Altération supergène, circulation des fluides et déformation interne du massif de Koniambo, Nouvelle-Calédonie : implication sur les gisements nickélifères latéritiques

Benoît Quesnel

ANNÉE 2015

THÈSE / UNIVERSITÉ DE RENNES 1
sous le sceau de l'Université Européenne de Bretagne

pour le grade de

DOCTEUR DE L'UNIVERSITÉ DE RENNES 1

Mention : Sciences de la Terre

Ecole doctorale Sciences de la Matière

présentée par

Benoît Quesnel

Préparée à l'unité de recherche Géosciences Rennes
OSUR (Observatoire des Sciences de l'Univers) – UMR 6118
UFR Sciences et Propriétés de la Matière

Altération supergène, circulation des fluides et déformation interne du massif de Koniambo, Nouvelle-Calédonie : Implication sur les gisements nickélifères latéritiques

Thèse soutenue à Rennes
le 11 décembre 2015
devant le jury composé de :

Alain Chauvet
Directeur de recherche, Université Montpellier 2 / *rapporteur*

Christophe Lecuyer
Professeur, Université Claude Bernard Lyon / *rapporteur*

Dominique Cluzel
Professeur, Université de Nouvelle-Calédonie, Nouméa / *examinateur*

Yves Lagabrielle
Directeur de recherche, Université Rennes 1 / *examinateur*

Stéphane Schwartz
Maître de conférences, Université Joseph Fourier, Grenoble / *examinateur*

Philippe Yamato
Maître de conférences, Université de Rennes 1 / *examinateur*

Philippe Boulvais
Maître de conférences, Université Rennes 1 / *directeur de thèse*

Pierre Gautier
Maître de conférences, Université Rennes 1 / *co-directeur de thèse*

Remerciements

« Il va falloir penser à déposer votre thèse en ligne Monsieur Quesnel », ah oui c'est vrai...Trois mois post soutenance ça passe vite quand même. C'est un mal que je soupçonne d'être courant chez les thésards ayant thésés, le syndrome du Procrastinator.

Après avoir reculé l'échéance, sachant que je n'allais pas me contenter d'un laconique « Vous avez tous été formidable », je me décide enfin à m'y mettre, préparez-vous cela durera quatre pages et des bananes, en adobe caslon pro, taille 11, interligne 1.0, du dense quoi.

Commençons par le commencement.

Tout d'abord un énorme merci à vous Philippe et Pierre (Le Val)! Tout débuta en cette année 2008 où, recueilli avec d'autres Padawan sub-vierges de connaissances géologiques, nous partîmes découvrir les joies du terrain au Pic Saint Loup. J'ai très vite compris que la géologie...ça allait me plaire! S'en sont suivies des années rennaises et un départ pour Lyon (merci Manu !) qui se solda par un retour en M2 à Rennes (pardon Manu...). Et c'est plus particulièrement pour ça que je dois vous remercier ! M'avoir proposé ce stage en Nouvelle Calédonie a signé le début d'une très belle aventure qui m'a permis de m'épanouir et d'évoluer pendant 4 ans, quand même! Pour faire un 'digest' simple efficace 'on s'est bien marré et on a bien bossé', dans l'autre sens ça marche aussi, encore une histoire de poule et d'œuf ça. J'espère que l'on aura l'occasion de continuer par ci par là en collaborant sur d'autres projets !

Un grand merci à toute l'équipe de permanents de Rennes avec qui il est toujours facile et agréable d'échanger ! C'est sans aucun doute en bonne partie pour cela que les thésards sont (globalement) heureux à Rennes ! Merci à toi Christian pour tout le boulot que l'on a pu faire ensemble et qui plus est dans une période pas forcément facile, la fin de thèse ! J'en profite également pour te remercier de ce compliment qu'un jour tu m'avais fait ' l'humour de Benoit frise toujours le bon gout, mais sans jamais l'atteindre'. Je te le retourne avec plaisir !

J'en viens maintenant au troisième directeur officieux de cette thèse, Michel! Merci à toi d'avoir été là et, de la même manière que Pierre et Philippe, d'avoir toujours rendu notre collaboration simple, efficace et chaleureuse ! Et cerise sur le gâteau, on va maintenant pouvoir continuer ensemble pendant deux ans!

Puisque l'on parle de Nancy ici, j'en profite pour remercier tous les nancéiens (Glin Glin, Christophe, Roland, Cédric, Matthieu, Antonin, Merca, PA ...) pour leur super accueil à chacune de mes visites! Attention j'arrive bientôt chez vous pour de bon !

Un très grand merci à Cédric et aux deux Pierre (le père noël a encore été généreux avec moi cette année Pierre, j'espère que ça continuera !) pour m'avoir respectivement accueilli à Londres et à Paris pour enfin savoir ce que les ZZ top avaient bien à me raconter. Ce fut un plaisir à chaque fois et j'espère pouvoir revenir dans un avenir proche travailler avec vous ! Et bien sûr merci à Simon (Saïmone with my nice and/or unbelievable French accent), John, Amelia, Thomas, Malorie, Nelly, Gérard, Amandine...

Un énorme merci à toi Clément, pour ton statut indéniable de guide d'exception en Nouvelle Calédonie! Tout ce terrain officiel sur le massif et officieux chez toi où ailleurs en Kanaky ont rendu mes séjours exceptionnels! Votre accueil à toi et Cindy je ne l'oublierai pas (par contre j'ai oublié mon anniversaire de l'année 2013...) ! J'espère que tout roulera pour toi à Valencia et ailleurs dans le monde pour l'avenir !

Enfin, un très grand merci à KNS d'avoir financé cette thèse et surtout de nous avoir donné autant de moyen pour faire le terrain et plus généralement cette thèse dans d'excellentes conditions ! Ce confort réside, en dehors de l'aspect matériel, dans la liberté intellectuelle que vous nous avez donné tout du long de ce projet. Enfin, merci Thierry, Nick, Fred, Manu, Max, Fabion, Laurine, Pierre, Patrice et toute l'équipe pour votre super accueil au service géol!

Merci également à l'ensemble du Jury d'avoir accepté de juger ce travail. Merci à Alain Chauvet et Christophe Lécuyer pour leur lecture intégrale du manuscrit (c'est déjà un point important, vous serez peut être les seuls...) et de m'avoir fourni le luxe de rapports encourageant ce qui, je ne vous le cache pas, m'a permis d'aborder la soutenance un peu plus (epsilon) sereinement ! Merci également à Stéphane Schwartz de m'avoir cuisiné de manière stimulante sur toutes ces sombres histoires de fluides et de serpentine. Merci à Dominique Cluzel, qui malgré son absence, a également su me cuisiner. Merci à toi Yves d'avoir accepté d'être le président de ce jury et d'avoir su manier de main de maître toute cette soutenance! Enfin merci à toi Pipo pour...bon je vais te remercier plus loin en fait !

Le travail c'est bien, quand on le fait avec des personnes formidables c'est encore mieux. Mais bon, ne nous voilons pas la face, une thèse n'impactera pas trop le système nerveux du thésard si le thésard en question sait se déconnecter régulièrement et efficacement de ce travail ' brain consuming'. Et c'est ici qu'un secret fondamental réside. Il faut savoir bien s'entourer !

Cercle numéro 1, peut-être le plus important, LA FAMILIA ! Papounet et Mamounette (ce sera mon bout de phrase régressif) merci pour tout, je ne peux pas être plus clair ! De ma 'genèse' à mon 'envol' (oui je mets entre guillemet car si je suis honnête il reste tout de même un certain nombre de points sur lesquels mon autonomie laisse à désirer, je vous laisse choisir lesquels) le fait de vous avoir et de vous sentir toujours bienveillants, forcément, ça aide grandement à se sentir bien dans sa vie ! Par bienveillance j'entends notamment le fait de savoir conseiller avec sagacité votre progéniture dans ses

choix lorsque ceux-ci vous paraissent niais. On notera ce jour de l'année 2007 où j'ai pu m'entendre dire ' Mais mon pti bonhomme, tu sais qu'il faut passer le concours de la police pour faire criminologue ?'. L'effet de cette bombe fut sans appel, j'ai continué la géologie pendant 8 ans... Mam' je m'excuse néanmoins d'avoir un peu 'merdé' en choisissant mon sujet de thèse. En effet je n'étudie pas les diamants... Mais la garniérite, tu sais, c'est vert et c'est plutôt joli !

Par Familia j'entends bien évidemment les soeurettes ! Marge et Kakane (héhéhéhéhé, ne vous inquiétez pas, peu de personnes liront ce manuscrit) merci d'avoir été et d'être d'iiiiincroyables soeurs et de m'avoir permis de ne pas devenir un jeune homme trop stupide. Votre 'input' féminin dans mon éducation n'a très certainement pas pu me faire du mal :) !

Enfin, toujours dans ce grand cercle numéro 1 qu'est la Familia j'en profite pour tous vous remercier ! Mamie et Mamina pour votre rôle de grand-mère toujours, et ce sera le mot récurrent, bienveillantes ! Et bien sûr Annie, Philippe, Hubert, Babou, Gnougnou, Marraine, Jean-Jacques, FX, Catherine, Philippe, Agnès, Adriano el coriño, Cam la zine, JC, Soph, Léa-Gab, Max, Violaine, Simon, Laëtitia Roro merci à vous tous pour cette ambiance familiale hors pair !

Bon à présent...cercle numéro 2...les coupaings...

Que vous veniez de ma contrée originelle normande, de celle d'adoption bretonne ou encore de bien plus loin, l'une des réussites de mes années rennaises aura été de pouvoir profiter et compter sur vous tous !

Alors il y a bien entendu les Normands (parfois)-Rennais, Zyg (ou Stéph' la nuit), Jeannette, Tranbert, Tibo, Clemtoch, Chonchon, Tordon, José, Fredo Mercure, Jamy (Jamass parfois), Zelax, Sarah (tatouille), Patrick Swayse (je te mets ici, tu es presque une normande, c'est un fait) Tomus, Fonstel, No', Redal, Philblard, Miré, Beubeu, Benj et tant d'autres avec qui nous avons pu écumer à peu près tout ce qu'il y avait à faire à Rennes. Jazz, Thermique et Camembert, voilà trois mots qui me viennent à l'esprit même s'il pourrait y avoir une infinité de combinaisons possible ! Le plus important ici est de constater que depuis le lycée ou même bien avant, on évolue ensemble et on ne se lasse pas !

Les Bretons, plus précisément, ceux avec qui un simple coup de marteau donné sur des sédiments merdeux a suffi pour nous lier jusqu'à aujourd'hui ! Pécile et Baptou (vous avez vu, on vous croirait mariés là! Mouhahahahahahaha. Amour et accordéons !), Agathe (Truck), Nono (c'était quand même beau chez nous !), Crabik (battles viriles d'expresso et 'délicates' ballades lyonnaises en vélo, tout est résumé ici !), Maxou (El Bombero), Maxfrein (Shine On You Crazy Diamond au milieu du lagon, what else ?), Halal Crétin (commentateur de courses de tracteurs imaginaires et punk de salon) et Froux (' Hééééééééé ', on notera tes qualités 'd'inondateur de lieux non inondables' et 'd'embobineur' de maréchaussée). Bon même si tu n'as jamais brisé de la roche à main nue comme nous, Bonzoine, je me dois de te dire un ' ALARMA-AMENO ' ému à cet endroit précis !

Bien sûr, il y a eu la Nouvelle-Calédonie ! Un énorme merci à vous Matt', Bérengère, Olive, Augustin, Solène, Camille, Carine, Johann et Etienne ! Grâce à vous les missions ont tout de suite pris une tournure savoureuse faite de lagon et de ti'punch ! Je remercie également Constance pour sa chaleureuse hospitalité !

Nous y voilà... la fin de ces remerciements approche. Grosso modo 4 ans à trainer mes guêtres à Géosciences et plus globalement l'OSUR...Ca en fait des copains à remercier...Car oui, ce qu'il faut savoir c'est que l'on est tous copains à Géosciences, une sorte de petite communauté sub-utopique ! Je vais donc commencer par Blore tiens ! Un mélange étonnant entre une barbie et un punk... Comment une si petite chose peut être aussi bruyante ? Dieu seul le sait. Bref tout ça pour dire Blore que cette dernière année n'aurait pas été aussi marrante si nous n'avions pas décidé d'unir l'univers Géoscienteux et Ecobiesque ensemble ! Une réussite (i.e. on a fini nos histoires de thèse en trois ans, et on est docteur, what else bis) ! Il y a également les révolutionnaires. Et oui la Cheul et la Boche, le Django du 18ème et le malouin dur au cœur (trop) tendre! Vos combats galvanisent les foules lorsque l'on parle de société, malheureusement un peu moins lorsque l'on parle de Judo. Bref... Stéph, 30ans déjà, et pourtant... Excité comme un petit enfant lorsque l'on parle de sport, nous avons tous compris que ce n'était qu'un substitut pour toi. Fais-nous confiance, nous serons toujours là pour te ramener sur le jaune chemin... Dani(elo), le poète ibère ! Les ballades noctambules en vélo avec toi c'est toujours un plaisir. La Bab, ton art délicat de l'hospitalité et surtout de la gastronomie ' On est pas arrivé en haut de la chaine alimentaire pour bouffer de la salade merde ! ' restera à jamais gravé en moi ! La Deul, oui je le sais maintenant, le FCGB et le Cougna sont les mamelles de l'humanité ! Pipo...alalala, ça aura été cheval quand même ! J'ai peu de doutes sur le fait que l'on se revoit régulièrement entre ' ici et là-bas ' ! LMNOPK ! Redj...Redj Redj Redj... Que dire... Je pense qu'un ' Je suis très heureux d'avoir pu te voir devenir quelqu'un de bien! ' suffira. Diane Albert, j'espère que tu es maintenant fières des racines normandes de tes frères siciliens (oui je sais tu viens de petit taureau... Mais pour moi tu sais l'Italie, ce n'est qu'une botte). La Ol', je ne te remercie pas de m'avoir appris que chocolatine était un mot qui existait vraiment. Tu le sais, je trouve ça déplorable. Mais je te remercie pour ce petit accent du sud qui avouons le met quand même du soleil à Breizhland. Il y a bien sûr mes deux exceeeeptionnels colocs du bureau des frisés. Rustine ! Tu m'as tout de suite excellemment intégré alors que je n'étais qu'un minuscule (je ne suis toujours pas très grand je sais) M2. Ce fut une année idéale et malgré les années passant et la distance parfois augmentant, le reste perdure ! Totoff ! Si on ne vient pas de passer deux années formidable dans ce bureau 115/1 je me fais bonze (bien que ce soit au final assez tentant). Le Ballouard spirit (un mix entre amour des déguisements de caribous et estimations de R^2 abusives) restera! Bon Tartèse, j'espère que t'es fier de ce bureau quand même ! Je te remercie aussi pour toutes ces conversations scientifiques de haut vol que j'ai pu avoir avec toi... On sent que t'es devenu un badass depuis Londres ! Enfin, je ne peux décemment pas continuer ainsi, je me dois d'accélérer ces remerciements si je ne veux pas mettre plus de temps à les écrire que ma thèse...

Alors merci à tous, Jeannette, Sté', Marie Degerman (oui tu es la seule à avoir ton nom complet, c'est cadeau), Dédé, Cécile, Feña, La Sim', La Nohr', La Gauz', Duncan MacHarrault, La Croiss', La Chatt', La Schuit', Hud'jo, La Ponte (ou JPeg), La Oual, Gemmayonaise, Cholène, Chmarylou, Caro, Vicky, Anthony, Julien, Tristan, Benji, Feng, Anne-Morwenn, Tamara, Luca, Jean, Nanard, Nico, Fanchon (héhéhéhé), Sage, Polo, Justine, La Ross', Gloria, Pilou, Carlos, Louise, Antoine, Clément, Rebecca, Sarah Ben Mamaar (ha ba non toi aussi tu as le droit à ton nom complet), Alix, Edwige, Marie, Hélène, Charlotte, Luc, Lorine, Pedram, Nikol, Sen...

Pour conclure, et je pense que vous l'aurez compris (j'espère), un immenses merci à vous tous !

Un immense mea culpa à ceux dont j'aurai pu omettre le nom, mais vous savez, aujourd'hui les jeunes, avec internet et les smartphones ils n'ont plus de mémoire...C'est dramatique...

' Big bisous ' (Dolto et al, 1977)

Table des matières

Résumé

Le gisement nickélifère latéritique de Nouvelle-Calédonie, développé au toit de la Nappe des Péridotites, représente près de 20% des ressources mondiales en nickel. Afin de mieux comprendre la formation de ce gisement, notre étude, portant sur le massif de Koniambo, se singularise par la volonté de ne pas se focaliser uniquement sur la zone minéralisée. L'approche employée a combiné :

i) l'analyse de la déformation interne de l'ensemble du massif,
ii) la caractérisation isotopique de deux sous-produits supposés de l'altération supergène que sont les veines de quartz et les veines de magnésite,
iii) la modélisation 3D du gisement nickélifère, basée sur les données de plus de 6000 forages de subsurface et sur l'étude d'affleurements ponctuels au sein de la zone minéralisée.

L'évolution spatiale et temporelle de la déformation associée à la serpentinisation est décrite au travers des ~800 m d'épaisseur structurale du massif de Koniambo. La partie supérieure du massif, très fracturée, préserve la marque d'au moins deux événements précoces de déformation. Le premier est associé au réseau de failles à antigorite et le second au réseau de failles à serpentine polygonale. La semelle serpentineuse, épaisse de ~200 m, est constituée de brèches et mylonites et enregistre un cisaillement tangentiel diffus associé à la serpentine polygonale et à la magnésite. La semelle représente ainsi un niveau de décollement majeur en base de nappe. Entre la semelle et le haut du massif, un niveau intermédiaire est identifié, caractérisé par la présence de zones de cisaillement plurimétriques probablement connectées à la semelle.

La caractérisation 3D de la distribution du nickel au sein du niveau saprolitique, à l'échelle du gisement comme à l'échelle de l'affleurement, permet de mettre en évidence l'existence de processus impliquant une redistribution non pas seulement verticale, comme il est classiquement admis, mais aussi latérale, mécanique ou associée à des fluides, à l'origine d'importants enrichissements locaux. L'analyse isotopique des veines de quartz associées au minerai garniéritique met en évidence les conditions d'hydrothermalisme de basse température associées à leur formation. La caractérisation structurale et isotopique (couplage « isotopes stables » et « clumped isotope thermometry ») des veines de magnésite situées dans la semelle serpentineuse permet de documenter leur caractère syn-tectonique et la nature météorique et de basse température du fluide dont elles sont issues. Ceci nous amène à proposer que la tectonique active a pu faciliter l'infiltration de l'eau météorique impliquée dans le processus de latérisation depuis le sommet jusqu'à la base de la nappe.

Abstract

The New Caledonia nickel laterite ore deposit, developed at the top of the Peridotite Nappe, hosts about 20% of the nickel resources worldwide. In order to better understand the formation of this deposit, our study, focusing on the Koniambo Massif, is not restricted to the ore zone but concerned with the whole peridotite pile. Our approach combined:

i) the analysis of the internal deformation of the massif,
ii) the isotopic characterization of quartz and magnesite veins which are suspected to represent by-products of the laterization process,
iii) the 3D modelling of the laterite nickel ore deposit, based on a dataset of ~6000 subsurface boreholes and the study of some outcrops located into the mineralized area.

The spatial and temporal evolution of the deformation associated with serpentinization is described across the ~800 m-thick rock pile of the Koniambo Massif. The upper part of the massif is densely faulted and preserves the record of two early deformation events. The first one is associated with syn-antigorite faults and the second one with syn-polygonal serpentine faults. The ~200m-thick serpentine sole is composed of breccias and mylonites and records pervasive tangential shearing associated with polygonal serpentine and magnesite. Thus, the serpentine sole represents a major décollement at the base of the nappe. Between the sole and the upper part of the massif, an intermediate structural level is identified, characterized by the presence of plurimetric shear zones that probably merge with the sole.

The 3D characterization of the nickel distribution in the saprolite level, at both deposit and outcrop scales, gives evidence for processes implying not only vertical (as commonly assumed) but also lateral nickel redistribution. This lateral transport is mechanical or associated with fluids and leads to significant local enrichments. The isotopic characterization of the quartz veins associated with garnieritic ore shows that they formed under low temperature hydrothermal conditions. The structural and isotopic (coupling “stable isotope” and “clumped isotope thermometry”) characterization of the magnesite veins located at the serpentine sole shows that they are syn-tectonic and derived from low temperature meteoric water. As a result, we propose that active tectonics has enhanced the infiltration of the meteoric waters involved in the laterization process down to the base of the nappe.

Introduction générale

1. Les gisements nickélifères

Le nickel est un métal omniprésent dans notre société cela étant principalement dû à son utilisation dans la fabrication d'acier inoxydable. L'ensemble du nickel contenu dans les gisements nickélifères continentaux, dont la teneur moyenne en nickel est au minimum de 1 %, est estimé à au moins 130 millions de tonnes (U.S. Geological Survey, 2015). Sur ces 130 millions de tonnes, 60 % sont contenus dans les gisements de type latéritiques et 40 % dans les gisements de type sulfurés (U.S. Geological Survey, 2015). Les gisements sulfurés sont génétiquement liés au magmatisme basique et ultrabasique et même si leur formation diffère dans le détail, ces gisements résultent néanmoins du processus général suivant (voir Jébrak et Marcoux, 2008, pour une revue des différents types de gisement):

i) génération d'un magma riche en nickel et souvent pauvre en soufre
ii) contamination en soufre du magma
iii) démixtion d'un liquide sulfuré et complexation du nickel
iv) accumulation des gouttelettes sulfurées par gravité
v) formation d'un gisement sulfuré

Figure 1 Localisation de certains des plus grands gisements nickélifères de type sulfurés. Modifié d'après Schulz et al. (2010).

La figure 1 présente la répartition mondiale des principaux gisements sulfurés nickélifères associés i) à des basaltes de plateaux (ex : Noril'sk-Talnakh), ii) à des complexe lités (Bushveld, Duluth), iii) à des komatiites (ex : Australie occidentale) et pour le seul cas du gisement de Sudbury iv) à un astrobleme.

La formation du second type de gisements nickélifères, les gisements dit latéritiques, est associée aux processus d'altération météorique. Au sens large, les gîtes de surface continentale sont des concentrations superficielles de substances utiles ou de minerais, résultant de l'altération sur place d'un protolithe, par action de l'eau météorique. Les latérites sont des roches ferrugineuses, pauvres en silice représentant le résultat de l'altération d'un protolithe soumis à des conditions climatiques tropicales. Dans le cas des gisements nickélifères latéritiques, les latérites se sont développées via l'altération d'un protolithe ultrabasique ou basique (par exemple péridotites, basalte, gabbro). Cette altération se caractérise par l'hydrolyse des différents silicates composant la roche ultrabasique. Il en résulte la mise en solution des éléments mobiles (i.e. Si, Mg, Ni) et le maintien du fer à l'état ferrique dans le profil d'altération sous forme d'oxy-hydroxydes de fer. Les éléments mobiles sont exportés plus bas dans le profil et le nickel recristallise sous forme de nouveaux minéraux dans une zone limitée formant ainsi le gisement nickélifère latéritique, Si et Mg étant exportés plus loin, plus bas. La figure 2 présente la distribution mondiale des principaux gisements nickélifères latéritiques dont la plupart sont localisés dans la zone tropicale humide.

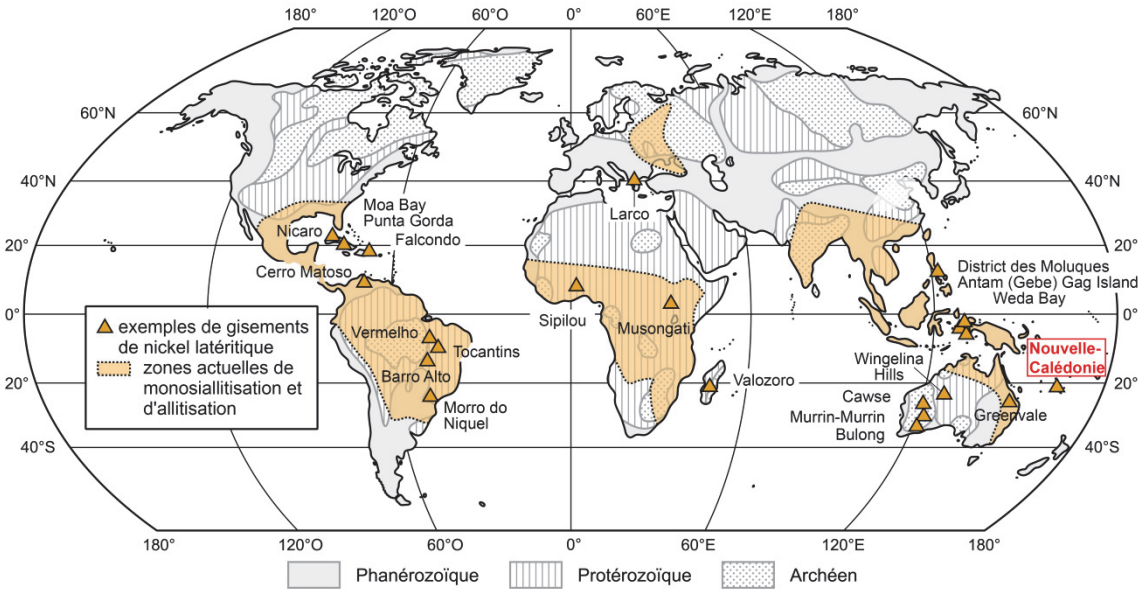

Figure 2 Localisation de certains des principaux gisements nickélifères latéritiques (Modifié d'après Jébrak et Marcoux, 2008)

Alors que les gisements latéritiques représentent près de 60% des ressources mondiales en nickel, du fait de la difficulté de leur exploitation (faibles teneurs, processus de traitement complexe), la production de nickel issue de ces gisements ne représentait que 40% de la production mondiale jusque dans les années 2000 (Butt and Cluzel, 2013). Du fait de la demande croissante en nickel, du développement de nouvelles méthodes de traitement et de la diminution de la disponibilité du nickel provenant des gisements sulfurés, la part de production de nickel associée aux gisements latéritiques ne cesse de croître depuis (Dalvi et al., 2004).

2. Le nickel en Nouvelle-Calédonie

Le gisement néo-calédonien (Fig. 2), reconnu pour sa richesse et exploité depuis la fin du 19ème siècle, représente aujourd'hui près de 20% des ressources mondiale en nickel. Si la Nouvelle-Calédonie représente historiquement l'un des principaux producteurs de nickel, l'augmentation du nombre de gisements exploités dans le monde fait qu'elle ne se place aujourd'hui au 6ème rang des producteurs mondiaux (Fig.3).

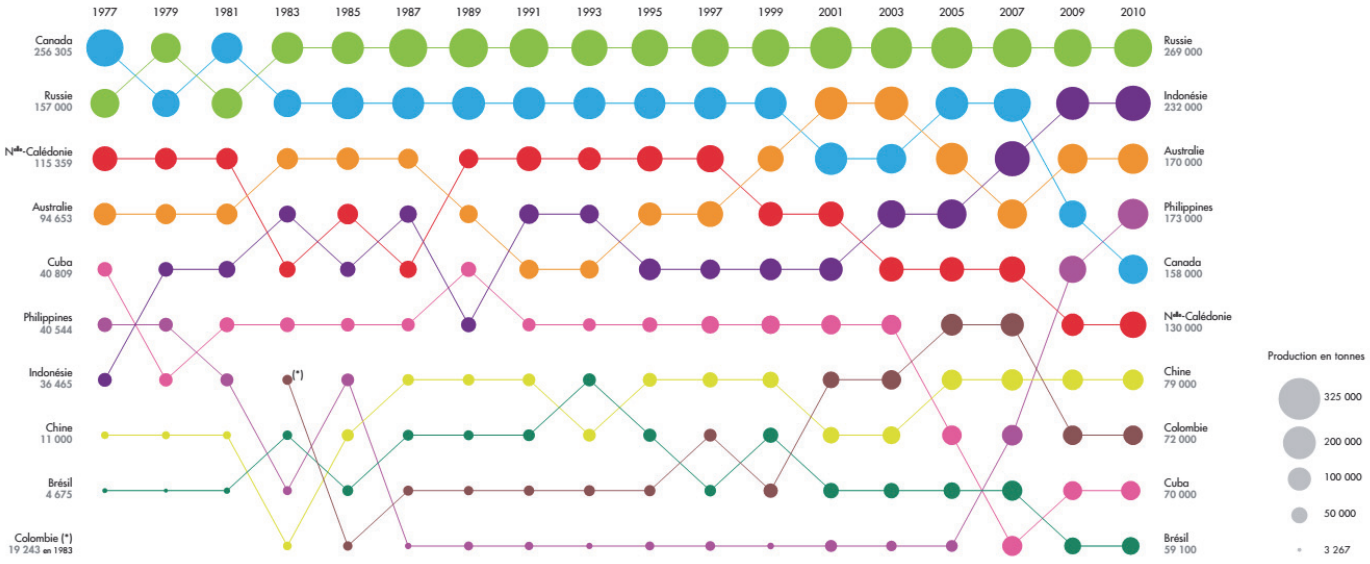

Figure 3 Classement des principaux pays producteurs de nickel. Extrait de Baille et al. (2013).

Depuis les accords de Matignon en 1988, favorisant l'entrée des indépendantiste Kanaks dans le monde minier, l'exploitation du nickel est devenue l'un des paramètres clé du rééquilibrage économique et social entre les trois provinces créées à cette époque en Nouvelle-Calédonie (Province Nord, province Sud, Province des îles Loyauté). La signature de ces accords a marqué le départ d'une

période de stabilité marquée notamment, sur le plan minier, par le début des redistributions entre les provinces des différents actifs miniers. L'accord de Nouméa, signé en 1998, continue sur cette voie i) en transférant la responsabilité des ressources minières aux provinces, ii) en créant une nouvelle instance décisionnelle, le Conseil des Mines, consultée obligatoirement pour toute question relative au nickel et iii) en prévoyant la mise en place d'un schéma de mise en valeur des richesses minières. En 2006, la création de la DIMENC (Direction de l'Industrie, des Mines et de l'Energie de la Nouvelle-Calédonie), composée de six services complémentaires (Energie, Mines et métallurgie, Industrie et Géologie), contribue, pour le compte de l'Etat et des différentes collectivités de Nouvelle-Calédonie, au développement durable de l'industrie minière néo-calédonienne. En 2008, la création du CNRT (Centre National de Recherche Technologique) Nickel et Environnement entre dans cette même dynamique d'exploitation durable du gisement nickélifère. Organisme financé à la fois par l'Etat, par les collectivités territoriales (Gouvernement de NC, Provinces Nord, Sud et des îles Loyauté) et par les industriels présents sur place (SLN, Société Le Nickel ; Vale Inco NC ; KNS, Koniambo Nickel SAS), le CNRT a pour objectif de financer la recherche selon trois axes complémentaires, « Nickel et technologie », « Nickel et Société », Nickel et environnement ».

En 2009, le congrès de Nouvelle-Calédonie adopte à l'unanimité le schéma de mise en valeur des richesses minières constituant la création d'une loi réformant le code minier vieux de 50 ans et créant l'établissement d'un « Fonds Nickel » chargé :

i) de financer la réhabilitation environnementale progressive des zones dégradées par l'activité minière,
ii) de soutenir les communes et les entreprises du secteur minier en favorisant le maintien ou la reconversion des emplois en cas de crise et/ou de fermeture de centres miniers

Ce travail de thèse a été possible via l'engagement financier de l'entreprise Koniambo Nickel SAS exploitant actuellement le massif de Koniambo (situé au nord-ouest de l'île) sur lequel cette étude se focalise. Le « Projet Koniambo » résulte de la volonté, suite à l'envolée des cours du nickel depuis 2002, de favoriser le maintien des plus-values liées à l'activité minière en Nouvelle-Calédonie via l'installation de deux nouvelles unités métallurgiques chargées de la transformation du minerai (l'une dans la Province Nord à Koniambo et la seconde dans la Province Sud à Goro). Associée au groupe

Glencore, la SMSP (Société Minière Sud Pacifique), propriété des Kanaks depuis la signature des accords de Matignon, est propriétaire à 51% de ce projet.

3. Vers une meilleure compréhension des gisements nickélifères latéritiques

L'exploitation du nickel en Nouvelle-Calédonie est fondamentale pour la viabilité de son économie. De manière générale, la demande croissante en nickel à l'échelle mondiale implique d'améliorer notre compréhension des gisements nickélifères latéritiques connus pour être complexes notamment du fait de la forte variabilité des teneurs au sein d'un même gisement (Golightly, 1981). De nombreuses études portent sur la caractérisation de ces gisements et peuvent être classées en trois grandes catégories d'approches :

i) les travaux portant sur la caractérisation d'un gisement particulier, souvent basé sur l'étude d'un ou plusieurs profils-types étudiés à l'échelle d'un affleurement ou d'un forage (Nouvelle-Calédonie : Trescases, 1975 ; Colombie : Gleeson et al., 2004 ; Indonésie : Fu et al., 2014 ; Brésil : Colin et al., 1990 ; République Dominicaine : Gallardo et al., 2010; Australie : Zeissink, 1969 ; Elias et al., 1981 ; Balkans : Eliopoulos et al., 2012 ; Afrique de l'Ouest : Deblond et Tack, 1999 ; Nahon et al., 1982) ;

ii) les travaux synthétiques comparant les spécificités des différents gisements à l'échelle mondiale afin d'en déterminer les paramètres généraux de formation (Golightly, 1981 ; 2010 ; Gleeson et al., 2003 ; Freyssinet, 2005 ; Butt et Cluzel, 2013). De ces travaux ressort l'importance de facteurs tels que la chimie et la structure du protolithe, la géomorphologie et la topographie, la tectonique, les processus biogéniques et bien entendu le climat.

iii) La troisième catégorie d'études regroupe les travaux se focalisant directement sur les phases porteuses du nickel afin d'en définir les caractéristiques dans le but de comprendre leurs conditions de formation et les processus menant à l'intégration du nickel (Brindley et Hang, 1973; Manceau et Calas, 1985; Wells et al., 2009 ; Dublet et al., 2012 ; 2015 ; Galí et al., 2012; Villanova de Benavent, 2014).

L'ensemble de ces études ont pour point commun de se focaliser sur l'objet minéralisé afin d'en comprendre la formation, et ce, en étant souvent basé sur l'étude d'un ou plusieurs affleurements isolés. En Nouvelle-Calédonie, la dynamique actuelle est de comprendre le gisement nickélifère à grande échelle ce que reflètent les missions et les moyens mis à disposition du Service Géologique de la Nouvelle-Calédonie (SGNC), service dépendant de la DIMENC, et du CNRT. Cartographie de la distribution et de la pétrologie des formations superficielles (Convention « Régolite » avec le BRGM et programme « Typologie des latérites »), cartographie par télédétection hyperspectral aéroportée (projet CARTHA) ou encore cartographie géophysique (magnétisme, radiométrie aéroportée) du régolite (programme « Radiométrie ») sont autant de projets en cours témoignant de cette volonté de compréhension à grande échelle du gisement nickélifère néo-calédonien.

Notre étude s'inscrit dans cette dynamique « grande échelle » en ayant pour originalité de ne pas se focaliser uniquement sur le gisement lui-même. En effet, via

i) la modélisation 3D, basée sur plus de 6000 forages de subsurface, du gisement nickélifère de Koniambo et l'étude d'affleurements au sein de la zone minéralisée,
ii) la caractérisation isotopique de deux sous-produits supposés de l'altération supergène que sont les veines siliceuses et de magnésite distribués en partie hors de la zone minéralisée et
iii) l'analyse de la déformation interne de l'ensemble du massif de Koniambo,

nous proposons ici une étude permettant notamment d'établir les relations existant entre altération supergène, déformation et circulation des fluides à l'échelle de la Nappe des Péridotites.

4. Organisation du manuscrit de thèse

Ce manuscrit s'organise en trois parties constituées principalement d'articles scientifiques (publiés, soumis ou en cours de préparation) suivis de quelques développements. Les articles scientifiques sont précédés d'un résumé en français.

La **première partie** constitue un bref aperçu de la géologie de la Nouvelle Calédonie principalement focalisé sur la Nappe des Péridotites et son altération.

La **seconde partie** consiste en un descriptif de la stratégie et des outils adoptés dans cette étude afin de caractériser les interactions fluides-déformation. Le premier chapitre décrit les méthodes de caractérisation minéralogique utilisées afin d'établir sur le terrain un contrôle minéralogique associé à

l'analyse structurale. Le second chapitre décrit les principes de la méthode des dièdres droits utilisée pour effectuer une partie de l'analyse de la déformation. Enfin, le troisième chapitre décrit les principes des méthodes d'isotopie classique et de « clumped isotope thermometry » utilisées afin de caractériser les conditions de formation des occurrences de magnésites et des silices.

La **troisième partie** de cette thèse représente le corps de ce travail et s'organise en trois chapitres.

Le **premier chapitre** se focalise sur le niveau saprolitique, principal hôte du gisement nickélifère. La première partie de ce chapitre porte sur la caractérisation 3D à l'échelle du gisement, via le traitement de la base de données de forages, de la géométrie de la couverture latéritique et de la distribution du nickel dans le niveau saprolitique. Nous mettons ainsi en évidence l'existence de processus impliquant le transport mécanique latéral et le lessivage de matériel porteur de nickel à l'origine d'enrichissements locaux en nickel dans le niveau saprolitique. Ce travail fait l'objet d'un article en préparation en vue d'être soumis dans un volume spécial de la revue ***Mineralium Deposita*** s'intitulant « Ore forming processes in surfacial environments », volume spécial qui fait suite à une session dédiée au congrès SGA (The Society for Geology Applied to Mineral Deposits) à Nancy en août 2015.

La seconde partie de ce chapitre porte sur la description et la caractérisation d'un nouveau type de minerai, que nous appelons « target-like ore », résultant de la dispersion latérale du nickel initialement contenu dans le minerai garniéritique par des processus d'évapo-précipitation liés aux mouvements actuels à sub-actuels du niveau hydrostatique. Ce travail fait l'objet d'un article publié en 2015 dans la revue ***Mineralium Deposita***.

Le **second chapitre** porte sur la caractérisation isotopique et structurale des occurrences de veines de magnésite localisée à l'extrême base de la Nappe des Péridotites, à la semelle de serpentine. Nous mettons ainsi en évidence l'origine météorique et basse température de la magnésite confirmant ainsi son lien à la latérisation. Le caractère syn-déformation de sa formation nous amène à proposer un modèle dans lequel l'activité tectonique active facilite l'infiltration de l'eau météorique associée au processus de latérisation. Ce travail fait l'objet d'un article publié en 2013 dans la revue ***Geology***.

Le **troisième chapitre** se compose de deux parties portant sur la déformation et la circulation des fluides à l'échelle de la nappe. La première porte sur la caractérisation spatiale et temporelle de la déformation enregistrée au sein de l'ensemble du massif de Koniambo. Nous mettons ainsi en évidence l'enregistrement de plusieurs épisodes de déformation dont les structures associées à chacun d'eux sont réparties verticalement dans trois niveaux distincts au sein du massif. Nous proposons également que la localisation de la déformation à la base de la nappe, illustrée par l'existence d'une semelle de serpentine mylonitisée, résulte simplement de la juxtaposition de la nappe, faite de péridotites serpentinisées peu résistantes, sur le substrat composé de roches basiques plus résistantes. Ce travail fait l'objet d'un article soumis à ***Journal of Structural Geology***.

La seconde partie de ce chapitre porte principalement sur la caractérisation isotopique des différentes occurrences de silices. Nous mettons ainsi en évidence que les silices amorphes, localement associées à la magnésite, témoignent également de circulation de fluide de basse température à l'échelle de la nappe. A l'inverse, la composition isotopique des veines de quartz localisées au sein du niveau saprolitique, attestent d'une formation dans des conditions d'hydrothermalisme de basse température. Ce travail fait l'objet d'un article soumis à ***Geochimica et Cosmochimica Acta***.

Les conclusions générales, présentées au terme de ce manuscrit, synthétisent les différents points forts de cette étude et sont suivies d'une ouverture sur les différentes perspectives de travaux restant à réaliser. Quelques annexes sont proposées, dont un article dédié à l'étude microscopique de la formation de magnésite par réaction de dissolution de la serpentine (Ulrich et al., 2014).

Partie I

Contexte géologique de la Nouvelle-Calédonie

1. Généralités

Située dans le sud-ouest de l'océan Pacifique, la Nouvelle-Calédonie constitue un segment émergé de la ride de Norfolk localisée à environ 1300km à l'Est des côtes australiennes, à environ 1700km au sud-est de la Papouasie Nouvelle-Guinée et à environ 1500 km au nord de la Nouvelle Zélande (Fig.I.1).

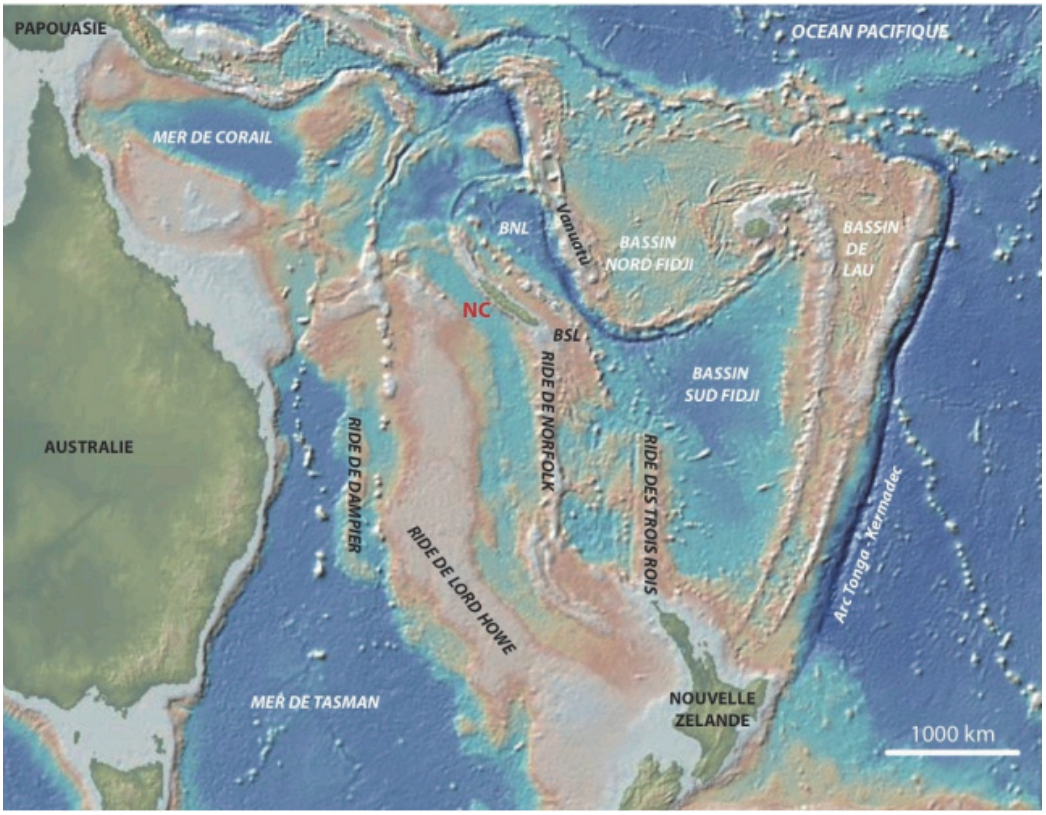

Figure I.1 Carte topographique du sud-ouest Pacifique (tirée du logiciel *GeomapApp*®) mettant en évidence les principales structures géologiques émergées et immergées. La Nouvelle-Calédonie (NC) constitue une partie du segment nord de la ride de Norfolk. BNL : Bassin Nord-Loyauté ; BSL : Basin Sud-Loyauté. D'après Ulrich (2010).

L'archipel néo-calédonien (Fig.I.2), d'une superficie de 18 575 km^2 est constitué d'une île principale, la Grande Terre (environ 400 km de long sur 50 km de large) et de divers îlots localisés dans sa périphérie. Les îles Loyauté (Ouvéa, Lifou, Tiga et Maré) sont localisées à environ 100 km au large de la côte est de la Grande Terre tandis que les îles Belep et l'île des Pins sont respectivement localisées à son extrémité nord et sud. La barrière corallienne ceinturant de manière continue la Grande Terre fait du lagon néo-calédonien le deuxième plus grand au monde après celui de l'Australie. Le relief de la Grande Terre est montagneux avec des points culminant à 1629 m (Mont Panié) et 1618 m (Mont Humboldt) pour les plus hauts d'entre eux. A l'est, le relief est particulièrement

montagneux avec de grands versants très abrupts disséqués par des rivières plongeant vers la mer. A l'ouest, le relief se caractérise par le développement de grandes plaines côtières occupant l'espace entre les massifs. Le vent dominant (alizé d'est sud-est) et le relief de la Grande Terre sont à l'origine de la variabilité climatique entre la côte ouest et la côte est. Les précipitations sont plus abondantes sur la côte est, permettant le développement d'une végétation luxuriante tandis que la côte ouest se caractérise par sa relative aridité.

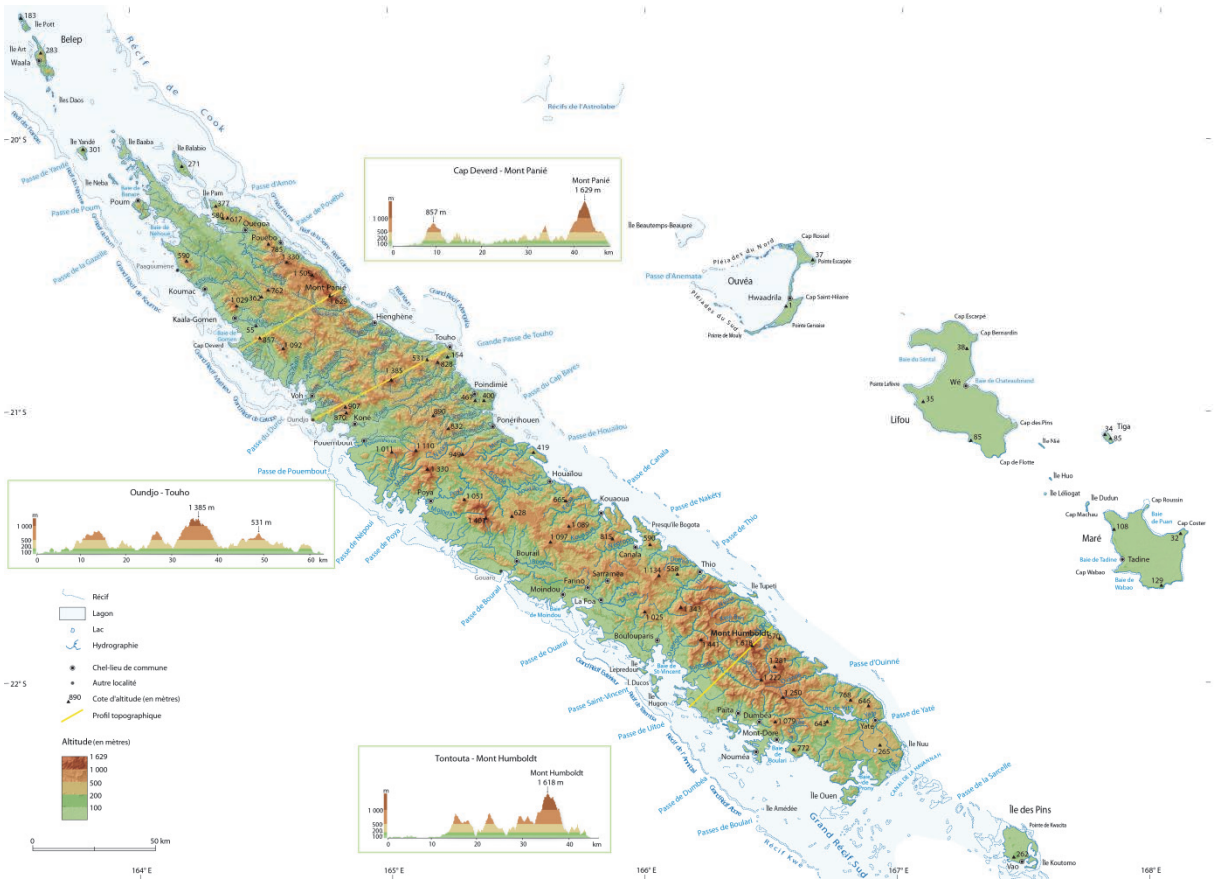

Figure I.2 Carte du relief de la Nouvelle-Calédonie mettant en évidence l'aspect montagneux et la dissymétrie générale de la Grande Terre. Carte modifiée d'après Bonvallot et al. (2013).

1. La Nappe des Péridotites

En Nouvelle-Calédonie, les péridotites sont abondantes à la surface de la Grande Terre (Fig.I.3). Elles affleurent sous la forme d'un grand « Massif du Sud » recouvrant le tiers sud-est de l'île ou sous forme d'une série de klippes alignées le long de la côte nord-ouest de l'île. La plupart des massifs de péridotites sont composés de harzburgites à l'exception des massifs du nord qui sont au moins en partie composés de lherzolites (Poum et Tiebaghi, e.g. Ulrich et al., 2010). La majeure partie du

volume péridotitique est extrêmement fracturé (Leguéré, 1976 ; Cluzel et Vigier, 2008) et présente un degré de serpentinisation variable mais modéré (Orloff, 1968).

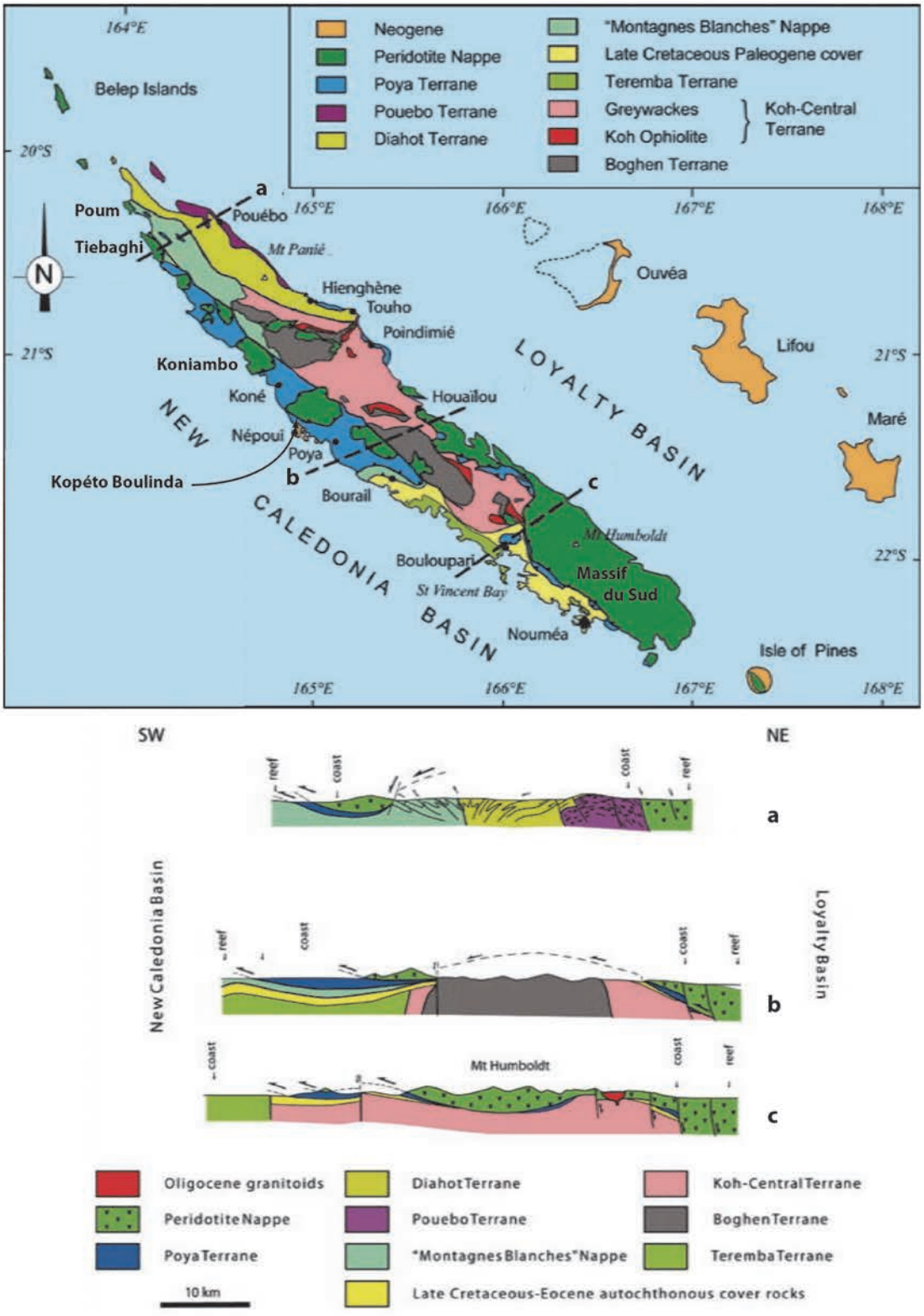

Figure I.3 Carte géologique de la Nouvelle-Calédonie (d'après Cluzel et al., 1999 ; Maurizot et Vendée-Leclerc, 2009). Carte modifiée d'après Cluzel et al. (2012).

La serpentine pure est localisée préférentiellement le long des discontinuitées structurales (fractures, failles et zones de cisaillements ; e.g., Leguéré, 1976 ; Lahondère et Maurizot, 2009 ; Lahondère et al., 2012). Seule l'extrême base des massifs péridotitiques présente un degré de serpentinisation élevé à total, formant une semelle de serpentine (e.g., Avias, 1967; Orloff, 1968; Guillon, 1975) atteignant une dizaine de mètres d'épaisseur dans le Massif du Sud et une centaine de mètres d'épaisseur dans les klippes du nord-ouest (Guillon, 1975 ; Maurizot et al., 2002). Dans les niveaux les plus hauts du Massif du Sud, les péridotites sont chapeautées par des niveaux de pyroxénites et de gabbros interprétés comme représentant la base d'une ancienne croûte océanique (Guillon, 1975 ; Prinzhofer et al., 1980; Paris, 1981). Localement, des rubans de dunites de 1 à 100 m d'épaisseur peuvent être observés dans la masse péridotitique représentant un litage compositionnel (e.g. Ulrich et al., 2010). L'ensemble des massifs de péridotites représentent les reliques d'une ophiolite aujourd'hui dépourvue de sa partie crustale (Avias, 1967 ; Prinzhofer, 1980 ; Paris, 1981) atteignant une épaisseur maximal de 1,5 km dans le Massif du Sud. Ces derniers reposent sub-horizontalement sur le substrat néo-calédonien selon un contact tectonique sub-horizontal (Fig.I.3, coupes a, b et c) marqué par l'intense déformation de la semelle de serpentine (Avias, 1967 ; Orloff, 1968 ; Guillon, 1975). Ils constituent les reliques d'une nappe ophiolitique aujourd'hui disséquée, la Nappe des Péridotites.

Le substrat néo-calédonien consiste en un assemblage complexe d'unités témoignant d'une histoire tectonique s'étalant du Permien à l'Eocène. Il est possible de distinguer deux groupes principaux, le premier correspondant à un ensemble Permien supérieur-Crétacé inférieur et le second Crétacé supérieur-Eocène. Les unités volcano-sédimentaires formant le premier groupe (Fig.I.3 ; unité de Boghen, unités de Koh et de la Chaîne Centrale et unité de Téremba) forment le socle néo-calédonien et ont été tectoniquement amalgamées lors d'un épisode tectonique attribuable à l'orogenèse Rangitata de Nouvelle-Zélande (e.g. Cluzel et al., 2001 et références associées). Les unités du second groupe (unité sédimentaire : couverture Crétacé supérieur-Eocène et Nappe des « Montagnes Blanches ; unités métamorphiques : unité de Pouébo et unité de Diahot ; la « formation des basaltes » de Paris, 1981 : unité de Poya) recouvrent le socle néo-calédonien et ont été formées puis accrêtées suite à l'ouverture de bassins marginaux à laquelle succéda la convergence Eocène entraînant la mise en place d'une subduction (Fig.I.4). L'arrivée de la ride de Norfolk dans la subduction entraina le blocage de cette dernière à environ 40 Ma (e.g. Cluzel et al., 2001; 2012). L'ophiolite de Nouvelle-Calédonie

représente dans ce modèle la lithosphère en position supra-subductive (Fig.I.4 ; Cluzel et al., 2001 ; Whattam et al., 2008).

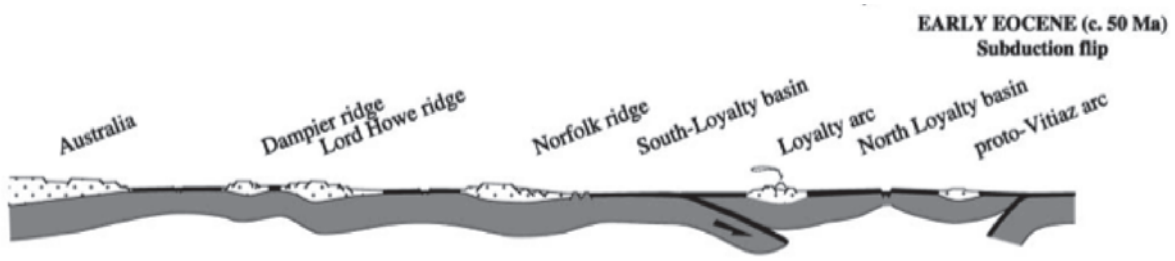

Figure I.4 Reconstitution géodynamique de la zone sud-ouest Pacifique à l'Eocène inférieur illustrant la phase de convergence qui mènera à l'obduction de la Nappe des Péridotites sur la ride de Norfolk à l'Eocène supérieur. D'après Cluzel et al. (2001).

Il existe un consensus sur le fait que la Nappe des Péridotites se soit mise en place du nord-est vers le sud-ouest (e.g. Avias, 1967 ; Guillon, 1975 ; Cluzel et al., 2012) sur le substrat néo-calédonien entre environ 35 Ma (âge des sédiments Priabonien supérieur chevauchés par la nappe près de Nouméa ; Cluzel et al., 2001) et 27 Ma (âge de l'intrusion de granodiorite de Saint-Louis recoupant le contact de base de la nappe dans le Massif du Sud ; Paquette et Cluzel, 2007). Cependant, le scénario menant à l'obduction de la Nappe des Péridotites est encore débattu dans la littérature (e.g. i) Cluzel et al., 2001; 2012 ; ii) Guillon et Routhier, 1971 ; Cluzel et al., 1995 ; Lagabrielle et al., 2013 ; iii) Spandler et al., 2005 ; iv) Baldwin et al., 2007). Nous reviendrons plus en détail sur chacun de ces scénarios dans le chapitre 3 de la partie III.

Enfin, un épisode post-obduction d'extension entraîna le développement de failles de détachement précoces à faible pendage recoupées par un ensemble de failles normales à fort pendage l'ensemble de ces structures ayant des orientations longitudinales à la Grande Terre (Lagabrielle et al., 2005 ; Lagabrielle et Chauvet, 2008). Le développement de ces structures serait responsables de l'amincissement de la Nappe des Péridotites et de l'actuelle morphologie en horst de l'île (Lagabrielle et al., 2005 ; Chardon et Chevillotte, 2006 ; Lagabrielle et Chauvet, 2008). Cette phase extensive pourrait être une conséquence du détachement en profondeur du panneau plongeant (Cluzel et al., 2005 ; Schellart et al., 2006 ; Lagabrielle et Chauvet, 2008).

2. L'altération supergène

2.1 Le profil d'altération type néo-calédonien

Les surfaces de latérites sont omniprésentes en Nouvelle-Calédonie et principalement localisées sur la partie sommitale des différents massifs de péridotites (Fig.I.5). Le développement de ces surfaces

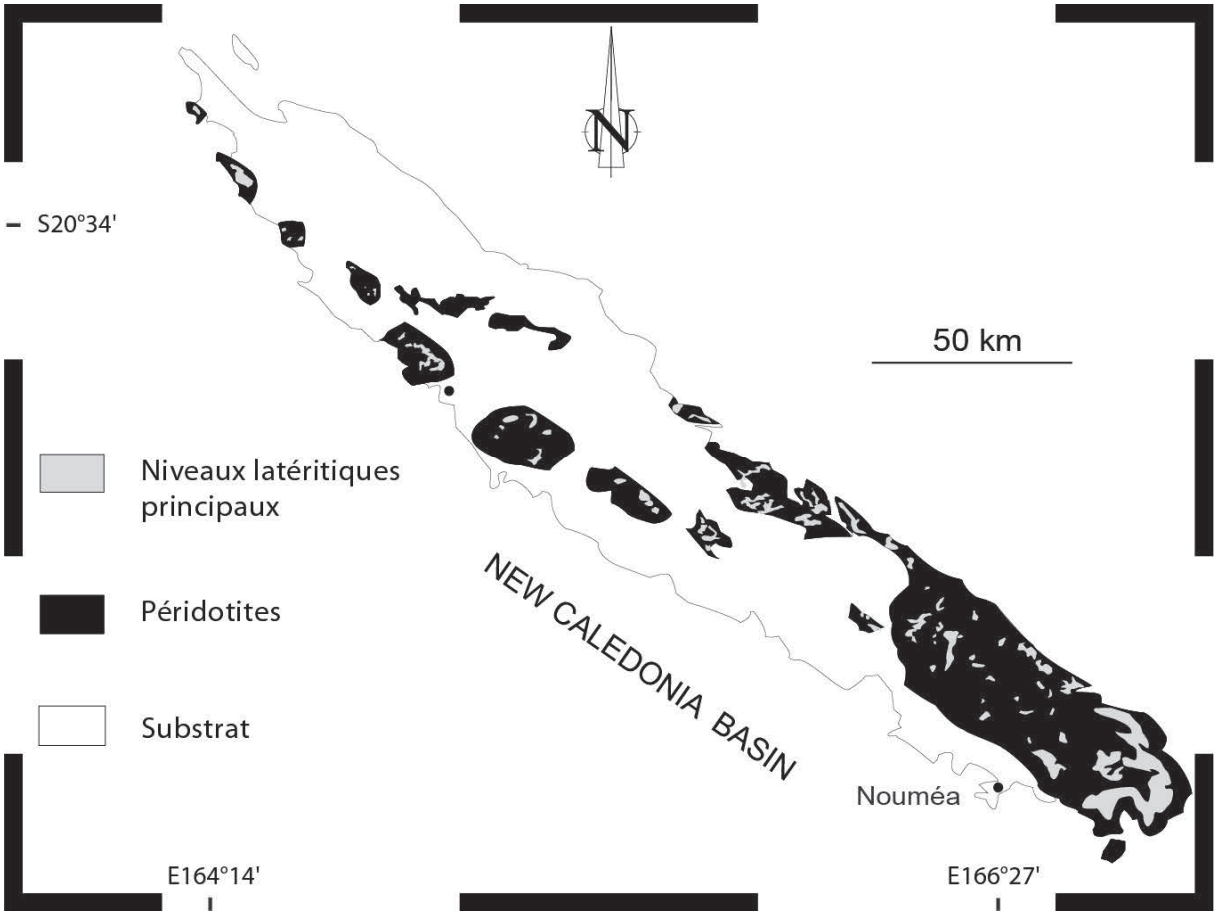

Figure I.5 Carte géologique simplifiée de la Nouvelle-Calédonie (D'après Cluzel et al., 2001). Les niveaux de latérites principaux sont représentés d'après Paris (1981).

résulte de l'altération des péridotites exhumées sous des conditions climatiques chaudes et humides. Cette altération se caractérise par l'hydrolyse des différents silicates ferromagnésiens (principalement l'olivine et les pyroxènes) composant les péridotites. Il en résulte la mise en solution des éléments mobiles (i.e. Si, Mg, Ni) et le maintien du fer à l'état ferrique dans le profil d'altération sous forme d'oxy-hydroxydes de fer (hématite et goethite) plus ou moins bien cristallisés. Le profil d'altération type de Nouvelle-Calédonie proposé par Trescases (1975) est présenté figure I.6 et comporte du sommet à la base :

- la cuirasse ferrugineuse d'aspect scoriacé, alvéolaire ou pisolitique composée de goethite et d'hématite.
- Un horizon de latérite rouge de granulométrie très hétérogène avec au sommet de l'horizon une prépondérance de la fraction grossière et à la base celle de la fraction fine. Une part importante de remaniement est identifiée dans la partie supérieure de l'horizon alors que la partie basse est in situ. La structure initiale de la roche mère est totalement effacée. Cet horizon est principalement constitué de goethite. Il atteint généralement de 1 à plusieurs mètres d'épaisseur.

- L'horizon de latérite jaune (ou saprolite fine), atteint généralement une épaisseur allant de 10 à 30 m. Ce niveau a une granulométrie très fine et est principalement composé de goethite partiellement cristallisée. La structure initiale de la roche est reconnaissable.

- La saprolite grossière est un horizon à fragments de roche peu altérée (saprolite rocheuse) emballés dans une matrice de saprolite terreuse. Le contact de cet horizon avec les horizons sus-jacent et sous-jacent est extrêmement tourmenté dans le détail. A la base de ce niveau, le volume de matrice terreuse diminue et les nombreuses fractures affectant les blocs de roche peu altérée peuvent être remplies de garniérite et/ou de silice. La garniérite consiste en un assemblage de différents silicates nickélifères où le talc et la serpentine sont les phases dominantes (Brindley et Hang, 1973 ; Brindley et Maksimovic, 1974).

- La roche mère consiste en des péridotites très « diaclasées » (Trescases, 1975) affectées par un dense réseau de fractures (Leguéré, 1976) pouvant être à l'origine de l'approfondissement local du profil d'altération. La roche mère est préservée de l'altération supergène.

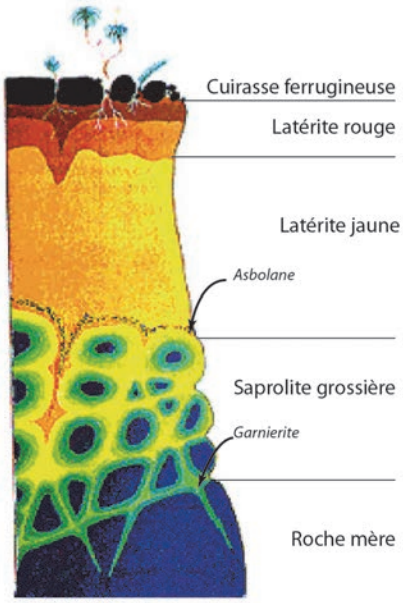

Figure I.6 Profil schématique de l'altération typique sur substrat péridotitique de Nouvelle-Calédonie. Modifié d'après Pelletier, 1989.

2.2 Distribution élémentaire dans le profil latéritique

Les éléments majeurs (Si, Mg, Fe) sont distribués de manière assez simple dans le profil latéritique (Tableau I.1). En effet, partant de la base du profil (i.e. la roche mère) jusqu'à son sommet (i.e. la cuirasse ferrugineuse), les teneurs en silice et magnésium décroissent de la roche mère jusqu'au sommet de la saprolite grossière où leur teneur devient brutalement très faible. Inversement, le fer augmente lentement de la roche mère jusqu'au sommet de la saprolite grossière où une augmentation brutale de sa teneur est notée. Ce comportement est cohérent avec la composition minéralogique des niveaux de latérite jaune, rouge et de la cuirasse ferrugineuse principalement composée d'oxyde de fer. Il en découle que le processus de latérisation génère le lessivage presque total de la silice et du magnésium. Cependant de forts enrichissements locaux en Si peuvent être observés, conséquence de la présence de veines de silice à la base du niveau de saprolite grossière.

	Profondeur	H_2O+	SiO_2	FeO	Fe_2O_3	Al_2O_3	CaO	MgO	Cr_2O_3	MnO_2	NiO	CoO
1	0-1,5 m	14,5	0,34	0,2	72,0	5,31	<0,10	<0,10	5,61	0,36	0,33	0,081
2	1,5-3,0	13,9	0,81	0,5	73,9	4,52	<0,10	1,0	3,05	0,46	0,52	0,060
3	3,0-4,5	13,6	0,50	0,8	74,2	4,60	<0,10	0,8	3,87	0,82	0,79	0,10
4	4,5-15,0	13,9	1,2	1,0	72,2	4,10	<0,10	0,9	4,12	1,00	0,85	0,16
5	15,0-19,5	13,8	3,0	1,2	64,8	5,50	<0,10	3,9	4,28	2,27	1,14	0,94
6	19,5-21,0	12,2	23,1	1,6	41,7	3,71	<0,10	11,0	3,68	0,69	1,05	0,08
7	21,0-22,0	13,1	34,2	3,5	18,7	1,41	0,11	24,2	1,40	0,27	1,11	0,025
8	>22 m	11,6	39,3	4,8	3,4	0,81	0,11	38,9	0,40	0,14	0,40	0,020

— non dosé
1. cuirasse
2. terres rouges
3. saprolite fine (sommet)
4. saprolite fine (milieu)
5. saprolite fine (base)
6. saprolite grossière (sommet)
7. saprolite grossière (base)
8. roche mère

Tableau I.1 Composition chimique moyenne des différents niveaux d'altération développés sur un substrat harzburgitique. Les valeurs sont exprimées en %. D'après Trescases (1975).

Les éléments mineurs (Cr, Al, Mn et Co) présentent une distribution plus ou moins complexe en fonction des éléments (Tableau I.1). Le chrome et l'aluminium se distribuent de manière assez simple augmentant de la roche mère jusqu'au sommet de la saprolite grossière où leur teneur augmente soudainement. Globalement les teneurs continueront d'augmenter parallèlement jusqu'au sommet du profil. Le chrome et l'aluminium peuvent donc être considérés comme des éléments immobiles.

De la même manière les teneurs en cobalt et manganèse évoluent parallèlement au sein du profil d'altération. Cependant leur distribution apparaît plus complexe car concentrés dans des niveaux variables du profil mais atteignant généralement de fortes teneurs à la base de l'horizon de saprolite fine. Cette augmentation est corrélée à la présence d'asbolane (Fig.I.6). La cuirasse ferrugineuse et l'horizon de latérite rouge sont systématiquement appauvris. Le cobalt et le manganèse n'ont donc pas de comportement clairement mobile ou immobile.

Le nickel a lui un comportement plus complexe. Au premier ordre, une décroissance simple des teneurs en Ni de la saprolite grossière à la cuirasse ferrugineuse est identifiée. Le nickel se concentre à la fois à la base du niveau de latérite jaune (incorporé préférentiellement dans la goethite partiellement cristallisée ; Dublet et al., 2015) et dans le niveau de saprolite grossière. Dans ce dernier, les teneurs en Ni sont extrêmement variables conséquence de l'aspect hétérogène de ce niveau. Le nickel peut à la fois être contenu dans la phase « terreuse », incorporé dans la goethite, mais également dans la garniérite remplissant de manière très erratique le réseau de fractures. Le nickel est donc considéré comme un élément peu mobile étant lessivé lors de l'altération supergène mais rapidement remobilisé.

Basé sur ces observations, un modèle *per descensum* (Fig.I.7) est proposé pour expliquer la formation du profil latéritique néo-calédonien (Trescases, 1975).

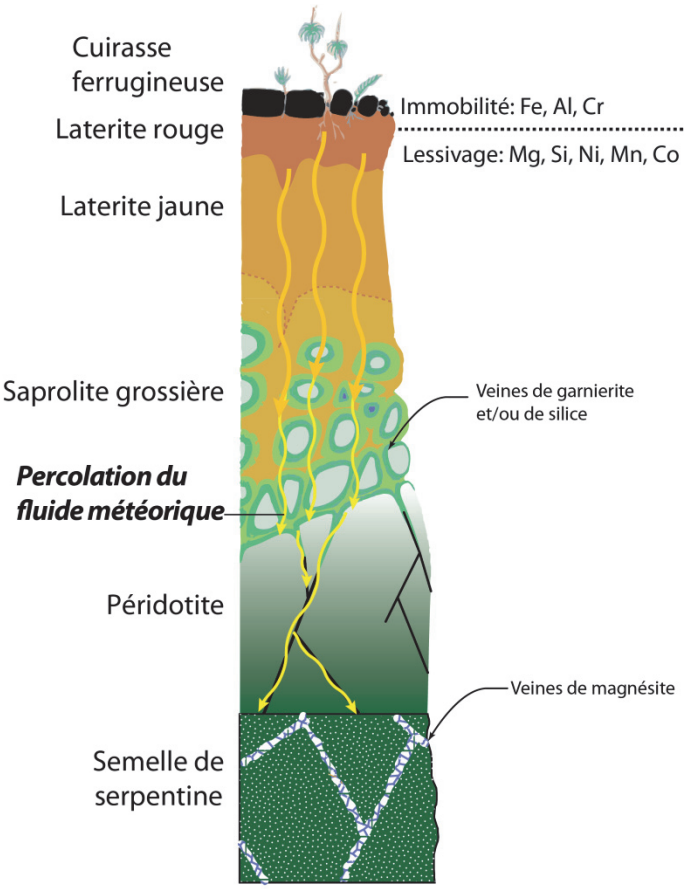

Figure I.7 Profil schématique de l'altération typique sur substrat péridotitique de Nouvelle-Calédonie (modifié d'après Pelletier, 1989) et son interprétation en terme de modèle de circulation de fluide *per descensum.*, modifié d'après Ulrich et al (2011).

La circulation d'eau météorique, favorisée notamment par le caractère extrêmement fracturé de la péridotite, a permis i) l'hydrolyse des différents constituants de la roche mère, ii) la mise en solution des éléments mobiles, iii) l'export de ces éléments dissouts et iv) leur réincorporation dans des phases néoformées. L'export de la silice et du nickel semble se faire sur une courte distance, le nickel lessivé se trouvant réincorporé dans la goethite et dans les veines de garniérite et la silice se trouvant réincorporée à la fois dans la garniérite, mais également sous forme de veines de silice au niveau saprolitique. Le fort contrôle structural de la minéralisation nickélifère est décrit dans la littérature (Leguéré, 1976) certains auteurs proposant que l'activité tectonique néogène ai i) facilité l'altération supergène via une meilleure circulation de l'eau météorique et ii) permis localement la redistribution du nickel dans le niveau saprolitique (Cluzel et Vigier, 2008). Le cas du magnésium est plus problématique. En effet compte tenu de l'intensité de son lessivage, les occurrences erratiques de garniérite ne suffisent pas à expliquer le devenir de l'ensemble du magnésium lessivé. A l'extrême base de la Nappe des Péridotites, au niveau de la semelle serpentineuse sous forme de veines, mais

également dans les sols sous forme de nodules, de nombreuses occurrences de magnésite ($MgCO_3$) sont identifiées. Il a très tôt été proposé (Glasser, 1904) que cette magnésite soit également un sous-produit de l'altération supergène.

2.3 Distribution spatiale et temporelle des surfaces latéritiques

L'existence de nombreuses surfaces d'aplanissement localisées à des altitudes variées a très tôt été décrite en Nouvelle-Calédonie (Davis, 1925). De trois à huit surfaces distinctes sont décrites dans la littérature (Trescases, 1975 ; Latham, 1977 ; Chevillotte et al., 2006 ; Chardon et Chevillotte, 2006). Les plus hautes sont exclusivement localisées sur les massifs de péridotites (Fig.I.8) les latérites y étant localisées. Sur la base d'argument géomorphologiques, Chardon et Chevillotte (2006) et Chevillotte et al. (2006) proposent que l'ensemble des surfaces d'aplanissement actuellement observé à une élévation supérieure à 200m (i.e. là où est localisée la grande majorité des latérites) soit pré-aquitanien. Des datations paléomagnétiques d'échantillons de cuirasse ferrugineuse chapeautant le profil latéritique du massif de Tiebaghi (Fig.I.3) ont permis d'estimer un âge compris entre ~10 Ma et ~55 Ma centré sur 25 Ma (Sevin et al., 2012). Sevin et al. (2014) ont récemment proposé que l'altération de la Nappe des Péridotites résulterait principalement d'une période de quiescence tectonique post-obduction et antérieure à l'uplift régional de l'île (~22 Ma). Dans la continuité de ce scénario, les auteurs proposent que l'alignement des surfaces latéritiques actuellement préservées sur les points hauts de certains massifs de péridotites témoigne de la formation d'une surface principale à cette période (voir également Latham, 1977 et Sevin et al., 2012). Les latérites localisées topographiquement plus bas et essentiellement composées de matériel latéritique remanié seraient donc plus jeunes que 22 Ma (la majeure partie de ces latérites sont considérées comme plus jeune que 20 Ma par Chevillotte et al., 2006).

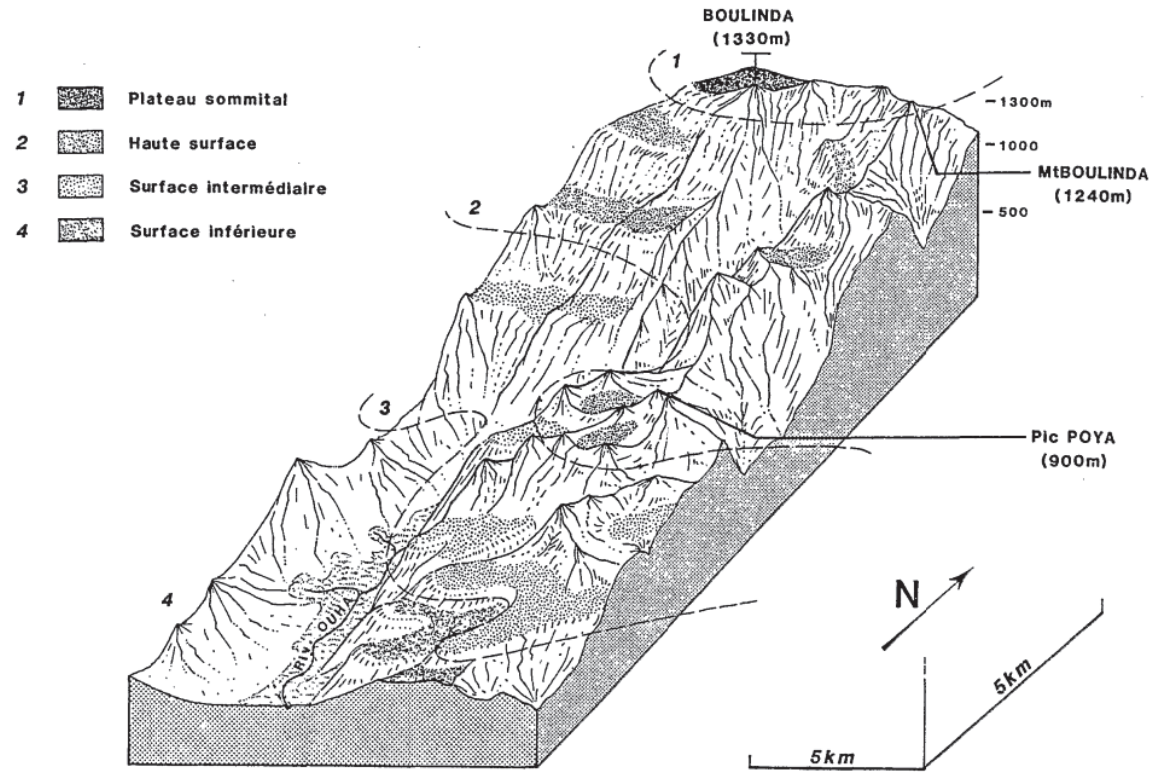

Figure I.8. Exemple d'étagement des surfaces d'aplanissement localisées sur le massif de Boulinda (Fig.I.3). D'après Latham (1986)

3. Le massif de Koniambo

Le massif de Koniambo (Fig.I.9) est l'une des klippes de péridotites localisée sur la côte nord-ouest de la Nouvelle-Calédonie (Fig.I.3). Ce massif culmine à environ 900 m et repose sur le substrat selon un contact sub-horizontal (Carroué, 1972 ; Maurizot et al., 2002). Principalement composé de harzburgites, des rubans de dunite de 1 à 100 m d'épaisseur témoignent d'un litage compositionnel. Le degré de serpentinisation croit du sommet à la base du massif pour atteindre un taux de serpentinisation presque total à la base. Ce niveau totalement serpentinisé forme la semelle de serpentine. La semelle de serpentine est connu pour être particulièrement épaisse (Guillon, 1975) atteignant près de 200 m. Au sein du massif, la serpentinisation est à la fois pervasive et localisée dans les nombreuses structures affectant le volume rocheux (Leguéré, 1976 ; Lahondère et Maurizot, 2009 ; Lahondère et al., 2012). Les surfaces latéritiques sont principalement localisées à des élévations supérieures à 400 m (mise à part le plateau Kaféaté localisé proche du niveau marin). Ces surfaces latéritiques sont fortement disséquées et localement remaniée. Selon Latham (1986) et Chevillotte

(2005) trois surfaces principales peuvent être identifiées. Les surface les plus hautes et les surfaces les plus basses sont respectivement interprétées comme étant les plus ancienne et les plus jeunes. L'ensemble de ces surfaces est localisé topographiquement plus bas que la surface de latérite principale proposée par Latham (1977), Sevin et al. (2012) et Sevin et al., (2014). Cela implique, suivant le raisonnement de Sevin et al. (2014) que l'ensemble des surfaces latéritiques aujourd'hui préservé sur le massif de Koniambo soit plus jeune que ~22 Ma. Suivant le raisonnement géomorphologique de Chevillotte et al. (2006), l'ensemble de ces surfaces devrait être plus jeune que 20 Ma.

Les latérites localisées sur la partie sommitale du massif sont actuellement exploitées par l'entreprise Koniambo Nickel SAS pour leur forte teneur en Nickel.

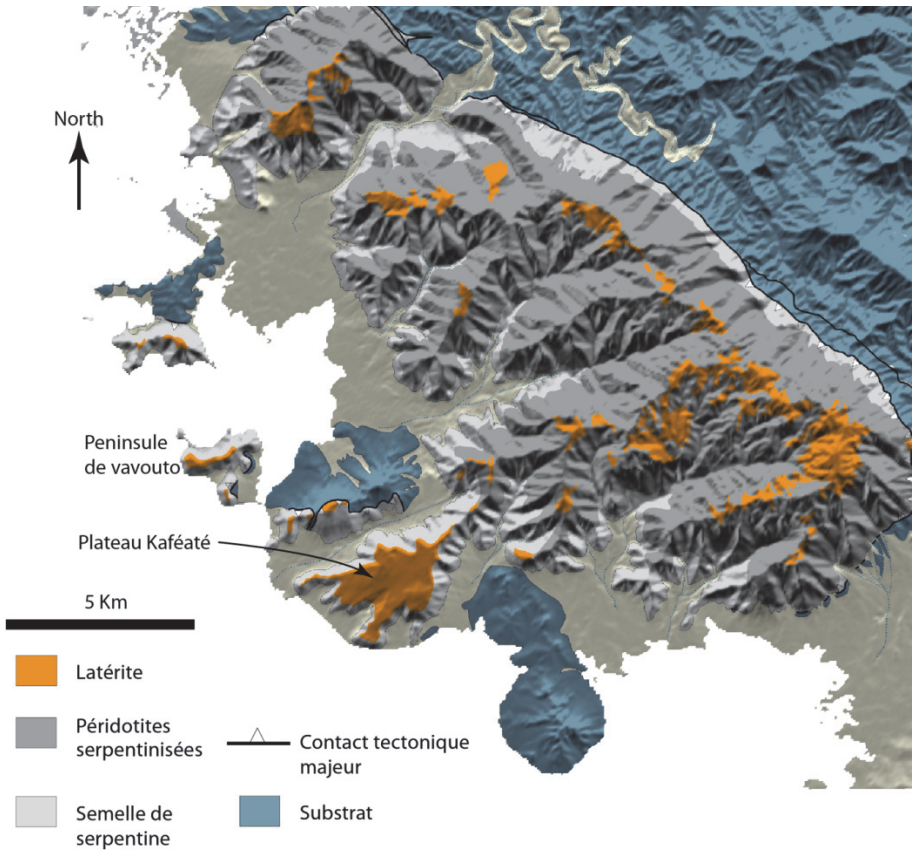

Figure I.9 Carte géologique du massif de Koniambo modifiée d'après Maurizot et al. (2002). La carte géologique est drapée sur un MNT (Modèle Numérique de Terrain) à 10 m.

Partie II

Outils et stratégie de caractérisation des relations fluides-déformation

Stratégie

La mise en place récente d'un site minier, par l'entreprise Koniambo Nickel SAS, sur le massif du Koniambo (Fig.I.3) a permis d'avoir accès à des affleurements d'une qualité exceptionnelle en termes de fraîcheur, de dimension et de distribution spatiale. Des affleurements localisés dans la partie sommitale (Fig.II.1a), dans les niveaux intermédiaires (Fig.II.1b) et à l'extrême base (Fig.II.1c) du massif nous ont permis d'avoir une vision continue de la géologie de la nappe des péridotites. Dans la dynamique de compréhension des relations existant entre la déformation, l'altération supergène à l'origine de la minéralisation nickélifère et la circulation des fluides, une approche pluridisciplinaire mêlant analyse structurale, caractérisation minéralogique, analyse isotopique et modélisation 3D a été menée.

L'analyse structurale de la nappe nous a permis de décrire les différentes structures ayant accommodé la déformation et, du fait de la continuité des affleurements étudiés, de discuter de la signification mécanique de leur distribution à l'échelle de la nappe. Ces structures sont associées à différents types de remplissage minéralogique (serpentine, magnésite, silice, garniérite) témoignant de paléo-circulations de fluides. Certains de ces remplissages (serpentines et magnésite) se sont avérés être d'excellents marqueurs de la déformation et ont permis de fournir des critères cinématiques robustes nécessaires à l'étude structurale. La reconnaissance sur le terrain de ces différentes minéralogies et la détermination de leur chronologie de formation nous a permis de discuter de la chronologie relative des structures et par extension, de l'évolution temporelle de la déformation au sein de la Nappe des Péridotites.

Afin de compléter cette approche géométrique, l'analyse isotopique de certains de ces remplissages a été utilisée comme outil de caractérisation physico-chimique (température et composition) des fluides ayant circulé au sein de la nappe et ayant permis leur formation. Cette étude s'est focalisée sur l'analyse isotopique de deux sous-produits supposés de l'altération supergène, la magnésite et la silice.

Enfin, l'intégration en 3D de données lithologiques et géochimiques provenant d'une base de données de plus de 6000 forages de sub-surface, répartis sur l'ensemble de la partie sommitale du massif de Koniambo, a permis de discuter à la fois de la géométrie des surfaces latéritiques et de la mobilité élémentaire résultant de l'altération supergène.

Dans la suite de cette partie, nous décrirons les outils utilisées afin d'effectuer les caractérisations minéralogiques, structurales et isotopiques. La description de la méthode d'intégration en 3D de l'ensemble des données de forage ne sera pas détaillée dans cette partie puisque faisant l'objet de l'article #1 présenté dans le chapitre 1 de la partie III.

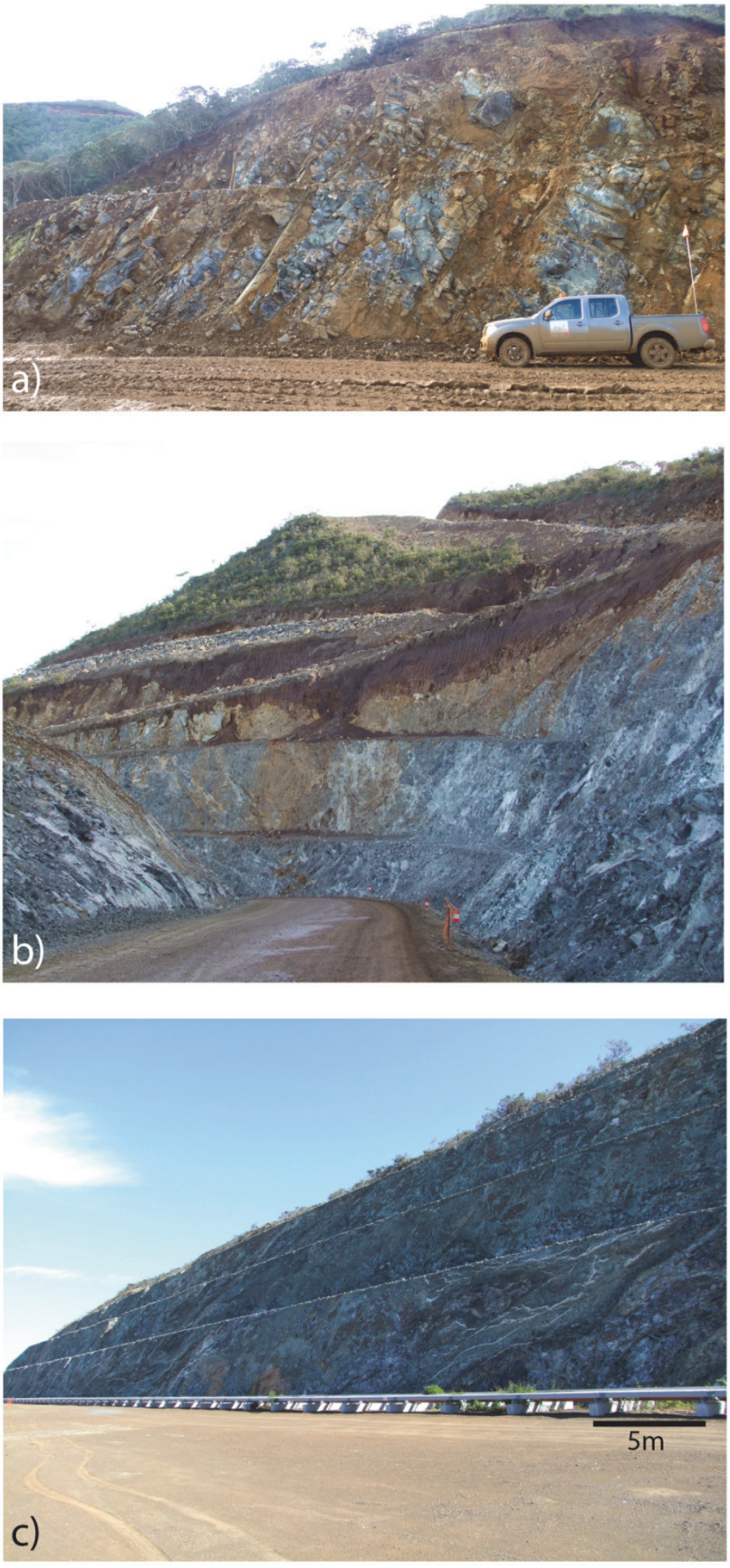

Figure II.1. Sélection de photos d'affleurements localisés à différents niveaux structuraux du massif de Koniambo. a) Exemple d'affleurement localisé le long de la route principale de la zone exploitée dans la partie sommitale du massif. Un grand nombre d'affleurements de qualité ont pu ainsi être étudiés à la fois le long des axes de circulations et au sein des zones exploitées. b) Exemple d'affleurement localisé dans le niveau intermédiaire du massif le long de la route d'accès à la mine. Cette route nous a permis d'avoir accès à des affleurements de manière quasi continue de la base au sommet du massif. c) Exemple d'affleurement visible sur l'une des deux coupes d'échelle kilométrique étudiée, localisée à la base du massif au niveau de la semelle de serpentine.

Chapitre 1

Caractérisation minéralogique

Sur le terrain, quatre types de remplissage peuvent être identifiés au sein des structures (serpentine, magnésite, silices et garniérite). Si pour la plupart d'entre eux, il est aisé de les distinguer macroscopiquement sur le terrain, la variabilité minéralogique intrinsèque des serpentines et des silices a nécessité d'utiliser la spectroscopie Raman afin d'en définir les différents polymorphes.

1. Principe de la spectrométrie Raman

Depuis sa découverte en 1928 (Raman et Krishnan, 1928), l'effet Raman et ses applications ont largement été détaillés dans la littérature (e.g. Smith et Dent, 2005). Le principe de la spectroscopie Raman consiste à déterminer les constituants chimiques d'un matériau en utilisant la réponse spécifique de ces derniers à l'interaction lumière-matière. Ces constituants vont être excités par une source électromagnétique, l'énergie ainsi transmise leur permettant d'osciller autour de leur position d'équilibre. Chaque constituant ayant une signature spécifique, il sera alors possible de les identifier. Lorsque appliqué à des polymorphes d'une même espèce minérale (et donc de même composition chimique) la spectroscopie RAMAN permet de mettre en exergue des variations structurelles du matériau. En effet, la réponse d'un matériau à l'interaction lumière-matière est également dépendante de la structure cristalline de ce dernier. Les polymorphes d'une même espèce minérale se distinguant par un agencement différent des atomes formant des structures cristallines distinctes, il sera alors possible de les différencier.

2. La magnésite

La magnésite se reconnait très facilement sur le terrain par sa couleur blanche et sa texture en chou-fleur (Fig.II.1.1a). Elle se trouve principalement sous forme de veines de puissance centimétrique à pluri-centimétrique localisées principalement au niveau de la semelle de serpentine (Fig.II.1.1b) ou sous forme de nodules pluri-centimétriques dispersés dans les sols (Fig.II.1.1c).

Figure II.1.1. Exemple d'occurrences de magnésite visibles sur le terrain. a) réseau de veines de magnésite localisé dans la semelle de serpentine du massif de Koniambo. b) Veine de magnésite localisée à la semelle de serpentine du massif de Koniambo présentant sa texture caractéristique en chou-fleur. c) Nodules de magnésite avec une texture en chou-fleur localisé dans un niveau de sol (massif de Koniambo).

3. La garniérite

Le terme garniérite désigne l'ensemble des phyllosilicates nickélifères historiquement exploités par les mineurs en Nouvelle-Calédonie depuis le 19ème siècle (Pelletier, 2003). Ces minéraux sont principalement des talcs nickélifères formant la solution solide kérolite-pimélite (Cathelineau et al., 2015b). Aisément reconnaissable sur le terrain, la garniérite se caractérise par sa couleur vert foncé à bleu turquoise, se présentant exclusivement sous forme de veines centimétriques (Fig.II.1.2a) à décimétriques (Fig.II.1.2b) localisées dans le niveau saprolitique du profil latéritique. La garniérite se localise à la fois dans les fractures majeures affectant la péridotite mais également au sein de fractures mineures définissant les limites de blocs décimétriques de péritotite.

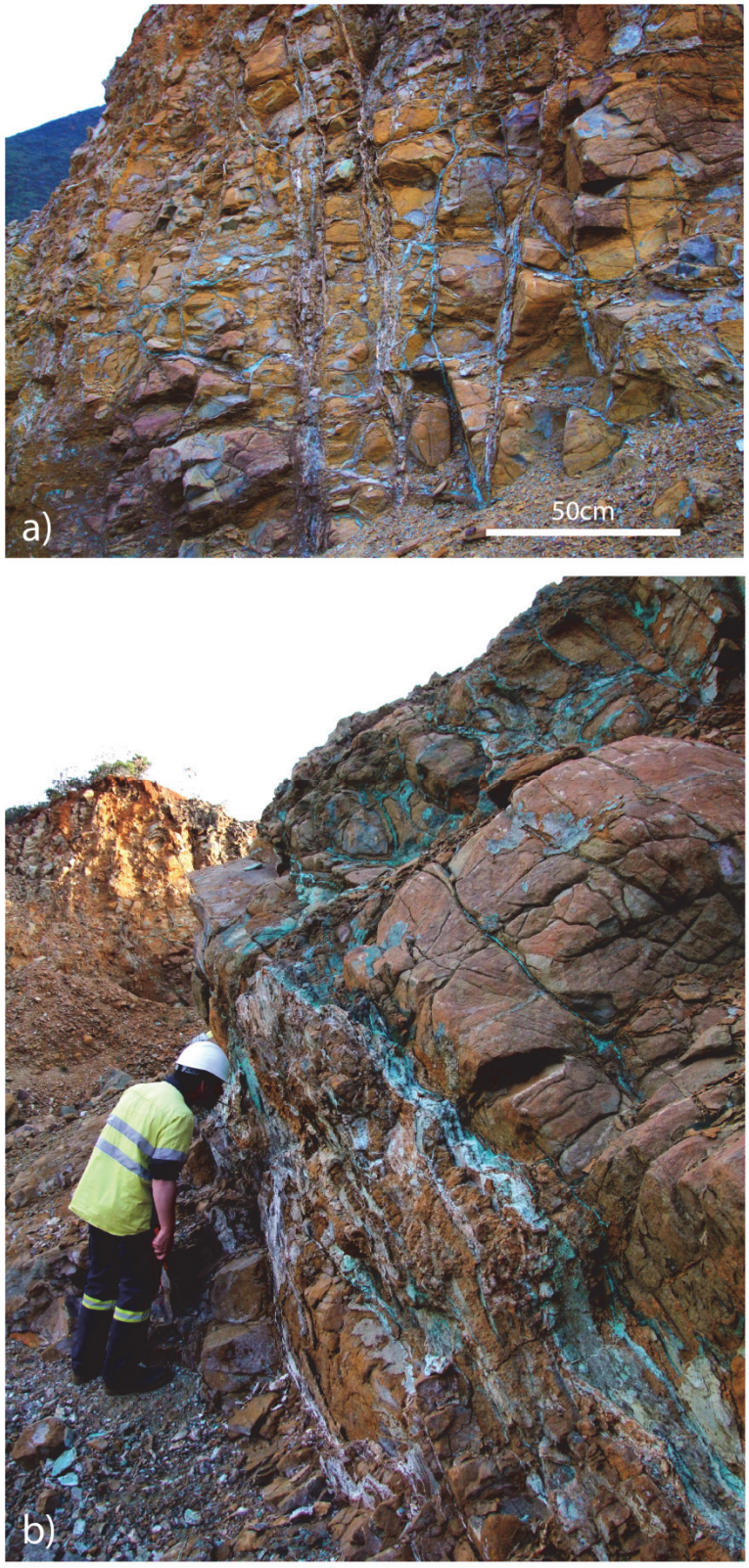

Figure II.1.2 Réseau de veines de garniérite particulièrement bien développé (massif de Koniambo).

4. Les polymorphes de la silice

Sur le terrain une grande variété de silice est rencontrée (Fig.II.1.3). Variables en termes de couleur et de texture, la caractérisation fine des différents types de silice ne sera pas l'objectif de ce travail. Néanmoins, l'analyse d'échantillons de référence nous permet de montrer que la grande majorité des silices observables sur le terrain présentent des spectres RAMAN caractéristiques du quartz (Annexe 1, voir Kingma et Hemley, 1994 pour les spectres de référence).

Figure II.1.3. Exemples de différents types d'occurrences de silice rencontrés sur le massif de Koniambo. a) Réseau de veines de quartz en arborescence. b) Macro-échantillon provenant de la veine présentée en a) mettant en évidence la coexistence de différents types de quartz au sein d'une même veine. c) veines massive de quartz recoupant une veine de garniérite. d) Remplissage d'une fracture par des films de quartz pluri-millimétriques associés à de la garniérite (en vert).

f,g) Silice amorphe translucide associée à de la magnésite. h) Silice amorphe brune nappant un bloc de péridotite serpentinisée.

Ces occurrences de quartz se présentent sous forme de veines mono-phasées ou pluri-phasées de largeur centimétrique à décimétrique (Fig.II.1.3a,b,c,d,e) localisées principalement dans le niveau saprolitique du profil latéritique.

Seul deux types de silice divergent clairement de cette tendance générale tant en terme d'occurrences que de nature minéralogique. Ces silices présentent des spectres RAMAN caractéristiques de silice amorphe (Annexe 1, voir Pop et al., 2004 pour les spectres de référence) et se présentent sous forme :

i) de silice translucide associée à la magnésite (Fig.II.1.3f,g) localisée au niveau de la semelle de serpentine et

ii) de silice brune nappant des blocs de péridotite serpentinisée (Fig.II.1.3h) localisée dans le niveau intermédiaire du massif.

5. Les polymorphes de la serpentine

Sur le terrain, des occurrences des quatre polymorphes de la serpentine (lizardite, antigorite, chrysotile et serpentine polygonale) peuvent être observées. Si la serpentine est omniprésente dans les massifs de péridotite de Nouvelle-Calédonie, cette étude ne s'intéressera qu'aux occurrences de serpentine localisées dans les structures étudiées. Basée sur les travaux antérieurs portant sur la caractérisation de la serpentinisation en Nouvelle-Calédonie (Lahondère et Maurizot, 2009 ; Lahondère, 2012 ; Ulrich, 2010), sur l'expérience de terrain des géologues miniers et sur notre propre expérience, l'identification macroscopique des trois polymorphes classiquement décrit en Nouvelle-Calédonie (lizardite, l'antigorite et le chrysotile) a été faite sans difficultés.

La lizardite se caractérise par une couleur noire et une texture homogène. Elle se présente à la fois de manière diffuse au sein de la péridotite sous forme d'un réseau à l'échelle granulaire, que sous forme de veines centimétriques à pluri-décimétriques (Fig.II.1.4.c). Elle est également souvent présente en bordure de faille, de zones de cisaillement ou de joints dans lesquels un type distinct de serpentine apparaît (Fig.II.1.4.a). Le chrysotile est principalement caractérisé par son habitus asbestiforme (Fig.II.1.4.b) et sa couleur blanche. Il se trouve la plupart du temps sous forme de micro-veinules

donnant un aspect zébré à la roche (Fig.II.1.4.a) et plus rarement sous forme de veines d'épaisseur décimétrique à pluri-décimétrique.

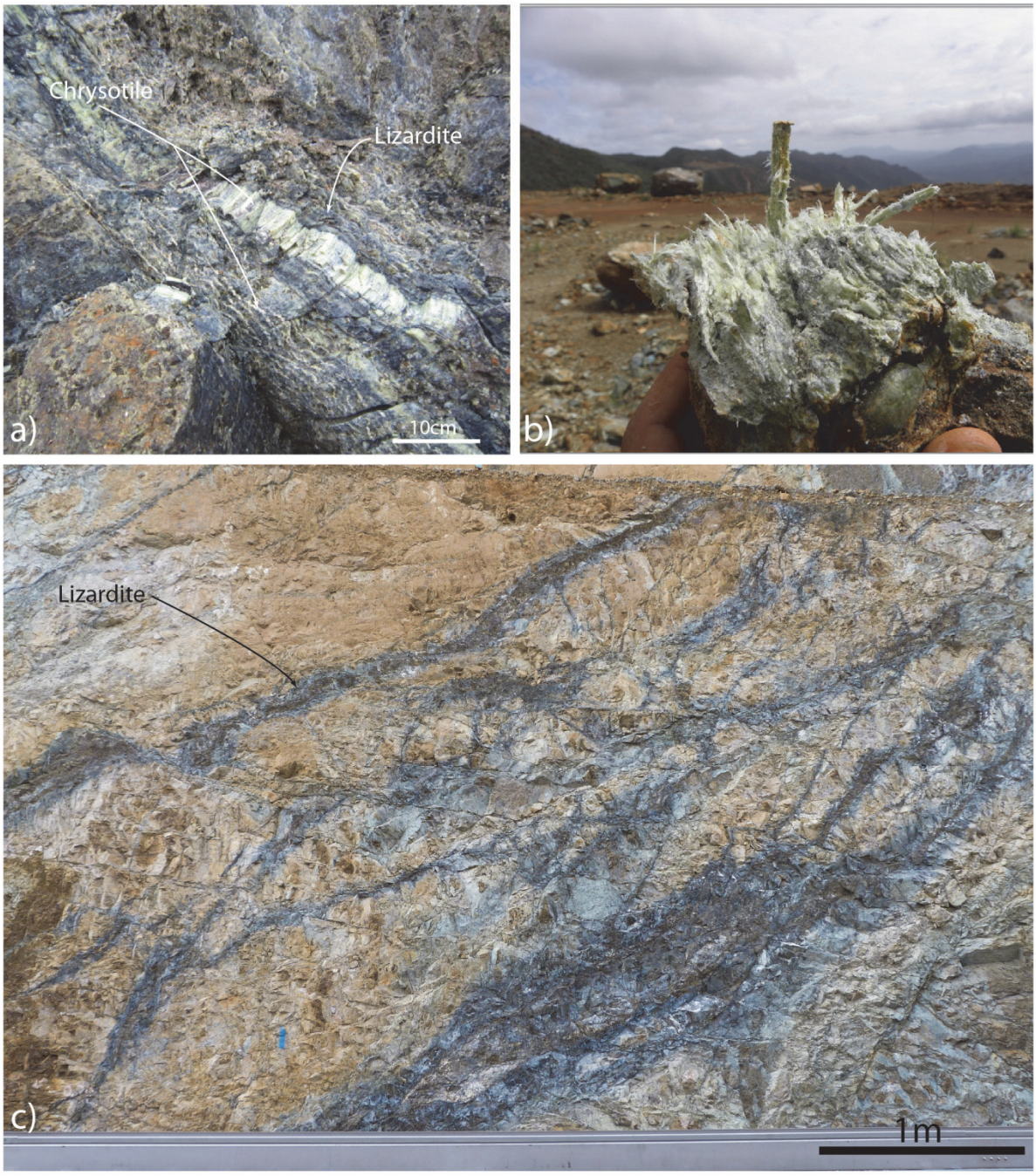

Figure II.1.4. a) Occurrences de veines de chrysotile millimétriques et décimétriques avec en bordure de veines la présence de lizardite (massif de Koniambo). b) Macro-échantillon de chrysotile montrant sa texture asbestiforme typique (grande veine de chrysotile de Trazy, massif de Koniambo, image extraite de Lahondère et al., 2012). c) Exemple de réseau de veines décimétriques à pluri-décimétrique de lizardite (semelle de serpentine, massif de Koniambo).

L'antigorite généralement de couleur vert sombre, lorsque non affectée par l'altération supergène, se reconnaît principalement sur le terrain par son aspect fibro-lamellaire (Fig.II.1.5) avec des fibres atteignant fréquemment plusieurs centimètres de long (Fig.II.1.5b). Les plus belles occurrences d'antigorite sont principalement localisées sur les miroirs de failles (Fig.II.1.5) ou sous forme de remplissage de zones de cisaillements.

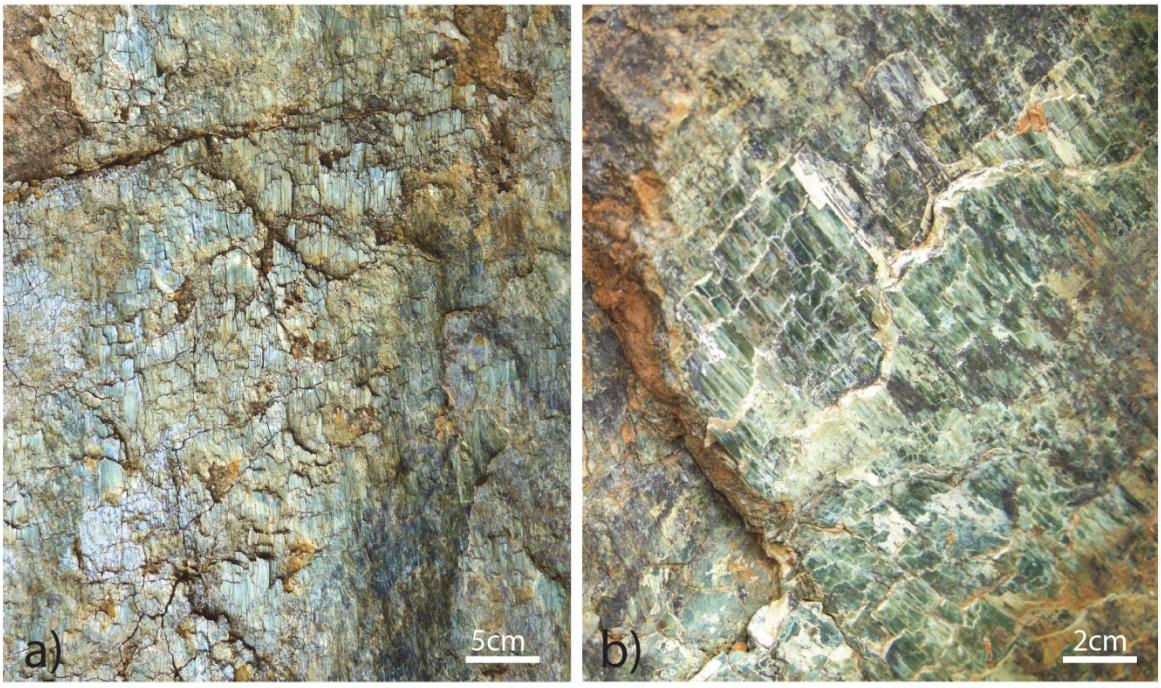

Figure II.1.5.a,b) Occurrences d'antigorite localisées sur des miroirs de failles (massif de Koniambo). L'antigorite présente une géométrie en marches d'escalier témoignant de sa cristallisation lors du jeu de la faille.

La serpentine polygonale, très peu décrite en Nouvelle-Calédonie (Ulrich, 2010) se caractérise par sa couleur mat vert clair et son aspect homogène (Fig.II.1.6). A l'instar de l'antigorite, les remplissages à serpentine polygonale présentent également des géométries en marches d'escalier lorsque localisés sur des miroirs de faille (Fig.II.1.6a,b). Néanmoins, la serpentine polygonale diffère de l'antigorite par le développement de fibres plus courtes (Fig.II.1.6a,b,d). On la retrouve également localisée au sein de zones de cisaillement ou sous forme de films recouvrant des blocs de péridotite (Fig.II.1.6c,d).

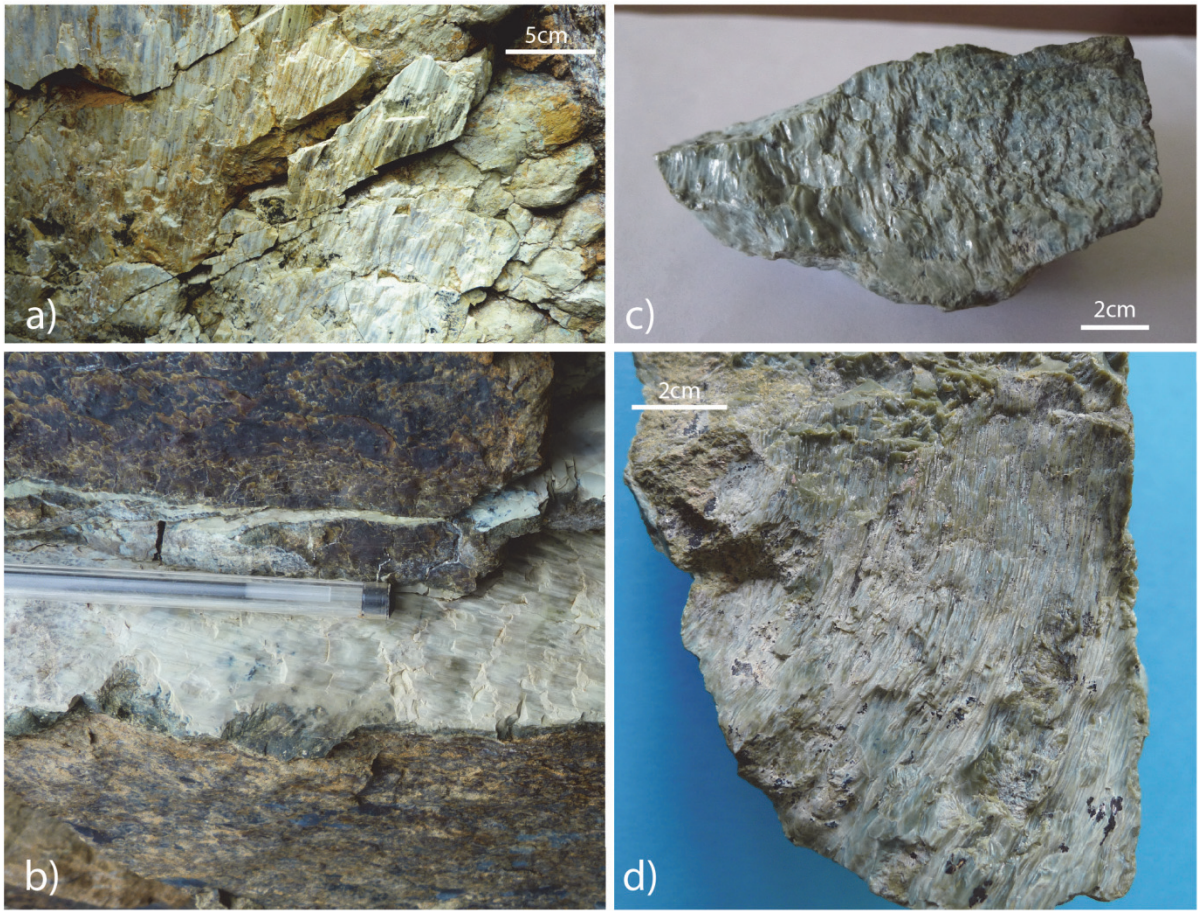

Figure II.1.6. a,b) Occurrences de serpentine polygonale en marches d'escalier localisée sur des miroirs de failles. c,d) Film de serpentine polygonale recouvrant un bloc de péridotite serpentinisée (semelle de serpentine du massif de Koniambo). La serpentine polygonale peut avoir un aspect homogène et strié (c) ou fibreux et présentant une géométrie en marches d'escalier.

Du fait du peu de descriptions macroscopiques disponibles dans la littérature, des analyses Raman ont été effectuées sur des échantillons considérés comme macroscopiquement représentatifs de la serpentine polygonale (cf partie III, chapitre 3 article #4). En effet, de nombreuses études (Lemaire, 2000 ; Auzende et al., 2004; Ulrich, 2010; Schwartz et al., 2013) ont montré que la spectrométrie Raman était particulièrement adaptée afin de différencier les différents polymorphes de la serpentine. Nos analyses se sont focalisées sur la partie du spectre correspondant aux liaisons hydroxyles (entre ~3500cm^{-1} et 3800 cm^{-1}) reconnues pour être les plus discriminantes (Fig.II.2.7).

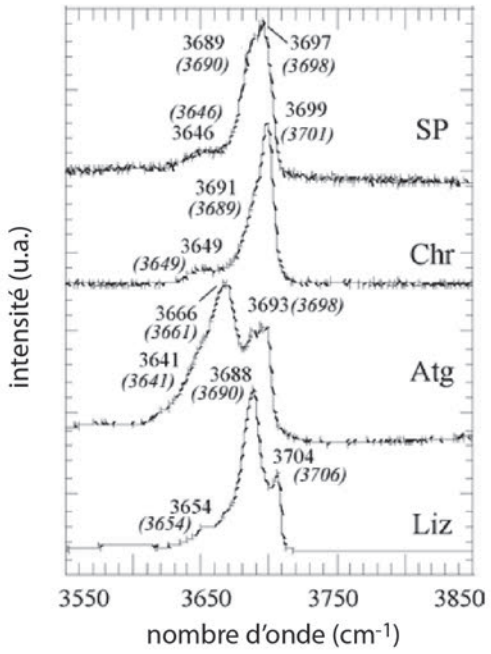

Figure II.1.7. Spectres Raman de référence pour les quatre variétés de serpentines (Lemaire, 2000). Les nombres en italiques sont montrés en guise de comparaison et sont issus de l'étude d'Auzende et al (2004). L'échelle des ordonnées est en unités arbitraires (u.a.). Liz : lizardite ; Atg : antigorite ; Chr : chrysotile ; SP : serpentine polygonale. Extrait de Ulrich (2010).

Chapitre 2

Analyse de la déformation

L'analyse de la déformation enregistrée au sein de la Nappe des péridotites s'est principalement focalisée sur la caractérisation de zones de cisaillement et de plans de failles. La cinématique des zones de cisaillement a été déterminée selon des critères classiquement utilisés tels que l'obliquité de la schistosité par rapport aux limites de la zone de cisaillement, la présence de bandes de cisaillement obliques à la zone de cisaillement principale et/ou le boudinage ou le plissement de niveaux plus compétents. La cinématique des failles a principalement été déterminée par l'analyse des fibres présentant une géométrie caractéristique de croissance en zone abritée puisqu'étant un critère robuste de détermination du sens de mouvement de la faille.

Dans cette étude nous considérerons que compte tenu de la dimension des zones de cisaillement étudiées, ces dernières témoignent d'une importante accommodation de la déformation et peuvent donc être considérées comme représentatives de la cinématique de la déformation à l'échelle de la zone d'étude. A l'inverse, l'abondance et la faible extension spatiale des failles étudiées témoignent d'une faible accommodation de la déformation sur chacune d'elle. Une stratégie de mesure systématique, couvrant la plus large zone possible, des failles présentant l'ensemble des critères nécessaires à l'analyse cinématique a donc été menée. La base de données ainsi récoltée a été traitée statistiquement afin de reconstituer, à l'échelle de la zone étudiée, la cinématique de déformation.

1. La fracturation des roches

La fracturation d'une roche résulte d'un état de déséquilibre atteint lorsque les contraintes appliquées à un volume de roche atteignent une valeur limite contrecarrant la cohésion interne de cette dernière et entraînant sa rupture. En 1776, Coulomb défini le « critère de rupture » basé sur le postulat que le glissement le long d'un plan quelconque localisé à l'intérieur d'un volume de matériau était entravé, à la fois par la cohésion (τ_0) mais également par le coefficient de friction (μ) interne de ce dernier. Lorsque les contraintes appliquées au matériau sont suffisantes pour en permettre la rupture (i.e sa perte de cohésion) et contrecarrer la friction interne, le glissement peut alors théoriquement se faire selon deux plans dit « conjugués » (Figure II.2.1a). Ces deux plans sont caractérisés par l'angle (θ) qu'ils forment avec la direction de contrainte principale (σ_1) bissectant le dièdre aigu formé par les deux plans conjugués.

Mohr (1882), proposa une représentation graphique simple du critère de rupture de Coulomb (Figure II.2.1b) dans un diagramme contrainte cisaillante (τ) versus contrainte normale (σ_n) suivant l'équation :

$$\tau_c = \tau_0 + \mu.\sigma_n \qquad (1)$$

Où τ_c est la contrainte de cisaillement critique, τ_0 est la cohésion et μ le coefficient de friction interne du matériau μ est lié à l'angle de friction interne φ_0 par l'équation :

$$\mu = \tan \varphi_0 \qquad (2)$$

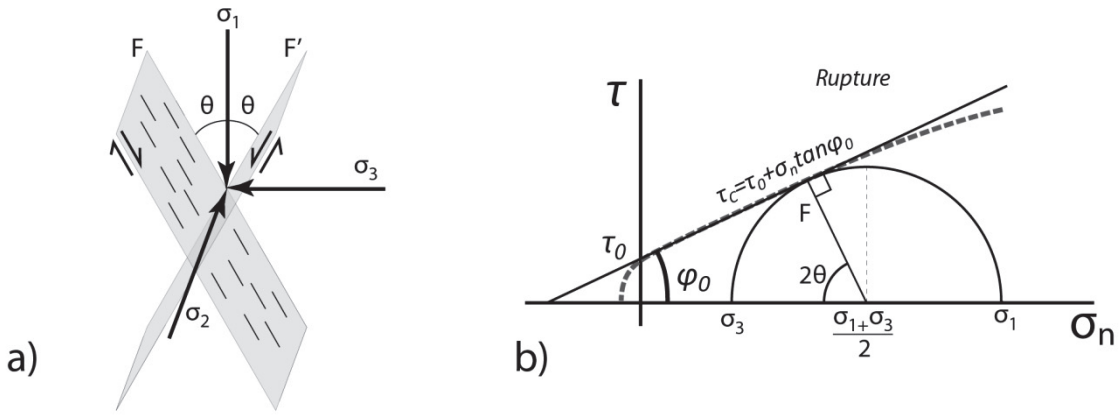

Figure II.2.1. a) direction des contraintes principales σ_1, σ_2, σ_3 déduites des plans conjugués F et F'. b) Représentation de Mohr du critère de rupture de Coulomb. L'angle entre le plan de faille et la contrainte principale σ_1 est noté θ.

Théoriquement, chaque matériau peut avoir des coefficients de cohésion et de friction propres. Si cela est vrai pour la cohésion, Byerlee (1978) montra qu'il n'en était pas de même pour le coefficient de friction des roches. Basé sur l'étude de différentes roches pré-fracturées (sans cohésion initiale), ce dernier présenta une compilation des valeurs de cisaillement critique (Figure II.2.2). Pour des roches soumises à une pression de confinement inférieure à 2Kbar, la friction apparait variable étant principalement fonction de la rugosité du plan de mouvement propre à chaque type de roche. Cependant, pour des roches soumises à une pression de confinement supérieure à 2Kbar, la friction apparaît relativement constante, la variation de rugosité du plan de mouvement devenant négligeable sous de telles contraintes. Byerlee proposa donc que les propriétés de friction de la plupart des roches étaient les mêmes (seules les roches riches en H_2O telles que les argiles ou les serpentinites diffèrent radicalement de cette tendance, Figure II.2.2) tel que $\mu = 0.6$ ou $\varphi_0 = 30°$.

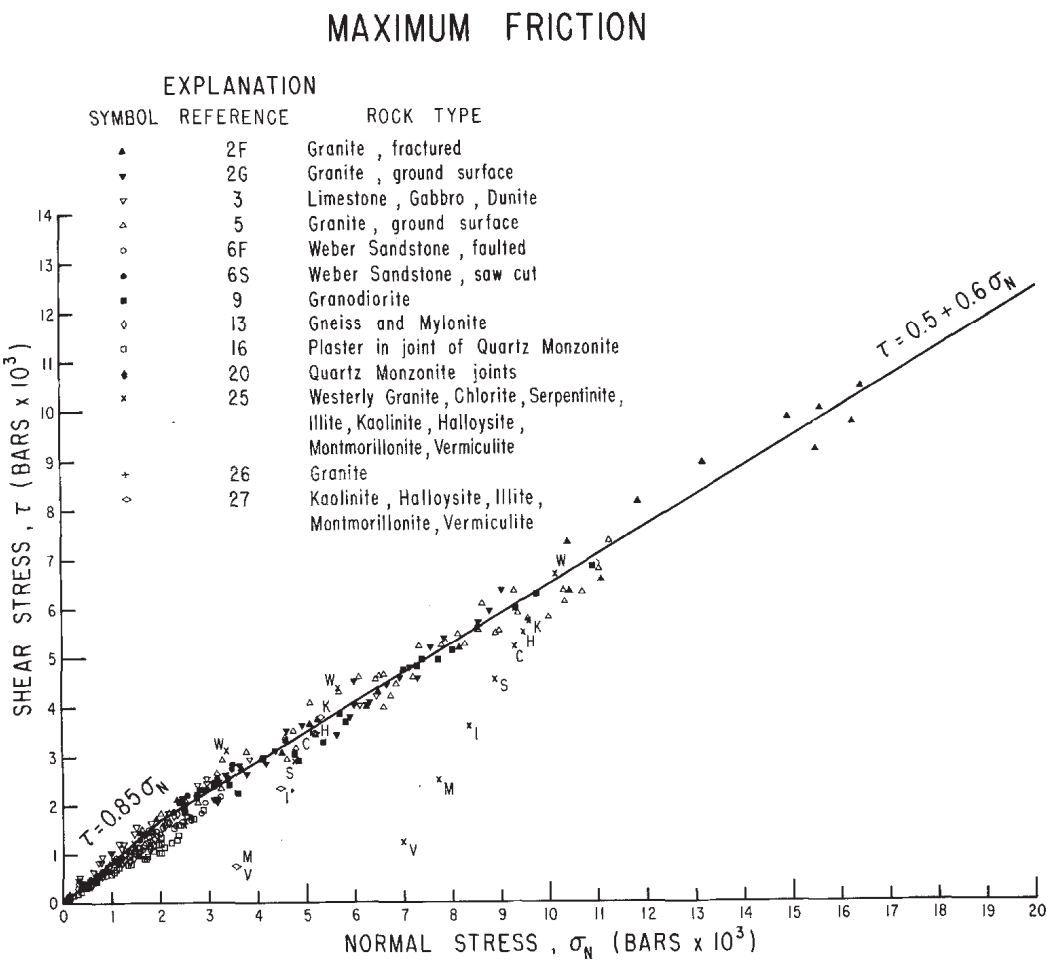

Figure II.2.2. Diagramme contrainte cisaillante versus contrainte normale présentant les coefficients de friction maximum de différents types de roches terrestres, extrait de Byerlee 1978.

Basé sur cette estimation empirique et sur les relations géométriques existant entre l'angle de friction φ_0 et l'angle θ (Figure II.2.1b) il a dès lors été possible de définir une relation générale tel que :

$$\theta = \frac{90° - \varphi_0}{2} = 30° \qquad (3)$$

Cette relation générale illustre le fait que lors d'un glissement sur le plan d'une faille néoformé ou réactivé, la contrainte principale σ_1 formera un angle de 30° avec ce dernier. Cependant, comme dit précédemment, cette relation n'est valable que pour une pression de confinement supérieure à 2Kbar et n'en reste pas moins basée sur une estimation moyennée. Dans la réalité des faits, les angles

approximatifs θ sont connus pour la plupart des roches, et cela à des pressions de confinement variables et vont de 40° à 70°.

2. Le traitement de population de failles

2.1 Les méthodes de traitement de population de failles

Les concepts de relation angulaire existant entre les contraintes principales (σ_1, σ_2, σ_3) et l'orientation des plans de fractures ont très tôt été utilisés par les géologues. Les premières méthodes de détermination des axes des paléo-contraintes se sont focalisées sur l'étude des systèmes de failles conjuguées (Hoskins, 1896 ; Van Hise, 1896). Moyennant la connaissance du coefficient de friction interne du matériau, ce n'est que plus tard que ces concepts furent appliqués à l'étude de failles isolées pourvues de stries indiquant la direction du mouvement, cette dernière étant perpendiculaire à l'intersection des deux plans conjugués (Compton, 1966). Dans la continuité de ces travaux, de nouvelles méthodes géométriques ont été proposées afin d'obtenir la direction des paléo-contraintes non pas à partir de l'étude d'une faille isolée mais à partir d'une population de failles donnant ainsi une signification régionale au champ de contraintes déterminé. Si la méthode du plan de mouvement (Arthaud, 1969) a été la première à être proposée, c'est la méthode des dièdres droits (Angelier et Mechler, 1977) qui aura le plus large écho et s'avérera être à la base de nombreux programmes informatiques aujourd'hui utilisés pour le traitement statistique de populations de failles.

2.1.1 La méthode des dièdres droits

Pour une faille donnée, dont le sens du jeu est connu, il est possible de définir quatre dièdres limités par le plan de faille lui-même et son plan auxiliaire (Fig.II.2.3a,b). Le plan auxiliaire est tracé comme étant perpendiculaire à la strie de mouvement et donc au plan de faille. Il est alors possible de définir deux dièdres en compression (P) et deux dièdres en tension (T). Le principe de cette méthode repose sur le respect de deux conditions. La première implique que pour l'ensemble des failles analysées, ces dernières doivent avoir joué en fonction d'un état de contrainte uniforme pour le volume de roche considéré (i.e la zone d'étude). La seconde consiste à admettre que la direction de déplacement le long du plan de faille soit parallèle à la contrainte cisaillante maximum résolue sur le plan de faille. Ceci équivaut à dire que les contraintes principales σ_1 et σ_3 sont respectivement contenues quelque part dans le cadran en compression ou en extension. Ainsi, si pour chaque faille les dièdres en compression contiennent σ_1 et les dièdres en extension contiennent σ_3, et si les axes porteurs de σ_1 et σ_3 sont homogènes à l'échelle de la zone étudiée (condition 1), l'intersection des dièdres en compression

contient σ_1 et l'intersection des dièdres en extension contient σ_3 (Fig.II.2.3c). Afin de minimiser la zone d'intersection des dièdres propres à chaque faille, la population de failles analysée devra contenir un nombre important de mesures de failles d'orientations variées.

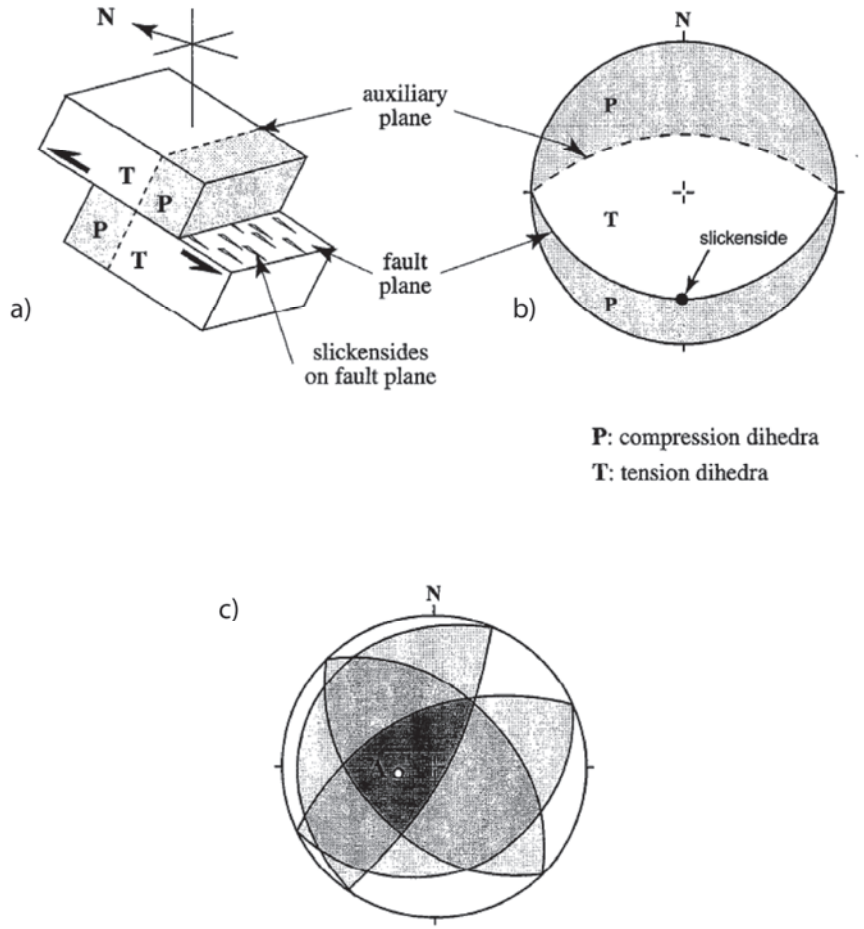

Figure II.2.3. Principe de construction des dièdres par la méthode géométrique des dièdres droits (Angelier et Mechler, 1977). a) un plan de faille strié et son plan auxiliaire définissant deux secteurs en compression et deux secteurs en extension. La position relative des deux secteurs est fonction de la cinématique du plan de faille. b) représentation stéréographique (projection sur l'hémisphère inférieur) du plan de faille et de son auxiliaire et des quatre dièdres correspondants. c) l'intersection des dièdres permet de déterminer un domaine réduit contenant l'axe de raccourcissement compatible avec la population de failles. D'après Pfiffner et Burkhard, 1987.

2.2 Contrainte versus déformation

Basé entre autres sur la méthode des dièdres droits, un certain nombre de méthodes d'analyse statistique numérique de population de failles ont été développés depuis les années 1970 (Célérier et al., 2012 pour une revue de ces différentes méthodes). Ces méthodes peuvent être distinguées en deux catégories :

i) celles assumant que le résultat du traitement d'une population de faille permet de contraindre la direction des axes des contraintes principales (Angelier et Mechler , 1977 ; Ciscato, 1996 ; Lisle, 1987)

ii) et celles assumant que le résultat contraint la direction des axes principaux de la déformation (Marret et Allmendinger, 1990, 1991). L'interprétation des résultats de traitement de population de faille en terme de contrainte ou en terme de déformation est source de débat dans la littérature (Twiss et Unruh, 1998 ; Tikoff et Wotjal, 1999 ; Gapais et al., 2000) et reste une question ouverte. Cependant, et ce quelle que soit la méthode, la fiabilité des résultats dépend de la quantité et de la variabilité en terme d'orientation des plans de failles analysés. Il en découle que ces méthodes sont généralement applicables à des zones ayant subi une déformation substantielle et donc fortement faillées. Durant la déformation, les différentes failles accumulant du mouvement, les différents blocs qu'elles délimitent vont nécessairement tourner et donc altérer la relation géométrique initiale entre la faille et le champ de contrainte ou de déformation régionale (Kissel et Laj, 1989). En dépit de cette contrainte fondamentale sur la signification régionale des résultats obtenus suite au traitement d'une population de faille, Gapais et al (2000) ont pu montrer que les axes déduits pouvaient être interprétés comme représentant les axes de la déformation finie de l'ensemble de la zone d'étude. Compte tenu du caractère intense de la déformation de notre zone d'étude (Fig.II.1a), nous interpréterons par la suite nos résultats comme représentatif des axes de la déformation finie.

2.3 Traitement des données

L'ensemble de nos mesures de failles a été traité via l'utilisation du logiciel *Faultkin* (Marret et Allmendinger, 1990 ; Allmendinger et al., 2012). Ce logiciel permet le traitement statistique de populations de failles suivant la méthode des dièdres droits. Seules ont été prises en compte les failles sur lesquelles ont pu être mesuré de manière univoque l'azimut et le pendage du plan, l'azimut ou le pitch de la strie ainsi que le sens de mouvement. N'ayant pas pu hiérarchiser l'importance relative de chaque faille, ces dernières auront le même poids dans le traitement statistique.

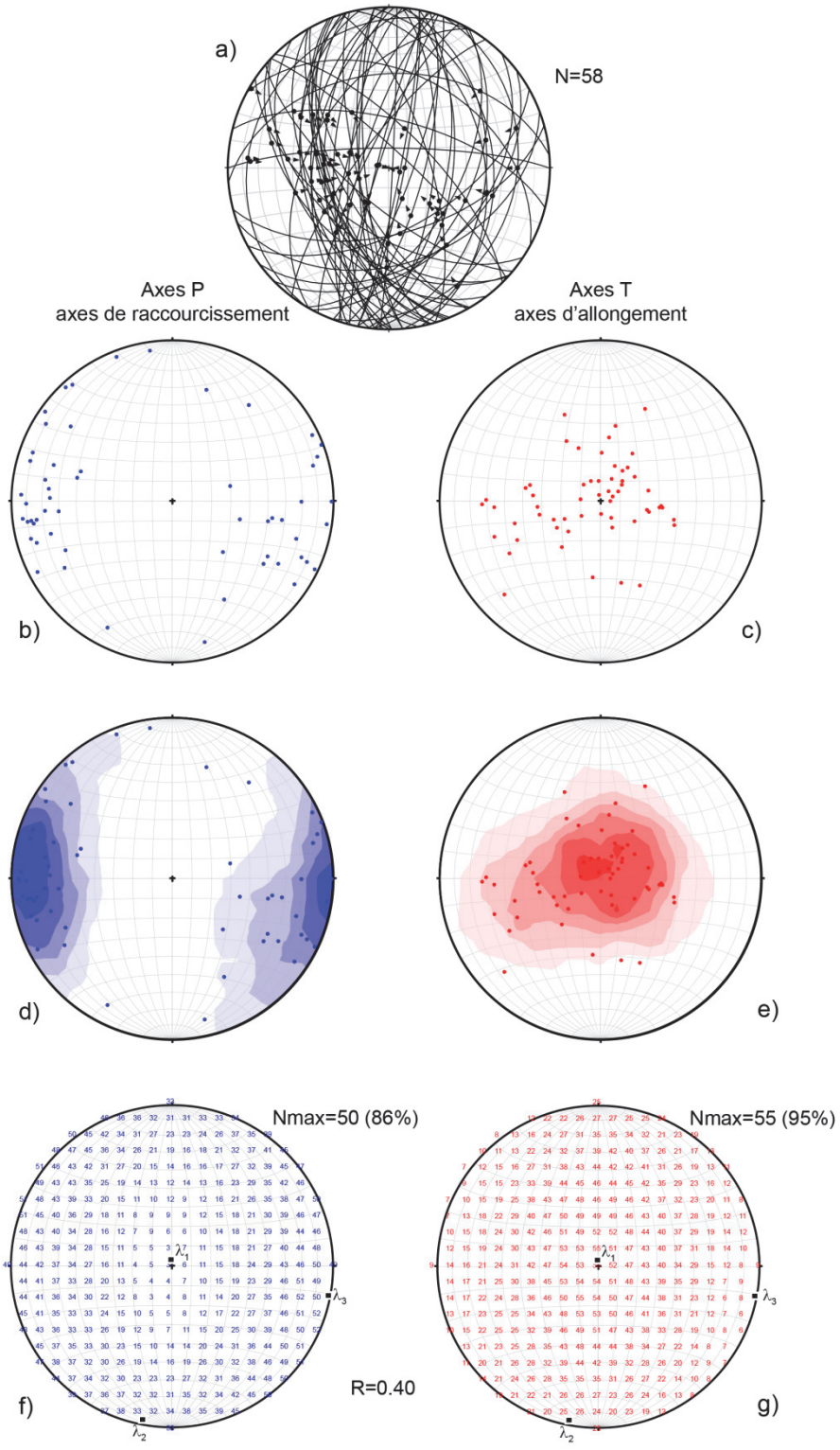

Figure II.2.4. Résultats du traitement d'une population de failles par le logiciel *Faultkin* (projection de Schmidt sur l'hémisphère inférieur). a) représentation de chaque plan de faille (grand cercle), de la strie (point) et du sens du mouvement (flèche) d'une population de failles. N indique le nombre de failles composant la population b, c) représentation des axes en raccourcissement (en bleu) et allongement (en rouge) calculé pour chaque plan de faille. d, e) contourage selon la méthode de Kamb décrivant la distribution des axes en raccourcissement et en allongement. f, g) résultat du calcul de Nmax à chaque nœud de la grille indiquant le nombre de failles dont les axes de raccourcissement et les axes d'allongement sont

respectivement compatibles avec l'orientation de l'axe principal de raccourcissement (λ_3) et de l'axe principal d'allongement (λ_1) calculé par la méthode de distribution statistique de Bingham pour l'ensemble de la population.

Pour une population de failles donnée (Fig.II.2.4a) sont calculés les axes P et T propres à chaque faille (Fig.II.2.4b,c) bissectant respectivement les dièdres en compression ou en tension (Fig.II.2.3a) Analytiquement, les axes P et T sont assimilables aux axes principaux de la déformation incrémentale pour une faille (Marret et Allmendinger, 1990). Ainsi, les axes P sont appelés axes de raccourcissement et les axes T axes d'allongement. Le contourage des axes de raccourcissement et des axes d'allongement selon la méthode de Kamb (Kamb, 1959) permet de décrire leur variabilité directionnelle (Fig.II.2.4d,e). La direction des axes principaux de la déformation finie ($\lambda 1$: axe principal d'allongement, $\lambda 2$: axe intermédiaire, $\lambda 3$: axe principal de raccourcissement) est déterminée selon la méthode de distribution statistique de Bingham. L'orientation des axes est calculée de manière à maximiser le nombre de failles compatibles au sein de l'ensemble de la population (Fig.II.2.4f,g). Il est dès lors possible d'estimer la fiabilité des résultats en estimant le rapport Nmax/N égale au rapport du nombre de failles compatibles avec l'orientation des axes principaux de la déformation sur le nombre total de failles analysées.

Une mesure quantitative (R) de la forme de l'ellipsoïde de la déformation est obtenue par le rapport des tenseurs réduits tel que :

$$R = \frac{\varepsilon_2 - \varepsilon_3}{\varepsilon_1 - \varepsilon_3} \qquad (4)$$

Où ε_1, ε_2, ε_3 sont les valeurs propres du moment du tenseur de Bingham. Théoriquement des valeurs du rapport R égales à 0, 0.5 et 1 indiquent respectivement un ellipsoïde de la déformation en constriction, déformation plane et aplatissement. Nous choisissons arbitrairement pour cette étude de considérer les valeurs comprises entre 0 et 0.35 comme représentative d'une déformation à dominante constrictive et les valeurs comprises entre 0.65 et 1 représentatives d'une déformation à dominante en aplatissement. Les valeurs autour de 0.5 indiquent une déformation à dominante plane.

2.4 Déformation hétérogène

Dans le cas idéal d'une population de failles ayant jouées sous un champ de déformation/contraintes homogène, le nombre de failles compatibles (Nmax) est égal au nombre de failles analysées (N). Cependant, la mesure systématique de failles localisées dans des zones substantiellement déformées amène souvent à l'obtention d'une population de failles hétérogène (Nmax/N faible). Cette hétérogénéité est souvent interprétée comme symptomatique d'un mélange de failles ayant jouées sous des champs de déformation/contrainte distincts. Plusieurs méthodes de séparation de population de failles hétérogène en sous populations homogènes sont proposées dans la littérature (voir Célérier et al., 2012 pour une revue de ces méthodes). Selon Célérier et al (2012) les méthodes raisonnant en termes de contraintes seraient plus adaptées à la séparation de sous populations homogènes alors que les méthodes raisonnant en déformation seraient plus adaptées pour contraindre une déformation moyenne dans un volume de roche donné. Dans le cas de cette étude, l'utilisation du logiciel *Faultkin* dans le but de distinguer des sous populations de failles homogènes n'est donc pas pertinente. L'identification de la minéralogie des marches d'escalier ayant servi à déterminer la cinématique associée à chaque plan de faille a donc été utilisée comme critère indépendant de séparation de la population de failles globale en sous populations.

Chapitre 3

L'utilisation des isotopes stables comme paléo-thermomètre

Partie II : Chapitre 3 – L'utilisation des isotopes stables comme paléo-thermomètre

Dans le cadre de cette étude, l'analyse des isotopes du carbone et/ou de l'oxygène a été effectuée sur deux sous-produits supposés de l'altération supergène, la magnésite ($MgCO_3$) et la silice (SiO_2). Si la composition isotopique en carbone de la magnésite nous permettra de discuter de l'origine possible du fluide à partir duquel elle s'est formée (voir article#3 partie III. chapitre 2 et article #5 partie III. chapitre 3), la composition isotopique en oxygène d'un minéral est classiquement utilisée afin d'en estimer la température de formation. L'utilisation de ce paléo-thermomètre dit « classique » nous permettra de discuter de la température de formation de la magnésite et des divers types de silices échantillonnés. De manière complémentaire à l'utilisation du paléo-thermomètre « classique », la température de formation des magnésites a également été estimée par la méthode récemment développée de « clumped isotope paleothermometry » (voir article #5 partie III. Chap.3. Le but de ce chapitre est donc de mettre en perspective les principes fondamentaux à l'origine de ces deux méthodes et d'en expliquer l'utilisation en tant que paléo-thermomètre.

1. Le paléo-thermomètre isotopique « classique »

1.1 Principe du fractionnement isotopique

Le fractionnement isotopique est le phénomène qui modifie la proportion relative des différents isotopes d'un élément contenu dans un composé par le passage de ce composé d'un état physique à un autre. Dans le cas de deux phases à l'équilibre, le fractionnement isotopique peut être décrit comme une réaction d'échange des différents isotopes entre ces deux phases. Cet échange dépend à la fois de la masse des différents isotopes mise en jeu et de la température à laquelle il se produit.

Si l'on prend le cas du fractionnement isotopique de l'oxygène entre l'eau liquide et la vapeur, la réaction d'échange des isotopes de l'oxygène peut s'écrire :

$$H_2{}^{18}O_{Liq} + H_2{}^{16}O_{Vap} \Leftrightarrow H_2{}^{16}O_{Liq} + H_2{}^{18}O_{Vap} \qquad (1)$$

Le coefficient de fractionnement de l'oxygène (équivalent à la constante d'équilibre K_{eq} d'une réaction d'échange) peut alors s'écrire :

$$\alpha^{0}_{\frac{Vap}{Liq}}(T) = (H_2{}^{18}O/H_2{}^{16}O)_{Vap}/(H_2{}^{18}O/H_2{}^{16}O)_{Liq} = ({}^{18}O/{}^{16}O)_{Vap}/({}^{18}O/{}^{16}O)_{Liq} \quad (2)$$

La manière dont les isotopes « lourds » (^{18}O) et « légers » (^{16}O) vont se répartir entre l'eau liquide et la vapeur dépend du second principe de la thermodynamique établissant que la stabilité d'un système est obtenue lorsque son énergie est au minimum. Ainsi, il apparaît (voir Albarède, 2008 pour l'explication physique) qu'il est moins coûteux en termes d'énergie de faire passer les isotopes « légers », plutôt que les isotopes « lourds », dans la phase vapeur. Ceci implique que la valeur du coefficient de fractionnement entre eau liquide et vapeur sera supérieure à 1. Sa valeur exacte dépendra de la température à laquelle la réaction d'échange se produira, le coefficient de fractionnement étant dépendant de la température suivant l'équation :

$$ln\alpha^{0} = \frac{A}{T^2} + C \quad (3)$$

où A et C sont des constantes et T la température.

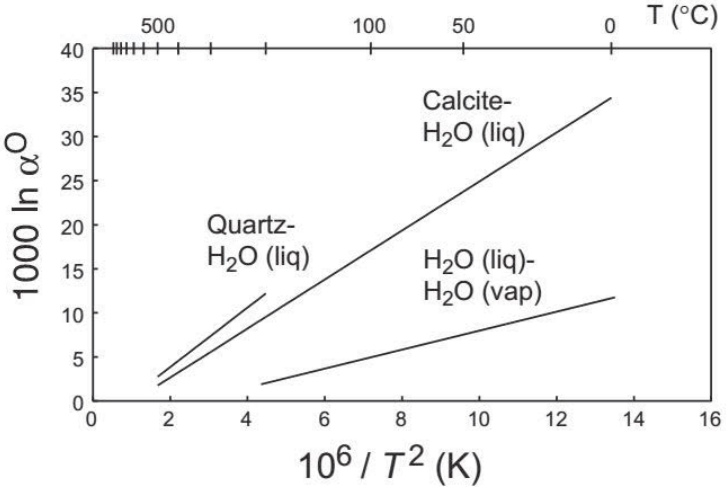

Figure II.3.1. Diagramme présentant l'évolution du fractionnement des isotopes de l'oxygène en fonction de la température entre une phase minérale et l'eau ou entre l'eau liquide et la vapeur. Extrait d'Albarède (2008) d'après Urey (1947).

La figure II.3.1, présente la variation du coefficient de fractionnement des isotopes de l'oxygène entre différentes phases minérales et l'eau, ou entre l'eau liquide et la vapeur. Il apparaît que le ^{18}O s'incorporera préférentiellement dans la phase minérale et que le coefficient de fractionnement diminue très fortement avec la température.

1.2 L'utilisation du fractionnement de l'oxygène comme paléo-thermomètre

Comme nous l'avons vu ci-dessus, la valeur du fractionnement isotopique d'un élément entre deux phases données est dépendant de la température. L'omniprésence de l'oxygène dans les différents minéraux terrestres a justifié l'utilisation du fractionnement isotopique de ce dernier dans le développement d'un paléo-thermomètre permettant de retrouver la température de formation d'un minéral donné à partir d'un fluide (e.g. Urey, 1947; McCrea, 1950; Epstein et al., 1953 ; Emiliani, 1966 ; Craig and Boato, 1955).

Dans la pratique, le rapport ($^{18}O/^{16}O$) mesuré dans un minéral est normalisé en fonction de rapports de référence arbitraire correspondant soit au rapport ($^{18}O/^{16}O$) de l'eau de mer moyenne (SMOW : « standard mean ocean water ») ou au rapport ($^{18}O/^{16}O$) d'une bélemnite de la formation de Pee Dee (PDB). Cette normalisation est notée :

$$\boldsymbol{\delta^{18}O = \left[\frac{\left(^{18}O/^{16}O\right)_{échantillon}}{\left(^{18}O/^{16}O\right)_{référence}} - 1\right] \times 1000} \qquad (4)$$

Une approximation très utile des propriétés de fractionnement isotopique de l'oxygène consiste à comparer la différence Δ des $\delta^{18}O$ des deux phases impliquées avec le coefficient de fractionnement α tel que:

$$\Delta_{2-1} = \delta^{18}O_2 - \delta^{18}O_1 = 1000 ln\alpha_{2-1} \qquad (5)$$

Dans la pratique, la valeur du coefficient de fractionnement entre le minéral étudié et le fluide peut être déterminée expérimentalement ou estimée théoriquement sur une gamme de température donnée. Le $\delta^{18}O$ du minéral étudié étant connu il est dès lors possible d'estimer la paléo-température de formation du minéral ce qui est équivalent à estimer la température du fluide à partir duquel il a cristallisé. La grande limite de cette méthode réside dans le fait que la composition initiale du fluide est inconnue. Néanmoins, partant du fait que les gammes de composition isotopique en oxygène des principaux réservoirs de fluides terrestres sont variables et connues (Craig et Boato, 1955), il est possible, moyennant l'utilisation d'indicateurs indépendants (bonne connaissance de la géologie de la zone d'étude, composition en $\delta^{13}C$, inclusions fluides etc…) de faire une hypothèse robuste sur la valeur du $\delta^{18}O$ du fluide initial.

La grande force de la méthode, récemment développée, de « clumped isotope thermometry » réside justement dans le fait qu'il n'est pas nécessaire de faire une telle hypothèse. Seulement applicable aux carbonates, cette méthode permet d'estimer la température de formation d'un minéral indépendamment de la connaissance du fluide à partir duquel il s'est formé.

2 La « clumped isotope thermometry »

La méthode « clumped isotope thermometry » s'intéresse à la manière dont les isotopes « lourds » du carbone (^{13}C) et de l'oxygène (^{18}O) sont distribués dans la structure cristalline d'un carbonate. En pratique, cela revient à mesurer l'excès de liaisons ^{13}C-^{18}O au sein de la structure cristalline d'un carbonate par rapport à une distribution aléatoire de ces isotopes au sein du minéral. L'abondance des liaisons ^{13}C-^{18}O étant fonction de la température, il est dès lors possible d'obtenir la température de formation (ou de rééquilibration) du carbonate (Ghosh et al., 2006; Schauble et al., 2006 ; Eiler, 2007 ; Guo et al., 2009). A l'inverse de la méthode standard de thermométrie basée sur le fractionnement de l'oxygène entre deux phases à l'équilibre thermodynamique, la « clumped isotope thermometry » permet de déterminer la température de formation du carbonate indépendamment de la composition de la phase coexistante (e.i. la phase fluide à partir de laquelle le carbonate s'est formé). En effet, la manière dont le ^{13}C et le ^{18}O se distribuent au sein du réseau cristallin du carbonate est indépendante de la composition du fluide à partir duquel il s'est formé. Qui plus est, moyennant la connaissance du coefficient de fractionnement de l'oxygène entre le type de carbonate analysé et l'H_2O, il est également possible de déterminer la composition en oxygène du fluide initial.

2.1 Le principe du « clumping »

Au sein d'un minéral carbonaté équilibré thermodynamiquement, les isotopes lourds du carbone (^{13}C) et de l'oxygène (^{18}O) auront tendance à se regrouper (« to clump » en anglais) dans un même ion carbonate pour former $^{13}C^{18}O^{16}O\ ^{16}O^{2-}$. Ce phénomène fait que la proportion d'ions $^{13}C^{18}O^{16}O\ ^{16}O^{2-}$ au sein du minéral est plus haute que celle attendue pour une distribution aléatoire des isotopes. Cela découle des lois thermodynamiques impliquant que le regroupement des isotopes lourds au sein d'une molécule donnée en augmente sa stabilité (i.e. le point zéro d'énergie d'une molécule composée des isotopes lourds est plus bas que pour une molécule composée d'isotopes lourds et légers, ou légers figure II.3.2).

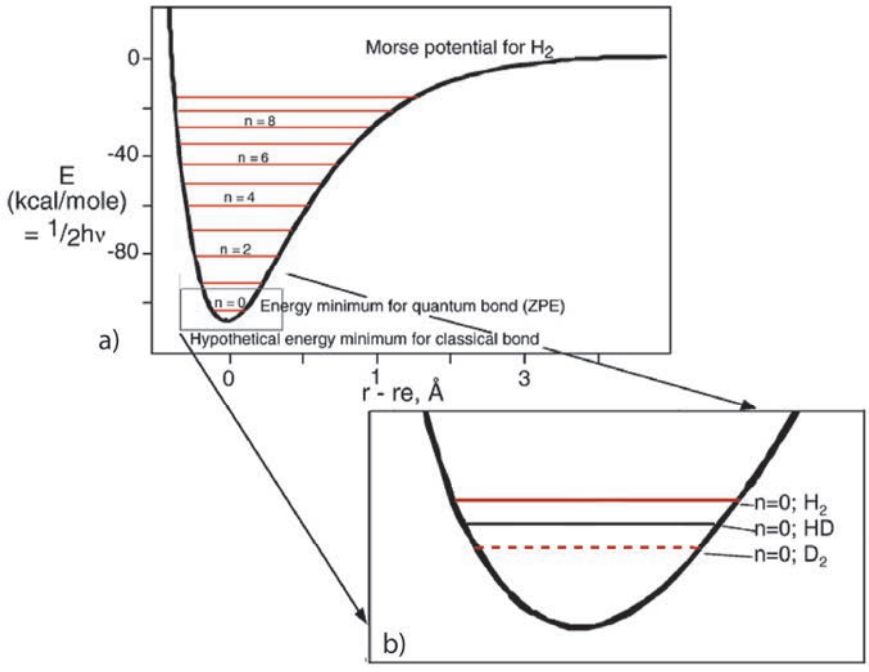

Figure II.3.2 a) Illustration de la quantité d'énergie contenue par la liaison d'une molécule de dihydrogène en fonction de la différence entre la distance inter-atomique (r) et la distance inter-atomique lorsque la liaison est à son niveau d'énergie le plus bas. La courbe représente l'énergie potentielle de la molécule de dihydrogène. Les lignes horizontales représentent les différents niveaux d'énergie correspondants aux différents états vibrationnels possibles de la liaison. L'état vibrationnel le plus bas (n=0) correspond à l'énergie minimale nécessaire pour créer la liaison (point zéro d'énergie) b) Représentation de l'effet de la substitution isotopique sur la valeur du point zéro d'énergie. Il apparaît que l'énergie nécessaire pour créer la liaison dihydrogène est minimale dans le cas d'une double substitution par l'isotope lourd de l'hydrogène (D). Modifié d'après Eiler (2007).

Dans le cas de l'ion carbonate, l'isotopologue $^{13}C^{18}O^{16}O^{16}O^{2-}$ (dit doublement substitué) est donc plus stable que les isotopologues $^{13}C^{16}O^{16}O\ ^{16}O^{2-}$, $^{12}C^{18}O^{16}O\ ^{16}O^{2-}$ et $^{12}C^{16}O^{16}O\ ^{16}O^{2-}$. Cette réaction de substitution des isotopes lourds peut être exprimée sous forme d'une réaction d'échanges tel que :

$$M^{13}C^{16}O^{16}O^{16}O + M^{12}C^{18}O^{16}O^{16}O \Leftrightarrow M^{13}C^{18}O^{16}O^{16}O + M^{12}C^{16}O^{16}O^{16}O \quad (6)$$

La constante d'équilibre K_{eq} de cette réaction varie en fonction de la température et représente la base de la méthode de « clumped isotope thermometry» (Ghosh et al., 2006 ; Schauble et al., 2006).

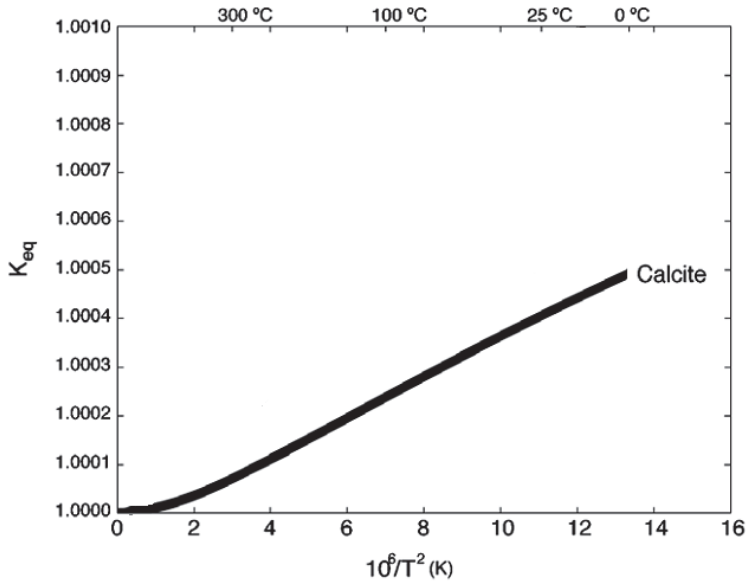

Figure II.3.3. Constante d'équilibre K_{eq} estimée théoriquement pour la réaction $^{13}C^{16}O^{16}O^{16}O + Ca^{12}C^{18}O^{16}O^{16}O \Leftrightarrow Ca^{13}C^{18}O^{16}O^{16}O + Ca^{12}C^{16}O^{16}O^{16}O$. Modifié d'après Schauble et al (2006).

Comme le montre la figure II.3.3, K_{eq} diminuant lorsque la température augmente, l'abondance de l'isotopologue doublement substitué sera d'autant plus importante que la température sera faible. Pour une température suffisamment haute, l'effet de « clumping » sera parfaitement contrebalancé par l'entropie apportée au système menant à une distribution purement aléatoire des isotopes lourds.

L'effet de « clumping » s'atténuant avec l'augmentation de la température, la méthode de paléo-thermométrie basée sur ce phénomène sera donc plus adaptée à l'étude de minéraux carbonatés formés à relativement basse température.

2.2 Le paléo-thermomètre « clumped isotope »

Le CO_2 possède 12 isotopologues (i.e. molécules de composition chimique identique mais de composition isotopique différente) si l'on exclut ceux dont le carbone est sous forme ^{14}C (Table.II.3.1).

Mass [a]	Isotopologue	Relative abundance
CO_2 [d]		
44	$^{12}C^{16}O_2$	98.40%
45	$^{13}C^{16}O_2$	1.11%
	$^{12}C^{17}O^{16}O$	748 ppm
46	$^{12}C^{18}O^{16}O$	0.40%
	$^{13}C^{17}O^{16}O$	8.4 ppm
	$^{12}C^{17}O_2$	0.142 ppm
47	$^{13}C^{18}O^{16}O$	44.4 ppm
	$^{12}C^{17}O^{18}O$	1.50 ppm
	$^{13}C^{17}O_2$	1.60 ppb
48	$^{12}C^{18}O_2$	3.96 ppm
	$^{13}C^{17}O^{18}O$	16.8 ppb
49	$^{13}C^{18}O_2$	44.5 ppb

Table II.3.1. Abondance des différents isotopologues du CO_2. L'abondance est estimée en assumant que les rapports $^{17}O/^{16}O$ et $^{17}O/^{16}O$ sont égaux à ceux du standard VSMOW, que le rapport $^{13}C/^{12}C$ est égal à celui du standard VPDB et que les différents isotopes du carbone et de l'oxygène sont distribués aléatoirement entre tous les isotopologues. Modifié d'après Eiler et al (2007).

Comme nous l'avons vu ci-dessus, l'abondance des liaisons ^{13}C-^{18}O au sein d'un minéral carbonaté est fonction de la température à laquelle il s'est formé (rééquilibré). En pratique, il est possible de quantifier l'excès de liaison ^{13}C-^{18}O en mesurant l'abondance de l'isotopologue de masse 47 du CO_2 ($^{13}C^{18}O^{16}O$) par rapport à l'abondance que cet isotopologue aurait pour une distribution aléatoire des isotopes ^{13}C et ^{18}O au sein du minéral. Cette mesure consiste en l'analyse au spectromètre de masse du CO_2 extrait du minéral carbonaté par réaction avec de l'acide phosphorique. Il est important de souligner que lors de cette analyse, les isotopologues $^{12}C^{17}O^{18}O$ et $^{13}C^{17}O^{17}O$ sont mesurés en même temps que l'isotopologue $^{13}C^{18}O^{16}O$ et biaisent donc de facto la mesure et les calculs de température

qui en découlent. Cependant, du fait de leur faible abondance par rapport à l'isotopologue $^{13}C^{18}O^{16}O$, leur contribution sur le résultat final est considérée comme insignifiante. L'excès de la masse 47 au sein d'un échantillon est exprimé sous la forme du paramètre Δ47 qui est défini comme la déviation du rapport isotopique R^{47}= [47]/[44] par rapport à la valeur que ce rapport aurait pour une distribution aléatoire des différents isotopologues tel que :

$$\Delta 47 = \left[\left(\frac{R^{47}}{R^{47^*}} - 1\right) - \left(\frac{R^{46}}{R^{46^*}} - 1\right) - \left(\frac{R^{45}}{R^{45^*}} - 1\right)\right] \times 1000 \qquad (7)$$

où R^{45}, R^{46} et R^{47} sont respectivement les rapports d'abondance des masses 45, 46 et 47 par rapport à la masse 44 (correspondant à l'isotopologue du CO_2 le plus abondant, $^{12}C^{16}O^{16}O$). Les rapports R^{45^*}, R^{46^*} et R^{47^*} sont les rapports qu'auraient R^{45}, R^{46} et R^{47} dans l'échantillon pour une distribution aléatoire des isotopologues. Ces rapports sont calculés suivant les équations suivantes :

$$R^{45^*} = R^{13} + 2.R^{17} \qquad (8)$$

$$R^{46^*} = 2.R^{18} + 2.R^{13}.R^{17} + (R^{17})^2 \qquad (9)$$

$$R^{47^*} = 2.R^{13}.R^{18} + 2.R^{17}.R^{18} + R^{13}.(R^{17})^2 \qquad (10)$$

où R^{13}, R^{17} et R^{18} sont respectivement les rapports $^{13}C/^{12}C$, $^{17}O/^{16}O$ et $^{18}O/^{16}O$ mesurés dans l'échantillon. R^{13} et R^{18} dérivent des valeurs de $\delta^{13}C_{PDB}$ et $\delta^{18}O_{VSMOW}$ mesurées dans l'échantillon. R^{17} est estimé à partir de R^{18} assumant qu'une relation dépendante de la masse lie ^{17}O et ^{18}O.

Ghosh et al (2006) ont été les premiers à proposer une calibration permettant de retrouver la température de formation de différents carbonates à partir de la mesure du Δ47 du CO_2 extrait par digestion de carbonates (précipités expérimentalement dans des conditions contrôlées ou d'origines biogéniques dont les températures de formation étaient connues ou estimées) dans l'acide phosphorique (Fig.II.3.4).

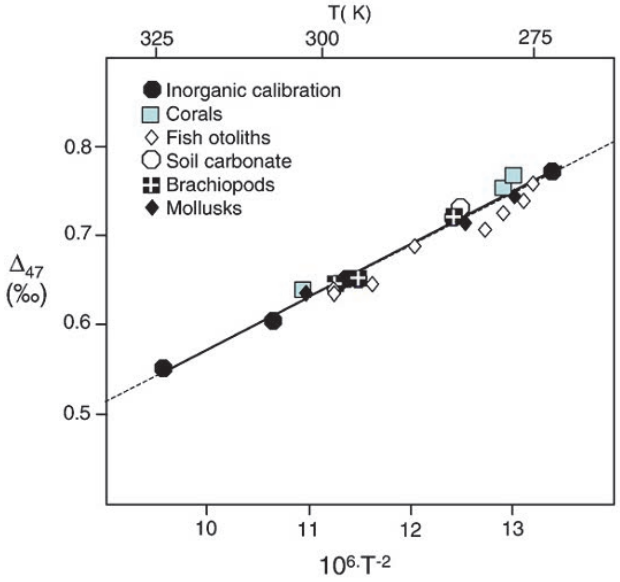

Figure II.3.4. Variation du Δ47 mesuré à partir du CO_2 extrait de différents types de carbonate par digestion à l'acide phosphorique par rapport à la température de croissance du minéral. Les carbonates analysés sont, des calcites inorganiques précipitées expérimentalement à des températures différentes (Ghosh et al., 2006), des carbonates biogéniques naturels dont les températures de formation sont connues ou peuvent être estimées (Ghosh et al., 2006, 2007 ; Came et al., 2007) et des carbonates formés naturellement dans des sols dont la température moyenne annuelle de la zone d'échantillonnage est connue (Ghosh et al., 2006). La ligne correspond au résultat de la régression linéaire des données de calcite inorganique et correspond à la première calibration empirique du Δ47 en fonction de la température ($\Delta47 = 56200/T^2 - 0.02$) proposé par Ghosh et al (2006). Extrait de Eiler (2007).

Ces premiers résultats suggéraient qu'une unique droite de calibration pouvait être dérivée pour l'ensemble des phases carbonatées impliquant l'inexistence d'effets de fractionnement spécifiques aux différents types de carbonates ou d' « effet vital » (pour les carbonates d'origine biogénique) influençant la relation Δ47 vs. température. Cependant cette étude portait exclusivement sur l'analyse de carbonates calcitiques et aragonitiques. Guo et al (2009) ont par la suite proposé des calibrations théoriques de la relation Δ47 vs. température mettant en évidence des variations en fonction du type de carbonate analysé (Fig.II.3.5).

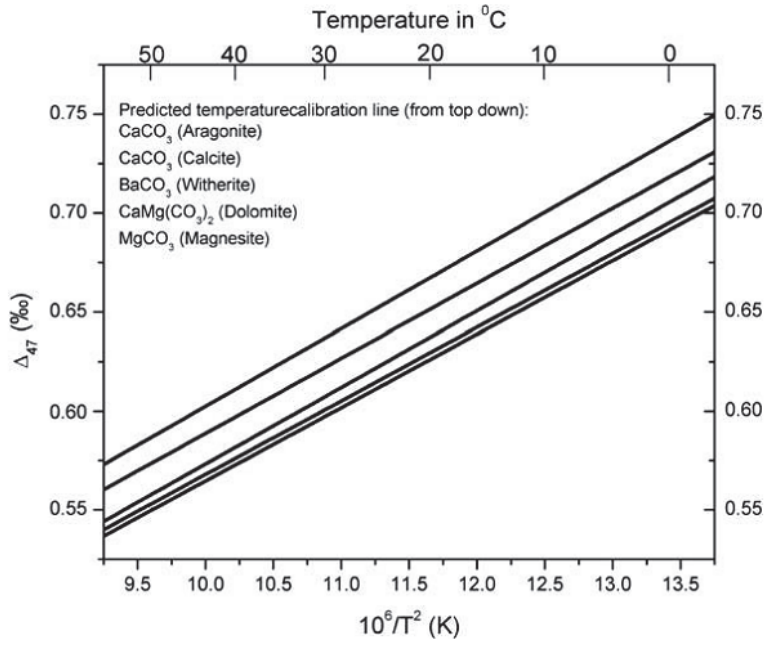

Figure II.3.5. Calibrations théoriques du Δ47 en fonction de la température de formation du minéral pour différents types de carbonate. Cette calibration prend en compte la variation de l'effet de clumping en fonction de la température prédite pour différents carbonates à l'équilibre thermodynamique (Schauble et al., 2006) et le fractionnement cinétique du Δ47 induit par la digestion du carbonate dans l'acide phosphorique à 25°C. D'après Guo et al (2009)

De nombreuses calibrations empiriques ont par la suite été effectuées afin d'établir des droites de calibration spécifiques à chaque type de carbonate et pour des gammes de températures variées (calcite inorganique naturelle ou synthétique et calcite biogénique : Ghosh et al., 2006; Ghosh et al., 2007; Dennis et Schrag 2010; Tripati et al., 2010; Thiagarajan et al., 2011; Henkes et al., 2013; Grauel et al., 2013 ; Kluge et al., 2015 ; dolomite naturelle ou synthétique: Ferry et al., 2011; et sidérite synthétique : Fernandez et al., 2013). Ces calibrations empiriques s'avère être concordantes avec celles estimées théoriquement, prenant en compte l'incertitude sur la mesure du Δ47.

A l'heure actuelle, la méthode de « clumped isotope thermometry » reste en développement nécessitant l'amélioration de la précision des mesures de Δ47, l'amélioration et la création de nouvelles droites de calibrations ainsi que l'identification de facteurs pouvant biaiser la relation Δ47 vs température (voir Eiler, 2011 et Affek, 2012 pour une revue relativement récente des principales limites de la méthode) tels que :

i) l'effet du pH et de la salinité de la solution à partir de laquelle le minéral se forme (Hill et al., 2014)

ii) l'effet de la vitesse de croissance du minéral

iii) l'influence d'effets vitaux liés à la formation de carbonates biogéniques

iv) l'effet de la diagenèse.

Comme nous l'avons dit dans l'introduction de ce chapitre, la méthode de « clumped isotope thermometry » a été utilisée dans cette étude afin de déterminer la température de formation de la magnésite. A ce jour, seule la calibration théorique de Guo et al (2009) établit la relation Δ47 vs. température spécifique à la magnésite. Cependant, le travail de Falk et al (2015) propose, se basant sur la concordance d'échantillons de magnésite formés expérimentalement ou de magnésites naturelles dont la température de formation peut être estimée, de choisir parmi les calibrations empiriques disponibles pour d'autres types de carbonates afin d'estimer la température de formation de la magnésite. Nous discuterons de ce choix à la suite de l'article #5 présenté dans le chapitre 3 de la partie III.

Partie III

Résultats :

Altération supergène, circulation des fluides et déformation interne de la Nappe des Péridotites.

Chapitre 1

Le niveau saprolitique, zone clé de la redistribution élémentaire par l'altération supergène

Partie III : Chapitre 1 – Le niveau saprolitique, zone clé de la redistribution élémentaire par l'altération supergène

Introduction

A ce jour, le gisement latéritique néo-calédonien représente près de 20% des ressources mondiales en nickel. La formation des latérites résulte de l'altération des péridotites sous des conditions climatiques chaudes et humides. Comme décrit précédemment (cf Partie I. Contexte géologique), cette altération se caractérise par l'hydrolyse des différents constituants de la péridotite entraînant la mise en solution des éléments mobiles (i.e. Si, Mg, Ni) et le maintien du fer à l'état ferrique sous forme d'oxy-hydroxydes de fer (hématite et goethite). Le modèle classiquement admis afin d'expliquer la formation du gisement nickélifère néo-calédonien implique la circulation *per descensum* d'eau météorique permettant le lessivage et l'export vertical des éléments mobiles mis en solution. Le nickel, lessivé de la partie supérieure du profil d'altération, se concentre à des teneurs d'intérêt économiques à la base du profil, au sein du niveau saprolitique. Ce niveau apparait dès lors comme étant une zone clé de la redistribution élémentaire par l'altération supergène.

Les travaux présentés dans ce chapitre visent à caractériser la distribution spatiale du nickel au sein du niveau saprolitique, à l'échelle du gisement comme à l'échelle de l'affleurement, et d'actualiser le modèle *per descensum* classique via la compréhension de processus complémentaires ayant permis la formation d'un gisement nickélifère aujourd'hui spatialement complexe.

Partie III : Chapitre 1 – Le niveau saprolitique, zone clé de la redistribution élémentaire par l'altération supergène

Résumé article #1

Résultant de l'altération supergène de la Nappe des Péridotites, les latérites sont abondantes en Nouvelle-Calédonie et forment l'un des plus grands gisements de nickel au monde. Se basant sur la base de données de forages de l'entreprise Koniambo Nickel SAS, ce travail présente une modélisation 3D de la couverture latéritique. Ce dernier montre que les latérites sont localisées le long de la crête du massif et sont organisées sous forme de patches hectométriques distribués à des altitudes variables et recoupés par la topographie. Trois types de géométrie peuvent être observés : i) une couverture limonitique épaisse (entre 20m et 40m) recouvrant la saprolite et principalement localisée sur les hauts topographiques, ii) une couverture limonitique fine (de quelques mètres à 20m d'épaisseur) principalement localisée dans des zones de pente douce et iii) une couverture limonitique absente, laissant la saprolite à l'affleurement, principalement localisée dans des zones de forte pente. Nos données montrent que les zones riches et pauvres en nickel sont organisées en patches hectométriques dont la distribution est globalement corrélée avec celle de l'épaisseur de la couverture limonitique. Les zones les plus riches en nickel sont localisées sur les pentes, sous une couverture fine à absente de limonite. A l'inverse, les zones les plus pauvres en nickel sont localisées sur les hauts topographiques sous les couvertures les plus épaisses de limonite. Le bilan de masse vertical du nickel effectué pour chaque forage montre que pour les zones à forte épaisseur de limonite, le bilan est sub-équilibré. A premier ordre cela suggère, étant donné qu'aucune perte significative en nickel n'est documentée dans les profils latéritiques de hauts topographiques actuels, que la circulation latérale d'eau riche en nickel dissout n'est probablement pas le processus principal menant à l'enrichissement significatif de la saprolite dans les zones de pente. Nous proposons dès lors que le transfert latéral successif et le lessivage de matériel remanié minéralisé en nickel provenant d'ancien hauts topographiques maintenant érodés puisse significativement augmenter la teneur en nickel de la saprolite localisée dans les zones de pente.

3D modelling of the laterites on top of the Koniambo Massif, New Caledonia: refinement of the *per descensum* lateritic model for nickel mineralization

In preparation for submission in a special volume of Mineralium Deposita:

Ore forming processes in surficial environments

Benoît Quesnel, Christian Le Carlier de Veslud, Philippe Boulvais, Pierre Gautier

Géosciences Rennes-OSUR, Université de Rennes1, France.

Michel Cathelineau

Université de Lorraine, CNRS, CREGU, GeoRessources laboratory, Nancy, France.

Maxime Drouillet

Koniambo Nickel SAS, Nouvelle Calédonie.

Abstract

Resulting from the weathering of the Peridotite Nappe, laterites are abundant in New Caledonia and host one of the largest nickel ore deposit worldwide. Based on a drilling dataset provided by the Koniambo Nickel SAS company, this work presents a 3D modelling of the lateritic cover. It shows that the laterites are located along the ridges of the massif and organized as hectometric–sized patches obliquely cut by the topography and distributed at various elevations. Three kinds of geometry can be observed: i) a thick limonite cover (between 20 m and 40m) overlying saprolite and mainly localized on the topographic highs, ii) a thin limonite cover (from few meters to 20m) mainly localized on areas with gently slopes and iii) an absent limonite cover, so the saprolite is exposed at the surface on steep slopes. Our data show that Ni-rich and Ni-poor areas are organized as hectometric–sized patches

which broadly correlate with the distribution of the limonite thickness. The richest areas are localized on slopes below thin or absent limonite cover. The poorest are localized in topographic highs under the thickest limonite covers. The vertical Ni mass balance performed for each borehole shows that in areas with thick limonite cover, Ni mass balance is sub-equilibrated. At first order, this suggests that, given that no significant loss of Ni is documented from the present-day topographic highs, lateral circulations of water rich in dissolved Ni is probably not the main process leading to the significant Ni enrichment in the saprolite from the slopes. We propose that successive lateral transfer and leaching of reworked Ni-bearing material, from ancient, now eroded topographic highs to downstream slope areas, was the main process leading to the largest Ni enrichment in the saprolite from the slopes.

1. Introduction

Lateritic nickel ore deposits are associated with the intense weathering of ultramafic rocks. Laterite development involves dissolution of the peridodite minerals, which leads to i) exportation of soluble elements (Si, Mg) and ii) in situ newly-formation of mineral phases (mainly oxi-hydroxides) hosting the insoluble elements (Fe, Al). Ni, with an intermediate behaviour, is concentrated at the base of the lateritic profile where it reaches economic concentration. This is particularly the case of New Caledonia (Trescases 1975, Freyssinet 2005) for which a typical lateritic profile is shown in figure 1. At the top, the limonite level is mainly composed of iron oxi-hydroxides (hematite, goethite). Beneath the limonite horizon, the saprolitic level represents an intermediate state of alteration between limonite and the fresh peridotite and hosts the most concentrated Ni ores. Earthy saprolite hosts a pervasive Ni ore, where goethite is the main Ni carrier, whereas rocky saprolite hosts an erratic fracture-controlled Ni high grade ore, known as garnierite (a Ni-rich talc-like phase).

For the New Caledonian Ni laterite ore deposit as for others worldwide, a downward model of fluid circulation is classically invoked to explain the geometry of the lateritic profile and the distribution of elements (Glasser, 1904; de Chetelat, 1947; Avias, 1969; Trescases, 1975; Fig. 1). According to this per descensum model, the supergene alteration of peridotites promotes vertical leaching and the passive export of Ni (and other mobile elements as Mg and Si) through

discontinuities crosscutting the peridotite. Nickel is then immobilized in the saprolite level, between the weathered zone and the fresh bedrocks, forming the pervasive and the erratic ores defined just

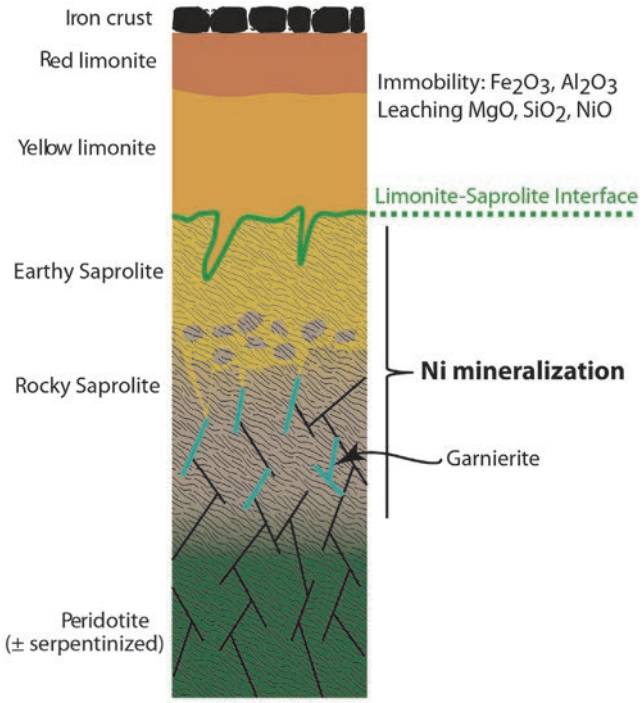

Figure 1 Typical laterite profile of New Caledonia developed on a peridotitic protolith.

above. Even if this model provides a simple way to explain the Ni laterite ore deposit formation, several studies provide information calling for renewed examination of the *per descensum* model. Firstly, evidences of low-temperature hydrothermalism conditions of formation of silica veins commonly associated to garnierite (Quesnel et al., 2015; Quesnel et al., submitted-a), of hydraulic brecciation involving silica and garnierite (Myagkiy et al., 2015) and syn-tectonic formation of garnierite veins (Cluzel and Vigier, 2008) suggest that the conditions of fluid circulation leading to the erratic ore formation are more complex than a simple downward percolation of meteoric waters. Secondly, evidences of actual to sub-actual Ni dispersion in the saprolite level related to water table movements (Cathelineau et al., 2015b) and geological observations showing that the Ni-richest area are commonly not spatially associated to the main laterite body (de Chetelat, 1947; Avias, 1969; Trescases, 1975) suggest that the formation of the Ni laterite ore deposit have to be thought as a 3D process, implying lateral Ni mobility.

In order to characterize the Ni mobility during laterization, most of the works discuss about the Ni behaviour based on one or few isolated vertical profiles (Trescases, 1975; Fu et al., 2014) and rarely

based on a significant samples dataset (Schellmann, 1989). Restricted by the difficulty to obtain large enough and regularly distributed boreholes database, these works can only be performed in 1D. Recently, Koniambo Nickel SAS initiated a large mining and industrial site for Ni production on the Koniambo massif (Fig.2). As a result, new outcrops and a large number of boreholes provide an exceptional data set for studying the Ni laterite ore deposits. When investigating a complex geological case study, 3D geometrical modelling coupled with field survey represents a first-order tool for integrating different kinds of data, building consistent geological structures and performing quantitative estimates. In this study, we combine 3D modelling with field observations and boreholes dataset in order to characterize the distribution and the geometry of the lateritic surfaces and more especially to estimate how and how much lateral Ni mobility have participated to the formation of Ni-rich laterite ore deposit.

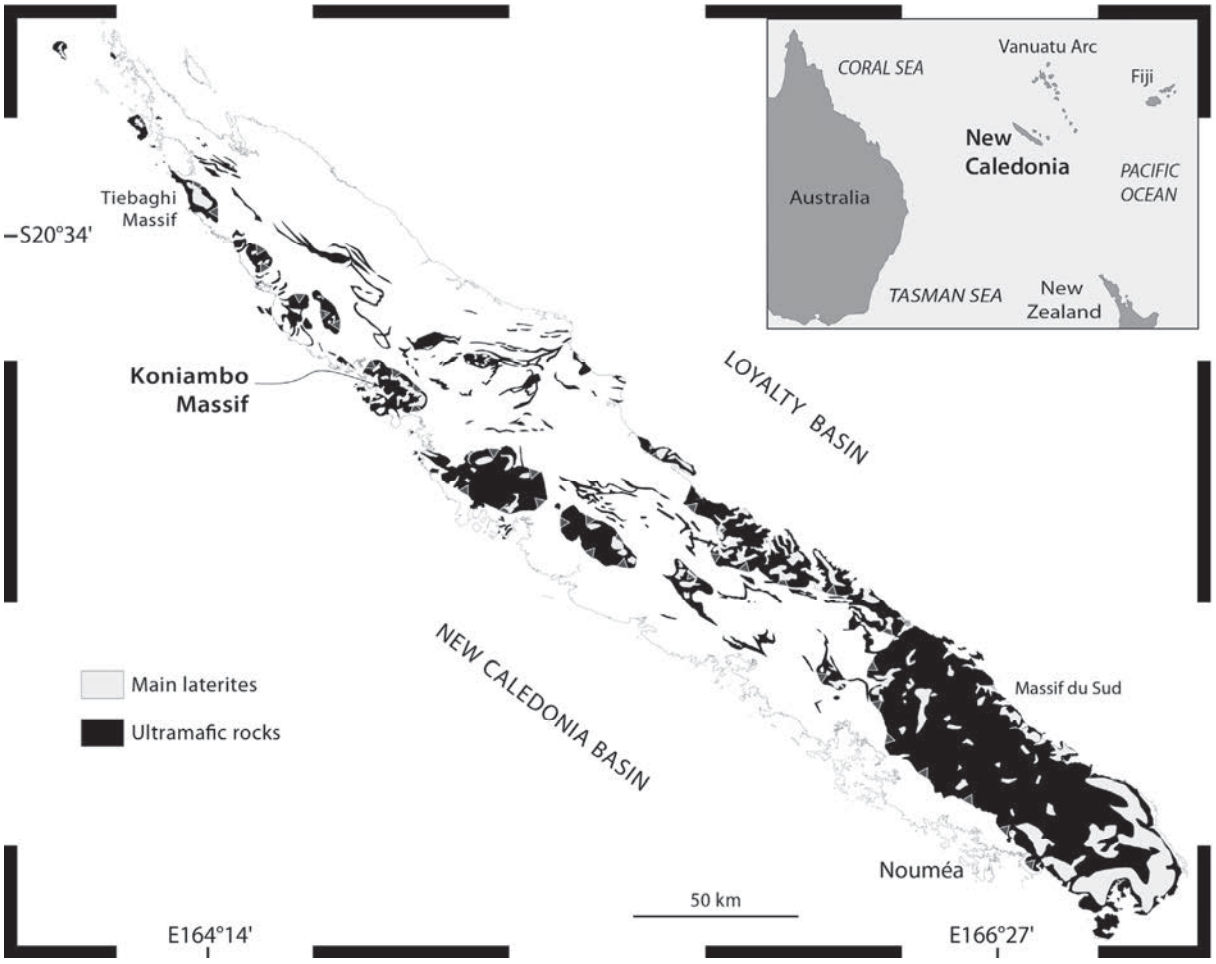

Figure 2 Simplified geological map of New Caledonia. Ultramafic rocks are from Maurizot and Vendé-Leclerc (2009) and laterites are adapted from Paris (1981).

2. Geological setting

To date, nickeliferous laterites from New Caledonia host 20% of the global resources in nickel. Laterites are actively worked by mining companies (KNS, SMSP NMC, SLN, Vale Nouvelle-Calédonie, Montagnat, Ballande) making New Caledonia the 6th nickel producer in the world (Baille et al., 2013). New Caledonia is located in the southwest Pacific Ocean, 1300 km east of Australia (Fig.2). The mainland consists in the northern extension of the Norfolk ridge and is approximately 50 km wide and 400 km long. Peridotites are abundant representing about 40% of the island surface. They occur as a main massif called "Massif du Sud" in the southern part of the island and as a series of klippes along the northwestern coast (Fig.2). They overlie a volcano-sedimentary basement with a sub-horizontal contact (Avias, 1967; Guillon, 1975). This geometry results of the Eocene obduction of the New Caledonia Peridotite Nappe on the Norfolk Ridge (Cluzel et al., 2001, 2012). The nappe is mostly composed of harzburgites except in the northernmost klippes where lherzolites dominate (e.g., Ulrich et al., 2010). In high elevation areas of the Massif du Sud, the peridotites are locally overlain by layered pyroxenites and gabbros, interpreted as representing the base of an oceanic crust (Guillon, 1975; Prinzhofer et al., 1980; Paris, 1981). In the peridotites, compositional layering is essentially represented by 1 to 100 m-thick layers of dunite within the main harzburgitic mass (e.g., Ulrich et al., 2010). In the main part of the nappe, the degree of serpentinization of the peridotites is variable but moderate (Orloff, 1968, Quesnel et al., submitted-b). Serpentinization becomes pervasive along the base of the nappe, forming a 'sole' in which deformation has been intense (Avias, 1967; Orloff, 1968; Guillon, 1975; Leguéré, 1976; Cluzel et al., 2012; Quesnel et al., 2013).

Laterites are well developed at the top of each massif of peridotites. The pseudo-karstic morphology of the peridotite nappe attests of a past efficient drainage system (Trescases, 1975; Genna et al., 2005). Laterites occur as several planation surfaces at distinct elevations. They probably did not form in a single event. On the northwestern klippes, the several planation surfaces are interpreted as resulting of the post-obduction progressive uplift of the island coupled with events of favourable climatic conditions (Latham, 1977, 1986; Chevillotte et al., 2006). For the "Massif du Sud", if some authors consider that uplift and climate also explain the formation of several planation surfaces (Chevillotte et al., 2006) others consider that this geometry should be, at least in part, influenced by

late brittle tectonic (Trescases, 1975; Latham, 1977). Most of these surfaces present evidences of reworked material (Trescases, 1975; Latham, 1977, 1986) attesting for alternate periods of wet and warm climate which led to laterization and dryer periods which led to erosion (Latham, 1977; Chevillotte et al., 2006). Dating these surfaces is still source of debate, however the older surfaces probably formed before ca.20 Ma (Latham, 1986; Chevilotte et al., 2006; Sevin et al., 2012; Quesnel et al., 2013).

The Koniambo massif is one of the klippes of the Peridotite Nappe located along the west coast of the main island (Fig. 2). It is 20 km long by 5 km wide (Fig.3). It is comprised essentially of harzburgites with interlayers of dunite that define a crude compositional layering (Maurizot et al., 2002; Ulrich, 2010). The degree of serpentinization increases from the top to the base of the massif (Maurizot et al., 2002) with: (i) a massive serpentinite level forming the base of the massif, (ii) a highly serpentinized level forming the intermediate part of the massif and (iii) a moderately serpentinized and highly fracturated (Leguéré, 1976) forming the upper part of the massif on which laterite developed. This massif is known to contain significant high grade nickel laterite mineralization (Xstrata 2012). The Koniambo massif rises from a narrow coastal plain to 940 m above sea level. The laterites are organized as distinct planation surfaces, highly dissected and partly reworked, localized at elevations above ~400m (Fig.3a, Maurizot et al., 2002). At lower elevations, laterites of the westerly-inclined Kaféaté plateau probably belong to a younger planation surface (Latham, 1977; Chevillotte et al., 2006).

3. Data and methodology

3.1. Data

Input data were mainly provided by the Koniambo Nickel SAS Company. They include:

- a 10m digital elevation model (DEM),
- a large database of about 6700 boreholes drilled in the laterites, mainly along the ridges of the massif. The well head altitudes range from 325 to 925m, but 50% of them lies in the range 675-815m (Fig.3b). For each borehole, major and some trace elements analyses, facies, some

specific features (e.g. presence of garnierite) and densities are available on samples taken in depth approximately every meter and altogether accounting for 260,000 data points. The maximum depth reached by these boreholes is 120m, but in average, this depth is only about 30m.

- the geological maps published in the literature or from the BRGM (French geological survey).

Two important points should be noted. Firstly, the boreholes are not regularly distributed with a spacing between adjacent boreholes ranging from few hundred of m to 5m. As the boreholes are concentrated along the ridges, the lower parts of the laterites, at intermediate altitude, are poorly if not sampled. Subsequently, some bias can occur during interpolation of data especially in areas where borehole density is low or as boundary effects at the edges of the studied area. On the contrary, the upper parts, corresponding to the highest Ni contents are oversampled. Secondly, each chemical analysis corresponds to a mean value measured on about 1m sample considered by the logging team as representative of a column of homogeneous material in a borehole. Thus, as no mineralogical or petrological study is available on these samples, this kind of analysis is less accurate that any detailed study based of a limited number of sample (e.g. Dublet et al., 2012, 2015), but they are more appropriate for large-scale mass-balance.

In this study we focus mainly on analyses of NiO, Al_2O_3, Fe_2O_3, Cr_2O_3, MgO and SiO_2 in wt.%. Loss on Ignition ranges from 0 to 20 %, with an average of 12%, similar to those obtained on altered rocks.

3.2. Alteration facies

Figure 1 shows the typical complete lateritic succession of New Caledonia characteristic of laterites developed under wet climate and tectonically active terranes with moderate relief (Golightly, 1981). From the top to the base of the profile, it is comprised of i) the iron duricrust, ii) the limonite horizon, mainly composed of iron oxi-hydroxides (goethite) and distinguished in two levels as a function of the alteration degree (red and yellow limonite) iii) the saprolite level which consists in a level of intermediate state of alteration between parent rock and limonite and which hosts the nickeliferous mineralization.

The earthy saprolite hosts the major part of the diffuse Ni mineralization related to oxi-hydroxides (Ni-goethite) whereas rocky saprolite, where the degree of alteration is lower and the structure of parent rock is partially preserved, hosts the erratic nickel ore occurring as a mix of (minor) Ni-serpentine and (dominant) Ni-talc like fractures infillings, the so called garnierite. A recent study of samples of garnierite from the Koniambo massif reveals that, in that case, nickel is essentially contained by the talc-like phase also known as kerolite (Cathelineau et., 2015a)

It is a common impression often gained from the literature that laterite facies occur as a regular succession of layers. However, two main types of configurations can be recognized on the field. The first, localized on topographic highs, present a thick laterite cover often preserved as complete profiles whereas the second is preserved as thin and incomplete profile localized on gently slopes (de Chetelat, 1947 his figure.7; Trescases, 1975 his fig.18; Avias, 1978 his figure.2). In addition, the preliminary study of boreholes indicates that the succession of laterite facies is highly irregular, both horizontally and vertically. Therefore, only two main groups are considered in this study, consisting of an uppermost limonitic zone and a lowermost saprolitic zone (Fig. 1).

3.3. 3D modelling

We used the gOcad 3D numerical modeller (Mallet 2002) to reconstruct the geometry of the lateritic cover and to quantify the distribution of geochemical tracers, including mass balance, in 3D. The gOcad modeller provides a discrete representation of geological objects in terms of regular meshes (grids) or irregular meshes (polygonal curves, triangulated surfaces, Mallet 2002). Triangulated surfaces appear to be particularly relevant for representing complex surfaces with irregularly distributed data points, which is the case in the present study.

The modelling process includes four steps. Firstly, a 3D database was built integrating all available data. A geo-referenced digital terrain model (DTM) consisting of geological maps draped over the DEM was constructed (Fig.3a). Secondly, surface maps and the lithological and geochemical information from the boreholes were integrated. Thirdly, the 3D reconstruction of geological structures from the borehole data, namely the limotine/saprolite interface, was performed by Discrete

Smooth Interpolation (DSI; Mallet 2002). Finally, different kinds of computations (vertical average, mass-balance on either limonite or saprolite levels) were performed, based on the previous 3D objects.

3.4. Methodology

Based on the available borehole data and on the 3D model, the methodology used to characterize the Ni distribution in the Koniambo massif can be summarized as follows:

- Study of the present-day geometry of the limonite cover (section 4.1 below);
- Study of elements spatial distribution with a special focus on the lateral variability of the Ni content in the saprolite level (section 4.2);
- Construction of Isocon diagrams (Grant, 1986) based on several representative boreholes in order to study the vertical general behavior of elements during weathering. (section 4.3);
- Calculation of 1D vertical mass-balance of Ni on the whole borehole dataset in order to study the lateral Ni distribution at the scale of the Ni laterite ore deposit (section 4.4).

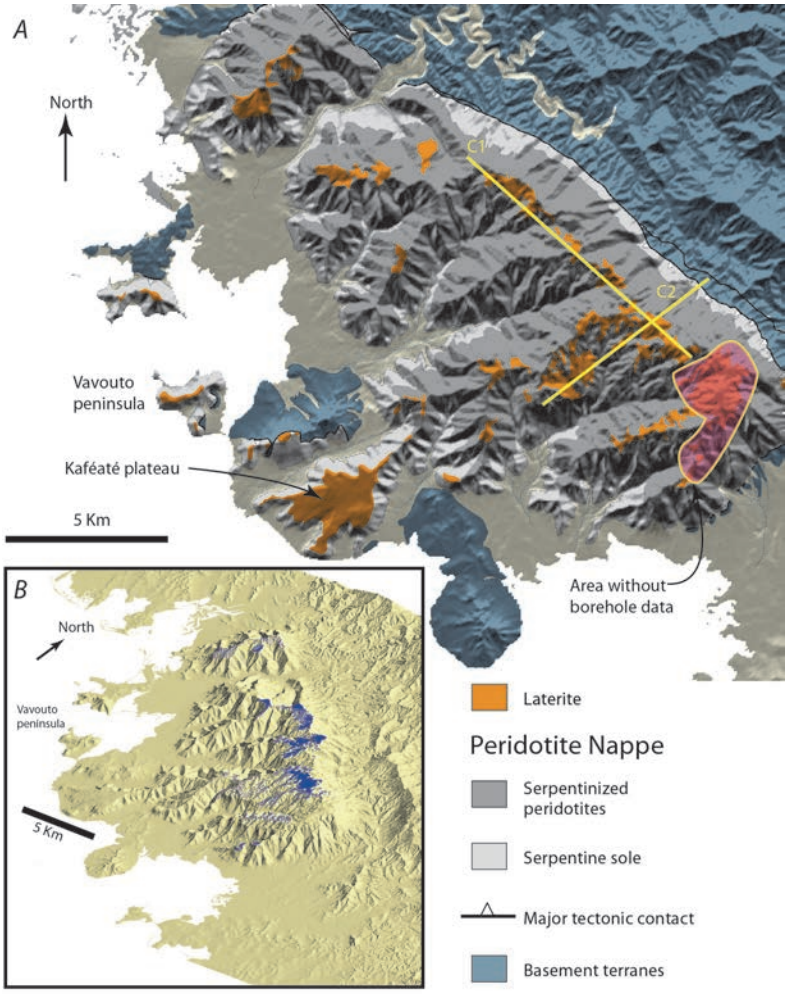

Figure 3 A) Geological map of the Koniambo massif adapted from Maurizot et al. (2002) draped on the 10m digital elevation model. C1 and C2 are the localization of the two cross sections presented on the figure 5. B) Localization of the whole borehole dataset where each blue point corresponds to one borehole.

4. Results

4.1. Geometry of the limonite cover

The laterites are developed along the ridges of the massif and on the gently slopes located close to the ridges. In contrast, almost no laterite is found along the steep slopes or in the valleys (Fig.3a). The largest and most continuous lateritic horizon occurs over the northwest-trending axial ridge of the massif. It is also in this area that most of the Ni deposits are located and exploited (Fig.3b). On the scale of the massif, the lateritic horizons define a broad surface with a slope of about 3° toward the SW. Some patches depart from this trend, being located underneath this surface.

A 3D surface corresponding to the limonite-saprolite boundary was modelled using borehole data. This interface is particularly interesting since it is known that most of the Ni mineralization is localized in the saprolite level, Ni being thought to come from the overlying limonite cover (Trescases,

1975, Freyssinet 2005). It should be noted that the level of detail of this surface is conditioned by the spatial density of boreholes. Globally (Fig.4a,b), the limonite cover is organized as hectometric–sized patches obliquely cut by the topography and distributed at various elevations (Fig4c1,c2). Three kinds of configuration may be observed. The first consists in topographic highs where the limonite cover is the thickest ranging between 20 m and 40m. The second consists in gently slope area where limonite cover is thin (from few meters to 20m), commonly localized downstream of the topographic highs with thick limonite cover. The third consists in absent limonite cover, allowing the saprolite to be exposed at the surface as a result of erosion because localized on steep slopes (Fig.4a,b,c1,c2).

More in detail, in places where the density of boreholes is high, the surface has a complex multiscale shape with two kinds of features: i) multiple small-scale depressions of metric to decametric vertical amplitude (Fig.5 a, b) and ii) larger closed depression areas (Fig. 5c).

Two cross sections (Fig. 4c1, c2), parallel or perpendicular to the main NW-SE ridge axis show the relationships between the limonite-saprolite interface and the topography. As described just above, the limonite cover is organized as hectometric–sized patches obliquely cut by the topography and distributed at various elevations. At first sight, the interface between limonite and saprolite is parallel to the topography (Fig. 4c1, c2) and may be extrapolated from one patch to the neighbour one suggesting a past continuity between them.

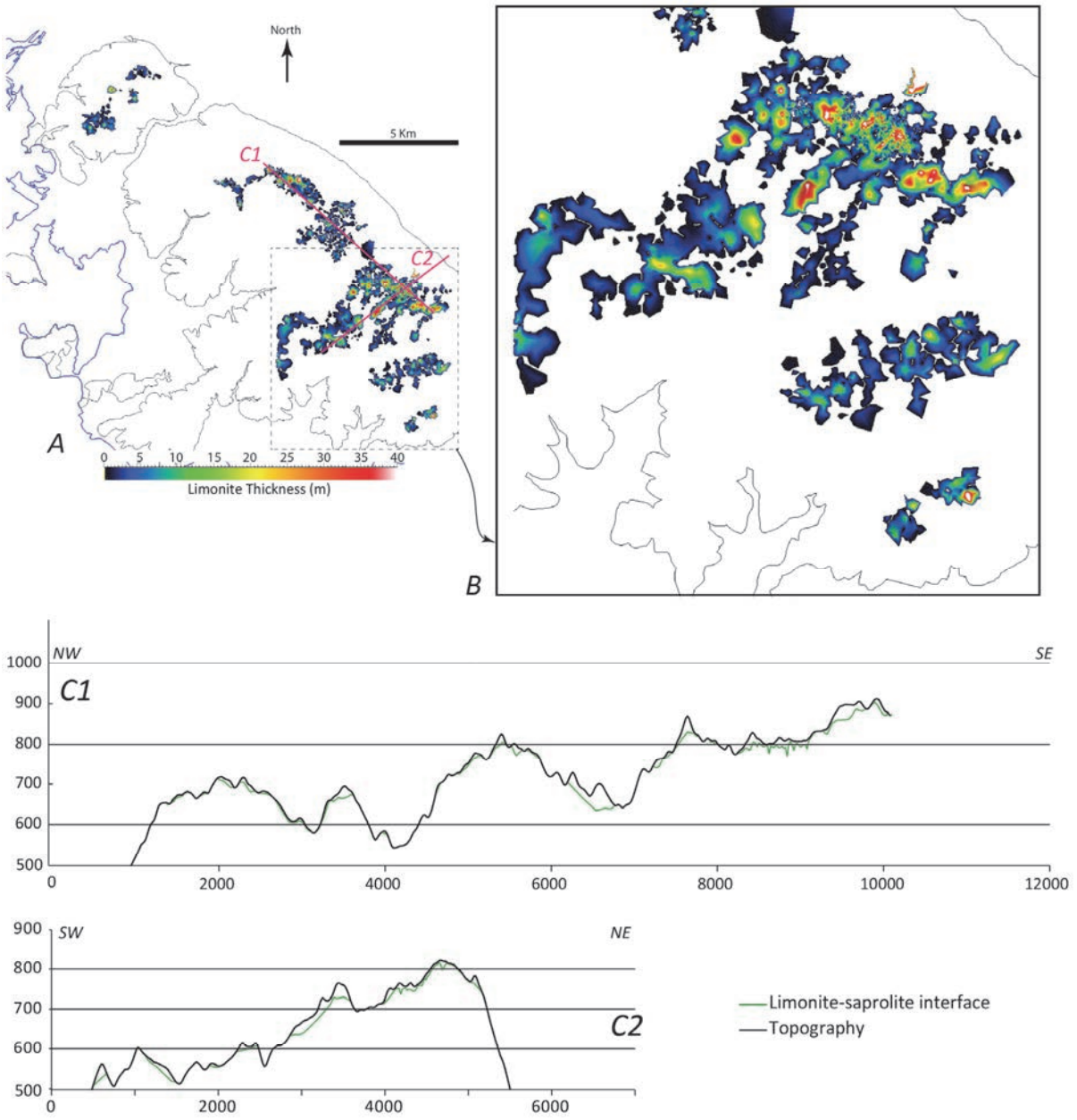

Figure 4 A) Interpolated map of the thickness of the limonite cover calculated from the whole boreholes dataset. B) Focus on the best covered area where density borehole is the highest and where they are the most regularly distributed. C1 and C2 are two perpendicular cross sections showing the lateral and vertical variability of the thickness of the limonite cover.

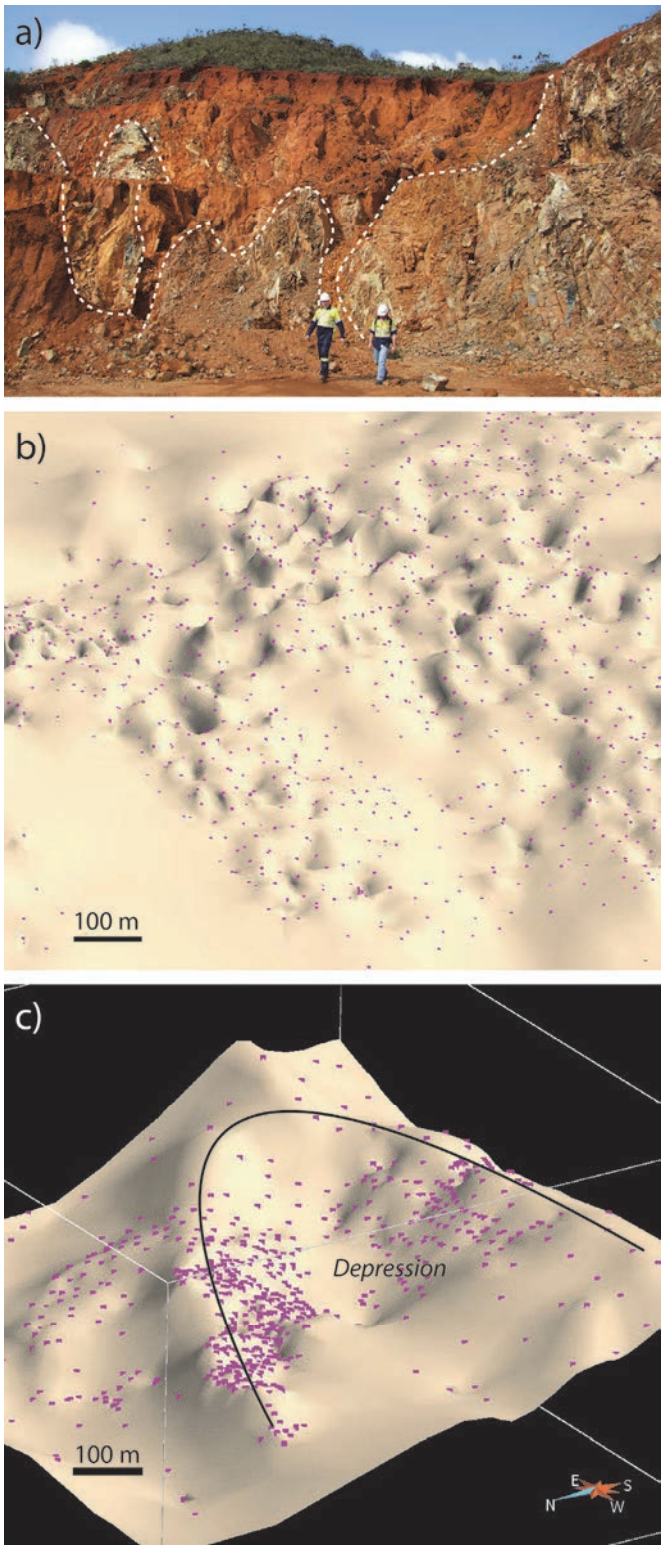

Figure 5 a) Field view of the limonite-saprolite interface. b and c) 3D model of the same interface (in pink boreholes localization, no vertical exaggeration).

4.2 Spatial distribution of elements

4.2.1 Bedrock geochemistry

Most of the boreholes reach the bedrock at variable depths from a few m to 120m. In order to rule out a possible variability of the Ni content of the bedrock which could lead to local variations of the laterites Ni contents, the geochemical homogeneity of the bedrock was checked. For that purpose, the bottom of each borehole was examined, discarding those that displays NiO content superior to 0.5 wt.%. Indeed, the initial Ni content of unweathered peridotites is known to be around 0.3 wt.%, both in New Caledonia and in other places worldwide (Ulrich, 2010; Herzberg et al., 2013). Consequently, a Ni content higher than 0.5 wt.% appears to be unrealistic for fresh peridotites. Statistics (1st and 3rd quartile, Table 1) on the 4260 remaining boreholes (from the initial 6700 ones) indicate that the bedrock is fairly homogeneous for the major elements, and without visible spatial trend. It should be noted that the peridotite rocks sampled here are a few hundreds of m above the main sub-horizontal contact of the peridotite nappe with the underlying Poya unit, and thus far from the significant serpentinization associated with this contact.

Element (wt.%)	Bedrock	Saprolite	Limonite
SiO_2	40.3 - 42	40.5 - 44.8	2.5 - 21
Al_2O_3	0.48 - 0.62	0.57 - 1	3.4 - 5.5
Fe_2O_3	7.6 - 8.3	8.6 - 13.5	53 - 70
MgO	39.2 - 42	26 - 37.3	0.8 - 3.2
NiO	0.25 - 0.36	0.6 - 2.3	1.1 - 1.7
Nb of samples	4 260	201 027	42 427

Table 1 1st and 3rd quartile of the bedrock, saprolite and limonite as documented from the whole borehole dataset.

4.2.2 Vertical distribution of elements from borehole data

Three boreholes (Fig.6 and Annexe 2) have been selected as representative of the three typical profiles defined just above (thick, thin or no laterite cover). In the limonite cover (well 1 and 5), the concentration of elements of interest is rather constant. Limonite is enriched in Fe_2O_3, Al_2O_3 and Cr_2O_3 relative to the peridotite protolith, with concentrations around 70wt.%, 5wt.% and 4wt.%, respectively. This level is depleted in MgO (~1wt.%) and SiO_2 (~3wt.%). NiO is slightly enriched, especially at the interface with saprolite and its concentration locally reaches 2wt.%. In the saprolite level, most of the elements concentrations are highly variable but oscillating around a mean value. In the well 1 and 3, SiO_2 concentration is around 40wt.%, MgO is around 30wt.%, Fe_2O_3 is around 10wt.%, Al_2O_3 is around 1wt.% and Cr_2O_3 is around 0.7wt.%. NiO is also highly variable but is enriched relative to peridotite with an average concentration of ~2wt.%. In the well 5, under a thin limonite cover, the saprolite appears enriched in SiO_2 (45wt.%) and NiO (3wt.%). MgO is slightly depleted in the first 30 meters and then increases with mean value around 20wt.% for the whole saprolite column. Fe_2O_3 shows the opposite trend with a slightly enrichment in the first 30 meters with a mean concentration value of 15wt.% and then decreases to a mean value of 10wt.%. In this well MgO and NiO are globally correlated whereas they are perfectly anti-correlated in the other wells (1 and 3). This likely reflects the presence of garnierite, consistently with the erratic and higher values of NiO. In the wells 1 and 3, the positive correlation between NiO and Fe_2O_3 likely reflects that goethite is the main Ni carrier in these levels as also shown by Dublet et al. (2012) in the same massif..

4.2.3 Lateral variability of the Ni content

For each borehole of the dataset, the vertically averaged content of chemical elements has been calculated in the laterite (when present) and in the saprolite. The use of the average concentration allows reducing the bias that could arise from boreholes with different lengths. In the limonite, the averaged Ni content is fairly constant (Table 1). In the saprolite, the averaged Ni content is more variable, between 0.6wt.% and 2.3wt.% (Table 1).

Figure 7b shows the variability of the Ni average content in saprolite at the scale of the exploited area which is localized along the ridge of the massif. The areas with a predominant blue colour have

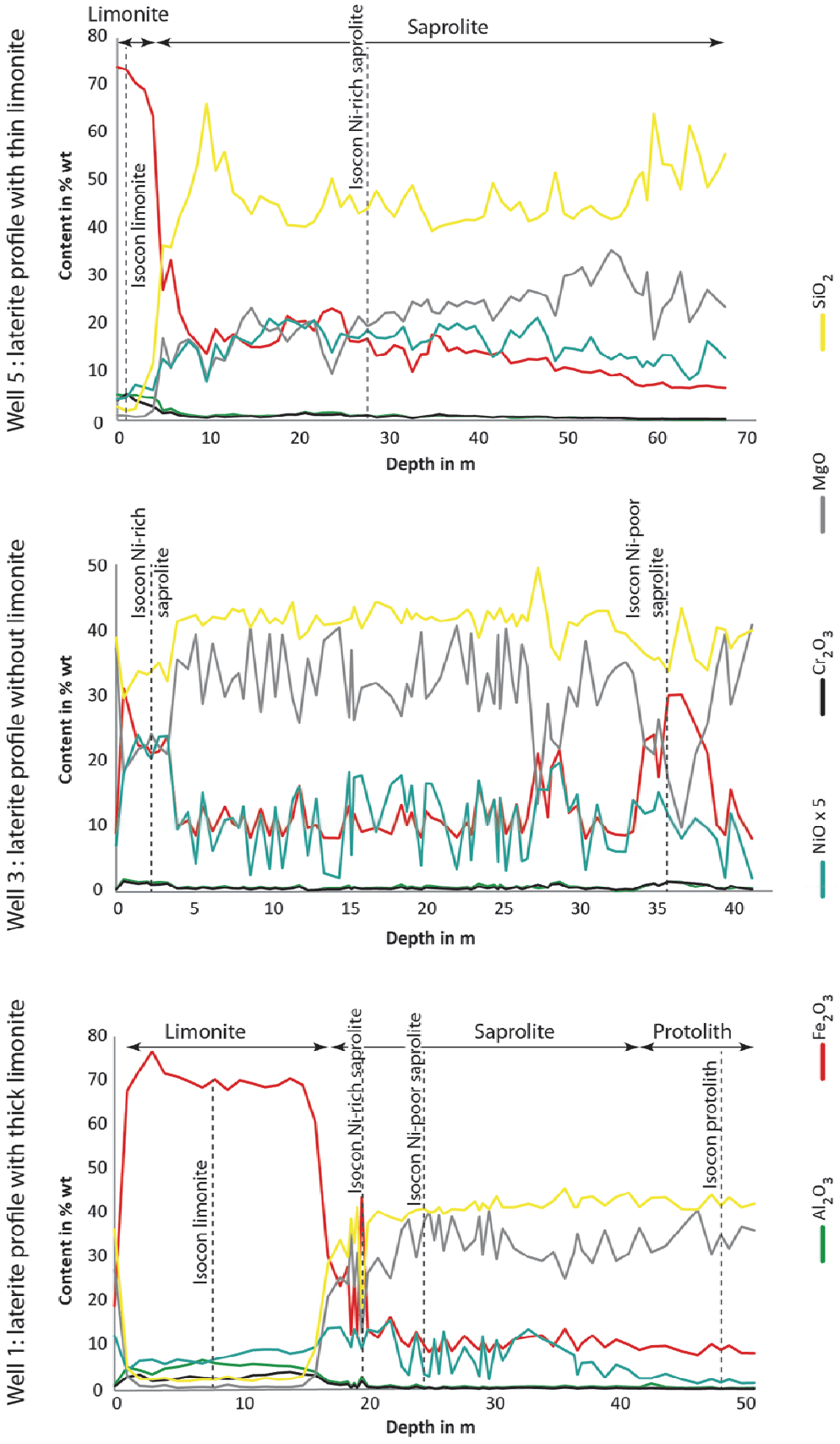

Figure 6 Variation of major and some trace elements through three typical laterite profile differentiated by the variability of the thickness of their limonite cover. The details of the chemical analyses are presented in the Annexe 2. The black dashed lines indicate the several that we consider as representative of limonite, saprolite and protolith composition (see also Annexe 3) and which be used to perform isocon method (Fig. 8).

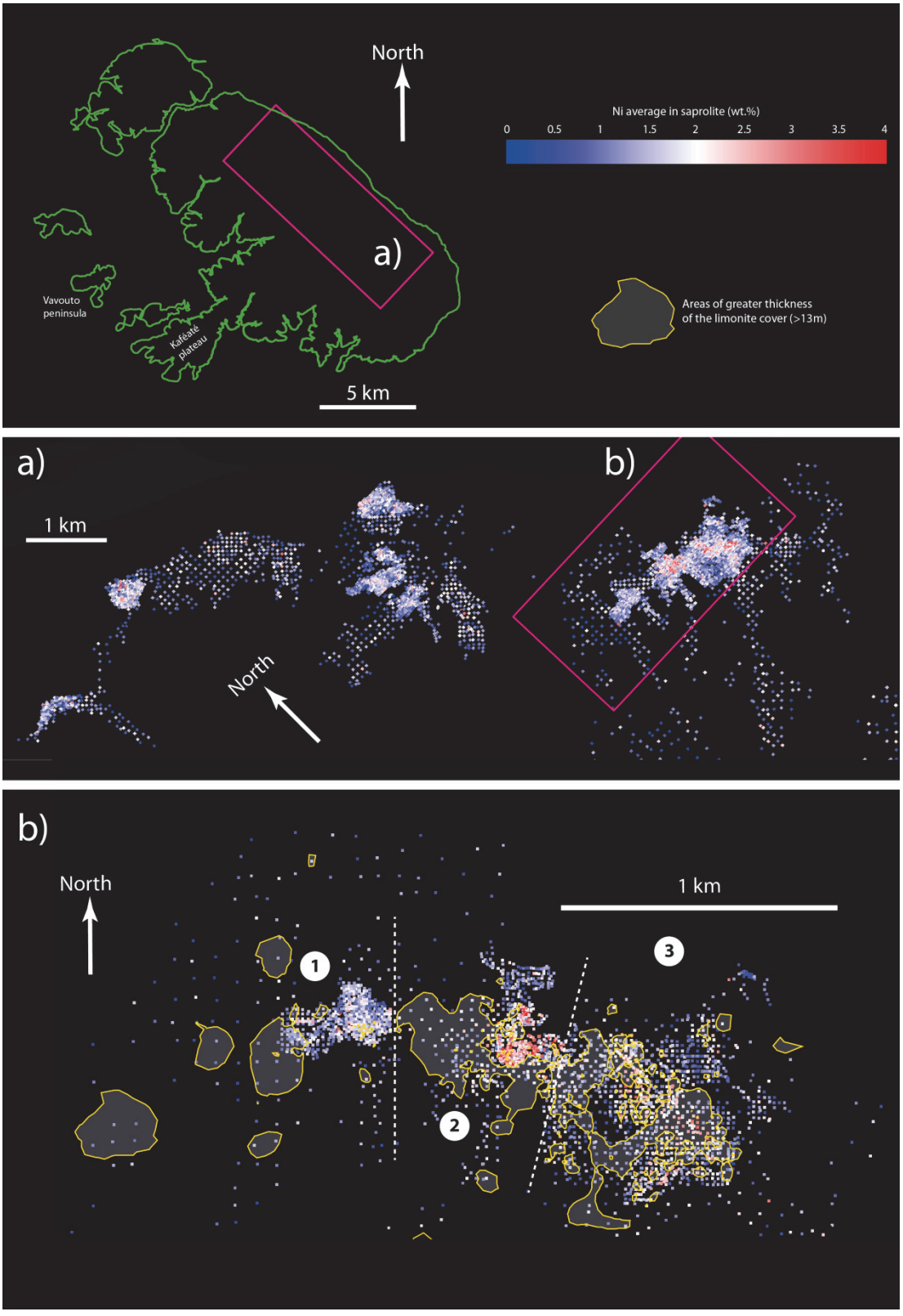

Figure 7 a) Average Ni content in the saprolite calculated for each borehole (each point on the figure) in the main exploited area. b) Focus on the Ni richest area where boreholes distribution is not too variable and where their density is high. The area of maximum thickness of the limonite cover is also represented

low Ni content (<2 wt.%) whereas areas with white to red colour have high Ni content (>2 wt.%). At the scale of the exploited area, the description of the distribution of the low and high Ni content areas remains difficult given that the density of boreholes is laterally highly variable. However, in the areas where boreholes density is high, Ni rich and Ni poor areas are organized as hectometric patches. If focussing on one of the richest areas, where borehole density is high enough and not too variable, we can describe the organization of these hectometric patches at a kilometric scale (Fig. 7c). In addition to the Ni concentration data, we also draw the area of maximum thickness of the limonite cover. At first order, it appears that there is an anti-correlation between the thickness of the limonite cover and the Ni content of the underlying saprolite. We divide this area in three sub-areas (1, 2, 3), as three different cases study, where the relationship between thickness of the limonite cover and Ni content is well expressed. In the sub-area 1, the zone with no limonite cover is slightly enriched in Ni with an average Ni content between ~1.5wt.% and 2wt.%. In the sub-area 2, the enrichment in Ni is extreme with an average Ni content between ~2.5wt.% and 4wt.% in the zone with no limonite cover whereas the average Ni content is around 1.5wt.% under thick limonite cover. Finally, in the sub-area 3, the relationship between thickness and Ni content is more complex with areas rich in Ni localized both under thick and thin limonite cover.

4.3. Behaviour of elements (construction of isocon diagrams)

4.3.1 Methodology

Mass balance calculations were carried out using the approach outlined in Grant (1986, isocon method) and Brimhall and Dietrich (1987). This approach uses the relationships between chemical composition, volume, and density in weathering profiles to quantify the process responsible for Ni enrichment in the laterite. These calculations are made possible at a large scale by extensive measurements of in situ bulk density, and whole-rocks geochemical analysis provided by Konimabo S.A.S. The main limitation of the method is that it is essentially a zero-dimensional model. Notwithstanding these limitations, this approach has been successfully applied to other Ni laterite deposits (Brimhall and Dietrich, 1987; Gleeson et al., 2004; Fu et al., 2014) and can offer some insight into the processes associated with the laterite formation.

The isocon method (Grant, 1986) provides a simple graphical solution to the Gresens' equations (Gresens, 1967). The Gresen's method consists in the analysis of changes in concentration (net gains or losses) of elements during metasomatism of rocks inducing changes in volume and mass.

On the diagram, the isocon is a best line passing through one or several components considered as immobile during the alteration and by the origin. The relative positions of mobile components (NiO, MgO and SiO_2) with respect to the isocon allow discussing their relative enrichment or depletion after weathering of the parent rock.

4.3.2 Choice of an immobile element

The isocon method has been applied to the three wells (1, 3 and 5) corresponding to the three typical lateritic profiles (thick, thin or no laterite cover). We apply the isocon method to several points representative of limonite, saprolite or protolith composition (Fig.8; Annexe 3) for the three studied boreholes. For each borehole, the lowermost sample was considered as the protolith.

One important point is the choice of an immobile element. In the case of harzburgite, Ti, Zr, Th, Al, Cr and Fe are classically considered as immobile elements during weathering (Golightly, 2010). However, Ti, Th and Zr, were not measured, Al and Cr are present in low concentrations in the bedrock and variable. Golightly, (2010) suggests that even if Fe is slightly more mobile than Cr, it may be a reliable invariant for its abundance, its ubiquity and given that its mobility is limited. Indeed, Fe tends to be combined with secondary minerals during laterite formation, as demonstrated by the ubiquitous presence of Fe-oxi-hydroxides. The validity of this assumption may however be questioned since pH and abundance of organic matter are known to increase the transfer of insoluble elements (Ma et al., 2007 and references herein). For instance, Ma et al. (2007), using Th as a immobile element, document a Fe mobility of 40% in the first meter of the laterites profile, decreasing to around 20% in the following few meters. At Koniambo, analyses of present-day water (Jeanpert & Dewandel, 2013) indicate pH condition from 5.5 near the surface to about 10 at depth, either in the laterite or in the serpentinized peridotite. Analyses (Jeanpert & Dewandel, 2013) indicate that Fe is present in surface water, at a content ranging mainly around 0 mg/l but with some analyses reaching 40 mg/l. Locally, waters with Fe contents greater than 50 mg/l have been measured, but marked by the presence of Fe-rich small particles, associated to a leaching of the duricrust. In summary, it is likely

that Fe may display a limited mobility close to the surface. Moreover, the fact that for the three wells Fe and Cr lie along the same isoline (Fig. 8) strengthens the idea that Fe is a valid invariant for mass balance computations.

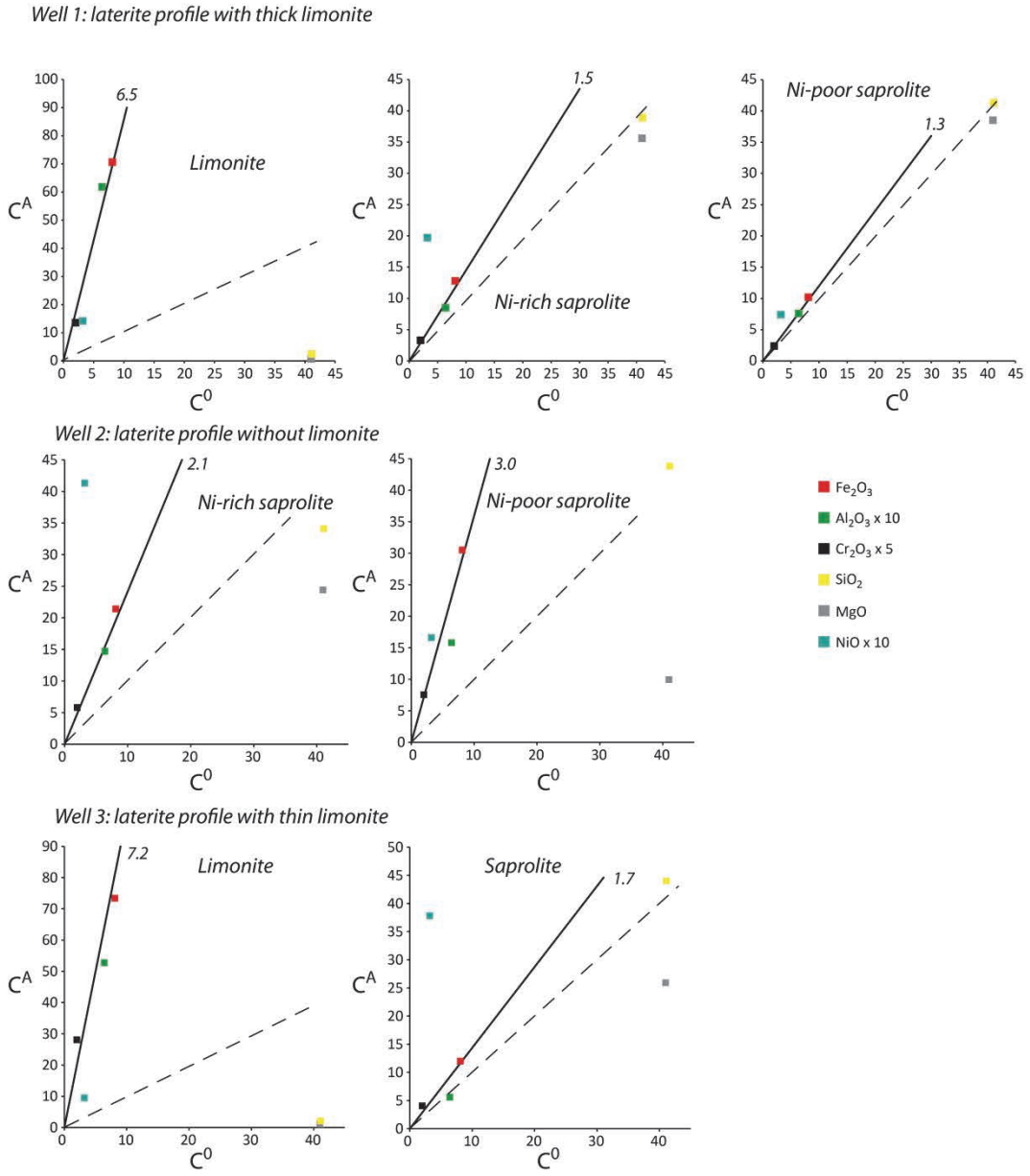

Figure 8 Isocon diagram based on the composition of representative points (localized on the figure 6) of limonite and saprolite for the three typical laterite profiles. The black line represents the isoline drawn to fit at best the points corresponding to invariant elements (Fe, Al, Cr). The number indicates the value of the volume change factor calculated considering Fe as invariant. The black dashed line represents the line of slope 1. The chemical composition of these points is presented in the Annexe 2. The results of the isocon calculation are presented in the Annexe 3.

4.3.3 Elements behaviour along the 1D vertical dimension

Assuming Fe as constant during weathering, it is possible to estimate the variation in volume and the quantitative gain or loss of each mobile element (Fig. 9 and see appendix).

In the limonite cover (well 1 and 5, fig.8; Annexe 3), MgO and SiO_2 are highly depleted with a loss of around 100% with respect to the parent rock. NiO is depleted with a loss of around 50% to 70% with respect to the parent rock. For both wells, the volume change is high, ranging from. 6.5 to 7.2 which means that one meter of limonite results of the weathering of 6.5 to 7.2 meters of peridotite.

In the saprolite, MgO and SiO_2 are systematically depleted whereas NiO is enriched (Fig.8). In details, for MgO, the relative loss ranges from around 25% to 95% and from 20% to 70% for SiO2 (Annexe 3). For NiO, the relative enrichment ranges from 40% to 80% in the so called "Ni-poor saprolite" and between 290% and 460% in the so called "Ni-rich Saprolite" (Fig. 8; Annexe 3). The highest enrichment in NiO is identified in the well 3 and 5 corresponding to saprolite covered by thin or without limonite level. The volume change associated with saprolite formation, ranges from 1.2 to 3, which is smaller than for limonite (Online Resource 2) which is consistent with the fact that saprolite is an intermediate state of alteration.

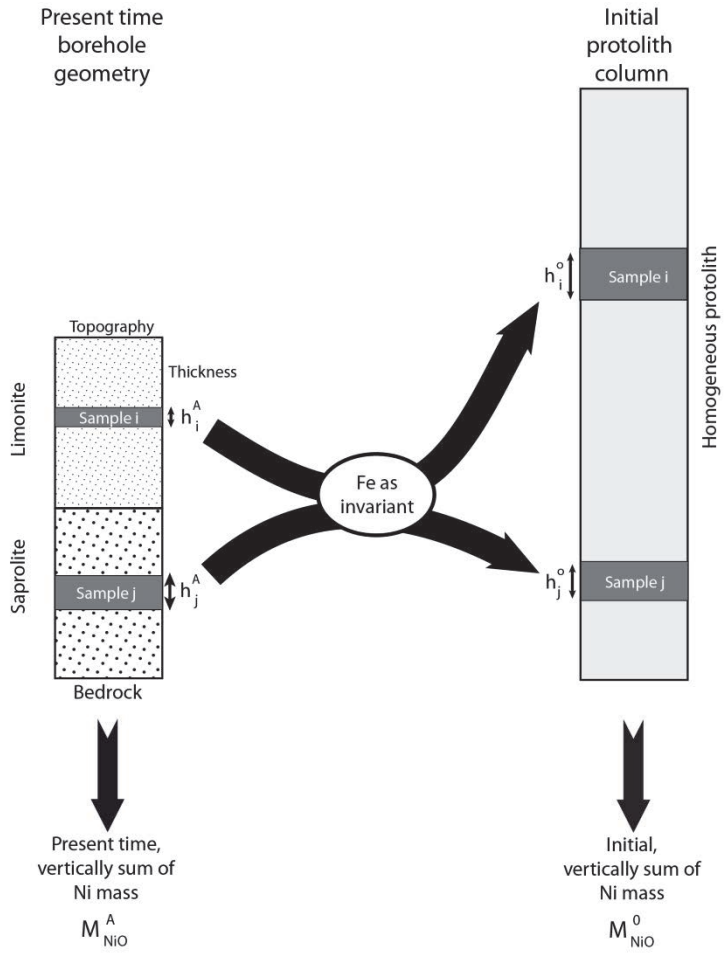

Figure 9 Schematic sketch of the principle of the mass balance calculation performed in this study.

4.4. Ni 1D mass-balance

We applied a 1D (vertical) Ni mass balance calculation (Fig. 9 and appendix) to the whole borehole dataset in order to characterize the Ni distribution at the scale of Ni laterite deposit.

The figure 10b shows the map of the Ni mass balance calculations applied for each of the ~6000 borehole in the main exploited area. The results range between ~5% (maximum loss) and 1300% (maximum gain) (Fig. 11). Two main types of area can be identified. The first areas have a Ni mass balance ranging from ~80% to 120% (in blue) which can be considered as vertically sub-equilibrated, i.e., no Ni is exported laterally from the area. The second areas have Ni mass balance ranging between ~150% and at least 300% (in red), which indicates that they are significantly enriched in Ni compared to the mass of Ni initially contained in the proto-column. These two types of area are organized as

hectometric–sized patches. It is noteworthy that these patches correlate with the distribution of limonite thickness (Fig.4a,b and Fig.10b). Indeed, figure 11 shows that the Ni mass balance tends to be equilibrated when the thickness of the limonite cover increase (Fig. 11). If focussing on the Ni richest areas, where borehole density is high enough and not too variable, the relationship between thickness of the limonite cover and Ni mass balance is particularly well expressed: in areas where Ni mass-balance is sub-equilibrated, the limonite cover is thick (Fig. 10c). Figure 12 shows the distribution of the sub-equilibrated and enriched areas compared to the topography. The Ni-equilibrated areas are localized on topographic highs (sub-areas 1, 2 on figure 12). Inversely, the Ni-enriched areas, under thin or absent limonite cover, are localized in the close vicinity of the Ni-equilibrated areas on slopes (sub-areas 1, 2 on figure 12). The sub-area 3 shows a slightly different geometry where the main equilibrated area is localized on a steep slope and mainly downstream of the enriched areas (figure 12). A first possibility to explain this geometry consists in the late tilting of the whole sub-area 3, and consequently the area with thick limonite cover which could have been initially localized on a high topographic. However, this possibility remains highly hypothetic given that no evidence of faults, along which such movement could have been occurred, are documented. Another possibility consists in the erosion of a thick limonite cover which could have been initially localized on the high topographic part of this area where Ni mass balance indicates, to date, a significant enrichment.

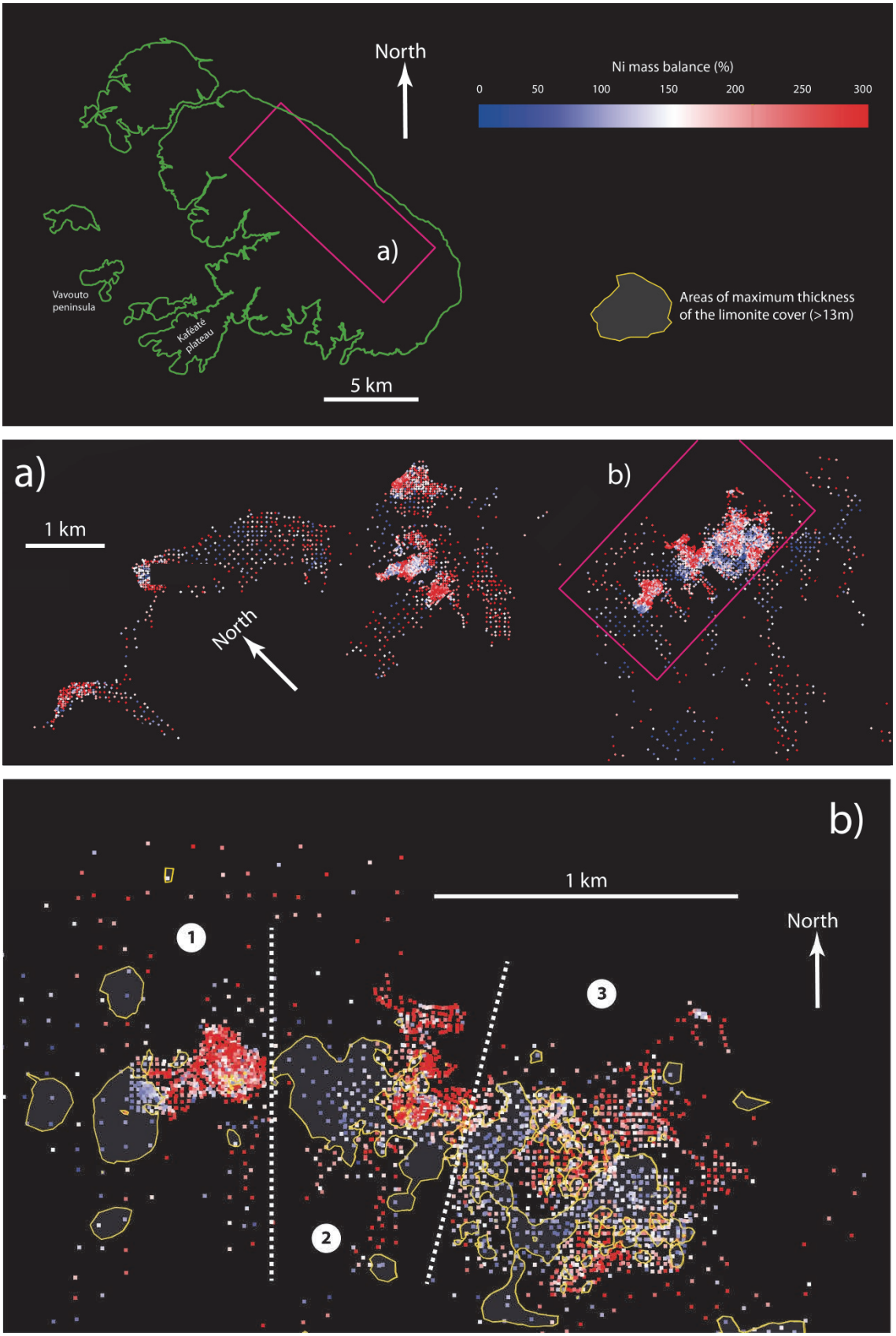

Figure 10 Ni mass balance for each borehole (each point on the figure). The blue color in the 80%-120% interval indicates sub-equilibrated vertical Ni balance whereas the red color indicates areas significantly enriched. Note that Ni mass balance values may be as high as 1300%. a) in the main exploited area. b) Focus on the Ni richest area where boreholes distribution is not too variable and where their density is high. The area of maximum thickness of the limonite cover is also represented.

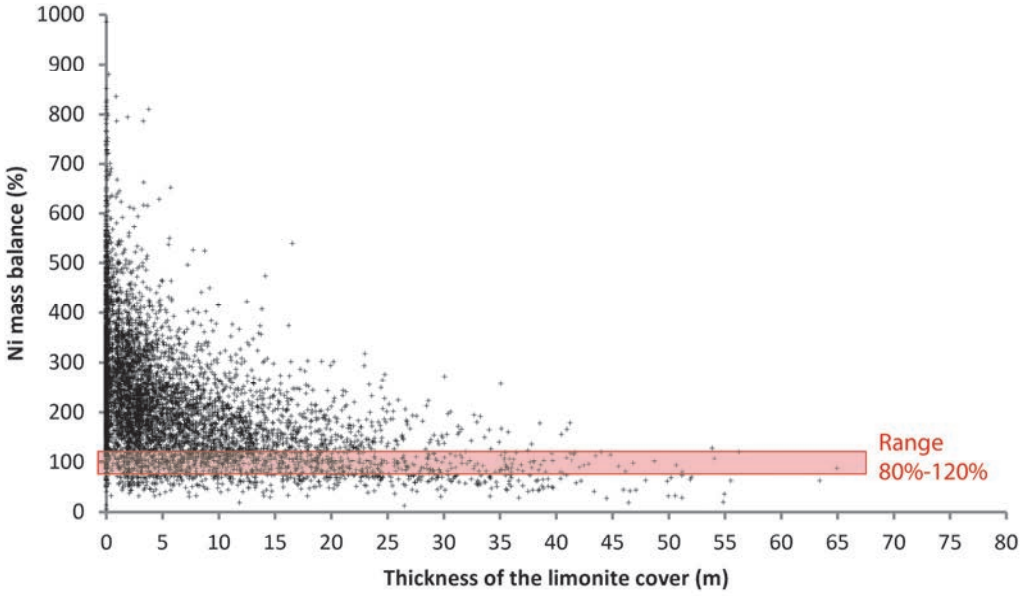

Figure 11 Diagram showing the variation of the Ni mass balance as a function of the thickness of the limonite cover for the whole borehole dataset.

This would give rise to consider that a significant bias in the Ni mass balance calculation remains which requires to reason only in relative and not in quantitative enrichment for the areas with thin or absent limonite cover. Indeed, for the thick limonite cover zones localized on the topographically high areas, it seems reasonable to consider that the laterite profile is, or close to be, complete. Consequently, the Ni mass balance can be consider as a quantitative result given that no or few material was lost by mechanical erosion. However, for the areas with thin limonite cover, mainly localized on slopes, the current thickness must to be considered as a minimal thickness given that these areas have probably been affected by mechanical erosion. The loss of a part of the limonite cover should lead to overestimate the enrichment in Ni compare to the proto-column. Indeed, a loss of 1m of limonite cover means not taking into account the Ni initially contained in a proto-column of around 6-7m (Annexe 3) in the Ni mass balance calculation. This leads to consider the enrichment in Ni in these areas as qualitative information given that, in most of the case, the Ni enrichment is over-estimated.

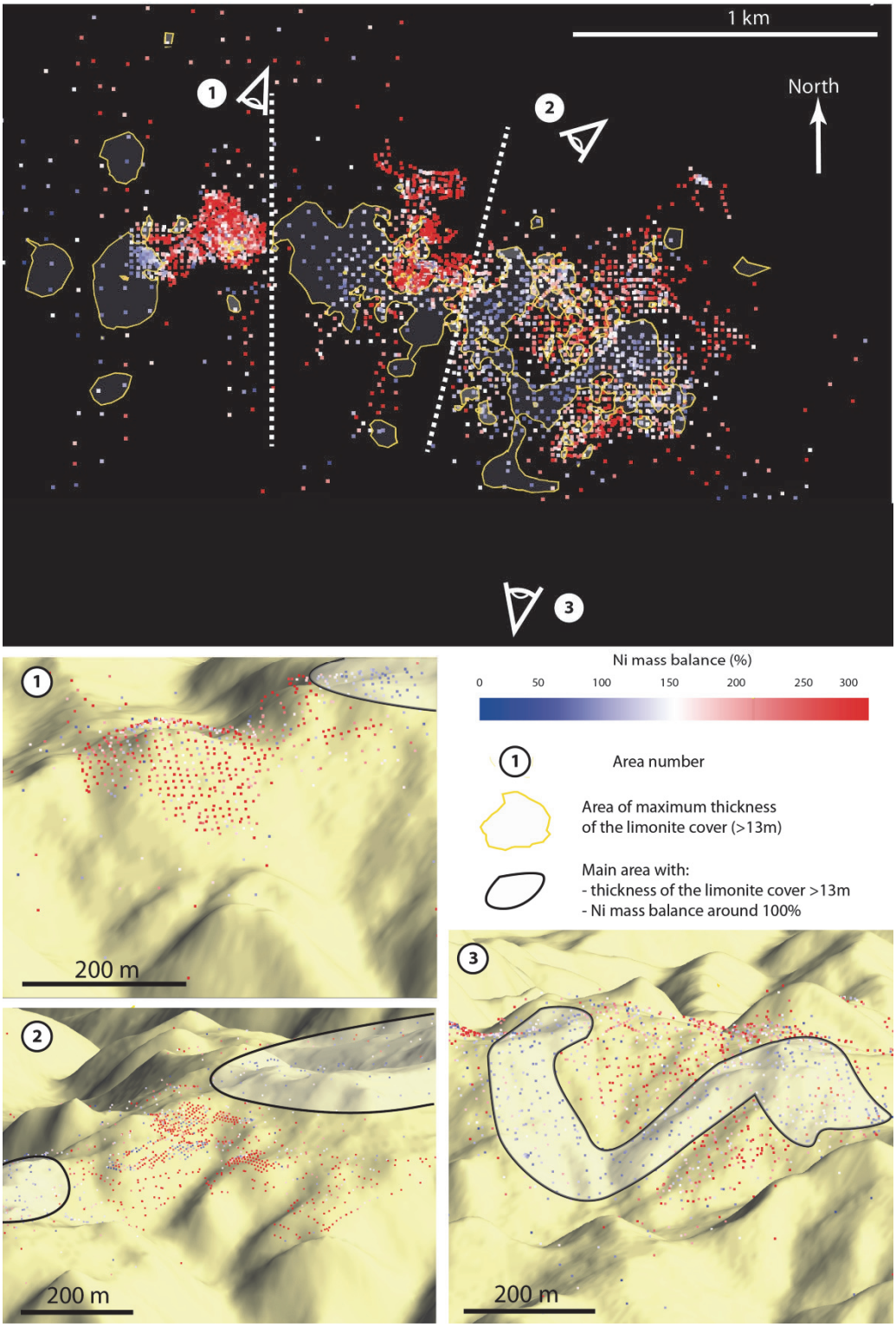

Figure 12 Distribution of the equilibrated and enriched areas determine by Ni mass balance calculation as a function of the topography (1.5 vertical exaggeration).

8. Discussion

8.1 Present day geometry of the lateritic cover

The thickness of the limonite cover varies at different scals. At large scale, its thickness is a function of the slope of the area where it occurs (Fig. 4c1,c2 and Fig. 12). The thickest covers occur mainly on the topographic highs whereas the moderate and thin covers occur respectively on gently and steep slopes. This distribution has already been described in New Caledonia by several authors (de Chetelat, 1947 his figure7; Trescases, 1975 his fig.18; Avias, 1978 his figure.2; Maurizot et al., 2002; Beauvais et al., 2007). It is difficult to estimate the initial thickness of the lateritic cover localized on slopes. First, these profiles are thin and incomplete which is probably the result of erosion (Latham, 1975; Trescases, 1975; Avias, 1978; Beauvais et al., 2007). On the other hand, these laterites are also, at least in part, composed of reworked materials (Latham, 1975; Trescases, 1975; Avias, 1978; Maurizot et al., 2002). This allochtonous material may have derived from the erosion of ancient (and today dismantled) or from present-day thick laterite profiles localized upstream. For the Koniambo massif, given that the present-day thick profiles localized on topographic highs can be considered as nearly complete with no evidences of significant dismantlement (the duricrust is preserved, Maurizot et al., 2002) the first solution seems the most likely. This is consistent with the origin of reworked materials proposed by Beauvais et al (2007) for laterites which occur on slopes of the Thiebaghi Massif (Fig.2).

At smaller scale, the interface between limonite cover and saprolite appears irregular with local depressions of metric to decametric vertical amplitude (Fig.4c1 and Fig. 5a,b). This geometry could reflect variations in density of the network of fractures affecting the bedrocks. Indeed, the intense fracturing of the upper part of the Peridotite Nappe is considered as one of the main parameters which led to karstification of the bedrock (Trescases, 1975; Leguéré, 1976). Consequently, areas with high density of fractures are the most likely to develop an efficient drainage system leading to development of i) preferential dissolution zones leading to karstification and ii) local deepening of laterite profile. Alternatively, Guilloux-Frottier et al. (2015) proposed that exothermic reaction of hydration of olivine could induce fracturing of the bedrock and provide enough temperature to trigger hydrothermal convection. This fluid flow regime may also be at the origin of the observed corrugated geometry of

the limonite/saprolite interface. At larger scale, the limonite-saprolite interface can form endoreic areas (Fig.5c) which can be interpreted as doline where material could be in part autochtonous but also composed of reworked materials derived from erosion of ancient thick lateritic profiles localized in the vicinity (Latham, 1975; Trescases, 1975; Genna, 2005).

The Tiébaghi massif, north of Koniambo (Fig. 2), is known to have a massive and continuous lateritic cover localized on the plateau (Beauvais et al., 2007) whereas the Koniambo lateritic cover is highly dissected by erosion, forming high relief morphology. The massive lateritic cover is also affected by erosion which is mainly localized on the plateau margins (Beauvais et al., 2007). Our 3D model supports the hypothesis that the thick limonite areas have to be extrapolated from one area to the neighbour one. This suggests that these surfaces may represent relicts of a past massive and continuous lateritic cover as the one observed on the Tiébaghi massif.

8.2 Significance of lateral Ni variability

Ni grade in the saprolite level is laterally variable both at large and small scales (Fig.7). At small scale, the Ni grade is organized as patches without clear organization. Several parameters are invoked in the literature to explain such variations. The structure of the bedrock can have an influence on the localization of the Ni mineralization. Areas of high density of fractures likely provide local preferential drainage leading to local deepening of weathering and Ni main concentration. Some major faults can also form barriers to water flow leading to preferential concentration of Ni along them (Leguéré, 1976). On the other hand, Cathelineau et al (2015b) showed that movements of the water table, under the current topographic surface, leads to local redistribution of the nickel initially contained in clusters of veins filled by garnierite through dissolution/redistribution/precipitation processes.

At large scale, our data show that Ni-rich and Ni-poor areas are organized as hectometric–sized patches which broadly correlate with the distribution of the limonite thickness (Fig.7). The richest areas are localized below thin or absent limonite cover whereas the poorest are localized under thickest limonite cover. This is consistent with early observations done New Caledonia by de Chetelat (1947) and Avias (1969) who identified Ni-rich areas under thin or absent limonite cover localized on slopes. This observation has also been reported by Gleeson et al. (2004) for the Ni laterite deposit of Cerro Matoso in Colombia. This result seems paradoxical given that a downward model of Ni mobility is

classically invoked to explain progressive enrichments of saprolite level, Ni coming from the weathered overlying column of rock. Indeed, following this model, a higher enrichment in Ni in saprolite should be expected below the thickest limonitic cover. Three possibilities could explain the unexpected enrichment in zones with thin or absent limonite cover.

The first consists in the fact that laterite profiles localized on slope were affected by erosion and are currently incomplete. The high Ni concentration in these areas could be explained if the initial limonitic cover has been thicker than the thick limonite cover currently preserved on the topographic highs (Fig. 13a). Even if it is impossible to estimate the thickness of eroded material, it seems unlikely that such lateritic profiles have been able to one day develop on where is now slope areas.

The second possibility (Fig. 13b) involves lateral circulations of water enriched in dissolved Ni coming from directly upstream thick laterite profiles occurring in topographic highs. This process has already been evoked for the New Caledonian case based on the fact that karstic network would have been able to enhance such lateral circulations (de Chetelat, 1947; Avias, 1969; Trescases, 1975; Join et al., 2005). The Ni mass balance performed at the deposit scale shows that for areas with complete lateritic profiles, the mass balance is equilibrated with no exportation of nickel (Fig. 10; 12). At first order, this suggests, given that no significant loss of Ni is documented, that lateral circulations of water rich in dissolved Ni is probably cannot be the main process leading to the significant enrichment of saprolite.

We favour a third possibility (Fig. 13c), which implies lateral mechanical transport of Ni-bearing material. Indeed, evidences of reworked materials are identified in thin laterite covers localized on slopes (Latham, 1975; Trescases, 1975; Avias, 1978; Maurizot et al., 2002) and should be an additional source of Ni. Even if erosion is active on slopes, successive input and successive leaching of Ni-rich material, coming from upstream lateritic profiles, could lead to significantly increase the Ni-grade in the underlying saprolite level. This model of nickel enrichment could be tested through a detailed petrological and chemical study focussed on a restricted area including systematic and accurate chemical analyses of immobile elements (Ti, Zr, Th, Al, Cr). Doing so, precise Ni mass balance of both the thick and thin lateritic profiles would be feasible and would allow quantifying i) the variability of reworked material abundance, ii) the variability of its Ni content and iii) the loss of material inherent to erosion process especially on slope areas.

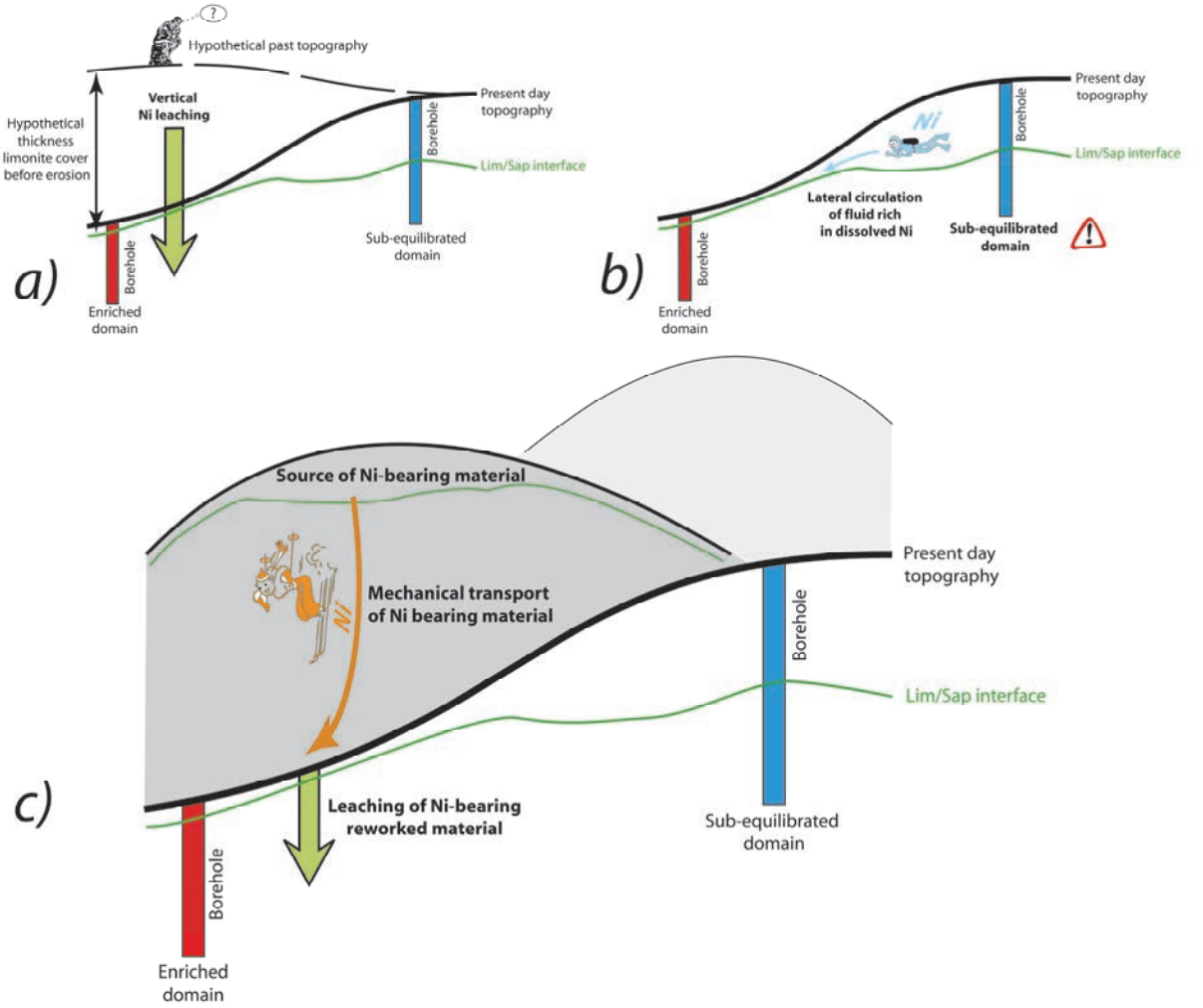

Figure 13 Sketches illustrating the three possibilities invoked in the text (see section 8.2) to explain the unexpected Ni enrichment in the saprolite from the slope. Based on our results, we propose that process c) is probably the most relevant.

Conclusion

On the Koniambo massif, two types of lateritic profiles can be recognized. The first type is thick and nearly complete profiles, localized on topographic highs, are . The second type is localized on gently slope and are thin and incomplete. Contradictorily to what it is expected following the classical *per descensum* model of Ni laterite ore deposit formation, we show that the Ni-richest areas are localized under thin or absent limonitic cover. Based on the Ni mass balance performed for each borehole on a kilometric scale area, we propose that successive lateral transfer and leaching of

reworked Ni-bearing material, from high topographic areas to downstream slope areas, is the main process leading to significantly increase the Ni-grade in the underlying saprolite level.

Appendix

1. Mass balance with Isocon method

The use of an Isocon diagram (Grant, 1986) allows visualizing the relative concentration changes of different components of a parent rock after its alteration. The isocon method consists in a rearrangement of the Gresen's equations as a linear relationship between the concentration of a component in the altered rock and that in the unaltered protolith. On the diagram, the Isocon line is a best line passing through one or several components considered as immobile during the alteration of the rock and by the origin. If it is assumed that Fe is invariant (see part 4.3 for more details), the relative variation in concentration of others elements in a sample is given by the equation:

$$\left(\frac{\Delta C_i}{C_i^O}\right) = \left(\frac{C_{Fe_2O_3}^O}{C_{Fe_2O_3}^A}\right)\left(\frac{C_i^A}{C_i^O}\right) - 1 \qquad (1)$$

where

- Superscripts *O* and *A* are used for the original (protolith) and altered (final) samples, respectively,
- C_{i}^A and C_{i}^O are the concentrations of altered rock and protolith respectively of the ith element,
- $\Delta C_i = C_{\mathrm{i}}^A - C_{\mathrm{i}}^0$,
- $C_{Fe_2O_3}^A$ and $C_{Fe_2O_3}^O$ are the Fe concentrations of altered rock and protolith respectively.

Then, the mass change may be expressed as:

$$\left(\frac{M^A}{M^O}\right) = \left(\frac{C_{Fe_2O_3}^O}{C_{Fe_2O_3}^A}\right) \qquad (2)$$

where M^A and M^O are respectively the mass of sample and the reference mass of protolith sample.

Similarly, the volume change may be expressed as:

$$\left(\frac{V^A}{V^O}\right) = \left(\frac{M^A}{M^O}\right) . \left(\frac{\rho^O}{\rho^A}\right) \quad (3)$$

where ρ^A and ρ^O are respectively the volume of sample and the reference mass of protolith sample.

2. 1D vertical Ni Mass balance

The Ni mass balance is calculated by comparing for each borehole the present-day Ni mass in the laterite with the Ni mass in the estimated original column, assuming a purely 1D vertical process.

The first step consists of calculating the mass of Ni contained in the entire lateritic column of each borehole by summing the mass of Ni contained in the different sampled levels. For each borehole, the current mass of Ni contained in the entire altered column (limonite + laterite) M^A_{NiO} is given by:

$$M^A_{NiO} = \sum_{samples\ i} \frac{\rho^A(z_i) V^A(z_i) C^A_{NiO}(\mathrm{z_i})}{100} \quad (4)$$

where z_i is the altitude of the ith sample in the borehole, $\rho^A(z_i), V^A(z_i)$ and $C^A_{NiO}(\mathrm{z_i})$ are respectively, the density, the volume and the nickel concentration of that sample. We considered a horizontal section of 1 m^2, so the volume $V^A(z_i)$ of each sample is 1x1x$h^A(z_i)$ with $h^A(z_i)$ the thickness of the sampled level.

The second step consists in calculating the mass of Ni contained in the proto-column that we consider to be composed of harzburgite partially serpentinized with the following characteristics:

$$\rho^o = 2250 \text{ kg.m}^{-3}$$

$$C^O_{Fe_2O_3} = 8.1 \text{ wt.\%}$$

$$C_{NiO}^{0} = 0.2 \; or \; 0.3 \text{ wt.\%}$$

The initial mass of Ni contained in the proto-column M_{NiO}^{O} is calculated using the following equation:

$$M_{NiO}^{O} = \sum_{Samples} \frac{V^{O}(z_i)\rho^{O}C_{NiO}^{O}}{100} \quad (5)$$

where ρ^{O} and C_{NiO}^{O} are respectively, the constant density and the nickel concentration in the proto-column given just above. $V^{O}(z_i)$ is the initial volume the ith sample, 1x1x$h^{O}(z_i)$ where $h^{O}(z_i)$ is the initial thickness, calculated assuming Fe is invariant by the following the equation (see Fig. 9).:

$$h^{O}(z_i) = \frac{C_{Fe_2O_3}^{A}(z_i)h^{A}(z_i)\rho^{A}(z_i)}{C_{Fe_2O_3}^{O}\rho^{O}} \quad (6)$$

The last step consists in comparing the Mass of Ni respectively contained in the current column and the proto-column as:

$$\Delta M = \frac{M_{NiO}^{A}}{M_{NiO}^{O}} \quad (7)$$

As the balance is integrated over the vertical column of each borehole, $\Delta M \cong 1$ indicates that Ni is vertically balanced for the corresponding borehole. By contrast, $\Delta M > 1$ indicates a gain of Ni whereas $\Delta M < 1$ indicates a loss of Ni from the estimated original protolith column. In these last cases, this means that lateral transfers of Ni – either chemical or physical – must be invoked.

Partie III : Chapitre 1 – Le niveau saprolitique, zone clé de la redistribution élémentaire par l'altération supergène

Résumé de l'article #2

Au sein du gisement de nickel latéritique de Nouvelle-Calédonie, le minerai le plus riche consiste en des veines composées de silicates nickélifères remplissant des fractures au sein du niveau saprolitique, mais également au sein de péridotites non-altérées. Ces veines ont des teneurs fortes en nickel dépassant d'au moins quelques pourcents la teneur moyenne exploitée (2.5 wt.%). Ces dernières sont généralement localisées de quelques dizaines de mètres à une centaine de mètres sous la surface actuelle, au niveau de la zone de battement de nappe, et sont affectées par des processus de dissolution-précipitation. Le nickel mis en solution re-précipite sous forme de films composés de silicates cimentant des espaces ouverts étroits affectant les blocs de roche. Cette minéralisation présente une zonation chimique et minéralogique de forme concentrique avec une bordure verte et une partie centrale blanche, composée, de la bordure vers l'intérieur du bloc,

i) d'une zone fortement oxydée et altérée,
ii) d'une zone riche en nickel composée de pimélite pure de couleur verte,
iii) d'une zone de couleur intermédiaire (limitée à quelques centimètres) composée d'un mélange de kérolite pauvre en nickel et de pimélite
iv) et d'une large zone composée de kérolite magnésienne de couleur blanche.

Cette étude propose que la zonation concentrique soit le résultat d'un processus d'évapo-précipitation dont le moteur est l'alternance de périodes d'hydratation et de déshydratation induites par le mouvement du niveau hydrostatique. Cette large dispersion du nickel pourrait en partie expliquer la teneur en nickel plutôt monotone de la zone exploitée à la base du régolithe avec des teneurs souvent comprises entre 2wt.% et 3wt.%.

Miner Deposita
DOI 10.1007/s00126-015-0607-y

ARTICLE

Nickel dispersion and enrichment at the bottom of the regolith: formation of pimelite target-like ores in rock block joints (Koniambo Ni deposit, New Caledonia)

Michel Cathelineau[1] · Benoît Quesnel[2] · Pierre Gautier[2] · Philippe Boulvais[2] · Clément Couteau[3] · Maxime Drouillet[3]

Received: 5 November 2014 / Accepted: 23 July 2015

Abstract In New Caledonian Ni deposits, the richest Ni silicate ores occur in fractures within the bedrock and saprolite, generally several tens of meters to hundred meters below the present-day surface. Fracture-related Ni silicate ore accounts for high Ni grades, at least a few weight percent above the average exploited grade (2.5 %). These Ni-rich veins are affected by active dissolution-precipitation processes at the level of the water table. Ni in solution is precipitated as silicates in thin layer cementing joints. This mineralization is characterized by chemical and mineralogical concentric zoning with an outer green rim around an inner white zone composed, from the edge to the centre of the block, (i) a highly oxidized and altered zone, (ii) a green pure Ni-rich pimelite zone, (iii) a zone (limited to a few centimetres) with a mixture of Ni-poor kerolite and Ni-rich pimelite and intermediate colours and (iv) a large white Mg-kerolite mineralization zone. This study proposes that the concentric zonation results from evapo-precipitation process related to alternate periods of hydration and drying, induced by water table movements. This extensive dispersion of Ni in concentrically zoned ores can partly explain the rather monotonous Ni grade of the bulk exploitation at the base of the regolith with values between 2 and 3 wt%.

Keywords Kerolite-pimelite · Garnierite · Ni-laterite · New Caledonia · Dissolution-precipitation

Editorial handling: T. Bissig and G. Beaudoin

✉ Michel Cathelineau
michel.cathelineau@univ-lorraine.fr

✉ Benoît Quesnel
benoit.quesnel@univ-rennes1.fr

[1] Université de Lorraine, GeoRessources Laboratory, CNRS, CREGU, BP 70239, F-54506 Vandoeuvre-lès-Nancy, France

[2] Géosciences Rennes, Université Rennes 1, UMR 6118 CNRS, 35042 Rennes Cedex, France

[3] Service géologique, Koniambo Nickel SAS, 98883 Voh, Nouvelle Calédonie, France

Introduction

Nickel silicate ores are generally thought to be closely associated with the weathering of peridotite leading to the formation of laterite profile (Trescases 1975; Schellman 1983; Gleeson et al. 2003; Freyssinet et al. 2005; Villanova-de-Benavent et al. 2014). In New Caledonia, the main ore genetic model for Ni ores is based on a single *per descensum* model where most elements (Mg, Ni and Si) are leached from the surface (Trescases 1975; Troly et al. 1979; Pelletier 1983, 1996). Nickel is then concentrated either in the fine-grained laterite where goethite is the main Ni bearer, the so-called lateritic ore (Manceau et al. 2000; Dublet et al. 2012), or below the laterites sensu stricto in the regolith as mixtures of hydrous Mg-Ni silicate and goethite, the so-called saprolite ores (Dublet et al. 2012). Ni-rich silicates also occur as fracture fillings, sometimes considered as syn-tectonic (Cluzel and Vigier 2008). These veins are filled with "garnierite", which is a term used for a mixture of different Ni silicates: mainly the kerolite-pimelite series, also called talc-like, as well as sepiolite and Ni-serpentine, also called "serpentine-like" (Brindley and Hang 1973; Springer 1974; Brindley and Maksimovic 1974). In most studies, Ni-rich silicates were described in detail using a series of appropriate analytical tools (X-ray diffraction (XRD) and infrared spectroscopy (IR) in some cases in combination with microprobe studies (Brindley and Hang 1973; Brindley and Maksimovic 1974; Brindley and Wan 1975; Brindley et al. 1977, 1979; Wells et al. 2009; IR:

Published online: 09 August 2015

Gerard and Herbillon 1983), extended X-ray absorption fine structure (EXAFS; Manceau and Calas 1985, 1986; Manceau et al. 1985) and some pioneer Raman works (Villanova- de-Benavent et al. 2012). Very few recent studies of Caledonian ores are available, apart those from Wells et al. (2009), Dublet (2012) and Cathelineau et al. (2015). Generally speaking, the geometric, time-space and paragenetic description of the ores is lacking.

Ni silicate ores have not been studied in detail at the Koniambo mining site (Fig. 1), which was recently re-opened as part of the Koniambo Nickel project, with the exception of the descriptions provided by Fandeur (2009). Recent observations in the new open pits have shown that two main types of Ni silicate occur. The first type (type 1) consists of mineralized faults and fractures filled by Ni silicates a few centimetres to decimetres in width, typically corresponding to what is described elsewhere in New Caledonia. These veins are filled by Ni-Mg kerolite-pimelite solid solution (as defined by Brindley et al. 1977). These minerals were described by Wells et al. (2009) at Goro (southern New Caledonia, Fig. 1) and Dublet (2012) at Koniambo. The Ni-Mg kerolite-pimelite series is characterized by a light greenish-blue colour. They correspond to the so-called garnierite fracture infilling considered as syntectonic by Cluzel and Vigier (2008). In the case of Koniambo, the term garnierite seems inappropriate, as the fracture ores are not mixtures of several Ni-rich silicates such as serpentine, kerolite and sepiolite as expected for garnierite but instead are only filled by bluish kerolite. The second type (type 2), which has not been described so far, consists of chemical and mineralogical concentric zoning, similar to a shooting target, and characterized by an outer green rim around an inner white zone coatings on joint planes that occur in the upper part of the open pits. The concentric zonation consists, from the edge to the centre of the joint, (i) a highly oxidized and altered zone, (ii) a green zone, (iii) a zone (limited to a few centimetres) with an intermediate colours and (iv) a large white zone. As there are now exceptional outcrops in the Koniambo Nickel mining area where two Ni ore types can be observed, a detailed structural and mineralogical study of the main ores has been carried out, especially on the so-called Cagou pit within the Koniambo mining domain (Fig. 1). The main objective of this study is to understand the genetic process of target-like ore formation. We determined the detailed mineralogy of the target-like ores and documented the geometric and time-space relationships between the two ore types at the field scale. We provide a new conceptual model of the Ni distribution, which takes into account the contribution of the two types of Ni silicates to the bulk grade of the exploited ore at the base of the regolith.

Geological setting

New Caledonia, in the SW Pacific, is an island characterized by the presence of significant relicts from the obducted peridotite nappe overlying basement formations from the Norfolk Ridge micro-continent (Fig. 1). Today, the Peridotite Nappe is essentially exposed in the *Massif du Sud* covering much of the

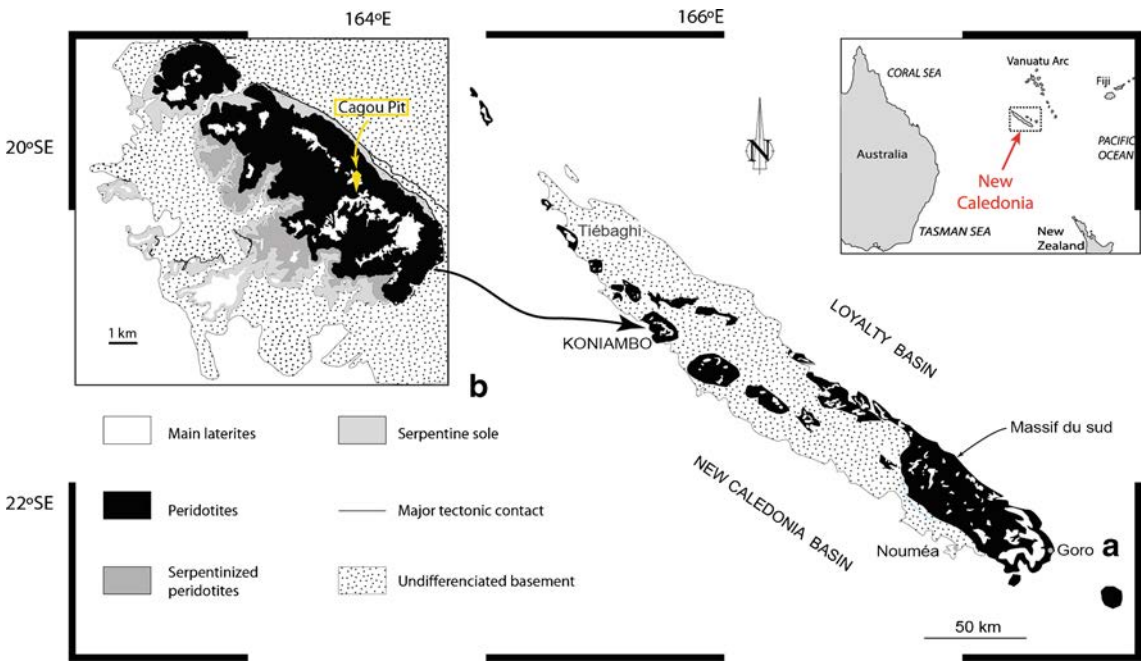

Fig. 1 **a** Simplified geological map of New Caledonia modified after Cluzel et al. (2001). The laterites are compiled from Paris (1981). **b** Geological map of the Koniambo massif modified after Maurizot et al. (2002). The *yellow diamond* indicates the location of the study site (Cagou pit from the Koniambo Nickel mining company) in the Koniambo massif

south-eastern third of the Grande Terre and as klippes along the north-western coast, including the Koniambo massif (Fig. 1). The south-westward emplacement of the Peridotite Nappe is considered to have occurred between 37 and 27 Ma (Cluzel et al. 2001, 2012; Paquette and Cluzel 2007; Maurizot et al. 2009). Outcropping peridotites then quickly underwent strong water-rock interactions under a hot and humid climate, favouring the formation of a thick laterite cover (Fig. 1; Trescases 1975). Laterite formation consists of the progressive dissolution of all silicates found in dunite and harzburgite (e.g. olivine and orthopyroxene) and the development of residual laterite, containing insoluble elements such as trivalent iron re-precipitated as goethite and/or hematite, and relicts of magmatic chromite. The accumulation of goethite over a significant period of time produced a 5 to 50 m deep profile including a lateritic duricrust and a plasmic horizon over a ferruginous saprolite, following the terminology from Butt and Cluzel (2013). Palaeomagnetic ages (around 25 Ma) obtained on lateritic duricrust from the Thiebaghi area (location in Fig. 1) suggest that the main laterite formation took place rather early, from the late Oligocene to the Miocene (Sevin et al. 2012).

Presently, the hydrologic and topographic features of the outcropping peridotite nappe are likely different to those of the main laterization stages. Mechanical erosion, helped by the constant hydrolysis of the peridotite minerals, predominates in topographically high areas, favoured by high orographic rainfall, with precipitation ranging from 2500 to 4000 mm (Printemps et al. 2007; Terry and Wotling 2011).

The Koniambo massif has been exploited intermittently since the end of the nineteenth century and particularly at the end of the twentieth century by SMSP. In 1998, the Koniambo Nickel project was started as part of a SMSP-Falconbridge venture and was followed by the industrial project conducted by SMSP-XSTRATA Nickel after 2007. Koniambo hosts around 158.6 million tonnes of saprolite that grades 2.47 wt% Ni at a cut-off grade of 2 wt% (Xstrata 2012).

The Koniambo massif is characterized by hills culminating at 930 m and steep slopes. At Koniambo, as in other parts of New Caledonia, the distribution of alteration facies does not follow the simple flat geometric distribution of the lateritic profile. The saprocks are overlain by oxidized horizons, mostly ferruginous saprolite. Above the ferruginous saprolite, on topographic highs, around 850 m above sea level, relicts of weathering profiles are preserved. The remnants of the lateritic profile, such as lateritic duricrust or pisolitic horizons as well as the plasmic horizon, are discontinuous and are in part redistributed due to slope effects following the degradation process affecting the laterite profile described elsewhere in New Caledonia (Chevillotte et al. 2006). The recent to present-day conditions are characterized by active dissolution processes which are remarkably illustrated by dissolution pipes within hard serpentinized peridotite. Highly transmissive karstic networks occur at depth. The local collapse is marked by sinkholes in the topography, as already observed elsewhere in New Caledonia (Trescases 1975; Genna et al. 2005). To summarize, two distinct conditions explain the geometric distribution of the alteration facies: (i) the present-day conditions, which mostly results in the dissolution and oxidation of the serpentinized ultrabasic rocks in a dynamic system which excludes the formation of a laterite profile due to permanent erosion, and (ii) older (Cenozoic) conditions which produced the lateritic profile. These profiles are almost entirely disturbed due to the competing effects of erosion and uplift and the subsequent flowing and reworking.

The studied zone, the Cagou pit (Fig. 1), is an open pit which provides a good cross-section of the lateritic profile including the bedrock, saprock and lower part of the ferruginous saprolite. As in all of the upper part of the Koniambo massif, the bedrock and saprocks are highly fractured. Some fractures and joints in the saprock contain Ni-Mg hydrous silicates (Fig. 2a, b). The ferruginous saprolite above the saprock contains significant Ni concentrations, which are related both to oxihydroxides (Ni-goethite) and a fine-grained Ni silicate, inferred as a Ni-rich serpentine (Dublet et al. 2012). These authors indicated that it is almost impossible to precisely identify this Ni silicate phase, even using EXAFS.

Materials and methods

Field studies and sampling

A structural description and measurements of most joints and fractures were carried out in the Cagou pit based on the systematic profiles along the approximately E-W pit face. Representative samples were taken in fractures, as well as on joints presenting the target-like ores, some of which are shown in Fig. 2. The target-like ores consist of thin layers, generally less than 500 μm thick. Therefore, most of the analytical works were carried out on sufficiently thick layers prepared as polished sections, with the exception of the Raman analysis which can be performed, without any preparation, on most samples.

Analytical techniques

The studied minerals are very fragile, and therefore, it was difficult to make polished thin sections. The layers were thus embedded in resin to establish the mineral paragenesis. We used a conventional reflected light microscope and scanning electron microscope (SEM), a JEOL equipped with an energy dispersive spectrometer using a Si(Li) semi-conductor detector and a HITACHI S-4800 SEM at SCMEM (Nancy, France). Minerals were identified based on the combined consideration of in situ chemical data using both semi-quantitative energy

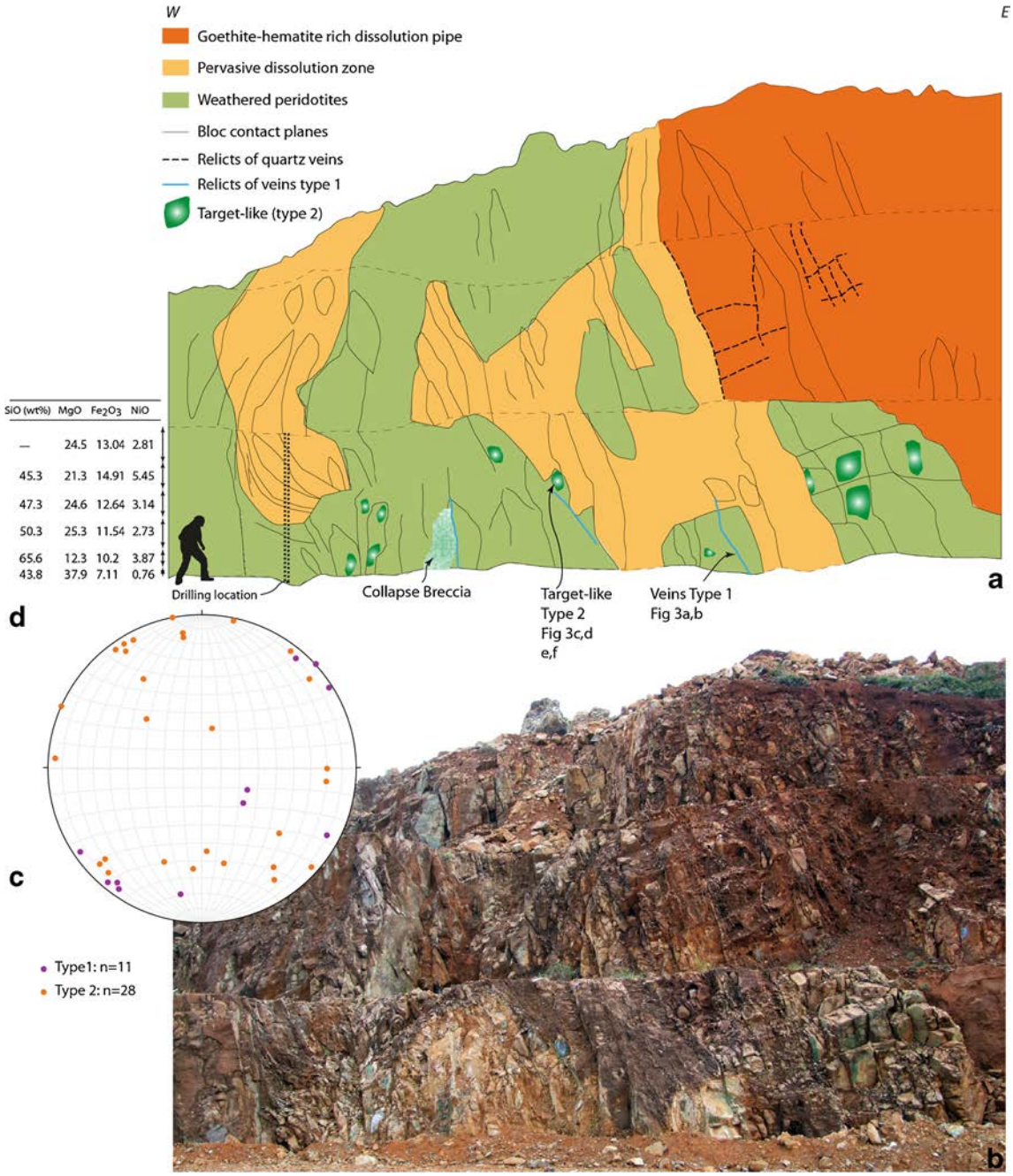

Fig. 2 **a** Sketch summarizing field observations on the studied cross-section in the Cagou pit. The *green*, *yellow* and *orange* colours represent the zones variously affected by dissolution and oxidizing processes. The location of the type 1 and type 2 ores is also reported. **b** Field view of the studied cross-section in the Cagou pit (Fig. 1). **c** Equal-area lower hemisphere stereographic projection of the kerolite veins and target-like bearing joints at the open pit scale. **d** Whole rock major element distribution along a drill hole located along the *dashed line*. Each chemical composition is representative of a given thickness of rock represented on the sketch by a *double black arrow*

dispersive (EDS) data using SEM and a quantitative analysis using an electron microprobe (EMPA), transmission electron microscopy data (TEM), and Raman spectroscopy data.

Electron microprobe analyses (EMPA) of the kerolite were performed at SCMEM (Nancy, France). Si, Al, Fe, Mn, Mg, Co, Ni and Na were analysed using a CAMECA SX100 instrument equipped with a WDS and calibrated using natural and synthetic minerals or compounds such as albite (Si, Na), Al_2O_3 (Al), olivine (Mg), hematite (Fe), $MnTiO_3$ (Mn), Co (Co) and NiO (Ni). Only traces of Al, Mn, Co and Fe were found. The analytical conditions were a current of 12 nA, an accelerating voltage of 15 kV and a counting time of 10 s (and 30 or 60 s for Ni in Ni-poor kerolite). The analyses have a spatial resolution of 1 to 2 μm. The total Fe is presented as FeO. Structural formulae of kerolite-pimelite were calculated arbitrarily on the basis of 22 negative charges per half unit cell,

i.e., an $O_{10}(OH)_2$ base, because the TEM observations and XRD data have not shown any other mineral layer than the kerolite-pimelite series. IMA's 50-50 rule for solid solution was applied, e.g., kerolite was used from a Ni/Ni + Mg ratio of 0 to 0.5, and pimelite from a ratio of 0.5 to 1, although the solid solution, in particular for ore type 1 consists of nearly continuous Ni/Ni + Mg ratios in between 0.2 and 0.7. The tetrahedral sheet was assumed to be filled with Si. The octahedral sheet was filled with Ni and Mg.

TEM photomicrographs, energy dispersive spectra and electron diffraction patterns were obtained on dried powder samples dispersed in ethanol and deposited on a micro grid (Formvar/Carbon 300 Mesh Ni, Agar Scientific, Essex, England). The Philips CM20 TEM operated at 200 kV and was equipped with an ultrathin window X-ray detector.

Raman spectra were recorded using a LabRAM HR spectrometer (Horiba Jobin Yvon) equipped with an 1800 g mm^{-1} grating and an edge filter. The confocal hole aperture was 500 μm, and the slit aperture was 50 μm. The excitation beam was provided by a Stabilite 2017 Ar^+ laser (Spectra Physics, Newport Corporation) at 514.53 nm and a power of 200 mW, focused on the sample using a ×50 objective (Olympus). The spot size was less than 1 μm. The acquisition time was limited by a weak luminescence, ranging between 2 and 6 s. The number of accumulations was set between 10 and 30 in order to optimize the signal-to-noise ratio (S/N).

Results

Mode of occurrence of the ores in the field

Figure 2b shows an E-W oriented profile in the Cagou pit, which shows the dissolution-oxidation front (reddish-brownish colours) and the underlying bedrock (whitish-pale brown serpentinized basic rocks). The overall saprock is affected by extreme fracturation, which is dominated by opened networks of subvertical discontinuities, connected with low angle joints. The main alteration zones and ore types are described below from the bottom of the regolith to the bedrock, based on Fig. 2a, b.

In the yellow zone, highly microfissured rocks have undergone significant rock dissolution. This is where hydrolysis of the main silicates that constitute the peridotite protolith (serpentine and relicts of olivine) takes place. The silica dissolved from the upper levels recrystallizes here as numerous quartz layers and microfissure infillings, explaining the high local SiO_2 contents (50 to 60 wt%). In the orange zone, saprocks are impregnated by iron oxihydroxides among which Ni-goethite is the predominant Ni-bearer, as already described in the Koniambo saprolitic horizons by Dublet et al. (2012). In the green zones, which are less affected by oxidation and dissolution, two types of joints and fractures bearing Ni silicates are observed: (i) fractures with kerolite-pimelite infillings (ore type 1) and (ii) target-like joints (ore type 2). A collapse breccia is also observed and corresponds to a pipe filled by centimetres to decimetres rock blocks that fell down into the pipe and were partially cemented by quartz and Ni-rich pimelite.

Figure 2c is the stereographic projection of the dip and direction of the discontinuities filled by the two main silicate ore types. Type 1 discontinuities split into two families with a strike close to N150 with a dip ~85 E-W for the first and close to N50 with a dip range between 30 N-W and 80 N-W for the second. Type 2 ore-bearing joints occur in nearly cemented joints without systematic strike and dip. They constitute planes in which longest length ranges from 30 cm to 1 m, rarely more than 1 m, and occur in the vicinity of the type 1 ore-bearing fractures. These target-like ore joints are revealed during exploitation of the open pit when rock blocks are broken by excavators. This observation possibly indicates that these mineralized joints represent closed and filled fractures. When opened during quarrying, target-like ores are quickly altered by present-day meteoric waters, hydrolysis inducing rapid mechanical and chemical degradation.

Figure 2d provides the NiO concentrations along a drill core, located on the studied profile (Fig. 2a) and taken before the pit was exploited. The NiO content ranges from 2.7 to 5.4 wt% in the main zone of the target-like occurrences.

Textural description of the ores

Type 1 ores consist of centimetres to decimetres thick fracture infillings containing mostly kerolite-pimelite solid solution (Fig. 3a). It may be affected later on by the reopening of the vein and sealing by red to brownish microcrystalline quartz and clear quartz microfractures. The texture of the kerolite-pimelite filling consists of successive botryoidal growth bands of bluish-green colour similar to those described in Villanova-de-Benavent et al. (2014) for type IV garnierite in Dominican Republic ores. *Type 2* target-like Ni ores occur exclusively as a layer in thin joints. Their extension ranges from a few decimetres to 1 m (Fig. 3c, d), corresponding to the average size of the rock blocks occurring within the first hundred meters below the surface (Fig. 2b). In the joint plane, pimelite is present as a green rim, whereas the centre of the joint is filled by whitish, translucent Ni-free kerolite (Fig. 3c, d). The main precipitation zone for the Ni-rich pimelite is limited to the first ~15 to ~20 cm at the edge of the rock block (Fig. 3c, d). Target-like features are concentric with, from the edge (close to the fracture) to the centre of the block, (i) a highly oxidized and altered zone (Fig. 3c, e), (ii) a pure Ni-rich pimelite zone (Fig. 3c–e), (iii) a zone (limited to a few centimetres) with an apparent mixture of Ni-poor kerolite and Ni-rich pimelite and intermediate colours (Fig. 3c–e), (iv) a large Mg-kerolite mineralization zone

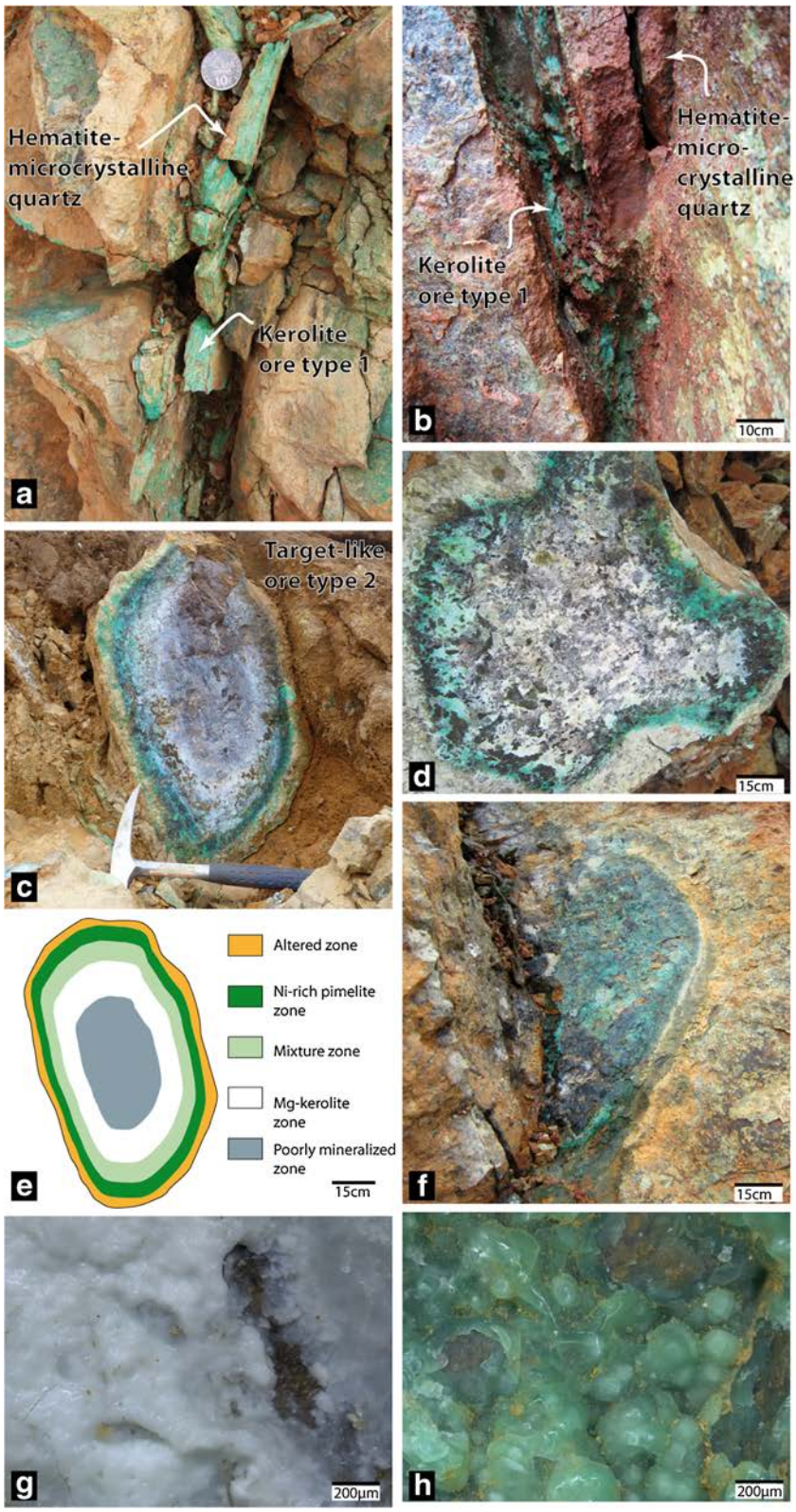

Fig. 3 Field occurrence of type 1 and 2 ores in the Cagou pit (see Fig. 1). **a** Type 1 kerolite-hematite bearing microcrystalline quartz (type 1 ore). **b** A relict of the type 1 kerolite-hematite bearing microcrystalline quartz partially dissolved by supergene alteration. **c**, **d** Zones of intense dissolution and the remaining harzburgite blocks showing, when broken during exploitation, a joint with a target-like (ore type 2). The colour green corresponds to the Ni-kerolite (pimelite) and the colour white to the Mg-kerolite. **e** Sketch summarizing the mineralogical variation from the edge to the centre of the target-like. **f** A relict of the target-like (ore type 2) quickly altered after exposure. **g**, **h** Zoom on the Mg-kerolite (**g**) and Ni-kerolite (pimelite) zones of a target-like ore showing the botryoidal habitus

(Fig. 3c–e) and (v) a poorly filled zone with a very thin Mg-kerolite layer (Fig. 3c, e). In zone iii, the intermediate colours result in fact from the superimposed deposit of thin layers of green pimelite and Ni-poor white kerolite. All the kerolite infillings form successive thin layers on the rock and have a botryoidal texture (Fig. 3g, h).

Both ore types are at present day affected by meteoric water percolation. The water circulating into ore type 1 fractures dissolves the Ni-Mg kerolite and partially dissolves the red to brownish microcrystalline quartz. Figure 3b shows the result of the supergene alteration of the type 1 ores: The relict consists of a totally unstructured vein, with reddish walls due to goethite and hematite impregnations. Furthermore, Fig. 3f shows that target-like ores are also affected by the present-day hydrolysis by meteoric water quickly after exposure to surface conditions. The relict consists of a partially dissolved and mechanically dismembered target-like ore.

Mineralogy and crystal chemistry

All the studied minerals (Table 1, Figs. 3, 4, and 5) are kerolite, also called talc-like, as defined by Brindley and Wan (1975) and Brindley et al. (1977). They are all characterized by a broad peak on the XRD diffractograms around 10± 0.5 Å due to poor crystallinity and small coherent domains; as usual, this value is slightly shifted from the interlayer value that was determined using HRTEM (9.5 Å). The type 1 ore does not show any XRD peak corresponding to serpentine, but the occurrence of a peak between 7.26 and 7.30 Å is frequently present in the type 2 ores and attributed to small sized inclusions of serpentinized host rocks within the thin joint infillings, which are impossible to separate from the kerolite. Raman spectra of the Ni-rich phases (pimelite from ore types 1 and 2) are characterized by a complex OH band in the high frequency range (Fig. 4). This band is totally distinct from the spectra of all serpentine polymorphs. Raman spectra of Mg-kerolite are close but distinct of that of chrysotile (Fig. 4) as already described by Cathelineau et al. (2015) for the whole solid solution.

Table 1 Average composition of kerolite from veins (ore type 1) and target-like features (ore type 2) of the analyses presented in Fig. 5, measured by EPMA

	Type 1		Type 2 (target-like ore)			
	Bluish kerolite		Pimelite (green)		Kerolite (white)	
wt%	Av	σ	Av	σ	Av	σ
SiO_2	52.09	1.89	38.49	1.80	52.25	3.10
Al_2O_3	0.01	0.01	0.03	0.05	0.02	0.03
MgO	23.98	2.71	2.27	1.15	35.92	1.42
K_2O	0.06	0.05	0.00	0.00	0.00	0.00
Cr_2O_3	0.00	0.01	0.00	0.00	0.00	0.00
MnO	0.02	0.03	0.02	0.04	0.04	0.13
FeO	0.02	0.02	0.12	0.14	0.41	1.16
CoO	0.07	0.06	0.44	0.31	0.04	0.06
NiO	14.31	4.28	49.65	1.44	0.10	0.11
Total	90.55		91.01		88.76	
n	50		8		20	
% NiO min	10.29		46.63		0.00	
% NiO max	27.33		51.06		0.37	
Si	3.78		3.50		3.62	
Al	0.00		0.00		0.00	
∑ Oct.	3.78		3.51		3.62	
Fe^{2+}	0.00		0.01		0.02	
Mg	2.59		0.31		3.72	
Ni	0.84		3.64		0.01	
∑ Oct.	3.43		3.95		3.75	

The Ni-Mg kerolite-pimelite series from type 1 ore exhibits strong chemical zonation due to Ni-Mg substitutions. The Ni contents cover a large range from 10 wt% NiO to 27 wt% NiO. Type 2 ores, conversely, display two narrow ranges of Ni concentrations recorded with rather constant concentrations (Fig. 4e, f): NiO ranges from 0 to 0.5 wt% in the white Mg-kerolite and from 43 to 49 wt% in the Ni-kerolite (pimelite). The two ranges are close to those of the end-member values for the Ni-Mg kerolite solid solution. All the analysed kerolites show a significant stoichiometric deviation from talc, given that an excess in the octahedral Ni (+Mg) occupancy is observed in correlation with a deficiency in the tetrahedral occupancy.

From all observations, it can be concluded that these minerals are rather distinct both from serpentine or talc and are not mixtures with any of these minerals. Although IMA does not recognize kerolite as a mineral phase, the term kerolite is used because this phase is distinct from talc, is not mixed with serpentine and has a rather narrow range around 0.50±0.03 for the Si/(Si + Mg + Ni) ratio, distinct from both that of talc (0.57) and serpentine (0.4) (Fig. 5). The value of this ratio has been largely discussed in the literature: Brindley and Hang (1972) explain this deviation either by the presence of an additional brucite layer or by a break in the tetrahedral sheet. Another hypothesis is the physical mixing with serpentine layers suggested for the Dominican ores by Villanova-de-Benavent et al. (2014). This mixing justifies, in that particular case, the use of the term garnierite, e.g., a mechanical mixing between serpentine, talc-like and sepiolite minerals. In our case, the deviation cannot be easily attributed to the presence of serpentine layers given that serpentine layers have been not observed under TEM and that the Si/(Si + Mg + Ni) ratio is constant with no chemical trend between kerolite and serpentine as that found on Dominican ores by Villanova-de-Benavent et al. (2014). Thus, the term garnierite cannot be used as the studied minerals are not a mix of talc-like and serpentine with a fixed abundance for the two phases.

Discussion

Field observations and the laboratory characterization indicate that two types of Ni silicate ores occur in the Koniambo massif

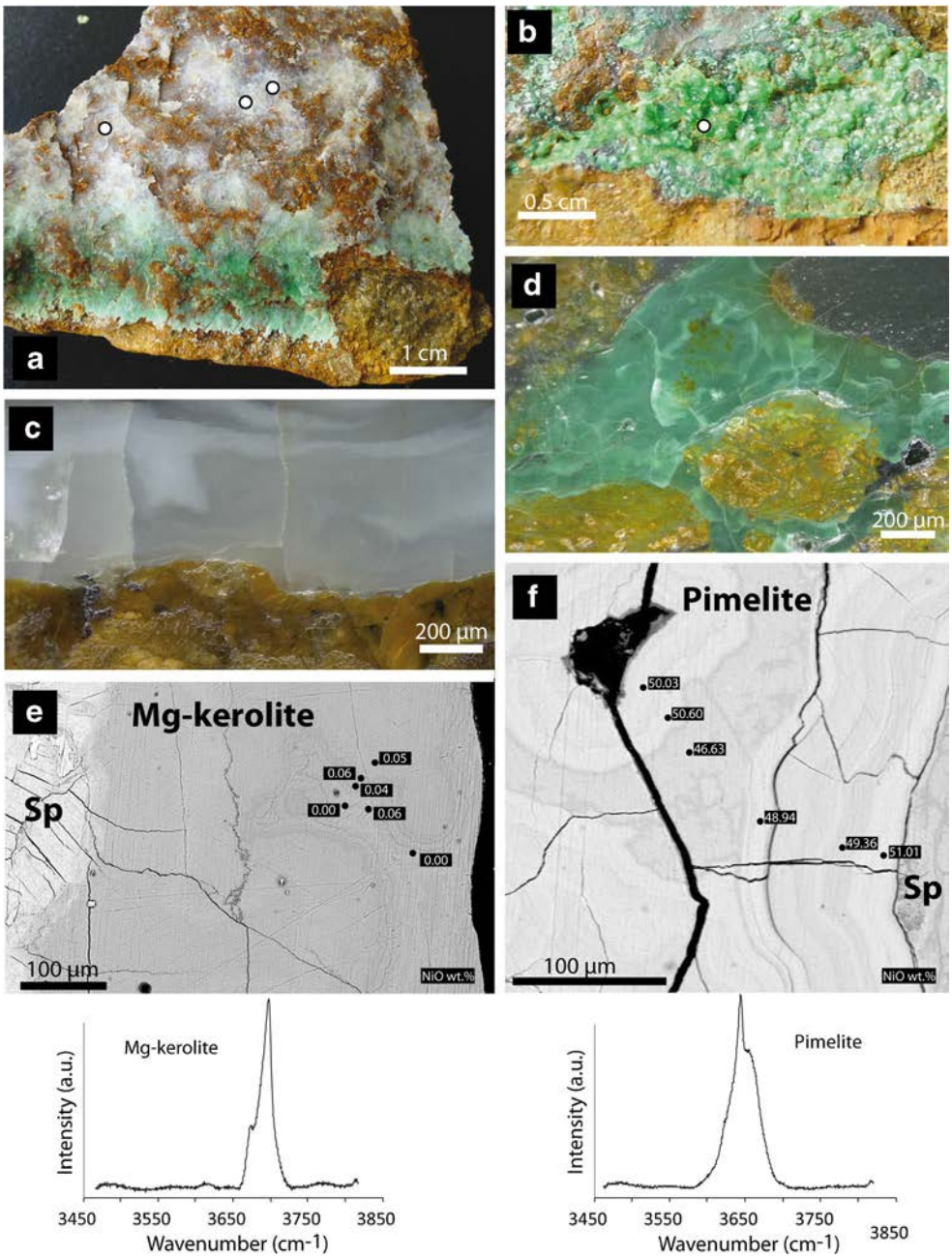

Fig. 4 **a**, **b** Samples of target-like (ore type 2) analysed by RAMAN (locations are shown by white dots). **b**, **c** Zoom on the Mg-kerolite and Ni-kerolite (pimelite) zones of a target-like. **e**, **f** Back-scattered electron image of the botryoidal habit of Ni-kerolite (**f**) and Mg-kerolite (**e**). Each growth band has a rather constant Ni concentration characterized by its specific mean Z (average atomic weight). Mg-Tl, Ni-Tl and Sp are respectively Mg talc-like, Ni talc-like and serpentine. The NiO concentrations are in wt% and were determined by electron microprobe analyses. RAMAN spectrum representative of the Mg and Ni kerolite from target-like (*bottom on the figure*)

near the oxidation zone. They are easily discriminated by the following features:

- Veins distributed as clusters of sub-parallel fracture infillings with a predominant strike and dip, at least at the open pit scale. The syntectonic characteristic is shown by the existence of hydraulic breccia and striated planes affecting both the silicate infillings and the fracture walls (Cluzel and Vigier 2008). They can be observed over a large depth range of few tens meters to few hundred meters below present day surface. Each vein is characterized by a large range of Ni-Mg content with complex chemical zoning. They are commonly associated with reddish micro-crystalline quartz.
- Target-like ores consist of a thin layer cementing a joint generally less than 0.5 mm in thickness, where the joint does not have a preferred orientation. These joints are interpreted to result from decompression that is typical of the first hundreds of meters below the surface; they are not syntectonic. The target-like ores are exclusively observed in a narrow zone of a few tens of meters in thickness, just below the high-oxidation zone in the saprolitic horizon.

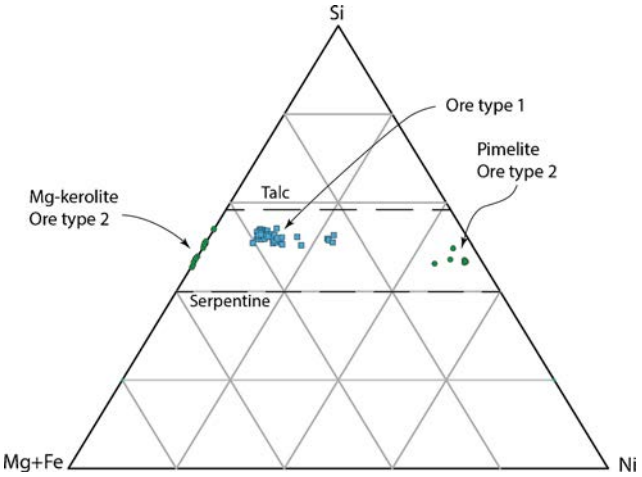

Fig. 5 Ternary Si-Mg + Fe-Ni diagram with analytical results for the kerolite veins (Ni-Mg solid solution, ore type 1) and target-like (Mg and Ni-kerolite end-members, ore type 2)

Time-space conditions favourable to target-like ore formation

The specific hydrologic conditions presently affecting the highest parts of the peridotite relief induce strong water-rock interactions characterized by a high rate of water infiltration, and subsequently, nearly continuous hydrolysis of all mineral phases except insoluble minerals (Fe-oxihydroxides) and inherited low solubility oxides (e.g., chromite) under oxidizing conditions. The almost complete dissolution of the serpentinized peridotite along the faults results in large open dissolution pipes, which are sub-vertical to dipping 60–70°. These large pipes are locally collapsed and cemented by white quartz and pimelite, as observed in breccia from the Cagou pit (Fig. 2a, b). These processes are rather distinct from those classically described for the slow downward progress of the nearly horizontal laterite fronts (Nahon and Tardy 1992; Freyssinet and Farah 2000).

All the observed features of the type 2 ore indicate that it formed under supergene conditions, close to the present-day topographic surface, and therefore during recent times. Target-like ores can develop once the very late exhumation of the peridotite massif and its erosion has induced mechanical decompression and subsequent jointing. The bulk permeability of the first hundreds of meters below the surface is thus increased by this process (Hencher et al. 2011). The high permeability of the saprocks allows rapid vertical transfer and short residence time for the incoming waters. Spatial relationships between the topographic surface and the occurrence of target-like ores around several tens of meters (30 to 50 m) below this surface suggest the potential link with the oscillating level of the water table. In this zone, the water table undergoes significant oscillations which are linked to the seasonal variations of water precipitation. In addition, the topology of the boundary of the water saturated zone is controlled by local hydrological conditions which primarily depend on the relief, here characterized by a hilly landscape. Target-like ores are therefore quite distinct from the ores that formed during fault activity.

Physical-chemical processes linked to target-like ore formation

The formation of target-like ores implies a mechanism of mineral precipitation from interstitial water present in the joints, e.g., an increase in $(Mg^{2+})/(H^{+})^2$ and $(Ni^{2+})/(H^{+})^2$ for a given pH (Fig. 6). Water close to the topographic surface is far from

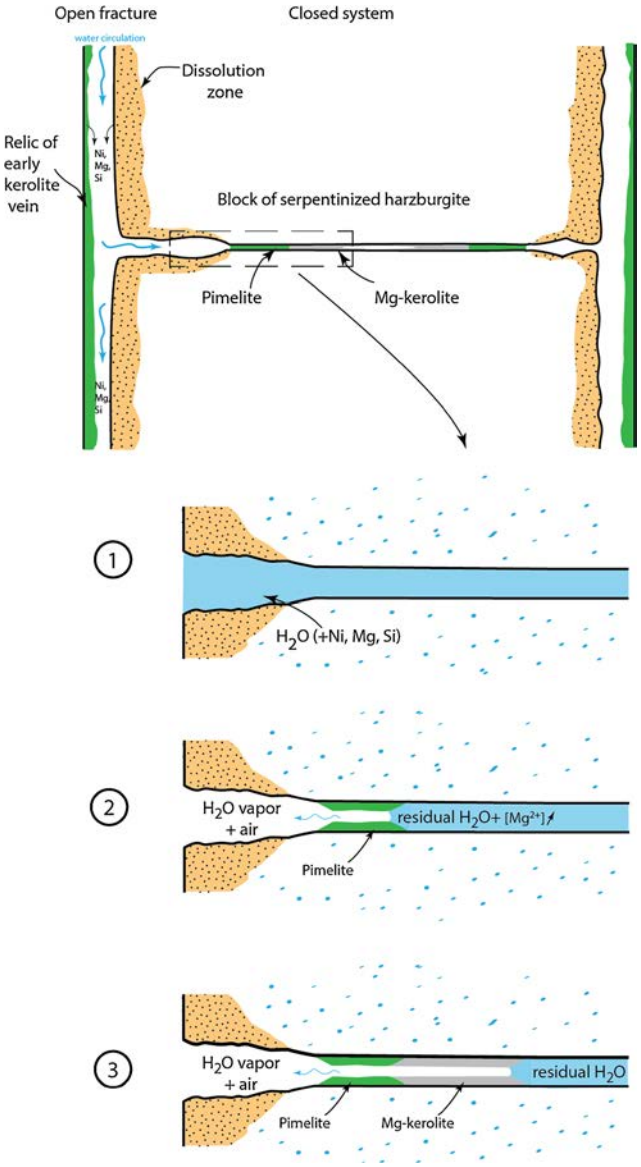

Fig. 6 Conceptual model of the Mg-Ni-kerolite target-like formation: Top cross-section peridotite block limited by joints, some partially filled with early type 1 ores, acting as a fluid pathway and affected by dissolution. Infiltration into the rather closed fracture occurs mostly through diffusion; fracture and sequence of target-like precipitation with (1) partial dehydration during an episode of water table lowering, with precipitation of Ni-kerolite (2) at the margins, and Mg-kerolite (3) at a higher degree of fissure dehydration (*bottom*)

mineral saturation, due to fast infiltration and a short residence time, thereby preventing any saturation with respect to silicates. The oversaturation of the solution with respect to the silicates therefore requires an additional mechanism that would increase cation activities in solution. The most likely mechanisms are (i) an increase in the residence time of the water, away from the main drainage open fractures, which would increase the rate of interaction with rocks when interstitial water is trapped in the micropores of the closed joints, a process which results in an increase in the cation/H^+ ratio due to the hydrolysis of pre-existing minerals, in rocks and fractures, and (ii) water evaporation, which occurs several times per day in between the rain events, in the rock volume located above the saturated zone. In this volume, interstitial water is connected with a major dissolution zone and drainage pipes and may be enriched in Ni, from the dissolution of all Mg (Ni) silicates including earlier ores, such as type 1 ores. Thus, the evaporation of waters containing Si, Mg and Ni may result in the saturation of pimelite or Mg-kerolite. The mineral distribution at the origin of the spectacular target-like colour zoning seems to come from chromatographic process due to the saturation of pimelite at the edge and saturation, with respect to Mg-rich kerolite, in the subsequent stages of the evaporation process at the centre of the block joint. It is suggested that the last zone to dry is in the centre of the joint, and there, water precipitates the remaining Si and Mg once Ni is already precipitated as pimelite near the joint boundary, or alternately, Mg-rich silicate could also have precipitated earlier. Pimelite is much more insoluble than Mg-kerolite, thereby explaining why this mineral precipitates first despite a Ni/Mg ratio in water close to 10^{-3}; this process was already described by Galí et al. (2012). The process is probably recurrent and repeated several times before reaching a significant volume of precipitated minerals but is limited to joints with a sufficiently low permeability, preventing rapid dissolution and the release of elements into the percolating waters. It is interesting to note that under these conditions, only the end-members of the kerolite-pimelite solid solution can precipitate. In open joints, the rate of infiltration is such that it prevents precipitation or favours mostly dissolution of all silicates.

The effects of water infiltration on the pre-existing target-like mineral are visible on the blocks exposed in the quarries. After a period of several months, the nice green glass translucent pimelite micro-spherolites are replaced by pulverulent amorphous phases resulting from pimelite hydrolysis, which are difficult to identify. Consequently, a large part of the nickel bearing joints are only revealed during mechanical fracturation during open pit quarrying, and this explains why, in the other joints or faults, most of the Ni-bearing minerals are partly dissolved.

Transfers at the bottom of the saprolitic horizon

The high number of open joints in the first several hundred meters of the peridotite, in addition to the high drainage zones such as the dissolution pipes, allows an efficient vertical transfer of water towards the water saturated zone (Fig. 7). Zones characterized by rapid vertical water transfer lack mineral precipitation. They are mostly characterized by residual iron oxyhydroxides, the trivalent iron being immediately reprecipitated in situ. Conversely, less open joint networks may be affected by the reprecipitation of Ni-Mg silicates such as the kerolite-pimelite series, mostly when located near clusters of early type 1 ore fractures which act as a source of Ni. Thus, pimelite occurs in a variety of joints; their distribution is rather distinct from the syntectonic kerolite fractures,

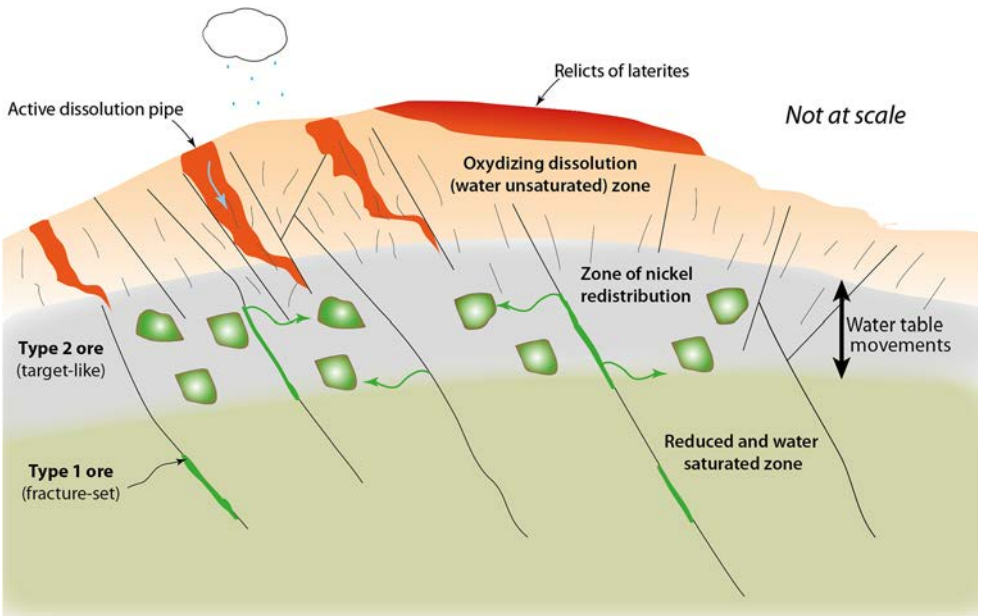

Fig. 7 Redistribution of the early ores located in discontinuities (ore type 1 as kerolite) at the interface between the oxidized and reduced zones within the water table oscillation zone. Newly formed ores (ore type 2 as pimelite) occur as target-like patterns in joint thin layers. This redistribution is independent of the occurrence of laterite, which formed much earlier

confirming that it represents a later Ni-precipitation in the joints that is genetically distinct from the earlier type 1. The abundance of type 2 ore pimelite joints at the bottom of the regolith suggests that type 2 ores significantly contribute to the grade of the main ore type exploited today in the open pits, besides Ni-rich iron oxyhydroxides, whereas type 1 ores in discontinuities only represent isolated and rich clusters, e.g., a very small portion of the exploited ores. As a result, type 1 ores are not considered when estimating the reserves due to their scarcity and erratic distribution, as well as to their very high, but not representative, Ni-grades.

Conclusion

Two types of silicate ores are distinguished in the saprolite from the Koniambo Massif:

- An early syntectonic mineralization, in relation with major discontinuities or sets of fractures, producing high-grade ores dominated by Mg-Ni kerolite-pimelite solid-solution phases.
- A later Ni silicate mineralization in narrow joints occurring as rims of pimelite around target-like joint fillings and produced by present-day or recent shallow supergene processes. The latter are favoured by the infiltration of meteoric waters in the decompressed bedrock and overlaying saprolite and subsequent water-rock interactions. The crystallization of pimelite at the bottom of the saprolite may explain the presence of the silicates found at the base of the oxidized saprocks, generally difficult to identify when mixed with iron oxyhydroxides.

The target-like ores result from a redistribution process. This process seems to be very recent, if not still active, and linked to the present-day topography and water table movements. It is probably independent of the main stages of laterite formation, which are thought to have occurred in earlier times, during the Cenozoic. This pervasive redistribution of nickel is likely responsible, in large part, for the rather large Ni anomalies within the saprocks, which make up the bulk of the exploited ore and for the rather monotonous Ni-grade within the saprolite, ranging from 2 to 3 wt%. Conversely, the type 1 ores, exclusively located in discontinuity networks, are responsible for high but erratic grades. However, the Ni-enriched zones are partly controlled by the early distribution of the type 1 fractures. This tends to indicate that the geometric distribution of type 1 Ni ores may have influenced the present-day distribution of exploitable ores.

From the mining point of view, this significant redistribution of the early concentrations is of primary importance for determining the mining volumes that can be exploited. Thus, the mineralized domains within the first hundred meters are far more extensive than the syntectonic type 1 kerolite fracture networks which constitute the richest ores exploited in New Caledonia during the very first stages of exploitation at the end of the nineteenth and the beginning of the twentieth century. It can be concluded that the main consequence of the redistribution of the earlier type 1 Ni-concentration is particularly interesting for mining as the large lateral redistribution ensures a rather homogeneous volume of mineralized rock.

Acknowledgments This work has been carried out thanks to the financial and technical help from Koniambo S.A. and Labex Ressources 21 (supported by the French National Research Agency through the national program.

"Investissements d'avenir", reference ANR-10-LABX-21–LABEX RESSOURCES 21), with analytical contributions from the UMR GeoRessources No 7356 laboratory platforms. The field work was based on an early introduction to this subject matter during a first 1-day visit to Koniambo in 2011 by C. Couteau and E. Fritsch (field trip organized as part of a CNRT project (French National Centre for Technological Research: "Nickel and its environment") and mostly thanks to 2-week stays both in 2012 and 2013 financed by Koniambo within the framework of B. Quesnel's PhD thesis. Sara Mullin, a translator specializing in scientific publications, improved the English. We thank the associate editor Thomas Bissig, the editor-in-chief George Beaudoin, and an anonymous reviewer for their constructive reviews which allowed to improve this paper.

References

Brindley GW, Hang PT (1972) The hydrous magnesium-nickel silicate minerals (so-called garnierites). Int Clay Conf 1:41–50

Brindley GW, Hang PT (1973) The nature of garnierites—I structures, chemical compositions and color characteristics. Clay Miner 21:27–40

Brindley GW, Maksimovic Z (1974) The nature and nomenclature of hydrous nickel-containing silicates. Clay Miner 10:271–277

Brindley GW, Wan HM (1975) Compositions, structures, and thermal behaviour of nickel-containing minerals in the lizardite–nepouite series. Am Mineral 60:863–871

Brindley GW, Bish D, Wan HM (1977) The nature of kerolite, its relation to talc and stevensite. Mineral Mag 41:443–452

Brindley GW, Bish D, Wan HM (1979) Compositions, structures, and properties of nickel-containing minerals in the kerolite–pimelite series. Am Mineral 64:615–625

Butt CRM, Cluzel D (2013) Nickel laterite ore deposits: weathered serpentinites. Elements 9:123–128. doi:10.2113/gselements.9.2.123

Cathelineau M, Caumon MC, Massei F, Brie D, Harlaux M (2015) Raman spectra of Ni-Mg kerolite: effect of Ni-Mg substitution on O-H stretching vibrations. J Raman Spectrosc, Proceedings GEORaman 2014 (11th), ST Louis (USA). doi:10.1002/jrs.4746

Chevillotte V, Chardon D, Beauvais A, Maurizot P, Colin F (2006) Long-term tropical morphogenesis of New Caledonia (Southwest Pacific): importance of positive epeirogeny and climate change. Geomorphology 81:361–375

Cluzel D, Vigier B (2008) Syntectonic mobility of supergene nickel ores of New Caledonia (Southwest Pacific). evidence from garnierite veins and faulted regolith. Resour Geol 58:161–170. doi:10.1111/j.1751-3928.2008.00053.x

Cluzel D, Aitchison JC, Picard C (2001) Tectonic accretion and underplating of mafic terranes in the Late Eocene intraoceanic fore-arc of

New Caledonia (Southwest Pacific). geodynamic implications. Tectonophysics 340(1–2):23–59

Cluzel D, Jourdan F, Meffre S, Maurizot P, Lesimple S (2012) The metamorphic sole of New Caledonia ophiolite: 40Ar/39Ar, U-Pb, and geochemical evidence for subduction inception at spreading ridge. Tectonics 31:TC3016. doi:10.1029/2011TC003085

Dublet G (2012) Relation entre spéciation et distribution du nickel dans les couvertures d'altération latéritique des roches ultrabasiques de Nouvelle-Calédonie. PhD thesis, UPMC Paris VI, 353 p

Dublet G, Juillot F, Morin G, Fritsch E, Fandeur D, Ona-Nguema G, Brown GE Jr (2012) Ni speciation in a New Caledonian lateritic regolith: a quantitative X-ray absorption spectroscopy investigation. Geochim Cosmochim Acta 95:119–133

Fandeur D (2009) Géochimie et cristallochimie du chrome au cours de l'altération de roches ultrabasiques en Nouvelle-Calédonie (Massif du Koniambo). PhD Thesis, Université Paris Diderot–IPGP, 321 p

Freyssinet P, Farah AS (2000) Geochemical mass balance and weathering rates of ultramafic schists in Amazonia. Chem Geol 170:133–151

Freyssinet P, Butt CRM, Morris RC, Piantone P (2005) Ore forming processes related to laterite weathering. Economic Geology, 100th Anniversary Volume: 681–722

Galí, Soler JM, Proenza JA, Lewis JF, Camas, Tauler (2012) Ni-enrichment and stability of Al-free garnierite solid- solutions: a thermodynamic approach. Clays Clay Miner 60:121–135

Genna A, Maurizot P, Lafoy Y, Augé T (2005) Contrôle karstique de minéralisations nickélifères de Nouvelle-Calédonie. Compt Rendus Geosci 337:367–374

Gerard P, Herbillon AJ (1983) Infrared studies of Ni-bearing clay minerals of the kerolite–pimelite series. Clays Clay Miner 31:143–151

Gleeson SA, Butt CRM, Elias M (2003) Nickel laterites: a review. Soc Econ Geol Newslett 54:9–16

Hencher SR, Lee SG, Carter TG, Richards LR (2011) Sheeting joints: characterization, shear strength and engineering. Rock Mech Rock Eng 44:1–22

Manceau A, Calas G (1985) Heterogeneous distribution of nickel in hydrous silicates from New Caledonian ore deposits. Am Mineral 70: 549–558

Manceau A, Calas G (1986) Nickel-bearing clay minerals: II Intracrystalline distribution of nickel: an X-ray absorption study. Clay Miner 21:341–360

Manceau A, Calas G, Decarreau A (1985) Nickel-bearing clay minerals: I. Optical spectroscopic study of nickel crystal chemistry. Clay Miner 20:367–387

Manceau A, Schlegel ML, Musso M, Sole VA, Gauthier C, Petit PE, Trolard F (2000) Crystal chemistry of trace elements in natural and synthetic goethite. Geochim Cosmochim Acta 64(21):3643–3661

Maurizot P, Lafoy Y, Poupée M (2002) Cartographie des formations superficielles et des aléas mouvements de terrain en Nouvelle-Calédonie, Zone du Koniambo: Bureau de Recherches Géologiques et Minières, Public Report RP51624-FR, 45 p

Maurizot P, Vendé-Leclerc M, Collot J (2009) Carte géologique de la Nouvelle-Calédonie au 1/500.000. Service Géologique de Nouvelle-Calédonie/DIMENC-BRGM, Nouméa

Nahon DB, Tardy Y (1992) The ferruginous laterites. In: Butt CRM, Zeegers H (eds) Regolith exploration geochemistry in tropical and subtropical terrains, vol 4, Handbook of Exploration Geochemistry. Elsevier, Amsterdam, pp 41–55

Paquette J-L, Cluzel D (2007) U–Pb zircon dating of post-obduction volcanic-arc granitoids and a granulite-facies xenolith from New Caledonia. Inference on Southwest Pacific geodynamic models. Int J Earth Sci 96:613–622. doi:10.1007/s00531-006-0127-1

Paris JP (1981) Carte géologique de la Nouvelle Calédonie, feuille Ouest, 1/200000. Bureau de Recherches Géologiques et Minières (BRGM)

Pelletier B (1983) Localisation du nickel dans les minerais "garnieritiques" de Nouvelle-Calédonie. Sci Geol Mem 73:173–183

Pelletier B (1996) Serpentines in nickel silicate ore from New Caledonia. In: Grimsey EJ, Neuss I (eds) Proceedings, nickel 096: mineral to market, Kalgoorlie. The Australasian Institute of Mining and Metallurgy, Carlton, pp 197–205

Printemps J, Ausseil A-G, Dumas P, Mangeas M, Dymond JR, Lille D (2007) An Erosion Model for Monitoring the Impact of Mining in New Caledonia. MODSIM conference

Schellman W (1983) Geochemical principles of lateritic nickel ore formation. In: Melfi AJ, Carvalho A (eds) Proceedings of the II International Seminar on Lateritisation Processes. Sao Paulo, Brazil, 1982, 119–135

Sevin B, Ricordel-Prognon C, Quesnel F, Cluzel D, Lesimple S, Maurizot P (2012) First palaeomagnetic dating of ferricrete in New Caledonia: new insight on the morphogenesis and palaeoweathering of "Grande Terre". Terra Nov. 24(1):77–85

Springer G (1974) Compositional and structural variations in garnierites. Can Mineral 12:381–388

Terry JP, Wotling G (2011) Identifying rain-shadow influences on river flows and flood magnitudes across the central massif divide of La Grande Terre Island, New Caledonia. J Hydrol 404:77–86

Trescases JJ (1975) L'évolution géochimique supergène des roches ultrabasiques en zone tropicale. Mem ORSTOM 78: 279 p

Troly G, Esterle M, Pelletier B, Reibell W (1979) Nickel deposits in New Caledonia, some factors influencing their formation. In: Evans DJI et al (eds) International Laterite Symposium. New Orleans, Louisiana, 19–21 February. Society of Mining Engineers, New York, pp 85–119

Villanova-de-Benavent C, Aiglsperger T, Jawhari T, Proenza JA, Galí S (2012) Micro-Raman spectroscopy of Garnierite minerals: a useful method for phase identification. Rev Soc Esp Miner 180:181–16

Villanova-de-Benavent C, Proenza JA, Galí S, García-Casco A, Tauler E, Lewis JF, Longo F (2014) Garnierites and garnierites: textures, mineralogy and geochemistry of garnierites in the Falcondo Ni-laterite deposit, Dominican Republic. Ore Geol Rev 58:91–109

Wells MA, Ramanaidou ER, Verrall M, Tessarolo C (2009) Mineralogy and chemical chemistry of "garnierites" in the Goro lateritic nickel deposit, New Caledonia. Eur J Mineral 21:467–483

Xstrata (2012) Mineral resources and reserves at 31 Dec. 2012. Annual Report, 50 p

Chapitre 2

La carbonatation de la semelle de serpentine, marqueur de circulation de fluide en base de nappe

.

Partie III : Chapitre 2 – La carbonatation de la semelle de serpentine, marqueur de circulation de fluide en base de nappe

Introduction

Les nombreuses occurrences de magnésite localisées au niveau de la semelle de serpentine témoignent de paléo-circulation de fluide à l'extrême base de la Nappe des Péridotites. Si la magnésite est depuis longtemps suspectée de représenter un sous-produit de l'altération supergène, il n'en reste pas moins qu'aucune étude n' a permis d'établir formellement ce lien. Dans ce chapitre, nous présentons une étude duale, couplant l'analyse structurale et géochimique de ces veines afin de caractériser le type et les conditions de circulation du fluide à l'origine de la magnésite et de discuter de son lien à la minéralisation nickélifère. Cette démarche permettra également d'aborder la question du type de processus menant à la carbonatation des roches ultramafiques.

Résumé de l'article #3

L'ouverture récente d'affleurements exceptionnels localisés sur le massif de Koniambo a permis l'étude de la semelle de serpentine de la Nappe des Péridotites de Nouvelle-Calédonie (sud-ouest Pacifique). De nombreuses veines de magnésite sont observées et ont des caractéristiques témoignant d'une mise en place synchrone de la déformation cisaillante à cinématique vers le sud-ouest. La composition en oxygène des magnésites est homogène (27.4‰ ≤ $\delta^{18}O$ ≤ 29.7‰) tandis que la composition en carbone varie fortement (-16.7‰ ≤ $\delta^{18}O$ ≤ -8.5‰). Ces nouvelles données documentent l'origine météorique du fluide à partir duquel les magnésites ce sont formées. Le processus de latérisation affectant la partie sommitale de la nappe et la carbonatation de la semelle de serpentine représentent des enregistrements complémentaires de l'infiltration d'eau météorique au travers de la nappe. Se basant sur le caractère syn-déformation des veines de magnésite, nous proposons que l'activité tectonique syn-latérisation a permis de faciliter l'infiltration de l'eau, favorisant l'export des éléments lessivés (dont le magnésium) menant à la carbonatation étendue de la semelle de serpentine. Cela appelle à réexaminer les autres ophiolites mondiales, au sein desquelles de la magnésite est observée, dans le but d'établir dans quelle mesure la tectonique active est un paramètre majeur dans le processus de carbonatation.

Syn-tectonic, meteoric water–derived carbonation of the New Caledonia peridotite nappe

Benoît Quesnel[1]*, Pierre Gautier[1]*, Philippe Boulvais[1]*, Michel Cathelineau[2]*, Pierre Maurizot[3], Dominique Cluzel[4], Marc Ulrich[2,5], Stéphane Guillot[5], Stéphane Lesimple[6], and Clément Couteau[7]

[1]Géosciences Rennes, Université Rennes 1, UMR 6118 CNRS, 35042 Rennes Cedex, France
[2]Georessources, Université de Lorraine, UMR CNRS 7359, CREGU, 54506 Vandoeuvre-lès-Nancy, France
[3]Bureau de Recherches Géologiques et Minières, 98845 Noumea, New Caledonia
[4]Pole Pluridisciplinaire de la Matière et de l'Environnement, Université de la Nouvelle-Calédonie, 98851 Nouméa, New Caledonia
[5]ISTerre CNRS, Université Grenoble 1, 38041 Grenoble, France
[6]Service Géologique de la Nouvelle-Calédonie, Direction de l'Industrie, des Mines et de l'Energie, 98851 Nouméa, New Caledonia
[7]Service Géologique, Koniambo Nickel SAS, 98883 Voh, New Caledonia

ABSTRACT

Exceptional outcrops recently exposed in the Koniambo massif allow the study of the serpentine sole of the peridotite nappe of New Caledonia (southwest Pacific Ocean). Many magnesite veins are observed, with characteristics indicating that they were emplaced during pervasive top-to-the-southwest shear deformation. The oxygen isotope composition of magnesite is homogeneous (27.4‰ < $\delta^{18}O$ < 29.7‰), while its carbon isotope composition varies widely (–16.7‰ < $\delta^{13}C$ < –8.5‰). These new data document an origin of magnesite from meteoric fluids. Laterization on top of the peridotite nappe and carbonation along the sole appear to represent complementary records of meteoric water infiltration. Based on the syn-kinematic character of magnesite veins, we propose that syn-laterization tectonic activity has enhanced water infiltration, favoring the exportation of leached elements like Mg, which has led to widespread carbonation along the serpentine sole. This calls for renewed examination of other magnesite-bearing ophiolites worldwide in order to establish whether active tectonics is commonly a major agent for carbonation.

INTRODUCTION

Carbonation of ultramafic rocks is the process by which CO_2-bearing fluids react with olivine and/or serpentine to form magnesite ($MgCO_3$) (e.g., Klein and Garrido, 2011). Based on stable isotope and structural evidence, Kelemen et al. (2011) recently showed that present-day carbonation of the Oman ophiolite is due to downward infiltration of meteoric waters in the absence of significant tectonic activity. Other stable isotope studies have also established the meteoric origin of the fluids from which magnesite has formed in a number of ophiolite occurrences (Barnes et al., 1973; Jedrysek and Halas, 1990; Fallick et al., 1991; Gartzos, 2004; Jurkovic et al., 2012; Oskierski et al., 2013). Some of these ophiolites include laterites and associated iron-nickel ore deposits capping the ultramafic rocks (e.g., Eliopoulos et al., 2012).

The main ophiolite of New Caledonia (southwest Pacific Ocean), referred to as the peridotite nappe, has also undergone intense laterization since its emergence. This has led to supergene nickel ore formation, a process which implies a well-drained percolation system through the peridotites (Trescases, 1975). Recently exposed outcrops in the Koniambo massif (Fig. 1A) show large surfaces of the serpentine sole that forms the base of the nappe (Figs. 1B and 2), providing unprecedented access to fresh samples. Numerous magnesite veins are observed along these outcrops, attesting to widespread carbonation.

Here we present oxygen and carbon isotope compositions of the magnesite veins and argue that they originate from meteoric water. Furthermore, in contrast with the situation depicted in Oman (Kelemen et al., 2011), many veins appear to have formed syn-tectonically. This leads us to infer potential genetic links between laterization, carbonation, and tectonics.

GEOLOGICAL SETTING

New Caledonia lies 2000 km east of Australia. About 40% of the island's surface consists of peridotite. Peridotites overlie rock units of the Norfolk Ridge microcontinent with a sub-horizontal contact marked by a strongly deformed serpentine sole (Avias, 1967). This geometry results from the southwestward obduction of the peridotite nappe, initially rooted in the Loyalty Basin, sometime between ca. 37 and 27 Ma (Cluzel et al., 2001, 2012; Paquette and Cluzel, 2007).

On top of the nappe, laterites have developed at the expense of the peridotites (Trescases, 1975). Several planation surfaces attest to distinct episodes of weathering since before ca. 20 Ma (Latham, 1986; Chevillotte et al., 2006; Sevin et al., 2012). This is consistent with biogeographic and phylogenetic studies indicating that New Caledonia was aerially exposed in the Late Oligocene (Grandcolas et al., 2008).

Magnesite is widespread in New Caledonia and occurs as veins within the serpentine sole of the peridotite nappe, and as nodular heaps in recent alluvial deposits and present-day soils. Since Glasser (1904), the origin of the veins is

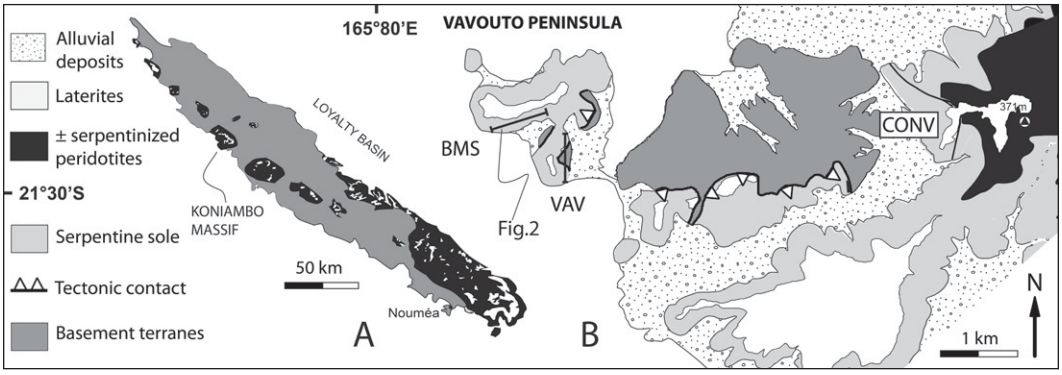

Figure 1. A: Simplified geological map of New Caledonia, southwest Pacific Ocean. B: Geological map of southwestern margin of Koniambo massif, adapted from Maurizot et al. (2002). BMS, VAV, and CONV indicate magnesite sampling sites. Laterites shown on this map belong to a planation surface that is younger than those having led to thicker laterites at higher levels of Koniambo massif (at elevations between ~400 and ~800 m; see text) (Latham, 1986; Chevillotte et al., 2006; Chardon and Chevillotte, 2006).

*E-mails: benoit.quesnel@univ-rennes1.fr; pierre.gautier@univ-rennes1.fr; philippe.boulvais@univ-rennes1.fr; michel.cathelineau@univ-lorraine.fr.

supposed supergene, possibly linked to the laterization process.

OBSERVATIONS AND SAMPLING

The Koniambo massif is one of the klippes of the peridotite nappe located along the west coast (Fig. 1A). Recently, Koniambo Nickel SAS initiated a large industrial site for nickel production. As a result, new outcrops of exceptional quality and size have been created in the serpentine sole of this massif (Figs. 1B and 2).

In the serpentine sole, rocks are strongly deformed, either schistose or intensely brecciated. A dense network of meter-thick shallow-dipping shear zones attests to pervasive non-coaxial deformation with a top-to-the-southwest sense of shear. Magnesite essentially occurs as veins, up to ~30 cm thick and irregularly distributed. Two main vein types are recognized (Figs. 3A–3C; Fig. DR1 in the GSA Data Repository[1]). Type 1 veins are located within or along the margins of the main shear zones. Open to tight drag folding of some of these veins indicates that they formed during, or possibly before, shearing. Type 2 veins are steeper and occasionally crosscut by the shallow-dipping shear zones, demonstrating that they do not represent younger structures. The obliquity of these veins with respect to the shear zones (Fig. 3D) and the local occurrence of magnesite as coarse fibers orthogonal to vein walls (Fig. 3C) are consistent with their interpretation as tension gashes opened during top-to-the-southwest shearing.

Both vein types have been sampled along two cross sections (BMS and VAV) located in the Vavouto peninsula, just above the basal contact of the peridotite nappe (Fig. 1B; Table DR1 in the Data Repository). Samples were also collected in other highly serpentinized zones in the Koniambo massif (sample CONV, Fig. 1B) and in the Kopeto massif ~50 km to the southeast (samples NEP and GAIACS).

CARBON AND OXYGEN ISOTOPE DATA

Isotopic analyses were performed at the stable isotope laboratory of the University of Rennes 1, France. Samples were finely crushed in a boron carbide mortar and reacted with anhydrous phosphoric acid at 75 °C for 24 h. The liberated CO_2 was analyzed on a VG SIRA 10 triple collector mass spectrometer. The experimental fractionation coefficient between magnesite and CO_2 is $\alpha_{CO_2\text{-magnesite}}$ = 1.009976 at 75 °C (Das Sharma et al., 2002). In the absence of a magnesite standard, in-lab calcite standard samples were analyzed together with the magnesite samples under identical conditions in order to control the general reliability of the protocol. The analytical uncertainty is estimated at 0.3‰ for oxygen and 0.2‰ for carbon.

Figure 2. Field view along part of BMS cross section (located in Fig. 1B), illustrating exceptional size and freshness of outcrops recently opened in serpentine sole of Koniambo massif.

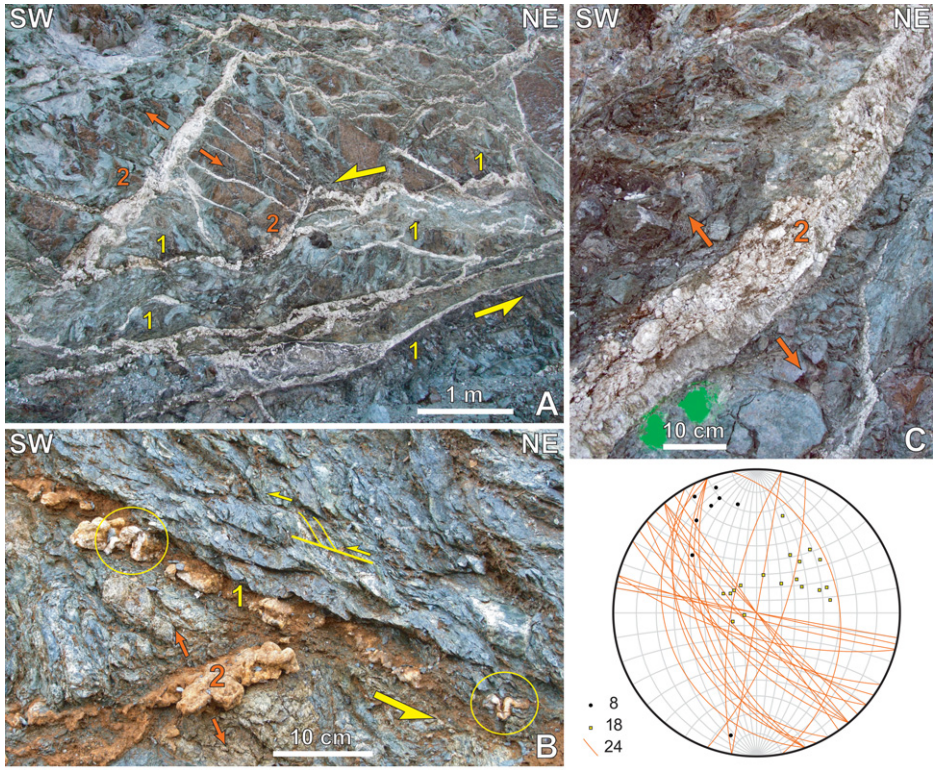

Figure 3. Field observations within serpentine sole of Koniambo massif. A–C: Field views illustrating relations between deformation and magnesite veins. Numbers 1 and 2 refer to the two main vein types as described in text. Two ellipses in B show sites where folding of a "type 1" vein is well visible. In C, magnesite occurs as coarse fibers suborthogonal to walls of this "type 2" vein (sample BMS Gio 9). D: Stereogram showing orientation, along BMS cross section, of major shear zones (shown as yellow squares representing poles of planes), of fold axes in the case of type 1 folded veins (shown as black dots), and of magnesite veins occurring in between shear zones (type 2 veins, shown as great circles).

[1]GSA Data Repository item 2013295, oxygen and carbon isotope data, and additional field observations, is available online at www.geosociety.org/pubs/ft2013.htm, or on request from editing@geosociety.org or Documents Secretary, GSA, P.O. Box 9140, Boulder, CO 80301, USA.

Results are presented in Figure 4 and Table DR1. All magnesite samples display comparable and high oxygen isotope values, irrespective of their structural position or sampling site (27.4‰ < $\delta^{18}O$ < 29.7‰); the carbon isotope composition is highly variable and negative (−16.7‰ < $\delta^{13}C$ < −8.5‰). Focusing on the samples from the Vavouto peninsula (BMS and VAV), the $\delta^{13}C$ and $\delta^{18}O$ values do not show any correlation.

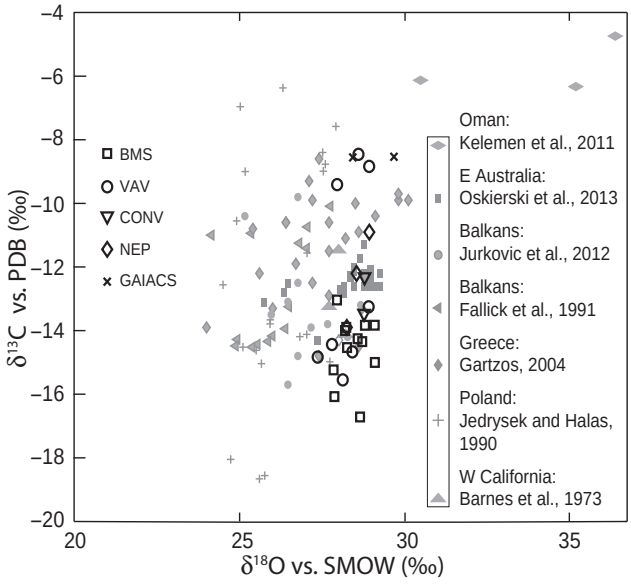

Figure 4. $\delta^{13}C$ versus $\delta^{18}O$ diagram of magnesite veins hosted by ultramafic rocks in different regions worldwide, for which a meteoric origin of fluids has been proposed. Black and gray symbols are from this study and the literature, respectively. The results are given versus SMOW (standard mean ocean water) for $\delta^{18}O$ and versus PDB (Peedee belemnite) for $\delta^{13}C$. BMS, VAV—Vavouto peninsula; CONV—Koniambo massif; NEP and GAIACS—Kopeto massif.

METEORIC ORIGIN OF CARBONATION

The isotopic compositions of magnesite reflect the conditions at which fluid/rock interactions occurred. As the $\delta^{18}O$ values are homogeneous, the physical conditions of carbonation, $\delta^{18}O$ value and temperature, were approximately constant in the fluid. Based on the two arguments to follow, we suggest that a strong interaction with meteoric fluids is the most likely process that led to carbonation along the serpentine sole. Firstly, although not precisely constrained, the carbon isotope fractionation between magnesite and CO_2 is known to be positive (Oskierski et al., 2013), therefore magnesite is expected to display higher $\delta^{13}C$ values than the fluid from which it precipitated. As a result, the largely negative $\delta^{13}C$ values in the magnesite veins rule out a seawater origin of the fluid because carbon dissolved in seawater has a $\delta^{13}C$ value close to 0‰. Secondly, as shown in Figure 4, our data set compares well with data from the literature on magnesite veins hosted by ultramafic rocks and for which a meteoric origin of the fluids has been proposed. Our data show a more restricted range in $\delta^{18}O$ values centered on the right side of the literature data cloud, the Oman data excluded. This observation may reflect a difference in the initial $\delta^{18}O$ value of rainwater due to distinct paleogeographic position or a slightly different temperature of formation. The higher $\delta^{18}O$ values from Oman probably reflect the fact that veins there were formed from spring waters, under lower temperatures (Kelemen et al., 2011). Our data show a large spread of $\delta^{13}C$ values that suggests at least two sources of carbon. The highest $\delta^{13}C$ values are close to those from Oman, which is consistent with an origin of CO_2 from the atmosphere. The lowest $\delta^{13}C$ values, around −15‰, point to an organic carbon contribution, either from surface soils or from a deep-seated source such as methane liberated from sediments buried below the peridotite nappe.

Under high fluid/rock ratios such as those inferred here because of the large size of magnesite veins and their abundance, the $\delta^{18}O$ value of magnesite is a function of temperature and of the $\delta^{18}O$ value of infiltrated water. To date, no isotopic data are available for meteoric precipitations in New Caledonia. We use a $\delta^{18}O$ range between −1‰ and −7‰, which corresponds to values of rainwater on isolated islands at inter-tropical latitude and low elevation (AIEA database; http://www-naweb.iaea.org/napc/ih/IHS_resources_isohis.html#wiser). Using the recent study of Chacko and Deines (2008) on oxygen fractionation between magnesite and water, a temperature range of 38–77 ºC can be estimated for the formation of the magnesite veins. This is consistent with heating of the meteoric waters while they were carried down to the serpentine sole.

LINKS BETWEEN LATERIZATION, CARBONATION, AND TECTONICS

The record of meteoric waters through carbonation along the serpentine sole implies that water circulated downward through the peridotite pile. An efficient drainage system has likely been provided by the dense network of fractures that characterizes the New Caledonia peridotites. This network is also recognized to have played a major role in peridotite weathering and the distribution of nickel ore (e.g., Leguéré, 1976). Hence, laterization on top of the peridotite nappe and carbonation along the serpentine sole may correspond to complementary records of meteoric water infiltration, as anticipated by Glasser (1904). In practice, laterization involves the leaching of large amounts of magnesium, a highly mobile ion that can be viewed as a tracer of fluid circulation from the surface down to the serpentine sole where it precipitated to form magnesite veins. Correlatively, nickel, which is less mobile, has accumulated at the base of the lateritic profile (e.g., Trescases, 1975). Throughout New Caledonia, the richest nickel ores are associated with a couple of planation surfaces associated with laterites up to 30 m thick (e.g., Chevillotte et al., 2006). They cap the Koniambo massif at elevations between ~400 and ~800 m, in agreement with the island-scale mean elevation of 640 m reported by Chevillotte et al. (2006). The outcrops of the Vavouto peninsula, where most of our magnesite samples come from, lie near sea level, and so does the basal contact of the peridotite nappe around much of the Koniambo massif. Therefore, downward infiltration of meteoric waters likely occurred across a vertical distance of at least ~600 m before magnesite formed along the serpentine sole. Greater vertical distances are also possible because older laterite-bearing planation surfaces are locally preserved at elevations up to ~1250 m in the nearby Kopeto massif and in southern New Caledonia (Latham, 1986; Chevillotte et al., 2006). This agrees with the above temperature range of ~38–77 ºC, which is consistent with fluids in thermal equilibrium with host rocks at depths around 0.5–2.5 km, using ~25 ºC as the initial temperature and 20–30 ºC/km for the geothermal gradient.

Because active slip typically increases the permeability of faults, water drainage through the peridotites could have been enhanced during active faulting. Indirect evidence for deformation-assisted fluid circulations across the peridotite pile is provided by the syn-kinematic character of the studied magnesite veins along the sole (Fig. 3; see also the Data Repository) and the observation that at least some of the nickel mineralizations underlying laterites developed during brittle deformation (Cluzel and Vigier, 2008; our own observations in the Koniambo massif).

The syn-kinematic magnesite veins of the Koniambo massif have been emplaced during top-to-the-southwest shearing deformation. Southwestward shearing recorded along the basal contact of the peridotite nappe may reflect obduction (e.g., Cluzel et al., 2001) or post-obduction reactivation of the contact as a southwest-dipping extensional detachment (Lagabrielle and Chauvet, 2008). Deformation occurred sometime between ca. 37 Ma and 27 Ma if related to obduction, or later, but before ca. 20 Ma, if related to post-obduction northeast-southwest extension

(Chardon and Chevillotte, 2006). The main laterites of New Caledonia were also formed before ca. 20 Ma (Chevillotte et al., 2006; Sevin et al., 2012). Hence, available time constraints make it possible that carbonation and laterization occurred at the same time, during tectonic activity.

As a result, we propose that syn-laterization tectonic activity enhanced water infiltration and played a major role in the exportation of leached elements like Mg, leading to widespread carbonation along the serpentine sole.

POTENTIAL IMPLICATIONS FOR OTHER CARBONATED OPHIOLITES

Syn-tectonic carbonation along the serpentine sole of the New Caledonia ophiolite contrasts directly with the well-documented case of post-tectonic subsurface carbonation of the Oman ophiolite (Kelemen et al., 2011). Studies documenting meteoric water–derived magnesite in other ophiolite occurrences lack a structural description that would allow the syn- versus post-tectonic character of carbonation to be evaluated (Barnes et al., 1973; Jedrysek and Halas, 1990; Fallick et al., 1991; Gartzos, 2004; Jurkovic et al., 2012; Oskierski et al., 2013). Nevertheless, syn-laterization tectonically driven carbonation of ultramafic rocks, as proposed here for New Caledonia, may have occurred in other areas worldwide. For instance, the ophiolites of the Dinaric-Hellenic segment of the Alpine orogen include (1) large volumes of magnesite originated from meteoric water (e.g., Gartzos, 2004; Jurkovic et al., 2012), (2) laterites capping the ultramafic rocks, with iron-nickel ore deposits (e.g., Eliopoulos et al., 2012), (3) various time constraints showing that obduction occurred in the Late Jurassic, and (4) the unconformity of Late Jurassic sediments on at least some of the laterites (Robertson et al., 2012). These features strongly suggest that laterization occurred during obduction, which opens the possibility that carbonation occurred simultaneously, fostered by tectonic activity. This pleads for renewed examination of the Dinaric-Hellenic and other carbonated ophiolites worldwide in order to establish whether active tectonics is commonly a major agent for carbonation.

ACKNOWLEDGMENTS

Thanks are due to Emmanuel Fritsch (Institut de Recherche pour le Développement) for his help during preliminary field work in the course of the Centre National de Recherche Technologique sur le Environment program. Kerry Gallagher improved the English. Peter Kelemen and two anonymous reviewers helped us in clarifying some aspects of the paper.

REFERENCES CITED

Avias, J., 1967, Overthrust structure of the main ultrabasic New Caledonian massives: Tectonophysics, v. 4, p. 531–541, doi:10.1016/0040-1951(67)90017-0.

Barnes, I., O'Neil, J.R., Rapp, J.B., and White, D.E., 1973, Silica-carbonate alteration of serpentine: Wall rock alteration in mercury deposits of the California Coast Range: Economic Geology and the Bulletin of the Society of Economic Geologists, v. 68, p. 388–398, doi:10.2113/gsecongeo.68.3.388.

Chacko, T., and Deines, P., 2008, Theoretical calculation of oxygen isotope fractionation factors in carbonate systems: Geochimica et Cosmochimica Acta, v. 72, p. 3642–3660, doi:10.1016/j.gca.2008.06.001.

Chardon, D., and Chevillotte, V., 2006, Morphotectonic evolution of the New Caledonia ridge (Pacific Southwest) from post-obduction tectonosedimentary record: Tectonophysics, v. 420, p. 473–491, doi:10.1016/j.tecto.2006.04.004.

Chevillotte, V., Chardon, D., Beauvais, A., Maurizot, P., and Colin, F., 2006, Long-term tropical morphogenesis of New Caledonia (Southwest Pacific): Importance of positive epeirogeny and climate change: Geomorphology, v. 81, p. 361–375, doi:10.1016/j.geomorph.2006.04.020.

Cluzel, D., and Vigier, B., 2008, Syntectonic mobility of supergene nickel ores of New Caledonia (Southwest Pacific): Evidence from faulted regolith and garnierite veins: Resource Geology, v. 58, p. 161–170, doi:10.1111/j.1751-3928.2008.00053.x.

Cluzel, D., Aitchison, J.C., and Picard, C., 2001, Tectonic accretion and underplating of mafic terranes in the Late Eocene intraoceanic fore-arc of New Caledonia (Southwest Pacific): Geodynamic implications: Tectonophysics, v. 340, p. 23–59, doi:10.1016/S0040-1951(01)00148-2.

Cluzel, D., Jourdan, F., Meffre, S., Maurizot, P., and Lesimple, S., 2012, The metamorphic sole of New Caledonia ophiolite: $^{40}Ar/^{39}Ar$, U-Pb, and geochemical evidence for subduction inception at a spreading ridge: Tectonics, v. 31, TC3016, doi:10.1029/2011TC003085.

Das Sharma, S., Patil, D.J., and Gopalan, K., 2002, Temperature dependence of oxygen isotope fractionation of CO_2 from magnesite–phosphoric acid reaction: Geochimica et Cosmochimica Acta, v. 66, p. 589–593, doi:10.1016/S0016-7037(01)00833-X.

Eliopoulos, D.G., Economou-Eliopoulos, M., Apostolikas, A., and Golightly, J.P., 2012, Geochemical features of nickel-laterite deposits from the Balkan Peninsula and Gordes, Turkey: The genetic and environmental significance of arsenic: Ore Geology Reviews, v. 48, p. 413–427, doi:10.1016/j.oregeorev.2012.05.008.

Fallick, A.E., Ilich, M., and Russell, M.J., 1991, A stable isotope study of the magnesite deposits associated with the Alpine-type ultramafic rocks of Yugoslavia: Economic Geology and the Bulletin of the Society of Economic Geologists, v. 86, p. 847–861, doi:10.2113/gsecongeo.86.4.847.

Gartzos, E., 2004, Comparative stable isotopes study of the magnesite deposits of Greece: Bulletin of the Geological Society of Greece, v. 36, p. 196–203.

Glasser, E., 1904, Rapport à M le Ministre des Colonies sur les richesses minérales de la Nouvelle-Calédonie: Paris, Annales des Mines, 560 p.

Grandcolas, P., Murienne, J., Robillard, T., Desutter-Grandcolas, L., Jourdan, H., Guilbert, E., and Deharveng, L., 2008, New Caledonia: A very old Darwinian island?: Philosophical Transactions of the Royal Society of London, Series B, v. 363, p. 3309–3317, doi:10.1098/rstb.2008.0122.

Jedrysek, M.O., and Halas, S., 1990, The origin of magnesite deposits from the Polish Foresudetic Block ophiolites: Preliminary $\delta^{13}C$ and $\delta^{18}O$ investigations: Terra Nova, v. 2, p. 154–159, doi:10.1111/j.1365-3121.1990.tb00057.x.

Jurkovic, I., Palinkas, L.A., Garasic, V., and Strmic Palinkas, S., 2012, Genesis of vein-stockwork cryptocrystalline magnesite from the Dinaride ophiolites: Ofioliti, v. 37, p. 13–26.

Kelemen, P.B., Matter, J., Streit, E.E., Rudge, J.F., Curry, W.B., and Blusztajn, J., 2011, Rates and mechanisms of mineral carbonation in peridotite: Natural processes and recipes for enhanced, in situ CO_2 capture and storage: Annual Review of Earth and Planetary Sciences, v. 39, p. 545–576, doi:10.1146/annurev-earth-092010-152509.

Klein, F., and Garrido, C.J., 2011, Thermodynamic constraints on mineral carbonation of serpentinized peridotite: Lithos, v. 126, p. 147–160, doi:10.1016/j.lithos.2011.07.020.

Lagabrielle, Y., and Chauvet, A., 2008, The role of extensional tectonics in shaping Cenozoic New-Caledonia: Bulletin de la Société Géologique de France, v. 179, p. 315–329, doi:10.2113/gssgfbull.179.3.315.

Latham, M., 1986, Altération et pédogenèse sur roches ultrabasiques en Nouvelle-Calédonie: Editions de l'ORSTOM (Office de la Recherche Scientifique et Technique Outre-Mer), Collection Etudes et Theses, 331 p.

Leguéré, J., 1976, Des corrélations entre la tectonique cassante et l'altération supergène des péridotites de Nouvelle Calédonie [Ph.D. thesis]: Montpellier, France, Université du Languedoc, 95 p.

Maurizot, P., Lafoy, Y., and Poupée, M., 2002, Cartographie des formations superficielles et des aléas mouvements de terrain en Nouvelle-Calédonie, Zone du Koniambo: Bureau de Recherches Géologiques et Minières Public Report RP51624-FR, 45 p.

Oskierski, H.C., Bailey, J.G., Kennedy, E.M., Jacobsen, G., Ashley, P.M., and Dlugogoski, B.Z., 2013, Formation of weathering-derived magnesite deposits in the New England Orogen, New South Wales, Australia: Implications from mineralogy, geochemistry and genesis of the Attunga magnesite deposit: Mineralium Deposita, v. 48, p. 525–541, doi:10.1007/s00126-012-0440-5.

Paquette, J.L., and Cluzel, D., 2007, U-Pb zircon dating of post-obduction volcanic-arc granitoids and a granulite-facies xenolith from New Caledonia: Inference on Southwest Pacific geodynamic models: International Journal of Earth Sciences, v. 96, p. 613–622, doi:10.1007/s00531-006-0127-1.

Robertson, A.H.F., Trivic, B., Deric, N., and Bucur, I.I., 2012, Tectonic development of the Vardar ocean and its margins: Evidence from the Republic of Macedonia and Greek Macedonia: Tectonophysics, v. 595–596, p. 25–54, doi:10.1016/j.tecto.2012.07.022.

Sevin, B., Ricordel-Prognon, C., Quesnel, F., Cluzel, D., Lesimple, S., and Maurizot, P., 2012, First palaeomagnetic dating of ferricrete in New Caledonia: New insight on the morphogenesis and palaeoweathering of 'Grande Terre': Terra Nova, v. 24, p. 77–85, doi:10.1111/j.1365-3121.2011.01041.x.

Trescases, J.J., 1975, L'évolution géochimique supergène des roches ultrabasiques en zone tropicale: Formation des gisements nickélifères de Nouvelle-Calédonie: Mémoires ORSTOM (Office de la Recherche Scientifique et Technique Outre-Mer), v. 78, 259 p.

Manuscript received 28 February 2013
Revised manuscript received 20 May 2013
Manuscript accepted 22 May 2013

Printed in USA

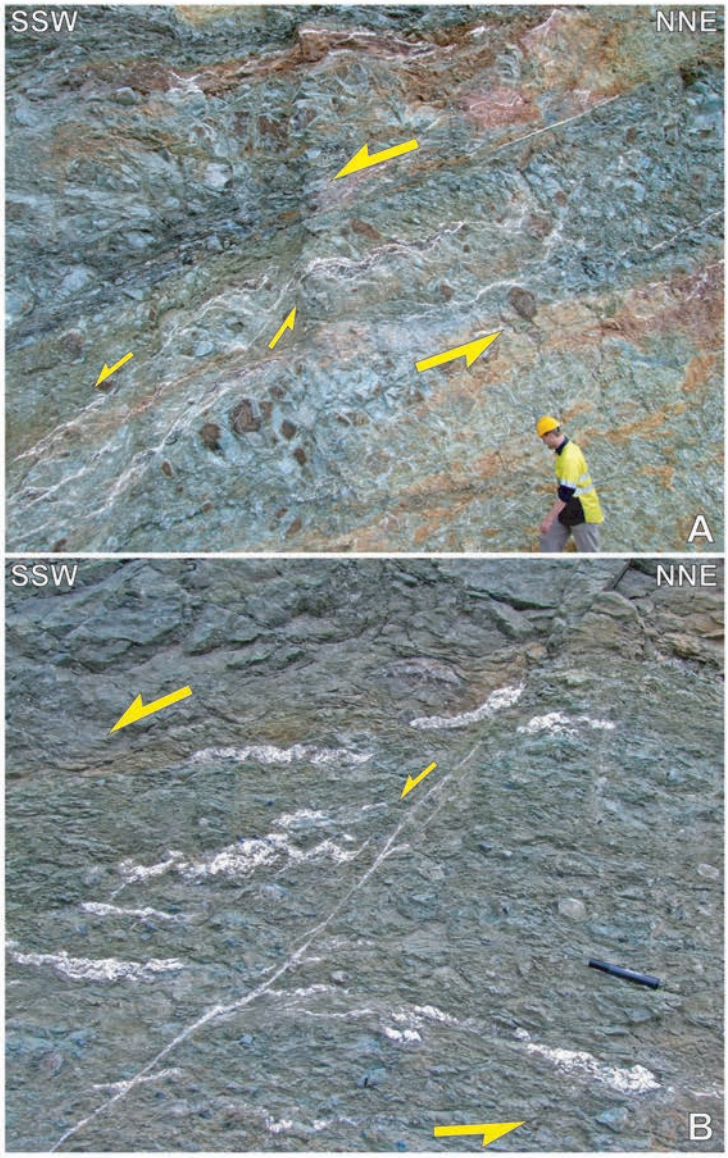

Figure DR1. Additional field views in the serpentine sole of the Koniambo Massif. A, a low-dipping shear zone and associated 'type 1' magnesite veins. In this exemple, three subtypes of vein may be distinguished: (i) a planar vein running along, and parallel to, the roof of the shear zone, (ii) subplanar veins inside, and oblique to, the shear zone, representing Riedel- or C'-type shear planes, (iii) a folded composite vein inside, and broadly parallel to, the shear zone. Folding seems to result from both buckling and drag folding along the shear planes. B, a mylonite zone hosting 'type 1' magnesite veins. A first subtype consists of sheared veins paralleling the schistosity. A second subtype consists of thinner veins along Riedel- or C'-type shear planes.

Magnesite				
Sample	**Localization**	**Host rock**	**$\delta^{18}O$**	**$\delta^{13}C$**
BMS Gio 1	Koniambo	serpentine	27,9	-13,0
BMS Gio 2	Koniambo	serpentine	29,1	-15,0
BMS Gio 3	Koniambo	serpentine	28,8	-13,8
BMS Gio 4	Koniambo	serpentine	27,9	-16,1
BMS Gio 5	Koniambo	serpentine	28,2	-14,5
BMS Gio 6	Koniambo	serpentine	28,6	-16,7
BMS Gio 7	Koniambo	serpentine	28,2	-13,9
BMS Gio 8	Koniambo	serpentine	28,7	-14,3
BMS Gio 9	Koniambo	serpentine	28,6	-14,3
BMS Gio 10	Koniambo	serpentine	28,2	-14,0
BMS Gio 12	Koniambo	serpentine	27,8	-15,2
BMS Gio 15	Koniambo	serpentine	29,1	-13,8
VAV 1 GIO 1	Koniambo	serpentine	28,6	-8,5
VAV 1 GIO 2	Koniambo	serpentine	28,9	-8,8
VAV 1 GIO 3	Koniambo	serpentine	27,9	-9,4
VAV 1 GIO 4	Koniambo	serpentine	28,9	-13,3
VAV 1 GIO 6	Koniambo	laterite	28,1	-15,5
VAV 1 GIO 7	Koniambo	serpentine	27,4	-14,8
VAV 1 GIO 8	Koniambo	serpentine	28,4	-14,7
VAV 1 GIO 9	Koniambo	serpentine	27,8	-14,4
CONV GIO 1	Koniambo	serpentine	28,8	-12,3
CONV GIO 2	Koniambo	serpentine	28,8	-13,5
NEP A1 Gio	Népoui	serpentine	28,2	-13,9
NEP A3 Gio	Népoui	serpentine	28,9	-10,9
NEP B1 Gio	Népoui	serpentine	28,5	-12,2
GAIACS 1	Gaiacs plain	serpentine	28,4	-8,6
GAIACS 2	Gaiacs plain	serpentine	29,7	-8,5

Table DR1. O and C isotope compositions of magnesite samples from this study. The results are given in ‰ versus SMOW for δ18O and ‰ versus PDB for δ13C.

Box 1: Analyses élémentaires (majeurs, traces et terres rares) des magnésites de Nouvelle-Calédonie

Problématique

Le couplage de l'analyse structurale et isotopique des veines de magnésite, provenant principalement du massif de Koniambo, nous a permis de mettre en évidence :

i) le caractère synchrone de la déformation et de la carbonatation de la semelle de serpentine et

ii) l'origine météorique et basse température du fluide à partir duquel les magnésites se sont formées.

Ces résultats nous ont amenés à proposer un modèle dans lequel le processus de latérisation est à l'origine du lessivage du magnésium nécessaire à la formation des magnésites. La déformation active est, dans ce modèle, le moteur permettant la circulation de l'eau météorique et l'export du magnésium jusqu'à la semelle de serpentine. Dans ce modèle *per descensum*, la source de magnésium étant allochtone, il est implicite que la formation des veines de magnésite à la base de la nappe résulte majoritairement d'une précipitation au sein des structures ayant permis la circulation du fluide. Alternativement, il est bien connu dans la littérature (Teir et al., 2007, 2009 ; Kelemen et Matter, 2008; Rudge et al., 2010; Klein et Garrido, 2011) que la formation de magnésite au sein de roches ultramafiques peut également résulter d'un processus de dissolution-précipitation résultant de la réaction entre un fluide riche en CO_2 dissout et la serpentine tel que :

Serpentine + CO2 (aq) → Magnésite + Silice (aq) + Eau

Se basant sur une caractérisation pétrographique et chimique détaillée d'échantillons de serpentine provenant de la semelle de serpentine du massif de Koniambo, le travail de Marc Ulrich (Annexe 4 :

Ulrich et al., 2014) a permis de mettre en évidence, qu'en plus du modèle *per descensum* de carbonatation menant à la formation de veines de magnésite localisées dans les fractures, la carbonatation s'exprimait également de manière pervasive au sein de la semelle de serpentine, conséquence du processus de dissolution-précipitation décrit ci-dessus.

Le traçage élémentaire a donc été pressenti comme un moyen de distinguer la magnésite résultant du modèle *per descensum* de celle formée in situ par réaction de dissolution-précipitation. En effet, lors du processus de latérisation, un certain nombre des éléments constitutifs de la péridotite ont un comportement peu mobile à immobile (Al, Cr, Ni, Mn, Fe et éléments de terres rares; Trescases, 1975; Marker et al., 1991; Ndjigui et al., 2008). Il semble donc raisonnable de supposer que la magnésite résultant du modèle *per descensum* sera particulièrement appauvrie en ces éléments. Inversement, la magnésite formée par le processus de dissolution-précipitation est susceptible d'incorporer une certaine quantité de ces éléments constitutifs de la serpentine ayant réagi avec le fluide riche en CO_2. L'analyse en éléments majeurs, traces et terres rares a donc été entreprise sur des échantillons de magnésite considérés comme représentatifs du modèle *per descensum* (i.e. les veines), du processus de dissolution-précipitation (i.e. des nodules isolés dans la serpentinite, annexe 5) et sur des échantillons de serpentine spatialement associés à ces nodules de magnésite (annexe 5).

L'analyse isotopique (O, C) des veines de magnésite présentée dans l'article #3 a permis de mettre en évidence une forte homogénéité des compositions en oxygène et inversement une forte variabilité de leur composition en carbone. De manière complémentaire à la volonté de tracer l'origine du processus ayant permis la formation des différents types de magnésite (veines versus nodules isolés), nous avons également cherché à identifier de possibles corrélations entre variabilité du $\delta^{13}C$ et compositions élémentaires. Ces dernières seraient susceptibles d'indiquer des conditions de formation différentes au sein d'une même famille d'occurrences de magnésite, à savoir les veines de magnésite.

Méthode :

L'ensemble des résultats a été obtenu par analyse in-situ via l'utilisation d'un LA-ICP-MS (Laser Ablation - Inductively Coupled Plasma - Mass Spectrometer) au laboratoire Géoressources de Nancy.

Echantillonnage :

Les échantillons des séries « BMS » et « VAV » correspondent à des veines de magnésite échantillonnées sur la péninsule de Vavouto (Article #3, Fig.1) au sein de la semelle de serpentine du massif de Koniambo. Les échantillons de la série « CONV » se localisent plus haut topographiquement dans le massif de Koniambo mais sont néanmoins localisés dans la semelle de serpentine (Article #3, Fig.1). Les échantillons des séries « NEP» et GAIACS » correspondent aux magnésites échantillonnées dans un périmètre proche (GAIACS) ou lointain (NEP=Népoui) du massif de Koniambo. Enfin les magnésites et les serpentines du « profil de dissolution » correspondent à une série d'échantillons censée refléter différents stades de formation de magnésite par dissolution de la serpentine (Annexe 5). Les échantillons K1, K2, K3, PG3 et KONA1 proviennent de la coupe BMS (Article #3, Fig.1). K1, K2 et K3 sont issus d'un même macro-échantillon. Enfin, les analyses de hazburgite et de serpentine du massif de Koniambo n'ont pas été réalisées au cours de cette étude ; les données utilisées proviennent du travail de Marc Ulrich (2010).

Résultats et discussion :

L'ensemble des résultats est présenté dans un tableau synthétique (Annexe 6).

Compositions en poids d'oxydes :

A partir des analyses de concentration en Si et Ca, les compositions en poids d'oxydes (MgO, CO_2, SiO_2 et CaO) des magnésites ont été calculées. La teneur en magnésium a été fixée ([Mg]= 282656 ppm) pour l'ensemble des échantillons sur la base des données de cartographie par microfluorescence X obtenues par Marc Ulrich (communication personnelle). Les résultats (Annexe 6) montrent que l'ensemble des échantillons bouclent entre 98.5wt.% et 116 wt.%. Les teneurs en CaO varient de 0.3 wt.% à 1.9 wt.% et pour SiO_2 entre 0.0 wt.% et 16.8 wt.%. L'ensemble des échantillons est donc bien des magnésites. Une analyse microsonde, qui permettrait d'améliorer le bouclage en prenant en compte de possibles variations de teneur en magnésium (particulièrement concernant l'échantillon BMS Gio 15), n'a pas été jugée nécessaire au vu, malheureusement, de résultats peu concluants (cf infra).

Compositions en terres rares :

Compte tenu de la très faible abondance en terres rares des magnésites, l'ensemble des analyses affichent majoritairement des teneurs inférieures à l'erreur associée à la mesure elle-même. Par conséquent aucun résultat ne sera présenté ici.

Compositions en éléments traces et majeurs :

Si pour la majeure partie des éléments analysés, aucune tendance ne se dessine, les diagrammes présentés figure 1 mettent néanmoins en évidence que la majeure partie des magnésites analysées s'alignent plus ou moins grossièrement sur une droite de mélange entre un pôle « magnésite pure » et un pôle « harzburgite-serpentine ». Le second point important réside dans le fait qu'aucune différence notable ne permet de distinguer, en termes de composition, les veines de magnésite de la magnésite du profil de dissolution. Cette tendance pourrait être le résultat :

i) d'un mélange homogène de tous ces éléments au sein de l'ensemble des magnésites résultant d'un processus de dissolution-précipitation suivant la réaction :

$(Mn, Fe, Cr, Ni, Mg)_3(Al, Si)_2O_5(OH)_4$ (s) + $3CO_2$ (aq) → $3MgCO_3$ (s) + $2SiO_2$ (aq) + H_2O (aq).

ii) De la présence de micro grains de serpentine et/ou de harzburgite au sein de la magnésite analysés simultanément lors de l'ablation laser.

iii) D'une différence de chronologie entre les veines de magnésite. Les premières à s'être formées seraient des magnésites se rapprochant du pôle pur magnésite. Les plus tardives, se formant alors que la latérisation s'intensifie, pourraient incorporer les éléments peu mobiles initialement restés dans la latérite.

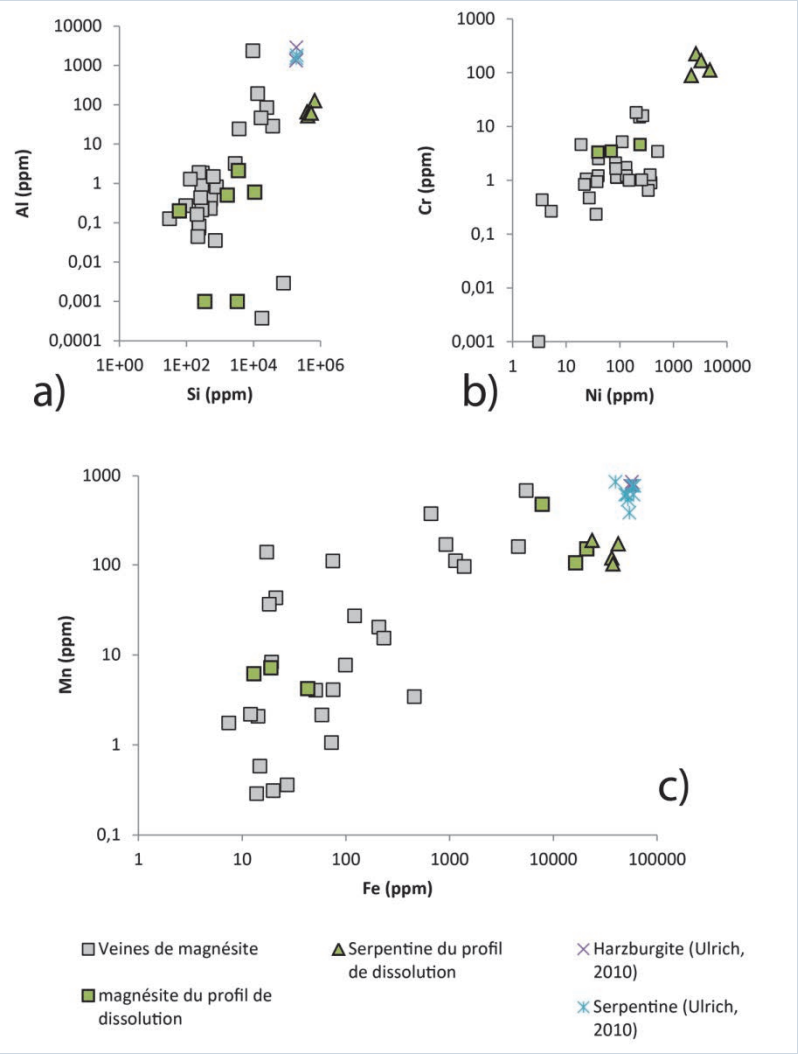

Figure 1 a,b,c) Diagrammes Al=f(Si), Cr=f(Ni) et Mn=f(Fe) où sont représentées les compositions élémentaires des veines de magnésite, des magnésites et des serpentines du profil de dissolution analysées dans cette étude ainsi que les compositions élémentaires d'échantillons de harzburgite et de serpentine provenant du massif de Koniambo analysées par Ulrich (2010).

Seuls quelques échantillons divergent de cette tendance générale. Sur le diagramme Al vs. Si présenté figure 1a, 4 échantillons ont des teneurs élevées en Si et proche de 0 ppm en Al (BMS Gio 15, NEP A3, K1-1, K2). Cette observation pourrait suggérer un épisode tardif de silicification (au moins pour l'échantillon BMS Gio 15) ou plus probablement, comme souligné par Ulrich et al.

(2014), que le processus de dissolution de la serpentine puisse localement générer un assemblage magnésite + silice.

Distribution Ni vs. $\delta^{13}C$:

Si pour la majeure partie des éléments analysés aucune tendance ne se dessine, les teneurs en nickel montrent des distributions intéressantes lorsque comparées aux valeurs de $\delta^{13}C$ (rien d'intéressant ne ressort lorsque confrontées au $\delta^{18}O$). La figure 2 met en évidence deux populations distinctes.

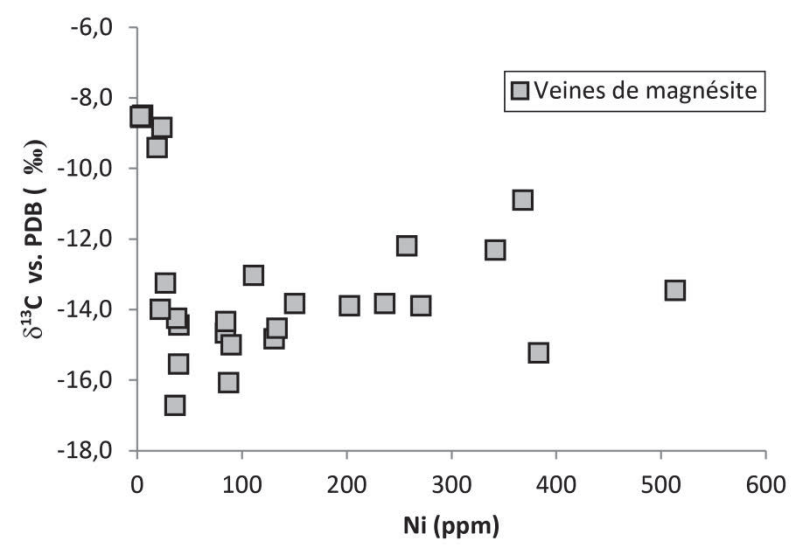

Figure 2 Diagrammes $\delta^{13}C$ =f(Ni) où sont représentées des veines de magnésite.

La majeure partie des veines de magnésite, première population, présentent une tendance positive reliant les basses valeurs en $\delta^{13}C$ à la teneur en Ni. La seconde population est composée des veines de magnésite ayant un $\delta^{13}C$ ~ -8‰ avec des teneurs très faibles en Ni. Au sein de l'article #3 nous proposons plusieurs hypothèses afin d'expliquer la grande variabilité du $\delta^{13}C$ de ces deux populations. Les valeurs les plus hautes en carbones (~ -8‰) sont cohérentes avec une contribution de CO_2 d'origine atmosphérique. Les valeurs les plus basses (~ -16‰) pourraient être symptomatiques d'une

contribution de carbone organique pouvant provenir aussi bien de sols que d'une source plus profonde (décarboxylation de sédiments riches en matières organiques chevauchés par la nappe par exemple). Trois hypothèses alternatives sont également proposées (Partie III. Chap 3. article #5), pour expliquer ces valeurs basses.

La première envisage la mise en jeu de fluides hyper-alcalins (dont le pH atteint des valeurs allant jusqu'à 11), conditions dans lesquelles des fractionnements cinétiques importants ont été documentés (e.g., Fourcade et al., 2007).

La seconde consiste en un appauvrissement cinétique du $\delta^{13}C$ s'effectuant lors de l'hydroxylation du CO_2 dissout dans le fluide à partir duquel le carbonate se forme (Dietzel et al., 1992).

Le troisième processus consiste en la production de carbone abiotique via des réactions dites de Fischer-Tropsch. Ces dernières consistent en une réaction catalytique entre le H_2, produit par la serpentinisation, et le monoxyde de carbone générant notamment du CO_2. Cette réaction engendre une augmentation du pH (Holm, 1996) et génère des produits organiques appauvris en $\delta^{13}C$ (McCollom et Seewald, 2006). Il est donc possible que les valeurs basses en $\delta^{13}C$ puissent être liées à une évolution du pH en fonction du degré d'interaction du fluide avec l'encaissant ultramafique. Constatant qu'une tendance positive relie la variabilité des valeurs basses en $\delta^{13}C$ à la teneur en Ni (deuxième population de veines décrite supra), il est intéressant de s'interroger sur la solubilité du Ni en fonction du pH. Au regard de la littérature, il apparait que la majorité des phases minérales porteuses de nickel (serpentine, talc) voient leur solubilité décroître lorsque le pH augmente (Wilson, 2004; Pokrovsky and Schott, 2000; Golightly, 2010). Théoriquement, l'augmentation du pH liée à l'augmentation du degré d'interaction du fluide avec l'encaissant pourrait donc en effet expliquer le fait que les veines de magnésite ayant un $\delta^{13}C$ intermédiaire (~ -12‰) aient des teneurs en Ni plus fortes que celles ayant un $\delta^{13}C$ extrêmement bas (~ -16‰). Cependant, compte tenu :

i) de l'aspect hypothétique de la relation $\delta^{13}C=f(pH)$,
ii) de la très faible solubilité des phases porteuses de nickel aux pH élevés suggérés et
iii) de l'aspect quelque peu erratique de la tendance positive reliant le $\delta^{13}C$ à la teneur en Ni

il semble que le pH ne soit pas l'unique moteur permettant d'expliquer les teneurs relativement fortes en Ni de certaines veines de magnésite. Si une tendance positive semble exister entre le $\delta^{13}C$ de beaucoup de magnésites et leur teneur en Nickel, il semble prématuré en l'état d'en faire une corrélation symptomatique d'un processus contrôlant ces deux paramètres.

Conclusion :

L'analyse élémentaire des différents types de magnésite n'a pas permis de mettre en évidence des différences significatives au sein de la population des magnésites. Cela suggère que le traçage élémentaire n'est probablement pas un outil efficace de discrimination du processus à l'origine de la carbonatation à l'échelle de la nappe. La tendance positive mise en évidence entre le $\delta^{13}C$ et la teneur en Ni des magnésites permet néanmoins de discuter de la variabilité des conditions de formation au sein d'une même famille d'occurrences de magnésite, à savoir les veines. L'influence du pH du fluide sur la composition isotopique en carbone et la teneur en Ni des veines de magnésite est suggérée ici, mais constitue en l'état une piste intéressante qu'il conviendra d'étudier spécifiquement à l'avenir.

Références :

Dietzel M., Usdowski E., Hoefs J. (1992) Chemical and 13C/12C- and 18O/16O-isotope evolution of alkaline drainage waters and the precipitation of calcite. Appl. Geochem., 7, 177–184.

Fourcade S., Trotignon L., Boulvais P., Techer I., Elie M., Vandamme D., Salameh E., Khoury H. (2007) Cementation of kerogen-rich marls by alkaline fluids released during weathering of thermally metamorphosed marly sediments. Part II: Organic matter evolution, magnetic susceptibility and metals (Ti, Cr, Fe) at the Khushaym Matruk natural analogue (Central Jordan). Appl. Geochemistry, 22, 1311–1328.

Golightly J.P. (2010) Progress in understanding the evolution of nickel laterites. Goldfarb R.J., Marsh E. E., Monecke T., eds., Chall. Find. new Miner. Resour. Metallog. Innov. Explor. new Discov. Soc. Econ. Geol. Spec. Publ., 15, 451–485.

Holms N. G. (1996) Serpentinization of oceanic crust and Fischer–Tropsch type synthesis of organic compounds. Origins Life, 26 (3–5), 205–206.

Kelemen P.B., Matter J. (2008) In situ carbonation of peridotite for CO2 storage. Proc. Natl. Acad. Sci., 105, 17295–17300.

Klein F., Garrido C.J. (2011) Thermodynamic constraints on mineral carbonation of serpentinized peridotite. Lithos, 126(3), 147–160.

Marker A., Friedrich G., Carvalho A, Melfi A (1991) Control of the distribution of Mn, Co, Zn, Zr, Ti and REEs during the evolution of lateritic covers above ultramafic complexes. J. geochemical Explor., 40, 361–383.

McCollom T.M., Seewald J.S. (2006) Carbon isotope composition of organic compounds produced by abiotic synthesis under hydrothermal conditions. Earth Planet. Sci. Lett., 243(1-2), 74-84.

Ndjigui P.-D., Bilong P., Bitom D., Dia A. (2008) Mobilization and redistribution of major and trace elements in two weathering profiles developed on serpentinites in the Lomié ultramafic complex, South-East Cameroon. J. African Earth Sci., 50, 305–328.

Pokrovsky O.S., Schott J. (2000) Kinetics and mechanism of forsterite dissolution at 25°C and pH from 1 to 12: Geochimica et Cosmochimica Acta, 64, 3313–3325.

Rudge J.F., Kelemen P.B., Spiegelman M. (2010) A simple model of reaction-induced cracking applied to serpentinization and carbonation of peridotite. Earth Planet. Sci. Lett., 291(1–4), 215–227.

Teir S., Eloneva S., Fogelholm C-J., Zevenhoven R. (2009) Fixation of carbon dioxide by producing hydromagnesite from serpentinite. Appl. Energy, 86(2), 214–218.

Teir S., Kuusik R., Fogelholm C-J., Zevenhoven R. (2007) Production of magnesium carbonates from serpentinite for long-term storage of CO2. Int. J. Miner. Process., 85(1–3), 1–15.

Tresacses J.J. (1975) L'évolution géochimique supergène des roches ultrabasiques en zone tropicale: formation des gisements nickelifères de Nouvelle-Calédonie. Mémoires ORSTOM (Office de la Recherche Scientifique et Technique Outre-Mer), 78, 259p.

Ulrich M. (2010) Péridotites et serpentinites du complexe ophiolitique de la Nouvelle-Calédonie, Thèse, Université de la Nouvelle-Calédonie et Université de Grenoble, pp 253.

Partie III : Chapitre 2 – La carbonatation de la semelle de serpentine, marqueur de circulation de fluide en base de nappe

Ulrich M., Muñoz M., Guillot S., Cathelineau M., Picard C., Quesnel B., Boulvais P., Couteau C. (2014) Dissolution–precipitation processes governing the carbonation and silicification of the serpentinite sole of the New Caledonia ophiolite. Contrib. to Mineral. Petrol., 167, 952.

Wilson M.J. (2004) Weathering of the primary rock-forming minerals: Processes, products and rates: Clay Minerals, 39, 233–266.

Chapitre 3

Déformation et circulation de fluide à l'échelle de la Nappe des Péridotites

Partie III : Chapitre 3 – Déformation et circulation de fluide à l'échelle de la Nappe des Péridotites

Introduction

La présence de magnésite à la semelle de serpentine, la présence de silice localisée à différents niveaux de la nappe et l'omniprésence de la serpentine (cf partie II.1) sont autant d'évidences attestant de l'existence de fluides ayant circulé à l'échelle de la Nappe des Péridotites. Les deux chapitres précédents se sont focalisés sur la caractérisation de la circulation des fluides au sein de deux zones stratégiques :

i) la zone saprolitique au sein de laquelle la minéralisation nickélifère se localise et
ii) la semelle de serpentine au sein de laquelle la carbonatation s'exprime presque exclusivement.

La minéralisation nickélifère est connue pour être fortement contrôlée structuralement (Leguéré, 1976) et certains auteurs (Cluzel et Vigier, 2008) ont également proposé que la tectonique active néogène aurait pu i) faciliter l'altération supergène via une meilleure infiltration de l'eau météorique et ii) permettre localement la redistribution du nickel dans le niveau saprolitique. Dans cette même dynamique, le chapitre précédent a permis de mettre en évidence le lien étroit existant entre la déformation de la Nappe des Péridotites et la carbonatation de la semelle de serpentine. Le modèle proposé suggère que la déformation active a facilité la circulation d'eau météorique du sommet jusqu'à la base de la nappe.

Ce dernier chapitre vise, dans un premier temps, à caractériser la déformation, non pas au sein d'une zone limitée, mais au sein de l'ensemble de la Nappe des Péridotites. Ce travail se focalise sur la caractérisation des structures porteuses de serpentine, témoignant de circulations précoces de fluides, jusqu'aux structures porteuses de magnésite témoignant d'une déformation synchrone de l'altération supergène. Elle permet de discuter de l'évolution spatiale et temporelle de la déformation au sein de l'ensemble de la nappe et des premières implications sur la mécanique d'obduction d'une nappe de péridotites.

Ensuite, nous nous focalisons sur la caractérisation des conditions de formation des différentes occurrences de silices qui, compte tenu de leur distribution spatiale, témoignent de circulation de fluide à l'échelle de la nappe. Du fait de leur lien supposé avec l'altération supergène, les conditions de formation des silices seront mises en perspective vis-à-vis des conditions de formation des occurrences

de magnésite.

Résumé de l'article #4

Dans ce travail, nous présentons une étude structurale des failles et des zones de cisaillement porteuses de serpentine affectant le massif de Koniambo, formant l'une des klippes de la Nappe des Péridotites de Nouvelle-Calédonie. Le massif est actuellement exploité pour ses ressources en Nickel donnant ainsi accès à des affleurements d'excellente qualité répartis sur les ~800 m de hauteur séparant sa base de son sommet. La partie supérieure du massif se caractérise par son dense réseau de fractures et de failles dont certaines sont porteuses d'antigorite ou de serpentine polygonale. Sur ces failles, l'antigorite ou la serpentine polygonale forment des fibres ayant une géométrie attestant d'une croissance en zone abritée et présentant des cinématiques distinctes. Ainsi, la partie supérieure du massif préserve au moins deux événements de déformation, le premier associé à l'antigorite (extension ONO-ESE) et le second associé à la serpentine polygonale (compression NO-SE). Le niveau basal de la nappe, ou « semelle de serpentine », est composé d'une brèche tectonique massive, composant la partie supérieure de ce niveau, et d'une couche de serpentinite mylonitisée composant la partie inférieure. La semelle enregistre un cisaillement tangentiel pervasif à cinématique vers le SO et représente un décollement à la base de la nappe. Le niveau intermédiaire est caractérisé par la présence de plusieurs zones de cisaillement conjuguées d'épaisseur métrique accommodant un raccourcissement NE-SO. De la même manière qu'à la semelle, ces zones de cisaillements sont associées à de la serpentine polygonale et de la magnésite représentant les principales phases minérales syn-déformation. Les zones de cisaillement s'enracinent probablement au sein du niveau de décollement basal ou sur son toit voir occasionnellement à sa base. En comparaison au cisaillement top SO enregistré le long de la semelle, la déformation enregistrée dans la partie supérieure du massif est plus ancienne.

Cartographiquement, ces trois niveaux structuraux se corrèlent bien aux variations spatiales de degré de serpentinisation de la péridotite. Par conséquent, il est tentant de considérer que l'intensité de la serpentinisation a joué un rôle majeur dans la manière dont la déformation a été distribuée au travers de la Nappe des Péridotites. Cependant, dans le niveau supérieur de la nappe, même la moins altérée des péridotites contient plus de serpentine que, selon les travaux théoriques et expérimentaux, ce qu'il serait nécessaire d'avoir pour être aussi peu résistant qu'une serpentinite pure. Par conséquent, aucun

gradient vertical de résistance due à des variations du degré de serpentinisation n'est attendu au sein de la nappe. Nous proposons dès lors que la localisation de la déformation le long de la semelle de serpentine résulte de la juxtaposition de la nappe, faite de péridotites serpentinisées peu résistante, sur le substrat composé de roches mafiques résistantes. Cette interprétation est en désaccord avec l'idée intuitive qui considèrerait que la nappe, faite de péridotites, serait plus résistante que le substrat. En plus de cette interprétation, et ce en dépit du peu d'évidences de terrain, la localisation de la déformation pourrait également avoir été facilitée par des surpressions de fluide le long de la base de la nappe.

The internal deformation of the Peridotite Nappe of New Caledonia: a structural study of serpentine-bearing faults and shear zones in the Koniambo Massif

Submitted to Journal of Structural Geology

Benoît Quesnel[1], Pierre Gautier[1], Michel Cathelineau[2,] Philippe Boulvais[1], Clément Couteau[3], Maxime Drouillet[3]

[1]Géosciences Rennes, Université Rennes 1, UMR 6118 CNRS, OSUR, 35042 Rennes Cedex, France, benoit.quesnel@univ-rennes1.fr; pierre.gautier@univ-rennes1.fr; philippe.boulvais@univ-rennes1.fr

[2] Georessources, Université de Lorraine, UMR CNRS 7359, CREGU, 54506 Vandoeuvre-lès-Nancy, France, michel.cathelineau@univ-lorraine.fr

[3] *Service géologique, Koniambo Nickel SAS, 98883 Voh, Nouvelle Calédonie, mdrouillet@koniambonickel.nc*

Keywords : New Caledonia, ophiolite, serpentine, magnesite, nappe, structural analysis

Abstract

We present a structural analysis of serpentine-bearing faults and shear zones in the Koniambo Massif, one of the klippes of the Peridotite Nappe of New Caledonia. The massif is currently exploited for nickel extraction, giving access to good rock exposures across a height of ~800 m. Three structural levels are recognized. The upper level is characterized by a dense network of fractures, many of which have been activated as faults. Antigorite and polygonal serpentine form slickenfibers along fault planes with distinct kinematics. As a result, the upper level keeps the record of at least two deformation events, the first associated with antigorite (WNW-ESE extension), the second with polygonal serpentine (NW-SE compression). The lower level coincides with the 'serpentine sole' of

the nappe, which consists of massive tectonic breccias overlying a layer of mylonitic serpentinites. The sole records pervasive tangential shear with top-to-SW kinematics and represents a décollement at the base of the nappe. The intermediate level is characterized by the presence of several meters-thick conjugate shear zones accommodating NE-SW shortening. Like the sole, these shear zones involve polygonal serpentine and magnesite as the main syn-kinematic mineral phases. The shear zones likely root into the basal décollement, either along its roof or, occasionally, around its base. With respect to top-to-SW shearing along the sole, the two deformation events recorded in the upper level are old.

The three structural levels correlate well with the previously recognized spatial variations in the degree of serpentinization. It is therefore tempting to consider that the intensity of serpentinization played a major role in the way deformation has been distributed across the Peridotite Nappe. However, even the least altered peridotites, in the upper level, contain so much serpentine that, according to theoretical and experimental work, they should be nearly as weak as pure serpentinite. Hence, no strong vertical gradient in strength due to variations in the degree of serpentinization is expected within the nappe. Our proposal is that strain localization along the serpentine sole results from the juxtaposition of the nappe, made of weak serpentinized peridotites, against the strong mafic rocks of its substratum. This interpretation is at odds with the intuitive view that would consider the nappe, made of peridotites, as stronger than its basement. In addition, despite limited field evidence, strain localization may have been promoted by higher fluid pressures along the sole of the nappe.

1. Introduction

Ophiolites commonly occur within orogenic belts as a result of the obduction of a piece of oceanic lithosphere upon a continental basement (Coleman, 1971; Dewey & Bird, 1971). The ultramafic rocks that constitute a large part of most ophiolitic nappes generally display evidence for pronounced fluid-rock interactions in the form of a spatially uneven development of serpentinization. Due to their low strength in comparison to peridotites (e.g., Escartín et al., 2001), serpentinites have the capacity to promote strain localization and greatly influence the style of deformation on the lithosphere scale (e.g., Hirth & Guillot, 2013). Several types of serpentine may be identified in a single ophiolite, which raises the question of their relative chronology and their geodynamic environment of formation (e.g., Coulton et al., 1995). Here the topic is on ophiolitic nappes remaining near the surface, excluding subducted oceanic material that is sometimes returned to the surface as a dismembered 'meta-

ophiolitic' sequence. In principle, serpentinization within a non subducted ophiolite may witness the successive stages of oceanic accretion, intra-oceanic subduction (the ophiolite lying in the upper plate), obduction, and post-obduction evolution. Post obduction events may involve post-convergence extension and/or collisional orogeny if the oceanic domain has ultimately been closed. The Peridotite Nappe of New Caledonia is one of the few ophiolites in the world to have escaped collision after obduction (e.g., Cluzel et al., 2012). In this case, deciphering early serpentinization events should be easier in that case. Recent work has shown that the Peridotite Nappe hosts various types of serpentine (Lahondère & Maurizot, 2009; Ulrich, 2010; Lahondère et al., 2012). According to Ulrich (2010), lizardite has formed first, before obduction, then antigorite has developed during the early increments of obduction, finally chrysotile has formed lately during obduction. For Lahondère et al. (2012), antigorite has formed before obduction, during the early stages of intra-oceanic subduction. However, although an intimate association between deformation and the occurrence of serpentines is recognized in these studies, no attempt has been made so far to characterize this deformation. More generally, structural studies carried out on the ultramafic section of ophiolitic nappes usually focus on serpentine-free high grade fabrics (e.g., Boudier et al., 1988; Suhr & Cawood, 1993; Cook et al., 2000). Studies including an analysis of serpentine-bearing faults and shear zones are relatively rare (Bailey et al., 2000; Titus et al., 2002; Schemmann et al., 2007; Laó-Dávila & Anderson, 2009; Federico et al., 2014). They do not adress the question of the vertical distribution of deformation associated with serpentinization across an ophiolitic nappe, mostly because post-obduction orogeny has severely disturbed the original structure in each studied case.

In addition to fluid-rock interactions leading to the serpentinization of peridotites, ultramafic rocks can also be a reservoir for long-term storage of atmospheric carbon by mineralization (Power et al., 2013). Beside experimental studies (e.g., Giammar et al., 2005; Andreani et al., 2009; Hövelmann et al., 2012), much work has focused on natural cases of peridotite carbonation (e.g., Dabitzias, 1980; Fallick et al., 1991; Boschi et al., 2009; Kelemen et al., 2011; Oskiersky et al., 2012; Ulrich et al., 2014). In New Caledonia, Quesnel et al. (2013) showed that carbonation of the Peridotite Nappe resulted from meteoric water infiltration down to the serpentine sole of the nappe, during shearing. At shallower depth, meteoric waters also led to laterization of the peridotites and development of worldclass nickel mineralizations, so that nickel ore deposits can be suspected to have formed during tectonic activity (see also Butt & Cluzel, 2013).

In New Caledonia, earlier studies concerned with the Peridotite Nappe have focused on i) the high

temperature intra-oceanic stages of deformation within the nappe (Prinzhofer et al, 1980; Titus et al, 2011), ii) the obduction process, however based essentially on the analysis of the rock units underlying the nappe (e.g., Cluzel et al., 2001, 2012; Spandler et al., 2005; Lagabrielle et al., 2013) and iii) post-obduction brittle extension that shaped the island as a large horst (e.g., Lagabrielle et al., 2005; Chardon & Chevillotte, 2006). Furthermore, much attention has been put on the chemistry and mineralogy of thick lateritic profiles formed at the expense of the peridotites, which led to the development of worldclass nickel mineralizations (e.g., Orloff, 1968; Trescases, 1975; Butt & Cluzel, 2013). In contrast, only limited work has concerned serpentines-bearing faults and shear zones that are ubiquitous throughout the Peridotite Nappe, despite the common statement that the distribution of nickel ore is highly dependent on this fault network (Leguéré, 1976; Cluzel & Vigier, 2008).

In this study, we had access to a recently opened large mining site in the Koniambo Massif, one of the klippes of the Peridotite Nappe in northwestern New Caledonia (Fig. 1). This site provides a quasi-continuous exposure of fresh rocks from the base of the nappe, near sea level, up to ~800 m elevation, where the main laterite capping the peridotites occurs. We focused on the study of structures and deformation associated with serpentines. These data enable to describe the internal deformation of the nappe in relation with successive serpentinization events. The implications of this study for the tectonic evolution of New Caledonia are not discussed here and will be the topic of a distinct paper.

2. Geological setting

New Caledonia is located in the southwest Pacific Ocean, 1300 km east of Australia (Fig. 1). On the main island, known as the "Grande Terre", the Peridotite Nappe overlies, with a sub-horizontal tectonic contact (Avias, 1967; Guillon, 1975), a substratum composed of several volcano-sedimentary units (Paris, 1981; Cluzel et al., 2001, 2012). The Peridotite Nappe is essentially exposed in the "Massif du Sud", covering much of the southeastern third of the Grande Terre, and as a series of klippes along the northwestern coast (Fig. 1). In the Massif du Sud, the thickness of the nappe is at least 1.5 km and may reach 3.5 km (Guillon, 1975). In this region, tight time constraints indicate that the nappe has been emplaced sometimes between ~35 and ~27 Ma (e.g., Cluzel et al., 2012). The nappe is mostly composed of harzburgites except in the northernmost klippes where lherzolites

dominate (e.g., Ulrich et al., 2010). In high elevation areas of the Massif du Sud, the peridotites are locally overlain by layered pyroxenites and gabbros, interpreted as representing the base of an oceanic crust (Guillon, 1975; Prinzhofer et al., 1980; Paris, 1981). Compositional layering is essentially represented by 1 to 100 m-thick layers of dunite within the harzburgites. In the main part of the nappe, the degree of serpentinization of the peridotites is variable but moderate (Orloff, 1968), serpentines occurring preferentially along a network of mm- to ~10 cm-thick fractures and shear zones (e.g., Leguéré, 1976; Lahondère & Maurizot, 2009; Lahondère et al., 2012). Fracture infillings and

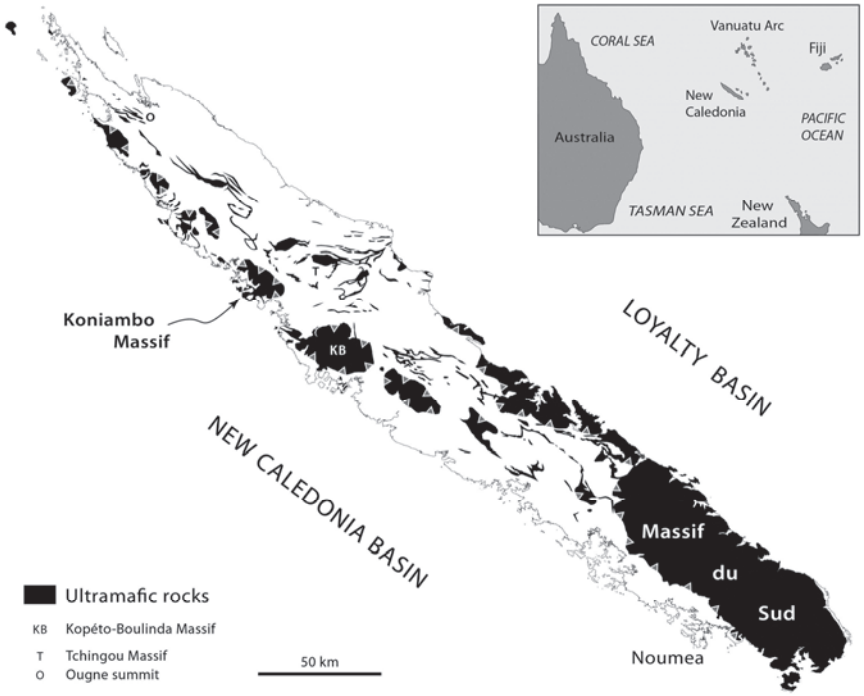

Figure 1 Simplified geological map of the Grande Terre, in New Caledonia, focusing on the ultramafic rocks exposures (adapted from Maurizot & Vendé-Leclerc, 2009). Most of these rocks are originally part of the Peridotite Nappe.

veins with various textures are described, containing lizardite±chrysotile or antigorite±chrysotile and/or an additional type of light-coloured serpentine not firmly identified (Lahondère & Maurizot, 2009; Lahondère et al., 2012). Serpentinization becomes pervasive along the base of the nappe, forming a 'sole' in which deformation has been intense (Avias, 1967; Orloff, 1968; Guillon, 1975; Leguéré, 1976; Cluzel et al., 2012; Quesnel et al., 2013). The thickness of this sole is a few tens of meters in the Massif du Sud but reaches a few hundred meters in the northwestern klippes (Guillon, 1975; Maurizot et al., 2002). For Leguéré (1976), the deformation recorded by the sole is older than the various sets of fractures observed at higher levels of the nappe. According to Ulrich (2010),

serpentinization of the sole involved three stages, firstly a pervasive development of lizardite, secondly the formation of antigorite within mm to cm-thick veins, finally the formation of chrysotile in local veinlet networks. In some of the veinlets, Ulrich (2010) also reports the partial replacement of chrysotile by polygonal serpentine. Recently, Ulrich et al. (2014) established that polygonal serpentine is more widespread in the sole than previously thought, forming light green serpentine veins associated with chrysotile veinlets.

Following their exposure to aerial conditions, the peridotites have been subject to intense weathering under dominantly warm and wet climatic conditions. This has led to the development of laterites up to ~30 m thick (e.g., Chevillotte et al., 2006). Leaching of the peridotites by downward infiltrating meteoric waters has resulted in a redistribution of elements, leading to high nickel concentrations at the base of the weathering profile, in the transition zone between coarse-grained saprolite and the bedrock (Orloff, 1968; Trescases, 1975; Leguéré, 1976; Paris, 1981; see also, e.g., Butt & Cluzel, 2013, their 'hydrous Mg silicate deposits' ore type). On a ~50 to ~500 m scale, the geometry of this transition zone is irregular and complex, and so is the distribution of nickel ore (e.g., Le Carlier de Veslud et al., 2015 on the example of the Koniambo Massif). This feature is usually attributed to the effect of uneven water drainage through the peridotites, drainage being enhanced along the network of fractures that crosscut the peridotites. The highest nickel concentrations coincide with the occurrence of bright green 'garnierite', a usual name for referring to a variety of Mg-Ni serpentine and talc-like minerals that are frequently mixed (e.g., Wells et al., 2009). A recent study of samples of garnierite from the Koniambo Massif reveals that, in that case, nickel is essentially contained by a talc-like phase also known as kerolite (Cathelineau et al., 2015a). Garnierite essentially occurs as mm to ~10 cm-thick veins locally arranged as dense 'boxworks' (e.g., Cluzel & Vigier, 2008). According to Cluzel & Vigier (2008), garnierite can also be found as striated coatings or slickenfibers along fault planes, attesting for its syn-tectonic nature. In addition, magnesite veins frequently occur along the serpentine sole of the Peridotite Nappe. Since Glasser (1904), magnesite is suspected to represent another by-product of the leaching of the peridotites by meteoric fluids (e.g., Ulrich, 2010). Quesnel et al. (2013) have confirmed this view using stable isotope evidence, and documented that at least some of the magnesite veins have been emplaced during pervasive shearing along the serpentine sole. Hence, weathering and deformation of the Peridotite Nappe were at least partly coeval (Cluzel & Vigier, 2008; Quesnel et al., 2013).

In the Koniambo Massif, the Peridotite Nappe is exposed from its base, near sea level, up to ~800 m elevation (Fig. 2a,b). Map relations (Carroué, 1972; Maurizot et al., 2002) show that the basal contact is subhorizontal around much of the massif but delineates a large open antiform in the west (Fig. 2b). At elevations above ~400 m, the nappe is capped by a highly dissected and partly reworked lateritic profile (Maurizot et al., 2002). At lower elevations, laterites of the westerly-inclined Kaféaté plateau probably belong to a younger planation surface (Latham, 1977; Chevillotte et al., 2006). The Koniambo Massif essentially consists of harzburgites with interlayers of dunite that define a crude

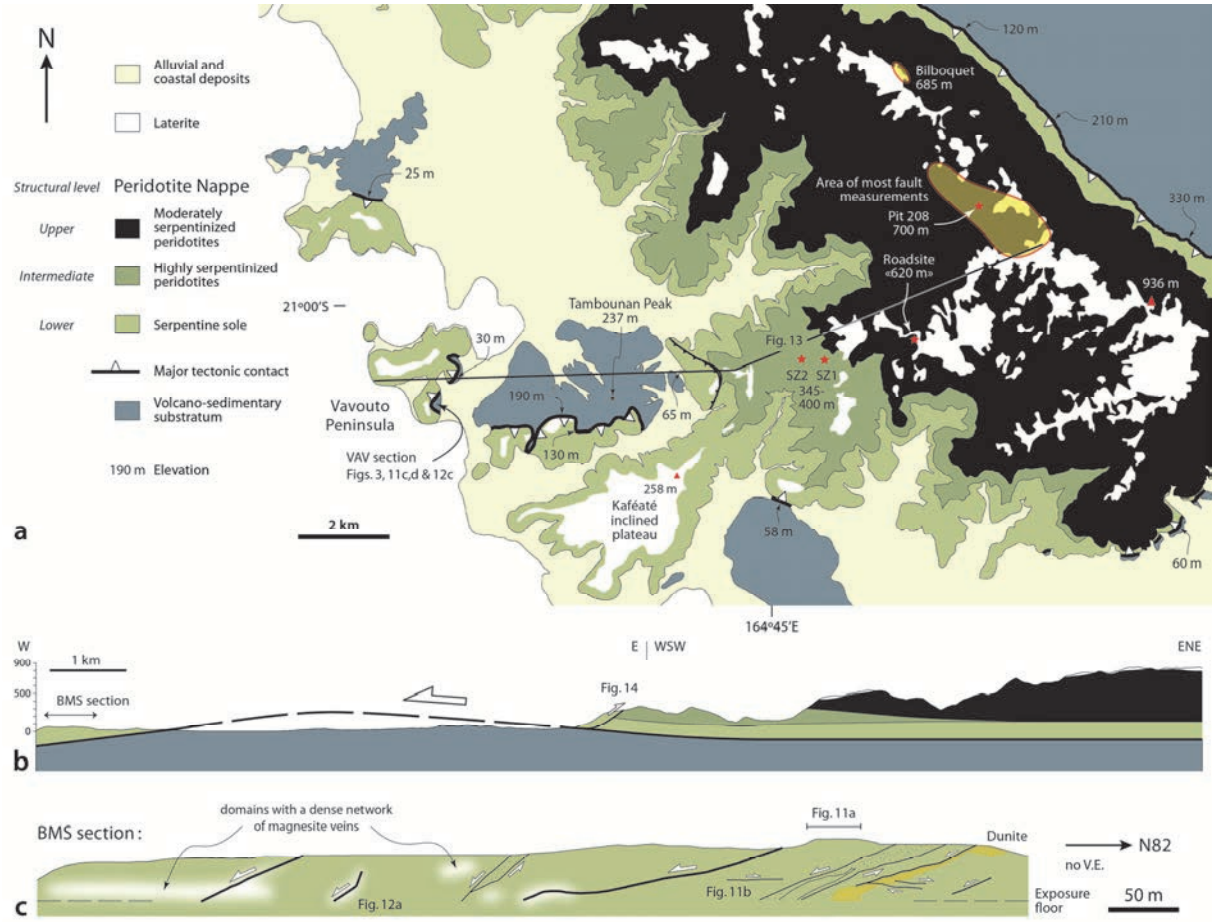

Figure 2 a) Geological map of the central and southern parts of the Koniambo Massif, adapted from Carroué (1972) and Maurizot et al. (2002). b) General cross-section of the Koniambo Massif, located in (a). c) Report of observations along the BMS section, in the Vavouto peninsula.

compositional layering with a fairly regular ENE-WSW strike and a ~50° southward dip (Maurizot et al., 2002). With regard to the degree of serpentinization, Maurizot et al. (2002) distinguished three main rock types, namely (i) moderately serpentinized peridotites in which the primary compositional layering is preserved, (ii) highly serpentinized peridotites and (iii) massive serpentinites. The latter

form the serpentine sole of the nappe, about 200 m thick. The highly serpentinized peridotites overlie the sole and form a distinct intermediate layer which, according to Maurizot et al. (2002), is ~200 m thick on the western flank of the massif but thins out further east (Fig. 2a,b). The moderately serpentinized peridotites occupy the higher part of the massif.

3. Methods

3.1. Strategy

Field work has focused on fresh rock exposures provided by the last ~5 years of mining activity in the Koniambo Massif. The serpentine sole is well exposed in the Vavouto peninsula, especially along two cross-sections named BMS (700 m long, striking N082, Fig. 2c) and VAV (a composite section ~330 m long with a mean N-S strike). The VAV section shows the basal contact of the nappe and its substratum made of basalts and minor cherts (Fig. 3a). Further east, the mine access road runs from the base of the nappe (height spot 65 m in figure 2a) to the upper part of the massif; it provides good outcrops of the intermediate level of highly serpentinized peridotites. The moderately serpentinized peridotites are exposed at higher levels of the access road and in a series of currently exploited open pits that focus on the transition zone between coarse-grained saprolite and the bedrock, for nickel extraction. We carried out preliminary field observations and sampled rocks with various textures and fabrics (veins, fracture infillings, fault coatings, cleavage domains within shear zones). We determined the mineralogical content of the samples, which then served as references for macroscopic assessment of the mineralogy within specific structures during renewed field work and structural analysis.

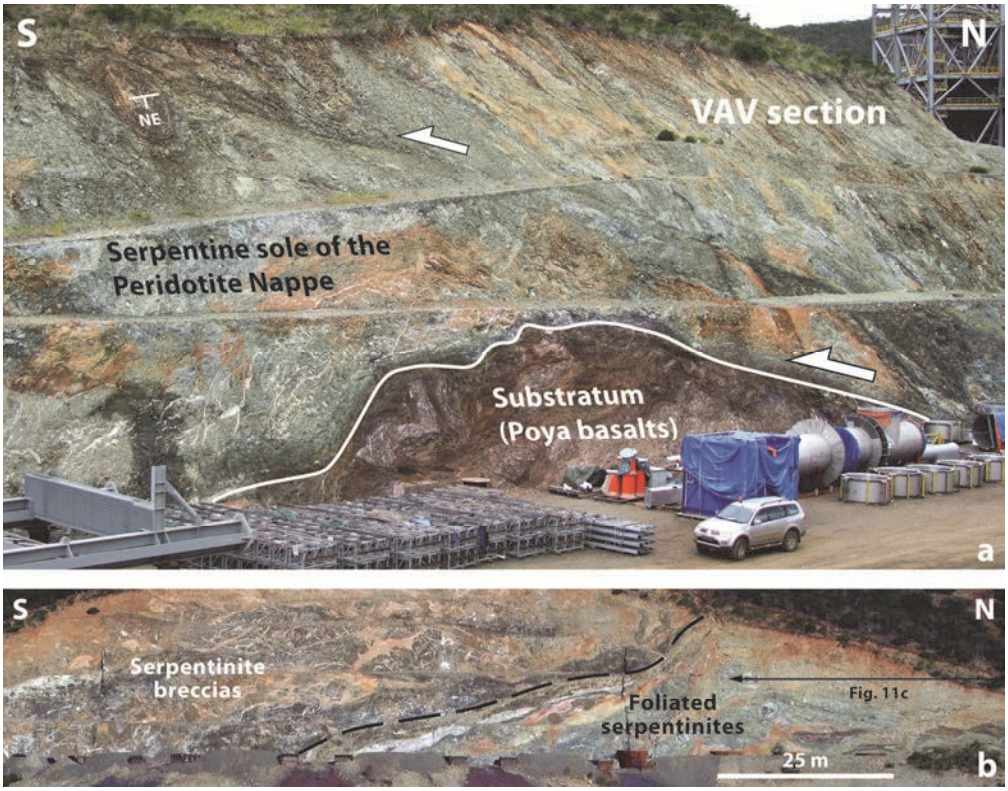

Figure 3 Two field views at the northern (a) and southern (b) ends of the VAV section, in the Vavouto peninsula (location in figure 2a).

3.2. Analytical methods

Reference samples have been characterized through a multi-technique approach including transmission electron microscopy, microprobe analysis (not presented here) and Raman spectroscopy. Raman spectroscopy measurements were carried out at the laboratory GéoRessources Nancy, France, using a Horiba Jobin-Yvon Labram HR800 spectrometer and a visible ionized argon laser source with a wavelength of 514 nm. The output power of the laser was 100 mW and measurements were performed using an Olympus lens of x50 to focus the laser beam onto an area 1µm in diameter. Spectra are the average of 6 to 10 acquisitions of 20 s each to optimize the signal/noise ratio. For serpentine identification, only one region of the Raman spectrum has been investigated, between 3520 cm^{-1} and 3870 cm^{-1} (Fig. 4). This region enables to characterize the hydroxyl groups which are the most discriminant for distinguishing the polymorphs of serpentine (Auzende et al., 2004; Ulrich, 2010; Schwartz et al., 2013; Ulrich et al., 2014).

For analyzing the deformation, we focused our attention on shear zones and on fault planes bearing clear striations or slickenfibers. The kinematics of shear zones has been determined using the obliquity of cleavage with respect to the shear zone walls (Fig. 5e,f) and, occasionally, the occurrence of a set of oblique shear bands. For determining the kinematics of faults, the offset of pre-kinematic markers or the presence of subsidiary Riedel shears has occasionally been used, however in most cases we favoured the use of accreted slickenfibers with a clear staircase geometry (Fig. 5a,b,c,d). The advantage of stepped slickenfibers is to provide a robust sense-of-slip indicator and to allow establishing which mineral or mineral assemblage was stable during a given fault slip event (Durney & Ramsay, 1973; see also, e.g., Hancock, 1985; Twiss & Moores, 1992). The bulk deformation of densely faulted areas has been assessed using the FaultKin software of Allmendinger et al. (2012). The basic tenets of this software, described by Marrett & Allmendinger (1990), are the same as in the right-dihedra approach (Angelier & Mechler, 1977; Angelier, 1994). There exists many other approaches and computational methods for retrieving possibly polyphased stress or strain states from a fault slip dataset (see Célérier et al., 2012 for a recent review) and it is outside the scope of this study to discuss their merits. Nevertheless, it should be noticed that the approach used by Marrett & Allmendinger (1990) is intended to provide a qualitative description of the strain ellipsoid, not the stress ellipsoid. Several authors have argued that, in essence, the analysis of fault slip data informs more about strain than about stress (e.g., Twiss & Unruh, 1998; Tikoff & Wojtal, 1999; Gapais et al., 2000). According to Célérier et al. (2012), methods aiming at retrieving paleostresses may be more suited for separating distinct subsets (presumed to witness successive tectonic events) within a given fault slip dataset whereas methods aiming at retrieving strain (e.g., Marrett & Allmendinger, 1990) may be more suited for yielding an average estimate of strain within a rock volume. In our case, the mineralogy of slickenfibers, which is of two types, has provided an independent criterion for separating the fault slip data into two subsets, therefore the 'strain' approach seems more appropriate. Using this separation criterion, we have obtained two strain ellipsoids that are very different in orientation and shape, which suggests that the criterion is robust. The situation met in this study is interesting in the sense that mineralogy provided a mean for attributing each fault slip datum to one of two subsets, at variance with the common case where a separation criterion (e.g., cross-cutting relations) is available for only a few faults, further separation being done by 'analogy' or 'consistency'. As a result, and because two contrasting strain ellipsoids have been obtained, the fault slip dataset of this study (see Annexe 7) might be used for testing the ability of the numerous existing methods of stress/strain inversion (cf.

Célérier et al., 2012) to retrieve two events from a single body of data. However, this remains beyond the scope of this paper.

4. Results

4.1. Reference samples

We here describe three hand specimens that are representative of field cases where serpentine occurs in association with deformation. The two first specimens come from higher levels of the Koniambo Massif. The first sample includes a ~1 cm-thick vein of light olive green serpentine with a massive aspect (Fig. 4a). The vein has been active as a fault plane as indicated by fine striations underlined by black oxides along a surface parallel to its margin. The Raman spectrum of the vein material (analysis A3802) shows two closely spaced main bands centered on ~3688 cm^{-1} and ~3694 cm^{-1}, which are diagnostic of polygonal serpentine (Auzende et al., 2004; Ulrich, 2010; Ulrich et al., 2014). The second sample includes a ~1 cm-thick vein of platy-fibrous serpentine (Fig. 4b). Outside the vein, the host rock shows a Raman spectrum (D3793) with two main bands centered on ~3688 cm^{-1} and ~3696 cm^{-1}, indicating the presence of polygonal serpentine. The vein itself is composite. Two insulated domains with diffuse boundaries are made of darker serpentine showing a Raman spectrum (A3790) with two main bands centered on ~3672 cm^{-1} and ~3700 cm^{-1}, typical for antigorite. The main part of the vein appears as an heterogeneous stack of fibers. The Raman spectrum of analysis C3792 in this domain shows a minor band centered on ~3671 cm^{-1}, attesting for the presence of antigorite. In addition, the main band

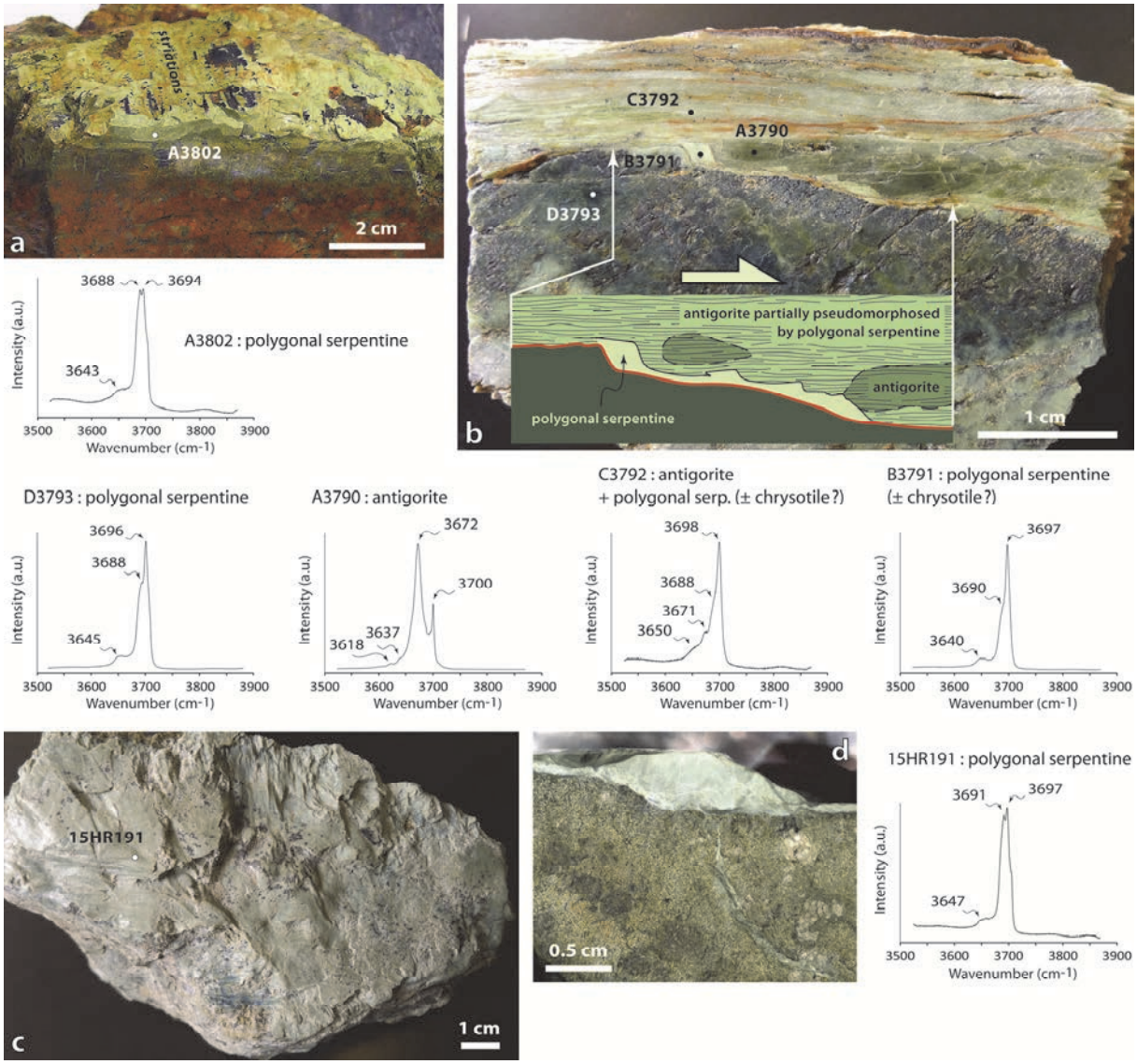

Figure 4 Close views of the first (a), second (b) and third (c & d) reference samples discussed in the text, and corresponding Raman spectra.

centered on ~3698 cm^{-1} and the adjacent poorly developed band at ~3688 cm^{-1} indicate the presence of polygonal serpentine or/and chrysotile. Finally, the margin of the vein is underlined by small domains of homogeneous light green serpentine. Their staircase distribution indicates that they formed as the result of a fault slip event. The Raman spectrum of analysis B3791 shows a main band centered on ~3697 cm^{-1} and an adjacent poorly developed band at ~3690 cm^{-1} which, again, points to the presence of polygonal serpentine or/and chrysotile. In that case, however, chrysotile is unlikely because the serpentine in this part of the vein is massive and does not display the habitus of well defined submillimetric fibers that is typical for chrysotile (Lahondère & Maurizot, 2009; Ulrich, 2010;

Lahondère et al., 2012). The small domains of polygonal serpentine have well defined boundaries, which suggests that they formed later than the adjacent domain of darker antigorite did. Furthemore, the platy-fibrous nature of the main part of the vein is typical for antigorite (e.g., Lahondère et al., 2012), therefore the occasional intimate association of antigorite and polygonal serpentine, like in analysis C3792, can be interpreted as the result of a partial pseudomorphosis of antigorite by fine-grained polygonal serpentine. Thus, the crystallization of polygonal serpentine appears to postdate that of antigorite.

The third sample comes from the Vavouto peninsula, within the serpentine sole. It consists of a fist-sized elongate clast taken from one of the major shear zones met along the BMS section (Fig. 2c). The clast, which is made of pervasively serpentinized harzburgite with few orthopyroxene relics, is embedded in a film up to 0.5 cm thick of homogeneous pale green serpentine (Fig. 4c,d). The Raman spectrum (analysis 15HR191) shows two closely spaced main bands centered on ~3691 cm^{-1} and ~3697 cm^{-1}, indicating that the film consists of polygonal serpentine.

4.2. Field determination of the serpentine polymorphs associated with deformation

Based on the characterization of the three above samples as well as other reference samples, we have established a number of macroscopic criteria for a field assessment of the mineralogy of fault zones and shear zones. Within fault zones, antigorite and polygonal serpentine are both able to build macroscopic slickenfibers with a clear staircase geometry. For distinguishing the two polymorphs, the main argument is textural. Antigorite has a well expressed platy-fibrous aspect (see also, e.g., Lahondère et al., 2012) with fibers frequently several centimeters long (Fig. 5a). As a result, fault planes covered with antigorite slickenfibers tend to produce shiny surfaces. In contrast, polygonal serpentine is massive, matte, and develops only short slickenfibers (Fig. 5b,c). A second argument is the fact that polygonal serpentine is pale green whereas antigorite is generally darker (Figs. 4b,c,d and 5a,b,c). However, this criterion is not always satisfactory in the saprolitic levels where weathering modifies the colours. In that case, polygonal serpentine tends to become olive green (Figs. 4a and 5c). In addition, some fault planes bear slickenfibers showing mixed properties, with a clear platy-fibrous nature but a pale green colour and a matte aspect (Fig. 5d). In that case, taking into account the

likeliness of a pseudomorphic replacement of antigorite by polygonal serpentine, as in the second reference sample above, we have assumed that the slickenfibers witness a syn-antigorite slip event.

Antigorite and polygonal serpentine are also involved in shear zones. The main argument for distinguishing them in the field is again textural, antigorite forming distinct lamellae (Fig. 5e) whereas polygonal serpentine is more massive despite the development of a pronounced cleavage (Fig. 5f).

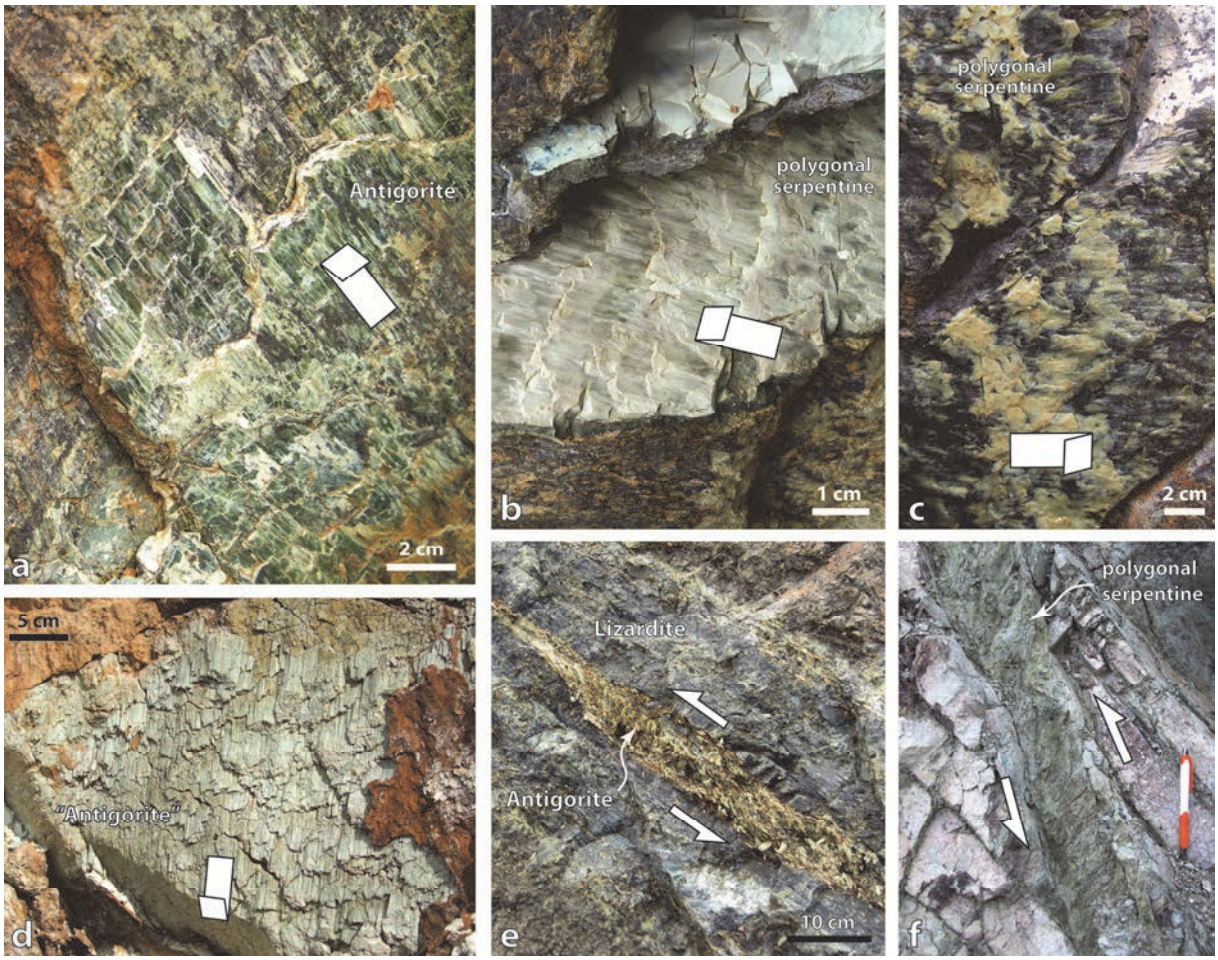

Figure 5 Field views of serpentine-bearing fault planes (a to d) and shear zones (e & f) in the Upper structural level.

Most of the shear zones we have observed involve polygonal serpentine. There is always a close coincidence between the shear zone walls and the margins of the serpentine body (Fig. 5e,f). The fabric in each shear zone being pronounced, shearing may essentially post-date serpentinization. Nevertheless, would shearing occur under physical conditions outside the stability range of a primary serpentine, it is expected that a new serpentine polymorph would easily crystallize during the pervasive

deformation. Hence, for shear zones with an homogeneous serpentine content, we assume that shearing and mineral growth were coeval.

In addition to antigorite and polygonal serpentine, lizardite and chrysotile were also observed in the field, with features similar to those reported by Ulrich (2010) and Lahondère et al. (2012). Dark lizardite is widespread, present as a diffuse grain-scale network in the peridotites and as infillings of ~1 mm to ~5 cm-wide joints. It is also found on the margins of many of the faults and shear zones that involve antigorite or polygonal serpentine (Fig. 5c,e). However, lizardite itself only rarely bears striations and, in our experience, never builds macroscopic slickenfibers, therefore we made no attempt to characterize the deformation associated with lizardite. Chrysotile occurs as very thin fibers always oriented at right angle to the vein walls within ≤ 1 cm-thick veinlets. Dense networks of subparallel veinlets are locally observed. Such veins can be interpreted as tension gashes, therefore, in principle, they could provide some clue on the tectonic regime that prevailed during chrysotile growth. Alternatively, tension gashes may open in the absence of a significant tectonic contribution, for instance due to fracturing assisted by fluid pressure. For this reason, and because these thin veins represent very small amounts of strain, we ignored them during the analysis of deformation.

Garnierite, the Ni-rich mineral mixture that usually contains finely crystallized serpentine, is easy to identify in the field due to its flashy green colour. It occurs as mm to ~10 cm-thick veins unevenly distributed along the base of the thick lateritic profile capping the Koniambo Massif. Macroscopically, the vein infilling is generally massive. In a study covering the Grande Terre, Cluzel & Vigier (2008) reported that garnierite can be found as striated coatings or slickenfibers along fault planes. During our study, we have observed very few fault surfaces where the striations were undoubtly carried by garnierite and, in that case, no sense-of-slip criterion was available.

4.3. Structural analysis

We identified three structural levels, which correlate with the rock horizons identified by Maurizot et al. (2002) on the basis of the intensity of serpentinization (Fig. 2a,b).

4.3.1 Upper structural level

The Upper structural level coincides with the domain of moderately serpentinized peridotites at higher levels of the massif. A dense network of fractures, most of them dipping steeply, crosscut the peridotites (Fig. 6a). The spacing between adjacent macroscopic fractures is always less than ~2 m. In between fractures, the least serpentinized peridotites show 'mesh' textures resulting from a partial replacement of olivine by lizardite along grain boundaries and grain-scale microfractures (Fig. 6b). As usually observed in the case of mesh textures (e.g., Wicks & Whittaker, 1977; Rouméjon & Cannat, 2014), the original texture of the peridotite is well preserved, hence syn- to post-serpentinization deformation appears negligible on that scale.

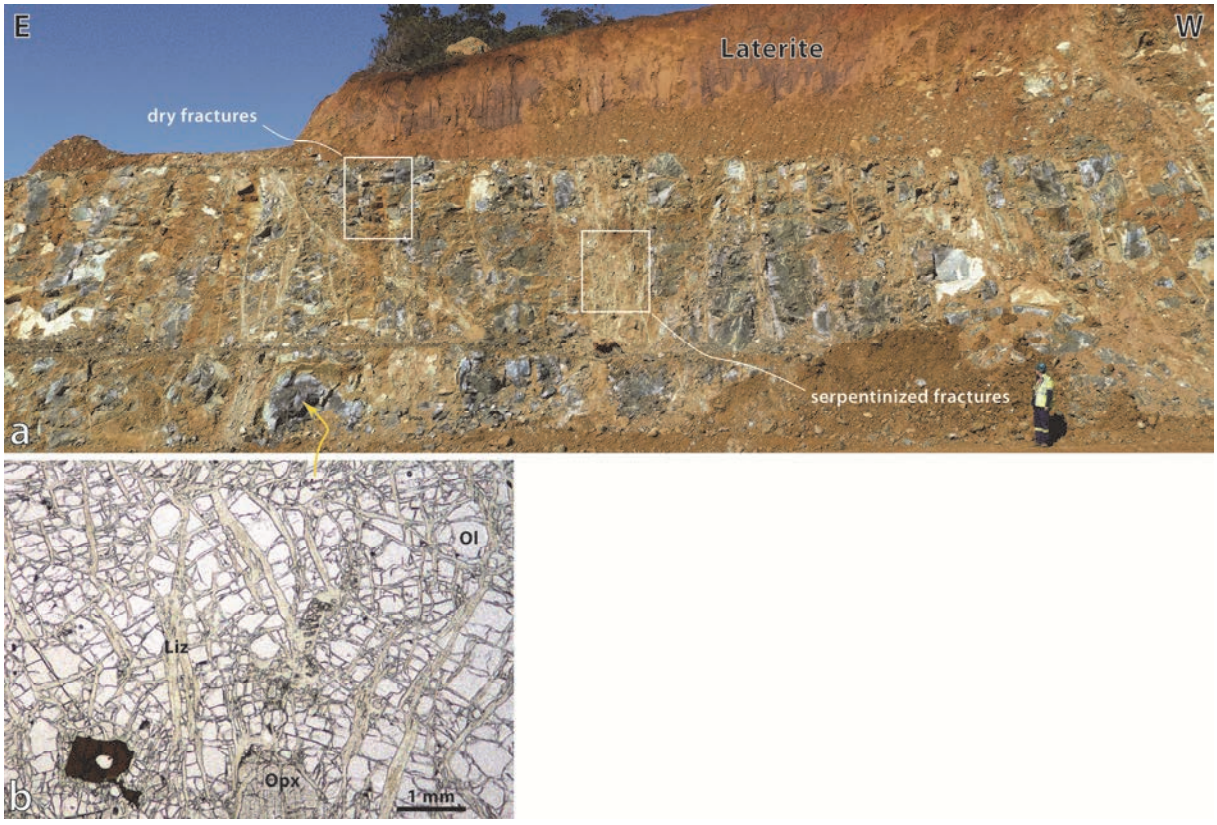

Figure 6 a) Field view of an open pit with a dense network of fractures, typical from the Upper structural level. b) Photomicrograph of a sample representative of the least serpentinized peridotites within the Koniambo Massif, from the Upper structural level, in between the macroscopic fractures. The sample shows a typical 'mesh' texture composed of lizardite (Liz) mesh rims surrounding olivine (Ol) and orthopyroxene (Opx) mesh cores.

On the outcrop scale, in addition to 'dry' joints, many fractures are filled with one or several types of serpentine (Fig. 6a). When serpentine is present, the structure resembles the 'kernel' pattern of joints frequently observed in partially serpentinized peridotites (O'Hanley, 1992), however the second-

order cross-fractures that are usually associated with this pattern are rarely present in our case. According to O'Hanley (1992), this happens when the degree of serpentinization of the peridotite in between the joints is high.

Garnierite veins occur across a height of about 5-20 m at the transition between the weathering profile and the bedrock. Silica veins are also frequent in the coarse-grained saprolite, some of them closely associated with garnierite (Fig. 7a). Most commonly, a single garnierite vein or a couple of veins with a steep attitude occur individually, the next vein lying at a distance of a few tens of meters. Networks of interconnected veins are less frequent (Fig. 7a). Garnierite veins generally follow pre-existing fractures filled with lizardite or/and antigorite or/and polygonal serpentine (Fig. 7b). The orientation of the largest garnierite veins is reported in figure 7c; a large part of them define a crude preferred NNE-SSW strike trend, which coincides with the orientation of most antigorite- and polygonal serpentine-bearing faults (Fig. 8a,b) (see below).

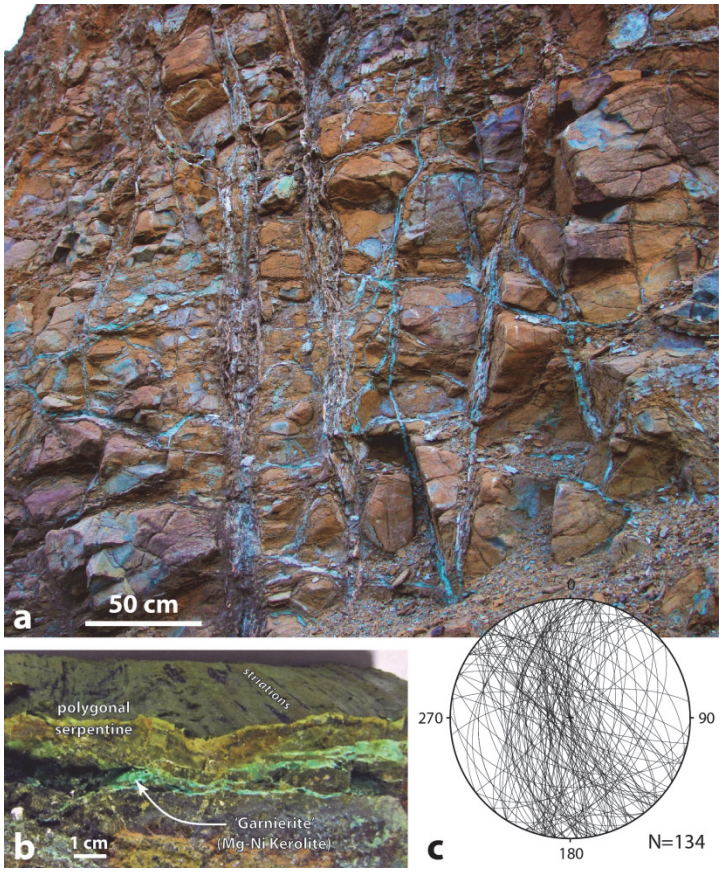

Figure 7 a) Field view of a network of garnierite±silice veins in the transition zone between coarse-grained saprolite and the bedrock, at higher levels of the Koniambo Massif. b) Close view of a sample with garnierite veinlets following the margin of a vein of polygonal serpentine. c) Stereogram (lower hemisphere, equal-area projection) showing the orientation of the largest garnierite veins in the studied pits.

Even where garnierite is not involved, serpentinized fractures frequently include more than one type of serpentine. When present together with another serpentine polymorph, lizardite occupies the margins of the fracture (Fig. 5c). When occurring together, antigorite and polygonal serpentine occupy the core vs. the margins of the fracture, respectively. As discussed with the second reference sample in Section 4.1 (Fig. 4b), polygonal serpentine has formed later, building distinct slickenfibers. This geometry is reminiscent of the process of antitaxial oblique vein growth (Durney & Ramsay, 1973). In most veins involving fibrous polygonal serpentine or/and antigorite, the fibers lie at a very low angle to the vein walls, hence these veins can be interpreted as fault zones (e.g Durney and Ramsay, 1973). A total of 125 such faults has been measured in a series of open pits covering a relatively small area on the top of the Koniambo Massif (Fig. 2a). The syn-polygonal serpentine vs. syn-antigorite nature of each fault displacement has been determined by assessing the mineralogy of associated slickenfibers (Fig. 5a,b,c,d) (see Section 4.2). As a result, two fault subsets have been defined, which compare well in

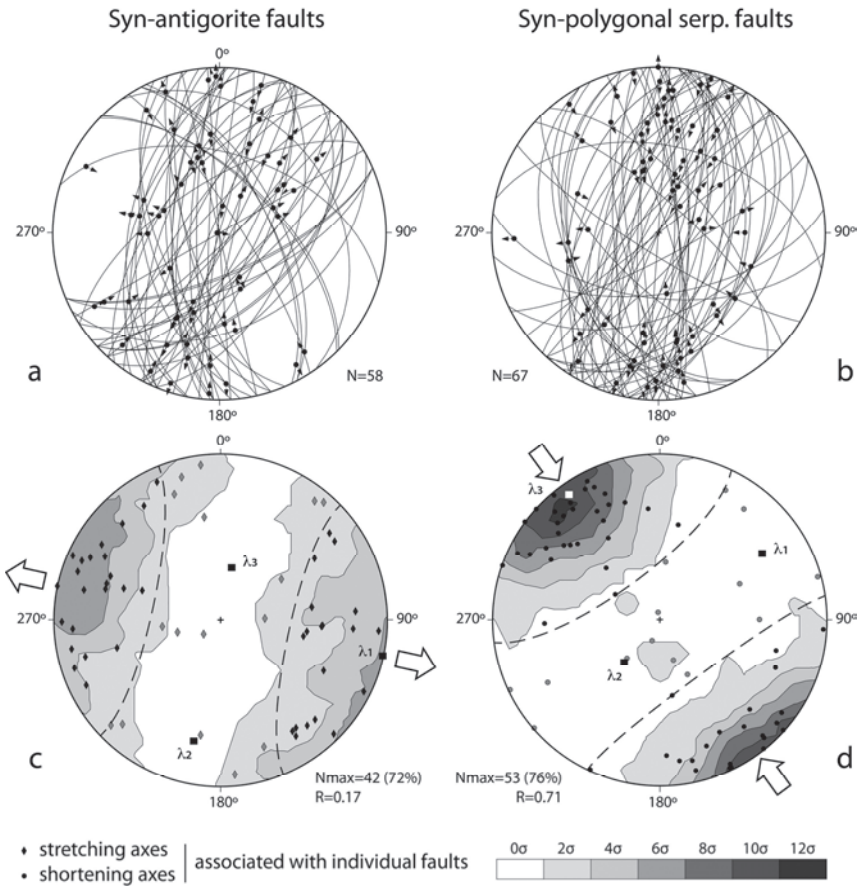

Figure 8 Stereograms (lower hemisphere, equal-area projection) showing the orientation of all measured syn-antigorite (a) and syn-polygonal serpentine (b) faults at higher levels of the Koniambo Massif (location in figure 2a), and the result of the

analysis of these fault slip data using the FaultKin software of Allmendinger et al. (2012) (c & d). The strain axes associated with individual faults are reported in black vs. grey when compatible vs. incompatible with the computed bulk strain ellipsoid, respectively (see the text). Dashed lines are small circles separating the domains of these two data types. Shades of grey vary as a function of the probability for the presence of the axis of maximum stretching (in c) or the axis of maximum shortening (in d).

terms of orientation but have distinct kinematics (Fig. 8a,b). The majority of the faults with dominantly dip-slip movement have a normal sense of slip when associated with antigorite vs. a reverse sense of slip when associated with polygonal serpentine. Fault slip analysis using the FaultKin software of Allmendinger et al. (2012) documents two strikingly different strain ellipsoids (Fig. 8c,d). The syn-antigorite faults yield a highly constrictional ellipsoid, as illustrated by the value of 0.17 computed for the R ratio ($R=(\varepsilon_2-\varepsilon_3)/(\varepsilon_1-\varepsilon_3)$ so that R equates 0 for pure constriction, 0.5 for plane strain, and 1.0 for pure flattening). Consequently, λ_1, the axis of maximum stretching, is the most accurately defined; it lies horizontally with a N102 trend (Fig. 8c). The axis of maximum shortening, λ_3, plunges steeply (64°) to the north-northeast. The syn-polygonal serpentine faults yield an ellipsoid in the flattening field (R=0.71). Consequently, λ_3 is the most accurately defined axis; it lies subhorizontally with a N144 trend, while λ_1 plunges shallowly in the N057 direction (Fig. 8d). Figure 9 illustrates the results of fault analysis on the scale of a pit ~200 m wide within the main area of investigation (Pit 208) and on an isolated site located 2 km further northwest (Bilboquet, see figure 2a for location). Fault slip analysis on these sites yields results that fit closely with those deduced from the bulk dataset.

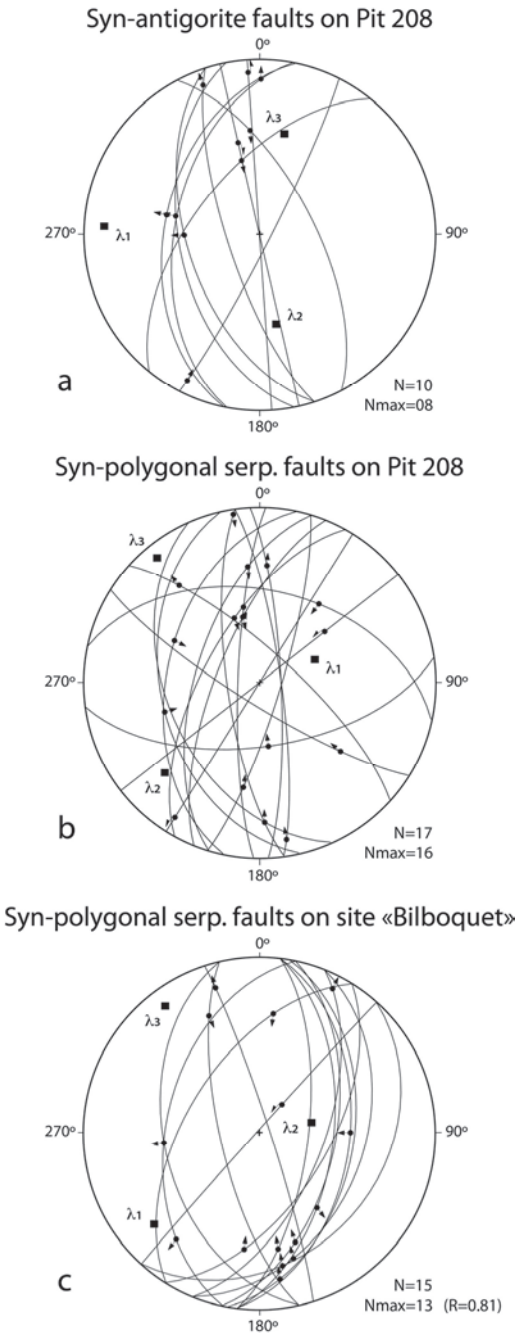

Figure 9 Stereograms (lower hemisphere, equal-area projection) showing the orientation of faults at two specific sites (location in figure 2a), and the result of the analysis of these fault slip data.

The ability of each computed ellipsoid to account for the related fault slip data can be evaluated by comparing the number of faults compatible with the ellipsoid (Nmax) with the total number of faults (N). Considering the bulk dataset, Nmax reaches 72% vs. 76% of N for the syn-antigorite vs. syn-polygonal serpentine faults, respectively (Fig. 8c,d). Hence, in both cases, about one quarter of the data is inconsistent with the computed ellipsoid. This is also illustrated by the orientations of stretching (Fig. 8c) or shortening (Fig. 8d) axes associated with individual faults, which show a scattered distribution. The FaultKin software does not indicate which faults are found incompatible

following the computation procedure. Nevertheless, these faults are likely those for which the individual strain axes differ the most in orientation from the computed ellipsoid. Assuming so, we have searched for the appropriate number of incompatible faults (16 syn-antigorite faults and 14 syn-polygonal serpentine faults); the individual axes of these faults are shown in grey in figures 8c and 8d. To account for the presence of incompatible faults, the three following explanations, not mutually exclusive, may be considered.

i) In a few cases, we might have misidentified the mineralogy of the slickenfibers.

ii) The 'incompatible' fault movements may result from the local accommodation of variable block displacements/rotations that are an inherent consequence of the highly localized nature of brittle deformation (e.g., Gapais et al., 2000).

iii) The change in mineralogy of the slickenfibers (from antigorite to polygonal serpentine), which reflects some change in physical or/and chemical conditions, has not necessarily occurred at exactly the same time the tectonic regime has been modified. The tectonic regime might have changed before or after the mineralogical change. In the first case, some antigorite-bearing faults could relate to the second tectonic regime; conversely, in the second case, some polygonal serpentine-bearing faults could relate to the first tectonic regime. As a fact, treated separately, the incompatible faults of each mineralogy tend to yield a strain ellipsoid resembling that obtained with the faults of the other mineralogy (or, regardless, the ellipsoid obtained with only the compatible faults of the other mineralogy, which is almost similar in terms of orientation of the strain axes). However, this might be just a fortuitous consequence of the fact that the two 'main' ellipsoids are strikingly different, so that most of the incompatible faults of one mineralogy are necessarily compatible with the ellipsoid of the other mineralogy. Moreover, at best, this third explanation could account for the incompatible faults of one mineralogy, not both. An alternative hypothesis is the existence of a third tectonic regime that would have prevailed at around the time of the mineralogical change, during which the incompatible faults of both mineralogies would have formed. However, the treatment of all the incompatible faults together yields a strain ellipsoid that is poorly consistent, with Nmax reaching only 67% of N. Hence, this alternative hypothesis is not satisfactory.

Further southwest and at lower elevation with respect to the open pits, the mine access road provides a large outcrop near the transition between the upper and intermediate structural levels

(Roadsite '620 m' in figure 2a). It shows fault planes with slickenfibers as well as shear zones a few centimeters thick (Fig. 5f), both involving polygonal serpentine. Fault slip analysis yields an ellipsoid in the flattening field (R=0.66), with λ_3 shallowly plunging southward (27°) along a N006 trend (Fig. 10). This is broadly consistent with the syn-polygonal serpentine strain field deduced from the open pits (Fig. 8d), though with a ~40° clockwise rotation in the direction of λ_3. In principle, this difference could reflect differential large-size block rotations post-dating the measured fault slip increments. However, in this area, the dunitic interlayers retain the same ENE-WSW strike and ~50° southward dip as elsewhere in the Koniambo Massif (Maurizot et al., 2002), therefore this hypothesis is unlikely. Hence, the difference is more likely to reflect a modification of the strain field through space (i.e. strain partitioning) or time.

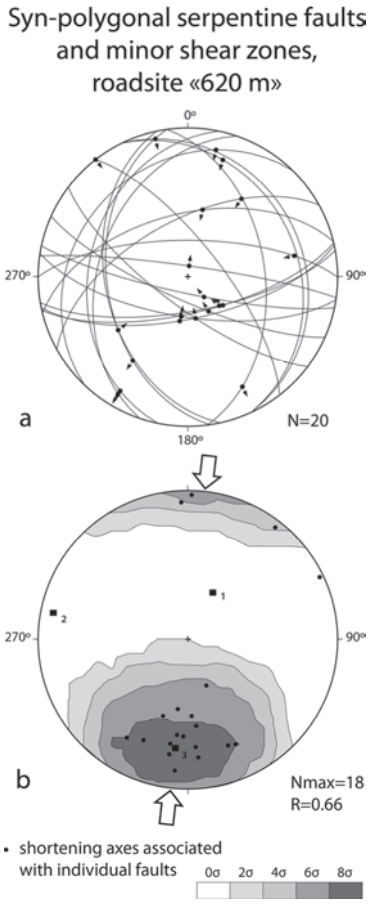

Figure 10 Stereograms (lower hemisphere, equal-area projection) showing the orientation of faults and minor shear zones at roadsite '620 m' (location in figure 2a), and the result of the analysis of this fault slip dataset. Shades of grey vary as a function of the probability for the presence of the axis of maximum shortening.

4.3.2 Lower structural level (the serpentine sole)

The best exposures of the serpentine sole are along the BMS and VAV cross-sections in the Vavouto peninsula (Figs. 2, 3, 11 and 12). Further east, the map contour of the basal contact of the

nappe implies a culmination of this contact slightly northwest of the Tambounan Peak (Fig. 2a). As a result, the surface probably dips westward beneath the peninsula, with a slope of ~6-7º (Fig. 2b). The contact is exposed at the eastern margin of the peninsula, displaying ~E-W-trending open folds on a ~100 m scale (Fig. 3a).

The rocks along the sole are brecciated and/or foliated. Breccias are well developed along the BMS section (Fig. 11a) and consist of clasts of serpentinized peridotite separated by serpentine joints (Fig. 4d). Many joints bear very fine striations (Fig. 4c) and can be interpreted as local shear planes. The striations have extremely variable orientations, which probably results from the complexity of clast displacements/rotations during brecciation. Major shear zones occur along the BMS section (Fig. 2c), marked by a reduction in clast size (Figs. 11a and 12a). The shear zone boundaries are dominantly diffuse, but locally change to sharp. The width of the main shear zones ranges from ~2 to ~10 m. In the shear zones, the greater density of fault planes subparallel to their walls tends to produce elongate clasts that locally define a crude foliation (e.g., in the upper part of figure 12b). Such a fault rock may be described as a 'foliated serpentinite cataclasite' (Manatschal et al., 2006). The shear zone boundaries are dominantly diffuse, but locally change to sharp (Figs. 11a and 12a). The width of the main shear zones ranges from ~2 to ~10 m. In the core of some shear zones, the planar fabric is more pronounced and locally oblique to the shear zone walls. In cases where this oblique fabric had the appearance of a closely spaced cleavage, it helped to assess the kinematics of the shear zone. In most cases, however, it is difficult to decide whether the fabric could alternatively represent a dense pattern of Riedel shears, hence implying the opposite sense of shear with respect to that deduced from an oblique cleavage (cf. Petit, 1987, his figure 1a,b). As a result, the kinematics of individual shear zones and shear planes along the BMS section has essentially been deduced from their effect (offset and drag folding) on pre-existing markers (Figs. 11b and 12b).

The largest part of the VAV section consists of serpentinites with a pronounced planar fabric (Figs. 3a and 11c). On a 10 cm scale, this fabric is underlined by a disjunctive anastomosing cleavage (Fig. 12c). When present, clasts are isolated, hence the rock retains a matrix-supported texture (Fig. 11d). This fault rock may be described as a 'incohesive sheared serpentinite' (Norrell et al., 1989) or a 'foliated serpentinite' (Manatschal et al., 2006). Generally, the clasts have an elongate and subangular to rounded shape with a consistent orientation throughout the rock (Fig. 11d). As a result, the rock

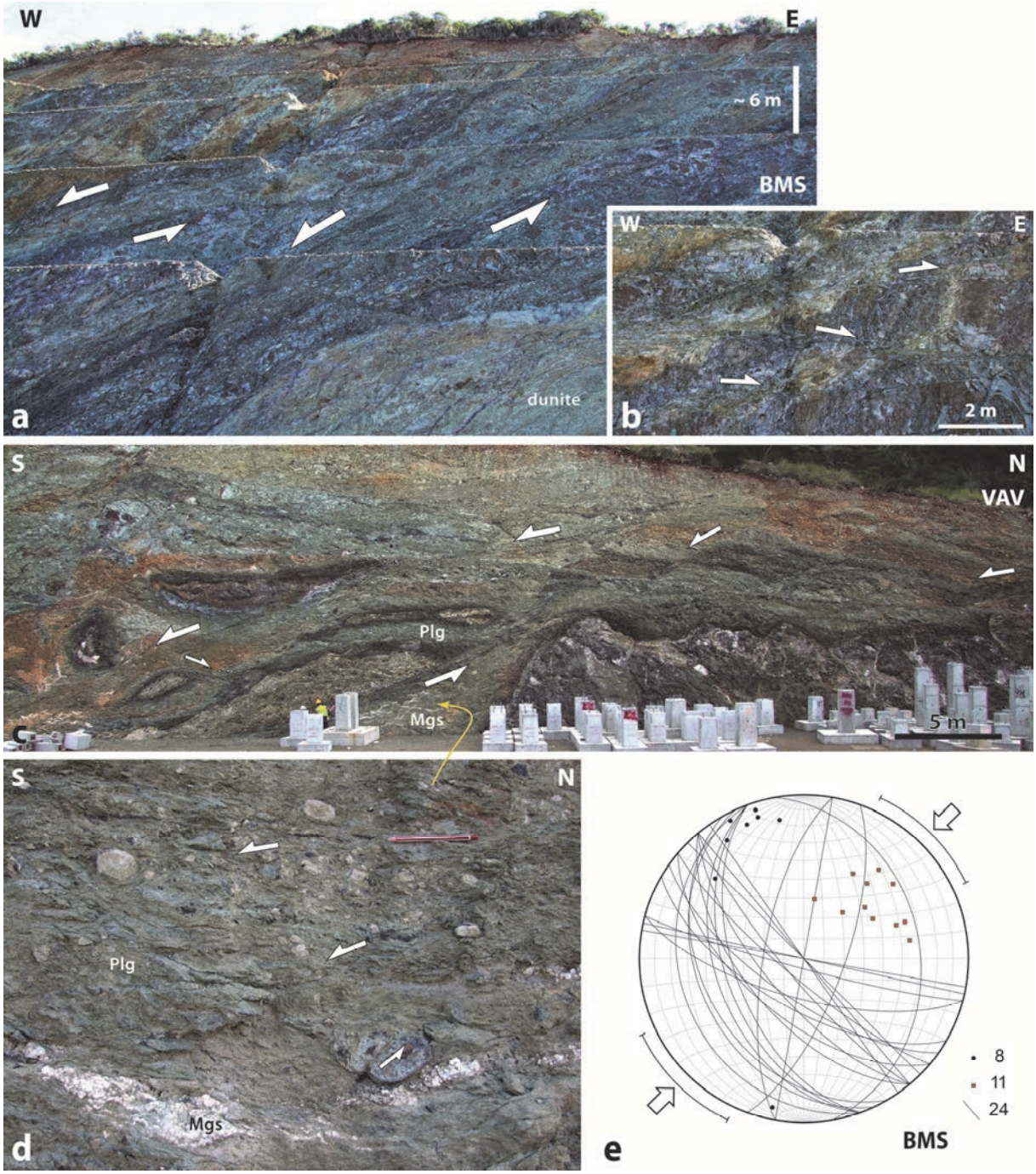

Figure 11 Field views of the serpentine sole in the Vavouto peninsula, along the BMS (a & b) and VAV (c & d) sections. Plg, polygonal serpentine; Mgs, magnesite. e) Stereogram (lower hemisphere, equal-area projection) showing the orientation, along the BMS section, of large shear planes (shown as orange squares representing poles of planes), of planar magnesite veins (shown as great circles) in between major shear zones, and of fold axes (shown as black dots) of folded magnesite veins within the shear zones.

has the typical appearance of a mylonite. In the uncommon case where the clast is very large, it shows the same features (cf. the ovoid clast in the upper left corner of figure 3a). Moreover, early compositional layering has been transposed into parallelism with the cleavage (Fig. 11c), attesting for very large strains. Hence, the foliated serpentinites of the VAV section may be referred to as mylonites, although Norrell et al. (1989) suggested to restrict the term 'serpentinite mylonites' to the case of cohesive antigorite schists with a ribbon texture. Under microscope, the fabric of the foliated serpentinites is irregularly distributed but locally pervasive (e.g., in the right part of figure 12d; the relations with the magnesite body are discussed further below). A component of ductile deformation is thus involved, with perhaps no or limited crystal plasticity but with a significant contribution of dissolution processes (cf. Ulrich et al., 2014). The northern end of the VAV section shows that the foliated serpentinites occur immediately above the basal contact of the nappe (Fig. 3a). The southern end of the section shows that they underlie the part of the sole dominated by breccias through a relatively sharp (~3 m-thick) transition zone (Fig. 3b). Hence, the foliated serpentinites form a distinct layer of most intensely deformed rocks at the base of the serpentine sole, with a thickness of at least 20 m.

According to Ulrich (2010), the serpentine sole of the Koniambo Massif keeps the record of an early pervasive development of lizardite, a later formation of antigorite in mm to cm-thick veins, and finally the formation of chrysotile±polygonal serpentine in local veinlet networks. Ulrich et al. (2014) recently modified this view by documenting a more widespread development of polygonal serpentine. As illustrated by the third reference sample in Section 4.1 (Fig. 4c,d), our observations indicate that the major shear zones along the BMS section involve pale green polygonal serpentine as the main syn-kinematic mineral phase (Figs. 11a and 12a,b). This also applies to the foliated serpentinites of the VAV section (Figs. 11c,d and 12c). Magnesite also occurs within this layer and along the BMS section, in the form of irregularly distributed veins and local stockworks (Figs. 2c, 11c and 12a). Magnesite occurs in close association with polygonal serpentine (Figs. 11c,d and 12a,b,c), which may suggest that the two phases were co-stable. Alternatively, this may mean that polygonal serpentine is the most reactive serpentine polymorph for in situ replacement by magnesite, or the most favourable substratum for magnesite precipitation (see discussion in Ulrich et al., 2014). Quesnel et al. (2013) briefly described the geometry of the magnesite veins of the Koniambo Massif and argued that at least some of them have been emplaced during pervasive shearing of the serpentine sole. Further evidence

of the syn-kinematic nature of the magnesite veins is shown in figure 12. In the macroscopic examples b and c, the veins are offset by local shear planes that contribute to the bulk shearing deformation. Hence, at variance with a common assumption for New Caledonia (e.g., Ulrich, 2010), not all the magnesite veins have been emplaced in a post-tectonic setting along a network of pre-existing discontinuites. In addition to the vein infilling habitus, elongate clusters of partly coalescent millimetric to centimetric nodules of magnesite are occasionally found (some of the veins actually consist of such clusters with well defined substraight boundaries, like in figure 12b). Figure 12d shows part of a pluricentimetric nodule under microscope. Its right margin is irregular, made up of submillimetric nodules of cryptocrystalline magnesite. This geometry, which suggests an unconstrained growth of magnesite, could be taken as an indication that magnesite has formed in the absence of contemporaneous deformation, after the development of the shear fabric visible in the host serpentinite. However, the upper margin of the nodule is straight and coincides with one of the shear bands related to this fabric. The relations between the nodule and the shear band, highlighted in the enlargement, are clearly more in line with the shear band post-dating the nodule than with the opposite. Overall, the relations seen in figure 12d are consistent with magnesite having grown during shearing.

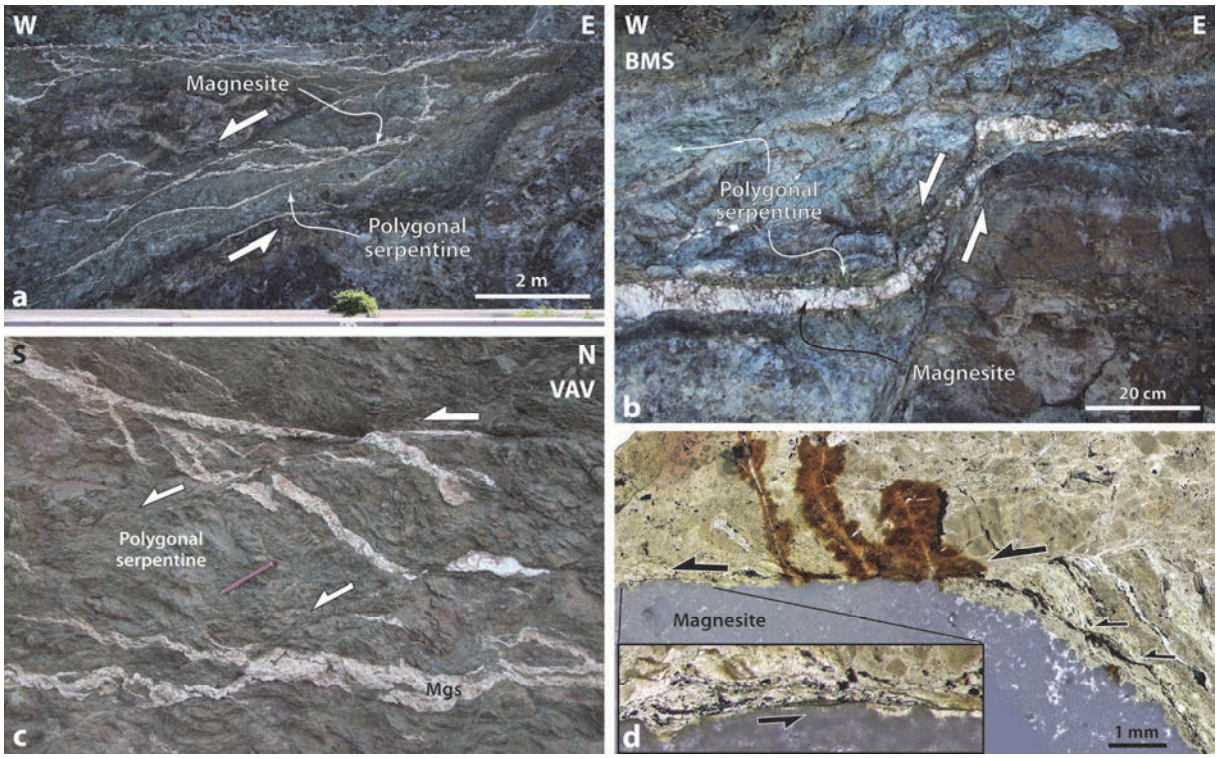

Figure 12 Field views (a to c) and microphotograph (d) illustrating the relationships between magnesite and deformation in the serpentine sole.

The asymmetric distribution of shear zones along the BMS (Fig. 2c) and VAV (Fig. 11c) sections documents non coaxial deformation across the serpentine sole. The exposure surface being smooth along both sections, the orientation of the main shear zones is difficult to evaluate. Nevertheless, a dozen of shear planes of significant size (several meters) have been measured along the BMS section (Fig. 11e). Their mean orientation is N141, 46° SW. This suggests top-to-SW kinematics for the bulk shearing deformation. Top-to-SW shearing is consistent with the orientation of steep planar magnesite veins in between the shear zones (mean value N134, 62°SW), interpreted as tension gashes (Quesnel et al., 2013), and with the orientation of folds developed at the expense of magnesite veins within the shear zones (Fig. 11e). Top-to-SW shearing is also consistent with the apparent top-to-west vs. top-to-south sense of shear observed along the ~W-E-trending BMS vs. ~N-S-trending VAV section, respectively. The orientation of the ellipsoid delineated by the large ovoid clast in the upper left corner of figure 3a also fits with this interpretation. Along the BMS section, the major shear zones with an apparent top-to-west sense of shear have a mean apparent dip of 24.5° (Fig. 2c). Assuming that the mean strike of these shear zones is N141 (i.e. the same as for the meter-scale shear planes) and taking into account the N082 strike of the BMS section, the mean true dip of the major shear zones can be estimated at ~28°. Taking into account the likely ~6-7° westward slope of the basal contact of the nappe beneath the Vavouto peninsula (Fig. 2b), the obliquity of the main shear zones with respect to the boundaries of the serpentine sole is probably around 22°. This obliquity is consistent with an interpretation of the shear zones as large C'-type shear bands (Berthé et al., 1979; Passchier & Trouw, 1996) developed during strong tangential shear across the serpentine sole. Smaller equivalent structures are visible in figures 11c, 12b and 12c. Finally, it should be noted that flat-lying antithetic shear planes also occur in the eastern part of the BMS section (Figs. 2c and 11b). In figure 11b, they crosscut the main southwest-dipping shear fabric, however their relationship with one of the major shear zones suggests that they may have developed contemporaneously.

4.3.3 Intermediate structural level

In the Intermediate structural level, the degree of serpentinization is overall high but laterally variable. The main part is similar to exposures of the Upper structural level, with a dense network of serpentine-bearing fractures. The distinctive feature of the Intermediate structural level is that this rock mass is crosscut by low-dipping shear zones a few meters thick, characterized by a pervasive development of light green polygonal serpentine (Fig. 13a). Two such shear zones, here named SZ1

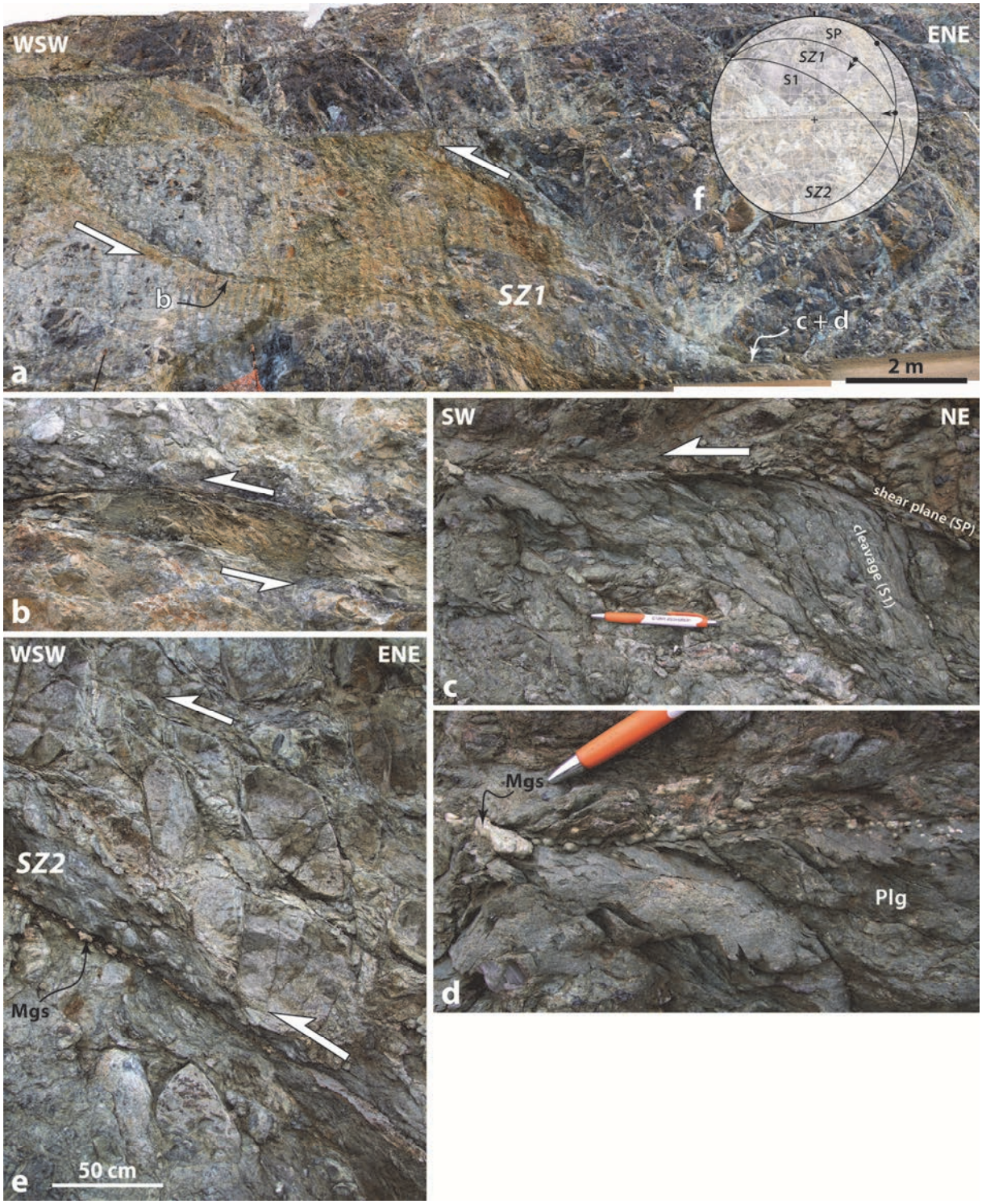

Figure 13 Field views of SZ1 (a to d) and SZ2 (e), two major low-dipping shear zones typical from the Intermediate structural level (location in figure 2a). Plg, polygonal serpentine; Mgs, magnesite. f) Stereogram (lower hemisphere, equal-area projection) showing the orientation of structural elements in the two shear zones (see the text).

and SZ2, occur at high levels of the Intermediate structural level (Fig. 2a). In this area, continuous rock exposure along the mine access road enables to note that no similar shear zone exists between SZ1 and SZ2. The NE-SW horizontal spacing between the two shear zones is ~450 m. Both SZ1 and SZ2 involve polygonal serpentine with a closely spaced cleavage as well as magnesite (Fig. 13b,c,d,e; for SZ2, see also Quesnel et al., 2013, their figure 3b). In the case of SZ1, striations were not observed. The direction of shearing is assumed to lie at right angle to the intersection between the cleavage and shear planes located along the margins of the shear zone (Fig. 13b,c), along a ~N34 trend (Fig. 13f). In the case of SZ2, a major fault plane in the core of the shear zone bears striations with a N39 trend while the relationship between cleavage and shear bands suggests a ~N85 trend for the direction of shearing (Fig. 13e,f). Both shear zones have top-to-SW kinematics. SZ1 has the attitude of a reverse-slip shear zone (Fig. 13a,b,c,f) while SZ2 combines reverse and dextral displacements (Fig. 13e,f).

At lower elevations, the mine access road crosscuts a prominent SW-dipping fault zone involving a ~30 m-thick pinch of fine-grained sediments (Maurizot et al., 2002) (Fig. 14a). These sediments are originally part of either the 'Poya terrane' (Maurizot et al., 2002) or, more likely, the 'Nepoui flysch' (D. Cluzel, personal communication, 2012). As a result, they represent a fragment of the volcano-sedimentary series that immediately underlie the Peridotite Nappe (Cluzel et al., 2001). Hence, the fault zone likely roots slightly beneath the basal contact of the nappe, or along it (Fig. 2b) if one takes into account the fact that sheets of serpentinite are frequently mixed with substratum rocks around several klippes of the nappe (e.g., Maurizot et al., 1985). Within the fault zone, the main fault superposes highly sheared serpentinites onto the sediments (Fig. 14a). Its orientation is N146, 38°SW and it bears pronounced striations with a N72 trend (Fig. 14b). Along this contact and across a structural thickness of at least 75 m above it, shear sense criteria indicate a reverse-slip (top-to-ENE) displacement (Fig. 14c,d). This movement is consistent with the incorporation of rocks from the substratum into the fault zone, and with the probable offset of the roof of the serpentine sole across it (Fig. 2a,b). Hence, the fault zone likely formed later than at least part of the tangential shear along the serpentine sole. In addition, this top-to-ENE fault, together with another shear zone with similar kinematics found ~1.4 km further east along the mine access road, can be viewed as conjugate shears with respect to the top-to-SW shear zones such as SZ1 and SZ2 (Fig. 15).

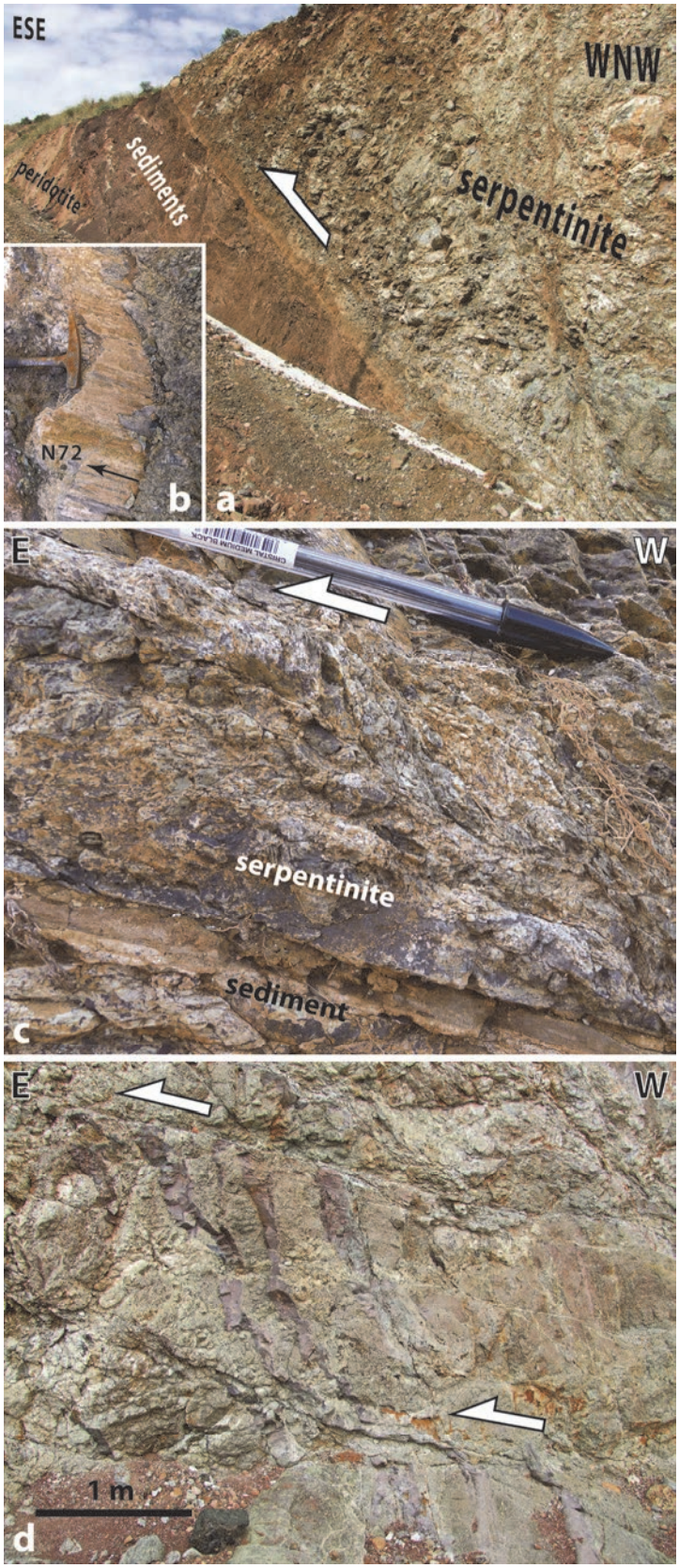

Figure 14 Field views of the reverse-slip fault zone with top-to-ENE kinematics shown in figure 2a,b.

5. Discussion

Here we summarize the results of our study of the Koniambo Massif and integrate them in a vertical section of the Peridotite Nappe focusing on the distribution of deformation associated with serpentines (Figs. 15 and 16). We discuss the observed variations of the orientation of the principal strain axes in terms of temporal and/or spatial changes. The intensity and style of deformation being strikingly different between the main mass of the nappe and its sole, we then examine the possibility that this difference results from variations in the degree of serpentinization of the peridotites. Finally, because this is probably not the case, we discuss which other processes could explain strong strain localization at lower levels of the nappe. The implications of this study for the mechanism of emplacement of the Peridotite Nappe and more generally the tectonic evolution of New Caledonia (see, e.g., Cluzel et al., 2012 and Lagabrielle et al., 2013, for two contrasting recent interpretations) are not discussed here and will be the topic of a distinct paper.

5.1. Summary of observations: the vertical distribution of deformation in the Koniambo Massif

Figure 15 summarizes the results of our structural analysis of the Koniambo Massif while figure 16 illustrates the possible relationships between the three structural levels identified in the Koniambo Massif.

The Upper structural level is characterized by a very dense network of fractures (Fig. 6a). Most fractures dip steeply and are filled with one or several types of serpentine. Many fractures have been activated as faults; in that case, we have observed that antigorite and polygonal serpentine are the two serpentine polymorphs able to build slickenfibers along the fault planes. Using the mineralogy of the slickenfibers as a criterion for separating the fault slip data into two subsets, we retrieved two strain ellipsoids that are very different in orientation and shape. The bulk deformation associated with antigorite is characterized by a highly constrictional ellipsoid with λ_1, the axis of maximum stretching, lying horizontally along a N102 trend. The bulk deformation associated with polygonal serpentine is characterized by an ellipsoid in the flattening field with λ_3, the axis of maximum shortening, lying subhorizontally along a N144 trend. The block diagram of figure 15 depicts schematically the deformation of the Upper structural level associated with polygonal serpentine, rather than with antigorite, because polygonal serpentine is also the main mineral phase associated with identifiable structures in the other structural levels. On roadsite '620 m', faults and minor shear zones associated

with polygonal serpentine imply a shallowly plunging λ_3 axis with a N006 trend. In the block-diagram, this site is shown at the top of the Intermediate structural level to highlight its location at lower elevation with respect to the main area of fault measurements (Fig. 2a). As explained in section 4.3.1, the ~40° difference in the direction of λ_3 between this area and roadsite '620 m' is unlikely to result from late differential rotations of large-size blocks. Rather, it probably reflects a modification of the strain field through space or time. We come back to this issue in the next Section.

The Lower structural level coincides with the serpentine sole. As a rule in New Caledonia (e.g., Avias, 1967; Leguéré, 1976; Cluzel et al., 2012), the serpentine sole of the Koniambo Massif is pervasively and intensely deformed. The remarkable exposures of the Vavouto peninsula show that breccias dominate while foliated serpentinites, interpreted as mylonitic rocks, form a distinct basal layer at least 20 m thick, well visible along the VAV section (Figs. 3 and 11c,d). The asymmetric distribution of shear bands and shear zones documents non-coaxial deformation with a top-to-SW sense of shear. Polygonal serpentine and magnesite are syn-kinematic phases with respect to this deformation (Figs. 4c,d and 12). Along the BMS section, major low-dipping shear zones are distributed with a ~100 m lengthscale, and some of them have a length of at least 200 m (Fig. 2c). As described in Section 4.3.2, their mean obliquity with respect to the basal contact of the nappe is estimated at ~22°. We interpret these shear zones as C'-type shear bands developed within a thick zone of strong tangential shear that coincides with the serpentine sole (Figs. 15 and 16; see also Lahondère et al., 2012, their figure 115). In line with this interpretation, no equivalent shear zone is observed above the serpentine sole.

The Intermediate structural level is characterized by the presence of several meters-thick reverse-slip shear zones (Figs. 13 and 14). Top-to-SW shear zones are synthetic to pervasive shearing along the serpentine sole and, likewise, involve polygonal serpentine and magnesite as syn-kinematic mineral phases (Fig. 13c,d,e). Therefore, although we had no opportunity to observe this contact in the field, we suppose that the shear zones root along the roof of the serpentine sole, the whole sole acting as a décollement (Fig. 15 and, in figure 16, geometric relationship 'r1'). In figure 16, the roof of the sole is schematically shown as a distinct fault; in reality, it is more likely to coincide with a zone across which the intensity of brecciation progressively diminishes (cf. the smooth shape of the curve in the strain-depth diagram). Alternatively, some shear zones may root at deeper level (Fig. 16, relationship 'r2'),

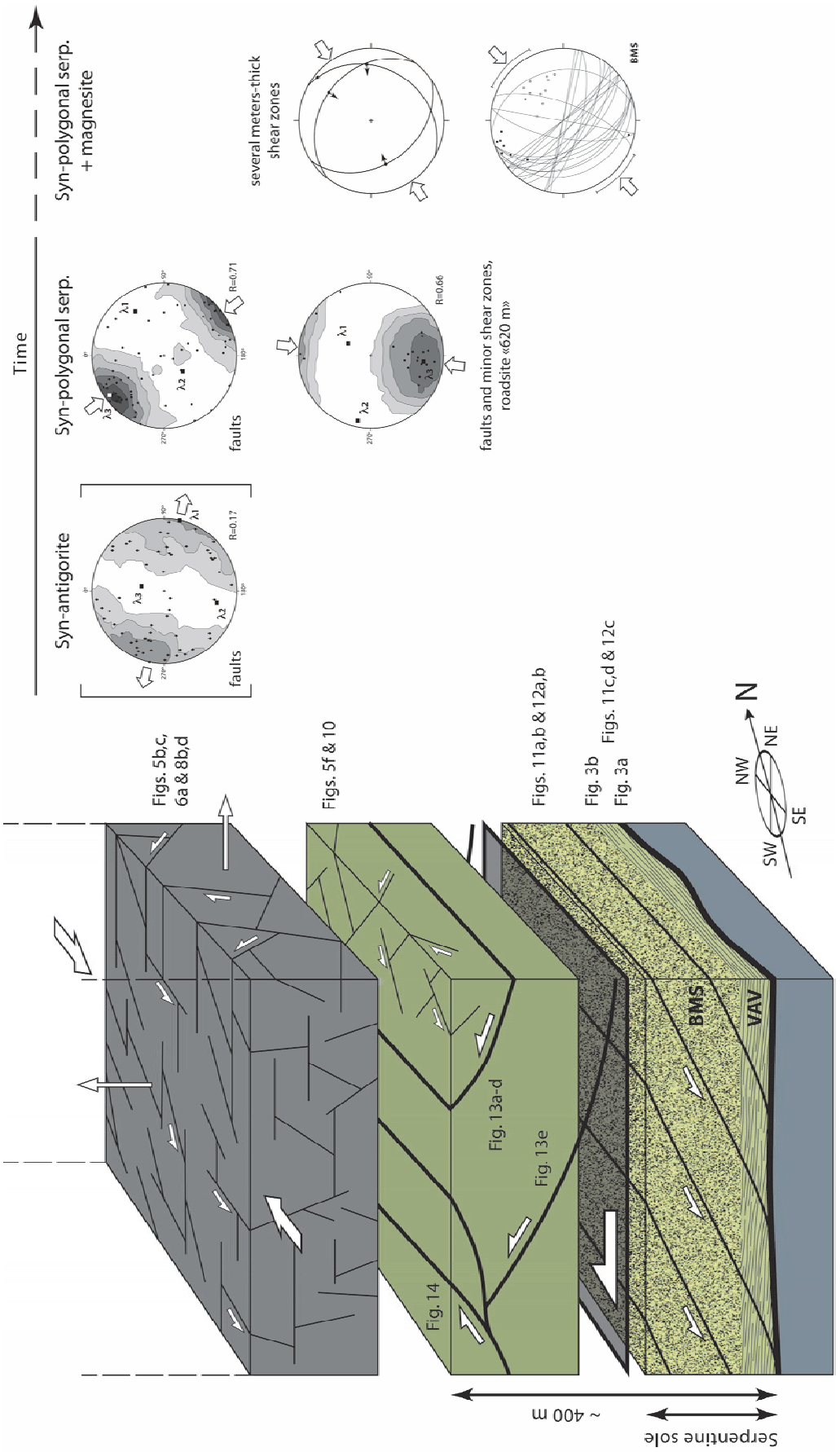

Figure 15 Block-diagram and time chart summarizing the results of this study.

for instance along the relatively sharp contact between the foliated serpentinites and the overlying serpentinite breccias (Fig. 3b) and/or along the basal contact of the nappe. This alternative is suggested by the presence of a relatively large top-to-SW reverse-slip shear zone at the northern end of the VAV section (Fig. 3a) and, though antithetic, by the characteristics of the fault zone of figure 14 (see Section 4.3.3 and below).

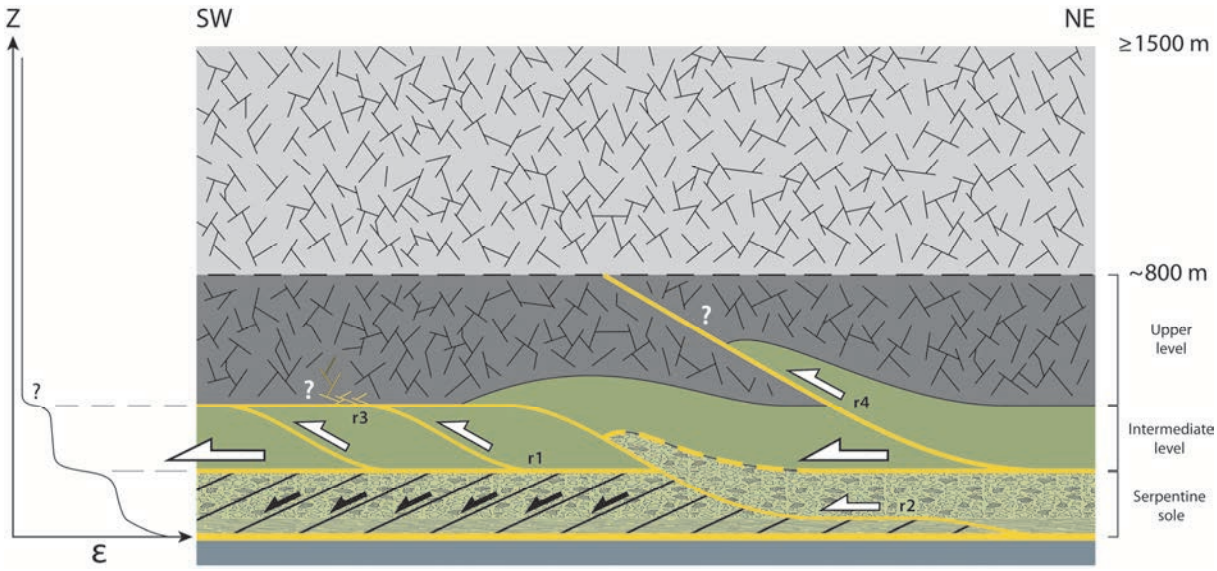

Figure 16 Schematic cross-section depicting the vertical distribution of deformation within the Peridotite Nappe by the time top-to-SW shearing occurred along the serpentine sole. 'r1' to 'r4' are geometric relationships discussed in the text. The thickness and the topography of the nappe are poorly constrained and are likely to have changed during deformation.

The NE-SW horizontal spacing between two consecutive top-to-SW shear zones, SZ1 and SZ2, is ~450 m. This is slightly less than the thickness of the Upper structural level in the Koniambo Massif (Fig. 2b) and much less than the thickness of the Peridotite Nappe in the Massif du Sud (≥ 1.5 km). This narrow spacing suggests that at least some of the shear zones do not cross the nappe up to the surface but remain confined to the Intermediate structural level. As a fact, although rock exposures are abundant in the open pits of the top of the Koniambo Massif, we have not observed any such shear zone in the Upper structural level. Based on this indirect evidence, it is here suggested that the shear zones may connect to another flat-lying décollement located along the roof of the Intermediate structural level (Fig. 16, relationship 'r3'). Like for the roof of the sole, this décollement might not coincide with a distinct fault but with a zone across which the reverse-slip displacement of the shear

zones could be absorbed through diffuse faulting. In addition, a few major shear zones may ramp up to the surface (Fig. 16, relationship 'r4'). No such shear zone is observed in the Koniambo Massif but one likely exists in the northern part of the nearby Kopéto-Boulinda Massif (see figure 1 for location). It is highlighted by a north-dipping serpentinite sheet about 200 m thick that emanates from the serpentine sole of this massif, at elevations around 200 m, and climbs among the peridotites up to an elevation of at least 500 m (Maurizot et al., 1985, their figure 4; Maurizot, 2007). The precise geometry and the kinematics of this probable shear zone remain to be documented.

Finally, top-to-NE shear zones also exist in the Koniambo Massif, as subsidiary structures in the serpentine sole (Figs. 2c and 11b,c), and as conjugate shears with respect to the top-to-SW shear zones in the Intermediate structural level (Figs. 14 and 15). Because it roots along or slightly beneath the base of the serpentine sole and likely offsets its roof (Fig. 2b), the reverse fault zone of figure 14 is probably a relatively late feature with respect to pervasive top-to-SW shearing along the sole. The shear zone labelled 'r2', in figure 16, would be an equivalent synthetic shear zone.

5.2. Temporal vs. spatial evolution of deformation

As summarized in figure 15, our analysis of serpentine-bearing faults and shear zones documents major variations in the orientation of the principal strain axes. At least part of these variations reflect a temporal evolution. This is the case within the Upper structural level, where fault slip data associated with antigorite and polygonal serpentine were collected in the same restricted area but yielded two strikingly different strain ellipsoids. Microstructural observations indicate that polygonal serpentine postdates antigorite (see Sections 4.1 and 4.3.1), in agreement with the time sequence identified by Ulrich (2010) in the serpentine sole of the Koniambo Massif (lizardite, then antigorite, then chrysotile sometimes associated with, or replaced by, polygonal serpentine). Hence, the Upper structural level keeps the record of a temporal change from WNW-ESE horizontal stretching, during antigorite crystallization, to NW-SE horizontal shortening, during polygonal serpentine crystallization.

The origin of the other variations in orientation of the principal strain axes is more difficult to assess because they involve the same serpentine polymorph (polygonal serpentine) and occur across distinct levels of the nappe. Therefore, the change from NW-SE shortening in the Upper structural

level to NE-SW shearing in the serpentine sole could reflect a spatial rather than a temporal evolution, i.e. vertical strain partitioning at a specific evolutionary stage of the nappe. The ~N-S direction of shortening recorded at an intermediate structural height, on roadsite '620 m', may support this view. Nevertheless, in our opinion, the observed changes in shortening direction are more likely to reflect a temporal evolution. A first reason is that it seems difficult to conceive a tectonic setting in which the nappe would undergo horizontal shortening at right angle to its direction of displacement (assuming the latter is given by the direction of shear along the basal décollement). A second reason is the fact that in the Intermediate structural level, the main shear zones, which accommodate NE-SW shortening, crosscut rocks with the same dense network of fractures as in the Upper structural level (Fig. 13a). We could not measure enough fault planes to determine the deformation pattern in the rock volume between the shear zones, nevertheless this crosscutting relation suggests that the event having produced NE-SW shortening in the Intermediate structural level (and top-to-SW shearing in the sole) is younger than most of the fracture sets observed in the Upper structural level.

Thus, we suspect that both the syn-antigorite and the syn-polygonal serpentine fault sets identifed in the Upper structural level are older than the top-to-SW shear deformation observed in the serpentine sole. This contrasts with the opinion of Leguéré (1976) who supposed that the various sets of fractures he identified in the main mass of the nappe are all younger than the deformation recorded by the sole. In addition, according to Leguéré (1976), these fracture sets provide evidence for a three-step temporal evolution involving an episode of ENE-WSW compression, then an episode of NNW-SSE compression, then an episode of NNW-SSE extension. This scenario applies to the Kopéto-Boulinda and Koniambo Massifs, but the same events and the same chronology, with some variations in the orientation of the strain axes, are given by Leguéré (1976) for the other klippes of the Peridotite Nappe he examined, spread over the Grande Terre. The episode of NNW-SSE compression, of fairly constant orientation across the Grande Terre (Leguéré, 1976), correlates well with the syn-polygonal serpentine event we identified in the Upper structural level of the Koniambo Massif. This supports the hypothesis that this event, although not easy to understand from the point of view of geodynamics, is not merely local but of regional significance. The episode of NNW-SSE extension, which is more variable in orientation on the scale of the Grande Terre (extension is locally WNW-ESE to W-E, cf. Leguéré, 1976), may correlate with the syn-antigorite event we identified. Finally, the episode of ENE-WSW compression, locally modified to a NE-SW compression (Leguéré, 1976), correlates with

the syn-polygonal serpentine±magnesite event we identified in the Intermediate structural level and the serpentine sole. If so, however, the chronology of events proposed by Leguéré (1976) differs strikingly from ours: his first event is our last one, and his last event is our first one. We ignore the reasons for this disagreement, but note that Leguéré (1976) does not provide details on the arguments he used for establishing his chronology. It is also possible that we failed to identify one or several late episodes of normal faulting that are reported from the sedimentary series surrounding the klippes of the Peridotite Nappe (Lagabrielle et al., 2005; Chardon & Chevillotte, 2006). According to Cluzel & Vigier (2008), garnierite, which is located within the klippes at the base of the weathering profile, is occasionally found as striated coatings along fault planes that essentially display normal-sense displacement, and within tension gashes with a *en échelon* geometry that also implies normal-sense shearing. Hence, as proposed by Leguéré (1976), relatively young extension is apparently recorded in the Peridotite Nappe, nevertheless we could not document it in our study of the Koniambo Massif.

5.3. The distribution of deformation vs. serpentinization

As described in Section 5.1 and figure 15, the three structural levels identified in the Koniambo Massif show strikingly different styles of deformation. These levels correlate fairly well with the subhorizontal lithological layering of the massif defined by Maurizot et al. (2002), which refers to variations in the intensity of serpentinization. Hence, it is tempting to consider that the intensity of serpentinization played a major role in the way deformation has been distributed across the Peridotite Nappe. Here we examine this hypothesis.

As implicitly considered in several studies (e.g., Avias, 1967; Cluzel et al., 2001), there is little doubt that the massive serpentinites of the sole acted as a weak décollement (Fig. 16). Compared to the Massif du Sud, where the serpentine sole is only a few tens of meters thick (e.g., Guillon, 1975), the northwestern klippes of the Peridotite Nappe are characterized by a prominent sole up to 200 m thick (Fig. 2b). This probably accounts for the large size of subsidiary structures developed within it, such as the major shear zones of the BMS section (Fig. 2c). All the serpentine polymorphs are present in the sole of the Koniambo Massif (Ulrich, 2010), however polygonal serpentine is the polymorph that is specifically associated with the most prominent structures accommodating top-to-SW

tangential shear (the basal layer of foliated serpentinites and the main shear zones, Figs. 11c,d and 12a,b). The same holds true for the shear zones on the Intermediate structural level (Fig. 13).

The Upper structural level coincides with the domain of moderately serpentinized peridotites of Maurizot et al. (2002). However, unlike in some parts of the Massif du Sud (e.g., Orloff, 1968), pristine peridotites are virtually absent from the Koniambo Massif. In the field, the least altered samples are identified as they seem to retain a granoblastic texture, yet their dark green colour is symptomatic of a significant serpentine content. Under microscope, these samples show 'mesh' textures (e.g., Rouméjon & Cannat, 2014) resulting from a partial replacement of olivine by lizardite (Fig. 6b; for another example from the Koniambo Massif, see Lahondère et al., 2012, their figures 309 to 312). The avancement of the reaction is most often enough for lizardite to form connected 'mesh rims' surrounding isolated olivine 'mesh cores'. According to theoretical and experimental evidence (e.g., Handy et al., 1999; Escartín et al., 2001), with such a texture, the peridotite, though moderately serpentinized, should be nearly as weak as pure serpentinite. Nevertheless, as well documented in the literature (e.g., Wicks & Whittaker, 1977; Rouméjon & Cannat, 2014), serpentine mesh textures are essentially pseudomorphic, therefore peridotites with these textures usually preserve their pre-serpentinization fabrics. This also applies to the Upper structural level of the Koniambo Massif, from the thin section (Fig. 6b; see also Lahondère et al., 2012) to the ~1 km scale (Maurizot et al., 2002). Moreover, the serpentine polymorphs that developed later than lizardite (antigorite, polygonal serpentine) are restricted to infillings of the macroscopic fractures (Figs. 5 and 6a). Many of these fractures have been activated as faults but the bulk mass of intimately serpentinized (lizardite-bearing) peridotites remained intact. As discussed in Section 5.2, syn-polygonal serpentine deformation recorded by the serpentine sole and the shear zones of the Intermediate structural level is likely younger than syn-polygonal serpentine faulting recorded by the Upper structural level. This further supports the picture of a rigid Upper structural level by the time shearing was accumulating along the sole. Hence, in the Koniambo Massif at least, it seems that the highly uneven vertical distribution of syn to post-serpentinization deformation across the Peridotite Nappe is not related to a vertical gradient in strength that would result from variations in the degree of serpentinization: within the range of observed variations, all the rocks should have approximately the same strength (cf. Escartín et al., 2001).

5.4. What promoted strain localization at lower levels of the nappe ?

The above discussion has shown that the degree of serpentinization is probably not the factor which led deformation to localize along the sole of the nappe. Though with a reverse vertical strain gradient, the situation met in the Koniambo Massif is reminiscent of observations made at slow-spreading oceanic ridges (MacLeod et al., 2002; Schroeder & John, 2004; Karson et al., 2006; Rouméjon & Cannat, 2014) and at the ocean-continent transition in magma-poor rifted margins (Manatschal et al., 2006). In these examples, large volumes of mantle peridotites have been pervasively serpentinized within an active tectonic setting, however most of these rocks remain massive, showing pseudomorphic mesh textures, whereas sheared serpentinites are restricted to an overlying high-strain zone, about 100 m thick, that defines a major extensional detachment.

An important feature of these oceanic detachment zones is that, in addition to serpentine, they commonly involve talc, chlorite and Ca-amphiboles such as tremolite (Escartín et al., 2003; Schroeder & John, 2004; Boschi et al., 2006; Picazo et al., 2012). The microstructural record in the related fault schists, as well as experimental evidence in the case of talc (e.g., Moore & Lockner, 2011), indicate that these minerals are weaker than serpentine. Hence, the apparent paradox of a large amount of the serpentine-rich rocks having escaped deformation might be explained by strain localization promoted by the occurrence of even weaker mineral assemblages in a restricted rock domain (e.g., Schroeder & John, 2004). Could this interpretation apply to the Koniambo Massif ? Ulrich (2010) has suspected the presence of talc in the serpentine sole of the massif, however subsequent analytical work has not confirmed this feature (Ulrich et al., 2014). In constrast, talc is well identified at higher levels of the massif where it participates, together with lizardite, to the pseudomorphic overprint of the high grade fabrics of some peridotites (Lahondère et al., 2012, their figures 301 to 306). In our experience, talc occurs on the margins of the lizardite-bearing macroscopic fractures and results from the destabilization of pyroxenes. Tremolite, sometimes associated with chlorite and/or talc, occurs as veins and fault infillings in the main mass of the Peridotite Nappe (Lahondère & Maurizot, 2009; Lahondère et al., 2012). According to Lahondère et al. (2012), it is spatially and genetically linked to the group of doleritic to felsic magmatic dykes that crosscut the peridotites at ~50-55 Ma (e.g., Cluzel et al., 2012). These dykes occur as isolated bodies, they do not seem to form a connected network, and they are not especially abundant in the serpentine sole. Hence, although their presence, together with tremolite veins, might have helped to localize deformation in some shear zones above the sole (e.g., in

the Kopéto-Boulinda Massif, cf. Lahondère et al., 2012), they are unlikely to have led to strain localization on the scale of the whole sole. Moreover, according to Lahondère et al. (2012), the crystallization of antigorite in the Peridotite Nappe is also contemporaneous with the emplacement of these dykes. Our analysis in the Koniambo Massif has shown that syn-antigorite deformation is old with respect to top-to-SW shearing recorded by the sole. As a result, tremolite can hardly be a late mineralization produced during strain localization, at variance with the situation in oceanic detachment zones (Schroeder & John, 2004; Boschi et al., 2006; Picazo et al., 2012).

To account for the localization of deformation at lower levels of the nappe, a simple alternative may be considered where the gradient in rock strength is not located within the Peridotite Nappe but arises from its juxtaposition against rocks of the substratum. In the Koniambo Massif, as for the other klippes of the northwestern coast, this substratum is essentially composed of basalts and dolerites (e.g., Guillon, 1975; Paris, 1981; Cluzel et al., 2001) (Fig. 3a). Such rocks are clearly stronger than serpentinites (e.g., Schroeder & John, 2004) and, following Escartín et al. (2001), also stronger than slightly serpentinized peridotites. Hence, a strength profile may be conceived where the whole Peridotite Nappe is weak, overlying a stronger subtratum. Deformation is then expected to concentrate in the part of the weak domain that is the closest to the strong one, i.e. on the soft side of the main rheological boundary. This hypothesis could account for strain localization along the sole of the nappe, however it may seem in conflict with the underlying basalts and dolerites being the main constituents of the 'Poya terrane', a complex package of kilometer-scale thrust sheets (Cluzel et al., 2001). On the scale of the Grande Terre, it is also common to note that the basement of the Peridotite Nappe has a complex geometry which contrasts with the simple flat-lying attitude of the nappe (e.g., Guillon, 1975; Paris, 1981; Cluzel et al., 2001, 2012). Nevertheless, within the Poya terrane, the internal deformation of the mafic rocks is limited (e.g., pillow lavas are well preserved), moreover the thrust sheets dip steeply (60-90°), even in close proximity to the flat-lying contact of the Peridotite Nappe (cf. Cluzel et al., 2001), which suggests that slicing of the Poya terrane may predate the emplacement of the nappe. Interestingly, where the Poya terrane underlies the nappe, the thickness of the serpentine sole is great (~100-200 m). This is the case in the Koniambo Massif and more generally in the klippes of the northwestern coast. In contrast, smaller klippes located further northeast, around the axis of the island, have a much thinner serpentine sole (~10-20 m) and a substratum made of pervasively schistose fine-grained sediments with a low grade metamorphic

overprint. Typical examples are the Tchingou Massif (e.g., Maurizot et al., 1985) and a series of kilometer-sized klippes around the Ougne summit (Maurizot et al., 1989) (see figure 1 for location). Assuming that the thickness of the sole depends essentially on the intensity of shearing, and assuming that the total amount of shear, linked to the displacement of the nappe, is approximately constant over the area under consideration, this large difference in sole thickness is consistent with the hypothesis that a lower vs. higher amount of strain is accommodated by the nappe when its substratum is made of soft metasediments vs. strong mafic rocks, respectively.

Finally, higher fluid pressures along the serpentine sole may also have promoted strain localization at this level of the nappe. Brecciation is widespread in the sole, which obviously results from shearing, but may also partly result from hydraulic fracturing. The magnesite veins, many of which were emplaced lately during shearing, are organized in networks that are locally consistent with this view (e.g., Quesnel et al., 2013, their figure 3a). Because serpentinization is more advanced at the sole than at higher levels of the nappe, it seems logical to suppose that the related fluids originate from below the nappe (Orloff, 1968; Ulrich, 2010). This was likely the case when antigorite crystallized (Ulrich, 2010; Lahondère et al., 2012) and also possible during the earlier formation of lizardite (Ulrich, 2010). This is less clear for polygonal serpentine, the younger polymorph that is associated with the most prominent structures accommodating top-to-SW shearing. Massive joint infillings (Fig. 4d) and slickenfibers (Fig. 5b,c) indicate that at least part of the mineralization in polygonal serpentine precipitated from a fluid. The close association of polygonal serpentine and magnesite (Figs. 11c,d, 12a,b,c and 13c,d,e) has two possible meanings. It may imply that the two phases were co-stable, or that polygonal serpentine was the most favourable substratum for a subsequent growth of magnesite. In the first case, polygonal serpentine would probably originate from the downward percolation of meteoric waters because this is demonstrably the case for magnesite (cf. Quesnel et al., 2013). If so, the abundance of polygonal serpentine in the sole implies that efficient pathways existed to carry the meteoric waters down there. Like for magnesite (Ulrich, 2010; Quesnel et al., 2013), these pathways could have been provided by the dense network of faults in the main mass of the nappe. However, whether these faults were active during the formation of polygonal serpentine at the sole is questionable because, as discussed in Section 5.2, syn-polygonal serpentine faulting at higher levels of the nappe probably predated top-to-SW shearing along the sole. Alternatively, polygonal serpentine at the sole may have precipitated from fluids emanating from below the nappe, for instance due to

dehydration of the underlying mafic rocks, whereas magnesite would have formed only later, from meteoric fluids.

6. Conclusion

Deformation associated with serpentinization shows important variations in intensity and style across the thickness of the Peridotite Nappe. Of the three structural levels identified in the Koniambo Massif, the Upper structural level is the thickest and is characterized by a dense network of fractures. Antigorite and polygonal serpentine form slickenfibers along fault planes with distinct kinematics. As a result, the Upper structural level keeps the record of at least two deformation events, the first associated with antigorite (WNW-ESE extension), the second with polygonal serpentine (NW-SE compression). The Lower structural level is represented by the serpentine sole. It consists of massive tectonic breccias overlying a layer of mylonitic serpentinites. The sole, which records pervasive tangential shear with top-to-SW kinematics, can be interpreted as a décollement at the base of the nappe. The Intermediate structural level is characterized by the presence of several meters-thick conjugate shear zones accommodating NE-SW shortening. Like the sole, these shear zones involve polygonal serpentine and magnesite as the main syn-kinematic mineral phases. Hence, a close link probably exists between the sole and the shear zones, and the different geometric relationships that may account for this link have been discussed (Fig. 16). With respect to top-to-SW shearing along the sole, the two deformation events recorded in the Upper structural level are old (certainly for the syn-antigorite WNW-ESE extension, probably for the syn-polygonal serpentine NW-SE compression).

The three structural levels correlate with the lithological layering of the massif defined by Maurizot et al. (2002), which refers to variations in the degree of serpentinization. It is therefore tempting to propose that the intensity of serpentinization had a major influence on the way deformation has been distributed across the Peridotite Nappe. However, even the least altered peridotites, in the Upper structural level, contain so much serpentine that, according to theoretical and experimental work (e.g., Handy et al., 1999; Escartín et al., 2001), they should be nearly as weak as pure serpentinite. Hence, no strong vertical gradient in strength due to variations in the degree of serpentinization is expected within the nappe. To account for strain localization along the serpentine sole, another explanation should be found. Our proposal, in Section 5.4, is that it results from the

juxtaposition of the nappe, made of weak serpentinized peridotites, against the strong mafic rocks of the underlying Poya terrane. This interpretation is at odds with the intuitive view that would consider the nappe, made of peridotites, as stronger than its basement. We acknowledge that this view is apparently supported by the fact that the nappe has a simple flat-lying attitude that contrasts with the complex internal structure of the basement (e.g., Guillon, 1975; Paris, 1981; Cluzel et al., 2012). Nevertheless, in support to our interpretation, we have noted that the serpentine sole is about ten times thinner when the substratum of the nappe is made of weak metasediments, compared to what it is when the substratum is made of mafic rocks. In addition, despite limited field evidence, strain localization may have been promoted by higher fluid pressures along the sole of the nappe.

Partie III : Chapitre 3 – Déformation et circulation de fluide à l'échelle de la Nappe des Péridotites

Complément de discussion : implication des résultats de l'analyse structurale sur le mécanisme de mise en place de la Nappe des Péridotites

Cette partie complémentaire vise à mettre en perspective les résultats de l'analyse structurale de la Nappe des Péridotites au regard des différents mécanismes de mise en place proposés dans la littérature. Cette discussion préliminaire fera office d'introduction au travail complémentaire à cette thèse, mené par Pierre Gautier, et faisant l'objet d'un projet d'article en cours d'écriture.

Très tôt, plusieurs auteurs ont proposé que l'emplacement de la Nappe des Péridotites et la formation des roches métamorphiques HP/LT aujourd'hui visibles au nord de l'île (unités de Pouébo et Diahot, Fig.I.3) étaient deux processus sub-contemporains suggérant un lien génétique entre les deux (e.g., Brothers, 1974; Paris & Lille, 1977). Cependant, la publication d'âges ^{39}Ar-^{40}Ar sur micas blancs interprétés comme datant le refroidissement des roches métamorphiques entre ~35-40 Ma (Ghent et al, 1994 ; Baldwin et al, 2007) et à la datation des sédiments entre ~34-35 Ma les plus jeunes chevauchés par la Nappe des Péridotites (Cluzel et al, 2001), mena à un consensus sur le fait que l'obduction de la Nappe des Péridotites s'est faite de manière contemporaine à l'exhumation des roches métamorphiques. Plusieurs scénarios de mise en place de la nappe du nord-est vers le sud-ouest sur le substrat néo-calédonien sont proposés dans la littérature et permettent de résoudre ce paradoxe apparent de manières différentes.

Balwin et al (2007), solutionnent le problème en proposant que ces deux processus n'aient pas été localisés au même endroit le long de la limite de plaque. La mise en place des massifs de péridotites localisées sur la côte nord-ouest de la Grande Terre et au sud-ouest du domaine métamorphique résulterait non pas de l'obduction elle-même, mais d'un événement post-obduction décrochant ayant généré au moins 150 km de déplacement dextre longitudinalement à l'île (voir aussi Brothers, 1974). Cependant, la faille principale la plus susceptible d'avoir accommodé ce déplacement reste très controversée, certains la décrivant comme une faille normale à vergence SW (e.g. Lagabrielle et Chauvet, 2008) et d'autres questionnant même jusqu'à son existence (e.g. Sevin et al, 2014).

Un deuxième scénario, considère que l'emplacement de la Nappe des Péridotites résulterait essentiellement d'un processus de glissement gravitaire (Guillon et Routhier, 1971 ; Cluzel et al, 1995 ; Lagabrielle et al, 2013) le long d'une pente à vergence SW dont l'origine serait la courbure d'échelle crustale du substrat sous-jacent.

Un troisième scénario propose un modèle de poussée par l'arrière, vraisemblablement soutenu par le contexte de convergence lithosphérique connu à cette époque (Cluzel et al, 2001 ; 2012). Même si ces auteurs soulignent également le synchronisme entre l'emplacement de la Nappe des Péridotites et l'exhumation des roches métamorphiques, ils n'adressent pas clairement le problème au regard de leur scénario. Pour Spandler et al (2005), l'exhumation des roches métamorphiques aurait pu se produire lors d'un court épisode de divergence (postérieur à 44 Ma et antérieur à ~34 Ma) entraînant une extension lithosphérique interrompant provisoirement le processus d'obduction de la nappe. L'emplacement de la nappe se serait fait ensuite selon le même modèle de poussée par l'arrière déjà proposé par Cluzel et al (2001).

Postérieurement à la mise en place de la nappe, un épisode d'extension NE-SW serait à l'origine du développement de failles de détachement précoces à faible pendage recoupées par un ensemble de failles normales à fort pendage, l'ensemble de ces structures ayant des orientations longitudinales à la Grande Terre (Lagabrielle et al, 2005 ; Lagabrielle et Chauvet, 2008). Le développement de ces structures serait responsable de l'amincissement de la Nappe des Péridotites et de l'actuelle morphologie en horst de l'île (Lagabrielle et al, 2005 ; Chardon et Chevillotte, 2006 ; Lagabrielle et Chauvet, 2008).

Notre analyse structurale de la Nappe des Péridotites montre que la semelle de serpentine et le niveau intermédiaire du massif de Koniambo ont tous deux enregistré un épisode de cisaillement vers le sud-ouest contemporain de la formation de la serpentine polygonale et de la magnésite (Fig.15). Au regard de l'évolution tectonique de la Nouvelle-Calédonie, cette déformation top sud-ouest pourrait aussi bien être attribuable à l'emplacement de la nappe sur le substrat néo-calédonien qu'à l'épisode d'extension post-obduction.

Dans l'hypothèse où le cisaillement top sud-ouest enregistré à la semelle de serpentine résulterait de l'emplacement de la nappe, plusieurs mécanismes de mise en place peuvent théoriquement être considérés (e.g. Merle, 1986). Comme nous l'avons mis en évidence précédemment et comme implicitement suggéré dans la littérature (e.g. Avias, 1967 ; Cluzel et al, 2001), la semelle de serpentine peut être considérée comme un niveau de décollement (Fig.16). La présence d'un tel niveau à la base de la nappe a pu favoriser son emplacement i) par un mécanisme de poussée par l'arrière ou ii) par un mécanisme de glissement gravitaire. Théoriquement, l'ensemble des mécanismes impliquant un niveau de décollement et menant à l'emplacement d'une nappe ont en commun l'enregistrement d'une

forte déformation non coaxiale le long de ce décollement, ce qui est en accord avec ce que nous observons à la semelle de serpentine. Par conséquent, la seule caractérisation des structures affectant la semelle de serpentine ne peut que difficilement nous renseigner sur le mécanisme ayant permis son emplacement. A l'inverse, la déformation enregistrée dans les niveaux sus-jacents au niveau de décollement différera en fonction du mécanisme impliqué (e.g. Merle, 1986).

Dans notre cas, la déformation enregistrée dans le niveau dit « intermédiaire » se caractérise par le développement de plusieurs zones de cisaillement à pendage faible à modéré, d'épaisseur métrique à plurimétrique et ayant une cinématique inverse (Fig.13 et 14). Dans l'hypothèse du glissement gravitaire, Lagabrielle et al (2013) proposent que la nappe ait pu glisser le long d'une pente d'environ 3° vers le sud-ouest. L'actuelle géométrie sub-horizontale du contact de base de la nappe (Fig.2) pourrait résulter d'un basculement de cette pente initiale. Par conséquent, les zones de cisaillement développées lors du glissement gravitaire dans les niveaux sus-jacents au niveau de décollement devraient également être basculées. Si l'on applique une rotation antihoraire d'environ 3° aux zones de cisaillement à vergence nord-est aujourd'hui observées dans la partie intermédiaire du massif (Fig.13), ces dernières garderont une cinématique inverse. De la même manière, appliquer un basculement antihoraire d'environ 3° à la zone de cisaillement inverse à vergence sud-ouest présentée figure 14 reviendrait même à renforcer son caractère chevauchant. Il semble dès lors raisonnable de considérer les zones de cisaillement localisées dans le niveau intermédiaire du massif comme représentant de vraies structures compressives. Comme expliqué dans la partie 5.1, il est probable qu'au moins certaines de ces zones de cisaillement représentent des structures en duplex imbriquées dans le niveau intermédiaire (Fig.16). De plus, il n'est pas exclu, même si cela reste hypothétique, que certaines des zones de cisaillement inverse puissent affecter l'ensemble de la nappe (Fig.16). Le caractère compressif des zones de cisaillements localisées dans le niveau intermédiaire implique que la déformation enregistrée au niveau de la semelle de serpentine ne puisse pas représenter une réactivation extensive du contact basal. En effet, compte tenu de la similarité en termes de cinématique de la déformation (cisaillement vers le sud-ouest) et de minéralogie, il semble difficile de considérer les structures localisées à la semelle de serpentine et au niveau intermédiaire comme représentant des événements distincts de déformation. Qui plus est, comme expliqué dans la partie 5.1, la zone de cisaillement présentée figure 14 représente très probablement une structure post-datant le cisaillement pervasif enregistré à la semelle de serpentine. Dans ces conditions, la déformation enregistrée à la semelle ne semble donc pas pouvoir représenter l'événement d'extension post-obduction. Comme discuté dans la

partie 5.1, l'obliquité (~22° par rapport au contact basal) et l'espacement (~100m) des zones de cisaillement à vergence sud-ouest localisées à la semelle de serpentine peuvent être interprétées comme des bandes de cisaillement de type C' au sein d'une zone épaisse ayant subi un fort cisaillement tangentiel (Fig.15 ; 16). Par conséquent, même si ces zones de cisaillements ont une cinématique normale, elles ne doivent pas être interprétées comme des évidences d'une extension généralisée. Dans l'hypothèse où ce que nous interprétons comme des bandes de cisaillement C' soit en réalité des failles normales, et considérant un espacement d'environ 100m entre ces failles, leurs extensions verticales devraient occasionnellement être visibles au-dessus de la semelle. Le fait qu'aucune évidence de ce type n'a pu être identifiée sur le terrain suggère que ces zones de cisaillement représentent des structures restreintes au décollement basal de la nappe, en accord avec l'interprétation en structure de type C'.

Si le caractère compressif des structures observées dans la Nappe des Péridotites est évidemment compatible avec un scénario de mise en place de la nappe par poussée par l'arrière, nous devons néanmoins examiner si de telles structures ont pu se développer dans un contexte de glissement gravitaire. En effet de nombreux exemples naturels de glissement gravitaire (e.g. le long de décollement salifère ou schisteux au niveau d'une marge continentale passive par exemple) ou résultant de modélisations analogiques montrent le développement de structures compressives dans la partie frontale de la nappe, à proximité du pied de pente topographique (e.g. Morley et Guerin, 1996; Fort et al., 2004; Loncke et al., 2006; Mourgues et al., 2009; de Vera et al., 2010). Dans certains cas, la compression peut se transmettre jusqu'à des niveaux relativement lointain du front de nappe (e.g. Fort et al., 2004). Cependant, il semble que les structures compressives soient toujours localisées dans la partie inférieure de la pente, atteignant éventuellement le milieu de cette dernière (e.g. de Vera et al, 2010). Un point important est donc de s'interroger sur la position relative du massif de Koniambo et plus généralement de l'ensemble des massifs de la côte nord-ouest par rapport à la paléo-pente topographique au moment de la mise en place de la nappe. L'étude, notamment, de l'évolution du bassin de Nouvelle- Calédonie (Fig.1) apportera un certain nombre de réponses que nous n'expliciterons pas dans le cadre de cette thèse car faisant partie d'un projet d'article (Gautier et al, 201x) complémentaire de ce travail.

Box 2: la serpentine polygonale

Géneralités

A l'instar du chrysotile, la serpentine polygonale, initialement appelée Povlen-type chrysotile (Krstanovic et Pavlovic, 1964; Middleton et Whittaker, 1976) est une variété fibreuse de serpentine. Du fait de sa ressemblance mais également de son association spatiale avec le chrysotile, les premières études sur cette espèce (*e.g.* Whicks et O'Hanley, 1988) ont considéré qu'il s'agissait d'une forme anecdotique de serpentine. Elle est caractérisée par des tubes plus courts, mais d'un diamètre plus grand (>100nm) que le chrysotile. La principale différence réside dans le fait que l'enroulement des feuillets perpendiculairement à l'axe d'un cylindre forme une structure polygonale composée de 15 ou 30 secteurs (Fig.1). Sur la base de ces observations, Middleton et Whittaker (1976) et Cressey et Zussman (1976) la décrivent comme une variété intermédiaire entre le chrysotile cylindrique et la lizardite plane.

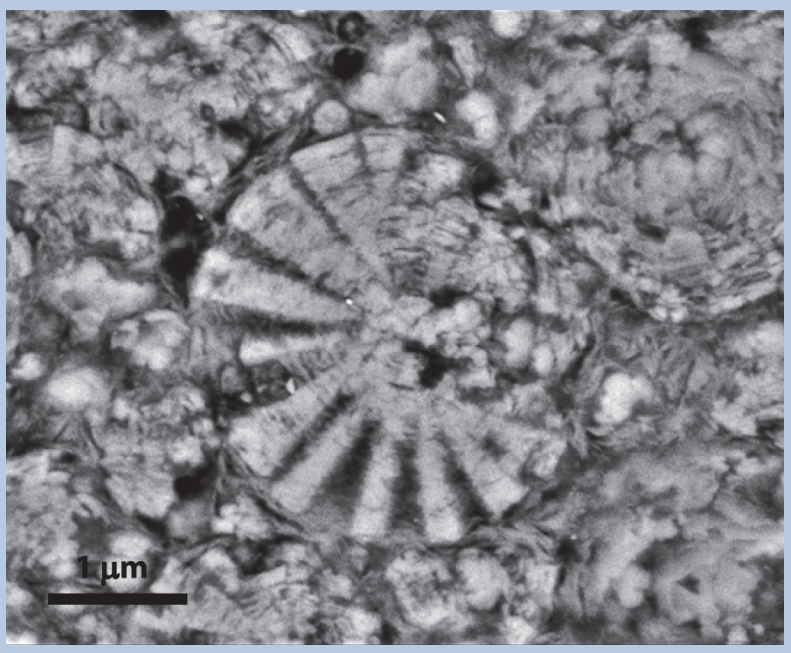

Figure 7 Image MEB * BSE d'une coupe perpendiculaire à l'axe d'une fibrille de serpentine polygonale composée de 15 secteurs. L'échantillon provient d'un recouvrement de bloc provenant de la semelle de serpentine du massif de Koniambo comme présenté figure 4c et d de l'article #4.

Initialement peu observée, il semble que la serpentine polygonale soit un polymorphe courant puisque identifié dans de nombreuses localités aux contextes géologiques variés (**Italie** : dans les serpentinites de Sasso della Matesca et Sasso di S. Zanobi, Morandi et Felice, 1979 ; dans les serpentinites de Gimigliano-Mount Reventino, Bloise et al., 2014 ; Dans les serpentinites de

Balangero, Mellini, 1986 ; **Kosovo** : sous forme d'une veine massive recoupant les serpentinites de Kačanik, Mugnaioli et al., 2007 ; **Atlantique** : dans la zone de fracture de Vema, Bonatti et al., 1984; **Etats-Unis** : dans les serpentinites de Woods Chrome Mine, Banfield et al., 1995 ; dans les serpentinites localisées le long de la faille de Santa Ynez, Andréani et al., 2004 ; **Afrique du Sud** : au sein des kimberlites de la baie d'Elwin, Mitchell et Putnis, 1988 ; **Nouvelle-Calédonie** : Ulrich, 2010 ; Annexe 4 ; cette étude). Cependant, dans la plupart de ces localités la serpentine polygonale est décrite comme peu abondante.

Macroscopiquement, la serpentine polygonale se caractérise par sa couleur vert pâle (Mugnaioli et al., 2007 ; Ulrich, 2010 ; cette étude) et son aspect plus massif. En effet, lorsqu'elle se présente sous forme de remplissage de faille (Fig.2) la longueur des « marches d'escalier » sera relativement courte, conséquence possible de la faible longueur des fibrilles de serpentine polygonal. A plus petite échelle, plusieurs méthodes de reconnaissance de la serpentine polygonale ont été investiguées (X-Ray, MET, MEB, SEM, SAED, RAMAN) notamment dans le but de la distinguer du chrysotile. Il en ressort que le MET et le MEB semblent être d'excellentes méthodes afin d'obtenir une image discriminante des deux polymorphes (Fig.1), mais nécessitant une préparation des échantillons relativement chronophage. L'utilisation de la méthode RAMAN est appréciée depuis quelques années (Lemaire, 2000 ; Auzende et al., 2004 ; Groppo et al, 2006; Ulrich, 2010; Ulrich et al., 2014) comme méthode rapide d'identification des différents polymorphes de la serpentine.

Figure 8 Occurrences de serpentine polygonale localisée sur un miroir de faille. Les fibres de serpentine polygonale ont une géometrie en marche d'escalier.

Conditions de formation

Baronnet et Devouard (1994) sont les premiers à proposer que la formation de serpentine polygonale pourrait être le résultat de la transformation du chrysotile par relargage de l'énergie élastique accumulée au court de sa croissance. La croissance de fibres de chrysotile atteignant un diamètre critique d'environ 100nm (Andréani et al., 2008) entraînerait une perte de courbure et le développement de structures planaires (Evans, 2004). Au regard de la littérature, il semble y avoir un consensus sur le fait que la transformation chrysotile-polygonale résulte simplement d'un processus continu de croissance minérale, la chimie du fluide, la pression, ou encore la déformation ne semblant pas avoir d'influence sur la formation préférentielle de serpentine polygonale (Banfield et al., 1995; Devouard et al., 1997; Grauby et al., 1998 Mugnaioli et al., 2007). En dépit du peu de données disponibles dans la littérature, il semble néanmoins que la température n'ait également pas d'influence sur la formation de la serpentine polygonale. L'analyse isotopique d'échantillons de serpentine polygonale provenant de la zone de fracture de Vema a permis d'estimer une gamme de température de formation entre ~80°C-120°C (Bonatti et al., 1984). Le travail expérimental de Devouard et al. (1997) montre qu'il est également possible de former de la serpentine polygonale à 300°C. Enfin, Mitchell et Putnis (1988) proposent que la serpentine polygonale identifée dans les Kimberlites de la baie d'Elwin, soit une phase primaire cristallisée entre 400°C-600°C à partir de la fraction résiduelle de magma.

Le cas néo-calédonien montre que la serpentine polygonale ne peut être considérée comme anecdotique compte tenu de son abondance (au moins en termes de nombre d'occurrences) sur le terrain (article #4 ; Annexe 4). Cette dernière s'observe comme remplissage de nombreuses failles (article #4 Fig.5b,c) , de zones de cisaillement décimétriques (artcile #4 Fig.5f) ou sous forme de films recouvrant des clastes de péridotite serpentinisée localisés dans des zones de cisaillement majeures (article #4 Fig.4c,d). Ces occurrences, très différentes de celles caractéristiques du chrysotile (principalement sous forme de veinules d'épaisseur plurimillimétrique en bordure de fracture, article#4 partie 4.2) pose la question du réel systématisme de la relation génétique entre ces deux polymorphes. Cependant, il apparaît que la serpentine polygonale est aujourd'hui localisée dans des structures au sein desquelles les fluides ont probablement pu circuler abondamment. Dans la littérature, il semble être

classiquement admis que la formation du chrysotile serait favorisée par un rapport fluide/roche élevé (Evans, 2004). Il ne semble donc pas déraisonnable de proposer que la serpentine polygonale observée aujourd'hui pourrait bien résulter de la transformation du chrysotile dans des structures au sein desquelles la circulation des fluides a été suffisante pour permettre la croissance continue du chrysotile jusqu'à sa transformation. La possible coexistence de ces deux polymorphes au sein d'une faille (spectres Raman B3791 et C3792, Fig.4, article# 4) pourrait représenter un stade intermédiaire de la transformation chrysotile-polygonale au sein d'une zone de circulation préférentielle des fluides. Une étude minéralogique fine des différents types d'occurrences de serpentine polygonale pourrait permettre de vérifier si oui ou non des reliques de chrysotile y sont systématiquement associées. Le type de fluide à l'origine de la serpentine polygonale reste quand à lui encore un inconnu (cf. dernier paragraphe de la partie 5.4 de l'article #4). La caractérisation de la composition isotopique en oxygène des différentes occurrences de serpentine polygonale néo-calédonienne pourrait probablement apporter de précieux éléments de réponses.

** Réglages MEB : les images électroniques à balayage ont été réalisées par Matthieux Harlaux en 2012 sur un microscope à vide secondaire MEB à effet de champ Hitachi S-4800 à cathode froide équipé d'un spectromètre EDS et optimisé pour la haute résolution du Service Commun de Microscopies Electroniques et de Microanalyses X (SCMEM) de Vandœuvre-lès-Nancy. L'acquisition des images en électrons rétrodiffusés (BSE) a été réalisée sur sections polies métallisées sous une tension d'accélération de 15kV.*

Références

Andréani, M., Grauby, O., Baronnet, A. et Munoz, M. (2008) Occurrence, composition and growth of polyhedral serpentine. European Journal of Mineralogy, 20(2), 159-171.

Andréani, M., Baronnet, A., Boullier, A-M., Gratier, J-P. (2004) A microstructural study of a « crack-seal » type serpentine vein using SEM and TEM techniques. Eur. J. Mineral., 16, 585-595.

Auzende, A-L., Daniel, I., Reynard, B., Lemaire, C., Guyot, F. (2004) High-pressure behaviour of serpentine minerals : a Raman spectroscopic study. Phys. Chem. Minerals, 31, 269-277.

Banfield, J. F., Bailey, S. W., Barker, W. W., and Smith, R. C. (1995) Complex polytypism: Relationships between serpentine structural characteristics and deformation: American Mineralogist, 80, 1116–1131.

Baronnet, A. et Devouard, B. (1994) Sectors of polygonal serpentine. A model based on dislocations. Phys. Chem. Minerals, 21, 330-343.

Baronnet, A., Devouard, B. (2005) Microstructures of common polygonal serpentines from axial HRTEM imaging, electron diffraction, and lattice-simulation data. The Canadian Mineralogist, 43, 513-542

Bloise, A., Critelli, T., Catalano, M., Apollaro, C., Miriello, D., Croce, A., Barrese, E., Liberi, F., Piluso, E., Rinaudo, C., Belluso, E. (2014) Asbestos and other fibrous minerals contained in the serpentinites of the Gimigliano-Mount Reventino Unit (Calabria, S-Italy). Environ. Earth Sci., 71, 3773-3786.

Bonatti, E., Lawrence, J.R., Morandi, N. (1984) Serpentinization of oceanic peridotites : temperature dependence of mineralogy and boron content. Earth and Planetary Science Letters, 70, 88-94.

Cressey, B.A. et Zussman, J. (1976) Electron microscopic studies of serpentinites. Can. Mineral., 14, 307-313.

Devouard, B., Baronnet, A., Van Tendeloo, G., Amelinckx, S. (1997) First evidence of synthetic polygonal serpentines. European Journal of Mineralogy, 9(3), 539-546.

Evans, B.W. (2004) The serpentinite multisystem revisited: Chrysotile is metastable, International Geology Review, 46(6), 479-506.

Grauby, O., Baronnet, A., Devouard, B., Schumaker, K., Demirdjian, L. (1998) The chrysotile–polygonal serpentine– lizardite suite synthesized from a 3 MgO– 2 SiO2–excess H2O gel. Eur. Mineral. Petrol. Geochem. (EMPGVII). Terra Nova, Suppl. 10(1), 24 (abstr.).

Groppo, C., Rinaudo, C., Cairo, S., Gastaldi, D. et Compagnoni, R. (2006) Micro-Raman spectroscopy for a quick and reliable identification of serpentine minerals from ultramafics. European Journal of Mineralogy, 18(3), 319.

Krstanovic, I., Pavlovic, S. (1964) X-ray study of chrysotile. American Mineralogist, 49, 1769-1771.

Lemaire, C. (2000) Application des spectroscopies vibrationnelles à la détection d'amiante dans les matériaux et à l'étude des serpentines. Thèse, Université de Paris 07, Paris: pp. 157.

Mellini, M. (1986) Chrysotile and polygonal serpentine from the Balangero serpentinite. Mineral. Mag., 50, 301-306.

Middleton, A.P. et Whittaker, E.J.W. (1976) The structure of Povlen-type chrysotile. Can. Mineral., 14, 301-306.

MitchellL, R.H. & Putnis, A. (1988) Polygonal serpentine in segregation-textured kimberlite. Can. Mineral. 26, 991-997.

Morandi, N. et Felice, G. (1979) Serpentine minerals from veins in serpentinite rocks. Mineralogical Magazine, 43, 35-40.

Mugnaioli, E., Logar, M., Mellini, M., Viti, C. (2007) Complexity in 15- and 30-sectors polygonal serpentine : longitudinal sections, intrasector stacking faults and XRPD satellites. American Mineralogist, 92, 603-616.

Ulrich, M. (2010) Péridotites et serpentinites du complexe ophiolitique de la Nouvelle-Calédonie. Ph.D. thesis, Université de la Nouvelle Calédonie & Université Joseph Fourrier (Grenoble, France).

Ulrich, M., Muñoz, M., Guillot, S., Cathelineau, M., Picard, C., Quesnel, B., Boulvais, P., Couteau, C. (2014) Dissolution–precipitation processes governing the carbonation and silicification of the serpentinite sole of the New Caledonia ophiolite. Contrib. to Mineral. Petrol., 167, 952.

Wicks, F.J. et O'Hanley, D.S. (1988) Serpentine minerals: structures and petrology. In Hydrous Phyllosilicates (S.W. Bailey, ed.). Rev. Mineral., 19, 91-167.

Partie III : Chapitre 3 – Déformation et circulation de fluide à l'échelle de la Nappe des Péridotites

Résumé de l'article #5

La composition en isotopes stables de veines fournit des informations sur les conditions des interactions fluide-roche et sur leur origine. En Nouvelle-Calédonie, des veines de magnésite et de silice sont observées au sein de la Nappe des Péridotites. Dans ce travail, nous présentons des données d'isotopes stables et de « clumped isotope » dans le but de contraindre les conditions de circulation de fluide et leur relation à la formation du gisement de nickel latéritique. Pour les veines de magnésite localisées à la base de la Nappe des Péridotites, les hautes valeurs en $\delta^{18}O$ entre 27.8‰ et 29.5‰ attestent d'une formation à basse température. Les analyses « clumped isotope » effectuées sur ces mêmes magnésites donnent des températures de formation comprises entre 26°C et 42°C, cohérentes avec l'équilibre isotopique entre la silice amorphe et la magnésite. L'origine météorique du fluide est bien établie via le calcul de la composition en oxygène du fluide initial dont les valeurs de $\delta^{18}O_{H2O}$ sont comprises entre -3.2‰ to +1.5‰. La silice amorphe associée à la magnésite, ou localisée dans le niveau de saprolite grossière, présente une gamme de composition en $\delta^{18}O$ comprise entre 29.7‰ et 35.3‰. Pour les veines de quartz communément associées à des talcs nickélifères et localisées dans la partie supérieure de la Nappe des Péridotites et dans le niveau saprolitique, la gamme de $\delta^{18}O$ est plus basse, comprise entre 21.8‰ et 29.0‰ suggérant une formation dans des conditions d'hydrothermalisme de basse température. L'équilibration thermique du fluide le long d'un gradient géothermique avant sa réinjection vers le sommet de la nappe et/ou l'influence de réactions exothermiques de serpentinisation pourraient être les sources de chaleur ayant permis la formation des veines de quartz dans de telles conditions.

Paired stable isotopes (O, C) and clumped isotope thermometry of magnesite and silica veins in the New Caledonia Peridotite Nappe

Submitted to Geochimica et Cosmochimica Acta

Benoît Quesnel*, Philippe Boulvais, Pierre Gautier

Géosciences Rennes, Université Rennes1, UMR 6118 CNRS, 35042 Rennes Cedex, France: benoit.quesnel@univ-rennes1.fr, philippe.boulvais@univ-rennes1.fr, pierre.gautier@univ-rennes1.fr

Michel Cathelineau

Géoressources, Université de Lorraine, UMR 7359 CNRS, CREGU, 54506 Vandoeuvre-lès-Nancy, France. michel.cathelineau@univ-lorraine.fr

Cédric M. John

Department of Earth Science and Engineering and Qatar Carbonate and Carbon Storage Research Centre (QCCSRC), Imperial College London, Prince Consort Road, London SW7 2AZ, UK. cedric.john@imperial.ac.uk

Malorie Dierick, Pierre Agrinier

Institut de Physique du Globe de Paris, Sorbonne Paris Cité, Univ Paris Diderot, UMR 7154 CNRS, F-75005 Paris, France. dierick@ipgp.fr, agrinier@ipgp.fr

Maxime Drouillet

Service géologique, Konimbo Nickel SAS, 98883 Voh, New Caledonia. mdrouillet@koniambonickel.nc

** corresponding author*

Partie III : Chapitre 3 – Déformation et circulation de fluide à l'échelle de la Nappe des Péridotites

Keywords: Peridotite, weathering, magnesite, silica, stable isotopes, clumped isotope thermometry, laterite, low temperature hydrothermalism.

Abstract

The stable isotope compositions of veins provide information on the conditions of fluid-rock interaction and their origin. In New Caledonia, magnesite and silica veins occur throughout the Peridotites Nappe. In this work, we present stable isotopes and clumped isotope data in order to constrain the conditions of fluid circulation and the relationship between fluid circulation and nickel ore-forming laterization. For magnesite veins occurring at the base of the nappe, the high $\delta^{18}O$ values between 27.8‰ and 29.5‰ attest to a low temperature formation. Clumped isotope analyses on magnesite give temperature between 26°C and 42°C that are consistent with amorphous silica - magnesite isotopic equilibrium. The meteoric origin of the fluid is well established with back-calculated $\delta^{18}O_{water}$ values between -3.2‰ to +1.5‰. Amorphous silica associated with magnesite or occurring in the coarse saprolite level displays a narrow range of $\delta^{18}O$ values between 29.7‰ and 35.3‰. For quartz veins occurring at the top of the bedrock and at the saprolite level, commonly in association with Ni-talc-like minerals, the $\delta^{18}O$ values are lower, between 21.8‰ and 29.0‰ and suggest low-temperature hydrothermal conditions (~40-80°C). Thermal equilibration of the fluid along the geothermic gradient before upward flow through the nappe and/or influence of exothermic reactions of serpentinization could be the source(s) of heat needed to form quartz veins under such conditions.

1. Introduction

Carbonate and silica veins occur in various geological contexts, and are the marker of past geological fluid circulations. Understanding the conditions of veins formation is of primary importance to decipher the role of fluids in the transfer of heat and matter, the transport and deposition of metals, and the mechanical properties of shear zones and faults. Stable isotopes are one of the historical tools used in the characterization of fluid-rock interactions (Urey, 1947; McCrea, 1950; Epstein et al.,

1953; Emiliani, 1966; Craig and Boato, 1955). Theoretically, stable isotopes give access to the fluid stable isotopic composition and the temperature of precipitation of minerals at a given fluid/rock ratio. However, estimates of temperature and fluid composition are interdependent. That is the reason why stable isotopes studies have to be undertaken with a strong knowledge of the local geology and in association with complementary methods of fluid characterization, like fluid inclusions studies or other geothermometers.

The recent development of the carbonate clumped isotope thermometer has rapidly been considered as a very promising tool in Earth Sciences (Eiler, 2007). This method is based on the thermodynamic phenomenon of "clumping" which consists in the preferential bonds formation between the heavy isotopes of carbon and oxygen in carbonate minerals. Unlike conventional carbonate thermometers, the clumped isotope thermometer allows temperatures of formation of carbonate to be estimated independently of the initial fluid isotopic composition. By extension, it can provide an estimate of the $\delta^{18}O$ value of the parent fluid since the $\delta^{18}O$ of the carbonate and temperatures are measured independently on the same aliquot of sample.

For the last two decades, the study of carbonate and silica veins developed in ultramafic rocks has attracted a renewed interest given the implications of this process for permanent carbon capture and storage through CO_2 mineralization (Kelemen and Matter, 2008; Kelemen et al., 2011; Oelkers et al., 2013; Ulrich et al., 2014), and in the understanding of lateritic nickel ore formation (Butt and Cluzel, 2013 and references herein). The New Caledonia Peridotite Nappe hosts one of the largest lateritic nickel ore deposit representing around 30% of the global reserves in nickel, thus making New Caledonia the 7th nickel producer in the world. In New Caledonia as in many other places worldwide (Caribbean, South America, Balkans, Russia, West Africa, South East Asian, Australia) Ni-laterites result from the intense weathering of ultramafic rocks exposed at the surface under hot and humid climate. Their development requires the dissolution of protolith minerals leading to i) the export of soluble elements and ii) the in-situ authigenesis of mineral phases hosting the insoluble elements. In the case of peridotites in New Caledonia, Si and Mg are exported whereas the laterites are enriched in iron oxi-hydroxides. Ni, with an intermediate behavior, is concentrated at the base of the lateritic profile where it reaches economic concentrations as Ni-bearing goethite (Trescases, 1975; Freyssinet, 2005). The erratic nickeliferous high-grade ore is located along fractures; it is known as garnierite, a mix of Ni-rich serpentine, Ni talc-like and Ni-sepiolite commonly associated with silica.

In New Caledonia (Fig. 1), numerous magnesite ($MgCO_3$), quartz and amorphous silica veins occur at different levels in the peridotite nappe and are thought to represent by-products of the laterization process (Glasser, 1904; Trescases, 1975). A *per descensum* model of fluid circulation was proposed in which Si and Mg are exported downward along fractures cutting through the nappe (Trescases, 1975).

Many studies have concentrated on the mineralogical characterization of the Ni bearing phases in other geological contexts (Brindley and Hang, 1973; 1980; Villanova de Benavent et al., 2014; Cathelineau et al., 2015a et b; Dublet et al., 2015), but only few studies focused on the understanding of the physical and chemical conditions of Si, Mg and Ni mobility. Based on stable isotope analyses ($\delta^{18}O$) of Ni talc-like minerals in garnierite from Morocco (Bou Azzer), Ducloux et al., (1993) showed that they could form between 25°C and 100°C. Part of this large spread in temperature is due to uncertainties in the oxygen isotope fractionation factors between Ni talc-like minerals, Ni serpentine-like minerals and water. These authors consider that this temperature range is consistent with a low temperature hydrothermal origin. For silica occurrences from New Caledonia, Saboureau and Trichet (1978) focused on fluid inclusions included in quartz. They identified two generations of quartz, respectively crystallized at <30°C and >120°C. Unfortunately, these samples were collected in soils and represent transported relicts of dismantled quartz occurrences. It is consequently difficult to place them in their genetic context. For magnesite, on the basis of stable isotopes analyses (C and O), most authors argue that carbonation occurs at low temperature and that the fluid is of meteoric origin but rarely propose to link carbonation and laterization processes as suggested in New Caledonia (Oman: Kelemen et al., 2011; Streit et al., 2012; West California: Barnes et al., 1973; Poland: Jedrysek and Halas, 1990; Balkans: Fallick et al., 1991; Jurkovic et al., 2012; Greece: Gartzos, 2004; East Australia: Oskierski et al., 2013; New Caledonia: Quesnel et al., 2013). In the same way, based on stable isotopes analyses (C, O and clumped isotope thermometry), some authors argue that carbonation events likely occurred at hydrothermal conditions (Balkans: Fallick et al., 1991; Norway: Beinlich et al., 2012; Oman: Falk and Kelemen, 2015).

In this study, we perform stable isotopes analyses on magnesite and silica veins and clumped isotope analyses on magnesite veins from New Caledonia, with a special attention to the Koniambo massif (Fig. 1,2) where the recent development of a mining site allows the access to numerous and exceptional outcrops. We show how the two isotopic methods are complementary and can help to constrain the conditions of veins formation. We also question the *per descensum* model of fluid

circulation proposed to explain the vertical distribution of the different mineralization in the peridotite nappe.

2. Geological setting

New Caledonia is located in the southwest Pacific Ocean, 1300 km east of Australia (Fig. 1). Peridotites are abundant on the island as a consequence of the Eocene obduction of a sliver of oceanic lithosphere (Cluzel et al., 2012). The Peridotite Nappe sub-horizontally overlies the substratum which is comprised of several volcano sedimentary units (Cluzel et al., 2012). The New Caledonian

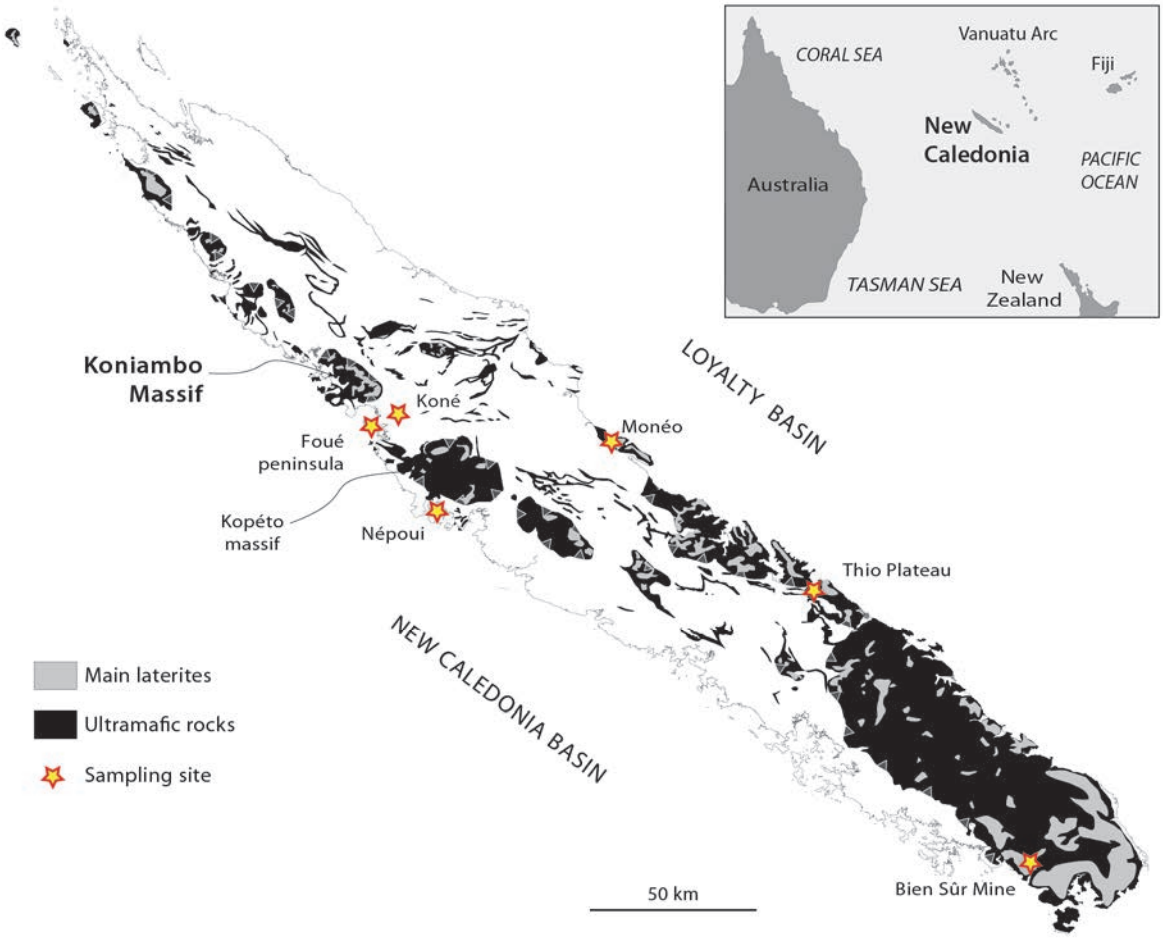

Figure 1 Simplified geological map of New Caledonia. Ultramafic rocks are from Maurizot and Vendé-Leclerc (2009) and laterites are adapted from Paris (1981).

Peridotite Nappe is exposed in the "Massif du Sud" and as a series of klippes along the northwestern coast (Fig. 1). Laterite occurs at the top of the peridotites (Fig. 1). Several planation surfaces attest to distinct episodes of weathering and/or epeirogenic movements during the Cenozoic (Latham, 1986;

Chevillotte et al., 2006; Sevin et al., 2012). Capping the laterite profile, a ferricrete composed of indurated iron oxides (hematite) mainly occurs as relicts 1 to 2 m thick. Below the ferricrete, the limonitic level is mainly composed of oxi-hydroxides (goethite) and reaches about 20 m in thickness. In this level, the structure of the rock is totally erased. At the base of the profile, the saprolitic level consists in an intermediate state of alteration between limonite and the underlying peridotite. This level reaches around 30m thick. The highly fractured structure of the protolith is preserved. The saprolite level hosts a diffuse Ni mineralization as well as an erratic nickeliferous high-grade ore, known as garnierite veins. Garnierite occurs as fracture infillings and consists in an association of Ni-rich serpentine and Ni talc-like minerals often associated with silica (Trescases, 1975; Cluzel and Vigier, 2008; Cathelineau et al., 2015b). Some garnierite occurrences formed syn-tectonically (Cluzel and Vigier 2008) and occurs occasionally as hydraulic breccia where a silica cement hosts clasts of serpentine and Ni talc-like minerals (Myagkiy et al., 2015). Fractures can also be filled solely by silica. Beneath the saprolite, the main part of the nappe consists of peridotites in which no silica occurs. Peridotites are highly fractured. Serpentinization is intensive in the deformed zones. At the base of the nappe, peridotites are pervasively serpentinized and highly sheared, constituting the so-called Serpentine Sole. The sole hosts numerous magnesite veins (Quesnel et al., 2013) commonly associated with amorphous silica (Ulrich et al., 2014). Elsewhere in New Caledonia, silica also occurs as infillings of late normal faults of regional extent, as pervasive silicification at the base of the nappe, locally known as the "Mur de silice" and as veins spatially associated to the Saint Louis and Koum Oligocene granitoid intrusions (Paquette and Cluzel, 2007; Jacob, 1985; Aye et al., 1986). These occurrences are not studied here as they do not relate to the supergene alteration system of the Koniambo Massif. This massif (Fig. 2) corresponds to one of the klippe occurring along the northwestern coast (Fig. 1). As everywhere on the island, the nappe is capped by a highly dissected and partly reworked lateritic profile (Maurizot et al., 2002). At lower elevations, laterites of the westerly-dipping Kaféaté plateau probably belong to a younger planation surface (Latham, 1977; Chevillotte et al., 2006).

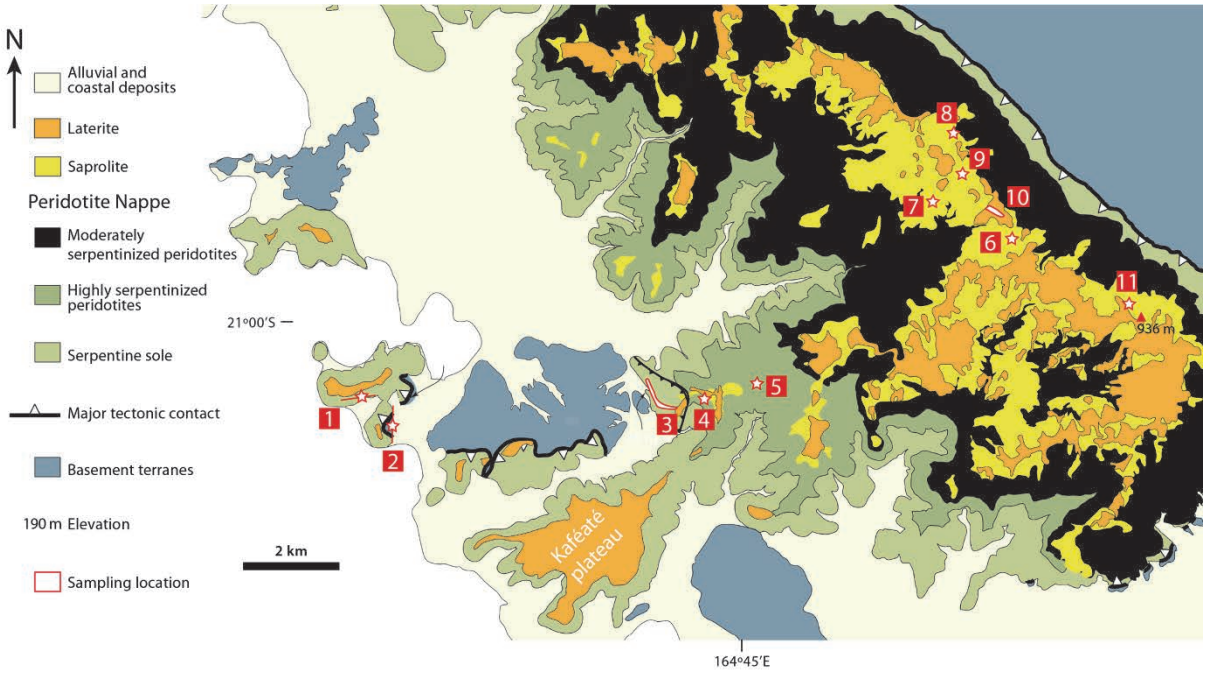

Figure 9 Geological map of the Koniambo massif adapted from Maurizot (2002). Numbers indicate sampling location and are reported in Table 1 for all samples coming from the Koniambo massif.

3. *Sampling and Samples*

3.1 Strategy

In the Koniambo massif, a recently opened mining site allows the sampling of the Peridotite Nappe nearly continuously from the Serpentine Sole to the lateritic profile (~800m). The Serpentine Sole is well exposed along cross-sections several hundreds of meters long and a few tens of meters high. The intermediate levels of the Nappe can be observed along an access road reaching the summit of the mining face where mining operations presently expose the laterite and the transition to the fractured peridotite. The veins have been collected at all levels in the Peridotite Nappe in order to get information on the circulation of fluids at the nappe scale on the 1D vertical direction.

On each sampling site (Fig. 2), the nature of the structure hosting veins has been described when possible. Samples have been collected in the core of veins to avoid host-rock buffering effects and to obtain the best preserved signature of the main fluid circulation event.

To obtain a first estimate on the representativeness of the Koniambo Massif with regards to the whole New Caledonia Peridotite Nappe, some samples have been collected at other locations within

New Caledonia (Fig. 1): magnesite veins in the nearby Kopéto Massif, quartz veins from the coarse saprolite level from Thio Plateau and Monéo and amorphous silica from Népoui and from the Bien Sûr Mine.

3.2 Magnesite

In the Koniambo massif, magnesite occurs mainly as veins in the Serpentine Sole (Fig. 3a, b). Some magnesite veins occur along fractures up to a few hundred of meters above this level (sampling sites 3 and 5, Fig. 2 and Table 1). In many cases, magnesite veins display a cauliflower texture which attests of a non-oriented growth. Some occurrences show a coarse fibrous texture where fibers of monomineralic magnesite are orthogonal to vein walls (Fig. 3b,c). At the Serpentine Sole level, magnesite veins occur preferentially within and along the margins of meter-thick low-dipping shear zones that are also marked by the development of serpentine (Fig. 3a,b). These veins are locally folded or offset by subsidiary shear planes (Fig. 3a). Most of the veins occurring outside the main shear zones have an orientation and coarse fibrous texture suggestive of tension gashes opened during the same shear regime (Fig. 3b,c; see also Quesnel et al., 2013). In soils (Fig. 3d), magnesite appears as nodules that can reach a few tens of cm in width. In general, magnesite samples are mono-mineralic but locally intimately associated with amorphous silica at the Serpentine Sole level.

Figure 3 Field observations of magnesite occurrences. A-C: Field views of magnesite veins occurring at the serpentine sole. A: field view illustrating relationship between magnesite veins and shear zone. The thickest vein occurs in the main shear band whereas the thinnest occur in C'-type shear bands. B,C: field view illustrating the fibrous texture of magnesite veins. D: field view of nodular magnesite occurring in a soil. Sample numbers are indicated and are reported in Table 1.

3.3 Quartz veins and amorphous silica

Quartz and amorphous silica samples have been examined using microscopies, and the nature of silica polymorphs has been checked by Raman spectroscopy. In the coarse saprolite level and the underlying bedrock, quartz veins occur as fractures infillings. These infillings correspond to the re-opening of ancient fractures commonly filled by serpentine, and in some cases by nickel-rich (or nickel-bearing) serpentine and/or talc-like minerals (Fig. 4c,d,f). They can occur as large branched networks of veins (Fig. 4a), as massive veins (Fig. 4c) or as thin films (Fig. 4d). Locally, quartz occurs as micro-crystalline brownish-reddish silica infillings (Fig. 4b, f; "brown silica" in Table 1), generally preceding the clearer yellow, whitish to clear quartz.

Two types of amorphous occurrences were studied: i) brownish amorphous silica occurs as very late coating or drapery-like on blocks of the coarse saprolite level, which constitutes a rather rare case, (Fig. 4e; "amorphous silica" in Table 1); ii) translucent amorphous silica closely associated with magnesite at the Serpentine Sole, as micro-spherule (Koniambo; Fig. 4g,h; first three rows in Table 1) or as microfracture infillings (Nepoui).

Similar quartz and amorphous silica samples were collected in other New Caledonian occurrences for comparison (Fig. 1 and Table 1).

4. Analytical techniques

4.1 Oxygen and carbon isotopes in magnesite

The isotopic analysis of 21 magnesite samples has been performed at the stable isotope laboratory of the University of Rennes 1, France. Samples were finely crushed in a boron carbide mortar, then reacted with anhydrous phosphoric acid at 75°C for 24h. The experimental fractionation factor between magnesite and CO_2 is $\alpha_{CO2\text{-}Magnesite}$=1.009976 at 75°C (Das Sharma et al., 2002). CO_2 was analyzed on a VG OPTIMA triple collector mass spectrometer. In the absence of magnesite standard, in-lab calcite standard (Prolabo Rennes) samples were analyzed together with the magnesite samples under identical conditions in order to control the general reliability of the protocol. The analytical uncertainty is estimated at ±0.3‰ for oxygen and ±0.2‰ for carbon. The results are reported using the δ notation relative to SMOW for O and to PDB for C.

Figure 4 A,C,D: field view of quartz veins occurring in the coarse saprolite level of Koniambo massif. B,F: sawed sections through two hand specimen showing complex textural relationships between B: brownish silica and yellow and white quartz and F: brownish silica, translucent quartz and clasts of serpentine (in green). G,E: field view of amorphous silica. G: translucent amorphous silica associated with magnesite at the Serpentine Sole. E: brownish amorphous silica occurring as late coating on blocks of the coarse saprolite. Sample locations are indicated by a yellow star and are reported in Table 1.

4.2 Magnesite clumped isotopes

The clumped isotope value of a carbonate sample can be deducted by measuring CO_2 following acidification, and using the Δ_{47} notation (in ‰) that compares the abundance of the rare ^{13}C-^{18}O bonds within a sample relative to a calculated stochastic distribution (Eiler and Schauble, 2004; Affek and Eiler, 2006):

$$\Delta_{47} = \left[\frac{R^{47}}{2R^{13} \cdot R^{18} + 2R^{17} \cdot R^{18} + R^{13} \cdot \left(R^{17}\right)^2} - \frac{R^{46}}{2R^{18} + 2R^{13} \cdot R^{17} + \left(R^{17}\right)^2} - \frac{R^{45}}{R^{13} + 2R^{17}} + 1 \right] \cdot 1000 \qquad (1)$$

The Δ_{47} value is calculated from the measured ratios (R^i) of masses 45, 46 and 47 to mass 44 and by calculating R^{13} ($^{13}C/^{12}C$) and R^{18} ($^{18}O/^{16}O$) from R^{45} and R^{46} assuming random distribution. R^{17} is calculated from R^{18} assuming a mass-dependent relationship between ^{18}O and ^{17}O. The higher the Δ_{47} is, the lower the temperature of formation of the mineral (e.g. Ghosh et al., 2006).

Clumped isotope analyses were performed on 7 samples of magnesite in the Qatar Stable Isotopes Laboratory at Imperial College, London, UK. Magnesite samples were finely crushed and samples of ~5 mg were digested online in a common acid bath composed of 105% ortho-phosphoric acid at 90°C during 1 hour. The liberated CO_2 gas was continuously trapped and purified by passage through a conventional vacuum line with multiple cryogenic traps and Porapak-Q trap held at -35°C (Dennis and Schrag, 2010) and was analyzed using a Thermo Finnigan MAT-253 gas source mass spectrometer. The analysis protocol followed procedures described by Huntington et al. (2009) and Dennis et al. (2011) comprising measurements that consisted of 8 acquisitions with 7 cycles per acquisition and an integration time of 26 s. Each cycle included a peak center, background measurements and an automatic bellows pressure adjustment aimed at a 15V signal at mass 44. The sample gas was measured against an Oztech reference gas standard ($\delta^{13}C$ =-3.63 ‰ VPDB, δ18O =-15.79 ‰ VPDB). Each sample was measured at least three times using separate aliquots to improve counting statistics. An internal standard (Carrara marble, "ICM", 0.312‰), a published inter-laboratory standard ("ETH3", Meckler et al., 2014, 0.634‰ before acid fractionation correction) and heated gases were analyzed regularly in order to correct for non-linearity (Huntington et al., 2009) and to transfer the measured values in the absolute reference frame (Dennis et al., 2011). Finally, an acid

fractionation factor of 0.069‰ was added to the Δ_{47} values in the absolute reference frame to account for acid fractionation at 90°C (Guo et al., 2009, Wacker et al., 2013). The analytical uncertainties of the Δ_{47} measurements were added by Gaussian error propagation using standard error of the mean.

4.3 Oxygen isotopes in quartz veins and amorphous silica

The isotopic analysis of 26 silica samples has been performed at the stable isotope laboratory of Institut de Physique du Globe de Paris, France. Samples were finely crushed and reacted with BrF_5 as an oxidizing agent overnight in Ni tubes at 550°C following the method of Clayton and Mayeda (1963). O_2 was directly analyzed on a Thermo-Fisher Delta V mass spectrometer. During the course of the analyses, the measurements of 14 NBS28 quartz standard allowed to control the general reliability of the protocol (mean = 9.67 ± 0.1 ‰, n= 14).
Fourteen other silica samples have been analyzed at the stable isotope laboratory of Géosciences Rennes (University of Rennes1, France). Samples were manually extracted and finely crushed and O_2 was liberated from minerals through reaction with BrF5 at 670°C overnight following the method of Clayton and Mayeda (1963). O_2 was then converted into CO_2 by reaction with hot graphite. Isotopic ratios were measured on a VG SIRA 10 triple collector. NBS 28 quartz standard and in-house A1113 granite standard were routinely analyzed together with samples; the analytical uncertainty is ±0.2‰. The O isotope composition is reported using the δ notation relative to SMOW.

5. Results

5.1 Magnesite

The stable isotopes compositions of magnesites (Fig. 5 a,b and Table 1) are comparable to those obtained by Quesnel et al. (2013). The oxygen isotope compositions of magnesites are homogeneous, with $\delta^{18}O$ values in the range of 27.8‰ - 29.5‰. The small variation in $\delta^{18}O$ values does not correlate with any structural or textural characteristics of magnesite. The $\delta^{13}C$ values vary between −15.3‰ and −9.1‰ (Fig. 5b,c and Table 1). The highest $\delta^{13}C$ values correspond to nodular magnesite from soil. The low values between −15.3‰ and −12.1‰ correspond to veins from the Serpentine Sole or from highly serpentinized peridotite (sample GMAR-5).

The Δ_{47} values and clumped isotope temperatures in magnesite are reported in Table 1 and illustrated in Figure 5d. The clumped isotope temperatures presented here are calculated using the Δ_{47} calibration for calcium carbonate of Kluge et al., (2015), because to date, no Δ_{47} calibration exists for magnesite. The temperatures range between 26-42°C (Fig. 5d and Table 1) with an average temperature of 30±5°C for the magnesite veins from the Serpentine Sole and a temperature of 42±2°C for a nodular soil magnesite.

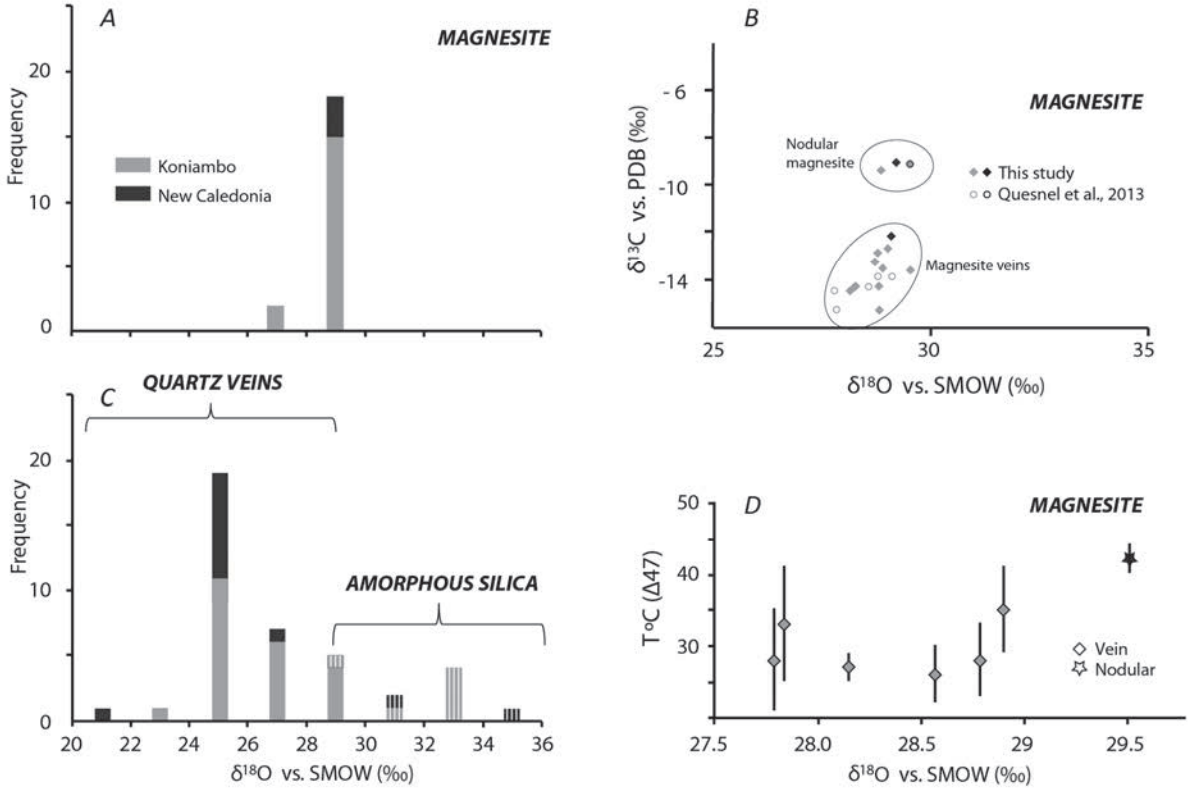

Figure 10 The light grey color represents samples from the Koniambo massif, those in dark grey are from elsewhere on the island. All the sample locations are reported in the figures. 1,2 and in Table 1. The isotopic values are given versus SMOW (Standard Mean Ocean Water) for $\delta^{18}O$ and versus PDB (PeeDee Belemnite) for $\delta^{13}C$. A: histogram of $\delta^{18}O$ values of magnesite samples (veins and nodules) B: $\delta^{13}C$ versus $\delta^{18}O$ diagram of magnesite samples. C: histogram of $\delta^{18}O$ values of quartz veins (including brownish silica) and amorphous silica (data with vertical white bars). D: diagram showing the temperature calculated from Δ_{47} analyses using the calibration of Kluge et al. (2015) as a function of the $\delta^{18}O$ values of 7 magnesite samples.

Sample	Localization	Nature	Silica	Magnesite						
			$\delta^{18}O$	$\delta^{18}O$	$\delta^{13}C$	$\Delta^{18}O_{(Qz\text{-}Mag)}$	Δ_{47}	Standard error	T°C(Δ_{47})	n=
KONIAMBO MASSIF										
GBMS-Si-1	Koniambo 1	Magnesite vein+amorphous silica	33.1	28.9	-13.5	4.2	0.671	0.016	35±6	3
BMS-Si-1'	Koniambo 1	Magnesite+amorphous silica	32.9	x	x					
BMS Gio 15*	Koniambo 1	Magnesite vein+amorphous silica	29.7	29.1	-13.8					
GBMS-2-13	Koniambo 1	Magnesite vein		28.3	-14.3					
GBMS-3-13	Koniambo 1	Magnesite vein		28.8	-14.3					
GBMS-4-13	Koniambo 1	Magnesite vein		29.0	-12.7					
GBMS-5-13	Koniambo 1	Magnesite vein		28.2	-14.3					
BMS Gio 9*	Koniambo 1	Magnesite vein		28.6	-14.3		0.695	0.012	26±4	3
BMS Gio 3*	Koniambo 1	Magnesite vein		28.8	-13.8		0.689	0.016	28±5	4
BMS Gio 12*	Koniambo 1	Magnesite vein		27.8	-15.2		0.675	0.024	33±8	3
GVAV-1-13	Koniambo 2	Magnesite vein		28.7	-13.2					
GVAV-2-13	Koniambo 2	Magnesite vein		28.8	-15.3					
VAV Gio 9*	Koniambo 2	Magnesite vein		27.8	-14.4		0.691	0.020	28±7	4
GMAR-2	Koniambo 3	Magnesite vein		28.2	-14.5		0.693	0.006	27±2	2
GMAR-3	Koniambo 3	Magnesite vein		28.8	-12.8					
GMAR-5	Koniambo 5	Magnesite vein		29.5	-13.6					
GMAR-4	Koniambo 3	Nodular magnesite in soil		29.5	-9.1					
CR-1	Koniambo 3	Nodular magnesite in soil		28.9	-9.4					
KNB3a	Koniambo	Qz	25.0							
MG1a	Koniambo	Qz	25.9							
MG3c	Koniambo	Qz	28.3							
MG5a	Koniambo	Qz	24.6							
FQZ 1	Koniambo 7	Qz	25.9							
Qz pim 1	Koniambo 7	Qz	26.0							
BAV Qz 1	Koniambo 7	Qz	25.9							
Si j 3	Koniambo 9	Qz	29.0							
Si Cl 3	Koniambo 9	Qz	28.1							
Si Cl Br 1	Koniambo 9	Qz	28.5							
FQZ 2	Koniambo 10	Qz	25.4							
Si Cl 1	Koniambo 10	Qz	27.5							
Si Cl 2	Koniambo 10	Qz	26.5							
Si j 4	Koniambo 11	Qz	28.0							
Test Pit	Koniambo 8	Brown silica+Qz	25.1							
KNB3b	Koniambo	Brown silica	27.6							
Si br 4	Koniambo 6	Brown silica	23.9							
Pit 207 haut	Koniambo 7	Brown silica	25.3							
Kon Bas Test Pit	Koniambo 8	Brown silica	25.1							
Si br 6	Koniambo 9	Brown silica	27.5							
Si br 2	Koniambo 10	Brown silica	27.2							
Si R 1	Koniambo 10	Brown silica	24.8							
BMS Si 13 2	Koniambo 1	Amorphous silica	33.4							
Si-Br-late	Koniambo 4	Amorphous silica	32.6							
Conv Si 1	Koniambo 4	Amorphous silica	30.4							
NEW CALEDONIA										
FOUE Gio	Foué peninsula	Magnesite vein		29.1	-12.1					
Bellevue Gio 1	Koné	Nodular magnesite in soil		29.2	-9.1					
DECH 1*	Koné	Nodular magnesite in soil		29.5	-9.1		0.652	0.005	42±2	3
NEP 4	Nepoui	Amorphous silica	35.3							
MONEO	Monéo	Brown silica+Qz	26.3							
NCBS1	Bien Sûr Mine	Tridymite	31.4							
Thio SP5	Thio Plateau	Brown silica	21.8							
"Fausse cargneule"	Thio Plateau	Qz	24.9							
BLV3 a	Thio Plateau	Qz	25.2							
3TX1 a	Thio Plateau	Qz	24.5							
Th Pl 3	Thio Plateau	Qz	25.1							
Th Pl 6	Thio Plateau	Qz	25.9							
Th Pl 9	Thio Plateau	Qz	25.8							
Th Pl 10	Thio Plateau	Qz	25.4							
Th Pl 11	Thio Plateau	Qz	25.5							

Table 1 Δ_{47}, $\delta^{18}O$ and $\delta^{13}C$ values of magnesite samples and $\delta^{18}O$ values of silica samples. "n" indicates the number of replicate samples analyzed by clumped isotope thermometry. T (Δ_{47}) uncertainty is estimated on the basis of the 1SE analytical uncertainty in measured Δ_{47} propagated through the Kluge et al (2015) equation.

5.2 Quartz veins and amorphous silica

The oxygen isotope compositions of quartz veins and amorphous silica display a large range of $\delta^{18}O$ values between 21.8‰ and 35.3‰ (Fig. 5a and Table 1). The values higher than 30‰ correspond to translucent or brownish amorphous silica and tridymite. Quartz veins from the coarse saprolite level have a total range of $\delta^{18}O$ values between 21.8‰ and 29.0‰, most values being between 24‰ and 28.5‰. There is no systematic difference between quartz and brown silica.

6. Discussion

6.1 Conditions of carbonation

6.1.1 Low temperature geochemistry

As shown previously, the oxygen composition of magnesite samples analyzed in this study are included in the same range ($27.4‰ \leq \delta^{18}O_{Magnesite} \leq 29.7‰$) than in Quesnel et al. (2013). A first range of temperature of formation of magnesite veins between ~40°C-80°C was estimated by Quesnel et al. (2013) using the oxygen fractionation factor between magnesite and water of Chacko and Deines (2008) and a $\delta^{18}O$ range of fluid composition between -1‰ and -7‰ which correspond to values of rainwater on isolated island at inter-tropical latitude and low elevation (IAEA database: http://www-naweb.iaea.org/napc/ih/IHS_resources_gnip.html). If the oxygen fractionation coefficient of Zheng (1999) had been used in the Quesnel et al. (2013) study instead, the calculated temperature range would be between ~10°C and 40°C. Clumped isotope thermometry is particularly useful in such situation when i) several distinct fractionation factors do not converge towards the same range of temperature of mineral formation and ii) uncertainties on the initial fluid composition is particularly large. To calculate the clumped temperature from Δ_{47} values, Falk and Kelemen (2015) used the calibration of Bristow et al. (2011) but in our case, we favor the use of the recent laboratory calibration for calcium carbonate of Kluge et al. (2015) performed in the same laboratory that our study. For our samples, the clumped isotope temperatures calculated using these two calibrations are similar, taking into account the uncertainties of the measurements. The clumped isotope temperatures obtained using

the calibration of Kluge et al. (2015) average around 30°C, and would suggest that the magnesite-water fractionation factor of Zheng (1999) is more applicable in the New Caledonian setting than the fractionation factor described in Chacko and Deines (2008).

We use the isotopic equilibrium between amorphous silica and magnesite to test the validity of the calculated clumped temperature of magnesite formation. We were able to obtain the $\delta^{18}O$ of magnesite, $\delta^{18}O$ of amorphous silica and Δ_{47} on magnesite measurements for one sample (GBMS-Si-1, Fig.4g,h and Table 1) where magnesite and amorphous silica are intimately associated and are interpreted here as cogenetic. Indeed, at the serpentine sole level, pervasive development of amorphous silica linked to magnesite formation by serpentine dissolution is documented (Annexe 4: Ulrich et al., 2014). The isotopic fractionation between silica and magnesite ($\Delta^{18}O_{\text{Amorphous silica-Magnesite}}$) measured on this sample is 4.2‰. Actually, there is no published isotopic fractionation factor between these two species. Considering that there is no significant fractionation between amorphous silica and quartz (Kita et al., 1985; Zheng, 1993; Sharp and Kirschner, 1994), this measured value is consistent with the theoretical value of the $\Delta^{18}O_{\text{Quartz-Magnesite}}$ of 4.2‰ at 26°C (Zheng, 1999). On the same sample, the Δ_{47} measurement allows calculating a temperature of 35±6°C (Table 1), consistent with the 26°C value estimated above. It thus appears that both methods agree with each other, despite the lack of a specific Δ_{47} calibration for magnesite. More generally, the range of clumped isotope temperatures between 26±4 and 42±2 calculated for magnesite confirms its low temperature of formation in the Koniambo massif.

It should be noted that when combining quartz-water and magnesite-water fractionation factors available in the literature to get the fractionation between quartz and magnesite, one obtains unrealistic estimates. For example, using the magnesite-water fractionation of Zheng (1999) and the quartz-water fractionation of Sharp and Kirschner (1994), one obtains a temperature of 136°C; and using the magnesite-water fractionation factor of Chacko and Deines (2008) with any of the quartz-water fractionation factor available in the literature, one obtains negative $\Delta^{18}O_{\text{Amorphous silica-Magnesite}}$ values.

6.1.2 Meteoric origin of the fluid

Since clumped isotope thermometry allows estimating the temperatures of formation of carbonate independently of the knowledge of the fluid composition, we can calculate the $\delta^{18}O$ of the fluid from

which magnesite formed. The fact that magnesite veins are commonly decimeter thick and abundant on the studied outcrops implies that a large amount of fluid has been involved in their formation. This suggests a high fluid/rock ratio during the fluid circulation through the nappe. The observation that the $\delta^{18}O$ values of magnesite are homogeneous, irrespectively of the nature of the host rock, (Fig. 5a) pleads for such conditions. Consequently, we consider that the calculated $\delta^{18}O$ value of the fluid represents its initial composition and not a composition buffered by the host rock during its circulation through the nappe. Given the consistency between temperature estimate using quartz-magnesite equilibrium and clumped isotopes, we use here the oxygen fractionation between magnesite and water from Zheng (1999). The calculated fluids for the 7 magnesite samples have $\delta^{18}O$ values ranging from -3.4‰ to +1.5‰. The 6 negative $\delta^{18}O$ values have an average of -2.5‰ with a minimum at -3.4‰ and a maximum at -0.6‰. They correspond to magnesite veins occurring at the Serpentine Sole. The highest value ($\delta^{18}O$ = +1.5‰) corresponds to a nodular magnesite occurring in a recent soil (DECH1). The oxygen isotope compositions of the fluid are homogeneous and consistent with the present day composition of rainwater on isolated island at inter-tropical latitude and low elevation ranging from -7‰ to -1‰ (AIEA database: http://www-naweb.iaea.org/napc/ih/IHS_resources_gnip.htlm). For the nodular magnesite, the positive oxygen fluid composition is interpreted as evaporation at surface conditions which leaves residual water enriched in ^{18}O. The higher clumped temperature of 42°C calculated for this sample seems consistent with the slightly higher temperature needed to precipitate magnesite through evaporation of surface waters.

6.2 Fractionation in the carbon isotope system

Whereas the $\delta^{18}O$ values of magnesite veins are homogeneous and suggest unicity of the fluid from which they formed, the large spread of $\delta^{13}C$ values implies several sources of carbon and/or specific fractionation effect in the carbon isotope system. The highest $\delta^{13}C$ values, around -9‰, suggest an atmospheric CO_2 contribution. This is consistent with the fact that magnesite with such $\delta^{13}C$ values are nodular magnesite from soil and are probably formed in-situ by evaporation as previously explained for sample "DECH1". Most of the magnesite samples from the Serpentine Sole have lower $\delta^{13}C$ values between -15.3‰ and -12.1‰. An organic carbon contribution from surface soil or from

decarboxylation of deep seated organic matter-rich sediments could explain such low values. Independently, several resurgences of hyperalkaline fluid with pH up to 11 related to present day serpeninization (Barnes et al., 1978, Monin et al., 2014) occur in New Caledonia (Launay and Fontes, 1985). At least two processes involving such fluid could explain low values of $\delta^{13}C$. The first one consists in the kinetic isotopic fractionation of C isotopes during hydroxylation of dissolved CO_2 when carbonate forms by diffusive uptake of dissolved CO_2 (Dietzel et al., 1992). Such process has been proposed to explain the extreme depletion of ^{13}C measured in various carbonate occurrences as calcite travertine deposit in Oman (Clark et al., 1992), sediments cemented by calcite from central Jordan (Fourcade et al., 2007) and also for magnesite deposits in Australia (Oskierski et al., 2013). The second type of processes consists in abiotic carbon production by Fisher-Tropsch reaction during serpentinization. This reaction consists in the catalytic reaction between H_2, produced by serpentinization, and CO to form CO_2 or light hydrocarbons. This reaction induces an increase of pH due to the occurrence of free OH^- (Holm, 1996) and produces organic products depleted in $\delta^{13}C$ (McCollom and Seewald, 2006). Often described as a reaction occurring at high temperature hydrothermal conditions (Berndt et al., 1996; Potter et al., 2004; McCollom and Seewald, 2006; Tara et al., 2007) some studies showed that it can also happen at low temperature (Charlou et al., 1991; Proskurowski et al., 2008; Neubeck et al., 2011; Etiope et al., 2011), consistent with the low temperature formation of the New Caledonian magnesite veins.

6.3 Conditions of quartz veins and amorphous silica formation

At the island scale, the $\delta^{18}O$ values of quartz veins and amorphous silica spread over a range of ~15‰. The fact that all quartz veins and amorphous silica occur in the peridotite and commonly in deformation zones (at the serpentine sole or as fractures or faults infillings) suggest that they are probably genetically linked to a unique fluid reservoir. We argued in section 6.1.2 that an amorphous silica sample ($\delta^{18}O$ = 33‰) formed in isotopic equilibrium with magnesite (sample GBMS-Si-1) from a meteoric water at low temperature (~26°C). Considering the low variability of paleogeography of New Caledonia during the 30 last million years (Paleomap project: http://gcmd.nasa.gov/records/PALEOMAP-Serf.html) and by consequence the limited variation of the isotopic composition of rainwater during that period, variations in temperature are the most likely

factor at the origin of the large spread in $\delta^{18}O$ values recorded by silica species.

The temperature of formation of amorphous silica in sample GBMS-Si-1 ($\delta^{18}O$ = 33.1‰) was estimated at 26°C. Given that quartz veins are commonly decimeter thick and abundant in the coarse saprolite level it is likely that the system worked under conditions of large fluid/rock ratios, in which case fluids keep their initial isotopic compositions during interaction with rocks. By consequence, the $\delta^{18}O$ of silica materials directly reflect the temperature of formation, as the $\delta^{18}O$ of the fluid is constant. The fractionation factors between quartz and water of Zheng (1993) and Sharp and Kirschner (1994) can be used but given that there is no important difference between them, we used here that of Zheng (1993) for more consistency in the paper.

The $\delta^{18}O$ values of amorphous silica samples range between 29.7‰ and 35.3‰, which correspond to temperatures between ~40°C and ~20°C (using the fractionation factor of Zheng, 1993; comparable estimates are obtained with other factors like the one of Sharp and Kirschner, 1994). The quartz veins occurring in the coarse saprolite level have $\delta^{18}O$ values between 21.8‰ and 29.0‰, which correspond to temperature between ~40°C and ~80°C, with most samples recording temperatures between ~40°C and ~65°C.

The main information obtained from the isotope systematics on quartz veins from the saprolitic level is that they formed under conditions of low-temperature hydrothermalism rather than at surface temperatures.

6.4 Heat sources for quartz veins formation

Magnesite and amorphous silica have ranges of oxygen composition narrower than that of quartz veins (Fig. 5a,c) which suggests more homogeneous conditions of formation. The clumped isotope temperatures for magnesite formation are between 26±4°C and 42±2°C, which is consistent with the range of temperature estimated for amorphous silica formation between ~20°C and ~40°C. Even if all amorphous silica are not intimately related to magnesite (typically brownish amorphous silica is not), the fact remains that both their similar temperature of formation and their narrow ranges of $\delta^{18}O$ values suggest that they are genetically linked to the same low temperature fluid. Following Quesnel et al. (2013), we can thus propose that magnesite and amorphous silica occurring at different levels of the

nappe record the fluid pathway through the nappe where rapid downward circulation was enhanced by active tectonics.

For quartz veins from the coarse saprolite level the large range of temperature between ~40°C and ~80°C indicates distinct conditions of formation. The range of temperature estimated for the quartz veins from the coarse saprolite level appears particularly high given their structural position. A first possibility is to invoke upward movements of hot fluids coming from depth. Even if it is difficult to estimate the past thickness of the nappe at the time of fluid circulation, the present-day topographic constraints allow estimating a minimum thickness. The mean elevation in the island scale is ~640m as reported by Chevillotte et al. (2006) and the Mont Panié, located on the northern part of the East coast, culminates at 1628m. Considering a surface temperature of ~25°C, a past thickness of the nappe between ~500 and ~2000m and a paleo-gradient of temperature in the peridotite nappe of 20°C.Km^{-1}, temperatures of ~35-75°C may have been reached at the base of the nappe. Rapid upward migration of fluids equilibrated at these temperatures might explain the temperatures recorded by the quartz veins. Occurrences of hydraulic breccia where quartz cements serpentine and garnierite clasts in the coarse saprolite level (Myagkiy et al., 2015) are consistent with this idea. The question of mechanism of precipitation of quartz in the saprolitic structural level remains. The first possibility consists in the precipitation of quartz lead by a change of pH condition. Indeed quartz solubility is function of pH increasing rapidly from pH>9. The pH measured in New Caledonian resurgences of water at the base of the nappe are basic with pH up to 11 (Monin et al., 2014) whereas pH in coarse saprolite level is around ~8 (Trescases, 1975). This abrupt decrease of pH at the saprolitic interface could explain quartz precipitation. Moreover, an additional mixing with *per descensum* meteoric water with pH ~7 (Trescases, 1975) and at surface temperature is also possible and could lead to quartz precipitation. Nevertheless, unlike the conditions of syn-tectonic magnesite formation, no clear evidence of syn-tectonic quartz veins formation is recorded and precludes associating the fluid overpressure to tectonic activity. Consequently, even if the upward fluid circulation linked to fluid overpressure may be in agreement with our data, it remains difficult to identify the cause of such large-scale upward migration of fluid.

An alternative hypothesis to explain the ~40-80°C temperature range of formation of quartz veins at the coarse saprolite level is to invoke exothermic reactions of serpentinization. Indeed, such reactions are known to produce heat (Fyfe, 1974) and may explain elevated temperature of fluid in

ultramafic-hosted hydrothermal systems (Kelley et al., 2001, Lowell and Rona, 2002, Schroeder et al., 2002). Even if serpentinization reactions can explain only a part of the heat contribution for high temperature hydrothermal systems, they could be sufficient for low temperature hydrothermal system like Lost City type (Mével, 2003). In New Caledonia, several present day resurgences of low-temperature and hyperalkaline fluid with pH up to 11 are interpreted as evidence of present-day serpentinization (Barnes et al., 1978, Monin et al., 2014). A recent study (Guillou-Frottier et al., 2015) proposes that such reactions could occur in the coarse saprolite during the weathering of the peridotite. These authors argue that serpentinization reactions should trigger convective fluid circulation by i) increasing of temperature by several tens of degrees and ii) increasing of permeability and porosity by fracturation induced by volume expansion (Kelemen and Hirth 2012). This model could explain the relatively high temperatures identified for the quartz veins formation and the local occurrences of hydraulic breccia where quartz cements serpentine and garnierite (Myagkiy et al., 2015). Our observation and isotopic data are consistent with this model.

7. Conclusion

On the basis of stable oxygen isotopes and clumped isotope analyses, we argue that carbonation and silicification of the New Caledonia Peridotite Nappe occurred under different temperature conditions. First, stable isotopes and clumped isotope analyses of magnesite and amorphous silica display a narrow range of $\delta^{18}O$ values attesting for formation under homogeneous conditions, at temperature of ~25 to 40°C for magnesite and between ~20°C and ~40°C for amorphous silica. The oxygen isotope composition estimated for the fluid at the origin of magnesite is consistent with meteoric water compositions. Second, $\delta^{18}O$ values of quartz veins from the coarse saprolite level display a large range, which is indicative of formation between ~40°C and ~80°C, typical temperatures of low temperature hydrothermalism.

These results lead to question the classical *per descensum* model of Ni-laterites ore deposit where silica, magnesium and nickel leached during supergene alteration of peridotite are exported by downward fluid circulation along fractures cutting through the nappe. Indeed, our results tends to show that carbonation of the Serpentine Sole and quartz veins formation at the coarse saprolite level are the results of two distinct fluid circulation systems. If the low-temperatures of magnesite formation,

specified here using clumped isotope thermometry, are consistent with the tectonically enhanced downward meteoric water circulation model previously proposed in Quesnel et al. (2013), higher temperatures of quartz veins formation would imply that a refinement of the classical *per descensum* model is needed. Thermal equilibration of the fluid along a normal geothermic gradient through the nappe or influence of exothermic reactions of serpentinization could explain such temperatures. Regardless of the exact explanation, it means that nickel lateritic mineralization, with which the quartz veins studied here are associated, developed under conditions of low-temperature hydrothermalism. This inference may be of importance with regards to the properties of migration of nickel during mineralization.

Acknowledgements

This study constitutes a part of B. Quesnel PhD which is supported financially and technically by Koniambo S.A. This study has benefited from equipment purchased by the Qatar Carbonate and Carbonate Storage Research Center sponsored by Qatar Petroleum, Shell, and the Qatar Science and Technology Park. PB and MC thank Emmanuel Fritsch for the geological tour he organized in the CNRT framework. Mineralogical investigations carried out at Nancy were done within the framework of Labex Ressources 21 (supported by the French National Research Agency through the national program "Investissements d'avenir", reference ANR-10-LABX-21–LABEX RESSOURCES 21).

Complément de discussion :

1. Absence de calibration du Δ_{47} spécifique à la magnésite : utilisation de la calibration de Kluge et al. (2015)

Comme il a été évoqué précédemment (partie II-chapitre3 ; article #5), mise à part la calibration théorique proposée par Guo et al. (2009), aucune calibration empirique du Δ_{47} par rapport à la température n'existe à ce jour pour la magnésite. Seule une c Falk et Kelemen (2015) ont proposé de tester l'applicabilité à la magnésite de différentes calibrations (empiriques et théoriques) du Δ_{47} disponibles dans la littérature. Ces auteurs ont donc comparé ces calibrations aux valeurs de Δ_{47} d'échantillons de magnésite précipitée expérimentalement à des températures allant de 120°C à 250°C ainsi que des échantillons de « playa magnesite » dont la température de formation est estimée entre 3°C et 10°C (Fig.III.3.1).

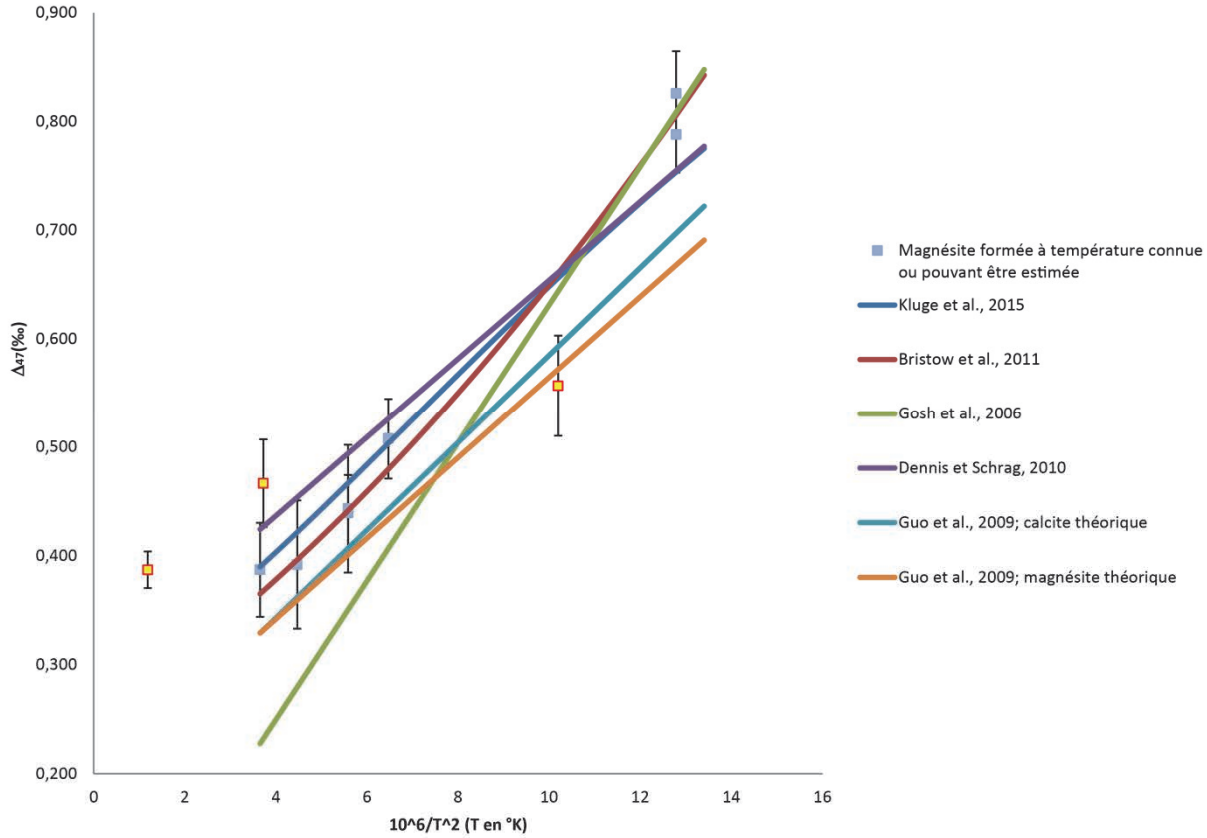

Figure III.3.1 Comparaison de droites de calibration du Δ_{47} en fonction de la température de formations pour divers carbonates avec des échantillons de magnésite dont la température de formation est connue ou peut être estimée. Ces

échantillons inclus des magnésites synthétiques formées à des températures allant de 40°C à 250°C (Deelman, 1999 ; Hänchen et al., 2008 ; Saldi et al., 2010; 2012) ; des échantillons naturels de « playa magnesite) provenant de Atlin, Colombie-Britannique dont la température de formation est estimée à ~3°C à 10°C (Power et al., 2014); des listvenites composées de magnésite+quartz provenant d'Atlin, Colombie-Britannique, formées à des températures comprises entre 210°C et 280°C (Andrew, 1985 ; Hansen et al., 2005); et des métapéridotites composées en partie de magnésite provenant du Val d'Efra, Suisse, formées durant le métamorphisme barrovien à des températures d'environ 645±10°C (Ferry et al., 2005). Les échantillons de magnésite représentés par des carrés jaunes et rouges correspondent aux échantillons dont la température de formation dépasse la température de fermeture du système « clumped » et/ou est relativement mal estimée. Modifiée d'après Falk et Kelemen (2015).

Sur les 10 échantillons analysés, trois divergent particulièrement (carrés rouges et jaunes) conséquence probable d'une formation à haute température (dépassant la température de fermeture de l'effet clumped) ou d'une mauvaise estimation de la température de formation (Falk et Kelemen, 2015). Ces échantillons mis à part, les valeurs de Δ_{47} mesurées (incertitudes prises en compte) recouvrent la plupart des droites de calibrations suggérant qu'il n'existe pas de différences significatives du paléo-thermomètre « clumped isotope » pour les différents types de carbonate. Cependant, comme soulignée par Falk et Kelemen (2015), la calibration de Bristow et al. (2011) semble être la plus adaptée afin d'estimer la température de formation de la magnésite. La calibration récemment publiée (postérieurement à la publication de Falk et Kelemen, 2015) de Kluge et al. (2015) présente une corrélation avec les échantillons de magnésite similaire à celle de Bristow et al. (2011) à moyenne et haute température, divergeant plus fortement à basse température (i.e. dans la gamme de température de formation des magnésites néo-calédoniennes). Dans le cadre de ce travail nous avons néanmoins choisi d'utiliser la calibration de Kluge et al. (2015) pour les raisons qui suivent :

i) la relation empirique Δ_{47} =f (température) utilisée par Bristow et al. (2011) est issue du travail de calibration mené par Magalie Bonifacie (IPGP Paris) sur des échantillons de carbonates formés expérimentalement, des dolomites hydrothermales et des calcites inorganiques synthétiques. Malheureusement ce travail n'étant à ce jour pas publié, aucun détail supplémentaire (protocole analytique, description des échantillons etc…) n'est disponible.

ii) Compte tenu de l'importante incertitude associée aux mesures du Δ_{47} (~0.040‰ en moyenne) à laquelle s'additionne l'incertitude sur l'estimation de la température de formation des échantillons de magnésite (et particulièrement pour les échantillons de basse température, voir Power et al., 2014), la comparaison de ces derniers avec les différentes

droites de calibration n'a ici que pour but de vérifier, au premier ordre, qu'il n'existe pas de déviation importante du thermomètre « clumped » spécifique à la magnésite. Par conséquent, l'apparente meilleure corrélation à basse température des magnésites avec la droite de calibration de Bristow et al. (2011) ne suffit pas à justifier à elle seule son utilisation.

iii) La comparaison des températures calculées pour nos échantillons de magnésite utilisant alternativement la calibration de Bristow et al. (2011) et celle de Kluge et al. (2015), ne mène qu'à de très légères différences de résultats ne remettant absolument pas en cause le caractère basse température de formation des magnésites néo-calédoniennes discuté dans ce travail (Tableau III.3.1).

Ech	Δ_{47}(‰)	Erreur standard	TºC Kluge et al., 2015	Incertitude sur la température	TºC Bristow et al., 2011	Incertitude sur la température
GBMS Si 1	0.671	0.016	35	6	37	5
BMS Gio 9	0.695	0.012	26	4	31	3
BMS Gio 3	0.689	0.016	28	6	32	4
BMS Gio 12	0.675	0.024	33	9	36	7
VAV Gio 9	0.691	0.02	28	7	32	5
GMAR 2	0.693	0.006	27	2	31	2
DECH 1	0.652	0.005	42	2	42	2

Tableau III.3.1 Comparaison des températures de formation des échantillons de magnésite néo-calédonienne analysés dans cette étude calculés en utilisant alternativement la calibration de Bristow et al. (2011) ou Kluge et al. (2015).

2. Comparaison des valeurs de $\delta^{18}O$ des échantillons de magnésite mesurés à Londres et à Rennes.

Sur l'ensemble des échantillons sur lesquels l'analyse « clumped » a été menée, le $\delta^{18}O$ a été mesuré à la fois au laboratoire de géochimie isotopique de Rennes ainsi qu'au laboratoire de l'équipe Carbonate Research de l'Imperial College de Londres. La comparaison des résultats obtenus dans ces deux laboratoires, sur les mêmes échantillons, met en exergue la faible reproductibilité inter-laboratoire des résultats (Tableau III.3.2 ; Fig.III.3.2). En effet des différences allant jusqu'à 1.6‰ pour le $\delta^{18}O$ et 2.2‰ pour le $\delta^{13}C$ sont observables. Il est intéressant de noter que les valeurs de $\delta^{18}O$ et de $\delta^{13}C$ (mis à part pour le $\delta^{13}C$ de l'échantillon BMS Gio 3) sont systématiquement plus élevées lorsque

mesurées à Londres. Graphiquement ces données apparaissent translatées vers la droite par rapport aux données obtenues à Rennes (Fig.III.3.2).

Les macro-échantillons de magnésite étant minéralogiquement très homogènes et les analyses ayant été faites sur les mêmes lots de poudre, il ne semble pas pertinent d'attribuer ces différences à de

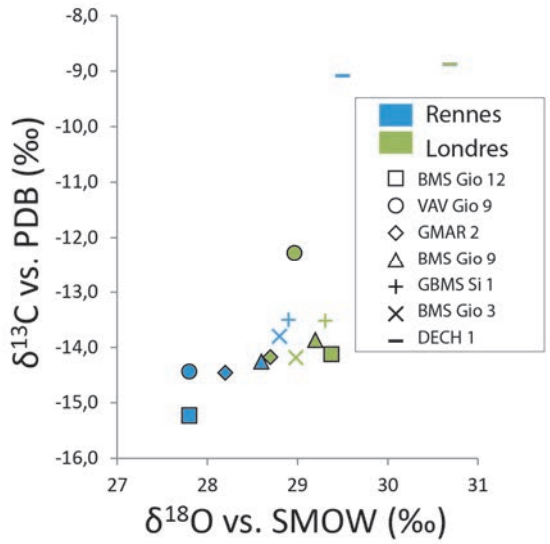

Figure III.3.2 Diagramme $\delta^{13}C$ versus $\delta^{18}O$ dans lequel sont représentées les compositions isotopiques des sept échantillons de magnésite néo-calédonienne obtenues à Rennes ou à Londres. Les résultats sont donnés versus SMOW (Standard Mean Ocean Water) pour le $\delta^{13}C$ et versus PDB (Pee Dee Belemnite) pour le $\delta^{13}C$.

possible variabilité locale de composition de l'échantillon. Sans faire appel à des différences d'architecture de ligne d'extraction (présence d'un piège Porapak-Q sur la ligne londonienne) ou de modèle de spectromètre de masse (Londres : Thermo Finnigan MAT-253; Rennes : VG OPTIMA triple collecteur) l'origine de ces différences réside plus probablement dans les conditions (température et durée) de réaction entre la magnésite et l'acide phosphorique. Au sein du laboratoire de Rennes, les échantillons de magnésite ont été mis à réagir par groupe à 75°C, en offline, jusqu'à ce que la réaction soit terminée, soit environ 15h à 20h selon les échantillons. Chaque échantillon n'a été analysé qu'une seule fois. Au sein du laboratoire de Londres, contraint par l'architecture de la ligne d'extraction, les échantillons de magnésite ont été mis à réagir un à un à 90°C en online pendant une durée de 1h à 2h. Chacune de ces réactions a été stoppée avant qu'elle ne soit terminée, le taux d'avancement étant mal contraint. Ces sept échantillons ont été répliqués de 2 à 3 fois chacun ne mettant en avant aucune déviation significative.

Ech	$\delta^{18}O$ Rennes	$\delta^{13}C$ Rennes	$\delta^{18}O$ Londres	$\delta^{13}C$ Londres	Ecart $\delta^{18}O$	Ecart $\delta^{13}C$
GMAR-2	28.2	-14.5	28.7	-14.2	0.5	0.3
BMS Gio 9	28.6	-14.3	29.2	-13.9	0.6	0.4
VAV Gio 9	27.8	-14.4	29.0	-12.3	1.2	2.2
BMS Gio 12	27.8	-15.2	29.4	-14.1	1.6	1.1
DECH 1	29.5	-9.1	30.7	-8.9	1.2	0.2
GBMS-Si-1	28.9	-13.5	29.3	-13.5	0.4	0.0
BMS Gio 3	28.8	-13.8	29.0	-14.2	0.2	-0.4

Tableau III.3.2 Comparaison du $\delta^{18}O$ et du $\delta^{13}C$ mesurés à Londres et à Rennes pour les échantillons sur lesquels la mesure du Δ_{47} a été effectuée.

L'influence de la température sur le fractionnement de l'oxygène lors de la réaction est connue et corrigée lors du calcul du résultat final (Das Sharma et al., 2002). Il semble donc peu probable que la variation de température puisse expliquer la variation de la valeur du $\delta^{18}O$. Expérimentalement, Das Sharma et al. (2002) ont montré que le taux d'avancement de la réaction entre l'acide phosphorique et la magnésite n'a que très peu d'influence sur la valeur du $\delta^{18}O$ mesurée (Fig.III.3.3).

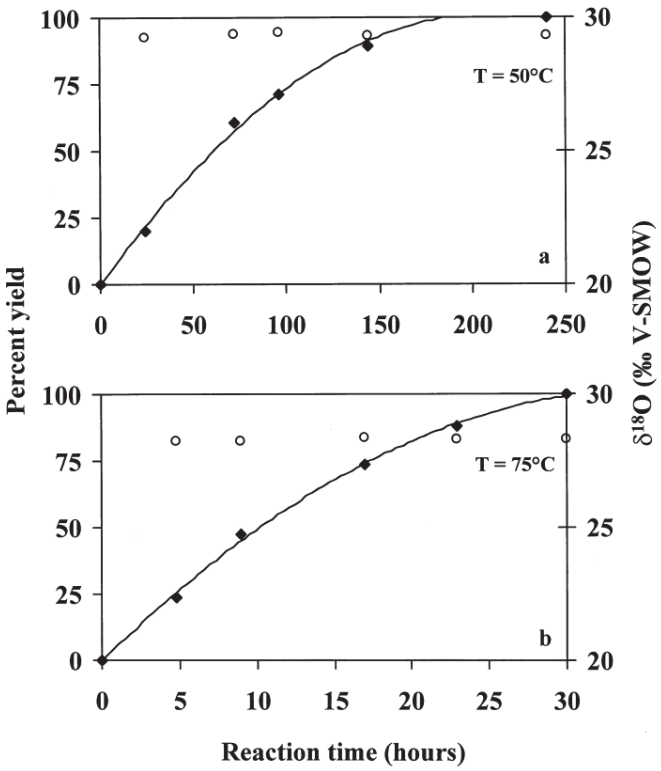

Figure III.3.3 Relation entre le taux d'avancement de la réaction entre acide phosphorique et magnésite (losange noir) et valeur du $\delta^{18}O$ (cercle) à a)50°C et b) à 75°C en fonction du temps de réaction.

Malgré cela, il nous semble probable, à défaut d'autre explication, que cela ait pu avoir une influence sur nos résultats. Cependant, seuls trois échantillons sur sept présentent une forte variabilité

en $\delta^{18}O$ (VAV Gio 9 ; BMS Gio 12 ; DECH 1) et seulement deux sur sept en $\delta^{13}C$ (VAV Gio 9 ; BMS Gio 12). L'absence de systématisme pourrait suggérer l'existence d'autres facteurs que le temps influençant l'avancement de la réaction. La variabilité de la granulométrie des poudres mises à réagir pourrait avoir une influence via l'augmentation ou la diminution de la surface réactive. Certains échantillons légèrement silicifiés pourraient également être plus difficiles à faire réagir. Au-delà de cela, l'échantillon DECH 1 met en évidence un découplage entre le $\delta^{13}C$ et le $\delta^{18}O$. Si l'écart en $\delta^{18}O$ est important (1.2‰) celui en $\delta^{13}C$ est presque nul (0.2‰). Ceci pourrait justifier, au moins pour cet échantillon, de l'existence d'un autre paramètre influençant la valeur du $\delta^{18}O$ indépendamment du taux d'avancement de la réaction.

Les articles #3 et #5 présentés dans cette thèse discutent de l'origine de la magnésite sur la base des données isotopiques acquises à Rennes. Le message principal résultant de ces discussions est que la magnésite de Nouvelle-Calédonie s'est formée à basse température à partir d'un fluide météorique. Cette interprétation reste valable, et est même renforcée, si l'on considère les données isotopiques acquises à Londres pour les sept échantillons de magnésite concernés. La figure III.3.4 est un analogue de la figure 4 de l'article #3 comparant les données isotopiques des magnésites néo-calédoniennes aux données isotopiques de magnésite provenant de différentes régions dans le monde mais systématiquement associées à des roches ultramafiques et interprétées comme ayant une origine météorique.

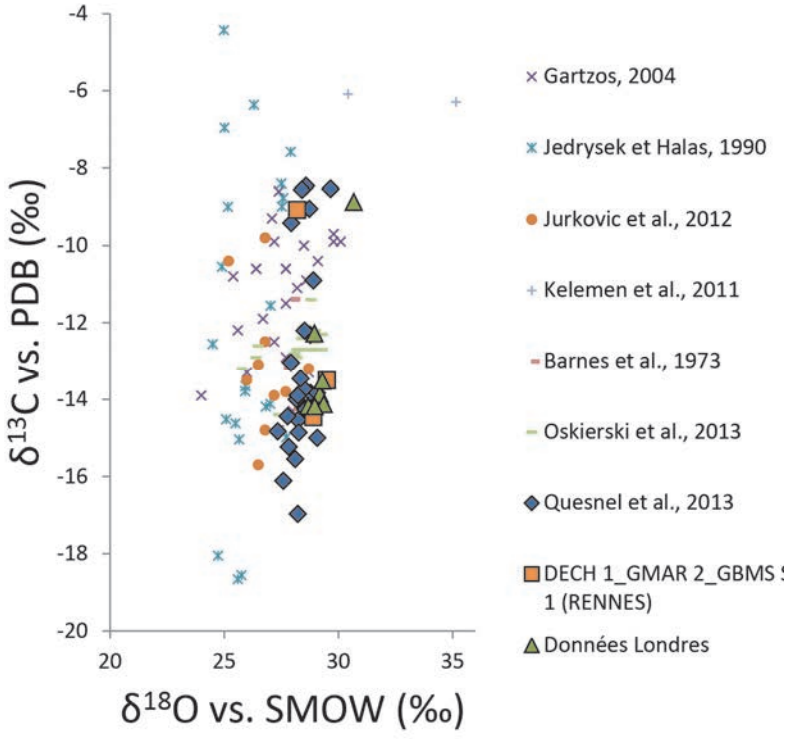

Figure III.3.4 Diagramme $\delta^{13}C$ versus $\delta^{18}O$ dans lequel sont représentées i) les compositions isotopiques de magnésites provenant de divers endroits dans le monde mais systématiquement localisées au sein de roches ultramafiques et interprétées comme étant d'origine météorique ; ii) les compositions isotopiques des magnésites néo-calédoniennes obtenues à Rennes ou à Londres. Les résultats sont donnés versus SMOW (Standard Mean Ocean Water) pour le $\delta^{13}C$ et versus PDB (Pee Dee Belemnite) pour le $\delta^{13}C$.

Les données de magnésite néo-calédonienne obtenues à Rennes sont systématiquement localisées à droite du cluster formé par les données de la littérature. Ce décalage est interprété comme pouvant résulter

i) d'une différence de $\delta^{18}O$ de l'eau météorique, possible conséquence de la position paléogéographique des sites étudiés ou

ii) d'une température de formation plus basse pour les magnésites néo-calédoniennes. Comme nous l'avons précisé, les valeurs de $\delta^{18}O$ obtenues à Londres sont systématiquement décalées à droite des données acquises à Rennes. Par conséquent, si l'on considère les données de Londres, l'interprétation basse température de la formation des magnésites néo-calédoniennes reste valable, voir même renforcée.

La question de l'influence du taux d'avancement de la réaction sur la valeur du Δ_{47} se pose également. Cependant, au regard de l'homogénéité des résultats obtenus (cf article #5, Fig.5d), de l'incertitude associée à ses mesures et de l'interprétation que nous en faisons, les possibles variations mineures du Δ_{47} peuvent être considérées, dans ce cas, comme non significatives. Nous précisons ici que la gamme de compositions en oxygène du fluide initial à partir duquel les différents échantillons de magnésites se sont formés a été calculée en utilisant le $\delta^{18}O$ mesuré à Rennes afin de s'affranchir de la possible influence du taux de réaction.

Conclusions générales et perspectives

L'objectif principal de ce travail peut se résumer à la volonté d'améliorer notre compréhension du gisement nickélifère néo-calédonien à grande échelle en ne se focalisant pas uniquement sur la zone minéralisée. Cette approche, qui semble au premier abord paradoxale, nous a permis d'obtenir des informations complémentaires de celles obtenues par l'étude du gisement lui-même menant à une réévaluation du modèle *per descensum* classiquement admis.

Ce travail a également permis, via l'analyse structurale, de caractériser l'évolution spatiale et temporelle de la déformation enregistrée dans l'ensemble de la Nappe des Péridotites et de discuter notamment de la réelle influence de la serpentinisation sur la localisation de la déformation.

1. Vers une actualisation du modèle per descensum

1.1 Evidences de processus secondaires menant à la redistribution du nickel

Via le traitement d'une base de données de plus de 6000 forages de sub-surface fournie par l'entreprise Koniambo Nickel SAS, nous avons pu modéliser en 3D la couverture latéritique et caractériser la distribution du nickel à l'échelle du gisement au sein du niveau saprolitique. Trois types de géométrie caractéristiques de la couverture latéritique peuvent être reconnus. Les zones où la couverture limonitique est la plus épaisse sont systématiquement localisées sur les hauts topographiques formant à l'échelle du massif des zones hectométriques disséquées par la topographie et distribuées à des altitudes variables. Lorsque localisée dans des zones de pente modérée, cette couverture s'affine, la succession classique des différents faciès étant souvent incomplète. Dans les zones de forte pente, enfin, l'absence de couverture limonitique laisse la saprolite à l'affleurement. Cette distribution de l'épaisseur de la couverture limonitique s'avère globalement corrélée à la teneur en nickel du niveau saprolitique. En effet les zones les plus riches en nickel sont majoritairement localisées sur les pentes, sous des couvertures fines à absente de limonite. A l'inverse, les zones les plus pauvres en nickel sont localisées sur les hauts topographiques sous des couvertures limonitiques épaisses. A l'inverse de ce qui est attendu suivant le modèle *per descensum* classique (i.e. que les saprolites les plus riches en nickel soient localisées sous les couvertures limonitiques les plus épaisses) cette observation pose la question de la possible mobilité latérale du nickel. En nous basant sur les bilans de masse verticaux du nickel effectués sur chacun des forages, nous avons pu mettre en évidence qu'aucune perte significative en nickel n'est documentée au sein des profils latéritiques épais des hauts

topographiques actuels. Ce résultat nous amène à suggérer que l'enrichissement en nickel des zones de pentes ne résulte pas de circulation latérale de fluides riches en nickel dissout provenant des zones amont comme très tôt évoqué dans la littérature (de Chetalat, 1947 ; Avias, 1969 ; Trescases, 1975). Ainsi, en nous basant sur l'identification de matériel remanié au sein des profils latéritiques localisés dans les zones de pentes (Latham, 1975; Trescases, 1975; Avias, 1978; Maurizot et al., 2002), nous proposons que le transfert latéral, mécanique, puis le lessivage de matériel enrichi en nickel provenant d'anciens hauts topographiques, maintenant érodés, puisse être à l'origine de l'enrichissement en nickel de la saprolite de pente.

De manière complémentaire, l'étude menée à l'échelle de l'affleurement du « pit Cagou » nous a permis de mettre en évidence la redistribution, actuelle à sub-actuelle, du nickel au sein du niveau saprolitique. En effet, l'identification d'une minéralisation nickélifère présentant une zonation chimique et minéralogique de forme concentrique (appelée « target-like ore ») avec une bordure verte (composée de pimélite) et une partie centrale blanche (composée de Mg-kérolite) témoigne d'une redistribution du nickel initialement contenu dans le minerai garniéritique. En effet, systématiquement localisé à proximité de cluster de veines de garniérite, les « target-like » résultent de la dispersion du nickel garniéritique via un processus d'évapo-précipitation dont le moteur est l'alternance de périodes d'hydratation et de déshydratation induites par les mouvements en zone vadose.

Par ces deux études complémentaires, nous mettons en évidence l'existence de processus secondaires impliqués dans la distribution observée du nickel au sein du niveau saprolitique. Ces résultats apportent de nouvelles clés de compréhension de la géométrie actuelle du gisement nickélifère néo-calédonien et pourraient représenter des éléments à prendre en compte dans la dynamique de prospection et d'exploitation de ce dernier.

1.2 Influence de la tectonique active sur l'altération supergène

La présence de magnésite localisée principalement au niveau de la semelle de serpentine témoigne de paléo-circulations de fluide à l'extrême base de la Nappes des Péridotites. Dans ce travail, via l'analyse isotopique classique et via l'utilisation de la « clumped isotope thermometry », nous avons pu documenter le caractère basse température (~30°C) et l'origine météorique des eaux à partir desquelles

la magnésite se forme. Depuis longtemps (Glasser, 1904), la magnésite est supposée être un sous-produit de l'altération supergène ; nos résultats confirment ce lien, en posant néanmoins la question de la manière dont le fluide supergène a pu circuler du sommet jusqu'à la base de la Nappes des Péridotites. A partir de l'analyse structurale des veines de magnésite, nous avons a pu montrer l'aspect synchrone de leur formation vis-à-vis de la déformation cisaillante, à cinématique vers le SO, enregistrée au sein de la semelle de serpentine. Ces résultats suggèrent donc que l'altération supergène et, par extension, la formation des latérites, a pu être synchrone d'un contexte tectonique actif. Nous proposons dès lors que l'activité tectonique a facilité l'infiltration de l'eau météorique impliquée dans le processus de latérisation et donc permettre l'export du magnésium lessivé menant ainsi à la carbonatation de la semelle de serpentine.

L'efficacité du drainage est connue comme étant un paramètre important dans le développement des latérites favorisant notamment l'approfondissement du front d'altération et menant à la formation de gisements particulièrement riche en nickel (Golightly, 1981, 2010 ; Freyssinet et al., 2005 ; Butt et Cluzel, 2013). Si l'influence de la tectonique active sur la redistribution locale du nickel dans le niveau saprolitique a déjà été souligné par Cluzel et Vigier (2008) pour le cas néo-calédonien, la complémentarité de notre étude réside dans le fait que nous documentons cette influence à l'échelle du Massif de Koniambo.

1.3 Evidences d'hydrothermalisme de basse température associées à la minéralisation nickélifère

De nombreuses veines de quartz sont localisées au sein du niveau saprolitique sous forme de remplissage de fracture. Ces veines sont souvent étroitement associées à la garniérite. De même que pour la magnésite, ces occurrences de quartz sont depuis longtemps considérées comme représentant également des sous-produits de l'altération supergène (Trescases, 1975). Dans le cadre de ce travail nous avons effectué la caractérisation isotopique de ces veines afin d'en estimer la température de formation. Nous basant sur leurs compositions isotopiques en oxygène ($21.8‰ \leq \delta^{18}O \leq 29.0‰$) nous avons pu estimer une gamme température de formation comprise entre ~40°C et 80°C. Ces températures, anormalement élevées compte tenu de la position structurale de ces veines au sein de la Nappe des Péridotites (i.e. principalement dans le niveau saprolitique), posent la question des possibles sources de chaleur impliquées. Deux hypothèses peuvent dès lors être proposées. La première consiste

en la possible existence d'une circulation de fluide en profondeur dans le massif de péridotites, de type hydrothermal convective. L'eau météorique impliquée dans le processus de latérisation pourrait être exportée jusqu'à la base de la nappe où elle se rééquilibrerait thermiquement puis migrerait rapidement vers le haut de la nappe. A l'instar de la magnésite, la tectonique active pourrait être le moteur d'une telle circulation permettant la descente du fluide puis sa remonté via des surpressions locales de fluide. Si les évidences de brèches hydrauliques à ciment de quartz et clastes de serpentine et de garniérite localisées dans le niveau saprolitique (Myagkiy et al., 2015) semblent cohérentes avec cette hypothèse, nous n'avons pas pu mettre en évidence le caractère synchrone de a déformation de la formation des veines de quartz. Compte tenu du caractère basse température de la formation des magnésites en base de nappe, la circulation du fluide à l'origine de la magnésite et celle du/des fluide(s) à l'origine des veines de quartz, doivent nécessairement être diachrones.

Alternativement, la source de chaleur nécessaire à la formation des veines de quartz dans des conditions d'hydrothermalisme de basse température pourrait provenir de réactions exothermiques de serpentinisation. En effet de telles réactions sont connues pour produire de la chaleur (Fyfe, 1974) et sont invoquées pour expliquer l'actuelle résurgence, à la base de la Nappe des Péridotites, de fluides hyper-alcalins, à des températures (jusqu'à 37°C) témoignant de conditions d'hydrothermalisme de basse température (Barnes et al., 1978 ; Monin et al., 2014). En outre, une étude récente (Guillou-Frottier et al., 2015) propose que de telles réactions auraient pu se produire au cours de l'altération supergène, au sein du niveau saprolitique, favorisant ainsi la circulation convective des fluides dans ce niveau en augmentant par incidence la température de ce dernier.

Si la question de la source de chaleur reste ouverte, il n'en reste pas moins que l'évidence d'hydrothermalisme de basse température au sein du niveau saprolitique et associée à l'altération supergène est documentée. Cette observation pose immédiatement la question de l'influence de telles températures sur le processus d'altération lui-même et plus spécifiquement sur la minéralisation nickélifère. Comme proposé par Guillou-Frottier et al. (2015), ces températures pourraient avoir généré des circulations de fluides convectives à la base du régolithe entrainant l'approfondissement local du profil latéritique. Il est également intéressant de s'interroger sur le comportement du nickel dans ces conditions. L'augmentation de la température au sein du niveau saprolitique pourrait-elle être le moteur de la précipitation des veines de garniérites dans ce même niveau ? En effet, comme décrit

ci-dessus, les veines de garniérites actuellement localisées dans la zone de battement de nappe (et donc à des températures de sub-surface) sont instables et se dissolvent favorisant ainsi la dispersion et la redistribution du nickel sous forme de « target-like ore ». Si les variations, au sein du profil latéritique, de pH, des conditions d'oxydo-réduction et de l'activité de la silice sont des paramètres connus dont dépend la formation de garniérite (; Trescases, 1975; Golightly, 1981, 2010 ; Gleeson et al., 2004; Galí et al., 2012; Villanova-de-Benavent et al., 2014) l'influence de la température reste donc une voie à explorer.

2. Evolution spatiale et temporelle de la déformation: influence de la serpentinisation sur la localisation de la déformation au sein d'une nappe obductée ?

La Nouvelle-Calédonie est l'un des rares sites mondiaux où l'obduction d'une nappe ophiolitique n'a pas été suivie d'une phase de collision. Cette particularité fait de la Nouvelle Calédonie une cible privilégiée de l'étude de la déformation associée au stade anté et syn-emplacement de la Nappe sur le substrat néo-calédonien. Aujourd'hui dépourvue de sa partie crustale, seule la base péridotitique de la nappe affleure. De manière générale, les roches ultramafiques présentent des évidences d'interaction fluide/roche importantes que reflète la présence abondante, mais distribuée de manière hétérogène, de serpentine. Du fait son caractère rhéologique peu résistant, la serpentine a la capacité de localiser la déformation. En Nouvelle-Calédonie, la serpentinisation s'exprime de manière pervasive au sein de la Nappe des Péridotites mais également de manière localisée. Plusieurs types de serpentine sont en effet associés aux structures résultant de la déformation de la Nappe posant la question de leur chronologie relative. L'objectif de l'analyse structurale effectuée dans cette thèse a donc été de caractériser l'évolution spatiale et temporelle de la déformation enregistrée au sein de l'ensemble de la Nappe des Péridotites, sur l'exemple du Massif de Koniambo, et de discuter de l'influence de la serpentinisation sur la localisation de la déformation.

La partie supérieure du massif se caractérise par son dense réseau de fractures et de failles dont certaines sont porteuses d'antigorite ou de serpentine polygonale. La partie supérieure du massif préserve au moins deux événements de déformation précoces, le premier associé à l'antigorite (extension ONO-ESE) et le second associé à la serpentine polygonale (compression NO-SE).

Le niveau basal de la nappe, ou « semelle de serpentine », est composé d'une brèche tectonique massive, composant la partie supérieure de ce niveau, et d'une couche de serpentinite mylonitisée

composant la partie inférieure. La semelle enregistre un cisaillement tangentiel pervasif à cinématique vers le SO et représente un décollement à la base de la nappe.

Le niveau intermédiaire est caractérisé par la présence de plusieurs zones de cisaillement conjuguées d'épaisseur métrique accommodant un raccourcissement NE-SO. De la même manière qu'à la semelle, ces zones de cisaillements sont associées à de la serpentine polygonale et de la magnésite représentant les principales phases minérales syn-déformation. Par conséquent ces zones de cisaillement sont probablement reliées à la semelle, plusieurs relations géométriques pouvant rendre compte de ce lien. En comparaison au cisaillement top SO enregistré le long de la semelle, la déformation enregistrée dans la partie supérieure du massif est plus ancienne.

Cartographiquement, ces trois niveaux structuraux se corrèlent bien aux différents niveaux lithologiques définis dans la littérature en fonction de leur degré de serpentinisation. Par conséquent, il est tentant de considérer que l'intensité de la serpentinisation a joué un rôle majeur dans la manière dont la déformation a été distribuée au travers de la Nappe des Péridotites. Cependant, dans le niveau supérieur de la nappe, même la moins altérée des péridotites contient plus de serpentine que, selon les travaux théoriques et expérimentaux, ce qu'il serait nécessaire d'avoir pour être aussi peu résistant qu'une serpentinite pure. Par conséquent, aucun gradient vertical de résistance dû à des variations du degré de serpentinisation n'est attendu au sein de la nappe. Nous proposons dès lors que la localisation de la déformation le long de la semelle de serpentine résulte de la juxtaposition de la nappe, faite de péridotites serpentinisées peu résistantes, sur le substrat composé de roches mafiques résistantes. Cette interprétation est en désaccord avec l'idée intuitive qui considèrerait que la nappe, faite de péridotites, serait plus résistante que le substrat. En plus de cette interprétation, et ce en dépit du peu d'évidences de terrain, la localisation de la déformation pourrait également avoir été facilitée par des surpressions de fluide le long de la base de la nappe.

Ce travail amène naturellement à s'interroger sur l'implication qu'ont la distribution et la chronologie des structures étudiées sur la mécanique d'emplacement de la Nappe des Péridotites. Cette question fait l'objet d'un projet d'article, mené par Pierre Gautier, et constitue un travail complémentaire aux développements préliminaires présentés dans cette thèse.

3. Perspectives

L'objectif principal de ce travail a été d'améliorer notre compréhension de la formation du gisement nickélifère néo-calédonien. Si un certain nombre d'éléments de réponses sont apportés dans cette étude, il n'en reste pas moins que de ce travail, découle un encore plus grand nombre de questions.

La mise en évidence de processus de remobilisation latérale du nickel, aussi bien mécanique qu'associés aux fluides, pose inévitablement la question de la généralisation de ces processus à l'échelle du gisement néo-calédonien mais plus généralement à l'ensemble des gisements nickélifères latéritiques mondiaux. Limitées par la difficulté d'avoir accès à des bases de données de forage de qualité comme celle que nous avons pu manipuler (en termes de nombre et de régularité de distribution des forages aussi bien que par la qualité des analyses chimiques associées), ces études sont souvent difficiles à mettre en place. Cependant, les processus que nous décrivons dans cette étude mériteraient d'être confirmés par l'étude d'autres gisements. En effet, s'ils s'avèrent être généralisables, il est indéniable qu'ils constitueraient une base directement exploitable par les entreprise minières notamment en terme d'exploration.

Toujours dans cette dynamique d'applicabilité des connaissances, l'étude structurale que nous avons menée sur l'ensemble de la déformation interne de la Nappe des Péridotites constitue le prérequis nécessaire à la compréhension des relations géométriques reliant la localisation du gisement nickélifère à la structure interne de la nappe. La volonté de compréhension de ces relations est d'ores et déjà matérialisée via le travail de Marion Iseppi dont la thèse (co-tutelle Université de Nouvelle-Calédonie-BRGM) s'intitule « Fracturation polyphasée et contrôles des gisements de nickel supergène de Nouvelle-Calédonie. Nouvelles méthodes d'exploration et modèles de gisements ».

D'un point de vue plus fondamental, au moins deux points forts mériteraient d'être investigués. Dans cette étude, nous avons pu mettre en évidence le lien existant entre la carbonatation des serpentinites néo-calédonienne et l'altération supergène et proposons que la déformation active a pu avoir une influence sur l'export des fluides impliqués dans l'altération supergène.

Trois questions découlent directement de cette observation :

i) la relation altération supergène et carbonatation est-elle vérifiable pour d'autres cas de carbonatation de roche ultramafique à l'échelle mondiale ?

ii) La tectonique active joue-t-elle un rôle fondamental dans le processus de carbonatation des roches ultramafiques?

iii) La tectonique active est-elle l'un des paramètres fondamentaux menant à la formation et à la forte minéralisation des gisements nickélifères latéritiques.

Les deux premiers points ont motivé la mise en place à Géosciences Rennes en 2015 d'un stage de Master 2 effectué par François-Xavier Masson sur la caractérisation de la carbonatation des ophiolites de Serbie. Compte tenu de l'histoire tectonique complexe ayant suivi la mise en place jurassique des latérites, le lien entre carbonatation et altération supergène n'a pu être directement établi. Cependant, il apparait clairement qu'au moins une partie des occurrences de magnésite serbe se sont formées de manière synchrone de la déformation enregistrée par l'ophiolite. Cette démarche mériterait d'être renouvelée sur d'autres analogues naturels de carbonatation de roches ultrabasiques.

Enfin, nous avons pu mettre en exergue que la minéralisation nickélifère au sein du niveau saprolitique était associée à la circulation de fluide dans des conditions d'hydrothermalisme de basse température. Ce résultats appellent à s'interroger à la fois sur les conditions de mobilité du nickel dans de telles conditions et sur l'influence qu'a pu avoir la circulation de tels fluides au sein du niveau saprolitique sur la localisation du gisement garniéritique. La compréhension des moteurs menant à la minéralisation nickélifère du niveau saprolitique fait l'objet du travail d'Andrey Myagkiy au laboratoire Géoressources de Nancy et dont le sujet de thèse s'intitule « Mineralization of Nickel in saprolitic ore of New Caledonia Dynamics of metal transfer and modeling of coupled geochemical and hydrodynamical processes ».

Force est de constater, qu'à ce jour, notre compréhension du gisement nickélifère néo-calédonien n'est que parcellaire mais continue d'évoluer et de susciter un vif intérêt scientifiques comme en témoignent les différentes thèses lancées sur cette problématique (Andrey Myagkiy et Marion Iseppi notamment) ainsi que les nombreux projets en cours menés par le CNRT et le service géologique de la DIMENC.

Références bibliographiques

A

Affek, H. P. (2012). Clumped isotope paleothermometry: principles, applications, and challenges. The Paleontological Society Papers, 18, 101–114.

Affek, H.P., Eiler, J.M. (2006) Abundance of mass 47 CO_2 in urban air, car exhaust, and human breath. Geochim. Cosmochim. Acta 70, 1–12.

Albarède, F. (2008) Geochemistry : an introduction. Second edition. Cambridge university press.

Allmendinger, R.W., Cardozo, N.C., and Fisher, D. (2012) Structural Geology Algorithms: Vectors & Tensors: Cambridge, England, Cambridge University Press, 289 pp.

Andréani, M., Grauby, O., Baronnet, A. et Munoz, M. (2008) Occurrence, composition and growth of polyhedral serpentine. European Journal of Mineralogy, 20(2), 159-171.

Andréani, M., Baronnet, A., Boullier, A-M., Gratier, J-P. (2004) A microstructural study of a « crack-seal » type serpentine vein using SEM and TEM techniques. Eur. J. Mineral., 16, 585-595.

Andreani, M., Luquot, L., Gouze, P, Godard, M., Hoisé, E., Gibert, B. (2009) Experimental study of carbon sequestration reactions controlled by the percolation of CO_2-rich brine through peridotites. Environ. Sci. Technol., 43, 1226-1231.

Andrew K. (1985) Fluid inclusion and chemical studies of goldquartz veins in the Atlin Camp, Northwestern British Columbia. B.Sc. thesis, Univ. British Columbia, Vancouver, BC, Canada. 116 pp.

Angelier, J. (1994) Fault slip analysis and paleostress reconstruction. In: Hancock, P.L. (Ed.), Continental Deformation. Pergamon Press, Oxford, pp. 53-100.

Angelier, J., Mechler, P. (1977) Sur une méthode graphique de recherche des contraintes principales également utilisable en tectonique et en sismologie: la méthode des dièdres droits. Bull. Soc. Géol. France ,19, 1309–1318.

Arthaud, F. (1969) Méthode de détermination graphique des directions de raccourcissement, d'allongement et intermédiaire d'une population de failles. Bull. Soc. géol. de France 7 (XI), 729–737.

Auzende, A.L., Daniel, I., Reynard, B., Lemaire, C., Guyot, F. (2004) High-pressure behaviour of serpentine minerals: a Raman spectroscopic study. Phys. Chem. Miner., 31, 269–277.

Avias, J. (1967) Overthrust structure of the main ultrabasic New Caledonian massives. Tectonophysics, 4, 531–541.

Avias, J. (1969) Note sur les facteurs contrôlant la genèse et la destruction des gîtes de nickel de la Nouvelle-Calédonie. Importance des facteurs hydrologiques et hydrogéologiques. C. R. Acad. Sc. Paris, 268, 244-246

Avias, J. (1978) L'évolution des idées et des connaissances sur la genèse et sur la nature des minerais de nickel, en particulier latéritiques, de leur découverte à nos jours. Bulletin B.R.G.M (Bureau des Recherches Géologiques et Minières), section II (3), 165-172.

Aye, F., Bonnemaison, M., Jacob, M. (1986) Etude gîtologique et géochimique des indices et anomalies en Sb, W, As, Au de la côte Est de la Nouvelle-Calédonie-programme CORDET-Rapport final du projet A4 (1983-84). Bureau des Recherches Géologiques et Minières report 85 NCL 079 GMX.

B

Bailey, W.R., Holdsworth, R.E., Swarbrick, R.E. (2000) Kinematic history of a reactivated oceanic suture: the Mamonia Complex Suture Zone, SW Cyprus. J. Geol. Soc. London, 157, 1107-1126.

Baille, J-S., Jegat, P., Marini, D., Louis, A. (2013) Atlas de la Nouvelle-Calédonie, IRD éditions.

Baldwin S.L., Rawling T., Fitzgerald, P.G. (2007) Thermochronology of the New Caledonian high-pressure terrane: implications for middle Tertiary plate boundary processes in the southwest Pacific. Geologogical society of America, special paper, 419, 117-134.

Banfield, J. F., Bailey, S. W., Barker, W. W., and Smith, R. C. (1995) Complex polytypism: Relationships between serpentine structural characteristics and deformation: American Mineralogist, 80, 1116–1131.

Barnes, I., O'Neil, J. R., and Trescases, J. J. (1978) Present day serpentinization in New Caledonia, Oman and Yugoslavia. Geochim. Cosmochim. Acta 42, 144–145.

Barnes, I., O'Neil, J.R., Rapp, J.B, White, D.E (1973) Silica-carbonate alteration of serpentine: wall rock alteration in mercury deposits of the California Coast Range. Economic Geology and the Bulletin of the Society of Economic Geologists, 68, 388-398.

Baronnet, A. et Devouard, B. (1994) Sectors of polygonal serpentine. A model based on dislocations. Phys. Chem. Minerals, 21, 330-343.

Baronnet, A., Devouard, B. (2005) Microstructures of common polygonal serpentines from axial HRTEM imaging, electron diffraction, and lattice-simulation data. The Canadian Mineralogist, 43, 513-542

Beauvais, A., Parisot, J.-C., Savin, C. (2007) Ultramafic rock weathering and slope erosion processes in a South West Pacific tropical environment. Geomorphology, 83,1–13.

Beinlich, A., Plümper, O., Hövelmann, J., Austrheim, H., Jamtveit, B. (2012) Massive serpentinite carbonation at Linnajavri, N-Norway. Terra Nova 24, 446-455.

Berndt, M.E., Allen, D.E., Seyfried, W.E. (1996) Reduction of CO_2 during serpentinization of olivine at 300ºC and 500 bar. Geology 24, 351-354.

Berthé, D., Choukroune, P., Gapais, D. (1979) Orientations préférentielles du quartz et orthogneissification progressive en régime cisaillant: l'exemple du cisaillement sud-armoricain. Bull. Minéral., 102, 265-272.

Bloise, A., Critelli, T., Catalano, M., Apollaro, C., Miriello, D., Croce, A., Barrese, E., Liberi, F., Piluso, E., Rinaudo, C., Belluso, E. (2014) Asbestos and other fibrous minerals contained in the serpentinites of the Gimigliano-Mount Reventino Unit (Calabria, S-Italy). Environ. Earth Sci., 71, 3773-3786.

Bonatti, E., Lawrence, J.R., Morandi, N. (1984) Serpentinization of oceanic peridotites : temperature dependence of mineralogy and boron content. Earth and Planetary Science Letters, 70, 88-94.

Bonvallot, J. (2013) Atlas de la Nouvelle-Calédonie, IRD éditions.

Boschi, C., Dini, A., Dallai, L., Ruggieri, G., Gianelli, G. (2009) Enhanced CO_2-mineral sequestration by cyclic hydraulic fracturing and Si-rich fluid infiltration into serpentinites at Malentrata (Tuscany, Italy). Chem. Geol., 265, 209–226.

Boschi, C., Früh-Green, G.L., Delacour A., Karson, J.A., Kelley, D.S. (2006) Mass transfer and fluid flow during detachment faulting and development of an oceanic core complex, Atlantis Massif (MAR 30ºN). Geochem. Geophys. Geosyst., 7, Q01004.

Boudier, F., Ceuleneer, G., Nicolas, A. (1988) Shear zones, thrusts and related magmatism in the Oman ophiolite: initiation of thrusting on an oceanic ridge. Tectonophysics, 151, 275–296.

Brimhall, G.H., Dietrich, W.E. (1987) Constitutive mass balance relations between chemical composition, volume, density, porosity, and strain in metasomatic hydrochemical systems: results on weathering and pedogenesis. Geochimica et Cosmochimica Acta, 51(3), 567-587.

Brindley, G.W and Hang, P.T (1972) The hydrous magnesium-nickel silicate minerals (so-called garnierites). Int. Clay Conf., 1, 41-50.

Brindley, G.W. & Hang, P.T. (1973) The nature of garnierites – I structures, chemical compositions and color characteristics. Clays Clay Minerals, 21, 27-40.

Brindley, G.W. and Maksimovic, Z. (1974) The nature and nomenclature of hydrous nickel-containing silicates. Clay Minerals, 10, 271-277.

Brindley, G.W. and Wan, H.M. (1975) Compositions, structures, and thermal behaviour of nickel-containing minerals in the lizardite–nepouite series. Am. Mineral, 60, 863-871.

Brindley, G.W., Bish, D., Wan, H.M. (1977) The nature of kerolite, its relation to talc and stevensite. Mineral. Mag, 41, 443-452.

Brindley, G.W., Bish, D., Wan, H.M. (1979) Compositions, structures, and properties of nickel-containing minerals in the kerolite–pimelite series. Am. Mineral, 64, 615-625.

Bristow T. F., Bonifacie M., Derkowski A., Eiler J. M. and Grotzinger J. P. (2011) A hydrothermal origin for isotopically anomalous cap dolostone cements from south China. Nature, 474, 68–71.

Brothers, R.N. (1974) High-pressure schists in northern New Caledonia. Contributions to mineralogy and petrology, 46, 109-127.

Butt, C. R. M. et Cluzel, D. (2013) Nickel Laterite Ore Deposits: Weathered Serpentinites. Elements, 9(2), 123–128.

Byerlee, J. (1978) Friction in rocks: Pure and Applied Geo- physics, v. 116, p. 615–626,

C

Came, R.E., Eiler, J.M., Veizer, J., Azmy, K., Brand, U., Weidman, C.R (2007) Coupling of surface temperatures and atmospheric CO_2 concentrations during the Palaeozoic era. Nature, 449, 198-201.

Carroué, J.P. (1972) Carte géologique de la Nouvelle-Calédonie à l'échelle 1/50000, feuille Pouembout. Bureau de Recherches Géologiques et Minières, map sheet and explanatory notes, p. 38.

Carroué, J.P. (1972) Carte géologique des territoires d'Outre-Mer, Nouvelle-Calédonie SF-58-III-3d et SF-58-III-4c, Ouaco-Voh / Bureau de recherches géologiques et minières ; Bureau de recherches géologiques et minières, Orléans

Cathelineau, M., Caumon, M.C., Massei, F., Brie, D., Harlaux, M. (2015 ou 2015a) Raman spectra of Ni-Mg kerolite: effect of Ni-Mg substitution on O-H stretching vibrations. J. Raman Spectrosc., Proceedings GEORaman 2014 (11th), ST Louis (USA).

Cathelineau, M., Quesnel, B., Gautier, P., Boulvais, P., Couteau, C., Drouillet, M. (2015b) Nickel dispersion and enrichment at the bottom of the regolith: formation of pimelite target-like ores in rock block joints (Koniambo Ni deposit, New Caledonia). Mineralium Deposita, in press.
Partie III.Chap 1 article #2

Célérier, B., Etchecopar, A., Bergerat, F., Vergely, P., Arthaud, F., Laurent, P. (2012) Inferring stress from faulting: from early concepts to inverse methods. Tectonophysics, 581, 206–219.

Chacko T., Deines P. (2008) Theoretical calculation of oxygen isotope fractionation factors in carbonate systems. Geochim. Cosmochim. Acta, 72, 3642–3660.

Chardon, D., Chevillotte, V. (2006) Morphotectonic evolution of the New Caledonia ridge (Pacific Southwest) from post-obduction tectonosedimentary record. Tectonophysics, 420, 473–491.

Charlou, J.L., Bougault, H., Appriou, P., Nelsen, T., Rona, P.A. (1991) Different TDM/CH4 hydrothermal plume signatures: TAG site at 26ºN and serpentinized ultrabasic diapir at 15º05VN on the Mid-Atlantic Ridge. Geochim. Cosmochim. Acta, 55, 3209–3222.

Chevillotte, V. (2005) Morphogenèse tropicale en contexte épirogènique modéré: exemple de la Nouvelle-Calédonie (Pacifique Sud-Ouest). Ph. D. thesis, Université de la Nouvelle- Calédonie, départemen sciences et techniques.

Chevillotte, V., Chardon, D., Beauvais, A., Maurizot, P., Colin, F. (2006) Long-term tropical morphogenesis of New Caledonia (Southwest Pacific): Importance of positive epeirogeny and climate change. Geomorphology, 81(3-4), 361–375.

Ciscato, B. (1996) Principal stress orientations from faults: aC++program. In: De Paor, D.G. (Ed.), Structural Geology and Personal Computers: Vol. 15 of Computer methods in the geosciences, pp. 325–342. Pergamon.

Clark, I.D., Fontes, J.C., Fritz, P. (1992) Stable isotope disequilibria in travertine from high pH waters: laboratory investigations and field observations from Oman. Geochim. Cosmochim. Acta 56, 2041-2050.

Clayton, R., Mayeda, K. (1963) The use of bromine pentafluoride in the extraction of oxygen from oxides and silicates for isotopic analyses. Geochim. Cosmochim. Acta 27, 43-52.

Cluzel, D., Jourdan, F., Meffre, S., Maurizot, P., and Lesimple, S. (2012) The metamorphic sole of New Caledonia ophiolite: 40Ar/39Ar, U-Pb, and geochemical evidence for subduction inception at

a spreading ridge: Tectonics, 31, TC3016. ***Uniquement cité dans l'article #3 présenté en Partie III chapitre 3.***

Cluzel D, Maurizot P, Collot J, Sevin B (2012) An outline of the geology of New Caledonia; from Permian-Mesozoic Southeast Gondwanaland active margin to Cenozoic obduction and supergene evolution. Episodes, 35, 72–86.

Cluzel D, Vigier B (2008) Syntectonic Mobility of Supergene Nickel Ores of New Caledonia (Southwest Pacific). Evidence from Garnierite Veins and Faulted Regolith. Resour Geol, 58, 161–170.

Cluzel, D., Bosch, D., Paquette, J.L., Lemennicier, Y., Montjoie, Ph., Ménot, R.P. (2005) Late Oligocene post-obduction granitoids of New Caledonia: a case for reactivated subduction and slab break-off. The Island Arc, 14, 254–271.

Cluzel, D., Aitchison, J. C., Picard, C. (2001) Tectonic accretion and underplating of mafic terranes in the Late Eocene intraoceanic fore-arc of New Caledonia (Southwest Pacific): geodynamic implications. Tectonophysics, 340, 23–59.

Cluzel, D., Aitchison, J., Clarke, G., Meffre, S., Picard, C. (1995) Dénudation tectonique du complexe à noyau métamorphique de haute pression d'âge tertiaire (Nord de la Nouvelle Calédonie, Pacifique, France). Données cinématiques. Compte rendus de l'académie des sciences, Paris 321, série IIa. 57-64

Cluzel, D., Aitchison, J.C., Black, P.M. and Picard, C. (1999) Origin and fate of Southwest Pacific marginal basins; an appraisal from New Caledonia, in Baldwin, L. and Lister G.S. (eds), Mid-Cretaceous to recent plate boundary processes in the Southwest Pacific: '99 Penrose Conference, Arthur's Pass, New Zealand, Abstracts Volume, 77–79.

Coleman, R. (1971) Plate tectonic emplacement of upper mantle peridotites along continental edges. J. Geophys. Res., 76, 1212-1222.

Colin F, Nahon D, Trescases JJ, Melfi A. J (1990) Lateritic weathering of pyroxenites at Niquelandia, Goias, Brazil: the supergene behavior of nickel. Econ Geol, 85, 1010–1023.

Compton, R.R. (1966) Analyses of Pliocene–Pleistocene deformation and stresses in northern Santa Lucia Range, California. Geological Society of America Bulletin 77, 1361–1380.

Cook, C.A., Holdsworth, R.E., Styles, M.T., Pearce, J.A. (2000) Pre-emplacement structural history recorded by mantle peridotites: an example from the Lizard Complex, SW England. J. Geol. Soc. London, 157, 1049–1064.

Coulomb, C.A. (1776) Sur une application des règles maximis et minimis à quelques problèmes de statique relatifs à l'architecture. Acad. Sci. Paris Mém. Math. Phys 7, 343–382.

Coulton, A.J., Harper, G.D., O'Hanley, D.S. (1995) Oceanic versus emplacement age serpentinization in the Josephine ophiolite: implications for the nature of the Moho at intermediate and slow spreading ridges. J. Geophys. Res., 100, 22245-22260.

Craig, H., Boato, G. (1955) Isotopes. Annual review of physical chemistry 6, 403-432.

Cressey, B.A. et Zussman, J. (1976) Electron microscopic studies of serpentinites. Can. Mineral., 14, 307-313.

D

Dabitzias, S.G. (1980) Petrology and genesis of the Vavdos cryptocrystalline magnesite deposits, Chalkidiki Peninsula, Northern Greece. Econ. Geol., 75, 1138–1151.

Dalvi, A.D., Bacon, W.G., Osborne, R.C. (2004) The past and the future of nickel laterites, I PDAC 2004 International Conference Trade Show and Investors Exchange, Toronto, Canada, March 7–10, 2004, Proceedings: Toronto, Canada, Prospectors and Developers Association of Canada, 27 p.

Das Sharma, S., Patil, D.J., and Gopalan, K. (2002) Temperature dependence of oxygen isotope fractionation of CO_2 from magnesite–phosphoric acid reaction. Geochim. Cosmochim. Acta 66, 589–593.

Davis, W.M. (1925) Les côtes et les récifs coralliens de la Nouvelle-Calédonie. An. Géogr., 34(191), 244-269 ; 322-359, 423-441, 521-556.

de Chetelat, E. (1947) La genèse et l'évolution des gisements de nickel de la Nouvelle-Calédonie. B. Soc. Geol. Fr., 5 (XVII), 105-160.

Deblond A., Tack L (1999) Main Characteristics and review of mineral resources of the Kabanga-Musongati mafic-ultramafic alignment in Burundi. J African Earth Sci, 29, 313–328.

Deelman J. C. (1999) Low-temperature nucleation of magnesite and dolomite.Neues Jahrbuch Fur Mineralogie-Monatshefte, 7, 289–302.

Dennis K. J., Affek H. P., Passey B. H., Schrag D. P. and Eiler J. M. (2011) Defining an absolute reference frame for 'clumped' isotope studies of CO_2. Geochim. Cosmochim. Acta 75, 7117–7131.

Dennis, K., Schrag, D. (2010) Clumped isotope thermometry of carbonatites as an indicator of diagenetic alteration. Geochim. Cosmochim. Acta, 74, 4110-4122.

Devouard, B., Baronnet, A., Van Tendeloo, G., Amelinckx, S. (1997) First evidence of synthetic polygonal serpentines. European Journal of Mineralogy, 9(3), 539-546.

Dewey, J.F., Bird, J.M. (1971) Origin and emplacement of the ophiolite suite: Appalachian ophiolites in Newfoundland. J. Geophys. Res., 76, 3179-3206.

Dietzel, M., Usdowski, E., Hoefs, J. (1992) Chemical and $^{13}C/^{12}C$- and $^{12}O/^{16}O$-isotope evolution of alkaline drainage waters and the precipitation of calcite. Applied Geochemistry, 7, 177-184.

Dublet G, Juillot F, Morin G, Fritsch, E., Fandeur, D., Brown, G.E. (2015) Goethite aging explains Ni depletion in upper units of ultramafic lateritic ores from New Caledonia. Geochim Cosmochim Acta, 160, 1–15.

Dublet G, Juillot F, Morin G, Fritsch, E., Fandeur, D., Ona-Nguema, G., Brown, G.E. (2012) Ni speciation in a New Caledonian lateritic regolith: A quantitative X-ray absorption spectroscopy investigation. Geochim Cosmochim Acta, 95, 119–133.

Dublet G. (2012) Relation entre spéciation et distribution du nickel dans les couvertures d'altération latéritique des roches ultrabasiques de Nouvelle-Calédonie. PhD thesis UPMC Paris VI. 353 p.

Ducloux, J., Boukili, H., Decarreau, A., Petit, S., Perruchot, A., Pradel, P. (1993) Un gîte hydrothermal de garnierites: l'exemple de Bou Azzer, Maroc. Eur. J. Mineral. 5,1205-1215.

Durney, D.W., Ramsay, J.G. (1973) Incremental strains measured by syntectonic crystal growths. In: de Jong, K.A., Scholten, R. (Eds.), Gravity and Tectonics. Wiley, New York, pp. 67–96.

E

Eiler J.M. (2007) "Clumped-isotope" geochemistry—The study of naturally-occurring, multiply-substituted isotopologues. Earth and Planetary Science Letters 262, 309–327.

Eiler, J.M. (2011) Paleoclimate reconstruction using carbonate clumped isotope thermometry. Quaternary Science Reviews, 30(25-26), 3575–3588.

Eiler, J.M., Schauble, E. (2004) $^{18}O^{13}C^{16}O$ in Earth's atmosphere. Geochim. Cosmochim. Acta 68 (23), 4767–4777.

Elias, M., Donaldson, M.J., Giorgetta, N.E. (1981) Geology, mineralogy, and chemistry of lateritic nickel-cobalt deposits near Kalgoorlie, Western Australia. Economic Geology, 76(6), 1775-1783.

Eliopoulos DG, Economou-Eliopoulos M, Apostolikas A, Golightly JP (2012) Geochemical features of nickel-laterite deposits from the Balkan Peninsula and Gordes, Turkey: The genetic and environmental significance of arsenic. Ore Geol Rev, 48, 413–427.

Emiliani, C. (1966) Isotopic paleotemperatures. Science 154, 851-857

Epstein, S., Buchsbaum, R., Lowenstam, H.A., Urey, H.C. (1953) Revised carbonate-water isotopic temperature scale. Bulletin of the geological society of America 64, 1315-1326.

Escartín, J., Hirth, G., Evans, B. (2001) Strength of slightly serpentinized peridotites: implications for the tectonics of oceanic lithosphere. Geology, 29, 1023–1026.

Escartin, J., Mével, C., MacLeod, C.J., McCaig, A.M. (2003) Constraints on deformation conditions and the origin of oceanic detachments: the Mid-Atlantic Ridge core complex at 15°45'N. Geochem. Geophys. Geosyst., 4, 1067.

Etiope, G., Schoell, M., Hosgörmez, H. (2011) Abiotic methane flux from the chimaera seep and Tekirova ophiolites (Turkey): understanding gas exhalation from low temperature serpentinization and implication for Mars. Earth and Planetary Science Letters 310, 96-104.

Evans, B.W. (2004) The serpentinite multisystem revisited: Chrysotile is metastable, International Geology Review, 46(6), 479-506.

F

Falk, E.S., Kelemen, P.B. (2015) Geochemistry and petrology of listvenite in the Samail ophiolite, Sultanate of Oman: Complete carbonation of peridotite during ophiolite emplacement. Geochim. Cosmochim. Acta, 160, 70–90.

Fallick, A.E., Ilich, M., Russell, M.J. (1991) A stable isotope study of the magnesite deposits associated with the Alpine-type ultramafic rocks of Yugoslavia. Econ. Geol., 86, 847–861.

Fandeur, D. (2009) Géochimie et cristallochimie du chrome au cours de l'altération de roches ultrabasiques en Nouvelle-Calédonie (Massif du Koniambo). PhD Thesis -Université Paris Diderot–IPGP.

Federico, L., Crispini, L., Vigo, A., Capponi G. (2014) Unravelling polyphase brittle tectonics through multi-software fault-slip analysis: the case of the Voltri Unit, Western Alps (Italy). J. Struct. Geol., 68, 175-193.

Fernandez A., Rosenheim B., Tang J. (2013) Calibration of the siderite CO2 clumped isotope paleothermometer. Paper presented at the 3rd International Workshop on Clumped Isotopes, Harvard University, Cambridge, MA, 10 Jan. 2013

Ferry J. M., Rumble D., Wing B. A., Penniston-Dorland S. C. (2005) A new interpretation of centimetre-scale variations in the progress of infiltration-driven metamorphic reactions: case study of carbonated metaperidotite, Val d'Efra, Central Alps, Switzerland. J. Petrol., 46, 1725–1746.

Ferry J.M., Passey B.H., Vasconcelos C., Eiler J.M. (2011) Formation of dolomite at 40-80 degrees C in the Latemar carbonate buildup, Dolomites, Italy, from clumped isotope thermometry. Geology 39 (6), 571-574.

Fort, X., Brun, J-P., Chauvel, F. (2004) Salt tectonics on the Angolan margin, synsedimentary deformation processes. AAPG bulletin, 88(11), 1523-1544.

Fourcade S., Trotignon L., Boulvais P., Techer I., Elie M., Vandamme D., Salameh E., Khoury H. (2007) Cementation of kerogen-rich marls by alkaline fluids released during weathering of

thermally metamorphosed marly sediments. Part II: Organic matter evolution, magnetic susceptibility and metals (Ti, Cr, Fe) at the Khushaym Matruk natural analogue (Central Jordan). Appl. Geochemistry, 22, 1311–1328.

Freyssinet P, Farah AS (2000) Geochemical mass balance and weathering rates of ultramafic schists in Amazonia. Chem Geol 170, 133-151.

Freyssinet, P., Butt, C. R. M., Morris, R. C., Piantone, P. (2005) Ore-forming processes related to lateritic weathering. Society of Economic Geologists, Economic Geology 100th Anniversary Volume, 681–722.

Fu, W., Yang, J., Yang, M., Pang, B., Liu, X., Niu, H., & Huang, X. (2014) Mineralogical and geochemical characteristics of a serpentinite-derived laterite profile from East Sulawesi, Indonesia: Implications for the lateritization process and Ni supergene enrichment in the tropical rainforest. Journal of Asian Earth Sciences, 93, 74–88.

Fyfe, W.S. (1974) Heats of chemical reactions and submarine heat production. Geophys. J. R. stra. Soc. 37, 213-215.

G

Galí, S., Soler, J.M., Proenza, J.A., Lewis, J.F., Cama, J., Tauler, E. (2012) Ni-enrichment and stability of Al-free garnierite solid-solutions: a thermodynamic approach. Clay Clay Miner., 60, 121–135.

Gallardo T, Tauler E, Proenza JA, et al (2010) Geology , Mineralogy and Geochemistry of the Loma Ortega Ni Laterite Deposit , Dominican Republic. Rev la Soc española Mineral, 13, 89–90.

Gapais, D., Cobbold, P.R., Bourgeois, O., Rouby, D., de Urreiztieta, M. (2000) Tectonic significance of fault-slip data. J. Struct. Geol., 22, 881–888.

Gartzos, E. (2004) Comparative stable isotopes study of the magnesite deposits of Greece. Bulletin of the Geological Society of Greece 36, 196–203.

Genna A., Maurizot P., Lafoy Y., and Augé T. (2005) Contrôle karstique de minéralisations nickélifères de Nouvelle-Calédonie. C. R. Geoscience 337, 367–374.

Gerard, P. and Herbillon, A.J. (1983) Infrared studies of Ni-bearing clay minerals of the kerolite–pimelite series. Clays Clay Miner. 31, 143-151.

Ghent, E.D., Roddick, J.C., Black, P.M. (1994) $^{40}Ar/^{39}Ar$ dating of white micas from the epidote to the omphacite zones, northern New Caledonia: tectonic implications. Revue canadienne des sciences de la Terre, 31(6), 995-1001.

Ghosh P, Eiler J, Campana S.E., Feeney R.F. (2007) Calibration of the carbonate 'clumped isotope 'paleothermometer for otoliths. Geochim Cosmochim Acta 71 (11), 2736-2744.

Ghosh P., Adkins J., Affek H., Balta B., Guo W., Schauble E. A., Schrag D. and Eiler J. M. (2006) $^{13}C–^{18}O$ bonds in carbonate minerals: a new kind of paleothermometer. Geochim. Cosmochim. Acta, 70, 1439–1456.

Giammar, D.E., Bruant Jr., R.G., Peters, C.A. (2005). Forsterite dissolution and magnesite precipitation at conditions relevant for deep saline aquifer storage and sequestration of carbon dioxide. Chem. Geol., 217, 257-276.

Glasser, E. (1904) Rapport à M le Ministre des Colonies sur les richesses minérales de la Nouvelle-Calédonie: Paris, Annales des Mines, 560 p.

Gleeson, S.A, Herrington, R.J., Durango, J., Velasquez, C.A., Koll, G. (2004) The mineralogy and geochemistry of the Cerro Matoso S.A. Ni laterite deposit, Montelibano, Colombia. Economic Geology, 99(6), 1197-1213.

Gleeson, S.A., Butt, C.R.M., Elias, M. (2003) Nickel laterites: a review. Society of Economic Geologists, Newsletter, 54, 11-18.

Golightly, J.P. (1981) Nickeliferous laterite deposits. Economic Geology, 75th Anniversary Volume, 710-735.

Golightly, J.P. (2010) Progress in understanding the evolution of nickel laterites. Society of economic Geologists, Special Publications, 15.

Grandcolas, P., Murienne, J., Robillard, T., Desutter-Grandcolas, L., Jourdan, H., Guilbert, E., and Deharveng, L., 2008, New Caledonia: a very old Darwinian island?: Philosophical Transactions of the Royal Society of London. Series B, Biological Sciences, v. 363, p. 3309–3317.

Grant, J.A. (1986) The isocon diagram—a simple solution to Gresens' equation for metasomatic alteration. Economic Geology, 81, 1976-1982.

Grauby, O., Baronnet, A., Devouard, B., Schumaker, K., Demirdjian, L. (1998) The chrysotile–polygonal serpentine– lizardite suite synthesized from a 3 MgO– 2 SiO2–excess H2O gel. Eur. Mineral. Petrol. Geochem. (EMPGVII). Terra Nova, Suppl. 10(1), 24 (abstr.).

Grauel A-L, Schmid T.W., Hu B., Bergami C., Capotondi L., Zhou L., Bernasconi S.M. (2013) Calibration and application of the 'clumped isotope' thermometer to foraminifera for high-resolution climate reconstructions. Geochim Cosmochim Acta, 108, 125-140.

Gresens, R.L. (1967) Composition-volume relationships of metasomatism. Chem. Geology, 2, 47-55.

Groppo, C., Rinaudo, C., Cairo, S., Gastaldi, D. et Compagnoni, R. (2006) Micro-Raman spectroscopy for a quick and reliable identification of serpentine minerals from ultramafics. European Journal of Mineralogy, 18(3), 319.

Guillon, J.H. (1975) Les massifs péridotitiques de Nouvelle-Calédonie: type d'appareil ultrabasique stratiforme de chaine récente. Mémoire ORSTOM (Office de la Recherche Scientifique et

Technique Outre-Mer), 76, 120p.

Guillon, J.H., Routhier, P. (1971) Les stades d'évolution et de mise en place des massifs ultramafiques de Nouvelle-Calédonie. Bulletin du BRGM, section IV, n°2. 5-38

Guillou-Frottier, L., Beauvais, A., Bailly, L., Wyns, R., Augé, T., Audion, A-S. (2015) Transient hydrothermal corrugations within mineralized ultramafic laterites. In: Proceedings of the 13th Biennal SGA (Society for Geology Applied to Mineral Deposits) meeting, 24-27 August 2015, Nancy, France, vol. 3, pp. 1169-1172

Guo W. F., Mosenfelder J. L., Goddard W. A. and Eiler J. M. (2009) Isotopic fractionations associated with phosphoric acid digestion of carbonate minerals: insights from first-principles theoretical modeling and clumped isotope measurements. Geochim. Cosmochim. Acta, 73, 7203–7225.

H

Haldemann, E.G., Buchan, R., Blowes, V.H., Chandler, T. (1979) Geology of the laterite nickel deposits, Dominican Republic. In:Evans, D.J., Shoemaker R.S., Velman, H. (eds.). International Laterite Symposium, New Orleans, Society of Mining Engineers, 57-84.

Hänchen M., Prigiobbe V., Baciocchi R., Mazzotti M. (2008) Precipitation in the Mg-carbonate system: effects of temperature and CO2 pressure. Chem. Eng. Sci., 63, 1012–1028.

Hancock, P.L., 1985. Brittle microtectonics: principles and practice. J. Struct. Geol. 7, 437-457.

Handy, M.R., Wissing, S.B., Streit, L.E. (1999) Frictional-viscous flow in mylonite with varied bimineralic composition and its effect on lithospheric strength. Tectonophysics 303, 175-191.

Hansen L. D., Dipple G. M., Gordon T. M. and Kellett D. A. (2005) Carbonated serpentinite (listwanite) at Atlin, British Columbia: a geological analogue to carbon dioxide sequestration.Can. Mineral.,43, 225–239.

Hencher, S.R., Lee, S.G., Carter, T.G., Richards, L.R. (2011) Sheeting Joints: Characterization, shear strength and engineering. Rock Mech Rock Eng, 44, 1-22.

Henkes G.A., Passey B.H., Wanamaker A.D. Jr., Grossman E.L., Ambrose W.G. Jr., Carroll M.L. (2013) Carbonate clumped isotope compositions of modern marine mollusk and brachiopod shells. Geochim Cosmochim Acta 106, 307-325.

Herzberg, C., Asimow, P.D., Ionov, D.A, Vidito, C., Jackson, M.G., Geist, D. (2013) Nickel and helium evidence for melt above the core-mantle boundary. Nature, 493, 393-397.

Hill, P.S., Tripati, A.K., Schauble, E.A. (2014) Theoretical constraints on the effects of pH, salinity, and temperature on clumped isotope signatures of dissolved inorganic carbon species and precipitating carbonate minerals. Geochimica et Cosmochimica Acta, 125, 610-652

Hirth, G., Guillot, S., 2013. Rheology and tectonic significance of serpentinite. Elements 9, 107-113.

Holms N. G. (1996) Serpentinization of oceanic crust and Fischer–Tropsch type synthesis of organic compounds. Origins Life, 26 (3–5), 205–206.

Hoskins, L.M. (1896) Flow and fracture of rocks as related to structure. In: Walcott, D. (Ed.), Sixteenth Annual Report of the United States Geological Survey to the Secre- tary of the Interior, 1894–1895, Part 1. USGS, pp. 845–874.

Hövelmann, J., Austrheim, H., Jamtveit, B. (2012) Microstructure and porosity evolution during experimental carbonation of a natural peridotite. Chem. Geol. 334, 254-265.

Huntington K. W., Eiler J. M., Affek H. P., Guo W., Bonifacie M., Yeung L. Y., Thiagarajan N., Passey B., Tripati A., Daëron M., and Came R. (2009) Methods and limitations of 'clumped' CO_2

isotope (Δ_{47}) analysis by gas-source isotope ratio mass spectrometry. J. Mass. Spectrom. 44, 1318–1329.

J

Jacob, M. (1985) Etude géologique, minéralogique et géochimique des anomalies en As, Sb, Au et W et indices minéralisés liés aux fractures regionals de la côte sud-est de la Nouvelle-Calédonie. Ph.D thesis, University Paul Sabatier, Toulouse, n°3138, 155p.

Jeanpert, J., Dewandel, B. (2013) Analyse préliminaire des donées hydrogéologiques du massif du Koniambo. Public Report BRGM/RP-61765-FR, 102 pp.

Jébrak et Marcoux (2008) Géologie des Ressources Minérales. Ministère des ressources naturelles et de la faune. 667 p.

Jedrysek, M.O., and Halas, S. (1990) The origin of magnesite deposits from the Polish Foresudetic Block ophiolites: Preliminary $\delta^{13}C$ and $\delta^{18}O$ investigations. Terra Nova 2, 154–159.

Join, J.L., Robineau, B., Ambrosi, J.P., Costis, C., Colin, F. (2005) Système hydrogéologique d'un massif minier ultrabasique de Nouvelle-Calédonie. C. R. Géosci., 337 (16), 1500–1508.

Jurković, I., Palinkaš, L.A., Garašić, V., Palinkaš, S.S. (2012) Genesis of vein-stockwork cryptocrystalline magnesite from the dinaride ophiolites. Ofioliti, 37, 13–26.

K

Kamb, W.B. (1959) Ice petrofabric observations from Blue Glacier, Washington in relation to theory and experiment. Journal of Geophysical Research, 64, 1891-1909.

Karson, J.A., Früh-Green, G.L., Kelley, D.S., Williams, E.A., Yoerger, D.R., Jakuba, M. (2006) Detachment shear zone of the Atlantis Massif core complex, Mid-Atlantic Ridge, 30°N. Geochem. Geophys. Geosyst., 7, Q06016.

Kelemen P.B., Matter J. (2008) In situ carbonation of peridotite for CO2 storage. Proc. Natl. Acad. Sci., 105, 17295–17300.

Kelemen, P.B., Hirth, G. (2012) Reaction-driven cracking during retrograde metamorphism: Olivine hydratation and carbonation. Earth and Planetary Science Letters 345-348, 81-89.

Kelemen, P.B., Matter, J., Streit, E.E., Rudge, J.F., Curry, W.B., Blusztajn, J. (2011) Rates and mechanisms of mineral carbonation in peridotite: natural processes and recipes for enhanced, in situ CO2 capture and storage. Annual Review of Earth and Planetary Sciences, 39, 545–576.

Kelley, D.S., Karson, J.A., Blackman, D.K., Früh-Green, G.L., Butterfield, D.A., Lilley, M.D., Olson, E.J., Schrenk, M.O., Roe, K.K., Lebon, G.T., Rivissigno, P., AT3-60 shipboard party (2001) An off-axis hydrothermal vent field near the Mid-Atlantic Ridge at 30°N. Nature 412, 145-149.

Kingma, K. J., Hemley, R. J. (1994) Raman spectroscopic study of microcrystalline silica. American Mineralogist, 79(3-4), 269–273.

Kissel, C., Laj, C. (1989) Palemagnetic rotations and continental deformation. In: NATO ASI Series, C254. Kluwer Academic Publishers, Dordrecht 516 p

Kita, I., Taguchi, S., Matsubaya, O. (1985) Oxygen isotope fractionation between amorphous silica and water at 34-93°C. Nature 314, 83-84.

Klein F., Garrido C.J. (2011) Thermodynamic constraints on mineral carbonation of serpentinized peridotite. Lithos, 126(3), 147–160.

Kluge, T., John, C.M., Jourdan, A.L., Davis, S., Crawshaw, J. (2015) Laboratory calibration of the calcium carbonate clumped isotope thermometer in the 25-250°C temperature range. Geochim. Cosmochim. Acta, 157, 213-227.

Krstanovic, I., Pavlovic, S. (1964) X-ray study of chrysotile. American Mineralogist, 49, 1769-1771.

L

Lagabrielle, Y., Chauvet, A. (2008) The role of extensional tectonics in shaping Cenozoic New-Caledonia. Bulletin de La Société Géologique de France, 179, 315–329.

Lagabrielle, Y., Chauvet, A., Ulrich, M., Guillot, S. (2013) Passive obduction and gravity-driven emplacement of large ophiolitic sheets: the New Caledonia ophiolite (SW Pacific) as a case study? Bull. Soc. Géol. France 184, 545–556.

Lagabrielle, Y., Maurizot, P., Lafoy, Y., Cabioch, G., Pelletier, B., Régnier, M., Wabete, I., Calmant, S. (2005) Post-Eocene extensional tectonics in Southern New Caledonia (SW Pacific): Insights from onshore fault analysis and offshore seismic data. Tectonophysics, 403, 1–28.

Lahondère, D. (2012) Serpentinisation et fibrogenèse dans les massifs de péridotite de Nouvelle-Calédonie : atlas des occurrences et des types de fibres d'amiante sur mine. Bureau de Recherches Géologiques et Minières. Public report BRGM/RP-61426-FR, 128p.

Lahondère, D., Lesimple, S., Cagnard, F., Lahfid, A., Wille, G., Maurizot, P., (2012) Serpentinisation et fibrogenèse dans les massifs de péridotite de Nouvelle-Calédonie. Bureau de Recherches Géologiques et Minières, Public Report BRGM/RP-60192-FR, p. 458.

Lahondère, D., Maurizot, P. (2009) Typologie et protocole d'échantillonnage des occurrences naturelles d'amiante en Nouvelle-Calédonie. Bureau de Recherches Géologiques et Minières. Public report BRGM/RP-57334-FR, 164p.

Laó-Dávila, D.A., Anderson, T.H. (2009) Kinematic analysis of serpentinite structures and the manifestation of transpression in southwestern Puerto Rico. J. Struct. Geol., 31, 1472-1489.

Latham, M. (1975) Géomorphologie d'un massif de roches ultrabasiques de la côte Ouest de la Nouvelle Calédonie : le Boulinda. Cah. ORSTOM, Sér. Géol. VII(1), 17-37.

Latham, M. (1977) On geomorphology of northern and western new caledonian ultramafic massifs. In International Symposium of Geodynamics in South West Pacific, Nouméa, Technip Paris éd, 235-244.

Latham, M. (1986) Altération et pédogenèse sur roches ultrabasiques en Nouvelle-Calédonie: genèse et évolution des accumulations de fer et de silice en relation avec la formation du modelé, 331 pp, Th. Sci. Dijon.

Launay, J., Fontes, J.C. (1985) Les sources thermales de Prony (Nouvelle-Calédonie) et leurs précipités chimiques. Exemple de formation de brucite primaire. Géologie de la France, 1, 83-100.

Le Carlier de Veslud, C., Quesnel, B., Gautier, P., Boulvais, P., Cathelineau, M., Drouillet, M. (2015) 3D modelling of supergene alteration of the Koniambo Massif, New Caledonian Peridotite Nappe. In: Proceedings of the 13th Biennal SGA (Society for Geology Applied to Mineral Deposits) meeting, 24-27 August 2015, Nancy, France, vol. 3, pp. 1173-1176.

Leguéré, J. (1976) Des corrélations entre la tectonique cassante et l'altération supergène des péridotites de Nouvelle Calédonie. PhD thesis, Univ. Du Languedoc, Montpellier, France, 95p.

Lemaire, C. (2000) Application des spectroscopies vibrationnelles à la détection d'amiante dans les matériaux et à l'étude des serpentines. Thèse, Université de Paris 07, Paris: pp. 157.

Lisle, R.J. (1987) Principal stress orientations from faults: an additional constraint. Annales Tectonicae I 2, 155–158

Loncke, L., Gaullier, V., Vendeville, B., Camera, L. (2006) The Nile deep-sea fan : An example of interacting sedimentation, salt tectonics, and inherited subsalt paleotopographic features. Marine and Petroleum Geology, 23(3), 297-315.

Lowell, R.P., Rona, P.A. (2002) Seafloor hydrothermal systems driven by the serpentinization of peridotite. Geophysical research letters, 29 (11).

M

Ma, J-L., Wei, G-J., Xu, Y-G., Long, W-G., Sun, W-D. (2007) Mobilization and re-distribution of major and trace elements during extreme weathering of basalt in Hainan Island, South China. Geochimica Cosmochimica Acta, 71(13), 3223-3237.

MacLeod, C.J., Escartín, J., Banerji, D., Banks, G.J., Gleeson, M., Irving, D.H.B., Lilly, R.M., McCaig, A.M., Niu, Y., Allerton, S., Smith, D.K. (2002) Direct geological evidence for oceanic detachment faulting: the Mid-Atlantic Ridge, 15°45'N. Geology, 30, 879-882.

Mallet, J.L. (2002) {G}eomodeling. Oxford University Press, New York, NY, Applied Geostatistics.

Manatschal, G., Engström, A., Desmurs, L., Schaltegger, U., Cosca, M., Müntener, O., Bernoulli, D. (2006) What is the tectono-metamorphic evolution of continental break-up: the example of the Tasna Ocean-Continent Transition. J. Struct. Geol., 28, 1849-1869.

Manceau A., Schlegel M. L., Musso M., Sole V. A., Gauthier C., Petit P. E. and Trolard F. (2000) Crystal chemistry of trace elements in natural and synthetic goethite. Geochim. Cosmochim. Acta , 64(21), 3643–3661.

Manceau, A. and Calas, G. (1986) Nickel-bearing clay minerals: II. Intracrystalline distribution of nickel: an X-ray absorption study. Clay Miner. 21, 341-360.

Manceau, A., Calas, G. (1985) Heterogeneous distribution of nickel in hydrous silicates from New Caledonia ore deposits. Am. Mineral., 70, 549–558.

Manceau, A., Calas, G., Decarreau, A. (1985) Nickel-bearing clay minerals: I. optical spectroscopic study of nickel crystal chemistry. Clay Minerals, 20, 367-387.

Marker A., Friedrich G., Carvalho A, Melfi A (1991) Control of the distribution of Mn, Co, Zn, Zr, Ti and REEs during the evolution of lateritic covers above ultramafic complexes. J. geochemical Explor., 40, 361–383.

Marques, J.M., Carreira, P.M., Rosário Carvalho, M., Matias, M.J., Goff, F.E., Basto, M.J., Graça, R.C., Aires-Barros, L., Rocha, L. (2008) Origins of high pH mineral waters from ultramafic rocks, Central Portugal. Applied Geochemistry 23, 3278-3289.

Marrett, R., & Allmendinger, R. W. (1990) Kinematic analysis of fault-slip data. Journal of Structural Geology, 12(8), 973–986.

Marrett, R.A., Allmendinger, R.W. (1991) Estimates of strain due to brittle faulting: sampling of fault populations. Journal of Structural Geology, 13, 735-738.

Maurizot P., Eberlé J.M., Habault C., Tessarolo C. (1989) Carte géologique de la Nouvelle-Calédonie à l'échelle 1/50000, feuille Pam-Ouégoa, 2e édition. Bureau de Recherches Géologiques et Minières, map sheet and explanatory notes, p. 81.

Maurizot, P. (2007) Cartographie d'aide à l'aménagement dans la zone Voh-Koné-Pouembout-Poya. Phase 1: Mise à jour de la carte géologique sur les communes de Koné et Pouembout et bilan des données existantes. Bureau de Recherches Géologiques et Minières, Public Report BRGM/RP-54898-FR, p. 76.

Maurizot, P. and Vendé-Leclerc, M. (2009) New Caledonia geological map, scale 1/500,000: Direction de l'Industrie, des Mines et de l'Energie – Service de la Géologie de Nouvelle-Calédonie, Bureau de Recherches Géologiques et Minières, Notice explicative par Maurizot, P. et Collot, J., 2009.

Maurizot, P., Feigner, D., Paris, J.P. (1985) Données nouvelles sur les « fils de serpentinite » de Nouvelle-Calédonie. Géol. France, 1, 61-67.

Maurizot, P., Lafoy, Y., and Poupée, M. (2002) Cartographie des formations superficielles et des aléas mouvements de terrain en Nouvelle-Calédonie, Zone du Koniambo: Bureau de Recherches Géologiques et Minières Public Report RP51624-FR, 45 p.

Maurizot, P., Vendé-Leclerc, M. (2009) New Caledonia geological map, scale 1/500000, DIMENC-SGNC, BRGM. Explanatory note by Maurizot, P. and Collo, J.

McCollom, T.M., Seewald, J.S. (2006) Carbon isotope composition of organic compound produced by abiotic synthesis under hydrothermal conditions. Earth and Planetary Science Letters 243, 74-84.

McCrea, J. M. (1950) On the isotopic chemistry of carbonates and a paleotemperature scale. Journal of Chemical Physics, 18, 849-857.

Meckler, A.N., Ziegler, M., Millan, M.I., Breitenbach, S.F.M., Bernasconi, S.M. (2014) Long-term performance of the Kiel carbonate device with a new correction scheme for clumped isotope measurements. Rapid Commun. Mass Spectrom., 28 (15), 1705-1715.

Mellini, M. (1986) Chrysotile and polygonal serpentine from the Balangero serpentinite. Mineral. Mag., 50, 301-306.

Mercier, J., Vergely, P. (1992) Tectonique. Dunod, Paris, 214 p

Merle, O. (1986) Patterns of stretch trajectories and strain rates within spreading-gliding nappes. Tectonophysics, 124(3-4), 211-222.

Mével, C. (2003) Serpentinization of abyssal peridotites at mid-ocean ridges. C.R. Geosciences 335, 825-852.

Middleton, A.P. et Whittaker, E.J.W. (1976) The structure of Povlen-type chrysotile. Can. Mineral., 14, 301-306.

MitchellL, R.H. & Putnis, A. (1988) Polygonal serpentine in segregation-textured kimberlite. Can. Mineral., 26, 991-997.

Mohr, O. (1882) Über die Darstellung des Spannungzustandes eines Korperelementes. Civilingenieure 28, 113–156.

Monin, C., Chavagnac, V., Boulart, C., Ménez, B., Gérard, M., Gérard, E., Quéméneur, M., Erauso, G., Postec, A., Guentas-Dombrowski, L., Payri, C., Pelletier, B. (2014) The low temperature hyperalkaline hydrothermal system of the Prony bay (New Caledonia). Biogeosciences Dicuss., 11, 6221-6267.

Moore, D.E., Lockner, D.A. (2011) Frictional strengths of talc-serpentine and talc-quartz mixtures. J. Geophys. Res. 116, B01403.

Morandi, N. et Felice, G. (1979) Serpentine minerals from veins in serpentinite rocks. Mineralogical Magazine, 43, 35-40.

Morley, C.K., Guerin, G. (1996) Comparison of gravity-driven deformation styles and behavior associated with mobile shales and salt. Tectonics, 15(6), 1154-1170.

Mourgues, R., Lecomte, E., Vendeville, B., Raillard, S. (2009) An experimental investigation of gravity-driven shale tectonics in progradational delta. Tectonophysics, 474(3-4), 643-656.

Mugnaioli, E., Logar, M., Mellini, M., Viti, C. (2007) Complexity in 15- and 30-sectors polygonal serpentine : longitudinal sections, intrasector stacking faults and XRPD satellites. American Mineralogist, 92, 603-616.

Myagkiy, A., Cathelineau, M., Golfier, F., Truche, L., Quesnel, B., Drouillet, M. (2015) Defining mechanisms of brecciation in Ni-silicate bearing fractures (Koniambo, New Caledonia). In: Proceedings of the 13th Biennal SGA (Society for Geology Applied to Mineral Deposits) meeting, 24-27 August 2015, Nancy, France, vol. 3, pp. 1181-1194.

N

Nahon DB, Tardy Y (1992) The ferruginous laterites. In: Butt CRM, Zeegers H (eds) Regolith exploration geochemistry in tropical and subtropical terrains. Handbook of Exploration Geochemistry 4, Elsevier, Amsterdam, pp 41-55.

Nahon, D.B., Paquet, H., Delvigne, J. (1982) Lateritic weathering of ultramafic rocks and the concentration of nickel in the western Ivory Coast. Economic Geology, 77(5), 1159-1175.

Ndjigui P.-D., Bilong P., Bitom D., Dia A. (2008) Mobilization and redistribution of major and trace elements in two weathering profiles developed on serpentinites in the Lomié ultramafic complex, South-East Cameroon. J. African Earth Sci., 50, 305–328.

Neubeck, A., Thanh Duc, N., Bastviken, D., Crill, P., Holm, N.G. (2011) Formation of H_2 and CH_4 by weathering of olivine at temperatures between 30 and 70°C. Geochemical Transactions 12(6).

Norrell, G.T., Teixell, A., Harper, G.D. (1989) Microstructure of serpentinite mylonites from the Josephine ophiolite and serpentinization in retrogressive shear zones, California. Geol. Soc. Am. Bull. 101, 673–682.

O

O'Hanley, D.S. (1992) Solution to the volume problem in serpentinization. Geology, 20, 705-708.

Orloff, O. (1968) Etude géologique et géomorphologique des massifs d'ultrabasites compris entre Houailou et Canala (Nouvelle-Calédonie). Ph.D. thesis, Université de Montpellier, France, 189 pp.

Oskierski, H.C., Bailey, J.G., Kennedy, E.M., Jacobsen, G., Ashley, P.M., Dlugogorski, B.Z. (2013) Formation of weathering-derived magnesite deposits in the New England Orogen, New South Wales, Australia: Implications from mineralogy, geochemistry and genesis of the Attunga magnesite deposit. Miner. Depos., 48, 525–541.

P

Paquette, J.L., and Cluzel, D. (2007) U-Pb zircon dating of post-obduction volcanic-arc granitoids and a granulite-facies xenolith from New Caledonia: Inference on Southwest Pacific geodynamic models. International Journal of Earth Sciences 96, 613–622.

Paris, J.P. (1981) Géologie de la Nouvelle-Calédonie, un essai de synthèse. Mémoires du Bureau de Recherches Géologiques et Minières, 113, 274 pp.

Paris, J.P., Lille, R. (1977) La Nouvelle-Calédonie du Permien au Miocène : données cartographiques, hypothèses géotectoniques. Bulletin du Bureau de Recherches Géologiques et Minières. Deuxième série, n°1, 79-95.

Passchier, C.W., Trouw, R.A.J. (1996) Microtectonics. Springer, Berlin, p. 289.

Pelletier B. (1989) Les Minerais de Nickel de Nouvelle-Calédonie, 10 p. SLN.

Pelletier, B. (1996) Serpentines in nickel silicate ore from New Caledonia. In "Proceedings, Nickel 096: Mineral to Market", E.J. Grimsey and I. Neuss, eds. Kalgoorlie, 27–29 November, The Australasian Institute of Mining and Metallurgy, Carlton, Victoria, Australia, 197-205.

Pelletier, B. (1983) Localisation du nickel dans les minerais "garnieritiques" de Nouvelle-Calédonie. Sci. Geol. Mem. 73, 173-183.

Pelletier, B. (2003) Les minerais de nickel de Nouvelle-Calédonie. Géologues, 138, 30-38

Petit, J.P., 1987. Criteria for the sense of movement on fault surfaces in brittle rocks. J. Struct. Geol. 9, 597-608.

Pfiffner, O.A., Burkhard, M. (1987) Determination of paleo-stress axes orientations from fault, twin and earthquake data. Annales Tectonicae, I (1), 48–57.

Picazo, S., Cannat, M., Delacour, A., Escartín, J, Rouméjon, S., Silantyev, S. (2012). Deformation associated with the denudation of mantle-derived rocks at the Mid-Atlantic Ridge 13°-15°N: the role of magmatic injections and hydrothermal alteration. Geochem. Geophys. Geosyst., 13, Q04G09.

Pokrovsky O.S., Schott J. (2000) Kinetics and mechanism of forsterite dissolution at 25ºC and pH from 1 to 12: Geochimica et Cosmochimica Acta, 64, 3313–3325.

Pop, D., Constantina, C., Tatar, D., & Kiefer, W. (2004) Raman spectroscopy on gem-quality microcrystalline and amorphous silica varieties from romania. Studia Universitatis Babes-Bolyai, Geologia, XLIX, 41–52.

Potter, J., Rankin, A.H., Treloar, P.J. (2004) Abiogenic Fischer-Tropsch synthesis of hydrocarbons in

alkaline igneous rocks; fluid inclusion, textural and isotopic evidence from the Lovozero complex, N.W. Russia. Lithos 75, 311-330.

Power I. M., Wilson S. A., Harrison A. L., Dipple G. M., McCutcheon J., Southam G., Kenward P. A. (2014) A depositional model for hydromagnesite–magnesite playas near Atlin, British Columbia, Canada. Sedimentology, 61, 1701–1733.

Power, I.M., Wilson, S.A., Dipple, G.M. (2013) Serpentinite carbonation for CO_2 sequestration. Elements 9, 115–121.

Printemps J, Ausseil A-G, Dumas P., Mangeas M., Dymond J.R. and Lille D. An Erosion Model for Monitoring the Impact of Mining in New Caledonia. MODSIM conference (Dec. 2007)

Prinzhofer, A., Nicolas, A., Cassard, D., Moutte, J., Leblanc, M., Paris, J. ., Rabinovitch, M. (1980) Structures in the new caledonia peridotites-gabbros: implications for oceanic mantle and crust. Tectonophysics, 69, 85–112.

Proskurowski, G., Lilley, M., Seewald, J.S., Früh-Green, G.L., Olson, E.J., Lupton, J.E., Sylva, S.P., Kelley, D.S. (2008) Abiogenic hydrocarbon production at Lost City hydrothermal field. Sciences 319, 604-607.

Q

Quesnel, B., Boulvais, P., Gautier, P., Cathelineau, M., John, C.M., Dierick, M., Agrinier, P. Drouillet, M. (2015). Formation of silica and magnesite veins in the massif of peridotites of Koniambo: geometric and stable isotopes data. In: Proceedings of the 13th Biennal SGA (Society for Geology Applied to Mineral Deposits) meeting, 24-27 August 2015, Nancy, France, vol. 3, pp. 1189-1192.

Quesnel, B., Boulvais, P., Gautier, P., Cathelineau, M., John, C.M., Dierick, M., Agrinier, P. Drouillet, M., (submitted-a). Paired stable isotope (O, C) and clumped isotope thermometry of magnesite and silica veins in the New Caledonia Peridotite Nappe. Submitted to Geochimica et Cosmochimica Acta.
Partie III. Chap 3. Article #5

Quesnel, B., Gautier, P., Boulvais, P., Cathelineau, M., Maurizot, P., Cluzel, D., Ulrich, M., Guillot, S., Lesimple, S., & Couteau, C. (2013) Syn-tectonic, meteoric water-derived carbonation of the New Caledonia peridotite nappe. Geology, 41(10), 1063–1066.
Partie III. Chap 3. Article #3

Quesnel, B., Gautier, P., Cathelineau, M., Boulvais, P., Drouillet, M. (submitted-b) The internal deformation of the Peridotite Nappe of New Caledonia : a structural study of serpentine-bearing faults and shear zones in the Koniambo Massif. Submitted to Journal of Structural Geology.
Partie III. Chap 1. Article #4

R

Raman, C.V, Krishnan, K.S. (1928) A new type of secondary Radiation. Nature, 121, 501-502

Robertson, A.H.F., Trivic, B., Deric, N., and Bucur, I.I. (2012) Tectonic development of the Vardar ocean and its margins: evidence from the Republic of Macedonia and Greek Macedonia: Tectonophysics, v. 595-596, p. 25-54.

Rouméjon, S., Cannat, M. (2014) Serpentinization of mantle-derived peridotites at mid-ocean ridges: mesh texture development in the context of tectonic exhumation. Geochem. Geophys. Geosyst., 15, 2354-2379.

Rudge J.F., Kelemen P.B., Spiegelman M. (2010) A simple model of reaction-induced cracking applied to serpentinization and carbonation of peridotite. Earth Planet. Sci. Lett., 291(1–4), 215–227.

S

Sabouraud, C., Trichet, J. (1978) Confirmation, par l'étude des inclusions intracristallines, de l'origine superficielle de quartz pyramides. Geoderma, 20, 191-199.

Saldi G. D., Schott J., Pokrovsky O. S., Gautier Q., Oelkers E.H. (2012) An experimental study of magnesite precipitation rates at neutral to alkaline conditions and 100–200°C as a function of pH, aqueous solution composition and chemical affinity. Geochim. Cosmochim. Acta, 83, 93–109.

Saldi G. D., Schott J., Pokrovsky O. S., Oelkers E. H. (2010) An experimental study of magnesite dissolution rates at neutral to alkaline conditions and 150 and 200°C as a function of pH, total dissolved carbonate concentration, and chemical affinity. Geochim. Cosmochim. Acta, 74, 6344–6356.

Schauble, E. A., Ghosh, P., Eiler, J. M. (2006) Preferential formation of 13C-18O bonds in carbonate minerals, estimated using first-principles lattice dynamics. Geochimica et Cosmochimica Acta, 70(10), 2510–2529.

Schellart, W.P., Lister, G.S. and Toy, V.G. (2006) A Late Cretaceous and Cenozoic reconstruction of the Southwest Pacific region: Tectonics controlled by subduction and slab rollback processes: Earth Science Reviews, 76, 191–233.

Schellman, W. (1983) Geochemical principles of lateritic nickel ore formation. In "Proceedings of the II International Seminar on Lateritisation Processes", A.J. Melfi and A. Carvalho, eds. Sao Paulo, Brazil, 1982, 119-135.

Schellmann, W. (1989) Composition and origin of lateritic nickel ore at Tagaung Taung, Burma. Mineralium Deposita, 24, 161–168.

Schemmann, K., Unruh, J.R., Moores, E.M. (2007) Kinematics of Franciscan Complex exhumation: new insights from the geology of Mount Diablo, California. Geol. Soc. Am. Bull., 120, 543-555.

Schroeder, T., Barbara, J., Ronald Frost, B. (2002) Geologic implications of seawater circulation through peridotite exposed at slow-spreading mid-ocean ridges. Geology, 30, 367-370.

Schroeder, T., John, B.E. (2004) Strain localization on an oceanic detachment fault system, Atlantis Massif, 30°N, Mid-Atlantic Ridge. Geochem. Geophys. Geosyst., 5, Q11007.

Schulz, K.J., Chandler, V.W., Nicholson, S.W., Piatak, Nadine, Seall, II, R.R., Woodruff, L.G., and Zientek, M.L. (2010) Mamatic sulfide-rich nickel-copper deposits related to picrite and (or) tholeiitic basalt dike-sill complexes—A preliminary deposit model. U.S. Geological Survey Open-File Report 2010–1179, 25 p. (available at http://pubs.usgs.gov/of/2010/1179/).

Schwartz, S., Guillot, S., Reynard, B., Lafay, R., Debret, B., Nicollet, C., Lanari, P., Auzende, A-L., (2013) Pressure–temperature estimates of the lizardite/antigorite transition in high pressure serpentinites. Lithos, 178, 197–210.

Sevin, B., Cluzel, D., Maurizot, P., Ricordel-Prognon, C., Chaproniere, G., Folcher, N., Quesnel, F. (2014) A drastic Lower Miocene regolith evolution triggered by post obduction slab break-off and uplift in New Caledonia. Tectonics, 33(9), 1787-1801.

Sevin, B., Ricordel-Prognon, C., Quesnel, F., Cluzel, D., Lesimple, S., & Maurizot, P. (2012) First palaeomagnetic dating of ferricrete in New Caledonia: new insight on the morphogenesis and palaeoweathering of "Grande Terre". Terra Nova, 24(1), 77–85.

Sharp, Z.D., Kirschner, D.L. (1994) Quartz-calcite oxygen isotope thermometry: a ncalibration based on natural isotopic variations. Geochim. Cosmochim. Acta, 58(21), 4491-4501.

Smith, E., Dent, G. (2005) Modern Raman spectroscopy: a pratical approach. Wiley, New York, 210 p.

Spandler, C., Rubatto, D. (2005) Late Cretaceous-Tertiary tectonics of the southwest Pacific : Insights from U-Pb sensitive , high-resolution ion microprobe (SHRIMP) dating of eclogite facies rocks from New Caledonia, 24, 1–16.

Springer G (1974) Compositional and structural variations in garnierites. Can. Mineral 12, 381-388.

Streit, E., Kelemen, P., Eiler, J. (2012) Coexisting serpentine and quartz from carbonate-bearing serpentinized peridotite in the Samail Ophiolite, Oman. Contrib. Mineral. Petrol. 164(5), 821-837.

Suhr, G., Cawood, P.A. (1993) Structural history of ophiolite obduction, Bay of Islands, Newfoundland. Geol. Soc. Am. Bull., 105, 399–410.

T

Taran, Y.A., Kliger, G.A., Sevastianov, V.S. (2007) Carbon isotope effects in the open-system Fischer-Tropsch synthesis. Geochim. Cosmochim. Acta 71, 4474-4487.

Teir S., Eloneva S., Fogelholm C-J., Zevenhoven R. (2009) Fixation of carbon dioxide by producing hydromagnesite from serpentinite. Appl. Energy, 86(2), 214–218.

Teir S., Kuusik R., Fogelholm C-J., Zevenhoven R. (2007) Production of magnesium carbonates from serpentinite for long-term storage of CO2. Int. J. Miner. Process., 85(1–3), 1–15.

Terry, J.P. and Wotling, G. (2011) Identifying rain-shadow influences on river flows and flood magnitudes across the central massif divide of La Grande Terre island, New Caledonia.J Hydrol (Amst), 404, 77-86.

Thiagarajan N., Adkins J., Eiler J.M. (2011) Carbonate clumped isotope thermometry of deepsea corals and implications for vital effects. Geochim Cosmochim Acta, 75 (16), 4416-4425.

Tikoff, B., Wojtal, S.F. (1999) Displacement control of geologic structures. Journal of Structural Geology 21 (8–9), 959–967.

Titus, S.J., Fossen, H., Pedersen, R.B., Vigneresse, J.L., Tikoff, B. (2002) Pull-apart formation and strike-slip partitioning in an obliquely divergent setting, Leka Ophiolite, Norway. Tectonophysics, 354, 101–119.

Titus, S.J., Maes, S.M., Benford, B., Ferré, E.C., Tikoff, B. (2011) Fabric development in the mantle section of a paleo-transform fault and its effect on ophiolite obduction, New Caledonia. Lithosphere, 3, 221–244.

Tresacses J.J. (1975) L'évolution géochimique supergène des roches ultrabasiques en zone tropicale: formation des gisements nickelifères de Nouvelle-Calédonie. Mémoires ORSTOM (Office de la Recherche Scientifique et Technique Outre-Mer), 78, 259p.

Tripati A.K., Eagle R.A., Thiagarajan N., Gagnon A.C., Bauch H., Halloran P.R., Eiler J.M. (2010) C-13-O-18 isotope signatures and 'clumped isotope' thermometry in foraminifera and coccoliths. Geochim Cosmochim Acta 74, (20), 5697-5717.

Troly, G., Esterle, M., Pelletier, B., Reibell, W. (1979) Nickel deposits in New Caledonia, some factors influencing their formation. In "International Laterite Symposium", D.J.I. Evans et al., eds. New Orleans, Louisiana, 19–21 February, New York, Society of Mining Engineers, 85-119.

Twiss, R.J., Moores, E.M. (1992) Structural Geology. W.H. Freeman and Company, New York, p. 532.

Twiss, R.J., Unruh, J.R. (1998) Analysis of fault slip inversions: do they constrain stress or strain rate? Journal of Geophysical Research 103 (B6), 12205–12222.

Twiss, R.J., Unruh, J.R. (1998) Analysis of fault slip inversions: do they constrain stress or strain rate? J. Geophys. Res., 103, 12205-12222.

U

U.S. Geological Survey (2015) Mineral commodity summaries 2015: U.S. Geological Survey, 196 p.

Ulrich M, Picard C, Guillot S, Chauvel, C., Cluzel, D., Meffre, S. (2010) Multiple melting stages and refertilization as indicators for ridge to subduction formation : The New Caledonia ophiolite. LITHOS, 115, 223–236.

Ulrich M. (2010) Péridotites et serpentinites du complexe ophiolitique de la Nouvelle-Calédonie, Thèse, Université de la Nouvelle-Calédonie et Université de Grenoble, pp 253.

Ulrich M., Muñoz M., Guillot S., Cathelineau M., Picard C., Quesnel B., Boulvais P., Couteau C. (2014) Dissolution–precipitation processes governing the carbonation and silicification of the serpentinite sole of the New Caledonia ophiolite. Contrib. to Mineral. Petrol., 167, 952.
Annexe 2

Ulrich M., Muñoz M., Guillot S., Chauvel C., Cluzel D., Picard C. (2011) Weathering effects on the mineralogical and geochemical composition of the New Caledonia ophiolite. *Mineralogical Magazine* **75(3)**, 2049

Urey, H.C. (1947) The thermodynamic properties of isotopic substances. Journal of the chemical society, 562-581.

U

Van Hise, C.R. (1896) Principles of North American Pre-Cambrian geology. In: Walcott, D. (Ed.), Sixteenth Annual Report of the United States Geological Survey to the Sec- retary of the Interior, 1894–1895: Part 1. USGS, pp. 571–843

de Vera, J., Granado, P., McClay, K. (2010) Structural evolution of the Orange Basin gravity-driven sustem, offshore Namibia. Marine and Petroleum Geology, 27(1), 223-237.

Villanova-de-Benavent C, Proenza J a., Galí S, et al (2014) Garnierites and garnierites: Textures, mineralogy and geochemistry of garnierites in the Falcondo Ni-laterite deposit, Dominican Republic. Ore Geol Rev, 58, 91–109.

Villanova-de-Benavent, C., Aiglsperger, T., Jawhari, T., Proenza, J.A., Galí, S. (2012) Micro-Raman spectroscopy of Garnierite minerals: a useful method for phase identification. Revista de la Sociedad Española de Mineralogía, 180, 181-16.

W.

Wacker U., Fiebig J., Schoene B. R. (2013) Clumped isotope analysis of carbonates: comparison of two different acid digestion techniques. Rapid Commun. Mass Spectrom., 27, 1631-1642.

Wells, M.A., Ramanaidou, E.R., Verrall, M., Tessarolo, C. (2009) Mineralogy and crystal chemistry of garnierites in the Goro lateritic nickel deposit, New Caledonia. Eur. J. Mineral., 21, 467–483.

Whattam, S.A., Malpas, J., Ali, J.R. and Smith, I.E.M. (2008) New SW Pacific tectonic model: Cyclical intraoceanic magmatic arc construction and nearcoeval emplacement along the Australia-Pacific margin in the Cenozoic. Geochemistry Geophysics Geosystems, 9, 1-34.

Wicks, F.J. et O'Hanley, D.S. (1988) Serpentine minerals: structures and petrology. In Hydrous Phyllosilicates (S.W. Bailey, ed.). Rev. Mineral., 19, 91-167.

Wicks, F.J., Whittaker, E.J.W. (1977) Serpentine textures and serpentinization. Can. Mineral., 15, 459-488.

Wilson M.J. (2004) Weathering of the primary rock-forming minerals: Processes, products and rates: Clay Minerals, 39, 233–266.

X

Xstrata (2012) Mineral resources and reserves at 31 Dec. 2012. Annual Report, 50p.

Z

Zeissink HE (1969) The mineralogy and geochemistry of a nickeliferous laterite profile (Greenvale, Queensland, Australia). Miner Depos, 4, 132–152.

Zheng, Y.-F. (1993) Calculation of oxygen isotope fractionation in anhydrous silicate minerals. Geochim. Cosmochim. Acta 57, 1079-1091.

Zheng, Y.F. (1999) Oxygen isotope fractionation in carbonate and sulfate minerals. Geochemical Journal 33, 109-126.

Annexes

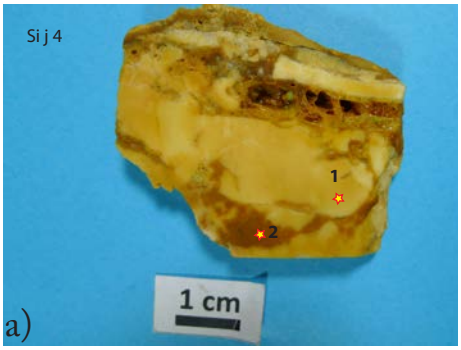

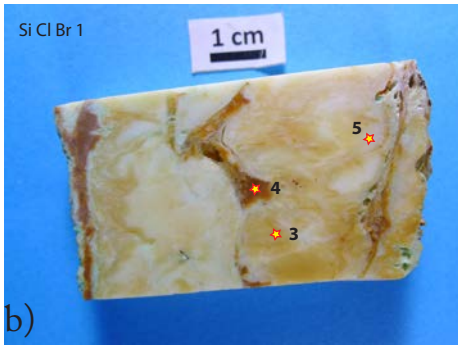

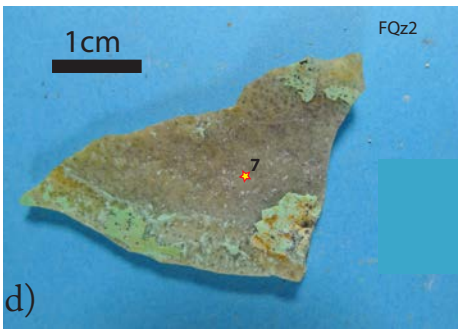

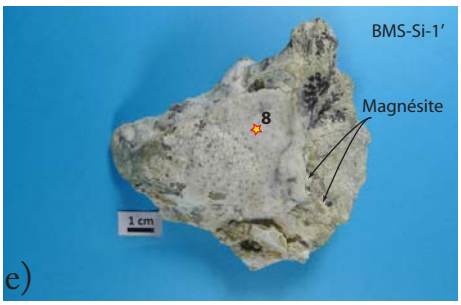

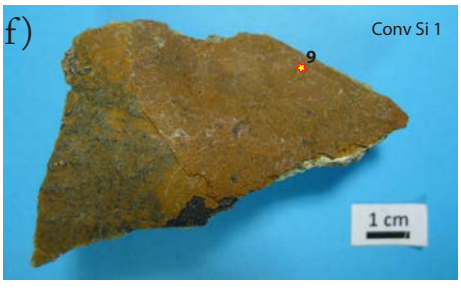

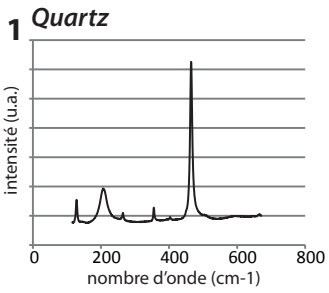

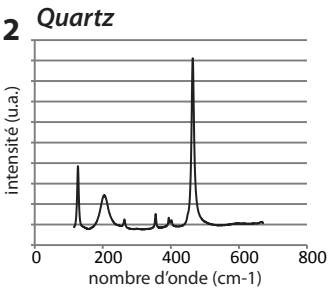

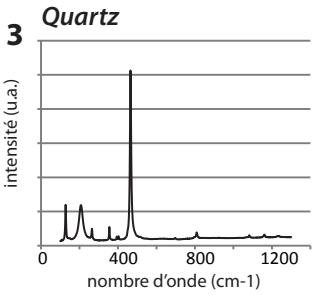

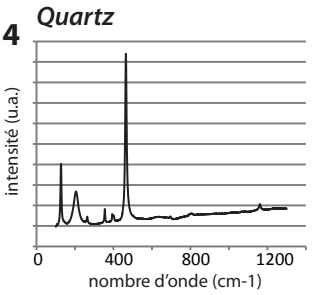

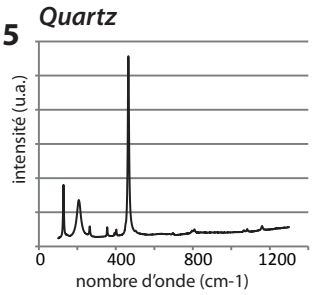

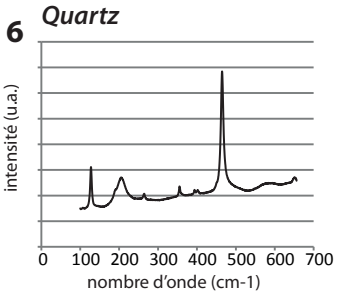

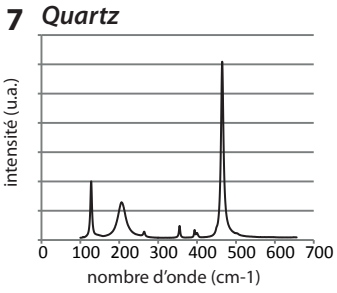

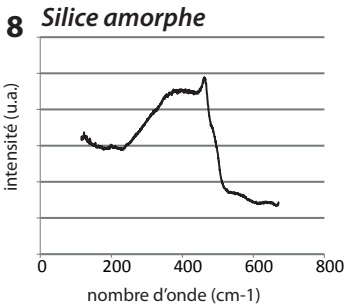

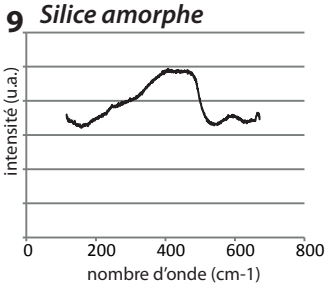

Annexe 1 - Les mesures par spectroscopie Raman ont été effectuées au laboratoire Géoressources de Nancy (France) sur un spectromètre Horiba Jobin-Yvon Labram HR800 et une source laser à argon ionisé d'une longueur d'onde de 514nm. La puissance de sortie du laser était de 200mW et les mesures ont été effectuées en utilisant une lentille Olympus ×50 afin de focaliser le faisceau laser sur une surface de 1µm de diamètre. Chaque spectre obtenu est le résultat de la moyenne de 20 acquisitions de 2 s pour le spectre 8, de 10 acquisitions de 5 s pour les spectres 3, 4, 5 et de 5 acquisition de 10 s pour tous les autres.chacune afin d'optimiser le rapport signal/bruit. Seule la région du spectre comprise entre 0 et 1400 cm^{-1} a été investiguée car étant la plus discriminante pour distinguer les différents polymorphes de la silice (Kingma et Hemley, 1994; Pop et al, 2004).

a,b,c,d) Echantillons des différents types de remplissage siliceux localisés dans les fractures au sein du niveau saprolitique du massif de Koniambo. L'analyse de ces échantillons de référence montre que ces remplissages sont majoritairement du quartz.

e) Silice amorphe translucide provenant de la semelle de serpentine. Ce type de silice amorphe est associé à de la magnésite plus ou moins bien développée. Dans le cas présent, la magnésite forme un film fin localisé sous la couche de silice amorphe.

f) Silice amorphe brune provenant de la zone intermédiaire du massif de Koniambo. Cette silice amorphe se présente sous forme de nappage de bloc de péridotite serpentinisée mais peut également être reconnue au niveau de la semelle de serpentine sous forme de remplissage de failles.

La localisation des différents échantillons de référence est présentée dans la figure 2 et le tableau 1 de l'article #5 (partie III.3).

Annexe 2

Well 1: Laterites profil with thick limonite

Depth	Al_2O_3	Cr_2O_3	Fe_2O_3	MgO	NiO	SiO_2
0.00	1.24	0.96	19.20	27.40	2.48	36.60
1.00	5.27	3.10	68.10	3.20	0.91	5.09
2.00	4.63	3.63	72.70	1.05	1.34	2.68
3.00	3.71	2.18	76.90	0.86	1.39	2.57
4.00	4.98	2.36	71.90	1.19	1.20	2.83
5.00	5.34	2.70	71.20	0.62	1.40	2.14
6.00	5.92	3.22	70.10	0.72	1.32	2.18
7.00	6.90	2.88	68.80	0.80	1.22	2.56
8.00	6.18	2.72	70.60	0.70	1.42	2.48
9.00	5.87	2.65	68.30	1.30	1.54	3.15
10.00	5.64	2.69	70.40	0.82	1.68	2.50
11.00	5.98	3.47	69.70	0.72	1.84	2.17
12.00	5.81	3.56	68.90	0.87	1.87	2.89
13.00	5.60	4.03	69.30	0.77	1.86	2.49
14.00	5.51	4.22	70.80	0.78	1.68	2.64
15.00	5.00	3.71	69.40	1.11	1.77	3.32
16.00	4.29	3.48	61.00	3.52	1.97	9.53
17.00	2.13	1.67	30.50	21.30	2.83	28.70
18.00	1.69	1.28	23.70	25.60	2.87	34.10
18.60	1.99	1.43	28.10	24.20	2.28	30.30
18.85	0.85	0.66	12.80	35.60	1.97	38.90
19.10	1.67	1.25	24.90	23.60	2.79	33.50
19.35	0.72	0.62	12.00	31.30	2.50	41.60
19.70	3.13	2.16	43.80	13.20	1.90	18.70
20.20	0.98	0.78	13.70	26.80	2.77	38.00
21.00	0.78	0.64	12.00	30.00	2.66	40.70
22.00	1.14	0.86	16.70	25.40	3.18	39.30
22.90	0.70	0.54	11.20	36.50	1.09	38.50
23.45	0.72	0.51	10.00	38.80	0.71	40.20
24.05	1.29	0.89	13.30	30.20	2.60	41.00
24.70	0.76	0.48	10.20	38.50	0.74	41.30
25.10	0.67	0.71	8.79	40.50	0.65	40.50
25.50	0.46	0.48	10.00	34.00	2.32	40.60
25.85	0.55	0.47	8.96	39.80	0.78	41.60
26.25	0.90	0.72	12.30	31.80	2.68	40.10
26.90	0.66	0.47	9.02	39.50	0.79	41.20
27.90	0.95	0.64	12.40	31.80	1.98	41.00
28.75	0.68	0.53	10.00	34.20	1.21	42.90
29.10	0.60	0.44	9.32	39.40	0.65	40.90
29.35	0.87	0.62	11.30	30.80	2.46	42.50
29.85	0.63	0.44	8.86	40.70	0.52	41.20
30.45	0.71	0.58	10.90	29.80	2.28	44.00
30.95	0.69	0.50	9.53	36.80	1.34	41.60
31.85	0.82	0.66	11.60	32.30	2.30	41.60
33.00	0.92	0.68	12.20	30.30	2.78	42.40

Well 3: Laterite profil without limonite

Depth	Al_2O_3	Cr_2O_3	Fe_2O_3	MgO	NiO	SiO_2
0.00	0.48	0.38	9.07	37.60	1.44	39.30
0.50	1.97	1.70	31.40	18.60	3.68	30.00
1.45	1.54	1.32	22.60	22.00	4.86	34.10
2.05	1.63	1.48	22.30	22.70	4.26	33.60
2.30	1.47	1.16	21.40	24.40	4.13	34.10
2.80	1.56	1.21	21.70	22.40	4.80	35.40
3.35	1.48	1.34	24.10	21.30	4.82	32.60
4.00	0.64	0.53	10.20	35.90	1.93	41.80
4.70	0.85	0.58	11.10	34.40	2.47	42.40
5.20	0.61	0.45	8.69	39.80	0.89	42.80
5.65	0.87	0.71	13.30	29.00	3.07	41.10
6.30	0.68	0.48	9.41	38.30	1.27	42.50
7.10	0.94	0.71	13.10	30.20	2.23	42.20
7.60	0.65	0.56	10.70	32.90	2.29	43.70
8.00	0.53	0.51	10.00	33.80	1.97	43.30
8.30	0.86	0.62	12.10	29.90	2.66	43.60
8.75	0.53	0.37	8.39	40.80	0.53	40.80
9.45	0.84	0.63	12.80	27.80	2.41	43.70
10.00	0.59	0.43	8.72	39.80	0.71	41.50
10.40	0.77	0.57	11.90	30.20	2.61	42.30
10.85	0.53	0.42	8.67	39.70	0.74	41.40
11.50	0.77	0.57	11.50	29.90	2.84	44.70
11.95	1.11	0.86	16.40	26.10	3.26	39.10
12.50	0.21	0.26	9.89	36.10	1.13	40.20
13.05	0.28	0.30	10.40	30.40	2.88	42.70
13.55	0.54	0.38	8.39	38.90	0.58	41.20
14.55	0.61	0.40	8.35	40.80	0.44	41.50
15.20	1.05	0.69	13.40	27.00	3.70	42.20
15.35	0.62	0.45	8.94	37.30	1.15	42.30
15.50	0.84	0.68	12.10	26.60	3.54	44.00
16.00	0.50	0.48	9.28	31.50	3.60	40.70
16.95	0.72	0.50	9.91	32.30	1.85	44.80
17.95	0.66	0.46	8.96	30.20	3.35	43.80
18.60	1.21	0.77	13.50	27.20	3.60	41.50
18.95	0.75	0.47	10.30	32.20	2.47	43.70
19.25	0.88	0.60	12.30	30.20	3.29	42.20
19.55	0.73	0.49	9.95	34.80	2.14	43.00
19.90	0.66	0.40	8.44	40.10	0.83	42.40
20.20	1.01	0.67	12.50	29.90	3.36	42.10
20.55	0.98	0.61	11.50	30.90	3.35	42.50
21.15	0.81	0.53	11.00	33.20	2.67	41.80
22.20	0.65	0.42	8.43	41.10	0.69	42.30
22.90	0.80	0.53	10.80	32.10	2.74	43.60
23.15	0.64	0.40	8.83	39.90	1.00	42.90
23.65	1.32	0.88	16.30	27.90	3.45	39.30

Well 5: Laterite profil with thin limonite

Depth	Al_2O_3	Cr_2O_3	Fe_2O_3	MgO	NiO	SiO_2
0.00	5.47	4.16	73.97	1.15	0.89	2.87
1.00	5.27	5.61	73.38	1.06	0.95	2.08
2.00	5.40	4.20	70.70	0.78	1.49	2.47
3.00	4.93	3.55	69.30	0.93	1.40	7.25
4.00	4.76	2.98	63.68	2.11	1.28	11.90
4.60	3.92	2.23	42.60	9.09	2.06	24.80
5.10	2.13	1.63	27.39	17.20	2.56	36.60
6.00	2.50	1.76	33.54	11.00	2.25	36.30
7.00	1.60	1.12	22.45	16.10	2.84	42.80
8.00	1.20	0.82	18.27	16.95	3.32	47.00
9.00	0.97	0.75	16.20	15.25	2.96	53.90
10.00	0.80	0.61	14.04	9.14	1.62	66.30
11.00	1.17	0.91	19.22	13.10	3.21	52.20
12.00	1.16	0.76	16.62	12.50	2.59	56.20
13.00	1.38	0.84	18.10	16.75	3.54	47.50
14.00	1.06	0.93	16.52	21.20	3.36	46.20
15.00	1.00	0.94	15.42	23.60	3.21	43.20
16.00	0.98	0.73	15.38	20.10	3.57	46.90
17.00	1.06	0.81	15.74	18.80	4.25	45.80
18.00	1.05	1.03	16.70	19.40	3.98	45.10
19.00	1.34	1.32	21.80	16.50	4.22	40.90
20.00	1.32	1.31	20.61	18.85	4.09	40.80
21.00	1.84	1.64	20.77	20.30	3.87	40.60
22.00	1.43	1.30	18.83	20.90	4.19	41.60
23.00	1.68	1.26	22.67	14.05	3.72	45.00
24.00	1.73	1.31	23.48	9.86	2.86	50.60
25.00	1.62	1.40	22.59	14.70	3.65	44.70
26.00	1.02	0.89	16.64	18.65	3.50	47.10
27.00	1.14	1.01	16.43	21.70	3.44	43.30
28.00	1.12	1.15	17.06	19.80	3.79	44.40
29.00	0.86	0.68	13.57	20.70	3.46	48.10
30.00	1.10	0.82	13.97	22.60	3.43	44.80
31.00	1.28	1.04	15.77	22.70	3.54	42.60
32.00	0.98	0.87	15.10	20.70	3.93	46.40
33.00	0.58	0.51	10.27	24.80	2.98	49.20
34.00	0.80	0.81	13.89	24.00	3.27	44.40
34.70	0.82	0.97	13.98	25.30	3.31	41.80
35.20	0.99	1.08	18.00	22.90	3.42	39.70
36.00	1.16	1.40	17.62	22.40	4.03	40.60
37.00	0.88	1.08	14.59	24.80	3.82	41.10
38.00	0.93	1.04	15.30	23.90	4.06	41.50
39.00	0.90	0.96	14.21	24.90	3.83	42.00
40.00	0.92	0.99	14.69	24.40	3.96	41.90
41.00	0.78	0.83	14.22	25.20	3.33	42.70
42.00	0.71	0.69	13.84	20.90	2.66	49.70

Well 1: Laterites profil with thick limonite

Depth	Al_2O_3	Cr_2O_3	Fe_2O_3	MgO	NiO	SiO_2
34.10	0.89	0.62	12.50	29.40	2.34	41.50
35.00	0.72	0.50	9.99	31.50	2.12	43.00
35.90	1.05	0.71	14.00	25.30	1.84	45.90
36.65	0.82	0.57	10.50	31.60	1.62	41.70
36.90	0.64	0.46	9.15	35.60	0.73	41.70
37.25	0.77	0.56	10.60	32.00	1.24	43.60
38.10	0.91	0.64	12.50	28.90	1.28	44.00
39.10	0.71	0.47	9.82	36.40	0.60	42.00
40.00	0.94	0.62	11.50	29.40	1.17	43.90
41.00	0.81	0.52	10.40	31.10	0.94	44.90
41.85	0.71	0.49	9.25	36.90	0.56	41.70
42.80	1.55	0.56	10.00	31.40	0.56	43.70
43.95	0.77	0.47	10.10	32.80	0.76	43.80
45.25	0.58	0.43	8.90	37.10	0.50	41.20
46.50	0.64	0.40	8.10	41.00	0.32	41.10
47.60	0.74	0.50	10.50	31.00	0.51	44.40
48.35	0.41	0.42	9.26	35.30	0.36	41.90
49.00	0.58	0.48	10.20	32.20	0.50	43.80
50.00	0.56	0.42	8.56	37.20	0.33	41.60
51.00	0.62	0.41	8.51	36.40	0.34	42.40

Isocon Limonite
Isocon Ni-rich Saprolite
Isocon Ni-poor Saprolite
Isocon protolith

Well 3: Laterite profil without limonite

Depth	Al_2O_3	Cr_2O_3	Fe_2O_3	MgO	NiO	SiO_2
24.20	0.92	0.58	11.20	33.80	2.08	43.40
24.65	1.16	0.77	14.30	29.00	2.86	42.20
24.90	0.66	0.42	8.90	39.70	0.94	43.30
25.03	1.18	0.80	14.40	28.30	2.91	43.80
25.42	0.58	0.44	8.98	40.60	0.66	41.60
25.85	0.69	0.64	11.30	32.50	2.29	42.90
26.10	0.94	0.78	13.60	29.20	2.69	41.00
26.45	0.65	0.44	9.12	38.20	0.96	42.80
26.80	0.96	0.67	11.40	34.80	1.03	41.80
27.50	0.58	1.17	21.40	13.70	3.17	50.10
28.15	0.73	0.68	11.60	29.10	3.15	42.10
28.35	1.33	1.25	19.10	23.70	3.78	37.90
28.90	1.62	1.30	21.90	22.10	4.00	35.90
29.50	0.91	0.67	12.20	31.60	2.48	41.70
30.05	0.87	0.73	13.40	28.60	3.02	41.10
30.60	0.57	0.43	8.29	38.80	0.68	42.60
31.35	0.80	0.63	11.50	28.80	2.71	43.40
32.05	0.57	0.51	9.29	33.20	1.33	43.40
32.55	0.14	0.31	8.88	34.60	1.25	40.30
33.20	0.23	0.43	8.76	35.50	1.24	39.90
33.70	0.20	0.37	9.35	33.80	2.85	38.60
34.45	0.92	1.11	23.40	22.50	2.42	36.80
35.05	1.39	1.35	24.30	21.30	2.52	35.90
35.35	1.04	1.05	17.80	26.70	3.08	36.20
36.00	1.64	1.64	30.40	17.20	2.37	34.00
36.85	1.58	1.51	30.50	9.94	1.66	43.80
37.75	0.80	1.34	25.80	21.20	2.28	36.00
38.55	1.20	1.14	21.40	26.00	1.96	34.20
39.15	0.60	0.53	10.40	34.50	1.63	40.80
39.70	0.53	0.43	8.82	39.80	0.44	40.50
40.05	0.56	0.96	15.80	28.90	2.43	37.60
40.55	0.74	0.66	11.90	33.10	1.78	39.40
41.45	0.53	0.39	8.25	41.20	0.43	40.40

Isocon Ni-rich Saprolite
Isocon Ni-poor Saprolite

Well 5: Laterite profil with thin limonite

Depth	Al_2O_3	Cr_2O_3	Fe_2O_3	MgO	NiO	SiO_2
43.00	0.88	0.83	14.44	23.40	2.94	45.80
44.00	0.56	0.81	11.98	25.90	3.78	44.00
45.00	0.56	0.77	12.32	25.00	3.47	45.70
46.00	0.65	0.79	12.82	27.30	3.96	41.70
47.00	0.72	0.82	12.69	26.80	4.29	42.30
48.00	0.73	0.81	13.07	26.00	3.59	43.70
49.00	0.57	0.60	10.48	21.90	2.49	51.90
50.00	0.65	0.63	11.14	30.20	3.05	43.20
51.00	0.69	0.60	10.78	30.70	3.01	42.20
52.00	0.64	0.53	10.24	32.10	2.93	44.10
53.00	0.67	0.57	10.10	28.20	3.48	44.90
54.00	0.65	0.60	10.54	31.70	2.85	43.10
55.25	0.54	0.51	9.46	35.70	2.55	42.10
56.25	0.54	0.53	9.76	34.10	2.80	42.70
57.00	0.32	0.41	8.92	30.50	2.59	44.90
58.00	0.22	0.32	7.51	27.00	2.65	50.20
58.75	0.20	0.29	7.19	26.20	2.25	52.00
59.25	0.17	0.28	7.40	31.10	2.47	46.10
60.00	0.24	0.27	7.48	16.90	2.28	64.10
61.00	0.26	0.30	7.90	23.50	2.75	53.70
62.00	0.13	0.26	6.92	25.50	2.73	53.40
63.00	0.13	0.27	6.94	31.20	2.18	48.40
64.00	0.14	0.27	6.82	20.60	1.71	61.70
65.00	0.14	0.29	7.20	23.50	2.01	56.30
66.00	0.15	0.27	7.28	27.40	3.32	48.80
67.00	0.14	0.26	7.01	25.40	3.01	51.70
68.00	0.12	0.26	6.84	23.80	2.61	55.70

Isocon Limonite
Isocon Ni-rich Saprolite

Annexe 2 - Chemical analyses of major and some trace elements through three typical laterite profiles. Each analysis is expressed in weight %

Well 1: Laterites profil with thick limonite

	C_i^O (wt.%)	C_i^A(wt.%)	ΔC_i (%)	ρ^A	$(V_O/V_A)_{Fe2O3=constant}$
Limonite					
Al_2O_3 x 10	6,4	61,8	10,8		
Fe_2O_3	8,1	70,6	0,0	**1,7**	**6,5**
Cr_2O_3 x 5	2,0	13,6	-22,0		
NiO x 10	3,2	14,2	-49,1		
SiO_2	41,1	2,5	-99,3		
MgO	41,0	0,7	-99,8		
Ni-rich saprolite					
Al_2O_3 x 10	6,4	8,5	-16,0		
Fe_2O_3	8,1	12,8	0,0	**2,1**	**1,5**
Cr_2O_3 x 5	2,0	3,3	4,4		
NiO x 10	3,2	19,7	289,6		
SiO_2	41,1	38,9	-40,1		
MgO	41,0	35,6	-45,1		
Ni-poor saprolite					
Al_2O_3 x 10	6,4	7,6	-5,7		
Fe_2O_3	8,1	10,2	0,0	**2,3**	**1,3**
Cr_2O_3 x 5	2,0	2,4	-4,7		
NiO x 10	3,2	7,4	83,6		
SiO_2	41,1	41,3	-20,2		
MgO	41,0	38,5	-25,4		

Annexe 3 - Details of calculation of isocon method. Each symbol is explained in the appendix

Well 3: Laterite profil without limonite

	C_i^O (wt.%)	C_i^A(wt.%)	ΔC_i (%)	ρ^A	$(V_O/V_A)_{Fe2O3=constant}$
Ni-poor saprolite					
Al_2O_3 x 10	6,4	15,8	-34,4		
Fe_2O_3	8,1	30,5	0,0	**1,8**	**3,0**
Cr_2O_3 x 5	2,0	7,6	0,3		
NiO x 10	3,2	16,6	37,8		
SiO_2	41,1	43,8	-71,7		
MgO	41,0	9,9	-93,6		
Ni-rich saprolite					
Al_2O_3 x 10	6,4	14,7	-13,1		
Fe_2O_3	8,1	21,4	0,0	**1,8**	**2,1**
Cr_2O_3 x 5	2,0	5,8	9,8		
NiO x 10	3,2	41,3	388,5		
SiO_2	41,1	34,1	-68,6		
MgO	41,0	24,4	-77,5		

Well 5: Laterite profil with thin limonite

	C_i^O (wt.%)	C_i^A(wt.%)	ΔC_i (%)	ρ^A	$(V_O/V_A)_{Fe2O3=constant}$
Limonite					
Al_2O_3 x 10	6,4	52,7	-9,1		
Fe_2O_3	8,1	73,4	0,0	**1,8**	**7,2**
Cr_2O_3 x 5	2,0	28,1	54,8		
NiO x 10	3,2	9,5	-67,2		
SiO_2	41,1	2,1	-99,4		
MgO	41,0	1,1	-99,7		
Ni-rich saprolite					
Al_2O_3 x 10	6,4	11,2	-16,9		
Fe_2O_3	8,1	17,1	0,0	**1,8**	**1,7**
Cr_2O_3 x 5	2,0	5,8	36,5		
NiO x 10	3,2	37,9	462,3		
SiO_2	41,1	44,4	-48,7		
MgO	41,0	19,8	-77,1		

Contrib Mineral Petrol (2014) 167:952
DOI 10.1007/s00410-013-0952-8

ORIGINAL PAPER

Dissolution–precipitation processes governing the carbonation and silicification of the serpentinite sole of the New Caledonia ophiolite

Marc Ulrich · Manuel Muñoz · Stéphane Guillot · Michel Cathelineau · Christian Picard · Benoit Quesnel · Philippe Boulvais · Clément Couteau

Received: 22 July 2013 / Accepted: 3 December 2013 / Published online: 18 January 2014

Abstract The weathering of mantle peridotite tectonically exposed to the atmosphere leads commonly to natural carbonation processes. Extensive cryptocrystalline magnesite veins and stock-work are widespread in the serpentinite sole of the New Caledonia ophiolite. Silica is systematically associated with magnesite. It is commonly admitted that Mg and Si are released during the laterization of overlying peridotites. Thus, the occurrence of these veins is generally attributed to a *per descensum* mechanism that involves the infiltration of meteoric waters enriched in dissolved atmospheric CO_2. In this study, we investigate serpentinite carbonation processes, and related silicification, based on a detailed petrographic and crystal chemical study of serpentinites. The relationships between serpentine and alteration products are described using an original method for the analysis of micro-X-ray fluorescence images performed at the centimeter scale. Our investigations highlight a carbonation mechanism, together with precipitation of amorphous silica and sepiolite, based on a dissolution–precipitation process. In contrast with the *per descensum* Mg/Si-enrichment model that is mainly concentrated in rock fractures, dissolution–precipitation process is much more pervasive. Thus, although the texture of rocks remains relatively preserved, this process extends more widely into the rock and may represent a major part of total carbonation of the ophiolite.

Keywords Serpentine · Magnesite · Carbonation · Silicification · New Caledonia ophiolite

Introduction

Carbon dioxide is currently one of the primary greenhouse gases having an impact on global warming. Therefore, numerous recent studies have focused on the potential of sequestration of CO_2 by mineral carbonation, either through ex situ (e.g., Bobicki et al. 2012; Power et al. 2011; Renforth et al. 2011; Balucan and Dlugogorski 2013; Harrison et al. 2013) or in situ processes (e.g., Cipolli et al. 2004; Hansen et al. 2005; Teir et al. 2007, 2009; Andreani

Communicated by J. Hoefs.

Electronic supplementary material The online version of this article (doi:10.1007/s00410-013-0952-8) contains supplementary material, which is available to authorized users.

M. Ulrich (✉) · M. Cathelineau
Laboratoire Géoressources, CNRS, UMR 7566,
Université de Lorraine, Nancy, France
e-mail: marc.ulrich@univ-lorraine.fr; mulrich@unistra.fr

M. Ulrich · M. Muñoz · S. Guillot
Institut des Sciences de la Terre, CNRS, UMR 5275,
Université de Grenoble 1, Grenoble, France

Present Address:
M. Ulrich
IPGS-EOST, UMR 7516, Université de Strasbourg,
Strasbourg, France

C. Picard
Laboratoire Chrono-environnement, UMR 6249,
Université de Franche-Comté, Besançon, France

B. Quesnel · P. Boulvais
Géosciences Rennes, CNRS, UMR 6118,
Université de Rennes 1, Rennes, France

C. Couteau
Service Géologique, Koniambo Nickel SAS,
Nouvelle Calédonie, France

et al. 2009; Rudge et al. 2010; Kelemen et al. 2011; Klein and Garrido 2011). Among the various mineral species that may undergo carbonation reaction, Mg-bearing minerals (as well as Ca-carbonates) are of a great interest as they are very common at Earth surface and thus represent an important reservoir for CO_2. In addition, magnesite ($MgCO_3$) has a long-term stability, contrarily to alkali carbonates, which are readily soluble in water (Lackner et al. 1995). Basically, magnesite is formed by the reaction between a Mg-rich source and CO_2-rich fluids (Bain 1924) and can integrate variable amount of cations (mainly divalent, e.g., Ca and Fe) by substituting Mg in the crystal structure. Based on the study of numerous magnesite deposits, Abu-Jaber and Kimberley (1992b) distinguished vein-type and massive-type magnesite, the second type forming deeper than the former. Numerous other parameters play a role in magnesite formation, such as temperature, the origin of the components or the mechanisms of precipitation. The temperature of magnesite formation extends from ambient to ~400 °C (Halls and Zhao 1995; Wilson et al. 2009; Klein and Garrido 2011). The origin of CO_2 is variable as it may be related to either weathering (atmospheric CO_2), metamorphic (deep seated CO_2) or magmatic (magmatic CO_2) sources (Abu-Jaber and Kimberley 1992b). The source of magnesium is usually local at the outcrop scale but can also be distant, e.g., coming from the weathering of magnesian rocks at the Earth surface and transported downward by meteoric water infiltration (Podwojewski 1995; Jurković et al. 2012). Mechanisms of magnesite precipitation are also variable. Abu-Jaber and Kimberley (1992b) reported two main ways of magnesite precipitation: (1) precipitation through a reaction that involves CO_2-rich fluid and Mg-rich rock, or alternatively Mg-rich fluids and CO_2-rich rock (i.e., the most common way to form magnesite); (2) the oversaturation of the fluid with respect to magnesite may be enhanced by the fluid evaporation and/or degassing (Dabitzias 1980; Fallick et al. 1991; Zedef et al. 2000; Ghoneim et al. 2003). In both cases, hydrated Mg-carbonate species may precipitate alternatively or in association with magnesite (e.g., Zedef et al. 2000; Beinlich and Austrheim 2012) Detailed studies of the precipitation mechanisms can thus provide major clues for the understanding of natural CO_2 sequestration.

Among the various rocks that have the potential to react with CO_2, ultramafic rocks, and particularly serpentinites, are probably the most efficient feedstock material for long-time storage through the formation of magnesite (Dabitzias 1980; Jedrysek and Halas 1990; Pohl 1990; Fallick et al. 1991; Abu-Jaber and Kimberley 1992b; Sherlock and Logan 1995; Goff and Lackner 1998; Gerdemann et al. 2003; Ghoneim et al. 2003; Cipolli et al. 2004; Schulze et al. 2004; Hansen et al. 2005; Teir et al. 2007, 2009; Kelemen and Matter 2008; Rudge et al. 2010; Klein and Garrido 2011; Jurković et al. 2012). Serpentine carbonation onsets by the dissolution of atmospheric CO_2 into water, where CO_2 forms different species as a function of pH. At pH < 6.5, carbonic acid (H_2CO_3) dominates, at pH between 6.5 and 10.5, bicarbonate (HCO_3^-) dominates and at higher pH, carbonate anion (CO_3^{2-}) dominates. Serpentine dissolution and magnesite precipitation are also pH-dependent (Klein and Langmuir 1987; Guthrie et al. 2001; Teir et al. 2007; Prigiobbe et al. 2009; Teir et al. 2009; Krevor and Lackner 2011). Experimentally, Teir et al. (2007) have shown that the best efficiency for serpentine to carbonate conversion is obtained in the pH range of 8–11, with an optimum at pH 9. Roughly similar pH conditions were measured for the optimum carbonation of olivine (Prigiobbe et al. 2009). At pH > 8, bicarbonate starts to dissociate into H^+ and CO_3^{2-} ions:

$$HCO_3^- \rightarrow H^+ + CO_3^{2-} \quad (1)$$

Interaction between CO_2-rich water and serpentine gives rise to the exchange of H^+ and Mg^{2+} cations on the mineral surface. This reaction produces silica and water, while free Mg^{2+} cations react with CO_3^{2-} anions to form magnesite:

$$Mg_3Si_2O_5(OH)_4 + 6H^+ \rightarrow 3Mg^{2+} + 2H_4SiO_4 + H_2O \quad (2)$$

$$Mg^{2+} + CO_3^{2-} \rightarrow MgCO_3 \quad (3)$$

The overall reaction can be summarized as follow:

$$\underset{\text{Serpentine}}{Mg_3Si_2O_5(OH)_4} + 3\underbrace{\left(2H^+ + CO_3^{2-}\right)}_{CO_{2(aq)}} \rightarrow \underset{\text{Magnesite}}{3MgCO_3} + \underset{\text{Silica}_{(aq)}}{2SiO_2} + \underset{\text{Water}}{5H_2O} \quad (4)$$

Worldwide, carbonation of serpentinite commonly leads to the formation of magnesite deposits in association with ophiolitic bodies, e.g., in California (Bodenlos 1950; Sherlock and Logan 1995), Egypt (Ghoneim et al. 2003), Greece (Dabitzias 1980), Italy (Cipolli et al. 2004), Norway (Beinlich et al. 2012) or Oman (Kelemen and Matter 2008). In New Caledonia, similar magnesite deposits have been described in the serpentine sole of the ophiolite, but few studies have focused on the origin of this magnesite (Glasser 1904; Trescases 1973; Ulrich 2010; Quesnel et al. 2013). Quesnel et al. (2013) propose that magnesite veins in the serpentinite sole formed tectonically, at temperatures between 40 and 80 °C. On the basis of stable isotope analyses (O and C), these authors propose that the fluid from which magnesite formed was originally meteoric water and that the carbon source is mostly atmospheric, with a possible biogenic contribution. They also suggest that magnesium originated from the dissolution of the peridotite at the

top of the ophiolite during laterization and was transferred down to the sole by the infiltration of meteoric waters under tectonically active conditions. The *per descensum* model is largely invoked to explain magnesite deposits in lateritic environments (Dabitzias 1980; Pefrov et al. 1980; Pohl 1990; Abu-Jaber and Kimberley 1992a, b; Foster and Eggleton 2002; Jurković et al. 2012; Oskierski et al. 2012). It requires a well-drained system where meteoric waters, charged with atmospheric CO_2, dissolve serpentine (and other Mg-silicates), a process that releases magnesium and silicon into solution. Meteoric waters then percolate downward thanks to a microfracturing permeability system, thus dissolving more magnesium. Within this frame, precipitation of magnesite is due to supersaturation of fluids, which are generated by the neutralization of carbonic acid by serpentine dissolution, as shown by reactions (2) and (3) (Bodenlos 1950; Pohl 1990; Fallick et al. 1991; Abu-Jaber and Kimberley 1992b; Giammar et al. 2005; Kelemen et al. 2011). Alternatively, the ultramafic pile may become a partially closed system, and therefore limit the exchange between atmospheric CO_2 and meteoric water (Jurković et al. 2012). Progressive dissolution of serpentine during the fluid migration downwards consumes H^+ ions, as shown by reaction (3). As CO_2 is not freely available anymore, such consumption of H^+ ions causes the increase in pH, enhancing magnesite precipitation (Jurković et al. 2012).

Considering the origin of magnesium as deriving from the laterization rises the question about the mechanism of magnesite precipitation in New Caledonia. In such a case, and similarly to magnesite deposits from Euboea (Greece, Boydell 1921), magnesite formation may be the result of direct precipitation from the fluids without interacting with hosted rocks of the deposit site. This hypothesis was favored by the composition of New Caledonia waters passing through peridotites and serpentinites (sampled in la Coulée river, Mont-Dore), showing that they are enriched in magnesium and CO_3^{2-} ions (Barnes et al. 1978). Alternatively, field investigations highlight a close relationship between serpentinite, magnesite and silica, suggesting that the two latter phases may originate from the dissolution of the former. In this case, magnesite would precipitate by in situ replacement of the serpentine, using magnesium released during the serpentine dissolution. In this study, we provide evidences of magnesite formation through such a process on the basis of mineral characterization using an original analytical method for the interpretation of micro-X-ray fluorescence (μ-XRF) images. We particularly focus on the formation process of magnesite veins coupled to intense silicification observed in the serpentinite sole of the New Caledonia ophiolite.

Geological settings and sample descriptions

New Caledonia is located in the SW Pacific, 2,000 km east of the Australian coasts (Fig. 1). It is composed of several islands that belong to the Norfolk ridge (La Grande Terre, Island of Pines, Belep Islands) and to the Loyalty ridge (Loyalty Islands). The main island, la Grande Terre, consists of a patchwork of terranes reflecting the geodynamic evolution of the SW Pacific region from late Permien to Eocene (e.g., Cluzel and Meffre 2002; Cluzel et al. 2001, 2012). Among these terranes, the ophiolite is the most prominent as it covers more than 25 % of the island. The so-called peridotite nappe is composed of a large and continuous massif located south of the island and some isolated klippes widespread along the west coast (Fig. 1). The ophiolite was formed between 83 Ma with the opening of the South Loyalty Basin and its subsequent closing at 34 Ma, timing of its obduction on the Norfolk continental basement (Cluzel et al. 2001; Crawford et al. 2003; Schellart et al. 2006; Whattam et al. 2008; Whattam 2009; Ulrich et al. 2010; Cluzel et al. 2012). Since its emergence, the uppermost part of the peridotite nappe has undergone an intense laterization. This led to the development of a thick laterite bed (up to 60 m thick; Sévin et al. 2012) that owns ~30 % of the world nickel resources. The whole ophiolite is formed of upper mantle rocks (mainly harzburgites) with minor cumulates (Prinzhoffer 1981). Peridotites are highly serpentinized, particularly at the base of the ophiolite which is made of a thick (up to 400 m thick, Audet 2008; Ulrich et al. 2010) and silicified serpentinite sole where large amount of magnesite veins have crystallized (Quesnel et al. 2013).

Samples presented in this study were collected in the serpentinite sole of the Koniambo massif (Fig. 1). Similar outcrops occur on the serpentinite sole from other peridotite massifs in New Caledonia (Ulrich 2010). In the field, the whole sole is highly deformed, finely schistose and/or intensely brecciated, and has recorded multiple serpentinization events (Ulrich 2010): Massive serpentinization, which is of a typical bottle green color in the field (Fig. 2), is cross-cutted by light-green-colored serpentine veins. The latter is associated with black magnetite impregnations and microcracks filled by fibrous serpentine (chrysotile). Magnesite occurs as millimeter to multi-decimeter stockwork veins with a typical cauliflower-like texture, crosscutting serpentinites (Fig. 2). The magnesite is mainly snow white colored, but can also appear greenish depending of the amount of intergrown serpentine. On the basis of structural observations, Quesnel et al. (2013) distinguished two types of veins. The first type of veins is observed along and/or within the margins of top to the SW-centimeter shallow dipping shear zones. The second type of veins corresponds to steeper veins occasionally crosscut by the

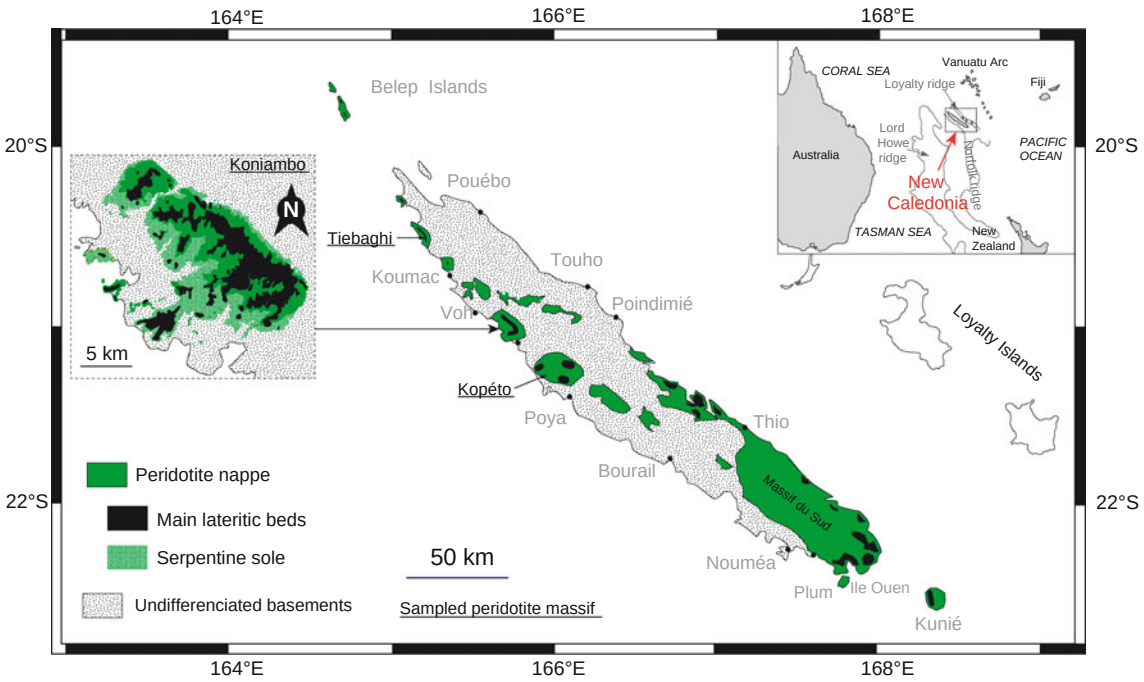

Fig. 1 Localization of the main ophiolitic occurrences composing the peridotite nappe. Simplified geological map of the Koniambo massif is modified from Maurizot et al. (2002)

low-dipping shear zones. Magnesite can also develop pervasively by precipitating in large and massive serpentine blocks (Fig. 2a–c). In this case, the magnesite seems to develop first at the expense of the light-green-colored serpentine to progressively extend to bottle green serpentine, a relationship that is not clear when magnesite fills the main shear zones, as described by Quesnel et al. (2013).

Analytical methods

X-ray diffraction

Analyses were performed at the Institut des Sciences de la Terre (ISTerre, Grenoble, France) on sample powders obtained after the crushing of separated magnesite veins and serpentinite host rock mineral fractions. X-ray diffraction (XRD) patterns were recorded with a Bruker D5000 powder diffractometer equipped with a Kevex Si(Li) solid state detector using $CuK\alpha_{1+2}$ radiation. Intensities were recorded at 0.02° 2θ step intervals from 5 to 80°, with a 6-s counting time per step. Size of the divergence slit was 0.298°.

Raman spectroscopy

Raman spectroscopy measurements were performed at the Ecole Normale Superieure of Lyon and at GéoRessources Nancy, France, in both cases using a Horiba Jobin–Yvon LabRam HR800 spectrometer and a visible ionized argon laser source with a wavelength of 514 nm. Output laser power was 100 mW, and measurements were performed using an Olympus lens of ×100 to focus the laser beam onto an area that was 1 µm in diameter. Analyses were carried out on macroscopic samples and on thin sections. Spectra result from the average of 5 acquisitions of 10–20 s to optimize the signal/noise ratio. Two regions of the Raman spectra were investigated: 150–1,250 cm^{-1} for structural bonding characterization and 2,800–3,900 cm^{-1} for the characterization of the hydroxyl groups.

Micro-X-ray fluorescence

Micro-X-ray fluorescence analyses were performed on a 5-mm-thick rock section (Fig. 2d) using EDAX Eagle III spectrometer at ISTerre (Grenoble, France). The X-ray tube consists of a Rh anode operating at 250 µA with an acceleration voltage of 40 kV. Polycapillary lenses were used to focus the X-ray beam down to 40 µm full-width-at-half-maximum at the sample surface. An energy-dispersive X-ray detector with resolution of 140 eV was used to measure fluorescence spectra. Chemical maps were recorded with a matrix of 256 × 200 pixels, a 40-µm step interval in both directions, and a dwell time of 1 s per pixel. For each map, the gray scale corresponds to the intensity of the Kα-lines of the different elements (Si, Mg,

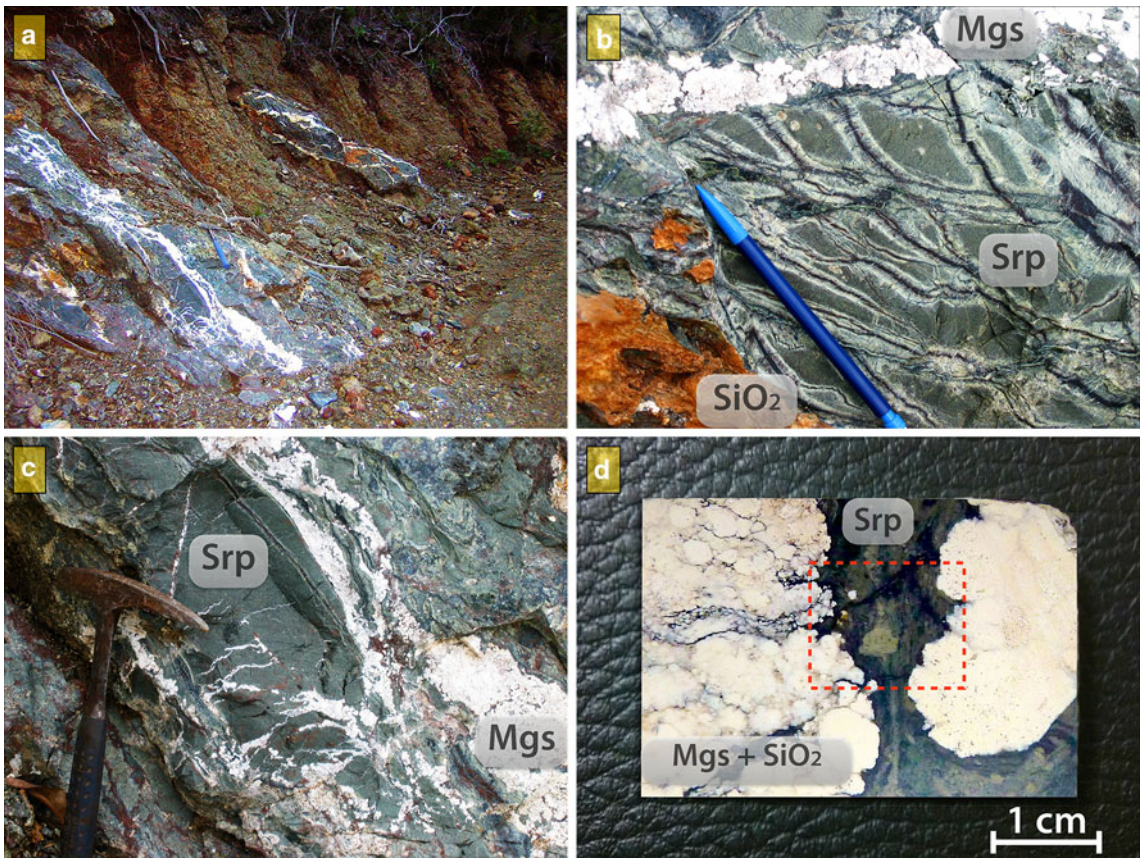

Fig. 2 **a**, **b**, **c** Snow-white-colored-magnesite veins crystallized in massive serpentinite blocs, Koniambo massif. Magnesite shows a typical cauliflower texture and is closely associated with silica veins (*in brown*). **d** Typical sample of carbonated serpentinite. *Orange dashed line* square localizes the mapped area by μ-XRF presented in Figs. 6, 7, 8 and in Figures S2 and S3

Table 1 In situ concentration measurements by μ-XRF for serpentine, magnesite, silica, sepiolite, magnetite and chromite used for the calculation of quantitative maps shown in Fig. 6 (see also electronic supplements, Figure S6)

Elements	Serpentine	Magnesite	Silica	Magnetite	Sepiolite	Chromite
MgO	40.25	46.84	–	–	24.72	12.34
Al_2O_3	0.41	–	–	–	0.46	23.22
SiO_2	43.60	0.39	100.00	–	62.66	0.08
K_2O	–	–	–	–	0.01	0.01
CaO	–	0.54	–	–	0.2	0.07
TiO_2	0.01	–	–	–	0.02	–
Cr_2O_3	0.02	–	–	–	0.02	48.20
MnO	0.03	–	–	–	0.67	0.20
FeO	2.51	0.02	–	100.00	0.55	15.82
NiO	0.17	–	–	–	0.11	0.06
CO_2	–	52.21	–	–	–	–
H_2O	13.00	–	–	–	10.58	–
Total	100.00	100.00	100.00	100.00	100.00	100.00

Fe, Al, Ni, Ti, Mn, Cr, Ca, K) calculated from the integration of a specified region of interest (ROI) of the energy range of XRF spectra. Then, ROI maps (see electronic supplements, Figure S4) are used to calculate phase maps thanks to a new routine, specially developed Matlab©-based code, following the same approach than that successfully applied first to the computing of mineral-phase maps from hyperspectral μ-XANES mapping (Muñoz et al.

2008). In the case of hyperspectral μ-XRF maps, the phase map calculation consists first of determining pure mineral phases that are expected to be present in the sample, in order to create standard spectra (or "pure" spectra). Then, for each pixel of the map, a linear combination of the different standard spectra is performed in order to fit each single spectrum. Results provide quantitative phase maps showing the distribution of minerals previously identified in the sample (e.g., based on XRD and/or Raman analyses). This approach is particularly useful to highlight relationships between minerals, especially for the characterization of finely divided mineral assemblages, i.e., when the beam is larger than grain size (such as here, typically below 1 micron). Concentration maps (in wt%) are finally recalculated on the basis of phase distribution maps considering the chemical composition of standards (Table 1).

Results

Mineralogy and chemical compositions

Bulk mineralogical compositions

Figure 3 shows the XRD patterns obtained on separated fractions of serpentinite and magnesite. The serpentinite mainly consists of serpentine with minor amount of magnetite and chromite. Serpentine occurs as lizardite and chrysotile. The occurrence of chrysotile is consistent with the presence of fibrous serpentine in microcracks as described above. Despite a careful separation, small peaks of magnesite and silica are present in the diffraction pattern of the serpentinite, suggesting that both minerals also occur at the micrometer scale within the hosted rock.

X-ray diffraction pattern of magnesite powder shows that the carbonate exhibits its most characteristic reflections at the following *d* values (in Å, arranged according to decreasing intensities): 2.74, 2.10, 1.70, 2.50 and 1.94 (Fig. 3). In addition, the diffraction pattern shows that magnesite systematically integrates small amounts of sepiolite ($Mg_4Si_6O_{15}(OH)_2{\cdot}6(H_2O)$), a mineral that is frequently described in association with carbonate in ultramafic environments (e.g., Birsoy 2002; Yaliçin and Bozkaya 2004; Boschetti and Toscani 2008). On the basis of this XRD pattern, magnesite is the only carbonate to crystallize. Neither dolomite nor calcite are formed, contrarily to numerous magnesite deposits previously described in the literature (Griffis 1972; Dabitzias 1980; Jedrysek and Halas 1990; Fallick et al. 1991; Abu-Jaber and Kimberley 1992b; Lugli et al. 2000; Zedef et al. 2000; Ghoneim et al. 2003; Jurković et al. 2012).

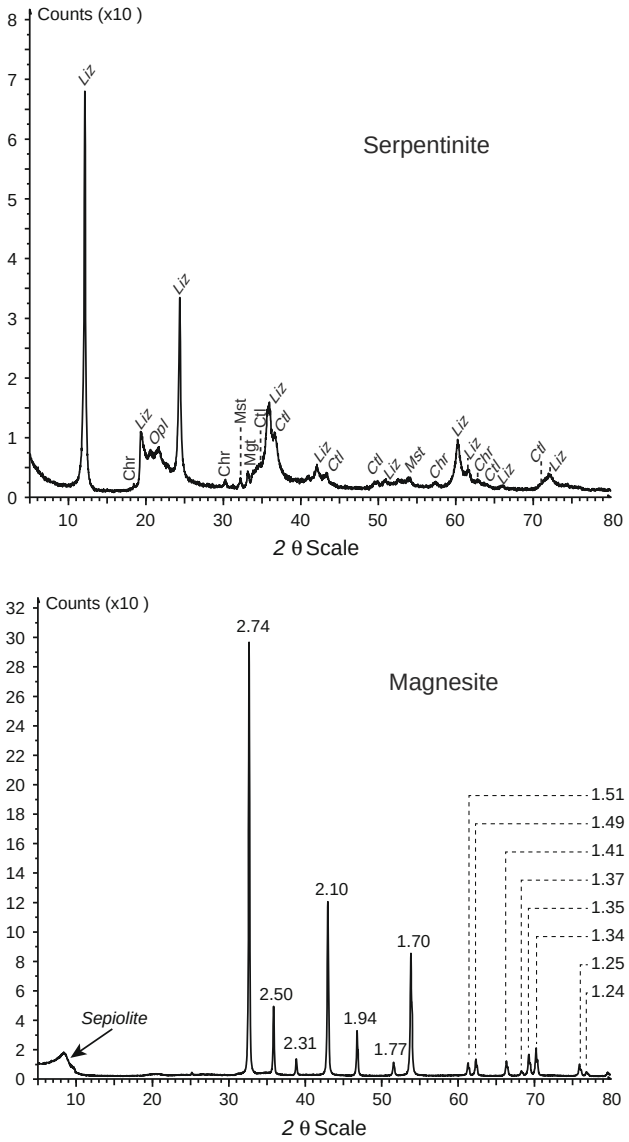

Fig. 3 Typical XRD patterns of serpentinite and magnesite. *Liz* lizardite, *Chr* chromite, *Opl* opal, *Mgs* magnesite, *Mgt* magnetite and *Ctl* chrysotile. Numbers upon the magnesite peaks correspond to *d* values, given in Å

Optical microscopy

Figure 4 shows the typical mineralogical textures of carbonated serpentinites composing the sole of the New Caledonia ophiolite. In thin section, the serpentinite does not exhibit any relic of primary minerals (i.e., olivine and pyroxene). However, the habits of grains and original textures of primary minerals (e.g., cleavage planes of orthopyroxene) have been preserved (typical pseudomorphic "mesh" texture, Fig. 4a, b) and indicate that the parent rock was a harzburgite. As highlighted by XRD analyses, opaque minerals associated with the serpentine are small grains of magnetite and chromite disseminated in

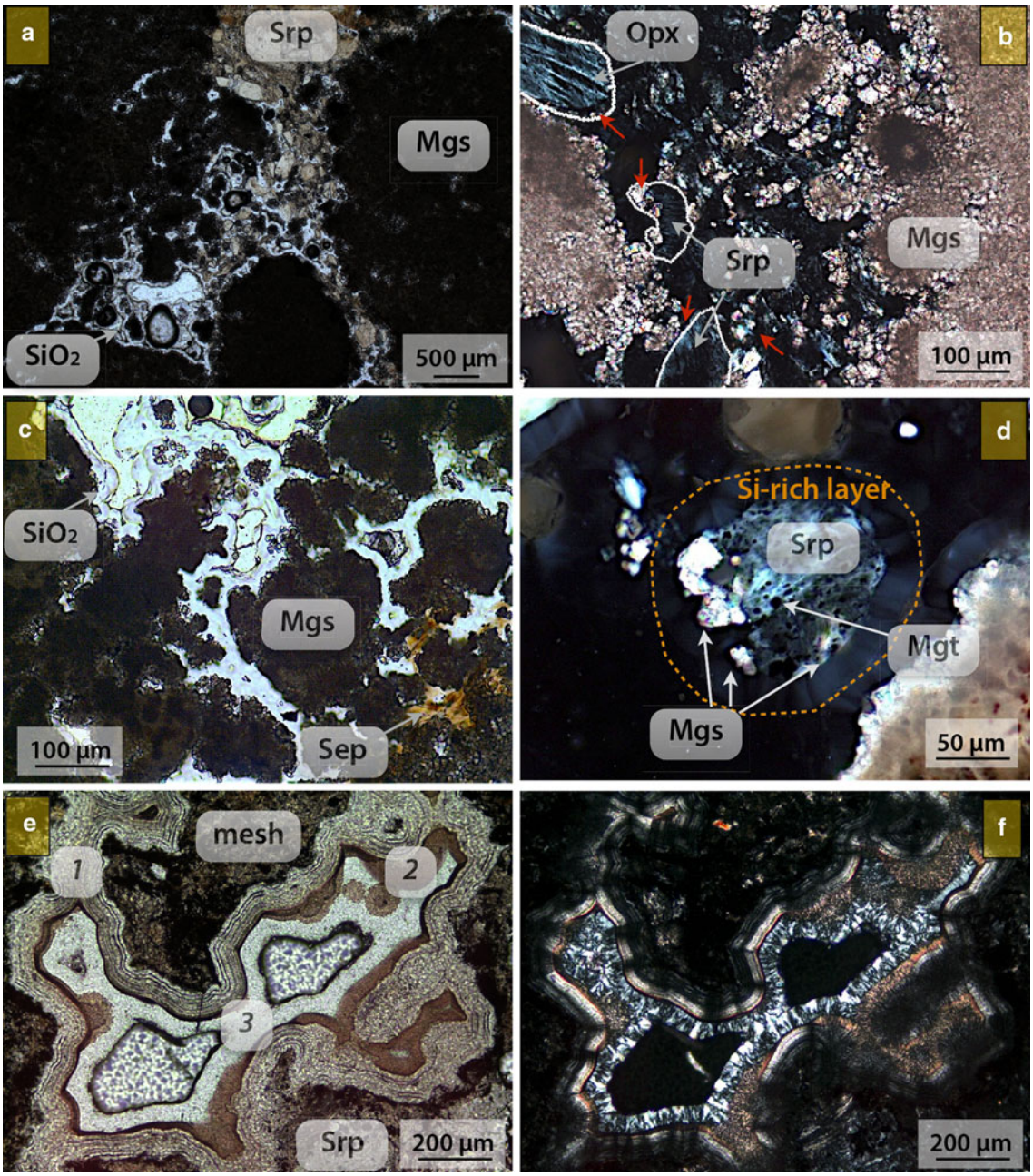

Fig. 4 **a** Microphotography under polarized light illustrating the development of magnesite and silica in serpentinite. **b** Microphotography under crossed-polarized light showing the development of magnesite along the rims of serpentine grains (indicated by the *red arrows*). Notice that the serpentinization also affects the orthopyroxene. **c** Magnesite grain aggregates surrounded by colloform amorphous silica gel. Associated brown and fibrous mineral corresponds to sepiolite (observation under polarized light). **d** Nucleation of magnesite grain on serpentine surface surrounded by colloform amorphous silica gel. Black dots inside of the serpentine grain correspond to magnetite (observation under crossed-polarized light). **e** Microtextures of a silica vein under polarized light (mesh: serpentine mesh; #1: opal-CT, #2 and #3: Chalcedony; identifications made by raman spectroscopy, see Fig. 5). **f** Same as **e** under crossed-polarized light. Mineral abbreviations: *Mgs* magnesite, *Mgt* magnetite, *Opx* orthopyroxene, *Sep* sepiolite and *Srp* serpentine

the mesh. In these rocks, magnesite occurs as finely disseminate grains (i.e., cryptocrystalline texture) that developed both at the rim and in cracks affecting serpentine grains (Fig. 4b, d). These grains progressively aggregate to form larger zones with a typical granular texture (Fig. 4a–c). The sepiolite, identified by XRD and optical microscopy, occurs as brown fibers interstitially to the magnesite nodules (Fig. 4c). Silica also occurs close to magnesite. Microscopic observations show that the nature of the silica is variable: it occurs as an amorphous solid (gel-like)

surrounding magnesite aggregates and serpentine grains in area where magnesite dominates (Fig. 4a, c, d). Where serpentine is dominant, silica consists of crystalline to fine grains, forming vugs with a typical colloform texture propagating in the serpentine mesh (Fig. 4e, f). In this case, the nature of silica ranges from amorphous-like near the rim of the vug to quartz-like at the center (Fig. 4c, e, f).

Raman spectroscopy

Raman analyses were performed to further identify minerals that compose the serpentinite. This technique is complementary to XRD, since it is particularly efficient to distinguish among the different varieties of serpentine (e.g., Lemaire 2000; Auzende et al. 2004) as well as silica polymorphs (e.g., Götze et al. 1998; Pop et al. 2004). Figure 5 shows Raman spectra collected on carbonated serpentinites. Results show that lizardite is the dominant serpentine variety that occurs as individual grains and in the mesh, and corresponds to the bottle-green-colored serpentine described in the macroscopic observations. Chrysotile (not shown in Fig. 5) has also been detected, as already highlighted by XRD. In addition, light green serpentine was identified as polygonal serpentine. It shows quite similar patterns to those of the lizardite at low wave numbers, but strongly differs at high wave numbers (from 3,500 to 3,800 cm^{-1}, corresponding to OH group), where the polygonal serpentine is characterized by a large peak composed by two bands centered at 3,689 and 3,700 cm^{-1} (e.g., Lemaire 2000; Auzende et al. 2004).

The Raman spectrum of magnesite is characterized by four distinct bands located at 209, 327, 737 and 1,094 cm^{-1} (Fig. 5), consistently with the work of Krishnamurti (1956). The lack of bands at 3,448 and 3,648 cm^{-1} (i.e., in the OH region; typical of hydromagnesite) shows that magnesite is anhydrous.

Silica polymorphs are clearly identified using Raman spectroscopy. Vug rims consist of opal-CT (Silica #1, Fig. 4e), while brown coronas (Silica #2, Fig. 4e) and white fine grains (Silica #3, Fig. 4e) inside of the vugs are identified as chalcedony (Fig. 5). Although significantly different in microscopic observations (Fig. 4e, f), both chalcedonies display very similar Raman spectra, except on the intensity of the band located at 501 cm^{-1} which is significantly higher in the white chalcedony (electronic supplements, Figure S1). Notice that in all silica polymorphs, the large bands observed between 3,100 and 3,900 cm^{-1} indicate the presence of molecular water.

XRF mapping

The elemental distribution, expressed in weight percent, in a typical serpentinite texture surrounded by magnesite is

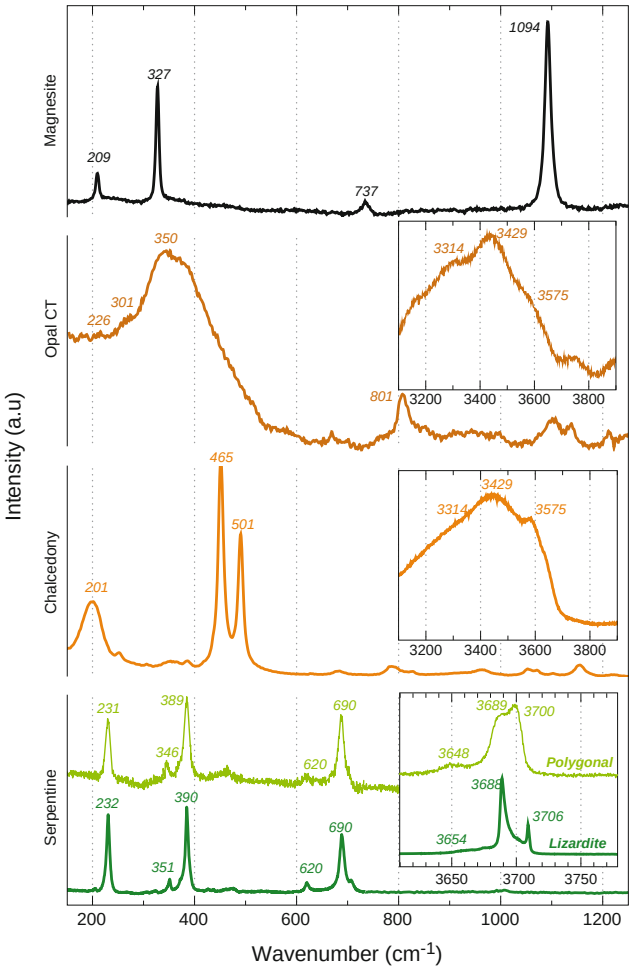

Fig. 5 Typical Raman spectra observed for serpentine (lizardite and polygonal), chalcedony, opal-CT and magnesite composing the serpentinite sole of the New Caledonia ophiolite

shown in Fig. 6. On the basis of chemical measurements, it was not possible to discriminate lizardite from polygonal serpentine, both having very similar compositions. Therefore, we only refer to serpentine in the following, focusing on the nature of processes that preferentially affect the serpentine grains or the mesh. The distribution maps of MgO and SiO_2 highlight serpentine grains (*s*) as well as mesh texture (*m*). The chemical composition of these grains is consistent with the stoichiometry of serpentine minerals, with about 43 wt% for both MgO + Fe_2O_3 and SiO_2. However, SiO_2 concentration in the mesh is significantly higher and can reach up to 65 wt%. To better understand such differences in chemical compositions, we calculated the phase distribution maps according to the minerals that are expected to be present in this sample (Fig. 7 and electronic supplements, Figure S4). Phase distribution reveals that the central zone of the mapped area mainly consists of serpentine minerals. The amount of serpentine is at least 50 % in the mesh and close to 100 %

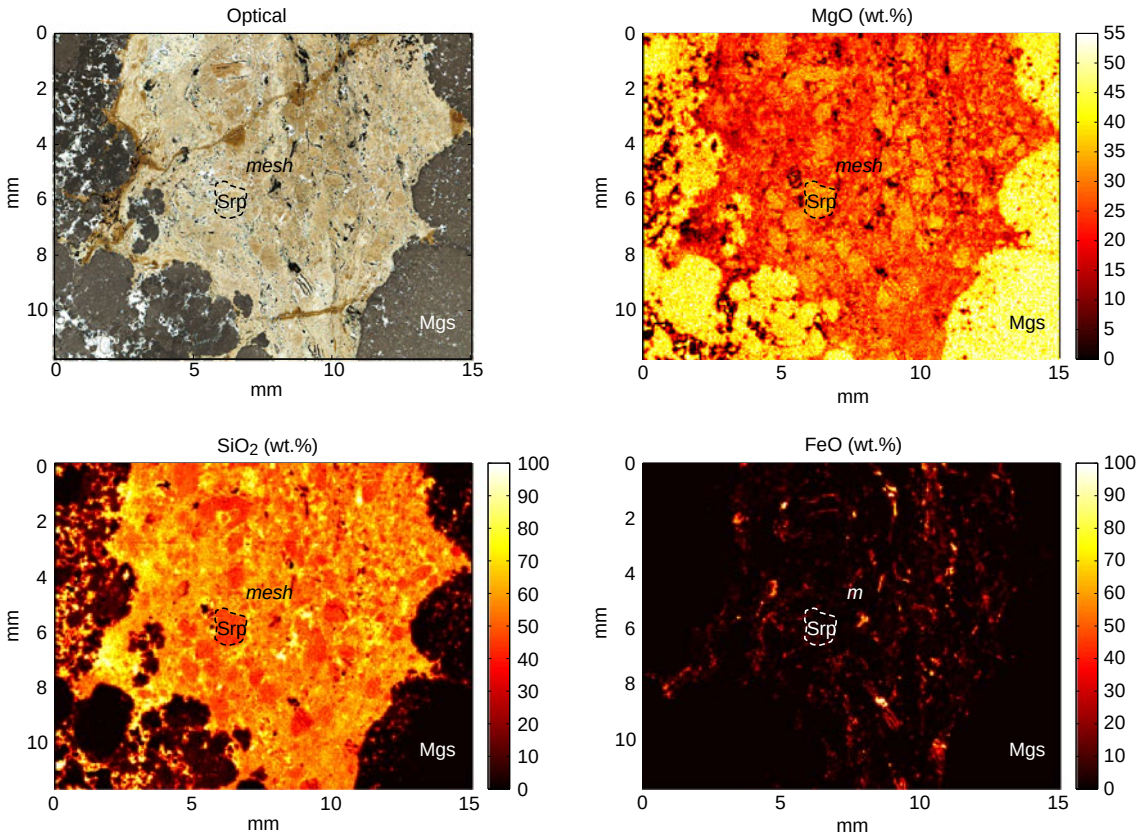

Fig. 6 Quantitative chemical maps of MgO, SiO_2 and Fe_2O_3 (in wt%) calculated on the basis of μ-XRF measurements (EDAX Eagle III). Complete procedure for the map calculation is detailed in the text

in grains. Silica distribution is relatively homogeneous in the mesh, with about 30 % silica, but shows peculiarities close to the magnesite, where the silica content reaches about 100 %. In contrast, the amount of silica in serpentine grains is well below 5 %. Finally, the calculation of phase distribution maps was obtained with about 20 % of magnesite in the serpentinite texture (i.e., the central area).

Figure 8 shows density correlation diagrams between serpentine, magnesite and silica based on the phase distribution maps for the two regions delimited by squares in Fig. 7. These diagrams statistically illustrate the description made above on the phase maps and reveal two distinct processes. In the region 1, the diagrams show a clear anticorrelation between silica and serpentine, corroborating that a great part of the pixels of this region corresponds to "silicified serpentine." At the opposite, the relationships between magnesite and serpentine on one hand and those between silica and magnesite on the other hand are less straightforward. To better understand these two diagrams, the region 2 (dashed square in Fig. 7) was delimited around a heterogeneous serpentine grain that appears partially altered (Fig. 9). This alteration occurs around fractures in the grain and is expressed by a lighter color of the serpentine in microscopic view. Considering this grain, a statistical analysis shows that silica and magnesite are correlated with each other, whereas they are both anticorrelated with serpentine (Fig. 8, region 2). This point is particularly interesting since the phase maps clearly highlight here a process of replacement of serpentine by an assemblage of magnesite and silica. Even if silica and serpentine are anticorrelated in both regions, carbonation and silicification processes do not follow rigorously the same trend. On the basis of our specific treatment of the XRF maps, we demonstrate here that the serpentinite is affected by two distinct weathering processes: while the mesh texture is mainly affected by a silicification process, the serpentine grains are mainly affected by the crystallization of a magnesite + amorphous silica assemblage.

Discussion

Serpentinite carbonation in New Caledonia has a supergene origin, following a *per descensum* model (Glasser 1904; Trescases 1973; Ulrich 2010; Quesnel et al. 2013). The atmospheric carbon dioxide is first dissolved in meteoric water. The CO_2-enriched fluids then circulate through the lateritic cover and dissolve the residual Mg-rich minerals

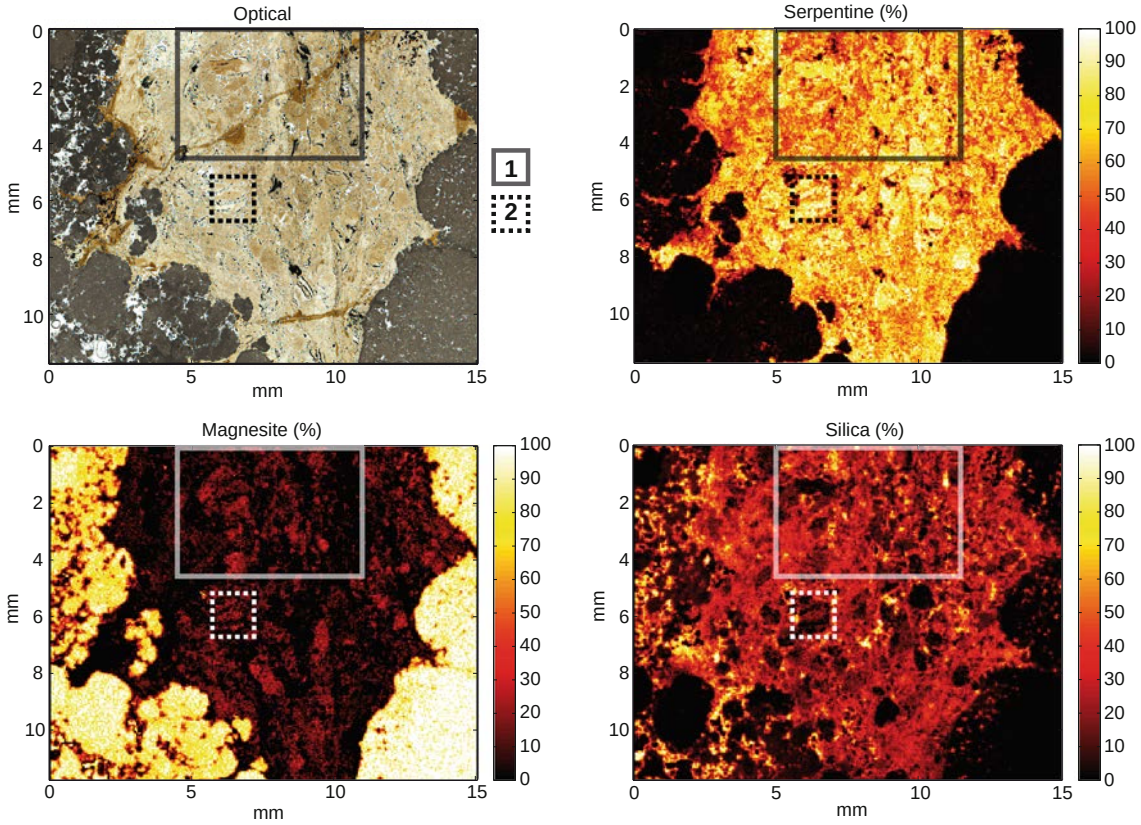

Fig. 7 Spatial repartition and quantification of mineral phases (in %) calculated on each pixel of the mapped area (Fig. 2d), based on μ-XRF measurements (EDAX Eagle III). Square-delimited regions correspond to areas used to construct correlation diagrams in Fig. 8

before driving to the precipitation of magnesite in fractures and to a porosity reduction in the serpentinite, within the serpentinite sole. This carbonation process leads to the formation of clusters of magnesite, potentially very large, and usually very localized to the serpentine-rich fractures or volumes. Although this process is most easily observed in the field, our results show that the serpentine dissolution leads to the local crystallization of magnesite and silica. This diffuse process is potentially the main mechanism of carbonation of the serpentinite sole.

Carbonation after serpentine dissolution

On the basis of our results of our mineralogical investigations, several features provide evidence that magnesite precipitation occurs through serpentine dissolution. First, the development of magnesite along the edges of adjacent serpentine grains is a characteristic of carbonation by in situ replacement of the serpentine (Figs. 4b, d, 9). When serpentine grains are preserved, carbonation is limited to the rims, the core remaining unaffected. At the opposite, the dissolution and replacement of the serpentine are more efficient in case of fractured grains (Fig. 9). This observation is consistent with experimental studies showing that intense grain fracturing is required to ensure complete carbonation (e.g., Haug et al. 2011; Kelemen et al. 2011; Hövelmann et al. 2012; van Noort et al. 2013). Another way to illustrate the progressive serpentine carbonation is given by Figure S2 (in electronic supplements). Here, the RGB map (for Red, Green, Blue, see the figure caption for more details) shows that magnesite is ubiquitous, formed by the replacement of the serpentine grains, and that only a few of the latter are preserved from the carbonation process. In addition, considering the stoichiometry and the molar volumes of the mineral species involved in reaction (4), volumes of magnesite and silica produced by the dissolution of 1 mol of serpentine (108 cm^3) are, respectively, 85 and 58 cm^3 ($V_{Mgs}/V_{Silica} \sim 1.45$), leading to a volume increase in about 30 %. Statistics calculated on the serpentine grain presented in Fig. 9 (corresponding to the region 2, Fig. 7) show that the assemblage consists of about 62 vol% of serpentine, 21 vol.% of magnesite and 15 vol.% of silica ($V_{Mgs}/V_{Silica} \sim 1.4$; Fig. 8). This assemblage compares well with the result of dissolution of 38 vol.% of serpentine, which leads to the formation of ~22 vol.% of magnesite and ~15 vol.% of silica. These estimates testify that results given in the phase maps are in good agreement with the stoichiometry of reaction (4).

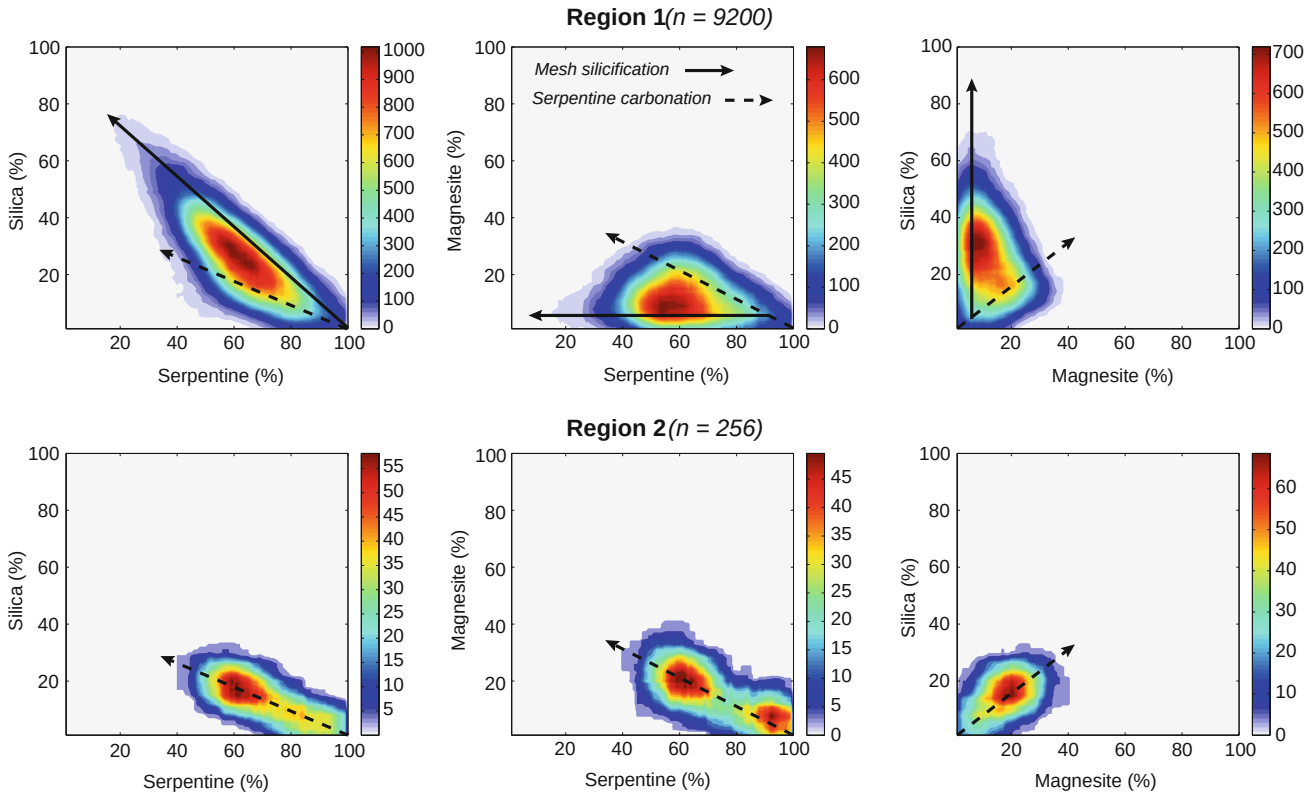

Fig. 8 Correlation diagrams (represented as density fields) between serpentine, magnesite and silica based on the phase distribution maps for the two square-delimited regions in Fig. 8. *n* corresponds to the total number of pixels composing each region. Colorbar values correspond to the number of pixels in one grid cell of a size of 5 % by 5 %

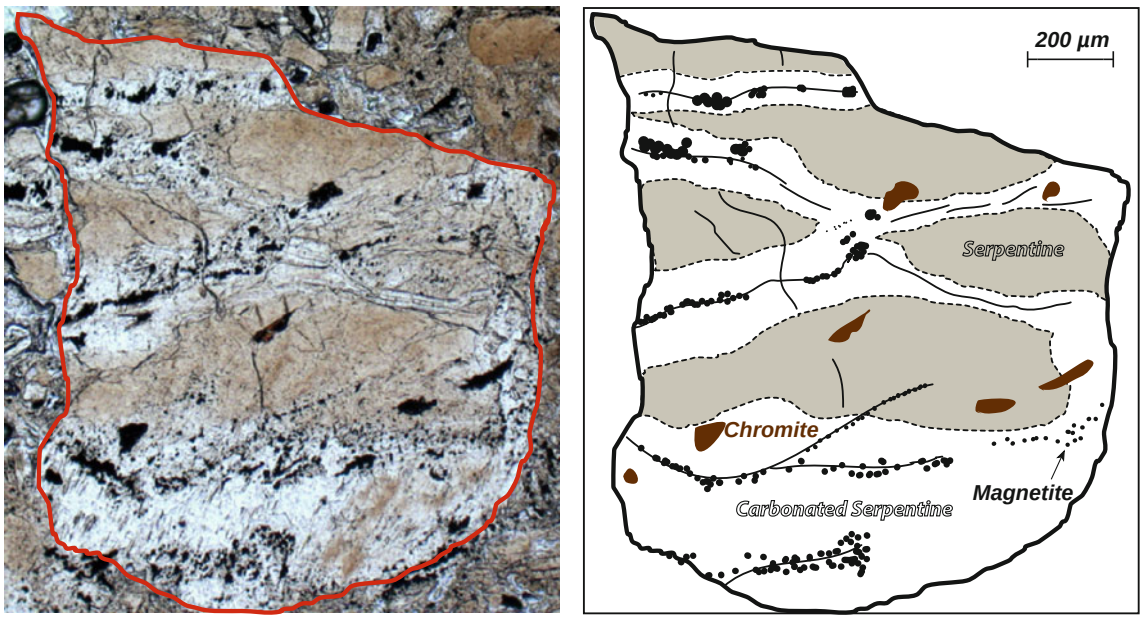

Fig. 9 Microphotography under polarized light and schematic representation of the partially carbonated serpentine grain (corresponding to the Region 2 in Fig. 7)

Second, carbonation by serpentine dissolution is also evidenced by the precipitation of an amorphous silica layer at the grain rims (Fig. 4d). This observation is consistent with the previous studies that systematically reported the formation of a Si-rich layer after Mg-bearing mineral breakdown (e.g., Luce et al. 1972; Lin and Clemency 1981;

Guthrie et al. 2001; Schulze et al. 2004; Giammar et al. 2005; Béarat et al. 2006; Sipilä et al. 2008; Andreani et al. 2009; Daval et al. 2011; King et al. 2011; Hövelmann et al. 2011, 2012). Third, sepiolite, which is described in our samples in association with magnesite (Figs. 3, 4c), also formed subsequently to the dissolution of serpentine (e.g., Jones and Galàn 1988; Birsoy 2002; Yaliçin and Bozkaya 2004; Andreani et al. 2009). Similar occurrences of sepiolite have been reported during natural (Yaliçin and Bozkaya 2004) and experimental (Andreani et al. 2009) carbonation of Mg-bearing minerals (serpentine and olivine). Actually, sepiolite may form in different ways:

$$\underset{\text{Serpentine}}{2Mg_3Si_2O_5(OH)_4} + \underset{CO_{2(aq)}}{2\left(2H^+ + CO_3^{2-}\right)} + \underset{\text{Silica}_{(aq)}}{2H_4SiO_4} \rightarrow \underset{\text{Magnesite}}{2MgCO_3} + \underset{\text{Sepiolite}}{Mg_4Si_6O_{15}(OH)_2\cdot 6H_2O} + \underset{\text{Water}}{3H_2O} \quad (5)$$

$$\underset{\text{Serpentine}}{3Mg_3Si_2O_5(OH)_4} + \underset{CO_{2(aq)}}{5\left(2H^+ + CO_3^{2-}\right)} \rightarrow \underset{\text{Magnesite}}{5MgCO_3} + \underset{\text{Sepiolite}}{Mg_4Si_6O_{15}(OH)_2\cdot 6H_2O} + \underset{\text{Water}}{4H_2O} \quad (6)$$

$$\underset{\text{Serpentine}}{Mg_3Si_2O_5(OH)_4} + \underset{CO_{2(aq)}}{2.5\left(2H^+ + CO_3^{2-}\right)} \rightarrow \underset{\text{Magnesite}}{2.5MgCO_3} + \underset{\text{Sepiolite}}{0.125Mg_4Si_6O_{15}(OH)_2\cdot 6H_2O} + \underset{\text{Silica}_{(aq)}}{1.25H_4SiO_4} + \underset{\text{Water}}{1.125H_2O} \quad (7)$$

All these reactions contribute to form magnesite, but they differ as reactions (5) and (6) conserve all Mg and Si in solids and are characterized by a volume gain ($\sim$60 and $\sim$30 %, respectively) while reaction (7) is balanced on volume. In addition, Eq. (5) consumes silica while Eq. (7) produces it. Only on the basis of cm-scale maps, it is difficult to estimate which reaction occured: in our sample, sepiolite represents <1 vol.% (see electronic supplements, Figure S4). Among the reactions written above, Eq. (7) is the one that produces the smallest amount of sepiolite, regarding the amount of magnesite that stoichiometrically precipitates. In contrast, Birsoy (2002) demonstrated that sepiolite formation is much more favored in the presence of Si-rich solution. In that case, sepiolite in our sample may derive from Eq. (5).

The fact that some serpentine grains are only partially transformed into magnesite indicates that the carbonation process was not completed. The reason why the reaction does not go to completion may be due to (1) silica precipitation, (2) pH increase and/or (3) porosity decrease. Numerous studies proposed that the formation of a Si-rich layer at the rims of serpentine grain during the first steps of dissolution might inhibit further Mg diffusion, potentially retarding or even stopping the process of carbonation (Gerdemann et al. 2003; Schulze et al. 2004; Alexander et al. 2007; Daval et al. 2011). Although Si-rich layer effectively reduces the accessibility of fluids to the reactive surface of minerals, recent investigations demonstrate that some permeability is maintained as carbonation remains active even after its development (Béarat et al. 2006; Andreani et al. 2009; Hövelmann et al. 2012). Thus, it is not obvious that precipitation of Si-rich layer led the serpentine carbonation to stop. Alternatively, following reaction (4), the dissolution of serpentine consumes 2 mol of H^+ for 1 mol of CO_3^{2-}, leading to a progressive increase in fluid pH. According to Barnes et al. (1978), fluids reacting with serpentinite in New Caledonia have pH ranging from 9 to 11. At pH 9, HCO_3^- dominates over CO_3^{2-}, making the serpentine dissolution possible following reactions (1) and (2). At pH 10.5, CO_3^{2-} species become dominant and at pH 10.8, HCO_3^- represent <20 % of the carbonate species in the fluid. In these conditions, magnesite precipitation is favored, but serpentine dissolution is scarce due to the lack of H^+ ions (e.g., Teir et al. 2007). Thus, intensive exchange between H^+ ions and Mg^{2+} cations on the serpentine surface leads to a progressive increase in pH that may inhibit further serpentine dissolution and subsequent carbonation. There is no evidence to argue against such process in New Caledonia, but it requires that atmospheric CO_2 is not freely available and thus a roughly closed system (Jurković et al. 2012). A third explanation may account for the inhibition of carbonation. Hövelmann et al. (2012) recently investigated the microstructure and porosity evolution as a function of carbonation reaction progress in natural peridotite. On the basis of their experimental results, they reported that a carbonation extend of $\sim$10 % leads to a closure of 50 % of the initial porosity. They demonstrated that magnesite precipitation in fracture pore space reduces the permeability and progressively stops the fluid pathway, preventing further reaction between the fluid and the silicate surface and ultimately ends the carbonation process. Contrarily to serpentinization, which is able to propagate through a reaction-induced fracturing mechanism (e.g., Plümper et al. 2012), carbonation is self-limited as the reaction will be inhibited due to magnesite growing that ultimately clogs the system. This implies that no volume gain occurs at the rock scale (Beinlich et al. 2012). Numerous studies highlight the necessity of active fracturing to ensure complete carbonation (e.g., Kelemen and Matter 2008; Kelemen et al. 2011). In our samples, no evidence of carbonation-induced fracturing has been observed so far, even if Quesnel et al. (2013) show the syn-kinematic character of magnesite veins at the outcrop scale. At the millimetric scale, volume gain associated with reaction (4) may have inhibited the complete carbonation of serpentinite by clogging the reacting zone. Such a process may prevent the infiltration of additional fluids, resulting in the partial carbonation of serpentine

grains as illustrated by Fig. 7 (see also electronic supplements, Figure S2).

Redox conditions during magnesite precipitation

The behavior of iron during carbonation has been poorly investigated. Such information would be indicative of redox conditions during magnesite precipitation. In serpentinite, iron is mainly hosted by iron oxides (magnetite, Fe_3O_4) surrounding serpentine grains or disseminated in the mesh texture (see electronic supplement, Figure S5). Iron content in serpentine is $\sim$2 wt% (expressed as FeO, Table 1). It substitutes Mg^{2+} cations in octahedral sites (O'Hanley 1996). During serpentine dissolution, iron is released from the mineral structure and may subsequently form Fe–Si-rich layer that progressively evolves into magnetite at the interface between serpentine and aqueous fluid (Fallick et al. 1991; Alexander et al. 2007; Andreani et al. 2009; Saldi et al. 2013). Alternatively, it may precipitate as siderite ($FeCO_3$) under rather high pCO_2 and specific pH range from 5.5 to 7.5 (Ohmoto et al. 2004) or be integrated in magnesite by substituting Mg^{2+} cations (Abu-Jaber and Kimberley 1992b; Hansen et al. 2005). In each of these minerals, iron oxidation is expected to differ according to oxidizing conditions: it is mostly oxidized in magnetite (i.e., 2/3 of iron is ferric iron) while it is in ferrous state in siderite or magnesite. In our sample, XRF analyses show that the iron content in magnesite is very low (Table 1), suggesting that its integration into the structure of the magnesite was very scarce. In addition, we never identified siderite in our samples so far. As stated above, siderite precipitates at pH conditions that are significantly lower than those of New Caledonia waters, so it is likely that pH was too high to make siderite precipitate. Magnetite is ubiquitous in our sample. Therefore, discriminating magnetite grains related to prior serpentinization events to those potentially derived from carbonation is not obvious. However, microscopic observations show that numerous magnetite grains have precipitated inside of partially carbonated serpentine grains (Figs. 4d, 9), while magnetite related to serpentinization generally forms outside of serpentine grains. Schematic representation in Fig. 9 highlights the systematic association of magnetite with cracks in the serpentine grain. According to Andreani et al. (2009), such grain fracturing may be considered as zones of localized fluid flow that favor the precipitation of magnetite during the first step of mineral dissolution. In contrast, their experiments show that carbonation initiates in domains of reduced fluid flow zones (fractures of a smaller size) where chemical gradients are small and thus facilitate local supersaturation, high pH and more reducing conditions. These results indicate that magnetite associated with the carbonation process may be used as a proxy to estimate the fluid flow rate at the serpentine grain scale: Fractures filled by magnetite correspond to high-fluid-flow zones characterized by more oxidizing conditions. In these regions, dissolution occurs but not magnesite precipitation (Andreani et al. 2009). Magnesium migrates to zones of reduced fluid flow, corresponding to regions dominated by magnesite or partially carbonated serpentine (Figs. 9, 10). In these areas, magnesite precipitates due to local supersaturation under more reducing conditions. This underlies that redox gradients occur even at grain scale.

Serpentine mesh silicification

Silica mobilization and precipitation

Intense silicification of the serpentine mesh was revealed during this study based on XRF measurements and Raman spectroscopy (Figs. 6, 7, 8, electronic supplements, Figures S2 and S3). For instance, the region 1 (Fig. 7) is composed of 62 vol.% of serpentine, 24 vol.% of silica and 7 vol.% of magnesite in average. The precipitation of 7 vol.% of magnesite consumes 12 vol.% of serpentine and forms 5 vol.% of silica, on the basis of reaction (4). Such excess of silica necessarily involves a contribution of silica from outside of the region 1. Phase maps show that pure silica mainly occurs in gaps between magnesite aggregates (left-side of the map, Fig. 7 and electronic supplements, Figure S2). However, when aggregates agglomerate subsequently to magnesite growth (right-side of the map, Fig. 7 and electronic supplements, Figure S2), silica is expelled from the magnesite. Numerous experimental studies indicate the progressive migration of silica rather than being rejected from the growing magnesite (Schulze et al. 2004; Hövelmann et al. 2011, 2012). As stated above, the first steps of serpentine dissolution release silica that immediately precipitates as a Si-rich layer. As carbonation reaction proceeds, the released silicon may feed the growth of the Si-rich layer, but Hövelmann et al. (2012) reported that such inward growth is limited. This limitation is mainly associated with pH increase in fluid during the carbonation process. At pH $>$ 9, magnesite precipitates while silica is solubilized and is therefore able to migrate away from the solid–fluid interface. Occurrence of water within silica is demonstrated by the Raman spectrum measured in the region of high frequencies (Fig. 5), which exhibits a typical spectrum of molecular water. As illustrated by XRF mapping, fluids enriched in silica subsequently to serpentine dissolution propagate in the serpentine meshwork. Similar observations have been reported in serpentinites from the Oman and the Ligurian ophiolites (Stanger 1985; Boschi et al. 2009; Lacinska and Styles 2012). According to Lacinska and Styles (2012), the well-preserved mesh texture (as observed in our samples) induces a combination of

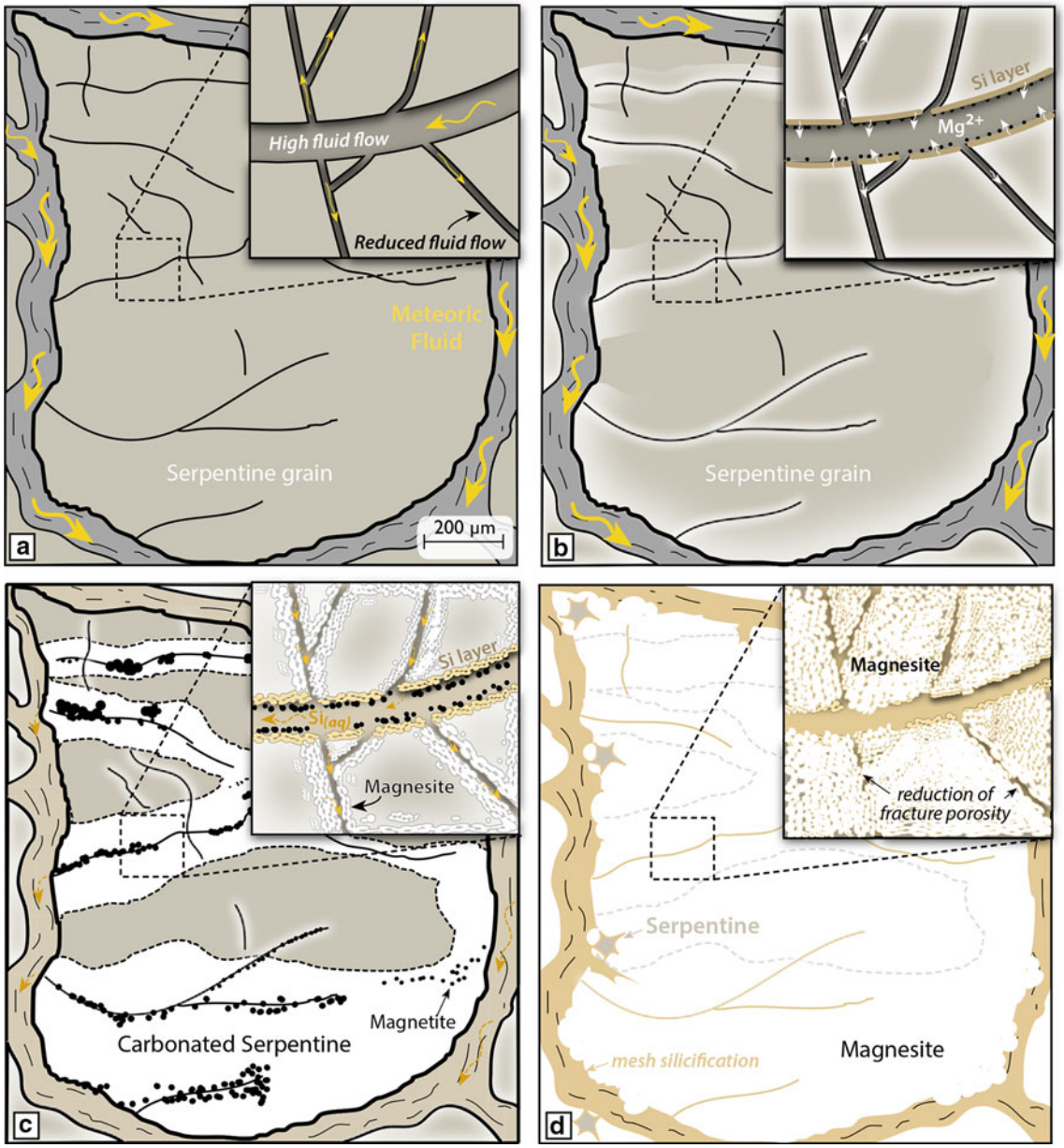

Fig. 10 Schematic sketch of coupled carbonation–silicification in dissolution–precipitation processes. **a** High pH meteoric waters (*yellow arrows*) percolating in serpentinite porosity start to dissolve the serpentine. **b** In zones of high fluid flow (see the text for more details), dissolution of the serpentine surface releases Mg^{2+} cations (*white arrows*) that migrate to zones of reduced fluid flow, leaving behind a Si-rich layer. Iron released during this dissolution step immediately precipitates as magnetite due to local oxidizing conditions favored by the constant renewal of water that characterizes zones of high fluid flow (Andreani et al. 2009). **c** Magnesite precipitates at the expense of serpentine surface in zones of reduced fluid flow due to local supersaturation and more reducing conditions. Released silica may precipitate as amorphous silica interstitially to magnesite aggregates, but increasing pH as the carbonation proceeds leads to its solubilization and subsequent migration in the serpentine mesh (*orange dashed arrows*). **d** Silica, in aqueous form, propagates in the serpentine mesh and finally precipitates in amorphous opal-A subsequently evolving to opal-CT, chalcedony and ultimately quartz. Complete serpentine replacement in a magnesite + silica assemblage may occur. Alternatively, the growing of magnesite may lead to the closure of initial porosity, preventing additional fluid circulations and thus ending the carbonation process before going to completion (Hövelmann et al. 2012)

iso-volumetric processes of slow rate dissolution of the mesh serpentine and immediate local precipitation of silica. They also argue that precipitation of silica is favored at near-neutral pH conditions. Such conditions differ from those we assume in our system (high alkali pH). However, Williams and Crerar (1985) attributed the precipitation of amorphous silica phases in nature due to the formation of dense colloids in supersaturate alkaline aqueous solutions.

In addition, progressive dissolution of silica causes pH of the solution to drop (Williams and Crerar 1985; Williams et al. 1985). Following these observations, we infer that such process may favor the dissolution of the serpentine mesh and the subsequent grain-by-grain replacement by amorphous silica phases, as postulated by Lacinska and Styles (2012). Such a process involves the removal of substantial amount of magnesium. As shown above, serpentine grain carbonation occurs stoichiometrically, i.e., magnesium released after serpentine grain dissolution, then immediately precipitates as magnesite. Thus, it is likely that the magnesium released during serpentine mesh silicification migrates out of the reaction zone. This assumption is consistent with the study of Boschi et al. (2009) that reported similar magnesium mobilization after serpentine dissolution and silica precipitation.

Silica evolution

Raman spectroscopy shows that silica formed in response to serpentine carbonation crystallizes as opal-CT and chalcedony (Fig. 5). Such silica polymorphs are commonly described in association with magnesite and are consistent with formation at low-temperature conditions (Boydell 1921; Bodenlos 1950; Dabitzias 1980; Pohl 1990; Abu-Jaber and Kimberley 1992b; Klein and Garrido 2011). According to Lacinska and Styles (2012), the formation of opal-CT indicates precipitation from supersaturated fluids. Williams et al. (1985) and Williams and Crerar (1985) show that the precipitation of silica polymorphs is driven by multiple steps of dissolution–precipitation. Systematically, studies made on the silica diagenesis report that saturated silica solutions do not form opal-CT directly, but follow a sequential crystallization with first the precipitation of amorphous opal-A (Graetsch et al. 1985; Williams et al. 1985; Williams and Crerar 1985; Heaney 1993; Lacinska and Styles 2012). Opal-A then evolves by means of dissolution–precipitation with concurrent ordering of the structure and removal of water, forming a pathway as follow: opal-A (amorphous) → opal-CT (cristobalite-tridymite assemblage) → chalcedony → quartz. According to Williams et al. (1985), the relationship between solubility and surface area or particle size is sufficient to explain such evolution. In our samples, only opal-CT and chalcedony have been identified so far. One possible explanation to account for the absence of opal-A is the complete replacement by opal-CT. The association with magnesite supports this hypothesis, since carbonates are thought to enhance the formation of opal-CT (Williams and Crerar 1985). Quartz has never been described associated with serpentinite in New Caledonia, so it is likely that the transition chalcedony to quartz does not occur. This reaction is very slow and is more likely to occur in a closed system, from the precipitation of fluids undersaturated in silica with respect to opal-A, opal-CT or chalcedony (Lund 1960 and references therein; Williams et al. 1985; Williams and Crerar 1985). In our samples, vugs containing chalcedony are systematically characterized by the presence of a hole on its center (Fig. 4). Similar observations were reported by Lund (1960) from silicified corals where both chalcedony and quartz precipitated. This author concluded that the hole served as a conduit for the continuous circulation of dissolved silica, resulting in the precipitation of chalcedony. At the opposite, when no hole was observed, chalcedony was completely replaced by quartz.

As an example, the concurrent reordering that occurs during the diagenetic pathway of silica is illustrated by the behavior of chalcedony (Figs. 4 and electronic supplement, Figure S1). Chalcedony, as many of the microcrystalline SiO_2 varieties, consists of an intimately intergrowth of α-quartz and moganite. Moganite is a silica polymorph that typically contains up to 3 wt% of water which is not a constituent of the structure. Using Raman spectroscopy, Pop et al. (2004) showed that during the opal-CT to chalcedony transition, moganite starts growing after α-quartz and preferentially in the most crystallized areas. It can be used as a proxy to evaluate the ordering of the chalcedony during its transition from opal-CT to quartz (Götze et al. 1998; Rodgers and Cressey 2001; Pop et al. 2004). In Fig. 4c, both silica #2 and silica #3 have been identified as chalcedony but differ in microscopic observation by their colors. In Raman spectroscopy, silica #2 and silica #3 almost display the same patterns, except the intensity of the band at 501 cm^{-1} (moganite) that is higher in the white chalcedony (electronic supplement, Figure S1). The moganite content (in wt%) of chalcedony can be calculated using the Raman band integral ratios $I_{(501)}/I_{(465)}$ (i.e., moganite/quartz) and applying the calibration curve proposed by Götze et al. (1998). We find that both chalcedonies are dominated by moganite, which represents 77 wt% in brown chalcedony (silica #2, Fig. 4c) and 81 wt% in white chalcedony. The enrichment of moganite traduces the progressive ordering of chalcedony which ultimately transforms in quartz given sufficient time (Williams and Crerar 1985; Heaney and Post 1992; Rodgers and Cressey 2001; Lynne et al. 2007).

Coupled carbonation–silicification in dissolution–precipitation processes: a summary

Based on our results and those from previous experimental studies, we infer that serpentine carbonation occurred due to the circulation of high pH meteoric waters dissolving the serpentine. Serpentine dissolution started at grain boundaries and in large grain fractures that correspond to regions where the fluid flow is the

highest (Fig. 10a). In these regions, intensive exchanges between H^+ and Mg^{2+} ions led to the development of a Si-rich layer and the precipitation of magnetite at the mineral/water interface (Fig. 10b). In contrast, magnesite precipitation was not favored in these zones of high fluid flow, which are characterized by strong chemical gradients and local oxidizing conditions (Andreani et al. 2009). Released magnesium therefore migrated to regions of reduced fluid flow, where magnesite nucleated at the expense of serpentine surfaces by a process of dissolution–precipitation due to local supersaturation and more reducing conditions (Fig. 10b–c). Here, the growth of magnesite was mainly fed by magnesium coming from the dissolution of adjacent serpentine grain. Potentially, distal contributions may have occurred (i.e., coming from the laterization, Barnes et al. 1978), since magnesite incorporate calcium while this element is not concentrated in serpentine (Table 1). Silica released during the carbonation process may first have precipitated in situ as amorphous silica (opal-A/CT), but progressive pH increase during the reaction facilitates the silicon solubilization and subsequent migration away from the fluid–solid interface (Fig. 10c; Schulze et al. 2004; Andreani et al. 2009; Hövelmann et al. 2011, 2012). Silica was then able to propagate in the serpentine mesh, silicifying the latter by precipitating first as an amorphous gel that progressively orders its crystalline structure to ultimately evolve as quartz if given sufficient time (Fig. 10c; Williams and Crerar 1985; Heaney and Post 1992; Rodgers and Cressey 2001; Lynne et al. 2007). Magnesium leached during the serpentine mesh carbonation migrated out from its original reacting zone and potentially fed larger magnesite deposits in syn-tectonic fractures, as previously proposed by Boschi et al. (2009) in the Ligurian ophiolite. Carbonation process ended when the overall serpentine was converted into an assemblage of magnesite + silica or, alternatively, when magnesite precipitation induced closure of the initial porosity (Fig. 10d; Hövelmann et al. 2012).

In agreement with recent studies from Andreani et al. (2009), Boschi et al. (2009) or Hövelmann et al. (2011, 2012), our study demonstrates the importance of active fracturing in the idea of in situ CO_2 sequestration. Although the volume extend expected during serpentine carbonation may lead to the system clogging, serpentine mesh silicification involves substantial removal of magnesium. This magnesium may migrate out of the reaction zone and subsequently precipitates as massive magnesite veins along the main structural discontinuities such as those described in New Caledonia by Quesnel et al. (2013). As previously underlined by Boschi et al. (2009), such a process may be considered as an alternative, efficient way for CO_2 sequestration.

Acknowledgments The authors gratefully thank Gilles Montagnac (ENS Lyon) and Marie-Camille Caumon (GeoRessources Nancy) for their help during Raman analyses. We also thank Valerie Magnin (ISTerre Grenoble) for her help during μ-XRF analyses and Clément Marcaillou (Eramet-SLN) and Olivier Vidal (ISTerre Grenoble) for their contributions on the development of the XRF-mapping software. This work has been possible thanks to the technical assistance of Koniambo SA. The financial support from Labex ANR-10-LABX-21-01 Ressources21 (Strategic metal resources of the 21st century) is gratefully acknowledged. We thank the editor Jochen Hoefs and the two anonymous reviewers for their careful revisions that helped to improve this manuscript.

References

Abu-Jaber NS, Kimberley MM (1992a) Origin of ultramafic-hosted magnesite on Margarita Island, Venezuela. Mineralium Deposita 27(3):234–241

Abu-Jaber N, Kimberley M (1992b) Origin of ultramafic-hosted vein magnesite deposits. Ore Geol Rev 7(3):155–191

Alexander G, Mercedes Maroto-Valer M, Gafarova-Aksoy P (2007) Evaluation of reaction variables in the dissolution of serpentine for mineral carbonation. Fuel 86(1–2):273–281

Andreani M, Luquot L, Gouze P, Godard M, Hoise E, Gibert B (2009) Experimental study of carbon sequestration reactions controlled by the percolation of CO2-rich brine through peridotites. Environ Sci Technol 43(4):1226–1231

Audet MA (2008) Caractérisation pétrographique et structurale des matériaux ophiolitiques du massif de Koniambo (Nouvelle Calédonie) et des minéralisations nickélifères supergènes, Unpubished Thesis, Université du Québec à Montréal et Université de la Nouvelle-Calédonie, pp 355

Auzende A, Daniel I, Reynard B, Lemaire C, Guyot F (2004) High-pressure behaviour of serpentine minerals: a Raman spectroscopic study. Phys Chem Miner 31(5):269–277

Bain GW (1924) Types of magnesite deposits and their origin. Econ Geol 19(5):412–433

Balucan RD, Dlugogorski BZ (2013) Thermal activation of antigorite for mineralization of CO_2. Environ Sci Technol 47:182–190

Barnes I, O'Neil J, Trescases J (1978) Present day serpentinization in New Caledonia, Oman and Yugoslavia. Geochim Cosmochim Acta 42:144–145

Béarat H, McKelvy MJ, Chizmeshya AV, Gormley D, Nunez R, Carpenter RW, Squires K, Wolf GH (2006) Carbon sequestration via aqueous olivine mineral carbonation: role of passivating layer formation. Environ Sci Technol 40(15):4802–4808

Beinlich A, Austrheim H (2012) In situ sequestration of atmospheric CO_2 at low temperature and surface cracking of serpentinized peridotite in mine shafts. Chem Geol 332–333:32–44

Beinlich A, Plümper O, Hövelmann J, Austrheim H, Jamtveit B (2012) Massive serpentinite carbonation at Linnajavri, N-Norway. Terra Nova 24:446–455

Birsoy R (2002) Formation of sepiolite-palygorskite and related minerals from solution. Clays Clay Miner 50(6):736–745

Bobicki ER, Liu Q, Xu Z, Zeng H (2012) Carbon capture and storage using alkaline industrial wastes. Prog Energy Combust Sci 38:302–320

Bodenlos A (1950) Geology of the red mountain magnesite district, Santa Clara and Stanislaus Counties, California, California. J Mines Geol 46:223–278

Boschetti T, Toscani L (2008) Springs and streams of the Taro–Ceno Valleys (Northern Apennine, Italy): reaction path modeling of waters interacting with serpentinized ultramafic rocks. Chem Geol 257(1–2):76–91

Boschi C, Dini A, Dallai L, Ruggieri G, Gianelli G (2009) Enhanced CO_2-mineral sequestration by cyclic hydraulic fracturing and Si-rich fluid infiltration into serpentinites at Malentrata (Tuscany, Italy). Chem Geol 265(1–2):209–226. doi:10.1016/j.chemgeo.2009.03.016

Boydell HC (1921) The magnesite deposits of Euboea, Greece. Econ Geol 16(8):507–523

Cipolli F, Gambardella B, Marini L, Ottonello G, Vetuschi Zuccolini M (2004) Geochemistry of high-pH waters from serpentinites of the Gruppo di Voltri (Genova, Italy) and reaction path modeling of CO2 sequestration in serpentinite aquifers. Appl Geochem 19(5):787–802

Cluzel D, Meffre S (2002) L'unité de la Boghen (Nouvelle-Calédonie, Pacifique sud-ouest): un complexe d'accrétion jurassique. Données radiochronologiques préliminaires U-Pb sur les zircons détritiques. Comptes Rendus Geosci 334:867–874

Cluzel D, Aitchison J, Picard C (2001) Tectonic accretion and underplating of mafic terranes in the Late Eocene intraoceanic fore-arc of New Caledonia (Southwest Pacific): geodynamic implications. Tectonophysics 340(1–2):23–59

Cluzel D, Maurizot P, Collot J (2012) An outline of the geology of New Caledonia; from Permian-Mesozoic Southeast Gondwanaland active margin to Cenozoic obduction and supergene evolution. Episodes 35(1):72–86

Crawford A, Meffre S, Symonds P (2003) 120 to 0 Ma tectonic evolution of the southwest Pacific and analogous geological evolution of the 600–220 Ma Tasman Fold Belt System. Geol Soc Aust Spec Publ 22:377–397

Dabitzias S (1980) Petrology and genesis of the Vavdos cryptocrystalline magnesite deposits, Chalkidiki Peninsula, northern Greece. Econ Geol 75(8):1138–1151

Daval D, Sissmann O, Menguy N, Saldi GD, Guyot F, Martinez I, Corvisier J, Garcia B, Machouk I, Knauss KG, Hellmann R (2011) Influence of amorphous silica layer formation on the dissolution rate of olivine at 90°C and elevated pCO_2. Chem Geol 284:193–209

Fallick AE, Ilich M, Russell MJ (1991) A stable isotope study of the magnesite deposits associated with the Alpine-type ultramafic rocks of Yugoslavia. Econ Geol 86(4):847–861

Foster L, Eggleton RA (2002) The Marlborough nickel laterite deposits. In: Roach IC (ed) Presented at the Regolith and Landscapes in Eastern Australia Conference, CRC LEME, vol 1, pp 33–36

Gerdemann S, Dahlin D, O Connor W, Penner L (2003) Carbon dioxide sequestration by aqueous mineral carbonation of magnesium silicate minerals. Greenhouse gas technologies, Elsevier Science, Amsterdam 8

Ghoneim M, Saleem I, Hamdy M (2003) Origin of magnesite veins in serpentinites from Mount El-Rubshi and Mount El-Maiyit. Eastern Desert Egypt, Archiwum Mineralogiczne, pp 41–63

Giammar D, Bruant R, Peters C (2005) Forsterite dissolution and magnesite precipitation at conditions relevant for deep saline aquifer storage and sequestration of carbon dioxide. Chem Geol 217(3–4):257–276

Glasser E (1904) Rapport à M. le Ministre des colonies sur les richesses de la Nouvelle-Calédonie, Dunod

Goff F, Lackner KS (1998) Carbon dioxide sequestering using ultramafic rocks. Environ Geosci 5(3):89–102

Götze J, Nasdala L, Kleeberg R, Wenzel M (1998) Occurrence and distribution of "moganite" in agate/chalcedony: a combined micro-Raman, Rietveld, and cathodoluminescence study. Contribut Mineral Petrol 133(1):96–105

Graetsch H, Flörke OW, Miehe G (1985) The nature of water in chalcedony and opal-C from Brazilian agate geodes. Phys Chem Miner 12:300–306

Griffis R (1972) Genesis of a magnesite deposit, Deloro Twp., Ontario. Econ Geol 67(1):63–71

Guthrie GD, Carey JW, Bergfeld D, Byler D, Chipera S, Ziock HJ, Lackner KS (2001) Geochemical aspects of the carbonation of magnesium silicates in an aqueous medium. NETL Conference on Carbon Sequestration, 14 pp

Halls C, Zhao R (1995) Listvenite and related rocks: perspectives on terminology and mineralogy with reference to an occurrence at Cregganbaun, Co., Mayo, Republic of Ireland. Miner Deposita 30(3):303–313

Hansen L, Dipple G, Gordon T, Kellett D (2005) Carbonated serpentinite (listwanite) at Atlin. British Columbia: A geological analogue to carbon dioxide sequestration, The Canadian Mineralogist 43(1):225–239

Harrison AL, Power IM, Dipple GM (2013) Accelerated Carbonation of Brucite in Mine Tailings for Carbon Sequestration. Environ Sci Technol 47:126–134

Haug TA, Munz IA, Kleiv RA (2011) Importance of dissolution and precipitation kinetics for mineral carbonation. Energy Procedia 4(C):5029–5036

Heaney P (1993) A proposed mechanism for the growth of chalcedony. Contrib Miner Petrol 115(1):66–74

Heaney P, Post JE (1992) The widespread distribution of a novel silica polymorph in microcrystalline quartz varieties. Science 255(5043):441–443

Hövelmann J, Austrheim H, Beinlich A, Anne Munz I (2011) Experimental study of the carbonation of partially serpentinized and weathered peridotites. Geochim Cosmochim Acta 75(22):6760–6779

Hövelmann J, Austrheim H, Jamtveit B (2012) Microstructure and porosity evolution during experimental carbonation of a natural peridotite. Chem Geol 334:254–265

Jedrysek MO, Halas S (1990) The origin of magnesite deposits from the Polish Foresudetic Block ophiolites: preliminary $\delta^{13}C$ and $\delta^{18}O$ investigations. Terra Nova 2(2):154–159

Jones BF, Galàn E (1988) Sepiolite and palygorskite. In: Bailey SW (ed) Hydrous phyllosilicates (Exclusive of Micas) reviews in mineralogy, 19. Mineralogical Society of America, Washington, pp 631–674

Jurković I, Palinkaš LA, Garašić V, Palinkaš SS (2012) Genesis of vein-stockwork cryptocrystalline magnesite from the Dinaride ophiolites. Ofioliti 37(1):1–14

Kelemen PB, Matter J (2008) In situ carbonation of peridotite for CO_2 storage. Proc Natl Acad Sci 105:17295–17300

Kelemen PB, Matter J, Streit EE, Rudge JF, Curry WB, Blusztajn J (2011) Rates and mechanisms of mineral carbonation in peridotite: natural processes and recipes for enhanced, in situ CO_2 capture and storage. Annu Rev Earth Planet Sci 39:545–576

King HE, Plümper O, Geisler T, Putnis A (2011) Experimental investigations into the silicification of olivine: implications for the reaction mechanism and acid neutralization. Am Mineral 96:1503–1511

Klein F, Garrido CJ (2011) Thermodynamic constraints on mineral carbonation of serpentinized peridotite. Lithos 126(3):147–160

Klein EM, Langmuir CH (1987) Global correlations of ocean ridge basalt chemistry with axial depth and crustal thickness. J Geophys Res Solid Earth 92(B8):8089–8115

Krevor S, Lackner KS (2011) Enhancing serpentine dissolution kinetics for mineral carbon dioxide sequestration. Int J Greenhouse Gas Control 5(4):1073–1080

Krishnamurti D (1956) Raman spectrum of magnesite. Proc Math Sci 43(4):210–212

Lacinska AM, Styles MT (2012) Silicified serpentinite—a residuum of a Tertiary palaeo-weathering surface in the United Arab Emirates. Geol Mag 1(1):1–11

Lackner KS, Wendt CH, Butt DP, Joyce EL Jr, Sharp DH (1995) Carbon dioxide disposal in carbonate minerals. Energy 20(11):1153–1170

Lemaire C (2000) Application des spectroscopies vibrationnelles à la détection d'amiante dans les matériaux et à l'étude des serpentines, Unpublished PhD, Université de Paris 7, Paris, pp 157

Lin F-C, Clemency C (1981) The dissolution kinetics of brucite, antigorite, talc, and phlogopite at room temperature and pressure. Am Mineral 66(7–8):801–806

Luce RW, Bartlett RW, Parks GA (1972) Dissolution kinetics of magnesium silicates. Geochim Cosmochim Acta 36(1):35–50

Lugli S, Torres-Ruiz J, Garuti G, Olmedo F (2000) Petrography and geochemistry of the Eugui magnesite deposit (Western Pyrenees, Spain): evidence for the development of a peculiar zebra banding by dolomite replacement. Econ Geol 95(8):1775–1791

Lund EH (1960) Chalcedony and quartz crystals in silicified coral. Am Mineral 45:1304–1307

Lynne BY, Campbell KA, James BJ, Browne PRL, Moore J (2007) Tracking crystallinity in siliceous hot-spring deposits. Am J Sci 307(3):612–641

Maurizot P, Lafoy Y, Poupée M (2002) Cartographie des formations superficielles et des aléas mouvements de terrain en Nouvelle-Calédonie, Zone du Koniambo, BRGM Public Report, (1:33000)

Muñoz M, Pascarellib S, Aquilantib G, Naryginac O, Kurnosovc A, Dubrovinskyc L (2008) Hyperspectral μ-XANES mapping in the diamond-anvil cell: analytical procedure applied to the decomposition of (Mg, Fe)-ringwoodite at the upper/lower mantle boundary. High Press Res 28:665–673

O'Hanley DS (1996) Serpentinites: records of tectonic and petrological history. Oxford University Press, Oxford, p 270

Ohmoto H, Watanabe Y, Kumazawa K (2004) Evidence from massive siderite beds for a CO_2-rich atmosphere before $\sim$1.8 billion years ago. Nature 429:395–399

Oskierski HC, Bailey JG, Kennedy EM, Jacobsen G, Ashley PM, Dlugogorski BZ (2012) Formation of weathering-derived magnesite deposits in the New England Orogen, New South Wales, Australia: implications from mineralogy, geochemistry and genesis of the Attunga magnesite deposit. Mineralium Deposita. doi:10.1007/s00126-012-0440-5

Pefrov VP, Vakanjac B, Joksimović D, Zekić M, Lapcević I (1980) Magnesite deposits of Serbia and their origin. Int Geol Rev 22(5):497–510

Plümper O, Royne A, Magraso A, Jamtveit B (2012) The interface-scale mechanism of reaction-induced fracturing during serpentinization. Geology 40(12):1103–1106

Podwojewski P (1995) The occurrence and interpretation of carbonate and sulfate minerals in a sequence of Vertisols in New Caledonia. Geoderma 65(3–4):223–248

Pohl W (1990) Genesis of magnesite deposits—models and trends. Geol Runds 79:291–299

Pop D, Constantina C, Tătar D, Kiefer W (2004) Raman spectroscopy on gem-quality microcrystalline and amorphous silica varieties from Romania, Studia UBB. Geologia 49(1):41–52

Power IM, Wilson SA, Small DP, Dipple GM, Wan W, Southam G (2011) Microbially mediated mineral carbonation: roles of phototrophy and heterotrophy. Environ Sci Technol 45:9061–9068

Prigiobbe V, Hänchen M, Costa G, Baciocchi R, Mazzotti M (2009) Analysis of the effect of temperature, pH, CO_2 pressure and salinity on the olivine dissolution kinetics. Energy Procedia 1(1):4881–4884

Prinzhoffer A (1981) Structure et pétrologie d'un cortège ophiolitique: le massif du Sud (Nouvelle-Calédonie): unpublished thesis. E.N.S.M, Paris 306 pp

Quesnel B, Gautier P, Boulvais P, Cathelineau M, Maurizot P, Cluzel D, Ulrich M, Guillot S, Lesimple S, Couteau C (2013) Syntectonic, meteoric water-derived carbonation of the New Caledonia peridotite nappe. Geology 41:1063–1066

Renforth P, Washbourne CL, Taylder J, Manning DAC (2011) Silicate production and availability for mineral carbonation. Environ Sci Technol 45:2035–2041

Rodgers KA, Cressey G (2001) The occurrence, detection and significance of moganite (SiO_2) among some silica sinters. Mineral Mag 65(2):157–167

Rudge JF, Kelemen PB, Spiegelman M (2010) A simple model of reaction-induced cracking applied to serpentinization and carbonation of peridotite. Earth Planet Sci Lett 291(1–4):215–227

Saldi GD, Daval D, Morvan G, Knauss KG (2013) The role of Fe and redox conditions in olivine carbonation rates: an experimental study of the rate limiting reactions at 90 and 150°C in open and closed systems. Geochim Cosmochim Acta 118:157–183

Schellart W, Lister G, Toy V (2006) A Late Cretaceous and Cenozoic reconstruction of the Southwest Pacific region: tectonics controlled by subduction and slab rollback processes. Earth Sci Rev 76(3–4):191–233

Schulze R, Hill M, Field R, Papin P, Hanrahan R, Byler D (2004) Characterization of carbonated serpentine using XPS and TEM. Energy Convers Manage 45(20):3169–3179

Sévin B, Ricordel Prognon C, Quesnel F, Cluzel D, Lesimple S, Maurizot P (2012) First palaeomagnetic dating of ferricrete in New Caledonia: new insight on the morphogenesis and palaeoweathering of "Grande Terre". Terra Nova 24:77–85

Sherlock R, Logan M (1995) Silica-carbonate alteration of serpentinite; implications for the association of mercury and gold mineralization in Northern California. Explor Min Geol 4(4):395–409

Sipilä J, Teir S, Zevenhoven R (2008) Carbon dioxide sequestration by mineral carbonation: Literature review update 2005–2007, Åbo Akademi Rep, VT, 1, pp 59

Stanger G (1985) Silicified serpentinite in the Semail nappe of Oman. Lithos 18:13–22

Teir S, Kuusik R, Fogelholm C, Zevenhoven R (2007) Production of magnesium carbonates from serpentinite for long-term storage of CO_2. Int J Miner Process 85(1–3):1–15

Teir S, Eloneva S, Fogelholm C-J, Zevenhoven R (2009) Fixation of carbon dioxide by producing hydromagnesite from serpentinite. Appl Energy 86(2):214–218

Trescases J (1973) Weathering and geochemical behaviour of the elements of ultramafic rocks in New Caledonia. Bureau Mineral Res Geol Geophys Dep Mineral Energy Canberra Bull 141:149–161

Ulrich M (2010) Péridotites et serpentinites du complexe ophiolitique de la Nouvelle-Calédonie, Unpublished Thesis, Université de la Nouvelle-Calédonie et Université de Grenoble, pp 253

Ulrich M, Picard C, Guillot S, Chauvel C, Cluzel D, Meffre S (2010) Multiple melting stages and refertilization as indicators for ridge to subduction formation: the New Caledonia ophiolite. Lithos 115:223–236

van Noort R, Spiers CJ, Drury MR, Kandianis MT (2013) Peridotite dissolution and carbonation rates at fracture surfaces under conditions relevant for in situ mineralization of CO_2. Geochim Cosmochim Acta 106 (C):1–24

Whattam SA (2009) Arc-continent collisional orogenesis in the SW Pacific and the nature, source and correlation of emplaced ophiolitic nappe components. Lithos 113(1):88–114

Whattam SA, Malpas J, Ali J, Smith IE (2008) New SW Pacific tectonic model: cyclical intraoceanic magmatic arc construction and near-coeval emplacement along the Australia-Pacific margin in the Cenozoic. Geochem Geophys Geosyst 9(3). doi:10.1029/2007GC001710

Williams LA, Crerar DA (1985) Silica diagenesis, II, general mechanisms. J Sediment Res 55(3):312–321

Williams LA, Parks G, Crerar DA (1985) Silica diagenesis, I, solubility controls. J Sediment Petrol 55(3):301–311

Wilson SA, Dipple GM, Power IM, Thom JM, Anderson RG, Raudsepp M, Gabites JE, Southam G (2009) Carbon dioxide fixation within mine wastes of ultramafic-hosted ore deposits: examples from the Clinton Creek and Cassiar chrysotile deposits, Canada. Econ Geol 104(1):95–112

Yaliçin H, Bozkaya Ö (2004) Ultramafic-rock-hosted vein sepiolite occurrences in the Ankara Ophiolitic Melange, Central Anatolia, Turkey. Clays Clay Mineral 52(2):227–239

Zedef V, Russell M, Fallick A, Hall A (2000) Genesis of vein stockwork and sedimentary magnesite and hydromagnesite deposits in the ultramafic terranes of southwestern Turkey: a stable isotope study. Econ Geol 95(2):429

Annexe 5 Echantillons du profil de dissolution et localisation des points de mesure des magnésites (en jaune) et des serpentines (en bleu) analysées.

	VAV1Gio1	VAV1Gio2	VAV1Gio3	VAV1Gio4	VAV1Gio6	VAV1Gio 7	VAV1Gio8	VAV1Gio9
[Si] (ppm)	299	38045	25219	31.3	289	529	235	95.6
[Ca] (ppm)	9692	5397	1402	11782	4968	13420	10424	9523
[Ni] (ppm)	5.30	23.7	19.0	27.0	39.5	131	84.1	39.9
[Fe] (ppm)	21.2	14.2	51.4	19.9	27.2	5480	4616	13.8
[Cr] (ppm)	0.27	1.06	4.60	0.47	1.21	1.73	2.10	2.51
[Al] (ppm)	1.84	28.3	84.3	0.13	0.93	0.40	0.07	0.27
[Mn] (ppm)	43.0	2.07	4.04	0.31	0.36	682	159	0.29
[Co] (ppm)	0.23	0.07	0.32	0.16	0.04	17.8	9.67	0.08
[Sr] (ppm)	8.08	3.29	1.289	3.53	2.03	15.2	19.8	0.75
[Cu] ppm	66.3	18.5	3.32	0.19	2.93	0.30	0.33	0.31
[Zn] ppm	24.3	8.01	6.130	22.8	6.01	63.8	9.15	13.2
$\delta^{18}O$	28.6	28.9	27.9	28.9	28.1	27.4	28.4	27.8
$\delta^{13}C$	-8.5	-8.8	-9.4	-13.3	-15.5	-14.8	-14.7	-14.4
MgO (wt%)	46.9	46.9	46.9	46.9	46.9	46.9	46.9	46.9
CO_2(wt%)	51.2	51.2	51.2	51.2	51.2	51.2	51.2	51.2
SiO_2(wt%)	0.1	8.1	5.4	0.0	0.1	0.1	0.1	0.0
CaO(wt%)	1.4	0.8	0.2	1.7	0.7	1.9	1.5	1.3
∑oxydes	99.6	107.0	103.7	99.8	98.9	100.1	99.7	99.4

	BMS Gio 1	BMS Gio 2	BMS Gio 3	BMS Gio 4	BMS Gio 5	BMS Gio 6	BMS Gio 7	BMS Gio 8	BMS Gio 9	BMS Gio 10	BMS Gio 12	BMS Gio 15
[Si] (ppm)	2877	9664	16958	512	238	294	13289	290	238	132	265	78740
[Ca] (ppm)	2574	4414	3471	3498	5439	1847	2759	8962	6114	3189	10689	7547
[Ni] (ppm)	111	89.6	236	87.3	133	36.1	271	84.6	37.9	22.0	383	150
[Fe] (ppm)	99.2	1142	72.8	209	233	17.3	459	664	18.3	58.8	75.2	7.46
[Cr] (ppm)	5.16	1.12	15.0	1.13	1.20	0.23	15.9	1.64	0.94	0.83	0.89	1.00
[Al] (ppm)	3.19	2357	46.2	0.23	0.08	0.24	191	0.21	1.88	1.28	0.43	0.00
[Mn] (ppm)	7.70	111	1.06	20.3	15.3	139	3.42	379	36.4	2.15	110	1.75
[Co] (ppm)	0.56	3.69	6.01	7.52	19.7	0.57	1.49	3.32	0.88	0.66	14.4	0.96
[Sr] (ppm)	0.29	1.13	0.73	8.07	1.99	13.6	1.06	2.09	1.72	1.12	3.04	1.37
[Cu] ppm	0.25	0.59	0.86	0.17	0.20	1.05	0.83	0.39	0.87	0.12	0.92	0.92
[Zn] ppm	4.86	8.39	4.38	2.85	3.14	3.85	6.17	5.37	3.93	1.48	10.8	5.45
$\delta^{18}O$	27.9	29.1	28.8	27.9	28.2	28.6	28.2	28.7	28.6	28.2	27.8	29.1
$\delta^{13}C$	-13.0	-15.0	-13.8	-16.1	-14.5	-16.7	-13.9	-14.3	-14.3	-14.0	-15.2	-13.8
MgO (wt%)	46.9	46.9	46.9	46.9	46.9	46.9	46.9	46.9	46.9	46.9	46.9	46.9
CO_2(wt%)	51.2	51.2	51.2	51.2	51.2	51.2	51.2	51.2	51.2	51.2	51.2	51.2
SiO_2(wt%)	0.6	2.7	3.6	0.1	0.1	0.1	2.8	0.1	0.1	0.0	0.1	16.8
CaO(wt%)	0.4	0.6	0.5	0.5	0.8	0.3	0.4	1.3	0.9	0.5	1.5	1.1
∑oxydes	99.1	101.4	102.2	98.7	99.0	98.5	101.3	99.5	99.1	98.6	99.7	116.0

	CONV Gio 1	CONV Gio 2	GAIACS 1	GAIACS 2	NEP A3 Gio	NEP B1 Gio	NEP A1 Gio
[Si] (ppm)	731	207	786	634	18120	222	3767
[Ca] (ppm)	2327	4010	10016	11091	12097	6044	3838
[Ni] (ppm)	342	514	3.57	3.09	368	257	203
[Fe] (ppm)	19.3	121	12.1	14.9	924	75.4	1385
[Cr] (ppm)	0.64	3.43	0.43	0.001	1.26	1.02	18.2
[Al] (ppm)	0.04	0.16	0.81	1.49	0.00	0.04	24.1
[Mn] (ppm)	8.27	27.0	2.18	0.58	168	4.09	95.7
[Co] (ppm)	0.42	2.37	0.02	0.03	21.1	2.66	15.0
[Sr] (ppm)	0.27	1.15	2.97	2.88	3.26	1.52	1.74
[Cu] ppm	0.13	0.26	2.89	5.14	0.27	0.33	0.69
[Zn]ppm	4.64	7.40	4.31	7.76	5.02	5.47	7.62
$\delta^{18}O$	28.8	28.8	28.4	29.7	28.9	28.5	28.2
$\delta^{13}C$	-12.3	-13.5	-8.6	-8.5	-10.9	-12.2	-13.9
MgO (wt%)	46.9	46.9	46.9	46.9	46.9	46.9	46.9
CO_2(wt%)	51.2	51.2	51.2	51.2	51.2	51.2	51.2
SiO_2(wt%)	0.2	0.0	0.2	0.1	3.9	0.0	0.8
CaO(wt%)	0.3	0.6	1.4	1.6	1.7	0.8	0.5
∑oxydes	98.6	98.7	99.7	99.8	103.7	98.9	99.4

Magnésite du profil de dissolution

	PG3	KONA1-1	KONA1-2	K1-1	K2	K3
[Si] (ppm)	10849	3572	1641	3273	355	62
[Ca] (ppm)	7151	2163	1988	941	3197	3195
[Ni] (ppm)	240	69.5	39.5	72.5	53.1	56.2
[Fe] (ppm)	7856	21142	16465	43.4	19.3	13.1
[Cr] (ppm)	4.61	3.47	3.34	0.00	0.00	0.00
[Al] (ppm)	0.66	2.13	0.49	0.00	0.00	0.22
[Mn] (ppm)	480	150	105	4.22	7.16	6.14
[Co] (ppm)	1.20	31.9	28.4	11.2	5.65	4.14
[Sr] (ppm)	30.4	3.53	2.16	0.45	0.39	0.42
[Cu] ppm	5.62	1.25	1.67	1.23	1.51	4.70
[Zn]ppm	23.8	41.6	34.3	6.57	5.20	5.52

Serpentine du profil de dissolution

	PG3-S	KONA1-1S	KONA1-2S	K1-1S
[Si] (ppm)	675700	399639	419964	533101
[Ca] (ppm)	143	126	210	241
[Ni] (ppm)	4823	2181	2649	3320
[Fe] (ppm)	42213	36639	37734	23717
[Cr] (ppm)	112	87.7	223	166
[Al] (ppm)	126	65.3	51.7	60.9
[Mn] (ppm)	171	119	102	186
[Co] (ppm)	129	83.2	88.9	39.9
[Sr] (ppm)	0.57	0.61	1.11	0.62
[Cu] ppm	3.29	2.26	5.03	2.47
[Zn]ppm	32.0	44.8	46.6	22.5

Harzburgite Koniambo

[Si] (ppm)	187600	190400
[Fe] (ppm)	57322	55455
[Al] (ppm)	1323	2860
[Mn] (ppm)	852	775

Serpentine Koniambo

[Si] (ppm)	193527	199220	224093	234547	211353	190867	247520	198053
[Fe] (ppm)	60277	57555	52500	49544	54211	51955	39744	59500
[Al] (ppm)						1535		1800
[Mn] (ppm)	774	774	542	616	387	616	852	616

Annexe 6 - Concentrations en éléments majeurs et traces et compositions en poids d'oxydes des veines de magnésite et des magnésites et serpentines du profil de dissolution. Les compositions en éléments majeurs et traces des harzburgites et des serpentines du massif de Koniambo proviennent de l'étude de Ulrich (2010).

Annexe 7

Fault slip data from open pits at higher levels of the Koniambo Massif (New Caledonia). Sense of slip: N, normal; T, thrust (reverse); LL, left-lateral; RL, right-lateral. For vertical fault planes, the sense of slip is indicated with its strike-slip component, even in cases where the dip-slip component is dominant. * is for data from Pit 208; x is for data from site 'Bilboquet'. See figures 2, 8 and 9 in the article #4.

	Mineralogy of the slickenfibers	Fault strike (right hand rule)	Fault dip	Striae trend	Striae plunge	Sense of slip
*	antigorite	27	85	206	8	LL
*	antigorite	332	65	355	40	T
*	antigorite	162	56	270	55	N
*	antigorite	167	90	347	45	RL
*	antigorite	192	45	282	45	N
*	antigorite	169	52	283	50	N
*	antigorite	176	90	356	8	LL
*	antigorite	219	60	347	54	T
*	antigorite	162	75	339	10	RL
*	antigorite	191	50	1	12	RL
	antigorite	42	70	53	27	LL
	antigorite	28	77	41	44	N
	antigorite	12	83	14	19	RL
	antigorite	202	52	16	8	LL
	antigorite	22	87	30	69	N
	antigorite	204	49	294	49	N
	antigorite	212	60	286	59	N
	antigorite	324	30	37	29	N
	antigorite	182	76	344	51	N

antigorite	215	73	19	43	T
antigorite	60	90	60	47	LL
antigorite	182	67	184	4	RL
antigorite	207	76	19	28	RL
antigorite	315	63	74	60	N
antigorite	202	63	323	59	N
antigorite	204	86	7	76	T
antigorite	187	89	277	89	T
antigorite	182	85	184	21	RL
antigorite	27	72	53	54	N
antigorite	332	60	144	13	LL
antigorite	314	62	65	60	N
antigorite	222	80	32	44	T
antigorite	42	84	221	12	LL
antigorite	334	65	150	9	RL
antigorite	287	50	297	11	RL
antigorite	327	80	330	15	RL
antigorite	25	68	159	61	T
antigorite	16	90	196	31	RL
antigorite	22	54	198	6	RL
antigorite	67	63	240	14	LL
antigorite	38	47	194	23	RL
antigorite	47	53	205	27	RL
antigorite	67	70	239	21	LL
antigorite	57	61	207	42	N
antigorite	237	65	293	61	N
antigorite	50	67	155	66	N

	antigorite	47	72	201	54	N
	antigorite	67	69	233	32	LL
	antigorite	157	60	198	49	N
	antigorite	47	85	53	50	T
	antigorite	167	74	336	33	RL
	antigorite	183	67	206	43	N
	antigorite	176	64	235	60	N
	antigorite	173	67	177	10	LL
	antigorite	62	42	171	40	T
	antigorite	186	70	338	52	T
	antigorite	47	52	177	45	T
	antigorite	180	79	359	6	RL
*	polygonal serp	32	90	212	10	LL
*	polygonal serp	156	46	178	21	RL
*	polygonal serp	167	43	253	43	T
*	polygonal serp	172	75	351	3	LL
*	polygonal serp	17	80	189	39	LL
*	polygonal serp	202	70	346	58	T
*	polygonal serp	182	80	348	54	T
*	polygonal serp	282	46	37	43	T
*	polygonal serp	82	60	172	60	T
*	polygonal serp	122	80	130	39	RL
*	polygonal serp	357	80	4	33	LL
*	polygonal serp	312	75	320	29	LL
*	polygonal serp	352	80	170	10	LL
*	polygonal serp	192	46	296	45	T
*	polygonal serp	197	60	354	34	LL

*	polygonal serp	209	64	339	58	T
*	polygonal serp	52	90	52	51	LL
	polygonal serp	152	44	326	6	LL
	polygonal serp	176	68	181	12	LL
	polygonal serp	319	64	16	60	T
	polygonal serp	42	75	211	36	LL
	polygonal serp	41	42	170	35	T
	polygonal serp	35	41	145	39	N
	polygonal serp	4	90	184	8	LL
	polygonal serp	360	75	360	0	LL
	polygonal serp	2	82	4	15	LL
	polygonal serp	172	45	223	38	N
	polygonal serp	192	63	196	7	LL
	polygonal serp	190	70	3	20	LL
	polygonal serp	152	34	191	23	N
	polygonal serp	184	70	1	9	LL
	polygonal serp	207	76	18	33	LL
	polygonal serp	212	80	19	52	T
	polygonal serp	212	85	27	44	LL
	polygonal serp	207	70	11	37	LL
	polygonal serp	27	75	71	69	T
	polygonal serp	177	82	350	40	LL
	polygonal serp	135	65	273	55	N
	polygonal serp	97	58	268	14	RL
	polygonal serp	17	76	192	19	RL
	polygonal serp	354	80	360	29	LL
	polygonal serp	2	75	6	14	RL

	polygonal serp	224	80	18	68	T
	polygonal serp	64	50	110	41	T
	polygonal serp	16	69	85	68	N
	polygonal serp	10	59	30	29	RL
	polygonal serp	199	83	19	2	LL
	polygonal serp	14	75	43	61	N
	polygonal serp	23	90	23	65	RL
	polygonal serp	62	78	75	47	N
	polygonal serp	192	77	354	53	N
	polygonal serp	202	52	16	8	LL
x	polygonal serp	167	72	337	28	LL
x	polygonal serp	192	46	218	24	LL
x	polygonal serp	167	45	264	45	N
x	polygonal serp	7	67	171	34	LL
x	polygonal serp	32	58	187	34	LL
x	polygonal serp	212	56	7	32	LL
x	polygonal serp	42	30	170	24	T
x	polygonal serp	342	85	343	15	LL
x	polygonal serp	222	89	39	73	LL
x	polygonal serp	7	47	90	47	T
x	polygonal serp	22	60	27	9	LL
x	polygonal serp	7	55	142	45	N
x	polygonal serp	10	45	172	17	LL
x	polygonal serp	22	40	165	27	T
x	polygonal serp	12	54	162	35	T